

13 July 2012 | \$10

# Science

HIV/AIDS in America

AAAS

## SPECIAL SECTION

# HIV/AIDS IN AMERICA

## INTRODUCTION

167 HIV/AIDS in America

## NEWS

- 168 The Many States of HIV in America  
A TALE OF 10 CITIES
- 172 *Birmingham, Alabama*: A Southern HIV/AIDS Program With All the Fixins
- 173 *Jackson, Mississippi*: By the People, For the People
- 174 *Atlanta, Georgia*: And the Band Played On, Vol. 2
- 175 *San Francisco, California*: A Concerted Effort to Lighten the Load
- 176 *Los Angeles, California*: Life in the Fast Lane: HIV and Meth
- 177 *San Diego, California, and Tijuana, Mexico*: My Virus Is Your Virus
- 178 *New York, New York*: Miracle on 34th Street: Success With Injectors Pay Now, Benefits May Follow
- 180 *Providence, Rhode Island*: HIV and the Cell: The Prisoner's Dilemma
- 181 *Baltimore, Maryland*: Dancing the Night Away; Keeping HIV at Bay
- 182 *Washington, District of Columbia*: HIV/AIDS Response Renovated in Capital

## REVIEW

- 183 Broadly Neutralizing Antibodies Present New Prospects to Counter Highly Antigenically Diverse Viruses  
*D. R. Burton et al.*

>> Editorial p. 133; News story p. 152; Science Express Policy Forum by S. Lynch et al.; Science Careers; Science Translational Medicine Research Article by C. Sundling et al.; Science Podcast and other features at <http://scim.ag/hiv2012>

## EDITORIAL

- 133 An AIDS-Free Generation?  
*Salim S. Abdool Karim*  
>> HIV/AIDS in America section p. 167

## NEWS OF THE WEEK

- 138 A roundup of the week's top stories

## NEWS & ANALYSIS

- 141 Higgs Boson Makes Its Debut After Decades-Long Search
- 143 Commission Spreads Blame for 'Manmade' Disaster
- 144 Genes Suggest Three Groups Peopled the New World
- 145 Earth and Planetary Scientists Search for Common Ground

## NEWS FOCUS

- 146 Rising Acidity Brings an Ocean of Trouble  
>> Report p. 220
- 149 Betting Big on Science: A Cautionary Tale
- 152 The View From the Top of the HIV/AIDS World  
>> HIV/AIDS in America section p. 167

## LETTERS

- 154 Canada's Weakening Aquatic Protection  
*B. Favaro et al.*  
Postmarketing Trials for Rare Diseases  
*V. A. Llera and E. J. A. Roldán*
- 155 The BUZZ: NSF's Big Pitch
- 155 CORRECTIONS AND CLARIFICATIONS
- 155 TECHNICAL COMMENT ABSTRACTS



pages 146 & 220

## BOOKS ET AL.

- 156 Infrastructure  
*B. M. Frischmann, reviewed by E. Schlager*
- 157 Born Together—Reared Apart: The Landmark Minnesota Twin Study  
*N. L. Segal, reviewed by D. I. Boomsma*

## POLICY FORUM

- 158 Challenges to the Future Conservation of the Antarctic  
*S. L. Chown et al.*

## PERSPECTIVES

- 160 Fragile Delivery to the Genome  
*D. E. Gottschling*  
>> Research Article p. 195; Report p. 243
- 161 Driving Dislocations in Graphene  
*L. L. Bonilla and A. Carpio*  
>> Report p. 209
- 162 Amazonian Extinction Debts  
*T. F. Rangel*  
>> Report p. 228
- 164 Frameshifting to PA-X Influenza  
*J. W. Yewdell and W. L. Ince*  
>> Research Article p. 199
- 165 Nature's Intricate Clockwork  
*B. R. Crane*  
>> Research Article p. 189



## COVER

The epicenter of the HIV/AIDS epidemic in the United States has shifted from the East and West Coasts to the Deep South, where young black men who have sex with men are now becoming infected at a high rate. One of these men is Joshua Alexander, 25, shown here sitting in front of his mother's house in Greenville, Mississippi. See the special section beginning on page 167. For the story behind the cover, go to <http://scim.ag/cov6091>.

Photo: Malcolm Linton

## DEPARTMENTS

- 131 This Week in Science
- 134 Editors' Choice
- 136 Science Staff
- 246 New Products
- 247 Science Careers



## BREVIA

- 188** Attenuated Vaccines Can Recombine to Form Virulent Field Viruses  
S.-W. Lee et al.  
Problems can arise when vaccines and wild strains of a chicken herpesvirus recombine.  
>> *Science Podcast*

## RESEARCH ARTICLES

- 189** Crystal Structure of the Heterodimeric CLOCK:BMAL1 Transcriptional Activator Complex  
N. Huang et al.  
Structure-function analyses reveal details of the interaction between two proteins that regulate daily rhythms in mammals.  
>> *Perspective p. 165*
- 195** MMS19 Assembles Iron-Sulfur Proteins Required for DNA Metabolism and Genomic Integrity  
O. Stehling et al.  
A protein thought to be involved in DNA repair is, in fact, responsible for inserting iron-sulfur clusters into enzymes.  
>> *Perspective p. 160; Report p. 243*
- 199** An Overlapping Protein-Coding Region in Influenza A Virus Segment 3 Modulates the Host Response  
B. W. Jagger et al.  
A previously unidentified influenza protein, partly old and partly new, turns off the expression of host genes.  
>> *Perspective p. 164*

## REPORTS

- 204** Spin-Polarized Light-Emitting Diode Based on an Organic Bipolar Spin Valve  
T. D. Nguyen et al.  
The light emission from an organic light-emitting diode depends on the spin polarization of the injected current.
- 209** Dislocation-Driven Deformations in Graphene  
J. H. Warner et al.  
Two-dimensional dislocation dynamics and the resulting strain fields are studied at high resolution in graphene.  
>> *Perspective p. 161*
- 212** A Reduced Organic Carbon Component in Martian Basalts  
A. Steele et al.  
Analysis of 11 martian meteorites reveals complex hydrocarbons associated with magmatic minerals in 10 of them.

- 216** Ice Volume and Sea Level During the Last Interglacial  
A. Dutton and K. Lambeck  
Global average sea level during the last interglacial period was 6 to 10 meters higher than it is today.
- 220** Rapid Progression of Ocean Acidification in the California Current System  
N. Gruber et al.  
Rising concentrations of atmospheric carbon dioxide threaten to amplify the severity of ocean acidification in upwelling zones.  
>> *News story p. 146*
- 223** Clovis Age Western Stemmed Projectile Points and Human Coprolites at the Paisley Caves  
D. L. Jenkins et al.  
The age of a Western Stemmed projectile point implies that this culture overlapped with the Clovis culture in North America.  
>> *Science Podcast*
- 228** Extinction Debt and Windows of Conservation Opportunity in the Brazilian Amazon  
O. R. Wearn et al.  
Deforestation scenarios predict species extinction rates and identify targets of conservation efforts.  
>> *Perspective p. 162*
- 232** Structural Basis for Allosteric Regulation of GPCRs by Sodium Ions  
W. Liu et al.  
A protein-engineering strategy yields a closer look at the receptor-bound water, sodium, and lipid molecules.
- 236** Molecular Architecture and Assembly Principles of *Vibrio cholerae* Biofilms  
V. Berk et al.  
When imaged in real time, biofilm development can be seen to rely on spatial and temporal intercellular contacts.
- 239** Oscillatory Dynamics of Cdc42 GTPase in the Control of Polarized Growth  
M. Das et al.  
The regulation of a yeast cell-growth enzyme is dynamic rather than on-off.
- 243** MMS19 Links Cytoplasmic Iron-Sulfur Cluster Assembly to DNA Metabolism  
K. Gari et al.  
A protein that associates with DNA metabolism enzymes serves as a platform for the integration of iron-sulfur clusters.  
>> *Perspective p. 160; Research Article p. 195*

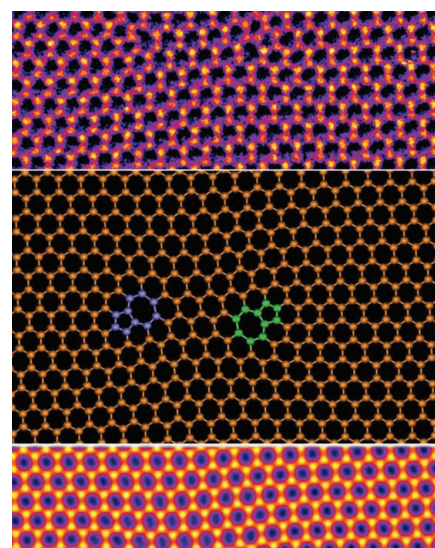
CONTENTS continued &gt;&gt;



page 157



pages 160, 195, &amp; 243



pages 161 &amp; 209

# SCIENCEONLINE

## SCIENCEEXPRESS

[www.sciencexpres.org](http://www.sciencexpres.org)

### Getting HIV Treatment to the Most People

S. Lynch et al.

10.1126/science.1225702

>> *HIV/AIDS in America* section p. 167

### The Provenances of Asteroids, and Their Contributions to the Volatile Inventories of the Terrestrial Planets

C. M. O'D. Alexander et al.

Hydrogen isotopic analysis of primitive meteorites implicates asteroids as early sources of Earth's water.  
10.1126/science.1223474

### Long-Range Incommensurate Charge Fluctuations in (Y,Nd)Ba<sub>2</sub>Cu<sub>3</sub>O<sub>6+x</sub>

G. Ghiringhelli et al.

Scattering experiments uncover an order competing with superconductivity in a cuprate family.  
10.1126/science.1223532

### Cartwheel Architecture of *Trichonympha* Basal Body

P. Guichard et al.

Electron microscopy provides a close-up view of the ninefold-symmetric stacked rings at the base of cilia and flagella.  
10.1126/science.1222789

### Identification of Small Molecule Activators of Cryptochrome

T. Hirota et al.

A small molecule binds to a core protein in the circadian clock and slows down time.  
10.1126/science.1223710

### Quantitative Modulation of Polycomb Silencing Underlies Natural Variation in Vernalization

V. Coutham et al.

*Arabidopsis* adjusts the onset of flowering to the length of winters via an epigenetic mechanism.  
10.1126/science.1221881

### GFAJ-1 Is an Arsenate-Resistant, Phosphate-Dependent Organism

T. J. Erb et al.

10.1126/science.1218455

### Absence of Detectable Arsenate in DNA from Arsenate-Grown GFAJ-1 Cells

M. L. Leavess et al.

Claims of arsenic substitution for phosphorus in the biomolecules of a Mono Lake bacterium are not independently reproduced.  
10.1126/science.1219861

## TECHNICALCOMMENTS

### Comment on "Plant Species Richness and Ecosystem Multifunctionality in Global Drylands"

T. Jucker and D. A. Coomes

Full text at [www.sciencemag.org/cgi/content/full/337/6091/155-c](http://www.sciencemag.org/cgi/content/full/337/6091/155-c)

### Response to Comment on "Plant Species Richness and Ecosystem Multifunctionality in Global Drylands"

F. T. Maestre et al.

Full text at [www.sciencemag.org/cgi/content/full/337/6091/155-d](http://www.sciencemag.org/cgi/content/full/337/6091/155-d)

## SCIENCENOW

[www.sciencenow.org](http://www.sciencenow.org)

### Highlights From Our Daily News Coverage

#### A Big Magnet in a Small Fish

Scientists have isolated magnetic cells that give some fish their sense of direction.

[http://scim.ag/Magnetic\\_Cells](http://scim.ag/Magnetic_Cells)

#### Space Weather Forecasted by South Pole Neutron Detectors

A team proposes a new way to monitor solar storms.

[http://scim.ag/Neutron\\_Detectors](http://scim.ag/Neutron_Detectors)

#### A Shotgun for Blood Clots

Nanoparticles home in on and dissolve blockages in veins and arteries.

[http://scim.ag/Blood\\_Clots](http://scim.ag/Blood_Clots)

## SCIENCE SIGNALING

[www.sciencesignaling.org](http://www.sciencesignaling.org)

### The Signal Transduction Knowledge Environment

10 July issue: <http://scim.ag/ss071012>

#### RESEARCH ARTICLE: Differential Regulation by Cyclic Nucleotides of the CNGA4 and CNGB1b Subunits in Olfactory Cyclic Nucleotide-Gated Channels

V. Nache et al.

Different subunits of olfactory CNG channels enable specific regulation of channel activity by cAMP or cGMP.

#### RESEARCH ARTICLE: Complementary Phosphorylation Sites in the Adaptor Protein SLP-76 Promote Synergistic Activation of Natural Killer Cells

H. S. Kim and E. O. Long

SLP-76 acts as a molecular checkpoint in the activation of NK cells of the immune system.

#### LETTERS: Comment and Response on "A Dynamic Network Model of mTOR Signaling Reveals TSC-Independent mTORC2 Regulation": Building a Model of the mTOR Signaling Network with a Potentially Faulty Tool

Comment: B. D. Manning

Response: P. Dalle Pezze et al.

Manning and Dalle Pezze et al. discuss whether phosphorylation of Ser<sup>2481</sup> of mTOR can serve as a specific readout of mTORC2 activity.

## SCIENCE CAREERS

[www.sciencereers.org/career\\_magazine](http://www.sciencereers.org/career_magazine)

### Free Career Resources for Scientists

#### A Capitol Job for a Midwestern Transplant

J. Cohen

Tiffany West helped turn Washington, D.C.'s HIV/AIDS effort into a widely admired program.  
<http://scim.ag/CapitolJob>

>> *HIV/AIDS in America* section p. 167

#### Out of India

J. Cohen

Moupali Das's roots led her to public health and caring for HIV/AIDS patients.

<http://scim.ag/OutofIndia>

>> *HIV/AIDS in America* section p. 167

#### Career Q&A: Laurel Haak and the ORCID Project

J. Austin

The newly appointed executive director of ORCID discusses her career and her latest challenge.

[http://scim.ag/QA\\_LaurelHaak](http://scim.ag/QA_LaurelHaak)

## SCIENCE TRANSLATIONAL MEDICINE

[www.sciencetranslationalmedicine.org](http://www.sciencetranslationalmedicine.org)

### Integrating Medicine and Science

11 July issue: <http://scim.ag/stm071112>

#### REVIEW: Deep Brain Stimulation for Psychiatric Disease

C. Hamani and Y. Temel

Animal models can help to improve deep brain stimulation for neuropsychiatric disease.

#### RESEARCH ARTICLE: High-Resolution Definition of Vaccine-Elicited B Cell Responses Against the HIV Primary Receptor Binding Site

C. Sundling et al.

Vaccine-elicited mAbs are different from infection-elicited antibodies against the HIV-1 Env CD4bs.

>> *HIV/AIDS in America* section p. 167

#### RESEARCH ARTICLE: Matrix Metalloproteinase Induction of Rac1b, a Key Effector of Lung Cancer Progression

M. L. Stallings-Mann et al.

#### FOCUS: Got a Light? Illuminating Lung Cancer

S. S. McAllister

New mouse models shed light on mechanisms of lung cancer progression and pinpoint a potential therapeutic target.

#### RESEARCH ARTICLE: Reproducible Quantification of Cancer-Associated Proteins in Body Fluids Using Targeted Proteomics

R. Hüttenhain et al.

A compendium of SRM assays for cancer-associated proteins provides a resource for accelerating and planning biomarker verification studies.

#### RESEARCH ARTICLE: PGC-1α Rescues Huntington's Disease Proteotoxicity

T. Tsunemi et al.

PGC-1α rescues Huntington's disease neurodegeneration by inducing a master regulator of autophagy.

## SCIENCEPODCAST

[www.sciencemag.org/multimedia/podcast](http://www.sciencemag.org/multimedia/podcast)

### Free Weekly Show

On the 13 July *Science* Podcast: a vaccine recombines in the wild, early North American inhabitants, HIV/AIDS in the U.S., and more.

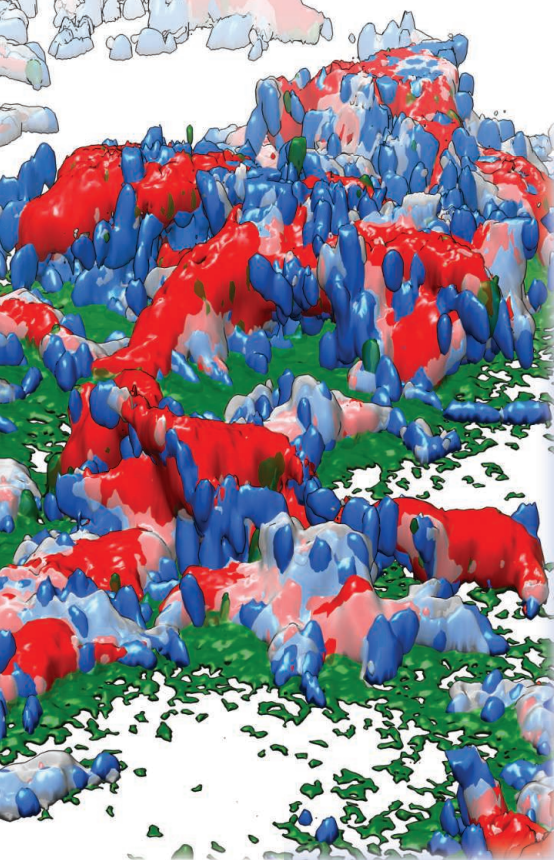
**SCIENCE** (ISSN 0036-8075) is published weekly on Friday, except the last week in December, by the American Association for the Advancement of Science, 1200 New York Avenue, NW, Washington, DC 20005. Periodicals Mail postage (publication No. 484460) paid at Washington, DC, and additional mailing offices. Copyright © 2012 by the American Association for the Advancement of Science. The title **SCIENCE** is a registered trademark of the AAAS. Domestic individual membership and subscription (\$1 issues): \$149 (\$74 allocated to subscription). Domestic institutional subscription (\$1 issues): \$990; Foreign postage extra: Mexico, Caribbean (surface mail) \$55; other countries (air assist delivery) \$85. First class, airmail, student, and emeritus rates on request. Canadian rates with GST available upon request, GST #1254 88122. Publications Mail Agreement Number 1069624. Printed in the U.S.A.

**Change of address:** Allow 4 weeks, giving old and new addresses and 8-digit account number. **Postmaster:** Send change of address to AAAS, P.O. Box 96178, Washington, DC 20090-6178. **Single-copy sales:** \$10.00 current issue, \$15.00 back issue prepaid includes surface postage; bulk rates on request. **Authorization to photocopy** material for internal or personal use under circumstances not falling within the fair use provisions of the Copyright Act is granted by AAAS to libraries and other users registered with the Copyright Clearance Center (CCC) Transactional Reporting Service, provided that \$30.00 per article is paid directly to CCC, 222 Rosewood Drive, Danvers, MA 01923. The identification code for *Science* is 0036-8075. *Science* is indexed in the *Reader's Guide to Periodical Literature* and in several specialized indexes.



ADVANCING SCIENCE, SERVING SOCIETY





## << Biofilms Up Close

Many bacterial infections involve biofilm formation. Cells within a biofilm are significantly more resistant to immune clearance and antibiotics compared to unattached, planktonic cells. Berk *et al.* (p. 236) applied super-resolution optical methods to image living bacteria with nanometer-scale precision as they form a biofilm. *Vibrio cholerae* biofilms were observed to have three distinct levels of spatial organization: cells, clusters of cells, and collections of clusters. Each cell cluster was wrapped in a flexible, elastic envelope. Several *V. cholerae* matrix proteins played complementary architectural roles during biofilm development. RbmA provided cell-cell adhesion, Bap1 allowed the developing biofilm to adhere to surfaces, and heterogeneous mixtures of VPS, RbmC, and Bap1 formed the dynamic, flexible, and ordered envelopes that encase the cell clusters.

## A Timely Structure

The physiology and behavior of most organisms are inextricably aligned with the day/night cycle. In mammals, these daily rhythms are generated by a circadian clock encoded by transcriptional activators and repressors operating in a feedback loop that takes about 24 hours to complete. A key participant in this loop is a heterodimeric transcriptional activator consisting of the CLOCK and BMAL1 proteins. Huang *et al.* (p. 189, published online 31 May; see Perspective by Crane) determined the crystal structure of a complex containing the PAS domains (implicated in protein-protein interactions) and the basic helix-loop-helix domains (implicated in DNA binding) from each protein. CLOCK and BMAL1 were observed to be tightly intertwined in an unusual asymmetric conformation, which may contribute to the stability and activity of the complex.

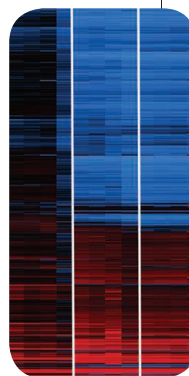
## MMS19 Joins the CIA

Iron-sulfur (Fe-S) proteins play a critical role in cell metabolism and particularly in DNA repair and replication. Mutants in eukaryotic gene *MMS19* are particularly sensitive to DNA damaging agents, suggesting that it is involved in DNA repair, but the mutations can also have other wide-ranging effects on the cell (see the Perspective by Gottschling). Now, Stehling *et al.* (p. 195, published online 7 June) and Gari *et al.* (p. 243, published online 7 June) show that in both yeast and humans, MMS19 functions as part of the cytosolic Fe-S protein assembly (CIA)

machinery. The MMS19 is part of a specialized CIA targeting complex that plays a role late in cytosolic Fe-S protein assembly to direct Fe-S cluster transfer from the CIA scaffold complex to a subset of Fe-S proteins, including a number associated with DNA metabolism.

## Influenza's Cryptic Constraint

Because of the well-known pandemic potential of influenza viruses, it is important to understand the range of molecular interactions between the virus and its host. Despite years of intensive research on the virus, Jagger *et al.* (p. 199, published online 28 June; see the Perspective by Yewdell and Ince) have found that the influenza A virus has been hiding a gene in its small negative-sense RNA genome. An overlapping open reading frame was found contained in the PA viral RNA polymerase gene, which is accessed by ribosomal frameshifting to produce a fusion protein containing the N-terminal messenger RNA (mRNA) endonuclease domain of PA and an alternative C-terminal X domain. The resulting polypeptide, PA-X, selectively degrades host mRNAs and, in a mouse model of infection, modulated cellular immune responses, thus limiting viral pathogenesis.



## Spin-Dependent Light Emission

Spintronic devices exploit electronic currents that are spin polarized, which have an excess of one spin current over the other. One way to detect this polarization would be to create a light-emitting diode that is sensitive to spin polarization. Along these lines, Nguyen *et al.* (p. 204) constructed a bipolar device in which an organic semiconductor was sandwiched between two ferromagnetic contacts whose relative polarization could be controlled by an applied magnetic field. Magneto-electroluminescence of the order of ~1% was observed at a bias voltage of ~3.5 V. The use of a deuterated organic polymer interlayer improved spin transport relative to polymers with hydrogen side groups, and a thin LiF buffer layer on the ferromagnetic cathode improved electron injection efficiency.

## Moving Dislocations

The mechanical properties of crystalline materials are limited by the presence and motion of defects caused by extra or missing atoms in the crystal lattice. Plastic deformation of a material causes these defects, known as dislocations, to move and multiply. Much is known about the motion of dislocations in three dimensions but less so in two. Warner *et al.* (p. 209; see the Perspective by Bonilla and Carpio) used graphene as a model material to track dislocation dynamics in real time. The strain fields in the graphene sheet were mapped, which suggests that the dislocation motion is connected to the stretching, rotating, and breaking of individual carbon bonds.

## Abiotic Martian Organics

Understanding the sources and the formation mechanisms of organic carbon compounds on Mars has implications for our understanding of the martian carbon cycle. Steele *et al.* (p. 212, published online 24 May) present measurements of organic material in 11 martian meteorites, including the Tissint meteorite, which fell in the Moroccan desert in July 2011. Ten of the meteorites contain complex hydrocarbons encased within igneous minerals. The results imply that the organics formed as the magma melt crystallized and are thus of abiotic origin.

Continued on page 132

## More Melting

The last interglacial period, around 125,000 years ago, was 1° to 2°C warmer than the present, and the sea level was thought to be 4 to 6 meters higher. However, **Dutton and Lambeck** (p. 216), now suggest that sea level was possibly as much as 10 meters above current levels. Such a large excess of seawater would mean that the Greenland and Antarctic ice sheets melted much more than previously assumed, which has implications for how much sea-level rise we should expect with anthropogenic climate warming.

## Acidification Blues

The increase in the concentration of atmospheric carbon dioxide threatens the health of the ocean's ecosystems because of the resulting acidification of the ocean and the decrease in its carbonate saturation state. **Gruber *et al.*** (p. 220, published online 14 June) used a regional ocean model to project how the saturation state of aragonite, a form of calcium carbonate that is produced by many marine organisms, will change in the California Current System through the year 2050. The sea floor along many parts of the California coast is likely to become exposed to year-round aragonite undersaturation within the next 20 to 30 years, a situation that could severely reduce the range of habitats for marine shellfish.

## They Walked Together

Paisley Cave in Oregon provides some of the earliest evidence for humans in North America. **Jenkins *et al.*** (p. 223) provide a wide variety of additional evidence of early human occupation of this site, including a series of radiocarbon ages extending back to nearly 12,500 radiocarbon years ago (about 14,500 calendar years ago). The find includes examples of projectile points representative of the Western Stemmed Tradition dating to about 11,100 radiocarbon years ago. The Western Stemmed Tradition has been thought to have evolved after the dominant Clovis technology, but the find suggests that the two cultures overlapped in time.



## Growing Extinction Debt

Predicting, and potentially preventing, extinction is a central goal of conservation biology. **Wearn *et al.*** (p. 228; see the Perspective by **Rangel**) describe a mathematical approach for predicting the time lags in extinction following habitat loss. The model was applied to the highly biodiverse Brazilian Amazon region, and used to reconstruct the spatial and temporal patterns of extinction and the accumulation of extinction debt from 1970 through to the present, and to extrapolate to 2050 under four deforestation scenarios. The Amazon basin sits at a critical point: Few species have been driven extinct to date, but an extinction debt is rapidly accumulating, which could lead to an increasing rate of extinction in the next four decades.

## GPCR Close-Up

Structures of G protein–coupled receptors (GPCRs) determined in the past few years, have provided insight into the function of this important family of membrane proteins. **Liu *et al.*** (p. 232) used a protein-engineering strategy to produce a stabilized version of the human A<sub>2A</sub> adenosine receptor (A<sub>2A</sub>AR). The high-resolution structure reveals the position of about 60 internal waters, which suggests an almost continuous channel in the GPCR and can explain the allosteric effects of Na<sup>+</sup> on ligand binding and how cholesterol may contribute to GPCR stabilization.

## Pole to Pole

How do fission yeast cells decide when to grow at a single end (or pole) of the cell or whether to grow in a multipolar manner? **Das *et al.*** (p. 239, published online 17 May) found that accumulation of the active form of the small guanine nucleotide–binding protein Cdc42 at the growing tip of the cell oscillated with a period of a few minutes. In cells growing at one pole, the oscillations were primarily present at that pole and during bipolar growth symmetrical anticorrelated oscillations were observed. Dynamic competition for Cdc42 between multiple growth zones could represent a flexible mechanism to modulate cell growth asymmetry.





Salim S. Abdool Karim is director of CAPRISA: Centre for the AIDS Programme of Research in South Africa, University of KwaZulu-Natal, and professor of Clinical Epidemiology, Columbia University. He was the co-principal investigator of the CAPRISA 004 trial of tenofovir gel and is a co-inventor of patents for tenofovir against herpes infections with scientists from Gilead Sciences. He is also an Executive Committee member of the Microbicide Trials Network, which is undertaking the VOICE trial of oral and topical PrEP. E-mail: karims1@ukzn.ac.za.

## An AIDS-Free Generation?

THE HIV PANDEMIC REMAINS A GREAT GLOBAL HEALTH CHALLENGE. WITH AN ESTIMATED 33.3 million people living with HIV today, is there really hope of achieving the vision of an AIDS-free generation? Optimists argue that strong political will and generous funding are the essential elements. But skeptics point to the deep-seated structural inadequacies in many health care systems, especially in Africa, where the need is greatest. However, both sides agree that a potential combination of therapeutic and prophylactic antiretroviral strategies brings the prospect of HIV control within reach. And this month, the International AIDS Conference in Washington, DC, “Turning the Tide Together,” will attempt to galvanize concerted global action to focus the world’s attention on this challenge.

Recent progress on the treatment and prevention of HIV infection has created a new-found sense of hope that the HIV epidemic can be overcome. AIDS mortality rates are declining globally, primarily due to antiretroviral therapy (ART), and efforts to eliminate mother-to-child transmission are progressing well. Since the 2010 Vienna AIDS conference, five studies have demonstrated that ART, when used as prescribed, either to treat HIV-infected individuals (treatment for prevention) or as oral/topical pre-exposure prophylaxis (PrEP), effectively prevents the sexual transmission of HIV.\* These promising results have spurred the Joint United Nations Programme on HIV/AIDS to set a global target of “zero new HIV infections, zero discrimination and zero AIDS-related deaths” through universal access to effective HIV prevention, treatment, care, and support.

Knowledge of HIV status is the common gateway to both treatment and prevention. But many people remain unaware of their HIV status. Denial, stigma, and a lack of understanding of vulnerability and risk lead to low rates of HIV testing, suboptimal condom use, and poor rates of circumcision. In addition to wider HIV testing, scale-up of ART therapy, both for the patient’s benefit and for the prevention benefit to partners, will be key to reducing HIV transmission and to reaching zero new HIV infections.

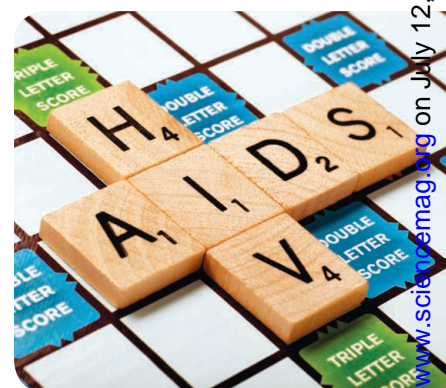
Even with effective scale-up of HIV testing, treatment, and prevention, there is still the major problem of high HIV incidence in young African women. HIV incidence in countries such as South Africa and Zambia is high in young women, who are seldom able to ascertain the HIV and treatment status of their male partners. In this setting, much more than ART scale-up is needed. Oral and/or topical PrEP, the only HIV prevention technology that empowers women to control their risk of infection, is therefore essential to achieve an AIDS-free generation in Africa. The United States recently took the lead when the Centers for Disease Control and Prevention released guidance on the use of oral PrEP in men who have sex with men; likewise, a U.S. Food and Drug Administration Advisory Committee has supported the licensure of oral PrEP for men and women. In contrast, the World Health Organization (WHO) has been dragging its feet—it has not yet released any guidance on PrEP use, especially for young women at high risk, despite compelling evidence that PrEP is effective in preventing HIV. Withholding PrEP until formal regulatory approval has been obtained raises serious ethical concerns.† Although desirable, such approval is not essential for WHO guidance, as evidenced by other WHO guidelines (such as misoprostil for abortion or tranexamic acid for trauma) that have recommended off-label use of existing medicines.

To turn the tide on HIV, WHO needs to act now to provide the guidance that will enable countries to implement combination prevention programs that include PrEP in high-risk populations such as young women. And the global community must respond by continuing to expand their support to address the current resource and health system constraints on the implementation of ART and prophylaxis in the worst AIDS-affected countries.

— Salim S. Abdool Karim

10.1126/science.1226535

\*S. S. Abdool Karim, Q. Abdool Karim, *Lancet* **378**, e23 (2011). †B. Haire, J. Kaldor, C. F. Jorden, *Am. J. Bioeth.* **12**, 21 (2012).



## MICROBIOLOGY

### Simple But Specific

Successful agricultural production is heavily dependent on bee pollinators, but key species have been suffering striking losses. Losses have been attributed to a combination of environmental change, pesticides, and pathogen pressure. Little is known about the normal microbiota of social species such as honey bees and bumble bees, except that they are distinctive. This is of interest because the microbiota plays an important role in shaping a species' nutrition and overall health. Engel *et al.* extended studies beyond the typical 16S rRNA analyses to develop a metabolic and functional picture of the honey bee's microbial metagenome. Although only eight bacterial species are typically present in the honey bee gut, pathway reconstruction indicated

strain-specific functions, which were particularly enriched for carbohydrate metabolism and transport for dealing with a nectar diet. A suite of pectin-degrading enzymes was also prominent, perhaps for pollen digestion or for pectin detoxification. And interestingly, of the candidate new species, *Snodgrassella* forms an intimate layer against the bee midgut and rectum, overlaid by a thick carpet of *Gilliamella*, which together appear to protect against parasite invasion. Despite the specialized nature of this microflora, it shows extensive strain diversity, and further discoveries about its functional and evolutionary interactions may help us to restore the world's pollinators to good health. — CA

*Proc. Natl. Acad. Sci. U.S.A.* **109**, 10.1073/pnas.1202970109 (2012).



## GEOCHEMISTRY

### It's All About the Sulphides

Both hydrated sulphates and carbonates have been observed on the surface of Mars. However, these two types of minerals form under very different conditions, with hydrated sulphates requiring acidic conditions that are incompatible with the formation or preservation of carbonates. Dehouck *et al.* explored the alteration of terrestrial basaltic minerals, similar to those found on Mars, under a simulated Mars-like atmosphere. After a 4-year-long exposure to a CO<sub>2</sub>-dominated humid atmosphere, samples without iron sulphide suffered only minor alteration, whereas mixtures of silicates and sulphides led to acidic conditions that favored the precipitation of hydrated sulphates. Infrared reflectance spectra of the samples showed good agreement with data from Mars. Thus, rather than being the result of planet-wide acidic conditions, as has been widely believed, martian hydrated sulphates may have formed from sulphide-rich basalts that produced locally acidic environments. With regional variations in bedrock composition controlling the distribution of alteration minerals on the surface of Mars, rather than a global change of atmospheric chemistry, it is possible for the carbonates to form coevally under the same atmospheric conditions. — MJC

*Geochim. Cosmochim. Acta* **90**, 47 (2012).

## APPLIED PHYSICS

### Astronomy Through a Fine-Tooth Comb

The observation of distant astrophysical events with the high precision afforded by large Earth- and space-based instruments continues to expand our knowledge of the universe. Untangling the mechanisms at play typically requires analyzing spectra, with the dynamical processes inferred from shifts in wavelengths of known emission lines. For example, recent work has focused on the identification of planets orbiting distant stars, their presence determined by periodic and

minute spectral lines shifts in the emission lines from their host star. These measurements require ever more precise and stable wavelength calibration of the astrophysical spectrographs. Phillips *et al.* demonstrate that laser-generated optical combs—broadband series of equally and precisely spaced wavelengths—can be used as an accurate and stable source to calibrate the spectrographs. The ability to tune and expand the extent of available wavelengths in the comb should provide the sensitivity to search for Earth-like planets orbiting distant stars, as well as to test other exotic astrophysical processes. — ISO

*Opt. Express* **20**, 13711 (2012).

## EDUCATION

### A Failure to Forget

Students with science misconceptions often have a hard time giving them up, especially if they have held them for a long time. When students are exposed to scientific evidence that conflicts with their earlier theories, what happens? Are the previous misconceptions overwritten or merely suppressed? Shtulman and Valcarcel devised and implemented a novel speed-reasoning task to investigate this question. Using software designed to record the speed and accuracy of answers, 150 college undergraduates, who had



completed an average of 3.1 college-level math and science courses, verified 200 statements about natural phenomena (20 statements in 10 areas of science such as evolution, mathematics, etc.). Participants were slower at verifying inconsistent statements than consistent ones, verified true statements faster than false statements, and were more accurate in domains where conceptual change occurs early in life, such as fractions, than they were for domains such as evolution, where conceptual change occurs later. These findings imply that although early, incorrect theories are suppressed by scientific theories, they are not truly replaced by them. This suggests that science instruction may benefit from helping students reanalyze their misconceptions rather than expecting students to simply forget them. — MM

*Cognition* **124**, 209 (2012).

#### PHYSIOLOGY

### Restless Flies Show Their Legs

Your leg may not seem to have much in common with that of a fly; however, it may be more than you think. Freeman *et al.* show that a relatively common human neurological disorder called restless legs syndrome, characterized by a strong urge to move one's legs and "fragmented" sleep, can be modeled in the fruit fly *Drosophila melanogaster*. A polymorphism in the gene *BTBD9* confers approximately 50% of the population-attributable risk in the human disorder. Deletion of the homolog in *Drosophila*, *dBTD9*, recapitulated features of this condition, such as altered rest activity cycles, disrupted sleep, and hyperlocomotion. Knockdown of *dBTD9* in a specific set of dopaminergic neurons also resulted in fragmented sleep. Also similar to the human disorder, aberrant dopamine levels were observed in the *dBTD9* mutant fly brain. Treatment of mutant flies with a dopamine agonist improved sleep patterns. In human cells, iron homeostasis was controlled by *BTBD9*. These findings support prior studies suggesting a role for dopamine regulation and iron metabolism in restless legs syndrome. Furthermore, the fly may serve as a useful model for understanding this disorder. — BAP

*Curr. Biol.* **22**, 1142 (2012).

#### BIOMEDICINE

### miRNAs: Optional for Cancer?

MicroRNAs (miRNAs) are small noncoding RNAs that control the expression of about half of the protein-coding genes in mammals. These regulatory RNAs have been implicated in a wide range of diseases, including cancer, where a large

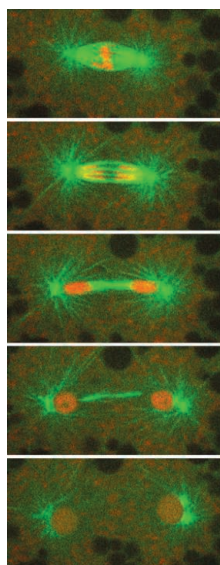
body of evidence suggests that they are essential for tumor survival and growth. The surprising results of a new study invite reexamination of this hypothesis. By genetic methods, Ravi *et al.* generated mouse sarcoma cells that were completely deficient in *DICER1*, an enzyme essential for miRNA production, and then experimentally verified the nearly total loss of miRNAs in these cells. In contrast to expectations, when these cells were injected into mice, they retained the ability to form tumors, although the tumors developed at a slower rate than those derived from control cells. Thus, global miRNA loss does not intrinsically preclude tumorigenesis. Whether these results highlight a quirk of tumors derived from mesenchymal cells or also apply to tumors of epithelial origin (which represent the majority of human solid tumors) remains to be determined, but is an important question given the current interest in miRNAs as potential targets for cancer therapy. — PAK

*Cancer Cell* **21**, 848 (2012).

#### CELL BIOLOGY

### Knowing Your Place

Often life starts in very large cells. In the fruit fly, thousands of micrometer-sized nuclei distribute in a half-millimeter-sized egg, but it is



a mystery how dividing nuclei distribute in the embryo. The positioning of nuclei in the embryo cortex is important for the subsequent cellularization required for successful development. Telley *et al.* studied a cell extract from individual early *Drosophila* embryos that was able to faithfully recapitulate repeated mitotic nuclear division cycles. When dividing nuclei were encapsulated in microchambers, the nuclear separation machinery was unable to adapt to reduced space. Thus, a distinct length scale of nuclear separation appears to be programmed into the early insect embryo, which is adapted to the requirements of the early developmental program of the syncytium. This scaling behavior involved actin-dependent microtubule aster migration and anaphase spindle elongation. — SMH

*J. Cell Biol.* **197**, 887 (2012).

## AAAS Travels



### Discover BURMA!

January 3-16, 2013

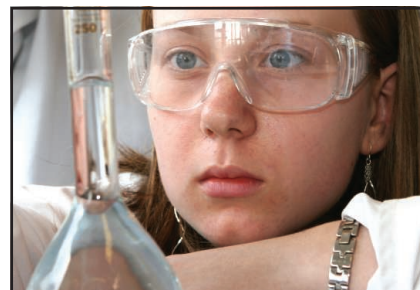
*Angkor Wat Extension Jan. 16-19*  
Burma is one of the least globalized lands in the world and one of Asia's most fascinating locations. Explore from Inle Lake and the fabled city of Mandalay to the stunning Bagan plain where thousands of temples dot the savanna. Products are still made by hand and oxcarts outnumber cars. Enjoy a terrific adventure in Burma! \$4,295 + air; Angkor Wat ext. \$1,295

**For a detailed brochure, please call (800) 252-4910**

All prices are per person twin share + air



BETCHART EXPEDITIONS Inc.  
17050 Montebello Rd, Cupertino, CA 95014  
Email: AAASInfo@betchartexpeditions.com  
www.betchartexpeditions.com



### AAAS is here – promoting universal science literacy.

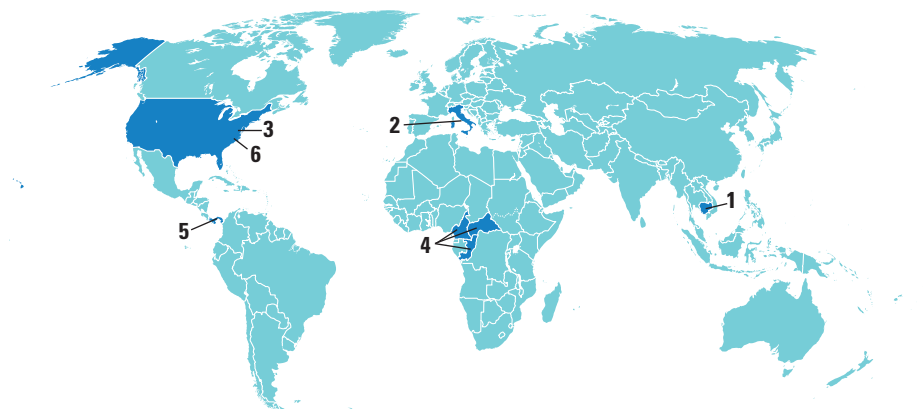
In 1985, AAAS founded Project 2061 with the goal of helping all Americans become literate in science, mathematics, and technology. With its landmark publications *Science for All Americans* and *Benchmarks for Science Literacy*, Project 2061 set out recommendations for what all students should know and be able to do in science, mathematics, and technology by the time they graduate from high school.

As a AAAS member, your dues help support Project 2061. If you are not yet a member, join us. Together we can make a difference.

To learn more, visit  
[aaas.org/plusyou/project2061](http://aaas.org/plusyou/project2061)



## AROUND THE WORLD



## Cambodia 1

**Mysterious Disease Kills Dozens In Cambodia**

Scientists have identified a possible culprit in the syndrome that has killed dozens of children in Cambodia since April, the Cambodian Ministry of Health and the World Health Organization announced on 8 July.

Between April and 5 July, 59 children in Cambodia fell ill with symptoms that include respiratory illnesses, fever, and convulsions, according to the health ministry. Of those patients, 52 died.



As of Monday, a conclusive diagnosis was not yet in. But laboratory work at Institut Pasteur du Cambodge in Phnom Penh pointed to hand, foot, and mouth disease, a contagious and sometimes fatal illness. Samples from 15 of 24 patients tested positive for Enterovirus 71, one of the pathogens that causes the disease.

Vietnam has been badly hit by hand, foot,

and mouth disease, so “we were expecting an outbreak sooner or later,” Institut Pasteur head virologist Philippe Buchy wrote in an e-mail. <http://scim.ag/Cambdisease>

## Rome 2

**Drastic Cuts Infuriate Researchers**

Italian scientists are up in arms over budget cuts at a dozen national research institutes, part of a spending review announced on 6 July that will strike €26 billion from the national government’s budget. “News about these cuts came out of the blue, and it’s outrageous,” says Fernando Ferroni, the president of the Italian National Institute of Nuclear Physics (INFN), which will be hardest hit.

INFN, which contributed to last week’s discovery of the Higgs boson, will see its €278 million budget cut by 3.8% this year and by another 10% both in 2013 and in 2014. Italy’s National Research Council (CNR), a €1 billion funding agency, faces cuts of 1.2% this year and 3.3% each of the next 2 years. The cuts have to be approved by the Italian parliament within 60 days.

Heads of the institutes received no warning but hope to change the mind of Italian research minister Francesco Profumo at a meeting scheduled for this week. “We shall do our best to convince our politicians that research is a key element for the economical growth of our country,” says CNR President Luigi Nicolais. <http://scim.ag/Italycuts>

## Washington, D.C. 3

**NSF Finds Icebreaker To Reach McMurdo**

The U.S. National Science Foundation (NSF) announced 3 July that it has struck a deal with a Russian shipping company to charter a heavy-duty icebreaker to clear a



path this winter to the largest U.S. scientific base in the Antarctic.

Two months ago, the Murmansk Shipping Company, which operates the icebreaker *Vladimir Ignatyuk*, informed NSF that the *Ignatyuk* would not be available for the 2012–13 season. The *Ignatyuk* had led the break-in and resupply of McMurdo Station during the 2011–12 season, but was concerned about the ship’s ability to continue to operate safely in the Antarctic pack ice. To allay those concerns, NSF hopes to locate additional vessels in the region who would be in a position to assist, should the need arise, says Kelly Falkner, acting director of NSF’s Office of Polar Programs.

NSF has also been stockpiling fuel at McMurdo; had there been no icebreaker available for the coming season, Falkner says, the station would have had enough fuel to continue operations at a reduced level through February 2014. <http://scim.ag/NSFice>

## Republic of Congo, Cameroon, and the Central African Republic 4

**New World Heritage Site Spans Three Countries**

The United Nations Education, Science, and Cultural Organization (UNESCO) designated the first tri-country World Heritage Site on 2 July. Conservationists hope the designation will help protect wildlife in the Republic of Congo, Cameroon, and the Central African Republic.

Known as the Sangha River Tri-National Protected Area (TNS), the site spans 25,000 square kilometers and is one of the few pristine wildernesses left in Central Africa; it is home to some of the region’s last populations of gorillas, chimpanzees, and elephants. But increasing human activity such as elephant poaching, logging, and clear-cutting for oil palm plantations threaten the site’s biodiversity.

Although TNS already receives funding from several other conservation organizations



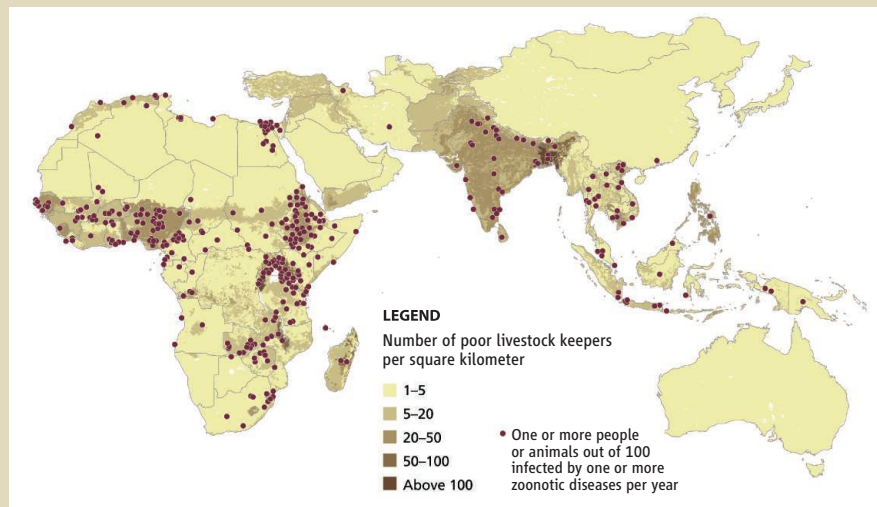
## THEY SAID IT

**"In conclusion, the new research shows that GFAJ-1 does not break the long-held rules of life."**

—An Editorial statement from *Science* accompanying two papers it released this week that refute claims that the so-called arsenic bacterium, GFAJ-1, survives without phosphorus.

**"I think it's unclear whether this is the last word."**

—Felisa Wolfe-Simon, lead author of the original report on GFAJ-1, to *The Washington Post*.



## Putting Zoonotic Diseases on the Map

New diseases emerge all the time, jumping the species barrier from animals to humans. A new study, led by the International Livestock Research Institute in Nairobi, maps the location of such zoonotic events over the last 72 years. While Western Europe and the United States (where the density of livestock is highest) are still hotspots, developing countries are catching up. More than half of the events that were newly identified in 2012 (the previous survey was done in 2004) occurred in poorer countries, with areas such as Southeast Asia and Brazil in the lead.

The world's increasing demand for meat and milk products presents an opportunity for people in developing parts of the world to lift themselves out of poverty, the authors write. But as more pigs and poultry are raised in concentrated spaces in these countries, the risk of zoonotic diseases rises: 56 zoonotic diseases together cause 2.5 billion cases of human illness and 2.7 million human deaths per year. Ethiopia, Nigeria, Tanzania, Togo, and India are bearing the brunt of the disease burden.

and foreign countries, the World Heritage Site designation cements a commitment that the three countries' governments made in 2000 to protect the area from destruction, says James Deutsch, director of Africa programs for the Wildlife Conservation Society.

There are many protected wildlife parks that run along country boundaries. Declaring TNS as the first trinational World Heritage Site represents "a strong step forward for conservation across Africa," Deutsch says.

### Panama City 5

## South Korea Considers 'Scientific' Whaling

South Korea announced it is considering hunting whales for scientific purposes at the annual meeting of the International Whaling Commission (IWC) last week. In a statement to IWC, South Korean delegation head Joon-Suk Kang said the country's non-lethal sighting surveys have not been able to suf-

ficiently assess whale stocks or identify their feeding habits and impact on fisheries. So the government is considering taking whales to "analyze and accumulate biological and ecological data on the minke whales migrating off the Korean peninsula," he said. The announcement was condemned by a host of governments and conservation groups.

A clause in the International Conven-



tion for the Regulation of Whaling (ICRW) allows any country to unilaterally decide to hunt whales for scientific research. Japan has used that clause to capture more than 16,000 minke and smaller numbers of other whales since a moratorium on commercial whaling took effect in 1986. The South Korean delegation said it will submit a research plan to IWC's Scientific Committee before taking any whales.

### Raleigh, North Carolina 6

## Revised Sea Level Rise Bill Goes To Governor

The North Carolina House of Representatives voted on 3 July to revise controversial legislation passed by the state senate that would have barred planning officials from considering acceleration in sea level rise due to climate change. The changes take out the requirement that planners use only linear estimates of future sea level rise, but also bar state agencies from considering accelerated sea level rise in decision-making until 1 July 2016.

Climate scientists gave a lukewarm reception to the changes. "This version is better than the original Senate version," says climate researcher Robert Jackson of Duke University in Durham, North Carolina. "It's still bad policy though because it requires the state to bury its head in the sand for 4 more years."

North Carolina's Senate already voted on 2 July (40 to 1) to adopt the revisions. Now, the bill will move on to the governor, who must sign off on it before it can become law. <http://scim.ag/NCSLbill>



## Higgs, Found

Back in 2009, British theoretical physicist Peter Higgs posed in front of his likeness in an oil painting by Scottish artist Ken Currie that had been commissioned by the University of Edinburgh in the United Kingdom. In the painting, one Higgs, holding his glasses, stares out, seemingly toward the viewer, while his mirror image is seen studying the remnants of a particle collision. It was more than 4 decades ago that Higgs, now professor emeritus at the University of Edinburgh, first suggested the existence of an elusive subatomic particle that would convey mass to all other fundamental particles in the universe.

When the painting was unveiled, Higgs expressed surprise, saying, "It is a great surprise to me that the university wanted to paint my portrait. I would not have predicted it 30 years ago." He got a considerably bigger surprise last week. On 4 July, scientists at CERN jubilantly announced that they had (most probably) found the particle that now bears his name (no, not God) (see story, p. 141).

## NEWSMAKERS

### Staring Down the Horns Of Budget Cuts

**Sonny Ramaswamy**, the new director of the \$1.2 billion National Institute of Food and Agriculture (NIFA), the U.S. Department of Agriculture's center for extramural research funding, says he hopes to raise the profile—and the budget—of agricultural research. But Ramaswamy, a charismatic entomologist who started in May, faces a tough fiscal environment. "Everybody's ox is going to be gored," he says, but adds that: "I'm cautiously optimistic that we're going to come out well."

Ramaswamy, 60, was dean of agricultural

research at Oregon State University since 2009. He reduced a proposed \$20 million cut from the OSU College of Agricultural Sciences' budget to \$8 million by canvassing the state to build support.

"You present the vision of what research can do," he says. Ramaswamy replaces NIFA's first director, molecular biologist Roger Beachy, who resigned in May 2011. Ramaswamy is undertaking a review of NIFA, which has received criticism for focusing on large, multi-institution grants at the expense of smaller projects.

"He's excited, he's working hard, and he's passionate speaker," says Karl Glasener, director of science policy for the American Society of Agronomy, Crop Science Society of America, and Soil Science Society of America.



## Science LIVE

Join us Thursday, 19 July, at 3 p.m. EDT for a live chat on **sports-related head injuries**.  
<http://scim.ag/science-live>

## BY THE NUMBERS

**172** Number of papers fabricated by Japanese anesthesiologist Yoshitaka Fujii over the past 19 years, an investigating panel reported 2 July. Should each paper be retracted, Fujii would hold the record for paper retractions for a single author.

**40:1** Ratio of stories about the reality television-famed Kardashian family to those about ocean acidification in major U.S. media outlets in 2011 and early 2012, according to a Media Matters for America study.

## FINDINGS

### Gene Mutation Protects Against Alzheimer's

Scientists have identified a rare gene mutation that appears to protect against Alzheimer's disease. In people 85 or older, the mutation is 7.5 times more common in those who don't develop the memory-robbing dementia, a team led by Kári Stefánsson at deCODE genetics in Reykjavik reports this week in *Nature*.

The mutation affects a gene called *APP*, which encodes a protein that breaks down into pieces, including the amyloid  $\beta$  peptide that forms the hallmark plaques in the brains of Alzheimer's patients. Previously, researchers identified mutations to *APP* that increase amyloid beta formation, causing an early-onset, inherited form of Alzheimer's disease. The new mutation found by Stefánsson's group appears to reduce amyloid formation.

The work bolsters the case that early- and late-onset Alzheimer's involve the same mechanisms, says Gerard Schellenberg, a molecular geneticist at the University of Pennsylvania. Clinical trials scheduled to begin later this year will give anti-amyloid drugs to people who are genetically predisposed to early-onset Alzheimer's disease, and Schellenberg says, "This study makes it seem more likely that if they find something [that prevents early-onset Alzheimer's], there's a good chance it will also work for late-onset disease." <http://scim.ag/Alzmuts>





**All smiles.** “I think we’ve got it,” quipped CERN Director General Rolf-Dieter Heuer (*center*) after ATLAS’s Fabiola Gianotti (*left*) and CMS’s Joseph Incandela presented the data.

p. 1657). “My nightmare—and it’s not just me, but a lot of us—is that the LHC discovers the Higgs and nothing else,” says Steven Weinberg, theorist and Nobel laureate at the University of Texas, Austin. “That would be like closing a door.”

Still, physicists say they’re optimistic that even bigger finds will follow. “We’ve reached deeper into nature than ever before and we didn’t come up empty,” says Joseph Incandela, an experimenter at the University of California, Santa Barbara, and spokesperson for the 3000 researchers working with a massive particle detector called CMS. “There aren’t any guarantees [of more discoveries], but there’s a strong likelihood.”

#### What’s a Higgs boson anyway?

The Higgs boson was born as the answer to a seemingly abstruse question: Why does the range of the electromagnetic force, which creates light and binds the atom, stretch infinitely far, whereas the range of the weak nuclear force, which causes a kind of radioactive decay, reaches across only the atomic nucleus?

In the early 1960s, theorists realized that they could both roll the electromagnetic and weak forces together and explain the differences in their ranges. To do that, they assumed that just as the electromagnetic force is conveyed by quantum particles called photons, the weak force is conveyed by particles called the W boson and the Z boson. But whereas the photon has no mass, the W and Z would be weighty, and their masses would shorten the range over which they act.

## PARTICLE PHYSICS

# Higgs Boson Makes Its Debut After Decades-Long Search

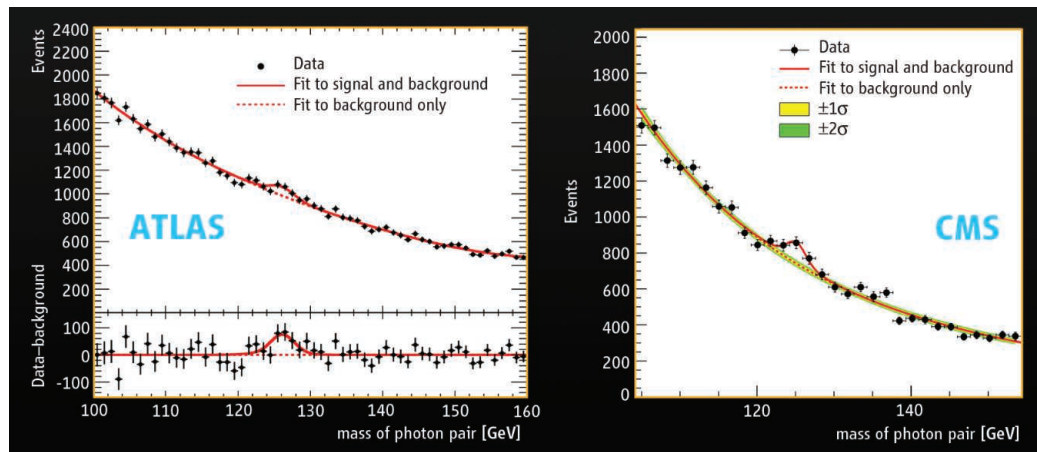
**MEYRIN, SWITZERLAND**—When physicists here at the European particle physics laboratory, CERN, reported last week that they had discovered the famed Higgs boson, or something much like it, they captivated the world. A hundred journalists descended upon the lab to hear scientists working with the world’s largest atom smasher, CERN’s Large Hadron Collider (LHC), present evidence of the Higgs, the key to physicists’ explanation of how all fundamental particles get their mass. Photographers swarmed Peter Higgs, the 83-year-old theorist from the University of Edinburgh in the United Kingdom, who dreamed up the most-coveted particle 48 years ago.

“I’d like to add my congratulations to everyone involved in this tremendous achievement,” Higgs said immediately after the special seminar. “For me, it’s really an incredible thing that it’s happened in my lifetime.” Otherwise, like a seawall resisting the surf, the demure Higgs refused to take questions. Greta Garbo would have admired his resolve.

The discovery of the Higgs marks a triumph for particle physicists. For the first time since 1995, they have unearthed a new fundamental particle. They have apparently confirmed a decades-

old prediction of how the universe works and found the last piece in their standard model of fundamental particles and forces, perhaps the most elaborate and precise theory in science. And they’ve reenergized their field, as attested by the hundreds of physicists who lined up all night for a chance to get into the auditorium for the talks.

But the advance also leaves particle physics at a curious crossroads. Physicists aren’t sure whether new particles or phenomena lie within the reach of the LHC or any conceivable atom smasher. If nothing else shows up, the discovery of the Higgs could mark the end of the road (*Science*, 23 March 2007,



**Twin peaks.** The coincident bumps in these plots reveal Higgs-like particles decaying into pairs of photons.

There was just one hitch: If theorists simply assigned masses to the W and the Z, the theory would go mathematically haywire. So instead, the masses of the W and Z had to come from interactions among the otherwise massless particles themselves. That's where the Higgs boson came in.

In 1964, Higgs and others independently realized that they could make a massless particle put on weight if they assumed that empty space was filled with a field a bit like an electric field. That "Higgs field" would then interact with and drag on other particles to produce the effects of inertia or mass. So in the late 1960s, other theorists adopted Higgs's scheme to give mass to the W and Z bosons, which were observed with precisely the predicted properties in experiments at CERN in 1983.

Physicists then simply assumed that the Higgs field gives rise to the masses of all the other fundamental particles. For example, the electrons that whiz around in atoms and the quarks that make up protons and neutrons in atomic nuclei get their mass by moving through the Higgs field.

Quantum theory assumes that any field consists of quantum particles. So just as an electric field consists of photons, the Higgs field consists of Higgs bosons. That does *not* mean that space is filled with scads of Higgses floating about. Rather, the massive particles lurk "virtually" in the vacuum, exerting their influence without stepping into the spotlight of bona fide existence.

The Higgs is much more than a bandage on the theory, says Stuart Raby, a theorist at Ohio State University, Columbus. "The standard model is framed on having a Higgs boson," he says. "If the Higgs weren't there, the whole theory would have to be rethought."

### Loose lips and long lines

To spot Higgs bosons, physicists must literally rip them out of the vacuum in violent particle collisions, as experimenters working with the LHC have done. The 27-kilometer-long circular collider smashes protons together at energies four times as high as any previous machine could reach—even though, because of technical flaws, the LHC is running at just over half its design energy. Collisions take place within two gargantuan particle detectors, called ATLAS and CMS, that have been hunting the Higgs since the LHC started tak-

ing data 27 months ago. Any Higgs bosons created in the collisions should decay into telltale combinations of familiar particles.

For example, the Higgs boson ought to sometimes decay into two photons. From the photons' energies, experimenters can infer the mass of their parent particle. So in a plot of the masses of the inferred particles, the Higgs should appear as a peak atop a background produced by random photon pairs. Both ATLAS and CMS see peaks at a mass of about 125 giga-electron volts (GeV), 133 times the mass of a proton (see figure, p. 141). The coincident peaks by themselves make a strong case for the Higgs. And ATLAS and CMS see other signs of the Higgs decaying into two Z bosons, as well as other combinations of particles.



**Hard pressed.** The eponymous Peter Higgs (right) faced an onslaught of media attention.

The data from either experiment alone would clinch the case for the new particle. Physicists measure the strength of a signal in multiples of the uncertainty in it, denoted sigma. A higher multiple implies a stronger signal, and the CMS data yield a signal just shy of particle physicists' 5-sigma standard for declaring discovery, CMS's Incandela reported. The chances that random background could produce a spurious signal as large are one in 3.5 million.

ATLAS's signal reaches the 5-sigma standard, reported Fabiola Gianotti, an experimenter at CERN and spokesperson for the 3000-member ATLAS team. As soon as she showed a slide stating that fact, the audience erupted into cheers. "I'm not done yet!" Gianotti responded. "There's more to come."

The presentations capped off 2 weeks of growing anticipation, fueled by rumors and anonymous leaks. Hours before the CERN auditorium opened at 7:30 a.m., people began lining up, creating a queue that snaked

through CERN's main building. Even 20 minutes before the seminar, dozens remained in line hoping against hope to get a spot inside the packed hall. "I want to stay close to this event for now," said Serena Persichelli, a graduate student from the Sapienza University of Rome. "Maybe at 9:00 I'll go somewhere else and watch the video feed."

### Is it really the Higgs?

Physicists still have to see how closely the particle they've discovered resembles the Higgs boson as described in the standard model. "This is *the* piece that was missing from the standard model jigsaw puzzle," says John Ellis, a theorist at King's College London. "Of course, when you find a piece from a jigsaw puzzle, you have to check that it's the one you want and not a piece from another puzzle."

First off, researchers will check the rates at which the supposed Higgs decays into various combinations of particles against the rates predicted by the standard model. In fact, physicists say, the rate for Higgses decaying into photon pairs already appears a bit high. To support such studies, CERN will postpone the end of the LHC's current run from November to February, says Stephen Myers, CERN's director of accelerators and technology. After that, the collider will undergo 20

months of repairs that should enable it to run at full design energy.

Ironically, most physicists seem to hope the new particle won't quite match the mug shot of the standard model Higgs boson. That's because strict agreement with standard model predictions would leave them with a theory that is complete, internally consistent, and devoid of any promise of new discoveries to come. Physicists would prefer a new puzzle to mull over.

In fact, they say the mere existence of the Higgs already gives them a conceptual one. In the standard model, interactions between the Higgs and the other particles ought to force the mass of the Higgs to skyrocket to a value a trillion times larger. Yet that doesn't happen. So new particles out there must somehow counteract the ballooning of the Higgs's mass, physicists suspect. A concept called supersymmetry, or SUSY, posits a heavy new partner for every known particle for exactly this reason. "In the context of SUSY, a Higgs with



a mass of 125 GeV is just what we're looking for," Raby says, "so it gives us hope that SUSY [particles] will be found at the LHC."

Still, the new particle was spotted decaying in the ways a standard model Higgs is supposed to. And that suggests that it cannot be too radically different from that plain-vanilla version, Ellis acknowledges.

The discovery was reported on 4 July, Independence Day in the United States, and for U.S. physicists it dredges up thoughts of what might have been. The Higgs could have been spotted years ago, they say, by an even bigger atom smasher called the Supercon-

ducting Super Collider (SSC), which physicists started building in Waxahachie, Texas, in 1991. But Congress killed the uncompleted SSC in 1993, after its cost ballooned to \$10 billion. "Go ahead, twist the knife," Weinberg says, when asked about the SSC. "As a theorist, I don't really care where the data comes from, but as an American I'm sad that America seems to have bowed out of this kind of science."

Even without the SSC, U.S. physicists may have gotten close to finding the Higgs. On 2 July, researchers working on data from the Tevatron at Fermi National Accelerator Lab-

oratory in Batavia, Illinois, a collider that shut down in September 2011, reported the final data from their Higgs search. They see a 2.9-sigma signal of the Higgs decaying mainly into particles called bottom quarks.

But the glory belongs to Europe. "It's a historic day," CERN Director General Rolf-Dieter Heuer told *Science* at the seminar. "We've been waiting for 50 years for this. That's the lifetime of a physicist." Physicists hope that the next, even bigger discovery will come within a few months or years. The survival of their field may depend on it.

—ADRIAN CHO

## FUKUSHIMA MELTDOWN

# Commission Spreads Blame for 'Manmade' Disaster

**TOKYO**—A powerful commission set up by Japan's parliament last week blamed Tokyo Electric Power Co. (TEPCO) and government regulators for what it called the "manmade" disaster at the Fukushima Daiichi Nuclear Power Plant. As the conclusions of the hard-hitting report sank in, Japan's scientific community pondered its responsibility in failing to provide sound advice to the government and the public during the crisis. "The scientific community at large lost some trust," commission chair Kiyoshi Kurokawa, a medical doctor and former president of the Science Council of Japan, told *Science*.

The powerful earthquake and tsunami on 11 March 2011 left the plant's reactors without power to cool their nuclear fuel, leading to multiple meltdowns and massive radiation releases that forced the evacuation of 150,000 people. Fukushima was an accident waiting to happen, the commission found. "There were many opportunities for taking preventive measures prior to March 11. The accident occurred because TEPCO did not take these measures," its report states, noting that upgrades needed to fix identified deficiencies in the plant's seismic and tsunami resistance were never carried out. In a strongly worded preface, Kurokawa blamed Japanese culture for "our reflexive obedience; our reluctance to question authority; our devotion to sticking with the program; our groupism; and our insularity."

According to the commission, the saga shows the dangers of "regulatory capture," in which an agency acts on behalf of the industry it oversees instead of representing the public interest. The Nuclear and Industrial Safety Agency, a part of the economy ministry that promotes nuclear energy, allowed TEPCO to delay upgrades and ignore problems, the

report found. Vulnerabilities identified at Fukushima raise questions about the rest of Japan's nuclear facilities, commission member Katsuhiko Ishibashi, a professor emeritus of seismology at Kobe University in Japan,



*"The scientific community at large lost some trust."*

—KIYOSHI KUROKAWA, COMMISSION CHAIR

said at a press briefing last week. "The seismic resistance of every nuclear power plant in Japan needs to be investigated," he said.

The industry was also overconfident in its own expertise. The commission claims in its report that because of a "not invented here" attitude, neither the power companies nor regulators learned any lessons from the Three Mile Island nuclear power plant accident in the United States or from the Cher-

nobyl disaster in Ukraine. The commission called this attitude an example of the closed nature of the entire nuclear industry, including its academic experts.

That analysis exposed what some see as another shortcoming of the scientific community. "There was always a very strong separation between nuclear and other scientists," says Hiroyuki Yoshikawa, an engineer and former president of the University of Tokyo. The split, which goes back to the 1960s when the government was pushing to jump-start nuclear power through imported technology, means that scientists have had little input into the nation's nuclear energy policies, and its nuclear engineers were cut off from advances in related fields that might have improved reliability and safety, Yoshikawa says. It is an example, he says, of how "there is not very good communication between scientists and the government."

The commission calls for the creation of an independent and professional nuclear regulatory body. Kurokawa thinks that the proposed agency's independence could be bolstered if the Science Council of Japan nominates candidates to head it. That, he says, would be an opportunity for scientists to engage with society.

Yoshikawa would like to go further. He is urging the government to establish the post of science adviser to the prime minister. He would also like to see the advisory Council for Science and Technology Policy revamped to take on the added responsibility of providing scientific input to health, energy, and industrial policies. With tens of thousands of Japanese still unable to return to their homes and the damaged reactors in a fragile state, the need for sound scientific advice is more urgent than ever.

—DENNIS NORMILE



POPULATION GENETICS

## Genes Suggest Three Groups Peopled the New World

Who were the first Americans? Twenty years ago, in a bold synthesis of linguistic, genetic, and dental data, researchers proposed that the first people on this continent arrived from Asia in at least three distinct waves. But the idea of diverse origins slowly fell out of favor, in part because studies found that Native Americans from Alaska to Chile were genetically similar, suggesting a single founding population.

Now the most comprehensive genetic study to date concludes that Native Americans do indeed descend from at least three groups of ancestors from Asia. “We can document at least three streams of Asian gene flow into America,” says team leader David Reich, a population geneticist at Harvard Medical School in Boston. “There were more migrations than we knew about.” But in contrast to the original three-wave hypothesis, Reich found that once in the New World, all three source populations intermingled extensively.

This complex picture caps decades of research by linguists, archaeologists, and geneticists who have tried to trace the steps of the first people to cross the Bering Strait to America at least 15,000 years ago. After linguist Joseph Greenberg of Stanford University and others suggested the three-wave model (*Science*, 15 January 1993, p. 312) 2 decades ago, linguists criticized Greenberg’s methods of grouping the diverse American languages into three large families of Amerindian, Eskimo-Aleut, and Na-Dene speakers. And genetic studies of sex chromosomes and of mitochondrial DNA, which trace only a maternal or paternal lineage, suggested a single founding population in Asia. “There really seemed to be a wholesale shift to the notion of a single migration,” says archaeologist David Meltzer of Southern Methodist University, Dallas, in Texas who was not part of the new study.

To test these models, Reich and Colombian geneticist Andrés Ruiz-Linares of University College London collaborated with 62 geneticists to assemble a comprehensive data set with representatives of most major linguistic groups. They analyzed samples from 493 Native Americans in 52 populations stretching from Alaska to Chile, as well as from 245 people from 17 groups in Siberia, as they report in *Nature* this week. (They were unable to get informed consent from tribes in the continental United States, however, and have no U.S. samples from outside Alaska.) The team genotyped 364,470 single-nucleotide polymorphisms (SNPs) from across the entire genome, giving a more reliable picture than past studies of a single gene or chromosome. The team used statistical and



**Diverse origins.** This Chipewyan woman (left) in Canada and Aleut boy (right) in Alaska descend in part from two distinct groups of ancient migrants to the New World.

tree-building methods to sort out relations among groups, and to subtract the effect of later interbreeding with Europeans.

The results do show a single founding population for most Native Americans, a group Reich’s team dubbed the “First Americans,” which is roughly similar to Greenberg’s ancestral Amerindian population. The DNA of this group is found in some proportion in all Native

**First wave.** This Zapotec woman from Mexico descends from the first people to colonize America.

Americans today. These people were the first to cross the Bering Strait, at least 15,000 years ago, and they then spread south rapidly, probably along the coast, as the genetic markers apparently spread more quickly along the coast than overland.

Two other groups crossed the strait later. One left its mark in Eskimo-Aleut-speaking populations in the far north, including the Aleut people of Alaska, who inherit almost half their ancestry from this group. The Aleut’s combined ancestry fits with anthropological data showing two distinct kinds of peoples arriving at different times in the Aleutian Islands (*Science*, 13 January, p. 158). This population also was ancestral to Inuits from Greenland (a link that previous studies had not found), showing that these people spread east across the far north rather than south. And the pattern of genetic markers in Siberia suggests that some people speaking Eskimo-Aleut languages and carrying First American DNA apparently returned westward to Asia.

The team found traces of a third ancestral group as well. Na-Dene-speaking Chipewyan from Canada inherit about one-tenth of their ancestry from this third group, who were more closely related to the Han Chinese. Although the three-wave model is not new, “it’s quite new that modern genetics supports it,” says geneticist Eske Willerslev of the University of Copenhagen. Research-

ers hope to study the DNA of other Na-Dene speakers, such as the Apache and Navajo, to see if they also carry ancestry from the third founding group. “Now that we’re starting to look at the genome in more detail, the peopling of the Americas is a far more complex and nuanced process than we thought,” Meltzer says.

—ANN GIBBONS



## PLANETARY SCIENCE

# Earth and Planetary Scientists Search for Common Ground

**BOULDER, COLORADO**—Discovered in 2005 orbiting a star 63 light-years from us, exoplanet HD 189733b doesn't generally get much attention from climate scientists on Earth. But maybe that should change, planetary scientist Adam Showman told planetary and earth scientists at a recent meeting here\*. Thermal observations of the gas giant have suggested that the planet's hot spot has shifted about 30 degrees away from the "high noon" position, suggesting strong winds. In trying to determine whether those winds moved east or west, Showman, who works at the University of Arizona in Tucson, and colleague Lorenzo Polvani of Columbia University consulted decades-old papers on simple models of tropical winds on Earth. In a paper published last year in *The Astrophysical Journal*, they proposed a theoretical mechanism for such winds, related in large part to the differences in temperature between day and night sides of a planet.

But the work with HD 189733b inspired Showman and Polvani to go further. They found that the models currently used to study terrestrial climate had left out some key physics concerning the transfer of momentum, so they published another paper making that point in *Geophysical Research Letters*—a journal that focuses on earth science. "We're learning about Earth by studying exoplanets and about exoplanets by studying Earth," says colleague Yohai Kaspi of the Weizmann Institute of Science in Rehovot, Israel.

Sharing work like Showman's—both interplanetary and interdisciplinary—was the goal of the unique 4-day meeting, which 125 researchers attended. Four separate NASA science divisions—Earth Science, Heliophysics, Astrophysics, and Planetary Science—cosponsored the event, a milestone for an agency infamous for bureaucratic stovepiping. The meeting's galaxy-spanning agenda included talks on topics as varied as how methane on Jupiter's moon Titan acts like water on Earth and new techniques for seeing wind currents on Mars, Venus, and Earth.

A key goal was to forge closer ties between communities that suffer from what geologist

Jeffrey Moore of NASA Ames Research Center in Mountain View, California, calls "ghettoization." For its part, the space agency was impressed. "What struck me was the enthusiasm," says NASA chief scientist Waleed Abdalati, an attendee. "The message I got from this meeting was that each of these disciplines has something to learn from the other."

Such cross-pollination used to be par for the course: Carl Sagan's views on global warming in the 1980s, for example, grew out of studies of Venus, and research on the role of

lites such as CloudSat and CALIPSO are helping tune models to understand how clouds form. "These tools could revolutionize our understanding of the cloud-formation processes on Venus, Titan, and early Mars," says David Crisp, an atmospheric physicist at NASA's Jet Propulsion Laboratory in Pasadena, California.

Yet observing our neighbors may also help answer many questions about Earth. Take dust clouds. "The physical processes responsible for dust raising, transport, sedimentation, and electric charge separation have been studied extensively by the Mars community in recent years," Crisp says. "It might be time to bring some of this back home" to study dust storms in Australia, central China, and the southwestern United States.

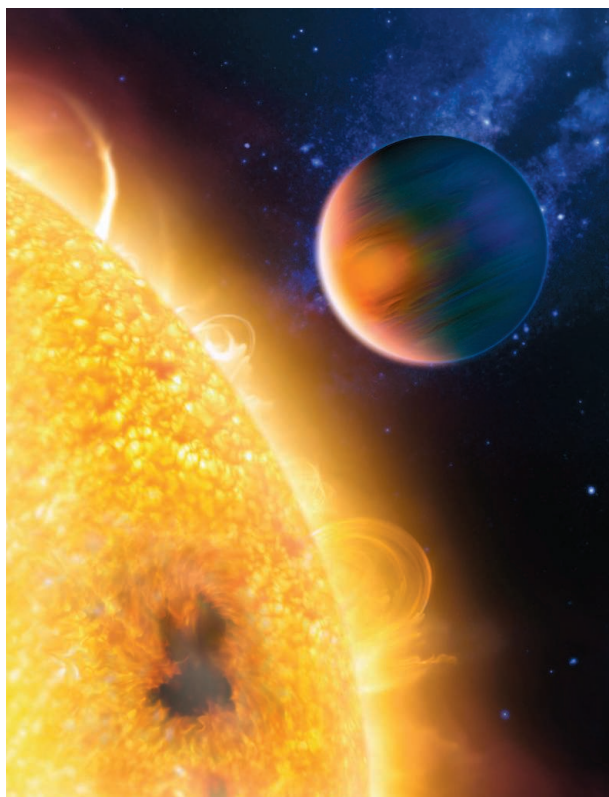
Some obstacles to more comparative climatology are organizational: Although NASA funded Showman's work on exoplanet winds, modeling the possible atmospheric dynamics of such distant worlds doesn't fit well into the mission of either NASA's astrophysics or planetary studies division. "So good proposals go unfunded," Bullock says.

Other obstacles are culturally ingrained. Moore would like to compare how water erodes basalt on Mars with how methane erodes water ice on Titan. But potential collaborators in each camp view him with suspicion. "There's such intense rivalry among these groups for funding," he says.

"The reaction we get from many earth scientists is 'You're doing this because you want our money,'" Bullock says. Indeed, although the Boulder meeting boasted some high-powered earth climatologists, earth scientists were notably in the minority. "There are just so many burning questions on Earth," Kaspi says.

Still, organizers are optimistic that NASA will be persuaded by a meeting summary likely proposing that several NASA divisions jointly fund such research in the future. While acknowledging his agency's tight budget, Abdalati says he'd like to revive the interdisciplinary spirit of planetary science's glory days. "If this can be the rekindling of something we used to do, ... that's great," he says.

—ELI KINTISCH



**Helpful alien.** Studies of exoplanet HD 189733b (artist's conception shown) revealed flaws in models of Earth's atmosphere.

chlorine in that planet's atmosphere inspired the scientists who discovered humanmade chlorinated compounds destroying the ozone layer. In recent decades, however, planetary and earth sciences have become increasingly specialized and disconnected from each other, says meeting co-organizer Mark Bullock, a planetary scientist at the Southwest Research Institute in Boulder.

When there is interchange, it generally flows from the more populous geosciences to planetary science. Cloud scientists at the meeting, for example, showed how new measurements from Earth-orbiting satel-

\*Comparative Climatology of Terrestrial Planets, 25–28 June.



# Rising Acidity Brings An Ocean of Trouble

**Carbon dioxide emissions have changed the chemistry of the world's oceans in ways that are already harming shell-building organisms and could lead to broad impacts on marine ecosystems**

**NETARTS BAY, OREGON**—Alan Barton hates beautiful summer days. Not the warm sunshine—here on the central Oregon coast, where it is cold and rainy for much of the year, sunshine is welcome. Rather, for Barton, an oceanographer who helps run an oyster larvae hatchery here, it's the breezes he can't stand.

When the wind blows from the north as it normally does in the summer, it pushes the surface waters out to sea, drawing up cold water from the deeper ocean. That water is enriched with carbon dioxide ( $\text{CO}_2$ ), given off by microbes as they metabolize organic matter that sinks to the ocean bottom. When the  $\text{CO}_2$ -rich water washes into Netarts Bay and the intake pumps and oyster larvae tanks at the Whiskey Creek Shellfish Hatchery, the excess  $\text{CO}_2$  causes the seawater's acidity to spike and reduces the amount of carbonate ions that oyster larvae use to build their shells.

The change can kill oyster larvae instantly or stunt their growth. In 2007 and 2008, Whiskey Creek lost 80% of its annual larvae production and nearly had to close up shop before Barton, working with regional scientists, fingered rising ocean acidity as the source of the problem. Now, the hatchery copes with fluctuations in pH by making sure

to draw water into its tanks only after acidity declines. But even that success has left Barton frustrated. "This is what I like to do," he says, shucking an oyster. "I hate thinking about carbonate chemistry."

The reprieve for Whiskey Creek and other shellfish hatcheries and farms along the West Coast of the United States could be short-lived. The burning of fossil fuels emits some 35 billion metric tons of  $\text{CO}_2$  into the atmosphere every year. That has already begun to change the fundamental chemistry of the world's oceans, steadily increasing their level of acidity. On page 220, scientists in Switzerland and the United States report projections from a new high-resolution computer model showing that over the next 4 decades, the combination of deep-water upwelling and rising atmospheric  $\text{CO}_2$  is likely to have profound impacts on waters off the West Coast of the United States, home to one of the world's most diverse marine ecosystems and most important commercial fisheries.

The new computer model is only one of several recent warning signs. Numerous laboratory and field studies over the past few years underscore rising concerns that ocean acidification could devastate marine ecosystems on which millions of people depend for

**Tip of the spear.** Acidity levels in Netarts Bay, Oregon, hit levels the rest of the ocean won't see for decades.

food and jobs. The new results "are a major concern," says Richard Feely, a chemical oceanographer at the National Oceanic and Atmospheric Administration's Pacific Marine Environmental Laboratory in Seattle, Washington. "It's dramatic how fast these changes will take place." George Waldbusser, an ocean ecologist and biogeochemist at Oregon State University, Corvallis, says it's not clear precisely how rising acidity will affect different organisms, but the changes will likely be broad-based. "It shows us that the windows of opportunity for organisms to succeed get smaller and smaller," he says. "It will probably have important effects on fisheries, food supply, and general ocean ecology."

## Nailing a killer

Concerns about ocean acidification have been ramping up for several years (*Science*, 18 June 2010, p. 1500). Although it hasn't captured the public imagination as vividly as its cousin, climate change, the "other  $\text{CO}_2$  problem" is just as insidious. One-quarter of  $\text{CO}_2$  in the air diffuses into the surface layer of the ocean. There, it reacts with water to create carbonic acid, which in turn splits into negatively charged bicarbonate ions and positively charged hydrogen ions that lower the water's pH. (pH measures available hydrogen ions  $[\text{H}^+]$  in solution; the more hydrogen, the lower the pH value.) Bicarbonate ions lose another  $\text{H}^+$  to become carbonate ions, which oysters, clams, and other organisms use to build their shells. But as acidity increases, less bicarbonate changes into carbonate, and some of the carbonate that is around recombines with  $\text{H}^+$  to reform bicarbonate. The upshot is that lower pH means more bicarbonate and less carbonate.

Since preindustrial times, ocean pH has dropped from 8.2 to 8.1. That might not sound like much, but the pH scale is logarithmic, like the Richter scale for measuring earthquakes. The 0.1 pH unit decline therefore corresponds to a 30% rise in acidity. By 2100, ocean pH is expected to drop to about 7.8, increasing the surface ocean's acidity by 150% on average.

Even with this distinct change, strictly speaking, the world's oceans will not become acidic. For that to happen, ocean pH would have to drop below neutral pH of 7.0, something no one is forecasting will happen. An alkaline pH of 7.8 or 8.1 is more acidic than the preindustrial baseline, however, so the process is popularly known as ocean acidification.



As the pH of seawater drops, it has other effects. The lower carbonate availability drops a measure known as the saturation state of different mineral forms of calcium carbonate, such as calcite and aragonite. Aragonite saturation is particularly sensitive to rising acidity, because that mineral form is more soluble. It also turns out to be the essential ingredient that oyster larvae rely on in their first days to build their shells. If the aragonite saturation state falls below a value of 1, a condition known as undersaturation, already-formed aragonite shells will dissolve. But trouble starts well before that. If the aragonite saturation state falls below 1.5, some organisms, such as oyster larvae, are unable to build shells during the first days of their lives, and they typically succumb quickly.

In 2008, when Barton and others were facing a full-scale collapse of their oyster hatchery, they didn't initially consider ocean pH as the culprit. Instead, they blamed a common bacterial assailant called *Vibrio tubiashii*. *Vibrio* had been a scourge of oyster hatcheries for decades, commonly asserting itself in August after the summer sun had caused widespread blooms in marine plant life, such as algae and seagrass. As those plants grow, they pull CO<sub>2</sub> out of the water to build their cells. That lowers CO<sub>2</sub> levels in the water and thus acidity levels. When the plants die and microbes gobble up the bounty, *Vibrio* moves in, proliferates, and can infect oyster larvae, hampering their development.

By the end of summer in 2007 and 2008, the number of *Vibrio* was "off the charts," Barton says. So he and his colleagues emptied their 62 larvae-rearing tanks—each of which can hold 23,000 to 76,000 liters of water—scrubbed them out, and installed filters to catch the bacteria. When they refilled the tanks, however, larvae kept dying. "After 2008, we thought we were done," says Sue Cudd, the hatchery's owner.

Later that year, they called in Feely, a specialist in ocean acidification. Feely, in turn, called in Waldbusser and Burke Hales of Oregon State University, Corvallis. Waldbusser and Hales brought sensitive detectors to track ocean pH as well as the partial pressure of CO<sub>2</sub> (pCO<sub>2</sub>) in the water. They found that Netarts Bay was experiencing wild swings in both pCO<sub>2</sub> and pH. In the May 2012 issue of *Limnology and Oceanography*, they reported that the low-pH swings were the primary cause of the oyster larvae die-offs.

After figuring out the source of the problem, Whiskey Creek and other oyster hatcheries in Washington state enlisted the help of Senator Maria Cantwell to secure \$500,000 from the U.S. government's economic stimu-



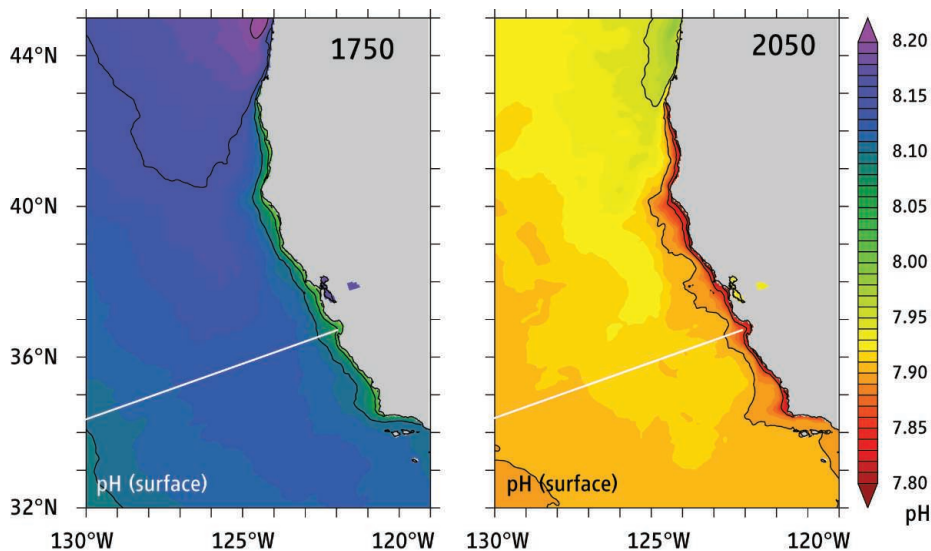
**Poster child.** Alan Barton shucks a Pacific oyster, often called the canary in the coal mine of ocean acidification.

lus program. The hatcheries used the money to set up a network of detectors to closely monitor pH, pCO<sub>2</sub>, temperature, salinity, and dissolved oxygen levels in Netarts Bay and two other prominent oyster-rearing grounds in Washington. "It was like putting headlights on a car," says Bill Dewey, a shellfish biologist and public affairs director for Taylor Shellfish Farms in Shelton, Washington. The detectors showed that pCO<sub>2</sub> levels plunged to as little as 200 microatmospheres

in the afternoon, as algae and other plants pulled CO<sub>2</sub> out of the water for photosynthesis. Overnight, when photosynthesis stopped but respiration continued, pCO<sub>2</sub> levels spiked to 2800. So now the hatcheries make sure to draw their seawater into their tanks at the lowest point of the day. If a large upwelling draws in corrosive waters, they try to hold off filling the tanks as long as possible. The strategy has largely worked. Whiskey Creek is back up to 80% of its historic larvae production levels. Taylor Shellfish has done even better, getting record numbers of larvae in their hatchery, although the natural larvae there haven't had a successful spawning season in 7 years. Now, Cudd says, "monitors are tools we can't live without."

### Troubled waters

But that good news looks likely to be temporary. The new computer simulations reported in this issue by a team led by Nicolas Gruber, an ocean biogeochemist at the Swiss Federal Institute of Technology in Zurich, spell trouble for shellfish in the relatively near future. Gruber and his colleagues focused on a broad region of Pacific Ocean upwelling, known as the California Current System (CCS), off the West Coast of the United States. Their regional ocean circulation model tied together the interplay of ocean and atmosphere, as well as the impacts ocean plants have in removing CO<sub>2</sub> from the water and microbes have in dumping that CO<sub>2</sub> back in when they metabolize algae and plants they eat. Because this model focused on the CCS, Gruber and colleagues could design it to study detailed changes at a resolution 400 times that of conventional global



**Rising tide.** Natural upwelling of CO<sub>2</sub>-rich waters caused pH values along the West Coast of the United States to drop even in preindustrial times (left), a change that will increase markedly by 2050 (right).

ocean models. The researchers considered various scenarios of CO<sub>2</sub> emissions over the next 4 decades and compared them with CO<sub>2</sub> levels in the atmosphere and ocean in 1750, before global industrialization (see figure, p. 147).

They found that the buildup of atmospheric CO<sub>2</sub> and its diffusion into the ocean will rapidly increase the amount of waters undersaturated in aragonite in the upper 60 meters of ocean, where most organisms live. Before industrialization, undersaturation of this top layer in the CCS almost never occurred. Today, Gruber says, undersaturation conditions prevail there 2% to 4% of the time. By 2050, CCS surface waters will be undersaturated for about half of the year. Just as bad, aragonite saturation levels above 1.5—the conditions under which larvae can thrive—will largely vanish from surface waters. Moreover, as increasing acidification of surface waters diffuses into the depths, undersaturation conditions (with the saturation state below 1) will exist year-round in deep waters, making life essentially impossible for shell-building organisms there. This combination could spell doom for Pacific oysters in the northwest, a \$110-million-per-year industry.

“The take-home message is the closeness of some of these events,” well within the life span of an individual person, Gruber says. Dewey agrees. “We’re at the tip of the spear here,” he says. Other regions won’t be far behind. Ocean regions with deep-water upwelling are prevalent around the globe, including sites off Chile in South America and the West Coast of Africa. Gruber says his group will next turn to modeling impacts in some of these areas.

Even if humans manage to stop dumping CO<sub>2</sub> into the atmosphere, the picture won’t improve for decades. Past studies that track different isotopes of carbon and other elements reveal that the deep corrosive waters that wash up along the West Coast have been circulating along the ocean bottom for 30 to 60 years. The water was last at the ocean surface and exposed to CO<sub>2</sub> from the air back in the 1950s and 1960s, when atmospheric CO<sub>2</sub> levels were only 310 to 320 parts per million, far lower than the 390 ppm today. That means even if global societies stopped emitting carbon today, CO<sub>2</sub>-rich waters already in circulation would cause CO<sub>2</sub> levels in the deep ocean to continue rising. “Even if we

fix it, we have 50 years of it getting worse before it gets better,” Dewey says.

### Beyond oysters

Other recent experiments suggest oysters are far from the only organisms in danger. Trouble, in fact, may be brewing along the first links in the food chain. Last year, for example, researchers led by Luc Beaufort of the European Center for Research and Teaching of Environmental Geosciences at Aix-Marseille University in France reported in the 4 August 2011 issue of *Nature* that as ocean pCO<sub>2</sub> rises, the ability of photosynthetic phytoplankton called coccolithophores to build shells decreases markedly. The team sampled 180 regions of ocean surface water and compared them with historical records found in 555 sediment cores. The amount of calcite the coccolithophores



**Oyster catcher.** Sue Cudd of Whiskey Creek Shellfish Hatchery holds a vial containing approximately 100 million oyster larvae that will be sold to oyster farms.

added to their shells dropped as much as 30% when pCO<sub>2</sub> levels rose from about 220 to 400 microatmospheres.

Not all coccolithophores suffered. One species, called *Emiliania huxleyi*—sampled off the coast of Chile in a natural upwelling zone—fared better in CO<sub>2</sub>-rich waters. Just how a combination of reduced coccolithophore biodiversity and supercalcifier survival will play out is unclear, the authors report.

In any case, the impacts will likely go far beyond coccolithophores. In 2009, Andrew Moy, an ice-core research scientist at the Antarctic Climate and Ecosystems Cooperative Research Centre in Hobart, Tasmania, and colleagues reported in *Nature Geoscience* that shell weights of other modern photosynthetic plankton, called foraminifera, are down as much as 35% from those in sediments dating back 50,000 years. Yet another class of plankton, called diatoms, is nearly as prolific. And in an article published online 6 May 2012 in *Nature Climate Change*, Ulf

Riebesell, a biological oceanographer at the Helmholtz Centre for Ocean Research in Kiel, Germany, and colleagues reported that in the South China Sea, diatom carbon use is down by as much as 40%. So if such sinks for atmospheric CO<sub>2</sub> decline, it could have a powerful feedback effect in the coming decades, reducing the amount of CO<sub>2</sub> the oceans can absorb and thereby increasing atmospheric CO<sub>2</sub> levels.

Past lab studies have raised concerns about another vital link in the food chain: pteropods. These tiny sea snails are particularly abundant in polar oceans near the Arctic and Antarctica. Like oyster larvae, pteropods use aragonite to form their shells. But polar seas naturally harbor lower carbonate concentrations, reducing saturation levels. Ocean chemistry monitoring cruises have already shown aragonite saturation

levels in the polar oceans dropping dramatically. If pteropods are unable to respond, that could imperil populations of salmon, krill, whales, and seals that depend directly or indirectly on their bounty. “Things are changing fundamentally in ways that are going to change the ecosystems of the ocean,” Dewey says.

A revealing look at what that change might bring comes from studies of underwater CO<sub>2</sub> seeps, where CO<sub>2</sub> bubbles out of the sea floor near volcanoes, naturally raising pCO<sub>2</sub> levels. Last year, researchers led by Katharina Fabricius, a coral reef ecologist with the Australian Institute of Marine Science in Townsville, reported in *Nature Climate Change* that they looked at three natural CO<sub>2</sub> seeps in tropical waters near Papua New Guinea with pCO<sub>2</sub> levels near levels expected throughout the global oceans in 2100. The biodiversity of coral species there dropped by 40%, and reef development stopped altogether in areas where the pH dropped below 7.7. In a separate study, Riebesell and colleagues found similar destructive impacts on cold-water corals.

Back along the Oregon coast, moderate north winds have returned. And Barton and his colleagues worry that conditions will once again deteriorate to levels other ocean regions won’t see for decades. “I have to admit I get a little annoyed when I hear people always talking about 2050 or 2100,” Barton says. “We’re already at 2050 in Netarts Bay.” It’s a future that doesn’t look kind.

—ROBERT F. SERVICE



## RESEARCH FACILITIES

# Betting Big On Science: A Cautionary Tale

To lure federal investment, South Dakota has spent nearly \$100 million to build an underground lab. Now its gamble is looking like a long shot

**LEAD, SOUTH DAKOTA**—It takes 11 minutes and 25 seconds for the rickety lift here in the abandoned Homestake gold mine to descend the 1478 meters to the Sanford Underground Research Facility (SURF). But that slow ride is a flash compared with the 11 years it took to realize the dream of building a subterranean lab in the mine. And like a dream, the lab's existence may be fleeting.

On 30 May, the state of South Dakota officially opened SURF, a gleaming little facility built with \$40 million in state money and \$50 million from a philanthropist. SURF has the potential to play an outsized role in particle physics in the United States. And two key experiments are already moving in.

But despite that promise, SURF is a far cry from what South Dakota officials had hoped for: an \$875 million national laboratory built by the U.S. National Science Foundation (NSF). Officials acknowledge that they built SURF with the intention of pressuring NSF to commit to the bigger project. Instead, NSF's governing body shot down the idea (*Science*, 17 December 2010, p. 1596), leaving its fate up to the U.S. Department of Energy (DOE).

DOE has requested \$10 million next year to run the place—mostly to pump ground water out of the mine and treat it. But it has

made no promise of support for 2014 and beyond. So South Dakota's investment could end up, literally, under water.

South Dakota's strategy was inherently risky, according to those who track how innovation can spur regional economic development. It's best to think small, they say, and to target research that provides a direct connection to industry. Also, don't depend on the federal government alone for your return on investment. "Given the fairly dismal recent history, it's better to begin with a fair amount of skepticism whether the federal government is going to follow through on its commitments," says Daniel Berglund, president of the nonprofit State Science and Technology Institute in Westerville, Ohio.

Predictably, South Dakota officials remain upbeat. "The future is still wide open," says Republican Governor Dennis Daugaard. "As landlords we've built the building, and I think we'll start attracting tenants now that we've seen a few begin to occupy their improved space."

But T. Denny Sanford, the lab's patron and a Sioux Falls businessman who made a fortune in the credit card industry, doesn't mask his frustration with the way things have played out. "I've never seen the federal gov-



BEFORE

**Finished basement.** In less than 2 years, this tunnel (*inset*) was turned into the Sanford Underground Research Facility.

ernment do anything right—except write the Constitution," he says. Asked if he wishes he'd specified that his donation couldn't be spent before NSF had committed to the project, Sanford smiles ruefully. "Oh yes," he says. "Live and learn."

## A heady wager

To understand what went wrong, it helps to know why South Dakota bet so heavily on a lab in an abandoned mine. Prospectors struck gold here in 1876, and the mine eventually yielded 1.1 million kilograms of the precious metal. For scientists, however, the most valuable discovery came from a mind-boggling experiment conducted in the mine almost 50 years ago.

In the 1960s, Raymond Davis Jr., a chemist at Brookhaven National Laboratory in

Upton, New York, used a crude detector to spot elusive subatomic particles called neutrinos emanating from the sun. In a bare cavern where SURF now stands, Davis filled a tank with 380,000 liters of chlorinated dry-cleaning fluid. The neutrinos converted the chlorine nuclei to argon, and Davis extracted and counted the argon nuclei, produced at the rate of one every few days.

The feat earned Davis a share of the 2002 Nobel Prize in physics and showed the benefits of going underground to avoid interference from background radiation and cosmic rays. So when the company that ran Homestake announced in 2000 that it would close the mine, physicists immediately proposed converting it into a lab.

Their original pitch to NSF was for a \$281 million lab reaching as deep as 2255 meters. There, ultrasensitive detectors would hunt for particles of the mysterious dark matter whose gravity binds the galaxy. Other detectors would search for a type of radioactivity called neutrinoless double beta decay that would prove that the neutrino is its own antiparticle. Such a finding would put a dramatic new twist on the relationship between matter and antimatter. The lab could also hold a huge detector to study neutrinos shot through Earth from DOE's Fermi National Accelerator Laboratory (Fermilab), 1300 kilometers away in Batavia, Illinois. It could even host work in geology, microbiology, and engineering.

Such labs already exist elsewhere. European researchers are pursuing similar physics experiments in Italy's Gran Sasso National Laboratory, at a depth of 1400 meters beneath the Apennines. Researchers in Japan work in the 1000-meter-deep Kamioka mine in Hida in central Japan. U.S. scientists use two smaller labs, one 700 meters deep at the Soudan mine in Minnesota and the second 670 meters below the surface at the Waste Isolation Pilot Plant, a nuclear waste repository in Carlsbad, New Mexico.

The effort to develop Homestake turned into political football, however. The Homestake Mining Company (which later merged

## State Support for DOE Projects



Facility	Location	Description	Total cost	State contribution
Center for Nanoscale Materials (pictured above)	Argonne National Laboratory, Illinois	Research center at existing x-ray synchrotron	\$72 million	\$36 million for the building
Guest House	Lawrence Berkeley National Laboratory, California	Hotel for lab visitors	\$10.9 million	\$10 million
National Synchrotron Light Source II	Brookhaven National Laboratory, Upton, New York	New x-ray synchrotron	\$912 million	Lower-priced electricity to entire lab
Facility for Rare Isotope Beams	Michigan State University, East Lansing	Proposed accelerator	\$615 million	\$94 million

**Chipping in.** Several states have contributed to major projects at DOE national labs, boosting local economies as well as enhancing the facilities.

with the Barrick Gold Corporation in Toronto, Canada) refused to sign the mine over to the federal government unless it was freed from any liabilities. South Dakota's congressional delegation, led by then-Senate Majority Leader Tom Daschle, a Democrat, crafted a deal to do that. But fiscal conservatives complained that it saddled taxpayers with the uncertain cost of environmental cleanup, and the deal fell through. Meanwhile, the company said it would stop pumping ground water out of the mine, which would cause it to flood.

In spite of its rocky road in Washington, D.C., the plan was popular among state politicians. A new national lab could spawn up to 8000 jobs and a billion dollars of commerce, promised Michael Rounds, a Republican who was South Dakota's governor from 2003 to 2011. The project also hit a political sweet spot, says Bernie Hunhoff, a Democrat and minority leader in the South Dakota House of Representatives. Liberal legislators from the eastern part of the state liked the investment in jobs, he says, and conservative legislators in the West liked the fact that, thanks to the mine's location, their districts would reap the benefits. "I think it would have been very hard to sell the project had it been in the eastern part of the state," Hunhoff says.

that the state should build an "interim lab." "If we believed that the project would hold long-term potential, then we would have to take that risk," Rounds says, "because it was pretty clear that Washington wasn't prepared to make that decision [to start building]."

Much of the money for the project would come out of one wallet. Rounds had discussed the idea with Sanford, and at the 2005 Governor's Invitational Pheasant Hunt the billionaire pulled the governor aside and committed to a \$50 million gift. "It was explained to me that the significance of this would be larger than the significance of [Ellsworth Air Force Base] in Rapid City," which houses 9000 people, Sanford recalls.

In October 2005, the state appropriated \$19.9 million for the interim lab. The gamble seemed to have paid off: Two years later, NSF chose Homestake as the site for DUSEL. By June 2009, workers had drained the 1478-meter level and begun work on the lab.

But the state's plans for DUSEL sprung a fatal leak after South Dakota had spent another \$5.4 million on pumping. In December 2010, the National Science Board, which sets policy for NSF, declined to continue design work for DUSEL, whose cost had climbed to \$875 million. The board was concerned about such a large investment in

In January 2004, the state and Barrick agreed to transfer ownership of, and liability for, the mine to the South Dakota Science and Technology Authority, which state legislators created especially for this project. The next month, legislators appropriated \$14.3 million to restart the pumps in Homestake, which had been flooding since the previous June.

But NSF took a step back from what was then called the Deep Underground Science and Engineering Laboratory (DUSEL): Officials decided its location should be determined in a competition and called for proposals. To get a jump on the seven other competitors, South Dakota officials and the team from the University of California, Berkeley, that was developing Homestake decided



infrastructure to support DOE experiments. The board's decision has forced officials at DOE's Office of Science to decide how much, if any, of the project they can afford.

### Swinging for the fences

South Dakota's predicament underscores the risks in investing in large projects. "A lot of states get into project envy," says Robert Atkinson, president of the Information Technology and Innovation Foundation (ITIF), a technology policy think tank in Washington, D.C. "Governors often want to see something tangible. It's in the ground, it's big, and they can say 'I did this.'"

South Dakota is not the first state to spend big to beef up its research capacity. In 2003, Florida pledged \$310 million to cover the first 10 years of operating expenses for a new branch of the California-based Scripps Research Institute in the city of Jupiter, Florida. The next year California voters approved a \$3 billion bond issue to create the California Institute for Regenerative Medicine to fund stem-cell research. It remains to be seen if either investment will pay off, says Atkinson, who argues that states are more successful when they invest in smaller projects and cultivate an "ecosystem" of technological development. "You're a lot better off with a bunch of singles than with one home run," he says.

States also do better to focus on fields with direct connections to industry, experts say. That is why officials with the Division of Science, Technology, and Innovation (NYSTAR) in New York state's Empire State Development department insist that researchers line up industrial partners before they apply for support. "There are very few technology investments that the state has made without showing that somebody else has skin in the game," says NYSTAR director Edward Reinfurt.

That philosophy hasn't prevented New York state from thinking big. Since 1993 it has invested more than \$1 billion in the College of Nanoscale Science and Engineering at the University at Albany, which officials claim has leveraged more than \$13 billion in mostly private investments from companies such as IBM and Intel. But that gargantuan investment was really a series of targeted investments that began with one \$500,000 grant, Reinfurt says.

It also helps if a state already has a strong

research base on which to build. "There's no doubt that having assets in place gives you a critical advantage," Reinfurt says.

### The payoff

South Dakota went all in when building SURF. The facility consists of two large halls connected by a long hallway lined with gleaming silver vents, gray electrical conduits, and white water pipes. The spotless epoxy floor shines under the fluorescent lighting. A visitor can quickly forget that the lab is not on the surface.

Lab officials are hoping that once scientists see the new lab, they'll flock to it. "It's here, it's world class, and the doors are open," says Kevin Lesko of Lawrence Berkeley National Laboratory in California, principal investigator on the project.

Lesko's confidence is bolstered by a report last year from the U.S. National Academies' National Research Council. It deemed the three main physics experiments to be done in a lab like DUSEL—a dark-matter search with a detector weighing between 1 and 10

are meant to be steppingstones to larger detectors. Scientists are hoping that biologists and geologists will jump at the chance to work underground at SURF.

It's equally plausible, however, that SURF will wither and die. The effort to develop Homestake has long been driven by plans to build a huge detector to field neutrinos shot from Fermilab. As originally conceived, that Long-Baseline Neutrino Experiment would use a 34,000-tonne detector filled with liquid argon in Homestake. But in March, officials at DOE's Office of Science said they could not afford to finance the \$1.9 billion experiment in one shot and asked Fermilab researchers for a plan to build it in stages, and for less money (*Science*, 30 March, p. 1553). Current options include a 10,000-tonne detector on the surface of Homestake or a larger detector in Minnesota's Soudan mine. (For a surface detector, physicists would limit interference from background radiation by timing the arrival of the neutrinos.)

So SURF's fate may rest with the outcome of the dark-matter and neutrinoless double beta decay experiments. However, the lab may not be deep enough for the full MAJORANA experiment, meaning that the LUX dark-matter search might be the only experiment in the lab. DOE would then face the question of whether to spend \$15 million per year to run the lab for one \$1.5 million experiment and its \$50 million follow-on effort. "Exactly what happens depends on the outcome of the [early] measurements," says James Siegrist, DOE's associate director for high-energy physics.

Even if DOE decides to support the lab over the long term, it seems likely to remain a research outpost occupied by a couple of dozen graduate students and postdocs and a small staff. (SURF currently employs 120 people.) That reduction in scope doesn't unduly bother state officials, who say they won't regret making a wager on the lab even if it were to close.

"The South Dakota psyche and culture is that we're risk takers and gamblers," says minority leader Hunhoff. "These are ranchers and farmers, and there are no bigger risk takers than ranchers and farmers." If the lab fails, it won't be one of the state's top 10 problems, he says. Of course, it also won't yield the economic jackpot that state officials were expecting.

—ADRIAN CHO



**Opening day.** VIPs get a crash course on how the LUX detector, to be housed in the cylindrical tank, will hunt dark matter.

tonnes, a search for neutrinoless double beta decay with a tonne-scale detector, and the study of neutrinos shot from a distant accelerator—"of paramount and comparable scientific importance."

Two DOE-funded experiments are already moving in. The Large Underground Xenon (LUX) detector will sit in the same spot as Davis's original detector and will search for evidence of dark-matter particles bumping into atomic nuclei in 350 kilograms of frigid liquid xenon. Down the hall, the MAJORANA Demonstrator will search for evidence of neutrinoless double beta decay in 60 kilograms of the isotope germanium-76. Both experiments





PROFILE: ANTHONY FAUCI

## The View From The Top of the HIV/AIDS World

**Science spends a day with immunologist and clinician Anthony Fauci, head of the single largest funder of HIV/AIDS research**

Anthony Fauci runs a marathon every day.

Fauci heads the single largest funder of HIV/AIDS research, the U.S. National Institute of Allergy and Infectious Diseases (NIAID), and the job requires an early start and a late finish. Part of the U.S. National Institutes of Health (NIH), NIAID will dole out nearly one-third of its \$4.5 billion budget to HIV/AIDS researchers in 2012—and Fauci's imprimatur is visible at every level. An immunologist who made fundamental findings about HIV's destructive ways, Fauci was also a key architect of the President's Emergency Plan for AIDS Relief that

provides anti-HIV drugs to millions of the world's poor.

NIAID funds a wide portfolio of research, and controversies repeatedly erupt around Fauci. A native of Brooklyn, New York, who studied at a Jesuit college, Fauci, 71, enjoys a good debate, and this past year alone has found him at the center of hot topics such as mutant forms of the H5N1 bird flu virus that scientists engineered to transmit in mammals and a mouse retrovirus erroneously linked to chronic fatigue syndrome. He is just as comfortable doing rounds with patients as he is testifying to

**Front runner.** Anthony Fauci has headed NIAID for 28 years and tries to fit in a run every day to let off steam.

Congress. He's a go-to source for journalists, and photos that clutter one office wall show Fauci hobnobbing with the likes of presidents Bill Clinton, George H. W. Bush, and George W. Bush, and Mother Teresa, Elizabeth Taylor, and rock star Bono.

Fauci's critics say he is an obsessive-compulsive autocrat with a serious limelight addiction. But in his 28 years occupying the NIAID director's office on the seventh floor of NIH's Building 31 in Bethesda, Maryland, no serious charge against him has stuck—and no one has challenged his commitment.

On 10 May, reporting for the special issue HIV/AIDS in America (see p. 167), *Science* jogged alongside Fauci for the day.

**6:30 a.m.** Fauci answers the flood of e-mails that poured in overnight, reads briefing material, and puts finishing touches on a few papers. It's the only peace he'll have all day.

**8:15 a.m.** A dash to the first-floor cafeteria for a croissant egg sandwich includes brief chats with secretaries, janitors, cashiers, and scientists—but no stopping. "Things are going to seem kind of hectic, because that's my life," he says. "We don't waste time here. I'm a bit of a grump."

**8:22 a.m.** Back in his office, Fauci's three assistants bounce in and out, sitcom fashion. He swears like a scientist, and his rapid-fire patter mixes the demanding and caustic with a dollop of charm. Boston on the 22nd for a *New England Journal of Medicine* panel! NIH Director Francis Collins at *exactly* 6 p.m. to talk about the H5N1 thing! Get the staffer on the phone who attached a three-page memo in an e-mail! "You violated Fauci rule number 26," he barks at the staffer over his speaker phone. "No e-mail longer than one page!" But he likes the memo, which describes a new independent report about NIAID.

"We couldn't look better if we wrote it ourselves," Fauci crows. "Don't ever send me more than a one-page memo again."

He's kidding. But he's not.

**8:51 a.m.** Fauci speed-walks up the hill to the NIH Clinical Center to see patients, which he does 3 days a week. The center recently started treating difficult HIV/AIDS cases from the local community. "It's like the '80s again," he says. "It's great for the fellows." He first sees a woman, 51, who presented with zero CD4 cells—normal is above 600, and 200 is the cutoff for AIDS—



and a skin rash diagnosed elsewhere as cutaneous T-cell lymphoma. "When they told me I had full-blown AIDS, that hurt me," says the woman, explaining that she had been diagnosed 10 years earlier. "I said to the doctor, 'What you telling me? I'm going to die?' And he said, 'Yeah.'" Clinical Center doctors started her on antiretroviral treatment, her rash resolved, and she now has a CD4 count of 122. Before leaving, Fauci notes that she used to live in Brooklyn. "Bensonhurst," she says. "I was born in Bensonhurst!" bellows Fauci, whose Brooklyn accent remains undiluted. "It's inexcusable for somebody to present here with zero CD4s," he says as he exits. She is hardly an anomaly.

**9:06 a.m.** Fauci visits five more patients who have been close to the brink: lymphoma in the stomach, acute renal failure, blinding retinopathy caused by cytomegalovirus. One patient is a nurse who, apparently in denial about his disease, had only 23 CD4s when he presented. Another is a wheelchair-bound man who had a rare case of TB that spread to his knee and an even-rarer complication called chylothorax after starting on antiretroviral drugs. Lymph fluid drained from his lungs filled two 1-liter bottles. "You almost never see this," Fauci said. "This is the 1940s."

**9:43 a.m.** Fauci checks in with his wife, Christine Grady, chief of the Clinical Center's Department of Bioethics. On the speed walk back down the hill to Building 31, he's sorting out the bioethical dilemma he's just witnessed in the clinic. "It's unconscionable in the capital of our nation," Fauci says. "What's going on here?"

**10:02 a.m.** Fauci's inner circle meets for a daily powwow about his schedule, including a commencement address at the University of Miami, an Institute of Medicine meeting on H5N1, and a request to sit on a panel about a revival of the AIDS play *The Normal Heart*, which was written by pioneering AIDS activist and Fauci-basher-turned-best-friend-forever Larry Kramer. "I said I'd only participate if he had De Niro play me," Fauci says.

**11:07 a.m.** "Hugh!" Fauci hollers, calling for his top deputy, the mild-mannered Hugh Auchincloss Jr. Fauci wants to make sure the ExCom—the executive committee meeting later today with his division directors—runs like clockwork. "I have a phenomenal impatience for people who go over their allotted time," Fauci says. One of his three adult daughters phones, and he speaks to her as though time does not exist.

**12:00 p.m.** Fauci changes into a T-shirt, shorts, and sneakers and heads off campus

for a 5-kilometer run, which is followed by a quick shower and a stop at the cafeteria for a yogurt and hummus with pretzels. He eats lunch at his desk, which is followed by a meeting with an investigator in his lab who updates him about cutting-edge HIV cure research.

**1:47 p.m.** "Patty!" Fauci, reviewing his schedule for his commencement talk in Miami, is pissed that he has to kill time at his beachfront hotel. "I have 5 hours of doing nothing," he complains to Patricia Conrad, his right-hand woman, who formerly worked at the White House. He then puts finishing touches on slides for the opening plenary that he will give at the 19th International AIDS Conference. Fauci may be the only presenter at the meeting who has finished preparing for his talk 2 months early.



**Political office.** Fauci's job blends science and medicine with diplomacy and policy.

**3:30 p.m.** The ExCom gathers 30 of NIAID's top brass in a conference room, and the bland review of budgetary issues segues into a spicy discussion about H5N1 and the ripple effects of the bird flu controversy. NIAID funds studies of many other pathogens, and Fauci asks whether it should continue to support any "gain-of-function" experiments that aim to better understand how a bug transmits or causes disease. "We have to get this aired out," Fauci says. "I would love to do this in a very transparent way."

**5:00 p.m.** At a gathering of Fauci's own lab members, a researcher reviews a study of a promising experimental hepatitis C drug. Fauci is wowed by possibilities: There are three times as many people in the United States infected with the hepatitis C virus as

with HIV, and the new drugs have little toxicity and can outright cure many infections.

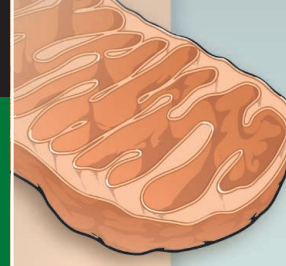
**6:01 p.m.** NIH Director Collins summons Fauci to his office for a private meeting to discuss H5N1.

**6:30 p.m.** Two high school girls interview Fauci about global ethics. "What's the most important issue you are now facing?" one of the girls asks. "My hope is that in the next 5 years, if we as a nation and a world have the political will to implement what we already have, we're going to probably see a dramatic turnaround in the AIDS epidemic," he says. The girls notice a photo of Fauci with Paul Farmer, the Harvard clinician widely celebrated for his HIV/AIDS work in Haiti. "What was it like meeting him?" one of the awestruck girls asks. Fauci, amused, dryly says that they met in

the late 1980s when he spoke to Farmer's medical school class at Harvard. When they ask him to name his favorite person, he graciously embraces their exuberance and offers that Farmer is one of them. "He really walks the walk," says the man who really runs the run.

**7:12 p.m.** A network television producer wants to preinterview Fauci for a possible appearance early tomorrow morning. "She said she wants you to send her home with something solid," Conrad says. Fauci phones the producer, who has a shaky grasp about HIV/AIDS and needs a 101 lesson, which he obligingly gives. By the time he hangs up at 7:30, he's spent. "It's going to be one of those days tomorrow," he says.

—JON COHEN



## LETTERS

edited by Jennifer Sills

## Canada's Weakening Aquatic Protection

CANADA'S REPUTATION AS A NATURAL WONDERLAND HAS TAKEN A BEATING LATELY FROM AN unlikely foe: its own government. Over the past months, deep budget cuts to departments with environmental responsibilities have been announced, including the closure of entire ecotoxicology labs and a unique large-scale aquatic research facility (1). There are also proposals to amend some of the strongest pieces of environmental legislation in the country, including the Fisheries Act. The Fisheries Act currently prohibits activities that harm the habitat of any fish species in any Canadian waters, either fresh or marine, but the new wording would limit protection only to those fishes involved in fisheries (2). This opens the door to unrestricted development on any water body as long as it does not contain federally listed endangered species or fish targeted by a fishery.

The government justifies changing the legislation by saying that it has been applied indiscriminately against ditches or other structures unlikely to bear fish, thereby interfering with landowners and farmers (3). They further argue that removing habitat protection would "[enable Canadians] to undertake activities on their properties without obtrusive interference" (4), implying that the law in its current form is inappropriately preventing routine activities from taking place.

This justification is not supported by the evidence. Between 2006 and 2011, only one proposal in thousands reviewed through the federal environmental assessment process was turned down, and its rejection was only partly due to potential destruction of fish habitat. Furthermore, a survey we conducted of 285 press releases, concerning 1283 convictions by the federal government for violations of the Fisheries Act between 2007 and 2011, showed that only 21 pertained to destruction of fish habitat (5). These low numbers could

reflect compliance with the habitat provision of the law, in which case there is no reason to alter it, or a poor enforcement capacity, which cannot be blamed on the law. Neither line of evidence suggests obtrusive interference by the federal government on behalf of fish habitat protection.

The Fisheries Minister argued that current policies go "well beyond what is necessary to protect fish" (6). The continued decline of Canadian fish and other aquatic species due to habitat loss and degradation suggests otherwise (7). The scientific case for protecting aquatic habitats is as strong as ever, and the justifications for weakening protection do not bear up to reasonable scrutiny. Canada should stand up to its responsibility as first signatory to the Convention on Biological Diversity and steward of the world's longest coastline and several of the largest lakes.

BRETT FAVARO,\* JOHN D. REYNOLDS, ISABELLE M. CÔTÉ

Earth to Ocean Group, Department of Biological Sciences, Simon Fraser University, Burnaby, BC V5A 1S6, Canada.

\*To whom correspondence should be addressed. E-mail: bfavaro@sfu.ca

## References

1. H. Hoag, "Canada's renowned freshwater research site to close," *Nature News* (21 May 2012).
2. Canada, Parliament, House of Commons, "An Act to implement certain provisions of the budget tabled in Parliament on March 29, 2012 and other measures," Bill C-38, 41st Parliament, 1st Session, 2011–2012 (Public Works and Government Services Canada, Ottawa, Canada, 2012).
3. Canada, Parliament, House of Commons, Debates, 41st Parliament, 1st session, No. 113 (2012).
4. P. O'Neil, "Fisheries Act changes introduced amid debate over new law's intent," *Vancouver Sun*, 26 April 2012.
5. B. Favaro, J. D. Reynolds, I. M. Côté, "List of published convictions under the Canadian Fisheries Act, 2007–2011" (<http://tmel.wordpress.com/research-2/brett-favaro/fisheries-act/>).
6. Canada, Parliament, House of Commons, Debates, 41st Parliament, 1st session, No. 109 (2012).
7. J. T. Quigley, D. J. Harper, *Env. Manage.* **37**, 351 (2006).

Published online 21 June 2012; 10.1126/science.1225523

Postmarketing Trials  
for Rare Diseases

WE FULLY AGREE WITH THE POLICY FORUM "Rethinking research ethics: The case of postmarketing trials" (4 May, p. 544), in which A. J. London *et al.* argue for rigorous, ethical, postmarketing (phase IV) trials for licensed drugs. We believe, moreover, that these phase IV studies should be mandatory for orphan products, which are developed specifically for rare and/or neglected diseases, as these products are usually approved after limited testing by the manufacturer's R&D department.

At present, there is an urgent need to produce reliable medical information about rare diseases, as the lack of data is a problem that affects vulnerable populations worldwide. It can take a long time to collect sufficient data (including health and social end points), but patients suffering from rare diseases have the right to be assisted with the same accuracy and efficacy as those with common diseases.

VIRGINIA A. LLERA\* AND EMILIO J. A. ROLDÁN

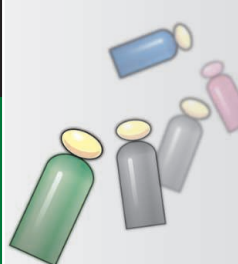
GEISER Foundation, Avellaneda 595, Mendoza (5500), Argentina.

\*To whom correspondence should be addressed. E-mail: fundgeiser@yahoo.com.ar



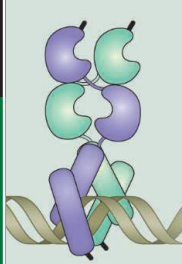
Lake Louise, Alberta, Canada





Another flu viral  
protein found

164



Mammalian clock  
mechanism

165



theBUZZ

## NSF's Big Pitch

On 25 May, a News & Analysis story titled "NSF's 'Big Pitch' tests anonymized grant reviews" (Y. Bhattacharjee, p. 969) described a National Science Foundation (NSF) study comparing the review results between grant proposals written in the standard format and versions rewritten as two-page summaries and stripped of investigator names. Results showed little overlap between the subset of grants in each group that reviewers rated as high priority, indicating that the format may affect funding selection. NSF plans to conduct further studies and track the success of the grants selected through the shorter, "Big Pitch" summaries. Many readers wrote in to comment on the study and its implications. Excerpts from some of those comments are below. You can read all the comments at <http://comments.sciencemag.org/content/10.1126/science.336.6084.969>.

### A selection of your thoughts:

...[Y. Bhattacharjee states] that NSF's Molecular and Cellular Biosciences (MCB) Division "plans to institute the (four-page preproposal) system soon." The MCB Division has no plans to change from the current policy of accepting full-length regular proposals. The article also did not acknowledge that two divisions within Biological Sciences at NSF participated in the "Big Pitch" experiment in proposal review: the MCB and the Division of Integrative Organismal Systems (IOS). —John Wingfield (Assistant Director, Directorate for Biological Sciences, NSF)

...If we maintain that preclinical/clinical research should be done blinded, this concept should be extended to the grant review process as well. Bold ideas do not necessarily require a proven "track record"; imagine the fate of the then-novel PCR invention proposal by the current system. The merit of any grant proposal should initially be reviewed blinded with minimum strings attached. This process would free up conflicting reviewers and result in innovative and transformative funded proposals. —Debomoy Lahiri

...[I]t is clear that the "plan" is everything for the standard 15-page proposal.... A great idea with an incomplete, unclear, or uncertain plan of action will not get funded; a good idea with a good plan will. For the two-page proposals, it will be impossible to give many details of the plan, so it will have to be judged in large part by judgment and supposition on what would be done. I am uncertain on whether this is a good idea or not.... Another side effect is that if it becomes much easier to submit proposals, PIs will simply submit more—doubling or tripling the number they submit over a funding cycle.... —Andrew Kennedy

...Even if you showed the same set of proposals to the same review panel on different days of the week, they would select different proposals. And in the end, this would not matter much (for the taxpayer) because the selected proposals were all very good. Favoring "proven track record" over "originality" is not bad per se, it's just a deliberate political choice. Many people do that when their own money is at stake.... —b eber

...It is a shame that many new ideas get shot down in favor of "proven track records," which often are repeating minor variations of the same work already published.... —David Donze

## CORRECTIONS AND CLARIFICATIONS

**News & Analysis:** "Young researchers deserve more support, reviews say," by M. Price (22 June, p. 1489). The story did not credit a co-chair of the reporting group: Sally Rockey, NIH deputy director of extramural research.

**News & Analysis:** "Action urged to curb racial bias in NIH grants," by M. Price (22 June, p. 1490). The story did not credit a co-chair of the reporting group: Lawrence Tabak, NIH principal deputy director.

**Reports:** "Baseline map of carbon emissions from deforestation in tropical regions" by N. L. Harris *et al.* (22 June, p. 1573). In Table 1, fourth column, "Gross forest cover loss, 2000–2005," the unit "Mha year<sup>-1</sup>" (million hectares per year) is incorrect. The correct unit is Kha year<sup>-1</sup> (1000 hectares per year).

**Perspectives:** "Beyond Turing's machines" by A. Hodges (13 April, p. 163). The volume in Ref. 4 was incorrect. The correct reference is: A. M. Turing, *Mind* 59, 433 (1950).

## TECHNICAL COMMENT ABSTRACTS

### Comment on "Plant Species Richness and Ecosystem Multifunctionality in Global Drylands"

Tommaso Jucker and David A. Coomes

Maestre *et al.* (Reports, 13 January 2012, p. 214) reported a general, but weak, positive relationship between plant diversity and ecosystem multifunctionality in global drylands. We show that the strength of this relationship changes consistently along multiple environmental gradients, becoming strongly positive in stressed habitats. This suggests that biodiversity loss may have especially strong consequences in harsh environments. Full text at [www.sciencemag.org/cgi/content/full/337/6091/155-c](http://www.sciencemag.org/cgi/content/full/337/6091/155-c)

### Response to Comments on "Plant Species Richness and Ecosystem Multifunctionality in Global Drylands"

Fernando T. Maestre, Santiago Soliveres, Nicholas J. Gotelli, José L. Quero, Miguel Berdugo

Jucker and Coomes claim that the relationship between plant species richness (biodiversity) and ecosystem multifunctionality (B-EMf) reported in our study changes along environmental gradients. We point out flaws in their analytical approach and then reanalyze our data to further demonstrate that the B-EMf relationship does not substantially change along environmental gradients. Full text at [www.sciencemag.org/cgi/content/full/337/6091/155-d](http://www.sciencemag.org/cgi/content/full/337/6091/155-d)

## Letters to the Editor

Letters (~300 words) discuss material published in *Science* in the past 3 months or matters of general interest. Letters are not acknowledged upon receipt. Whether published in full or in part, Letters are subject to editing for clarity and space. Letters submitted, published, or posted elsewhere, in print or online, will be disqualified. To submit a Letter, go to [www.submit2science.org](http://www.submit2science.org).

# Comment on “Plant Species Richness and Ecosystem Multifunctionality in Global Drylands”

Tommaso Jucker\* and David A. Coomes

Maestre *et al.* (Reports, 13 January 2012, p. 214) reported a general, but weak, positive relationship between plant diversity and ecosystem multifunctionality in global drylands. We show that the strength of this relationship changes consistently along multiple environmental gradients, becoming strongly positive in stressed habitats. This suggests that biodiversity loss may have especially strong consequences in harsh environments.

In light of global change and its consequences for plant and animal communities, exploring and quantifying the link between biodiversity and ecosystem multifunctionality (B-EMf) has become a priority for ecologists and stakeholders alike (1). Maestre *et al.* (2) measured 14 ecosystem properties related to the storage and flux of nutrients [carbon (C), nitrogen (N), and phosphorus (P)] in 224 vegetation plots distributed across all major dryland ecosystems. From these, the authors derived an index of ecosystem multifunctionality (M) that was significantly positively related to the richness of perennial vascular plants. Although weak (regression model  $R^2 = 0.03$ ), this pattern persisted even after having accounted for the confounding effects of

environmental covariates influencing M. Because of the global scale of the study, the focus on multiple ecosystem processes (1, 3) and the vulnerability of drylands to climate change, this study represents an important contribution to its field. However, we reveal that the association between biodiversity and ecosystem multifunctionality in drylands is more complex than initially thought and highlight how this relationship changes consistently and predictably along different environmental gradients, becoming progressively stronger and more positive as environmental stress increases.

The role of abiotic stress in shaping plant interactions has been extensively studied in ecology and is conceptualized in the stress-gradient hypothesis (SGH), which predicts competition (i.e., negative interactions) to dominate under favorable environments, whereas facilitative processes (i.e., positive interactions) increase as conditions become harsher (4). These same ecological processes (competition and facilitation)

help explain how biodiversity may enhance (or impede) ecosystem functioning (5), suggesting that the strength of the B-EMf relationship should vary along environmental gradients in response to changes in the net effect of species interactions (6). Therefore, the most basic expectation is that B-EMf patterns shift from weak or even negative where conditions are favorable and competition is prominent, to strong and positive under harsher environments (6, 7). Maestre *et al.* (2) focus on drylands, which encompass arid, semi-arid and dry-subhumid ecosystems and exhibit a considerable range of environmental conditions (e.g., mean annual precipitation: 66 to 1219 mm/year; elevation: 69 to 4668 m; soil sand content: 5 to 98%; mean annual temperature:  $-2$  to  $28^\circ\text{C}$ ). In light of this, we reanalyzed the data presented in the study to determine how accounting for differences in environmental stress would influence the effect of species richness on ecosystem multifunctionality.

We identified environmental stress gradients [as defined in (4)] from data available in Maestre *et al.* (2) and other data sources. Measures of terrain slope and soil sand content were obtained from the original study, while FetchClimate (<http://fetchclimate.cloudapp.net>) was used to extract environmental variables related to stress (8). We removed strongly correlated predictors and used principal components analysis (PCA) ordination to obtain a measure of water availability (8). Following Maestre *et al.*'s (2) method, Z scores were then computed for the selected environmental stress variables (water availability, sand content, terrain slope, temperature range, frost days, and wind speed), and for each plot a stress index (S) was calculated by averaging the Z score of all predictors. Based on this, we divided the data into three equal-number S classes (low, intermediate, and high,

Forest Ecology and Conservation Group, Department of Plant Sciences, University of Cambridge, Downing Street, Cambridge CB2 3EA, UK.

\*To whom correspondence should be addressed. E-mail: tj272@cam.ac.uk

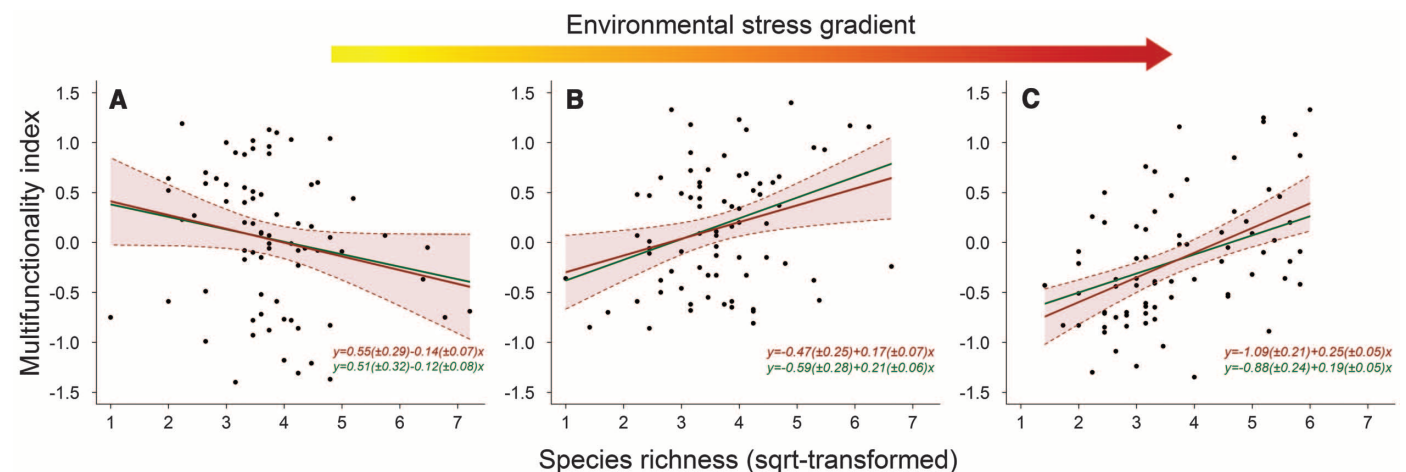


**Fig. 1.** Scatter plots of ecosystem multifunctionality (M) as a function of species richness [square-root transformed for comparability with (2)] along an increasing environmental stress gradient (from left to right): low (A), intermediate (B), and high (C) stress. Red and green lines represent the fitted OLS and SAR models, respectively. The shaded region in red corresponds to

the 95% confidence intervals of the OLS regression. Linear regression equations ( $\pm$ SE for parameter estimates) are reported for OLS (red) and SAR (green) models. Regression results were (A) OLS,  $R^2 = 0.046$ ,  $P = 0.065$ ; SAR,  $P = 0.113$ ; (B) OLS,  $R^2 = 0.083$ ,  $P = 0.012$ ; SAR,  $P < 0.001$ ; (C) OLS,  $R^2 = 0.224$ ,  $P < 0.001$ ; SAR,  $P < 0.001$ .



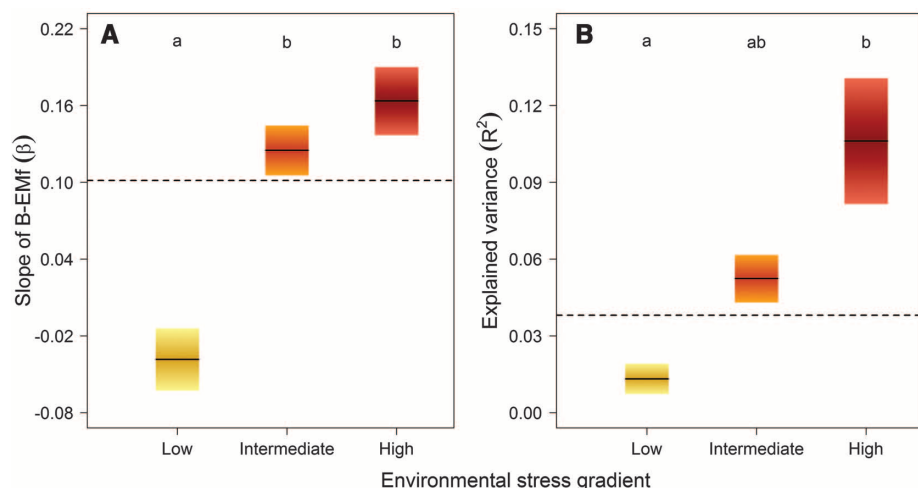


**Fig. 2.** Plots comparing the (A) slope ( $\beta$ ) and (B) explained variance ( $R^2$ ) of the B-EMf relationship for different levels of environmental stress. For each environmental stress variable used to calculate S, the data was divided into low, medium, and high stress classes, after which  $\beta$  and  $R^2$  values for each class were obtained from OLS regressions. Boxes represent mean (black line) and standard errors. Lower-case letters refer to statistically homogeneous subsets (analysis of variance with Tukey honestly significantly different test;  $\alpha = 0.05$ ). Dashed lines provide a comparison with Maestre *et al.*'s (2) original analysis, after correction for reduced sample size. This was achieved by fitting OLS regressions to random subsets of the data (75 randomly selected plots; replicated 999 times) and then plotting mean  $\beta$  (A) and  $R^2$  (B) values.

with 74 to 75 plots each) and repeated the authors' regression analysis [ordinary least-squares (OLS) and simultaneous autoregression (SAR)] for the three groups separately (9). In this way, we were able to test how both the strength (explained variance,  $R^2$ ) and slope (slope parameter,  $\beta$ ) of the B-EMf relationship changes across multiple environmental stress gradients.

We found that B-EMf patterns differed considerably among S classes, and did so in accordance with the predictions of the SGH (Fig. 1). The B-EMf relationship shifted from slightly negative in the low S plots ( $R^2 = 0.046$ ;  $\beta = -0.138$ ) to increasingly positive in the intermediate ( $R^2 = 0.083$ ;  $\beta = 0.168$ ) and high ( $R^2 = 0.224$ ;  $\beta = 0.247$ ) S class, respectively. To highlight the consistency of this result, we also considered each environmental stress variable used to calculate S individually and sorted the data according to their values. We then repeated the regression analysis separately for each of these environmental gradients, highlighting very similar B-EMf patterns across all of them. This com-

mon trend can be clearly seen when  $R^2$  and  $\beta$  estimates of the separate models are compared among stress classes, with  $R^2$  becoming increasingly strong and  $\beta$  shifting from negative to positive as stress increases (Fig. 2).

Along with focusing on B-EMf, the authors also investigated the effects of species richness on ecosystem functions related to C, N, and P individually. In repeating their analysis while accounting for environmental stress, we found the same pattern of increasing importance described for B-EMf in all three nutrient pools. While unsurprising for C and N (both of which covary strongly with M;  $r > 0.93$ ), this is important to note for P (which is less correlated with M;  $r < 0.55$ ). Although P availability was little affected by species richness in the authors' initial analysis, a strongly significant relationship emerged once stress had been accounted for.

Collectively, our analyses revealed that the general positive B-EMf relationship in global drylands reported by Maestre *et al.* (2) masks strong and contrasting underlying patterns. By

accounting for the effect of environmental stress on ecological interactions, we considerably improved model predictions and identified a consistent trend of shifting B-EMf patterns in relation to environmental stress. In conjunction with the original study, our results provide a strong basis for research aiming to disentangle large-scale B-EMf patterns in plant communities and highlight the value of considering both general relationships and their underlying variability. A better understanding of how biodiversity interacts to promote ecosystem functioning is crucial if areas of conservation priority are to be identified and attempts to mitigate the effects of global change are made. Our findings indicate that the effect of biodiversity loss on ecosystem multifunctionality might be particularly severe in harsh environments.

## References and Notes

1. J. Reiss, J. R. Bridle, J. M. Montoya, G. Woodward, *Trends Ecol. Evol.* **24**, 505 (2009).
2. F. T. Maestre *et al.*, *Science* **335**, 214 (2012).
3. B. J. Cardinale *et al.*, *Am. J. Bot.* **98**, 572 (2011).
4. F. T. Maestre, R. M. Callaway, F. Valladares, C. J. Lortie, *J. Ecol.* **97**, 199 (2009).
5. D. U. Hooper *et al.*, *Ecol. Monogr.* **75**, 3 (2005).
6. F. T. Maestre *et al.*, *Phil. Trans. R. Soc. B* **365**, 2057 (2010).
7. A. Paquette, C. Messier, *Glob. Ecol. Biogeogr.* **20**, 170 (2011).
8. For each study plot, FetchClimate was used to extract the following environmental variables: near-surface air temperature, precipitation rate, soil moisture, near-surface air humidity, diurnal temperature range, near-surface wind speed, percent of maximum possible sunshine, and frost day frequency. Pearson product-moment correlation coefficients ( $r$ ) were then used to identify strongly correlated variables ( $|r|$ : 0.55 to 0.89). Based on this, air temperature was excluded from further analysis, while component 1 of a PCA among soil moisture ( $r = 0.91$ ), precipitation rate ( $r = 0.87$ ), sunshine fraction ( $r = -0.85$ ), and air humidity ( $r = 0.68$ ) was included as measure of water availability. Therefore, the selected predictors were terrain slope and soil sand content [available in (2)], water availability, temperature range, frost days, and wind speed ( $|r| < 0.55$ ).
9. We tested the sensitivity of our results to the criteria adopted for subdividing the data by repeating the analyses with different numbers of subsets (2, 3, 5, and 7 stress classes). In all cases, B-EMf patterns along environmental gradients were highly comparable.

**Acknowledgments:** We thank P. De Frenne and F. Rodriguez-Sanchez for their insightful comments and are indebted to E. C. Randall for encouragement.

13 February 2012; accepted 21 May 2012  
10.1126/science.1220473

# Response to Comment on “Plant Species Richness and Ecosystem Multifunctionality in Global Drylands”

Fernando T. Maestre,<sup>1\*</sup> Santiago Soliveres,<sup>1</sup> Nicholas J. Gotelli,<sup>2</sup>  
José L. Quero,<sup>1</sup> Miguel Berdugo<sup>1</sup>

Jucker and Coomes claim that the relationship between plant species richness (biodiversity) and ecosystem multifunctionality (B-EMf) reported in our study changes along environmental gradients. We point out flaws in their analytical approach and then reanalyze our data to further demonstrate that the B-EMf relationship does not substantially change along environmental gradients.

We reported the existence of a positive and significant relationship between plant species richness (biodiversity) and ecosystem multifunctionality (B-EMf) in global drylands (1). Jucker and Coomes (2) extended our analyses to explore the effects of “environmental stress” on the B-EMf relationship. They constructed a stress index (S) based on abiotic variables and showed that the slope and  $R^2$  of the B-EMf relationship varies with stress. We first discuss the lack of suitability of their analytical approach and conceptual framework and then reanalyze our data in light of the interesting question raised by these authors.

There are technical flaws that invalidate the analyses made by Jucker and Coomes. First, they incorrectly calculated Z scores for water stress. We found a perfect negative correlation between their Z score for water availability and their untransformed variable (Fig. 1A). As a consequence, their measure of stress (S index) is positively correlated with average water availability (Fig. 1B), a correlation that makes no ecological sense in drylands (3). Second, their S index is based on averages of the Z scores of negatively correlated environmental variables (sand content and slope, Spearman's  $\rho = -0.464$ ,  $n = 224$ ,  $P < 0.001$ ). Different, but inversely correlated, stress factors can cancel one another out when calculating S and may suggest a relatively low stress level when it is actually high. This problem has been previously discussed in the context of multifunctionality indices (4), as we stated in our manuscript [page 7 of the supporting online material (SOM) in (1)]. These analytical flaws led Jucker and Coomes to mis-

classify our sites into inappropriate stress categories. For example, some sites in Chile (numbers 52 to 54 in our database) with annual rainfall well below 100 mm and a high sand content (~80%), but low slopes and no important frost or wind damage, were classified as “low stress” by Jucker and Coomes. In fact, these sites are extremely arid and are classified as highly stressed, following international and well-established classification schemes for drylands (5).

Apart from the analytical problems, Jucker and Coomes invoked the stress-gradient hypothesis (SGH) (6) to explain the stronger B-EMf relationship under harsher conditions. Claims made by these authors, such as “We found that B-EMf patterns differed considerably among S classes, and did so in accordance with the predictions of the SGH,” are incorrect because the predictions of the SGH have nothing to do with B-EMf relationships, but rather with the relationship between plant-plant interactions and stress. Although these interactions can help to explain the relationship between species richness and ecosystem functioning (7), they are not the only, nor even the most important, mechanism invoked to explain the B-EMf relationship. The sampling effect, the insurance hypothesis, and the resource complementarity hypothesis [reviewed in (8)] are other plausible explanations, which cannot be evaluated properly with the data gathered in our study.

Despite the analytical errors found in Jucker and Coomes' contribution, they raise an interesting question (does the B-EMf relationship change along environmental gradients), which clearly deserves exploration. We therefore repeated our model selection analysis (9), introducing interaction terms (species richness by abiotic variables) as potential predictors. Each interaction term was calculated as the product of the centered variables (plant species richness

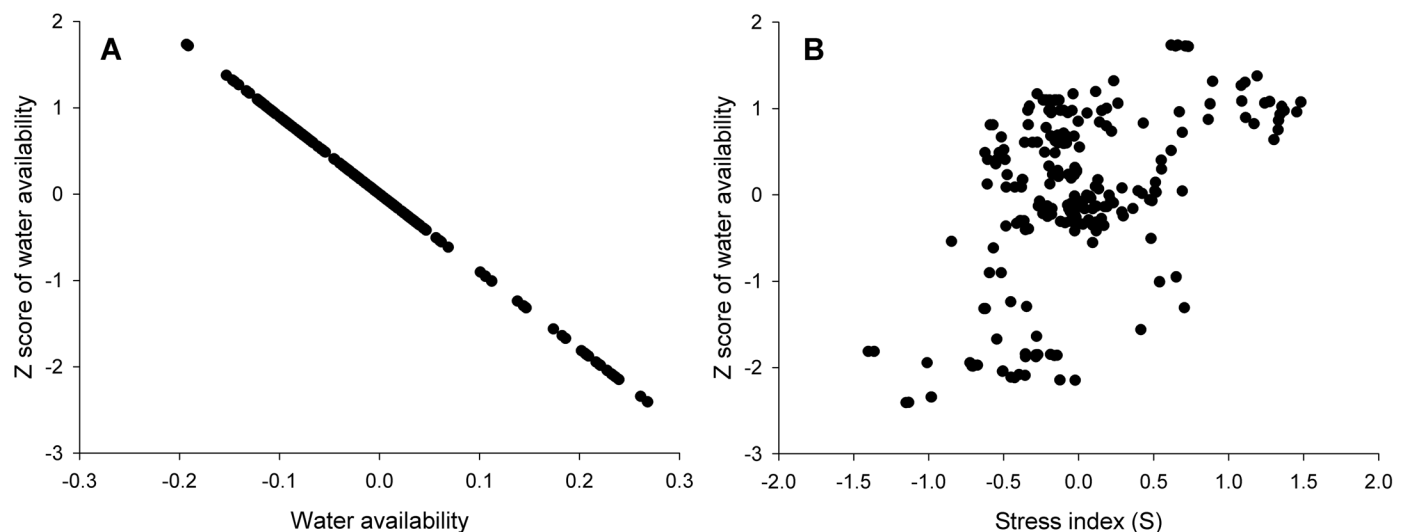


**Fig. 1.** Relationships between the Z score of water availability and the untransformed values of this variable (A), and between the Z score of water availability and the S index used by Jucker and Coomes (B). Results of nonparametric correlations in (B) are as follows: Spearman's  $\rho = 0.420$ ,  $n = 224$ ,  $P < 0.001$ .

<sup>1</sup>Área de Biodiversidad y Conservación, Departamento de Biología y Geología, Escuela Superior de Ciencias Experimentales y Tecnología, Universidad Rey Juan Carlos, Calle Tulipán Sin Número, 28933 Móstoles, Spain. <sup>2</sup>Department of Biology, University of Vermont, Burlington, VT 05405, USA.

\*To whom correspondence should be addressed. E-mail: fernando.maestre@urjc.es



and the corresponding abiotic measure) (10). If the inclusion of these interaction terms modifies the regression coefficients of other predictors, or substantially increases the variance explained by the model, it would imply that the B-EMf relationship changes along environmental gradients. We ran two new sets of models with our multifunctionality index as the dependent variable and compared them with our original set of models (Fig. 2A). Model set A included the original variables, plus four interaction terms between plant species richness and the four principal components analysis (PCA) components describing major climatic features of our study sites (1) (Fig. 2B). Model set B included the original variables plus four interaction terms between plant species richness and abiotic variables related to the degree of environmental stress

(average rainfall, average annual temperature, annual temperature range, and sand content) (Fig. 2C). We quantified the relative importance of the different predictors as described in our original manuscript [page 9 of the SOM in (1)]. Regardless of the combination of variables chosen, our results were robust and virtually identical to those presented in our original analyses (Fig. 2). The inclusion of the new interaction terms did not modify the regression coefficients of other predictors. Annual mean temperature and sand content were the two most important predictors of multifunctionality, followed by plant species richness, slope, and elevation. The interaction terms were always weaker than the original variables, and they collectively increased the variance explained by less than 0.5%. In both model sets, one of the richness by abiotic inter-

action terms were chosen in the best model. However, the addition of these interactions terms did not improve our original model. [Difference in Akaike information criterion (AIC) between the best model and our original model was below 2 in both cases (Table 1).] We also repeated the analyses using other interactions, and their outcome was the same (11). Overall, these results suggest that the significant relationship between plant species richness and ecosystem multifunctionality that we originally described does not substantially change along environmental gradients. We never claimed that the relationship between species richness and multifunctionality was universal, or even that it was constant, and acknowledged in our paper that other abiotic and biotic factors that are known to affect ecosystem functioning can be responsible for the

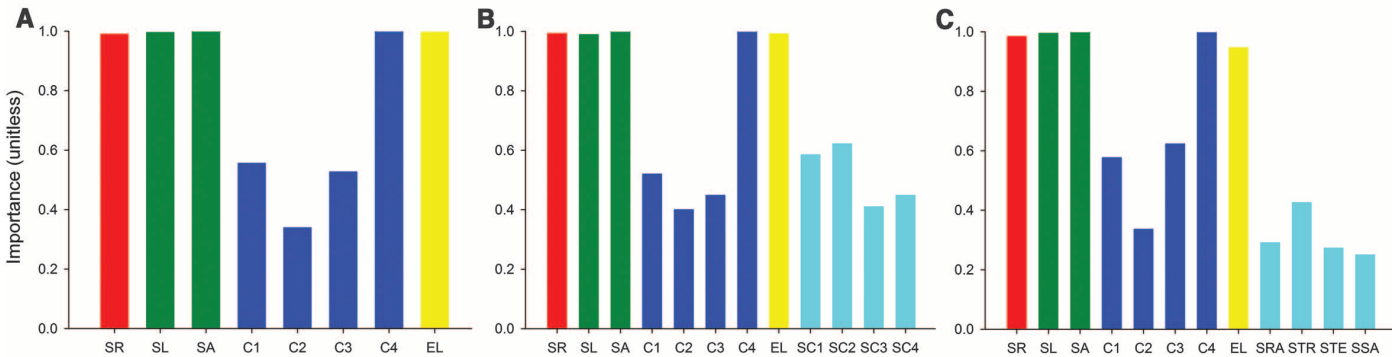


**Fig. 2.** Relative importance of perennial plant species richness (red column, SR) and other predictor variables in models of ecosystem multifunctionality. The height of each bar is the sum of the Akaike weights of all models that included the predictor of interest, taking into account the number of models in which each predictor appears. Interaction terms between plant species richness and abiotic variables are shown in light blue. (A) Original model analysis from Maestre *et al.* (1). (B) Original variables plus interaction terms with climate PCA variables. (C) Original variables plus interactions with

aridity-related variables. C1, C2, C3, and C4, first, second, third, and fourth components of a PCA conducted with climatic variables; SA, sand content; SL, slope angle (square root–transformed); EL, elevation (square root–transformed); SRA, STR, STE, and SSA, interaction terms between plant species richness and average annual rainfall, temperature range, and annual temperature and sand content, respectively; SC1, SC2, SC3, and SC4, interaction terms between plant species richness and C1, C2, C3, and C4, respectively.

**Table 1.** Best-fitting regression models of ecosystem multifunctionality of the new sets of models analyzed (A and B). Each column represents a different predictor variable (red, perennial plant species richness; green, abiotic variables; blue, climatic variables; gold, geographic variables; light blue, richness by abiotic variables interaction terms). The three best models within each set are presented, ranked according to their second-order AIC (AIC<sub>c</sub>) value. In set A, we also include the model originally presented in Maestre *et al.* (1) to allow comparison of the amount of variance explained

and the differences in AIC<sub>c</sub>. This model is the second-best model in set B. AIC<sub>c</sub> measures the relative goodness of fit of a given model; the lower its value, the more likely it is that this model is correct. Unshaded cells indicate variables that were not included in a particular model. *w<sub>i</sub>*, Akaike weights;  $\Delta AIC_c$ , difference between the AIC<sub>c</sub> of each model and that of the best model ( $\Delta AIC_c$  values below 2 indicate that the models being compared are approximately equivalent in explanatory power). Other abbreviations as in Fig. 2.

Model set	Abiotic				Climatic				Geographic			Interaction terms				R <sup>2</sup>	AIC <sub>c</sub>	ΔAIC <sub>c</sub>	w <sub>i</sub>
	SR	SL	SA		C1	C2	C3	C4	LA	LO	EL	SC1	SC2	SC3	SC4				
A																0.567	281.35	–	0.024
																0.571	281.36	0.014	0.023
																0.571	281.63	0.285	0.020
																0.564	282.75	1.405	0.012
B																			

scatter found in our results (1). We also believe that the amount of variance in the B-EMf relationship not explained by the variables we measured clearly deserves further attention (12). However, the main take-home message of both our original manuscript and this response is that, despite the multiple sources of variation, there is a significant positive B-EMf relationship in global drylands and that species richness is an important positive predictor of ecosystem multifunctionality. The latter result was consistent after accounting for other major environmental factors and their interactions with plant species richness.

#### References and Notes

1. F. T. Maestre *et al.*, *Science* **335**, 214 (2012).
2. T. Jucker, D. A. Coomes, *Science* **337**, 155 (2012); [www.sciencemag.org/cgi/content/full/337/6091/155-c](http://www.sciencemag.org/cgi/content/full/337/6091/155-c).
3. W. G. Whitford, *Ecology of Desert Systems* (Academic Press, San Diego, CA, 2002).
4. L. Gamfeldt, H. Hillebrand, P. R. Jonsson, *Ecology* **89**, 1223 (2008).
5. UNEP, *World Atlas of Desertification* (Edward Arnold, London, 1992).
6. M. D. Bertness, R. M. Callaway, *Trends Ecol. Evol.* **9**, 191 (1994).
7. C. P. H. Mulder, D. D. Uliassi, D. F. Doak, *Proc. Natl. Acad. Sci. U.S.A.* **98**, 6704 (2001).
8. D. U. Hooper *et al.*, *Ecol. Monogr.* **75**, 3 (2005).
9. K. P. Burnham, D. R. Anderson, *Model Selection and Multimodel Inference: A Practical Information-Theoretic Approach* (Springer, New York, ed. 2, 2002).
10. G. P. Quinn, M. J. Keough, *Experimental Design and Data Analysis for Biologists* (Cambridge Univ. Press, Cambridge, 2002).
11. Apart from the models described in the text, two additional sets of models were evaluated. One of them included the original variables plus four interaction terms between plant species richness and the climatic variables most correlated with the four PCA components (average rainfall, mean temperature and rainfall during the driest quarter, and mean temperature during the wettest quarter) [page 6 of the SOM in (1)]. The other set of models included the original variables plus the interaction between species richness and a widely used aridity index (precipitation/potential evapotranspiration) (5). The analyses of these sets of models produced virtually identical results to those presented in the text; the best models for each of the two model sets described here did not include any of the richness by abiotic variables interaction terms. Collinearity among independent variables in all the new sets of models conducted was negligible.
12. A. Paquette, C. Messier, *Glob. Ecol. Biogeogr.* **20**, 170 (2011).

**Acknowledgments:** We thank A. Escudero, D. Eldridge, M. Bowker, P. García-Palacios, and M. Delgado-Baquerizo for discussions on this response. This research was funded by the European Research Council under the European Community's Seventh Framework Programme (FP7/2007-2013)/ERC grant agreement 242658 (BIOCOM).

27 February 2012; accepted 21 May 2012  
10.1126/science.1220620



## ECONOMICS

## An Uncommonly Open Approach

Edella Schlager

In *Infrastructure: The Social Value of Shared Resources*, Brett Frischmann makes the counterintuitive argument that open access is the key for ensuring the provision of public and social goods such as the Internet or social capital. Conventional wisdom, based on microeconomic analysis, argues for limiting access and discriminating among uses of infrastructure (typically through various pricing policies) as the means for allowing providers to recoup their costs and boost incentives for additional investment. Such policies undervalue infrastructure because they focus on uses whose value may be captured by markets or government regulations and ignore the usage and positive spillovers (the social value) enjoyed by society at large. Frischmann (a specialist in intellectual property and Internet law at Yeshiva University) holds that social value is best encouraged and realized by open access policies.

Clearly, a balance between encouraging infrastructure supply and infrastructure use must be realized, and that is Frischmann's goal in this book—to offset conventional economic analysis and its almost exclusive focus on supply with a consideration of the varieties of demand for and uses made of infrastructure. As he argues, “Infrastructure valuation, management, and policy must pay closer attention to and be guided by the activities, systems, and ends enabled by infrastructure.” Frischmann extends conventional economic analysis to focus on ends by categorizing different forms of infrastructure according to the types of “user-generated outputs” they make possible. Infrastructures that predominantly generate private goods are appropriately governed by markets. However, infrastructures that predominantly generate public and social goods are more appropriately governed by policies that nurture the continued creation of social value. In a critically important policy insight, Frischmann notes that social value is nurtured by encouraging the widespread use of public and social

infrastructures. A commons management strategy, in which a resource is accessible to all members of a community on nondiscriminatory terms, meaning “terms that do not depend on the users’ identity or intended use,” facilitates greater access. Managing social and public infrastructures as commons

achieves two goals: Users are allowed the flexibility and freedom to choose how to make use of and to experiment with the infrastructure. And as society’s values and goals change over time, so too may the uses made of the infrastructure shift to meet those values. In other words, gov-

ernments and markets are not put in charge of determining the forms of social value to be created; rather, social value emerges endogenously because of commons management.

Avoiding jargon and carefully defining key concepts and terms, Frischmann makes a complex economic argument readily understandable to students, policy-makers, and scholars from many different backgrounds and disciplines. Furthermore, he systematically constructs and defends his argument in a way that is easy to follow. The book’s opening section provides a primer on infrastructure economics for lay readers. Frischmann then lays out his social value-centered infrastructure analysis. Given the counterintuitiveness of his policy proposal, he devotes several chapters to addressing the challenges raised to commons management. For instance, commons management would seem to invite congestion (too many users interfering with one another’s use). Commons management, however, does not mean open and free access, which would tend to encourage congestion. Rather it entails nondiscriminatory access and use, which makes it compatible with customary means of addressing congestion, such as expanding infrastructure capacity or using congestion pricing. (As long as the pricing is based on when and how much the infrastructure is used and not on by whom and for what purpose the infrastructure is used.)

The second half of the book consists of empirical applications of infrastructure analysis. The most compelling of these applications, by far, explore intellectual infrastructure and the Internet and the network

neutrality debate. In these settings, the demand for the social and public goods the infrastructure makes possible is clearly exhibited. For instance, consider the social capital created as people share their stories, make new friends, maintain contact with work colleagues, and share ideas using the Internet. We face the challenge of finding a workable balance between encouraging the production of new ideas, inventions, and markets—which requires allowing people to capture at least some of the benefits of their creations—and allowing for and supporting open, nondiscriminatory access to the ideas, speech, and communication that make those creations possible. Frischmann discusses how such tradeoffs are made in copyright and patent laws, which he describes as “semi-commons arrangements that mix both private rights and commons.” Patent law, for instance, protects creations for a relatively short period of time, eventually allowing the creations to enter the public domain to be freely used and capitalized upon. In addition, some things are not patentable; people cannot be excluded from their enjoyment. The boundaries between private and commons are constantly contested, and Frischmann clearly sides with more openness and less closure.

In his consideration of “environmental infrastructure,” the author misses an opportunity to probe the boundaries of his approach and perhaps even to extend it. Environmental infrastructure (the author mentions oceans, lakes, forests, and the atmosphere as examples) is simply too broad a category to insightfully analyze in a single chapter. But, more important, the environment differs in crucial ways from the other forms of infrastructure on which Frischmann builds his approach. One of the several such differences can be found in the downstream effects flowing from environmental infrastructure. The uses of human-constructed infrastructures largely (although not entirely) generate many public and social goods, not to mention positive externalities. The uses of natural infrastructures largely (although not entirely) generate many public bads and negative externalities. Reducing and limiting public bads and negative externalities is not comparable to promoting public goods and positive externalities. The discrepancy has substantial policy implications. A Frischmann commons approach (open, nondiscriminatory access and use) applied to environmental infrastructure will have—and has had—the effect of promoting public bads and negative externalities. Sustaining environmental infrastructures will require a careful matching of governing arrangements to biophysical

**Infrastructure****The Social Value of Shared Resources****by Brett M. Frischmann**Oxford University Press,  
New York, 2012. 435 pp. \$85,  
£55. ISBN 9780199895656.

The reviewer is at the School of Government and Public Policy, University of Arizona, Tucson, AZ 85721, USA. E-mail: schlager@email.arizona.edu

settings, and no single default rule is likely to be appropriate. Also, in this context one should note the author's narrow and specific meaning of the term "commons," which his functional perspective presents as "a type of resource management strategy." That contrasts with the broader, more expansive scope of the term, encompassing a wide variety of governing arrangements, that many scholars, including Nobel laureate Elinor Ostrom, have used in studying common pool resources.

The book provides a new and productive way of analyzing all forms of infrastructure, especially those that are sources of major social value. Frischmann helps us recognize the importance of understanding how different types of policies balance provision and use. With its many fresh ideas, *Infrastructure* itself is likely to generate social value through additional research and the creation of innovative policies.

10.1126/science.1223454

## GENETICS

# Similarities Despite Separation

Dorret I. Boomsma

No study of twins has generated as much publicity, media attention, and discussion in the field of behavior genetics as the Minnesota Study of Twins Reared Apart (MISTRA). This milestone study, founded and directed by Thomas Bouchard Jr., included 137 pairs of twins who were separated in infancy and reared apart. It was the first project of its kind to include both monozygous (MZ) and dizygous (DZ) twins (81 and 56 pairs, respectively). No other single study has produced results that are as important in evaluating one of the crucial assumptions of classical twin study design: the equal environments assumption, "the premise that the environmental factors affecting similarity in a given trait ... are the same for MZ and DZ twin pairs."

The study, which ran from 1979 to 1999, brought twin pairs, some of whom had not previously met, to Minnesota for a week of

### Born Together—Reared Apart: The Landmark Minnesota Twin Study

by Nancy L. Segal

Harvard University Press,  
Cambridge, MA, 2012. 416 pp.  
\$49.95, £36.95, €45.00.  
ISBN 9780674055469.



Together again. A 1987 reunion of British reared-apart twins.

assessments. The protocols recorded a wide range of phenotypes, including personality, physiological and dental traits, brain function, lifestyle, happiness, attitudes, and, of course, IQ and cognition. In a landmark 1990 paper, Bouchard and colleagues summarized the resemblances observed in 60 pairs of monozygotic twin pairs reared apart and compared them with resemblances measured in monozygotic twins reared together (1). Importantly, they also reported the reliability of the traits (the correlation between two testings of the same individual). They found no large differences between the two groups of twin pairs, validating the equal environments assumption. For example, correlations in mental abilities (IQ and some subscales) ranged between 0.64 and 0.78 for the twins raised apart, while those for twins raised together were between 0.76 and 0.88.

In *Born Together—Raised Apart*, Nancy Segal offers a comprehensive account of MISTRA. Segal (California State University, Fullerton), who has been involved with the project for most of its duration, documents its procedures, funding, and results. Online (2), she also provides a complete list of the assessments. She proceeds chronologically, from "early findings" to "twin studies of the future." However, reflecting shifts in the researchers' focus, individual chapters tend to concentrate on a few traits (e.g., "Sexual orientation, cognition, and medical traits" and "Psychopathology and religiosity"). The chronological organization does lead to some repetition, as results based on smaller sample sizes are presented in earlier chapters and then discussed again based on the larger data sets.

In the 1980s and 1990s, MISTRA was the

largest study of reared-apart twins. Nonetheless, sample sizes often turned out to be too small to allow firm conclusions. For example, to test Frank Sulloway's birth-order theory (firstborns in a family tend to be more traditional), Segal compared MZ twins having different birth order in their adoptive families (3). Even with the combination of data from MISTRA and the Swedish Adoption and Twin Study of Aging, she found no meaningful differences. However, this example illustrates another of the book's strong points: throughout, Segal includes and discusses data and findings from the few other studies on twins reared apart. These include earlier works by Horatio Newman, Frank Freeman, and Karl Holzinger on 19 U.S. pairs (4); by James Shields on 44 pairs in Great Britain (5); and by Niels Juel-Nielsen on 12 pairs from Denmark (6). Segal omits the work by Cyril Burt, who has been accused of fabricating data. After briefly discussing the charges against and defenses of Burt, she concludes that the affair is currently unresolved.

Segal writes very well. Much of the material may be familiar to twin researchers and behavioral geneticists, although they will enjoy the recollections by MISTRA's major investigators. All readers will find *Born Together—Raised Apart* a highly valuable account of the entire project.

## References

1. T. J. Bouchard Jr., D. T. Lykken, M. McGue, N. L. Segal, A. Tellegen, *Science* **250**, 223 (1990).
2. [www.drmancysegaltwins.org](http://www.drmancysegaltwins.org).
3. N. L. Segal, *Twin Res. Hum. Genet.* **11**, 103 (2008).
4. H. H. Newman, F. N. Freeman, K. J. Holzinger, *Twins: A Study of Heredity and the Environment* (Univ. Chicago Press, Chicago, 1937).
5. J. Shields, *Monozygotic Twins Brought Up Together and Brought Up Apart* (Oxford Univ. Press, London, 1962).
6. N. Juel-Nielsen, *Acta Psychiatr. Neurol. Scand. Monogr. Suppl.* 183 (1965).

10.1126/science.1226444



# Challenges to the Future Conservation of the Antarctic

Changing environments and resource demands present challenges to Antarctic conservation.

S. L. Chown,<sup>1,2\*</sup> J. E. Lee,<sup>1</sup> K. A. Hughes,<sup>3</sup> J. Barnes,<sup>4</sup> P. J. Barrett,<sup>5</sup> D. M. Bergstrom,<sup>6</sup> P. Convey,<sup>3</sup> D. A. Cowan,<sup>7</sup> K. Crosbie,<sup>8</sup> G. Dyer,<sup>9</sup> Y. Frenot,<sup>10,11</sup> S. M. Grant,<sup>3</sup> D. Herr,<sup>12</sup> M. C. Kennicutt II,<sup>13</sup> M. Lamers,<sup>14</sup> A. Murray,<sup>15</sup> H. P. Possingham,<sup>16</sup> K. Reid,<sup>17</sup> M. J. Riddle,<sup>6</sup> P. G. Ryan,<sup>18</sup> L. Sanson,<sup>19</sup> J. D. Shaw,<sup>6,16</sup> M. D. Sparrow,<sup>20</sup> C. Summerhayes,<sup>21</sup> A. Terauds,<sup>6</sup> D. H. Wall<sup>22</sup>

The Antarctic Treaty System, acknowledged as a successful model of cooperative regulation of one of the globe's largest commons (1), is under substantial pressure. Concerns have been raised about increased stress on Antarctic systems from global environmental change and growing interest in the region's resources (2, 3). Although policy-makers may recognize these challenges, failure to respond in a timely way can have substantial negative consequences. We provide a horizon scan, a systematic means for identifying emerging trends and assisting decision-makers in identifying policies that address future challenges (2, 3). Previous analyses of conservation threats in the Antarctic have been restricted to matters for which available evidence is compelling (4). We reconsider these concerns because they might escalate quickly, judging from recent rapid environmental change in parts of Antarctica and increasing human interest in the region (see the map). We then focus on a more distant time horizon.

The most immediate conservation threats to species, ecosystems, and resources around the Antarctic margin are consequences of regional warming, ocean acidification, and changes in sea-ice distribution. Marine resource extraction may exacerbate these threats. Current information suggests that toothfish and krill are particularly at risk into the future, but the full extent thereof is unclear due to the lack of comprehensive understanding of their life histories and spatial dynamics and difficulties in obtaining such information (5). Advancing marine ecosystem protection, which may help

ensure that resource extraction is conducted in a more sustainable fashion, is a major governance challenge.

Climate change is elevating risks of introduction of nonindigenous species that might become invasive (6). These risks will be exacerbated should tourist and research activity in the region continue to increase. The nonindigenous species threat is better recognized than any other in the region and has been addressed most comprehensively by policy-makers (7). Still, risks of transfer of organisms among biogeographically distinct regions of the Antarctic remain under-researched and poorly regulated (8).

Increasing human activity in the region means escalating risks of pollution from vessel emergencies (at least 12 over the past 5 years) (9) and from point-source discharges. Although marine noise pollution is not thought to pose a major threat in the region, inadequate research leaves policy responses dependent on information from elsewhere. Wildlife disturbance is likely to increase with growing numbers of visitors, especially to popular sites. Identification of long-term consequences of such disturbance is hindered by the lack of appropriate surveys.

Diversification of both science (e.g., intensified subglacial drilling activity) and tourism (e.g., polar crossings) challenge regulatory responses (10). Activities adjacent to protected areas may be reducing the values these areas were designated to protect (8). The Committee for Environmental Protection, responsible for advising Antarctic Treaty Parties about conservation measures and implementation (1), has yet to adopt a dynamic conservation planning approach

for protected areas. As conservation challenges increase with growing environmental change and human impacts, the need to undertake dynamic planning and implementation will grow. Such planning is a hallmark in many other areas and necessary tools are available or being developed (11), but data on the distribution of biodiversity will have to be improved.

Over the longer term (~50 years), growing global human populations and life-style expectations will increase resource demands (12) and, without greater commitment to mitigation, escalation of conservation challenges associated with greenhouse gas emissions. Consequences of climate change will bring pressure to consider geoengineering solutions (13). Activities that do not reduce CO<sub>2</sub> emissions will add to problems associated with ocean acidification, predicted to be most acute in the Southern Ocean (14).

As climate continues to change and technology advances, Antarctic resource extraction, driven by escalating global demand, will become more economically feasible. The Protocol on Environmental Protection to the Antarctic Treaty prohibits "any activity relating to mineral resources, other than scientific research." However, this can change should a binding legal agreement on exploitation be reached (Article 25.5) (15). Nations outside the treaty are not bound by its provisions. Although the challenges of working in the Antarctic are considerable, technologies for oil, gas, and mineral exploitation in remote regions have been developed or are advancing rapidly. Two recent developments bear out the proposal. First, several claimant states have made submissions to the United Nations Commission on the Limits of the Continental Shelf about the possibility of asserting shelf claims offshore of their Antarctic territories (16), claims for which are in abeyance under the treaty (1). Second, a submission to the XXXIV Antarctic Treaty Consultative Meeting announced that achievement of the Russian Federation's scientific objectives would help to "strengthen

<sup>1</sup>Stellenbosch University. <sup>2</sup>Monash University. <sup>3</sup>British Antarctic Survey. <sup>4</sup>Antarctic and Southern Ocean Coalition. <sup>5</sup>Victoria University of Wellington. <sup>6</sup>Australian Antarctic Division, Department of Sustainability, Environment, Water, Population and Communities. <sup>7</sup>University of the Western Cape. <sup>8</sup>International Association of Antarctica Tour Operators. <sup>9</sup>32 Lyme Street, London NW1 0EE, UK. <sup>10</sup>French Polar Institute Paul-Emile Victor. <sup>11</sup>Unité Mixte de Recherche Ecobio Centre National de la Recherche Scientifique, Université de Rennes. <sup>12</sup>International Union for Conservation of Nature. <sup>13</sup>Texas A&M University. <sup>14</sup>Wageningen University. <sup>15</sup>Desert Research Institute. <sup>16</sup>The University of Queensland. <sup>17</sup>Commission for the Conservation of Antarctic Marine Living Resources. <sup>18</sup>University of Cape Town. <sup>19</sup>Antarctica New Zealand. <sup>20</sup>Scientific Committee on Antarctic Research. <sup>21</sup>Scott Polar Research Institute. <sup>22</sup>Colorado State University.

\*Full affiliations for all authors are provided online. †Author for correspondence: steven.chown@monash.edu

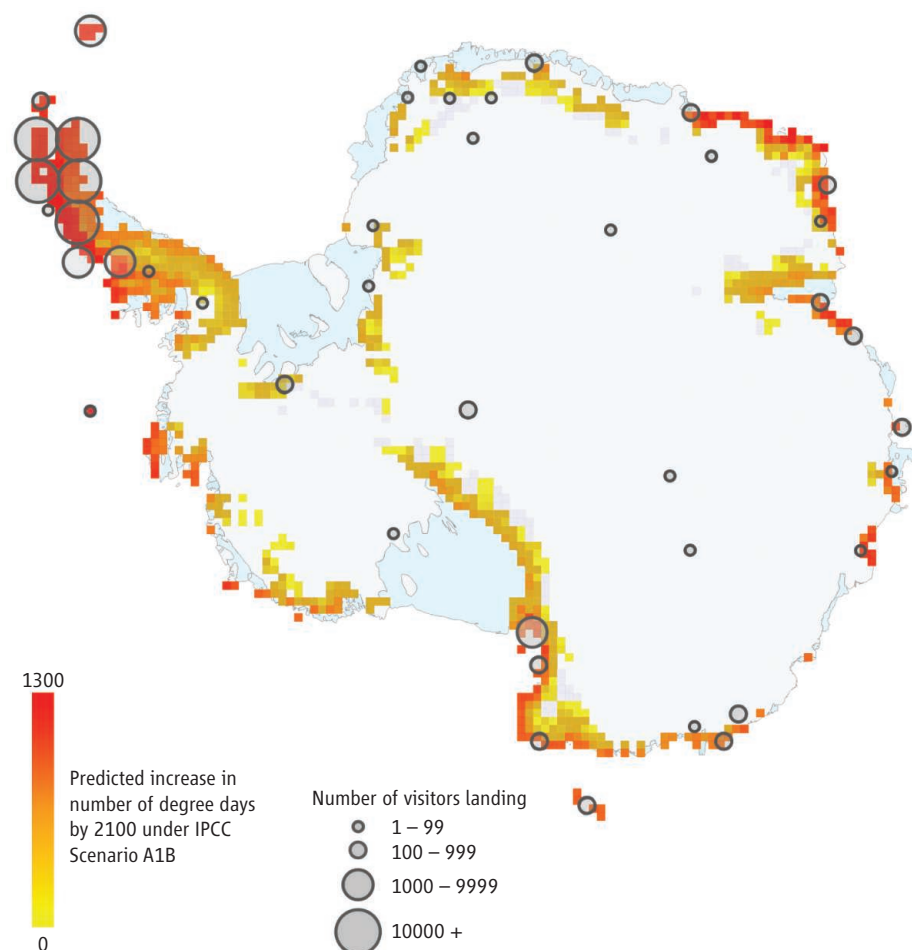


**Figure 1.** Predicted increase in degree days for vascular plants between 2007–2008 and 2010, overlaid with science and tourist visitor activity in 2007–2008. Data from (6, 8).

the economic capacity of Russia through the use of marine biological resources available in the Southern Ocean, and complex investigations of the Antarctic mineral, hydrocarbon and other natural resources” (17). Data to evaluate hydrocarbon and mineral deposits could be gathered, with attendant environmental risks, as part of legitimate scientific programs. Managing activities that bridge research and exploitation is a challenge for other international agreements.

Marine resource harvesting for human consumption is a current threat. Bio-prospecting in the region could represent a further challenge if it leads to substantive nondisclosure of information. Information sharing has been a challenge within the treaty (1), and profit-motivated restrictions would further hamper dynamic spatial conservation planning and management (8, 11).

Discussions about permanent settlements of parts of Antarctica have typically revolved around the activities of some claimant states. However, as tourism diversifies and includes more land-based compo-

nents, and as science and tourism ventures share resources (18), the probability of more permanent residents will increase, as is the case for those who serve these industries on the Arctic island of Svalbard. Permanent human settlements can be acceptable within the charge to use the continent for “peaceful purposes” but are likely to bring a broad range of conservation challenges. Although the treaty has provisions to deal with conservation threats, it does not currently regulate resident citizens.

The five decades since entry into force of the Antarctic Treaty have seen a quickening in the pace of global change, reflected in accelerating rates of ice loss in the Antarctic (19). Growing use of the continent together with such change will mean substantial impacts on ecosystems, including those that are globally unmatched, such as in the McMurdo Dry Valleys. The capability of current conservation governance arrangements to deal with these challenges may be outpaced.

The scientific community can help address these challenges by investigating

their nature, extent, and trajectories and by making the outcomes more rapidly and readily accessible to the policy environment. Action to adapt to and mitigate the consequences of change must be taken by all Antarctic visitors, operators, and national programs. The most potential for effective action lies with the Antarctic Treaty System itself. This will require improved ways to use scientific information effectively and an increase in the speed of decision-making. The greatest challenge will be addressing threats that are global in scale, but with impacts that are being realized most significantly in the Antarctic. To do so requires greater engagement with other international environmental policy instruments and organizations.

#### References and Notes

1. P. A. Berkman, M. A. Lang, D. W. H. Walton, Eds., *Science Diplomacy: Antarctica, Science, and the Governance of International Spaces* (Smithsonian Institution Scholarly Press, Washington, DC, 2011).
2. W. J. Sutherland et al., *Trends Ecol. Evol.* **27**, 12 (2012).
3. For a description of the approach and participants and additional information, see supplementary materials.
4. T. Tin et al., *Antarct. Sci.* **21**, 3 (2009).
5. L. K. Blight et al., *Science* **330**, 1316 (2010).
6. S. L. Chown et al., *Proc. Natl. Acad. Sci. U.S.A.* **109**, 4938 (2012).
7. Committee for Environmental Protection, *Non-native Species Manual* (2011); [www.ats.aq/documents/atcm34/www/atcm34\\_ww004\\_e.pdf](http://www.ats.aq/documents/atcm34/www/atcm34_ww004_e.pdf).
8. A. Terauds et al., *Divers. Distrib.* **18**, 726 (2012).
9. V. Ruoppolo, E. J. Woehler, K. Morgan, C. J. Clumper, *Polar Rec. (Great Britain)* 10.1017/S0032247411000763 (2012).
10. Antarctic Treaty Consultative Meeting XXXIV Information Paper 18, [www.ats.aq/documents/ATCM34/ip/ATCM34\\_ip018\\_e.doc](http://www.ats.aq/documents/ATCM34/ip/ATCM34_ip018_e.doc).
11. D. B. Segen, E. T. Game, M. E. Watts, R. R. Stewart, H. P. Possingham, *Environ. Model. Softw.* **26**, 1434 (2011).
12. G. Dyer, *Climate Wars: The Fight for Survival as the World Overheats* (Oneworld Publications, Oxford, 2010).
13. N. E. Vaughan, T. M. Lenton, *Clim. Change* **109**, 745 (2011).
14. B. I. McNeil, R. J. Matear, *Proc. Natl. Acad. Sci. U.S.A.* **105**, 18860 (2008).
15. Protocol on Environmental Protection to the Antarctic Treaty, [www.ats.aq/documents/recatt/Att006\\_e.pdf](http://www.ats.aq/documents/recatt/Att006_e.pdf).
16. C. C. Joyner, in (1), pp. 97–102.
17. Antarctic Treaty Consultative Meeting XXXIV Working Paper 55, [www.ats.aq/documents/ATCM34/wp/ATCM34\\_wp055\\_e.doc](http://www.ats.aq/documents/ATCM34/wp/ATCM34_wp055_e.doc).
18. Antarctic Treaty Consultative Meeting XXXII Information Paper 23, [www.ats.aq/documents/ATCM32/ip/ATCM32\\_ip023\\_rev1\\_e.doc](http://www.ats.aq/documents/ATCM32/ip/ATCM32_ip023_rev1_e.doc).
19. E. Rignot, I. Velicogna, M. R. van den Broeke, A. Monaghan, J. Lenaerts, *Geophys. Res. Lett.* **38**, L05503 (2011).

**Acknowledgments:** Views expressed here reflect authors’ personal perspectives, not necessarily the policy positions of their home organizations. This work was supported by the Scientific Committee on Antarctic Research, Antarctica New Zealand, the South African National Research Foundation, and a Martha T. Muse award (S.L.C.). A. Macey, N. Gilbert, and M. McGeoch provided useful comments.

#### Supplementary Materials

[www.sciencemag.org/cgi/content/full/337/6091/158/DC1](http://www.sciencemag.org/cgi/content/full/337/6091/158/DC1)

10.1126/Science.1222821



# Fragile Delivery to the Genome

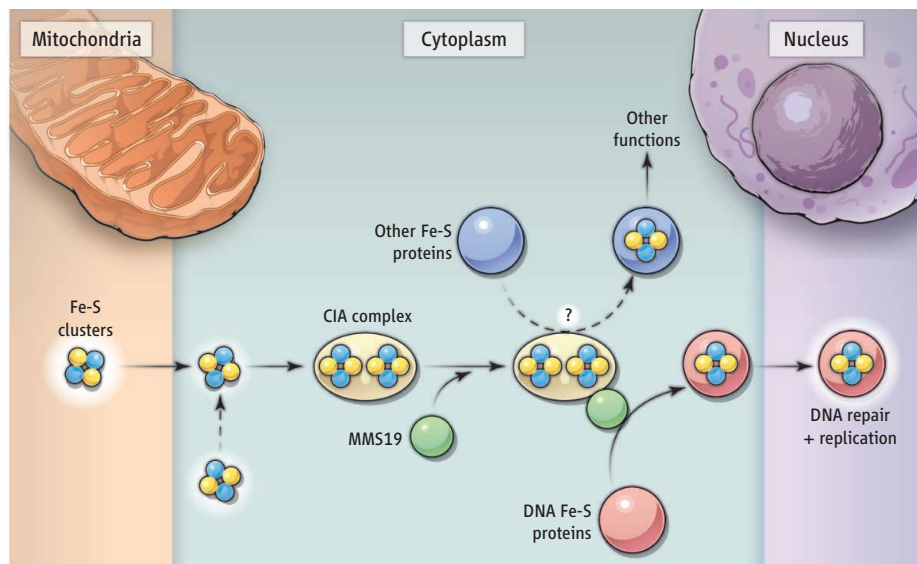
Daniel E. Gottschling

When an important, fragile package needs to be delivered with high assurance, a dependable envoy can ensure that it lands in the right hands. Iron-sulfur (Fe-S) clusters are one such package in the cell. Many proteins, including some that replicate and maintain the nuclear genome, require them. Two papers in this issue—by Gari *et al.* (1) on page 243 and Stehling *et al.* (2) on page 195—identify MMS19 as the envoy that delivers Fe-S clusters to enzymes that maintain genome integrity.

Fe-S clusters are cofactors in hundreds of proteins and are required in virtually all organisms from bacteria to humans (3, 4). They reside in multiple forms and they readily accept or donate electrons. Although this feature is used in “redox” catalysis in some enzymes, Fe-S clusters also serve in nonredox catalysis, act as redox sensors, and play a structural role in proteins.

It is thought that Fe-S clusters were critical to evolution on Earth by facilitating chemical transformations that created life in the anaerobic milieu (5). Ironically, once plants evolved and oxygen became prevalent in the world, Fe-S clusters became susceptible to destruction by oxidation. Once liberated from Fe-S clusters, the free iron could turn oxygen into reactive oxygen species that are toxic to the cell. Thus, the biosynthesis and introduction of Fe-S clusters into proteins has evolved in such a way as to preserve these fragile molecules in today's world.

Most biosynthesis of Fe-S clusters in eukaryotes occurs in the mitochondria, though in mammalian cells some *de novo* biosynthesis may also occur in the cytoplasm and nucleus (3, 6). Regardless of their origin—which is a point of contention—Fe-S clusters need to be escorted and presented to their cytoplasmic and nuclear apoproteins. This is handled by the conserved cytoplasmic iron-sulfur assembly (CIA) machinery. However, the CIA complex does not appear to provide any specificity to the loading of apoproteins, nor is it clear how this is accomplished. In part this is because the genes encoding CIA proteins are essential, but also because there is no obvious pro-



**Cluster escort.** Fe-S clusters that are synthesized in the mitochondria, and perhaps in the cytoplasm, are handed off to the CIA complex. MMS19 serves as an adaptor for apoproteins that require Fe-S clusters for activity, including many involved in DNA replication and repair. It is less clear how other Fe-S proteins obtain their Fe-S clusters from the CIA complex.

tein sequence signature that readily distinguishes Fe-S proteins (3).

Over 20 years ago, a DNA glycosylase involved in base excision repair was found to contain an Fe-S cluster that was essential for its activity (7). Dozens of DNA and RNA helicases and DNA and RNA polymerases, which are all enzymes critical for DNA replication and repair, have since been found to contain Fe-S clusters (4, 8)

Gari *et al.* and Stehling *et al.* converge on MMS19 but start at opposite ends of the problem (see the figure). Stehling *et al.* looked for factors that bound to known components of the CIA complex in yeast and discovered Mms19. Mms19 was required for *in vivo* incorporation of radioactive  $^{55}\text{Fe}$ —indicative of Fe-S cluster insertion—into various DNA repair enzymes. Furthermore, Mms19 was identified in biochemical complexes with these enzymes and several other DNA replication and repair proteins. This explains the phenotypes associated with a mutation of the yeast *MMS19* gene, including sensitivity to the DNA damaging agent methane methylsulfonate (MMS) (9).

Gari *et al.* identified, in human cells, MMS19 in a complex containing an Fe-S protein called regulator of telomere length 1, a DNA helicase. The interaction appeared

to reside only in the cytoplasmic fraction of cell extracts. The authors also discovered that cytoplasmic MMS19 bound to many other Fe-S proteins involved in nuclear DNA repair and replication, as well as components of the human CIA complex.

Gari *et al.* and Stehling *et al.* also found that not all cytoplasmic Fe-S proteins associated with MMS19, nor were they affected by its absence, supporting specificity of the interaction. Further, in the absence of MMS19, CIA components still bound to Fe-S clusters, suggesting that MMS19 acts late in the hand-off to apoproteins—i.e., binding to the target proteins and facilitating the transfer of Fe-S clusters. Reducing the amount of MMS19 in cells decreased the presence of various Fe-S proteins that interact with MMS19, supporting earlier observations that a bound Fe-S cluster stabilizes its resident protein (10). This suggests that cells have a feedback or quality control system that eliminates nonfunctional Fe-S proteins.

One nuanced distinction between the approaches of Gari *et al.* and Stehling *et al.* provided independent verification of MMS19's role in DNA replication and repair. When Stehling *et al.* introduced low levels of DNA damage via MMS or ultraviolet irradiation in dividing cells that lacked MMS19,

Division of Basic Sciences, Fred Hutchinson Cancer Research Center, 1100 Fairview Avenue North, Seattle, WA 98109-1024, USA. E-mail: dgottsch@fhcr.org

canonical DNA damage checkpoint pathways were hyperactivated (2, 11). By contrast, Gari *et al.* treated cells with hydroxyurea to deplete deoxynucleotide pools, and found that in the absence of MMS19, cells could not enter S phase of the cell division cycle (could not replicate DNA), and consequently did not elicit a DNA damage checkpoint signal (1, 12). Thus, in the study by Stehling *et al.*, DNA repair was compromised because of reduced MMS19 synthesis, whereas in the study by Gari *et al.*, DNA replication was compromised.

It is not yet clear how MMS19 recognizes the apoproteins it serves, nor whether it directly hands over Fe-S clusters to recipient proteins. There are Fe-S proteins that are not served by MMS19, but depend on the CIA complex, and those might be served by undiscovered MMS19-like adaptors. A more

fundamental question is why so many DNA enzymes require Fe-S clusters. It seems dangerous to place iron so close to DNA, where it could potentially unleash reactive oxygen species and damage the nucleotides. Are the Fe-S proteins simply an evolutionary artifact that cannot be removed by selection, or do they serve some other purpose, such as sensing aberrant DNA structures (13)?

An increase in yeast nuclear genome instability was associated with mitochondrial defects (14), suggesting that mitochondrial dysfunction inhibited the production of Fe-S cluster-containing proteins required for genome integrity. The findings of Gari *et al.* and Stehling *et al.* offer further tools to test this hypothesis. In addition, gene mutations in several of the DNA repair and replication proteins serviced by MMS19 have been associated with various cancers (15). Could it be

that MMS19 and its prospective associates serve as another set of oncogenic targets?

#### References and Notes

1. K. Gari *et al.*, *Science* **337**, 243 (2012); 10.1126/science.1219664.
2. O. Stehling *et al.*, *Science* **337**, 195 (2012); 10.1126/science.1219723.
3. T. A. Rouault, *Dis. Model. Mech.* **5**, 155 (2012).
4. M. F. White, M. S. Dillingham, *Curr. Opin. Struct. Biol.* **22**, 94 (2012).
5. J. A. Imlay, *Annu. Rev. Biochem.* **77**, 755 (2008).
6. A. Sheftel, O. Stehling, R. Lill, *Trends Endocrinol. Metab.* **21**, 302 (2010).
7. R. P. Cunningham *et al.*, *Biochemistry* **28**, 4450 (1989).
8. D. J. A. Netz *et al.*, *Nat. Chem. Biol.* **8**, 125 (2012).
9. L. Prakash, S. Prakash, *Genetics* **86**, 33 (1977).
10. J. Rudolf *et al.*, *Mol. Cell* **23**, 801 (2006).
11. A. Pelliccioli *et al.*, *EMBO J.* **18**, 6561 (1999).
12. Y. Sanchez *et al.*, *Science* **286**, 1166 (1999).
13. C. A. Romano *et al.*, *Biochemistry* **50**, 6133 (2011).
14. J. R. Veatch, M. A. McMurray, Z. W. Nelson, D. E. Gottschling, *Cell* **137**, 1247 (2009).
15. Y. Wu, R. M. Brosh Jr., *Nucleic Acids Res.* **40**, 4247 (2012).

10.1126/science.1225852

## MATERIALS SCIENCE

# Driving Dislocations in Graphene

Luis L. Bonilla<sup>1</sup> and Ana Carpio<sup>2</sup>

The movement of dislocations in crystals—defects such as an extra half-plane of atoms—can determine the strength of a material and how it will deform under a load, and how it accommodates strain (1). In most materials, tracking the movement of dislocations in three dimensions requires analysis of high-resolution transmission electron microscopy (TEM) images. Tracking atomic positions in graphene, a two-dimensional material, could simplify such studies, and on page 209 of this issue, Warner *et al.* (2) use a sophisticated TEM technique to see, create, and move dislocations in suspended graphene. These results can help guide efforts to improve our theoretical understanding of how defect motion affects the mechanical properties of materials.

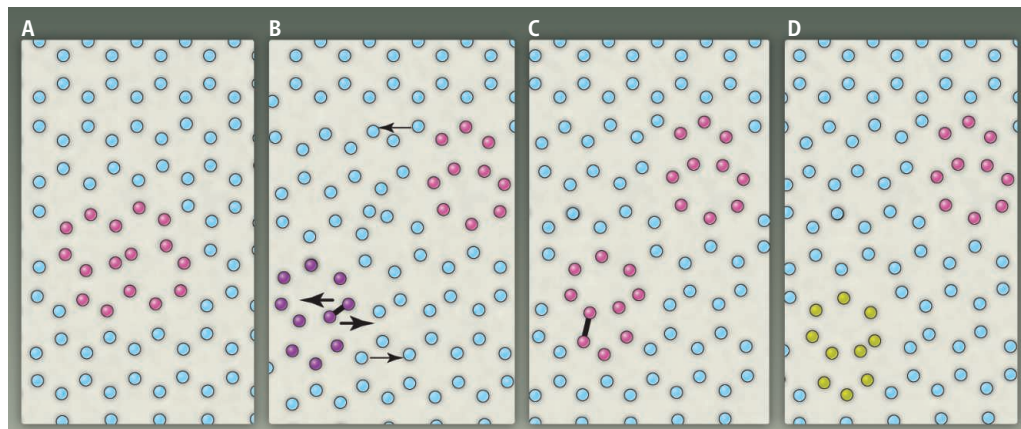
In graphene, mechanical characteristics can have striking consequences for its electronic properties. For example, strains may induce strong pseudo-magnetic

fields and Landau levels (3), whereas vacancies and point defects produce paramagnetism (4). Special grain boundaries—the interfaces between crystalline domains—may be used to filter electrons from different graphene “valleys” (different conduction bands for charge carriers) used in so-called “valley-tronic” devices (5).

In the experiments performed by Warner *et al.*, the electrons used for imaging

Electron microscopy has revealed time-resolved glide and climb motion of dislocations in graphene and imaged their strain and rotation fields.

were accelerated at low voltage so that they could not knock atoms off the graphene lattice (the maximum energy transferred from beam electrons is less than 17 eV at voltages lower than 90 kV). However, these energies were sufficient to rotate carbon-carbon (C–C) bonds, create defects, and knock atoms off defective sites. These defects are the cores of dislocations in the graphene lattice (6). For instance, a 90° C–C bond rotation requires



**Driving dislocations.** (A) A Stone-Wales defect (red) is shown in a graphene lattice (blue). (B) Dislocations are characterized by Burgers vectors (thin arrows), and the indicated pentagon-heptagon dislocations form from a dipole with Burgers vectors pointing in opposite directions along a primitive lattice direction (the horizontal axis). Warner *et al.* show that dislocations can advance parallel to their Burgers vector (glide) or in a different direction (climb), provided the electrons from the TEM beam can supply atoms with sufficient energy to overcome the corresponding energy barriers. Glide to the right involves moving two atoms as indicated by the thick arrows. (C) Configuration after dislocation glide. If the TEM beam knocks the marked atoms off, the left dislocation climbs vertically downward. (D) Resulting configuration after dislocation climb.

<sup>1</sup>Fluid Dynamics, Nanoscience and Industrial Mathematics Institute, Universidad Carlos III de Madrid, 28911 Leganes, Spain. <sup>2</sup>Applied Mathematics, Universidad Complutense de Madrid, 28040 Madrid, Spain. E-mail: ana\_carpio@mat.ucm.es; bonilla@ing.uc3m.es



9.2 eV and transforms four hexagons in the pristine lattice into a ring comprising two pentagons and two heptagons, a Stone-Wales defect (SWD) (see the figure, panel A).

The SWD is not a single dislocation but a dipole formed by two dislocations (the pentagon-heptagon pairs). The distortion of a lattice caused by a dislocation is described by a Burgers vector, and the SWD is a dipole because the Burgers vectors are of equal length and antiparallel. To revert back to the pristine, stress-free lattice, a SWD needs to be activated by about 4 eV, much less than the maximum energy the TEM can transfer to carbon atoms. In fact, the first TEM observations with reasonable atomic resolution revealed SWDs that disappeared within 4 s after their creation (7).

Under sufficient applied shear stress, a SWD splits into its two component dislocations that then glide apart [(6); see (8) for experimental evidence] (see the figure, panel B). From a pristine lattice, irradiation can create other dislocation pairs with zero overall Burgers vector. For example, nonagon-pentagon and pentagon-octagon-pentagon defects are the cores of vacancy and divacancy dislocation dipoles, respectively, created by the loss of one or two carbon atoms (6). More complicated defect rings and dynamics have also been observed (7–9).

Warner *et al.* have imaged dislocation dynamics in graphene in real time. They observed one dislocation in a dipole that glided one lattice constant toward the other along the direction marked by its Burgers vector. Later, it climbed another lattice constant away moving perpendicular to its Burgers vector (see the figure, panels C and D). The glide motion requires only atomic bond rotation (about 5 eV), whereas climbing involves removal of two atoms. The latter action has a higher energy cost (9 to 12 eV), and this energy is provided by the electrons from the TEM beam. The authors used density functional theory (DFT) to calculate the energy of defects located at different positions in the lattice once atoms have relaxed to a state compatible with boundary conditions and external stress constraints. Configurations that cost energy within the range provided by the TEM beam are plausible.

Despite DFT calculations showing that dislocation motion is consistent with energy barriers overcome by TEM irradiation, it remains unclear why dislocations move the way they do. What is the interplay among dislocations, strains, and irradiation? There are no complete theories of dislocation dynamics in graphene, although existing models based on discrete (6) or continuous elasticity

(10) could be a starting point. Future theories should also consider that strain fields (maps of the extent of compressive and tensile strain) around dislocations differ from those given by classical elasticity with line singularities (1). Using geometric phase analysis, Warner *et al.* have mapped dislocation strain fields. Formulas inspired by the semicontinuous Peierls-Nabarro model (1) give a better description than classical isotropic elasticity of strains at the dislocation cores. Furthermore, the lattice is rotated quite appreciably at the cores. These maps of strain and rotation fields could give additional clues about dislocation core structure.

Warner *et al.* have characterized dislocation motion in TEM-irradiated graphene with unprecedented accuracy. Their results should stimulate theory and experiments alike, as they offer the opportunity to understand plastic deformation in nanoscale materials. At the micrometer scale, there are effective computational theories of line dislocations that rely on empirical rules for dislocation interaction and motion (11).

Besides bridging the gap with the nanoscale, graphene could offer a benchmark for a quantitative theory of irradiation-driven dislocation dynamics. In addition, controlling electronic properties in graphene through strain engineering is a promising concept (3, 12). In this respect, learning how to produce appropriate dislocations and control their motion will be quite important.

## References

1. J. P. Hirth, J. Lothe, *Theory of Dislocations* (Wiley, New York, ed. 2, 1982).
2. J. H. Warner *et al.*, *Science* **337**, 209 (2012).
3. N. Levy *et al.*, *Science* **329**, 544 (2010).
4. R. R. Nair *et al.*, *Nat. Phys.* **8**, 199 (2012).
5. D. Gunlycke, C. T. White, *Phys. Rev. Lett.* **106**, 136806 (2011).
6. A. Carpio, L. L. Bonilla, *Phys. Rev. B* **78**, 085406 (2008).
7. J. C. Meyer *et al.*, *Nano Lett.* **8**, 3582 (2008).
8. C. Gómez-Navarro *et al.*, *Nano Lett.* **10**, 1144 (2010).
9. J. Kotakoski *et al.*, *Phys. Rev. B* **83**, 245420 (2011).
10. S. Chen, D. C. Chrzan, *Phys. Rev. B* **84**, 214103 (2011).
11. V. V. Bulatov, W. Cai, *Computer Simulations of Dislocations* (Oxford Univ. Press, Oxford, 2006).
12. F. Guinea, M. I. Katsnelson, A. K. Geim, *Nat. Phys.* **6**, 30 (2010).

10.1126/science.1224681

## ECOLOGY

# Amazonian Extinction Debts

Thiago F. Rangel

How many species are headed for extinction as a result of past and future deforestation in the Brazilian Amazon?

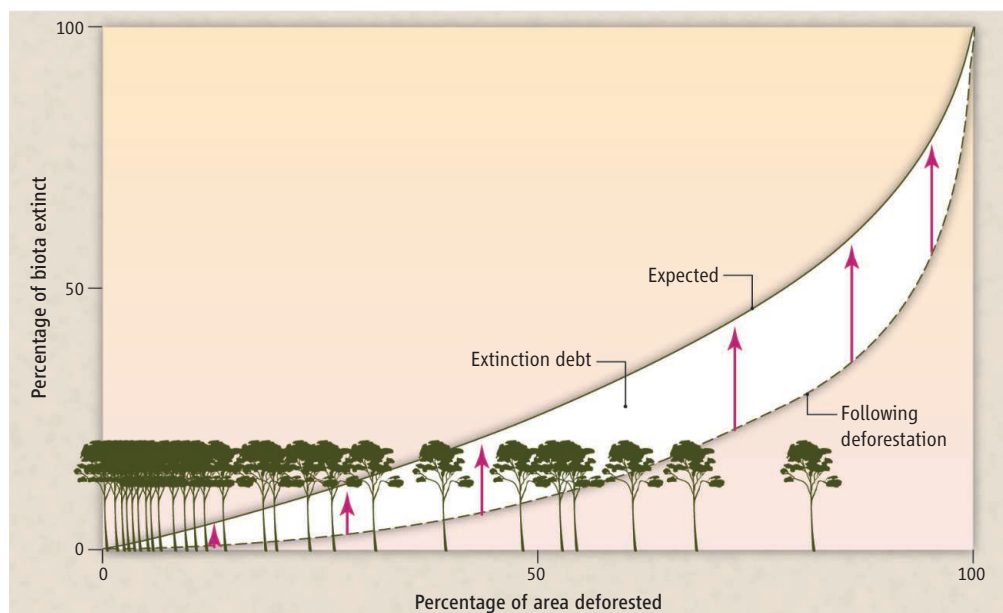
Habitat loss, climate change, and invasive species are the main drivers of the ongoing biodiversity crisis. These human-induced processes may have boosted the background rate of species extinction by 100 to 1000 times (1). However, species do not go extinct immediately when their habitat shrinks, climate changes beyond their tolerance limit, or an invasive species spreads. It may take several generations after an initial impact before the last individual of a species is gone. Conservation biologists are trying to estimate the time lag between habitat perturbation and species extinction. By inverting the reasoning, one can also estimate how many species are headed toward extinction as a function of past and current anthropogenic interference, the “extinction debt” (see the figure) (2). On page 228 of this issue, Wearn

*et al.* (3) apply this approach to the Brazilian rainforest.

The authors tackle an important but challenging question: Across the Brazilian Amazon, how many species will be lost from at least part of their historical distribution as a consequence of past and future deforestation? The starting point for answering this question is the assumption that larger areas of old-growth forest habitat should harbor more species than smaller areas, an example of the “species-area relationship” (4). Deforestation reduces forest cover and available habitat area, consequently extirpating some native species not only from the impacted area but also from the remaining forest as populations fall below viability thresholds.

Wearn *et al.* used cutting-edge statistical tools to devise a novel strategy to estimate the expected number of local species extinctions as a function of the extent of habitat loss. In contrast to the modest record of local extinction across the Brazilian Amazon so far, their findings suggest that more than 80% of the

Department of Ecology, Federal University of Goiás, CxP. 131, Goiânia, Goiás, Brazil 74970-001. E-mail: thiagorangel@icb.ufg.br



**Headed toward extinction.** Area is a good predictor of the number of species co-occurring in a given location. The effects of deforestation on biodiversity can therefore be estimated by the percentage of area deforested. The solid line describes the number of species expected to go extinct at a given location as a function of deforestation. However, species do not become locally extinct immediately after deforestation. The dashed line is a better descriptor of the short-term effects of deforestation on biodiversity. The area between the two lines is the “extinction debt,” or the percentage of species committed to extinction as a consequence of realized deforestation. The time between deforestation and extinction (arrows) provides a window of opportunity for biodiversity conservation. Wearn *et al.* now estimate the extinction debt resulting from current and future deforestation in the Brazilian Amazon.

local extinctions expected from historical deforestation have not yet happened. They estimate that deforestation during the past 30 years in some localities in the eastern and southern portion of the Amazon has already committed up to 8 species (30%) of amphibians, 10 species (25%) of mammals, and 20 species (14%) of birds to future local extinction. The authors focus on local extinction (when a species is extirpated from a location where it was historically present), but deforestation may potentially cause complete species extinction.

Moving beyond historical deforestation, the authors also project the magnitude of local extinction debts caused by deforestation expected to happen until 2050. They use four future deforestation scenarios of deforestation (5). At one extreme, if future deforestation rates in the Amazon exceed even the unprecedented levels of up to 28,000 km<sup>2</sup>/year recorded in the past decade (6), at least 10 species of amphibians, 15 species of mammals, and 30 species of birds are expected to be extirpated from around half the Amazon. At the other extreme, if cattle ranchers and soy farmers comply with current Brazilian environmental legislation and the expansion of the protected area network is maintained, the rate of deforestation may decrease below the current 6500 km<sup>2</sup>/year (7), possibly stabilizing around 2016 (6). Under this scenario, the accumulated local extinction debt in the most impacted areas should remain at about its current level.

The Brazilian Amazon is the largest continuous forest on Earth, representing more than 40% of the world’s existing tropical rainforest (8). It regulates regional climate and

hydrology, stores terrestrial carbon, and harbors vast biodiversity (7). In the past decade, Brazil has expanded its network of protected areas. Currently, around 54% of Brazilian Amazon is under some form of environmental protection (9). However, the current macroeconomic crisis is threatening Brazil’s long-term economic growth. To foster growth, the Brazilian government has been pushing a rapid expansion of infrastructure in the Amazon, with the construction of over 22 vast hydroelectric power plants in the Amazon basin (10). Several protected areas have been reduced in size or relocated. In addition, agricultural businesses have been strongly lobbying for a radical legislative reform to weaken forest protection. These reforms could potentially reverse the reduction in deforestation rate of the last decade (11), steering the future trajectory of extinction debts across the Amazon toward Wearn *et al.*’s worst-case scenario.

Extinction debts in the Brazilian Amazon are one debt that should be defaulted on. Wearn *et al.* offer the first step toward this goal by estimating the magnitude of the extinction debt. However, the “currency” used to measure the debt can be improved, given that the number of species is not the best proxy for biodiversity (12). Future studies should attempt to estimate the functional and phylogenetic diversity of species that has been lost or is threatened by deforestation.

Actions to further decrease the rate of deforestation (6) would help to slow the rate at which additional extinction debt is accumulated. However, reducing the rate at which extinction debts accumulate is not sufficient to preserve the Amazon’s biodiversity heritage; the existing extinction debt may even-

tually lead to the loss of species. To prevent species extinctions, it is necessary to take advantage of the window of opportunity for forest regeneration (13). Restored or regenerated forests initially show lower native species richness than the original forests they replaced, but they gradually recover species richness, composition, and vital ecosystem functions (14), reducing extinction debt and mitigating local species loss (15).

#### References and Notes

1. S. L. Pimm *et al.*, *Science* **269**, 347 (1995).
2. M. Kuussaari *et al.*, *Trends Ecol. Evol.* **24**, 564 (2009).
3. O. R. Wearn *et al.*, *Science* **337**, 228 (2012).
4. S. L. Pimm, P. Raven, *Nature* **403**, 843 (2000).
5. B. S. Soares-Filho *et al.*, *Nature* **440**, 520 (2006).
6. Recent experience has shown that several measures have effectively reduced deforestation rates, such as the development of new technology to improve productivity in areas already used for agriculture, satellite-based monitoring of forest fires and clearing, coupled with on-the-ground enforcement of obligatory forest reserves on private land, cancellation of credit for illegal deforesters, and economic compensation for farmers and ranchers who maintain additional forest (16).
7. E. A. Davidson *et al.*, *Nature* **481**, 321 (2012).
8. W. F. Laurance *et al.*, *Science* **291**, 438 (2001).
9. B. S. Soares-Filho *et al.*, *Proc. Natl. Acad. Sci. U.S.A.* **107**, 10821 (2010).
10. Brazil, official report on PAC program, [www.brasil.gov.br/pac](http://www.brasil.gov.br/pac).
11. J. P. Metzger, *Braz. J. Nat. Conserv.* **8**, 92 (2010).
12. D. P. Faith, *Biol. Conserv.* **61**, 1 (1992).
13. R. L. Chazdon, *Science* **320**, 1458 (2008).
14. R. L. Chazdon *et al.*, *Conserv. Biol.* **23**, 1406 (2009).
15. A. Gómez-Pompa, A. Kaus, *Proc. Natl. Acad. Sci. U.S.A.* **96**, 5982 (1999).
16. D. Nepstad *et al.*, *Science* **326**, 1350 (2009).

**Acknowledgments:** I thank R. Colwell, R. Chazdon, J. A. F. Diniz-Filho, and F. S. Cassemiro for helpful comments on the manuscript, and Conselho Nacional de Desenvolvimento Científico e Tecnológico (CNPq grants 564718/2010-6, 474774/2011-2, and 310117/2011-9) for research support.

10.1126/science.1224819



## VIOLOGY

# Frameshifting to PA-X Influenza

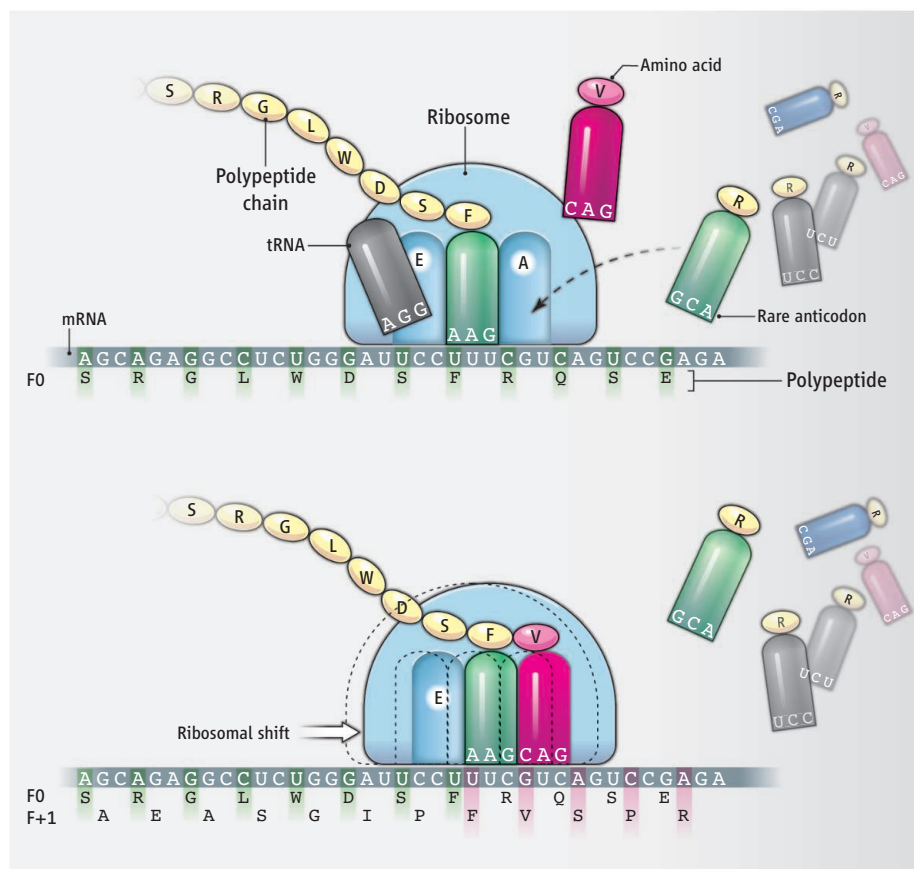
Jonathan W. Yewdell and William L. Ince

Influenza A virus (IAV) remains a major cause of human mortality and morbidity due to its remarkable genetic variability, which limits vaccine effectiveness. IAV's high intrinsic mutation rate is augmented by its segmented genome, which greatly facilitates beneficial interactions among its genes (*1*) and is likely a key to IAV's capacity to infect multiple mammalian and avian species. IAV must accomplish much with minimal genetic information—a mere 13.5 kilobases of RNA. To maximize its genome, IAV uses many tricks, including gene splicing, downstream translation initiation in normal or alternative overlapping frames, and, as Jagger *et al.* report on page 199 of this issue (2), ribosomal frameshifting, which generates a gene product that diminishes viral pathogenicity.

Because of the degeneracy of the genetic code, each amino acid can be encoded by as many as six different nucleotide triplets (codons). High codon conservation in a given gene region can reflect multiple factors, including RNA folding, RNA interaction with viral or cell macromolecules, transfer RNA (tRNA) preference (because synonymous codons are often decoded by distinct tRNA species), or the need to preserve a conserved overlapping open reading frame.

Analyzing nearly 1300 genome sequences from diverse isolates, Jagger *et al.* found that IAV gene segment 3 (there are eight segments), which encodes the PA subunit of the viral RNA polymerase, exhibits a highly conserved internal sequence that potentially encodes a 61-residue polypeptide in a +1 open reading frame [because of the triplet nature of the genetic code, each messenger RNA (mRNA) potentially encodes information in three reading frames]. Noting the lack of a proximal potential +1 canonical translation start codon or mRNA splice acceptor site to shift frames, the authors focused on a decanucleotide sequence. The near-absolute conservation of this sequence between IAV strains is striking, given the potential use of 15 synonymous codons for the three encoded amino acids and the presence of a CGU codon, which is rarely used by human

The genome of influenza A virus encodes a newly discovered protein that diminishes its pathogenicity.



**Ribosomal shift.** As the ribosome (60S subunit shown) transits PA mRNA in the standard reading frame (F0), the codon in the ribosomal A site is matched to the cognate aminoacyl tRNA, whose amino acid cargo is bonded to the elongating polypeptide. Deacylated tRNA is ejected from the E (exit) site. Ribosomal pausing as the slowly decoded arginine (R) codon CGU enters the A site and waits for its rare <sup>3</sup>GCA<sup>5</sup> anticodon allows the upstream phenylalanine (F) anticodon <sup>3</sup>AAG<sup>5</sup> to occasionally slip into the preferred +1 UUC codon, thus changing the reading frame to F+1 and altering the C-terminal peptide to generate the PA-X fusion protein.

or viral genes. Such rare codons are typically decoded more slowly because of the low concentration of their cognate tRNAs—a mechanism that can promote ribosomal frameshifting (3) (see the figure). Because the abundance of individual tRNA species can vary widely among mammalian cell types (4), this mechanism can potentially modulate frameshifting in different cell types.

Jagger *et al.* show that the translation of PA mRNA generates a protein that consists of the amino-terminal 191 amino acids of PA fused to 61 amino acids that result from +1 frameshifting. Expression of the PA-X protein from cDNA that encodes PA likely explains the observed decreased expression of a number of host cell proteins (5)—a phe-

nomenon that had long been attributed to PA protease activity despite the absence of sequence or structural features that suggest protease function (6). Rather than PA itself, it is PA-X, using the PA endonuclease domain, which selectively degrades host mRNAs, abrogating their translation and reducing expression of short-lived cellular proteins.

PA-X exhibits remarkable sequence conservation across strains, although it does come in two forms, with many strains of the recently introduced swine-origin IAV (SOIV) possessing a stop codon that truncates PA-X by 20 residues. This situation is eerily similar to PB1-F2, the first IAV gene product shown to be generated from a non-spliced alternative reading frame (encoding

Laboratory of Viral Diseases, National Institute of Allergy and Infectious Diseases (NIAID), Bethesda, MD 20892, USA. E-mail: jyewdell@niaid.nih.gov

87 to 90 amino acids in PB1) (7). PB1-F2 exhibits similar length polymorphism [typically, SOIVs encode an 11-residue fragment, and recent classical H1N1 viruses express a 57-residue form (8)]. Further, like PB1-F2 (8), PA-X is a viral accessory protein (i.e., dispensable for replication, but rather modulates host immune response).

Jagger *et al.* show that eliminating PA-X expression in the highly pathogenic 1918 IAV (whose associated pandemic caused perhaps 50 million deaths worldwide) enhances viral pathogenicity while inducing many changes in host gene expression, as determined by global transcriptional profiling. This may reflect, at least in part, the direct and cascading effects of host mRNA degradation by PA-X, although it is probable that PA-X, like many viral accessory proteins, is highly multifunctional. Although IAV pathogenesis is complex, it seems that PA-X diminishes viral damage by reducing the expression of select proinflammatory cytokines.

Intriguingly, PA-X and PB1-F2 exert opposite effects on pathogenesis, because PB1-F2 enhances morbidity and mortality (albeit in a viral strain- and host-dependent manner) (9). Presumably, the two proteins work together to optimally modulate host

immunity. It will be interesting to examine the effect of PA-X on secondary bacterial pneumonia, whose severity is enhanced by PB1-F2 in mouse-model infections (10).

How do PA-X and PB1-F2 contribute to viral transmission between hosts, given that transmission is the ultimate selective factor in viral evolution? IAV's high mutation rate ensures that genes that do not confer increased fitness quickly succumb to loss-of-function mutations.

Viral pathogenesis and transmission are intimately related: Viruses have no interest in incapacitating their hosts if it limits viral transmission. Indeed, few viruses exhibit both high lethality and transmissibility (among human viruses, smallpox is the only known example). What is IAV aiming for? Perhaps to diminish immunological memory to preserve a susceptible host population. Perhaps to induce sufficient sneezing, coughing, rhinorrhea, etc., to maximize transmission, but not such severe disease that the host remains at home in bed with minimal chance to infect others.

It may be exceedingly difficult to accurately model the effects of these evolutionary constraints in animal models, which are unlikely to recapitulate subtle immunologi-

cal, behavioral, or physical effects critical to human IAV transmission. Complicating matters is the constant flow of IAV between host species, which may preserve genes that confer a significant selective advantage in some species but not others, and de-optimize transmission for any one species. Identifying factors such as PA-X, however, is an essential step on the path to greater understanding.

#### References and Notes

1. S. Kryazhinskiy, J. Dushoff, G. A. Bazykin, J. B. Plotkin, *PLoS Genet.* **7**, e1001301 (2011).
2. B. W. Jagger *et al.*, *Science* **337**, 199 (2012); 10.1126/science.1222231.
3. M. F. Belcourt, P. J. Farabaugh, *Cell* **62**, 339 (1990).
4. K. A. Dittmar, J. M. Goodenbour, T. Pan, *PLoS Genet.* **2**, e221 (2006).
5. J. J. Sanz-Ezquerro, S. de la Luna, J. Ortín, A. Nieto, *J. Virol.* **69**, 2420 (1995).
6. S. Boivin, S. Cusack, R. W. H. Ruigrok, D. J. Hart, *J. Biol. Chem.* **285**, 28411 (2010).
7. W. Chen *et al.*, *Nat. Med.* **7**, 1306 (2001).
8. A. Krumbholz *et al.*, *Med. Microbiol. Immunol.* **200**, 69 (2011).
9. D. Zamarin, M. B. Ortigoza, P. Palese, *J. Virol.* **80**, 7976 (2006).
10. J. L. McAuley *et al.*, *Cell Host Microbe* **2**, 240 (2007).

**Acknowledgment:** Supported by the Division of Intramural Research, NIAID.

10.1126/science.1225539

## BIOCHEMISTRY

# Nature's Intricate Clockwork

Brian R. Crane

Much of human physiology and behavior is influenced by circadian rhythms (1). Whether you burned the midnight oil, rose at the crack of dawn, or enjoyed your rest last night, tiny clocks in your cells have been trying to keep you on schedule. Over the past decade, remarkable progress has been made in elucidating the molecular genetics of these single-cell oscillators (2, 3). More recently, structural biology has begun to contribute a detailed picture of our clock components. On page 189 of this issue, Huang *et al.* (4) move these efforts forward dramatically with a crystal structure of the heterodimeric transcriptional activator CLOCK:BMAL1, a protein complex that is a key component of the circadian oscillator in mammals.

The CLOCK:BMAL1 complex controls the expression of numerous genes, includ-

ing those that code for the oscillator proteins of the clock itself. The oscillator proteins are translated in the cytoplasm, but return to the nucleus to inhibit their own production by directly repressing the activator (see the figure, panel A) (2, 3). This transcription-translation feedback loop repeats over a ~24-hour period, with a phase that sets to the day-night cycle. In mammals, the activator consists of two proteins known as CLOCK and BMAL1. *Clock* was the first mammalian circadian rhythm gene to be identified in genetic screens and cloned (5), whereas the BMAL1 protein was found through its interaction with CLOCK (6).

Now, 15 years after cloning CLOCK, the same group has determined the crystal structure of CLOCK in complex with BMAL1. Both these proteins are made up of two domains that are found throughout biology, serving a range of functions. bHLH (basic helix-loop-helix) domains are DNA recognition modules found in many eukary-

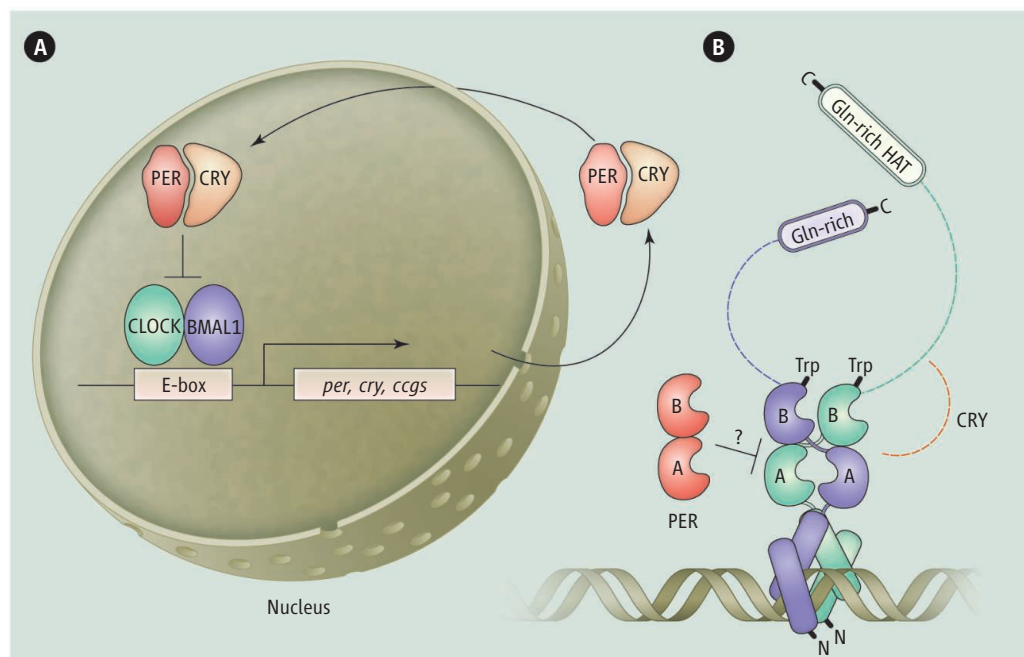
The crystal structure of a transcriptional activator reveals the inner workings of the mammalian circadian clock.

otic transcription factors (7). PAS (PER-ARNT-SIM) domains are signaling modules, conserved across all domains of life, that mediate protein-protein interactions and can bind small molecules (8). bHLH-PAS heterodimers include regulators such as Hif-2 $\alpha$ :ARNT, a molecule important for the response to hypoxia and growth of blood vessels (9). The study by Huang *et al.* provides the first detailed structure of a bHLH-PAS heterodimer.

The CLOCK:BMAL1 structure reveals typical interactions between the respective bHLH and PAS domains of each subunit, but also shows an interesting twist (see the figure, panel B). Both CLOCK and BMAL1 consist of an amino-terminal bHLH domain followed by a PAS-A domain in tandem with a PAS-B domain. As expected, the bHLH modules dimerize into a four-helix bundle that recognizes the E-box DNA sequences found in the regulatory regions of clock control genes. The PAS-A domains heterodi-

Department of Chemistry and Chemical Biology, Cornell University, Ithaca, NY 14850, USA. E-mail: bc69@cornell.edu





**The core oscillator of the mammalian circadian clock.** (A) The transcriptional-translational feedback loop that makes up the core oscillator of the mammalian circadian clock. CLOCK and BMAL1 bind to E-box DNA sequences to activate clock-controlled genes (cogs), including those that code for the oscillator proteins PER and CRY. PER and CRY are translated in the cytoplasm and then cycle back into the nucleus to directly repress CLOCK:BMAL1. As PER and CRY levels drop, CLOCK:BMAL1 reactivates another round of transcription. (B) The CLOCK (green) and BMAL1 (blue) proteins heterodimerize to bind DNA through their N-terminal bHLH domains. The structure reported by Huang *et al.* shows that the PAS A domains dimerize symmetrically; in contrast, the PAS B domains form a head-to-tail interaction, mediated by a conserved Trp residue on BMAL1 that binds into a pocket on the back side of CLOCK PAS-B. The analogous Trp on CLOCK projects into solvent for putative interactions with CRY. To inhibit transcription, the PER tandem PAS domains may interact with those of CLOCK:BMAL1. Unstructured regions of CLOCK and BMAL1 (dotted lines) are important for transcriptional activation and histone acetyltransferase (HAT) activity. Gln, glutamine; ccgs, clock-controlled gene sequences.

merize in the symmetric manner also seen in other PAS associations.

In contrast, the PAS-B domains do not interact symmetrically; CLOCK PAS-B twists relative to the dimer interface and makes a head-to-tail interaction with BMAL1 PAS-B. A conserved tryptophan (Trp) residue on an extended loop of BMAL1 PAS-B binds into a pocket on the back side of CLOCK PAS-B. The role of this conserved Trp recalls that of an analogous Trp found in the fly oscillator protein PERIOD (PER), which also contains tandem PAS domains and uses a similar Trp-mediated contact to homodimerize (10, 11).

The Trp-receiving pocket on CLOCK resembles the cofactor-binding pocket in other PAS proteins. CLOCK also conserves this Trp residue, but because the CLOCK PAS-B twists around, the CLOCK Trp projects away from the BMAL1 interface. Moreover, this residue is contained in a known recognition element for the other main oscillator component, the flavoprotein CRY (3). Thus, an aromatic residue plugging into the PAS receiver pocket not only mimics small-molecule recognition in other PAS proteins,

but may represent a common mechanism for latching PAS domains to their partners.

Given the close relationship between the PAS domains of the PERIOD proteins and those of CLOCK:BMAL1, Huang *et al.* suggest that the PERIOD PAS domains may compete with those of either CLOCK and BMAL1 in the act of repression. This intriguing idea has some parallels to how the light-sensitive PAS activator of the fungal clock (WC1:WC2) is attenuated by the PAS protein VVD (12–14). Thus, it is tempting to think that the clock mechanism is partly based on exchanges between PAS domains, binding and releasing each other, like the interlocking teeth of a watch gear.

The authors test the observed heterodimeric contacts in CLOCK:BMAL1 through cellular interaction and transcription assays with mutated proteins designed to disrupt the heterodimer. Transcriptional rhythms driven by the modified CLOCK:BMAL1 proteins are complex but clearly demonstrate the functional relevance of the crystallized dimer.

However, important regions of both CLOCK and BMAL1 are not contained

in the structure. An absent glutamine-rich carboxyl-terminal region of CLOCK involved in transactivation of the transcriptional machinery has been shown to have histone acetyltransferase activity (15). CLOCK acetylates not only histones but also BMAL1 on a similar disordered region. These activities are required for CLOCK:BMAL1 to regulate clock-controlled genes and thereby involve the clock activators in chromosome remodeling (15). How such activities play into gene regulation and coordinate with repression by PER and CRY (see the figure, panel A) remains to be seen.

The clock mechanism has additional interconnected loops that involve many cellular components with overlapping and redundant roles. Structures such as that reported by Huang *et al.* provide the opportunity to engineer protein variants with defined functionality. By introducing these modified proteins back into living systems of known genetic backgrounds, we can try to dissect how specific properties of the components play out within these cellular circuits. Ultimately, these studies may allow us to understand biological responses bestowed by different genetic makeups and even manipulate behavior at the level of biochemistry.

## References

1. U. Albrecht, *Neuron* **74**, 246 (2012).
2. P. L. Lowrey, J. S. Takahashi, *Adv. Genet.* **74**, 175 (2011).
3. J. C. Dunlap, *Cell* **96**, 271 (1999).
4. N. Huang *et al.*, *Science* **337**, 189 (2012); 10.1126/science.1222804.
5. D. P. King *et al.*, *Cell* **89**, 641 (1997).
6. J. B. Hogenesch, Y. Z. Gu, S. J. Jain, C. A. Bradfield, *Proc. Natl. Acad. Sci. U.S.A.* **95**, 5474 (1998).
7. W. R. Atchley, A. D. Fernandes, *Proc. Natl. Acad. Sci. U.S.A.* **102**, 6401 (2005).
8. Y. Z. Gu, J. B. Hogenesch, C. A. Bradfield, *Annu. Rev. Pharmacol. Toxicol.* **40**, 519 (2000).
9. T. H. Scheuermann, J. S. Yang, L. Zhang, K. H. Gardner, R. K. Bruick, *Methods Enzymol.* **435**, 3 (2007).
10. O. Yildiz *et al.*, *Mol. Cell* **17**, 69 (2005).
11. H. A. King, A. Hoelz, B. R. Crane, M. W. Young, *J. Mol. Biol.* **413**, 561 (2011).
12. B. D. Zoltowski, B. R. Crane, *Biochemistry* **47**, 7012 (2008).
13. C. H. Chen, B. S. DeMay, A. S. Gladfelter, J. C. Dunlap, J. J. Loros, *Proc. Natl. Acad. Sci. U.S.A.* **107**, 16715 (2010).
14. E. Malzahn, S. Ciprianidis, K. Kaldi, T. Schafmeier, M. Brunner, *Cell* **142**, 762 (2010).
15. B. Grimaldi, Y. Nakahata, M. Kaluzova, S. Masubuchi, P. Sassone-Corsi, *Int. J. Biochem. Cell Biol.* **41**, 81 (2009).

10.1126/science.1224611



## INTRODUCTION

# HIV/AIDS In America

THE EPIDEMIC OF ACQUIRED IMMUNODEFICIENCY SYNDROME WAS FIRST recognized in the United States. As clinicians from Los Angeles, California, reported in the 5 June 1981 issue of *Morbidity and Mortality Weekly Report*, they had seen odd immune problems and opportunistic infections in five young “active homosexuals.” Similar reports soon came in from all over the country and the world, making it clear that AIDS affected heterosexuals and homosexuals alike and also spread from mother to child and via tainted blood products and dirty needles. In the following years, U.S. researchers helped prove that HIV causes the disease, which led to a critical blood test to detect the novel retrovirus. The U.S. National Institutes of Health and the Centers for Disease Control and Prevention—prodded by AIDS activists such as Mark Harrington of the Treatment Action Group (pictured here)—steadily ramped up support for basic research as well as efforts to develop and test treatment and prevention interventions. In the early 2000s, the U.S. government poured billions of dollars into programs that now bring life-saving antiretrovirals to millions of people in cash-strapped countries.

By any measure, the United States has played a vital global role in unraveling HIV’s mysteries, providing help to the infected and protecting the vulnerable.

It may seem odd, then, that since 1990 this country has not hosted the International AIDS Conference, a megameeting that has gathered 20,000 participants every other year. But that will change on 22 to 27 July, when the gathering will take place in Washington, D.C. The meeting organizers shunned the United States because of an immigration ban on HIV-infected people imposed by Congress in 1987, which President Barack Obama ended in 2010.

In keeping with that shift, *Science* is focusing this special HIV/AIDS issue on America, now home to an estimated 1.2 million HIV-infected people—many of whom have little in common with the original five gay men in Los Angeles. The Deep South has become the epicenter; blacks—gay and straight—face a far higher risk of becoming infected than whites, and poverty is a major driver for all races. The biggest challenge the country faces today is diagnosing all of its HIV-infected people and helping them take full advantage of the existing treatments, which both stave off disease and make people less infectious. It is a problem shared worldwide.

Correspondent Jon Cohen, working with photographers Malcolm Linton and Darrow Montgomery, visited 10 U.S. cities this spring, and the package of stories that begins on p. 168 describes the varied epidemics and responses. A News Focus by Cohen spends a day with Anthony Fauci, who leads the NIH branch that funds more HIV/AIDS researchers than any institution in the world (p. 152). This special issue also includes an Editorial by Salim Abdool Karim (p. 133), who highlights problems rolling out what’s known as pre-exposure prophylaxis, as well as an update on HIV antibody research by Dennis Burton and colleagues (p. 183) that promises to inform AIDS vaccine development. Online, a slide-show offers more images and stories about the country’s epidemic, and *Science Careers* features profiles of two young HIV/AIDS public health workers making a big dent in big-city epidemics.

— LESLIE ROBERTS

## A Tale of 10 Cities

### CONTENTS

#### News

- 168 The Many States of HIV in America
- 172 *Birmingham, Alabama: A Southern HIV/AIDS Program With All the Fixins*
- 173 *Jackson, Mississippi: By the People, For the People*
- 174 *Atlanta, Georgia: And the Band Played On, Vol. 2*
- 175 *San Francisco, California: A Concerted Effort to Lighten the Load*
- 176 *Los Angeles, California: Life in the Fast Lane: HIV and Meth*
- 177 *San Diego, California, and Tijuana, Mexico: My Virus Is Your Virus*
- 178 *New York, New York: Miracle on 34th Street: Success With Injectors Pay Now, Benefits May Follow*
- 180 *Providence, Rhode Island: HIV and the Cell: The Prisoner’s Dilemma*
- 181 *Baltimore, Maryland: Dancing the Night Away; Keeping HIV at Bay*
- 182 *Washington, District of Columbia: HIV/AIDS Response Renovated in Capital*

#### Review

- 183 Broadly Neutralizing Antibodies Present New Prospects to Counter Highly Antigenically Diverse Viruses  
D. R. Burton et al.

See also Editorial p. 133; News Focus story p. 152; Science Express Policy Forum by S. Lynch et al.; Science Careers; Science Translational Medicine article by C. Sundling et al.; and Science Podcast at <http://scim.ag/hiv2012>

# Science





**Detention/retention.** HIV-infected inmates such as Rhode Island's Robert Quintana benefit from programs that link care on the inside and outside.

time" of his life. "On the one hand, I had the stigma of the virus itself, and on the other hand, people in church said you're damned because you're gay," says Alexander, a devout Baptist. "There were some very, very gloomy times when I'd sit at home and get to thinking, 'Why is this happening to me? I'm fighting a constant battle that I can't win.'"

Alexander soon vomited the overdose of antiretroviral drugs, and he now laughs about his "oxymoronic" attempt to commit suicide with the very drugs that he depends on to stay alive. But he, like many others, struggles to take antiretroviral drugs day after day, year after year. Efforts to help people like Alexander deal with their challenges have now moved to the top of the HIV/AIDS agenda in the United States.

Taking antiretroviral drugs as prescribed can fully suppress an HIV infection, keeping disease at bay for decades. There's another huge benefit, as well: A large study completed in 2011—*Science's* "Breakthrough of the Year" (23 December 2011, p. 1628)—provided irrefutable evidence that people who have undetectable levels of the virus in their blood rarely spread the infection to others. Yet as wealthy as the United States is, antiretroviral drugs are having nowhere near the treatment or prevention impact they could have on the country's epidemic. "We only have a little more than 1 million infected people in the United States, and per case, we probably have one of the highest expenditures in the world," says Carlos del Rio, a clinical researcher based at Emory University in Atlanta. "We ought to be able to do something to stop the epidemic. But the problem is that it's not just a medical disease. In fact, the least of the difficulty is the medical part of the disease. It's the social, structural things that are driving the epidemic."

This spring, *Science* met with HIV-infected people, at-risk communities, researchers, caregivers, health officials, and advocates in 10 cities, traveling to the Deep South and the West and East coasts to see the varied epidemics and the local responses up close. The package of stories on the following pages looks at everything from the social and structural issues to the medical and scientific challenges through the eyes of people on the front lines, as well as the research efforts under way to try to slow, if not one day bring to a halt, the spread of HIV.

# The Many States Of HIV in America

Treatment as prevention promises to help the infected and dramatically slow the spread of the virus, but the epidemic's changing demographics present myriad challenges in this diverse country

IN THE SPRING OF 2006, A YEAR AFTER JOSHUA Alexander took part in an HIV testing day at his college and found out he was infected, he tried to kill himself. He did not do it with a gun, a noose, or the tailpipe of a car. He chose instead to gulp down his entire supply of the anti-HIV drugs Truvada and Viramune.

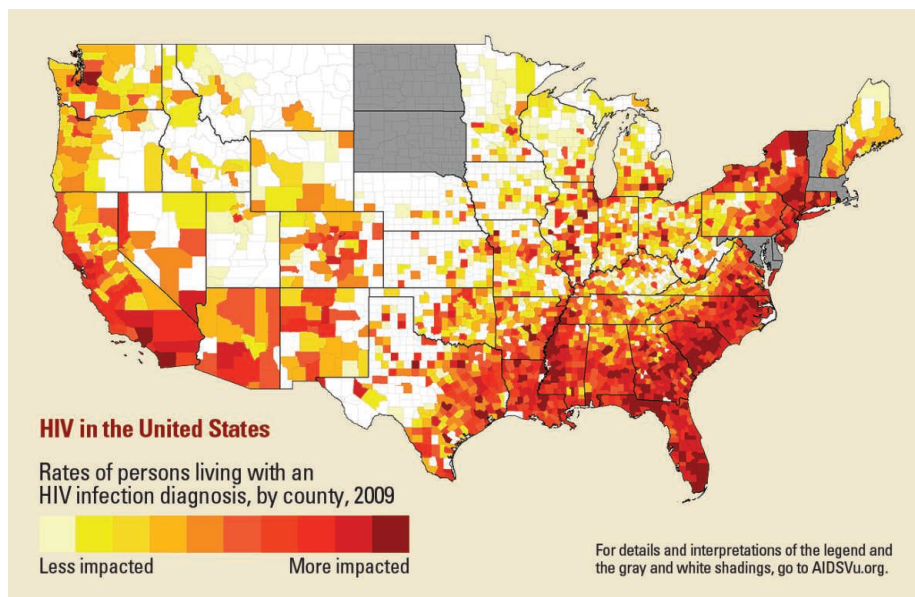
Alexander, then 19 (pictured at right with his family), had taken time off from Delta State University after he learned of his diagnosis and moved back to his

mother's home an hour away in Greenville, Mississippi, a small town bordered by cotton fields, catfish ponds, and an oxbow lake that branches off "Old Man River." About one-third of the town lives below the poverty line, and an abundance of boarded-up shotgun shacks and cottages tilt on the clay soil. But Alexander's mother had provided well for her five children, and money wasn't his main issue—his version of the Delta blues came from what he called "the double nega-

### Treatment cascade

When AIDS surfaced in the United States 31 years ago, it was largely a disease of economically stable, white, gay men living in big cities on the West and East coasts. But today, HIV disproportionately infects African-American men who have sex with men (MSM), like Alexander, and the epicenter of the epidemic is in the poverty-stricken Deep South. In addition to confronting deep-rooted homophobia and stigma for being infected, many face the added burdens of unemployment, homelessness, mental illness, incarceration, substance abuse, and lack of medical insurance and access to qualified care providers—all of which pose obstacles to even getting an HIV diagnosis, much less taking pills every day. “What’s happening among young, black MSM in the United States jumps out and screams,” says Phill Wilson, a leading HIV/AIDS advocate who founded the Black AIDS Institute in Los Angeles. “We have the richest country on the planet, and you have a population impacted more than the poorest parts of the planet.”

Del Rio’s work has helped popularize the notion of a “treatment cascade,” a series of factors that create a vast gap between HIV infection and control of the infection. Roughly 20% of infected people in the United States do not know their HIV status. Among those who do, many never seek care. Some see a doctor but fail to show up for subsequent appointments. Of those who start taking antiretroviral drugs, many have difficulty staying on them. Building on del Rio’s earlier work, the U.S. Centers for Disease Control and Prevention (CDC) highlighted the treatment cascade in its 2 December 2011 issue of *Morbidity and Mortality Weekly Report* (MMWR), showing that of the estimated 1.2 million infected people in the country, only 28% receive medication, adhere to their



prescriptions, and have fully suppressed viral loads (see graph, p. 171).

In July 2010, the Obama Administration issued the first-ever National HIV/AIDS Strategy, which lays out a plan for increasing the proportion of diagnosed MSM with undetectable viral loads by 20% within 5 years. The plan has the same goals for blacks and Latinos who are not MSM. “We need to focus our resources where the epidemic is,” says Grant Colfax, who directs the White House Office of National AIDS Policy. An openly gay clinician who formerly ran the prevention and research section of the widely praised San Francisco Department of Public Health, Colfax says hard-hit locales also have to spend more of their own money addressing the problem in their most affected communities. “There is no magic bullet here,” Colfax says. “Every epidemic is local, and we need to look at local solutions.”

### Diverse drivers

With an adult HIV prevalence of 0.6%, the United States ranks 39th in the world, on par with many countries in Europe and Latin America. But because of the relatively large U.S. population of 311 million, only six countries have more HIV-infected people, and its burden matches that of Zimbabwe and Uganda. “I’m always taken aback by that,” says Wafaa

El-Sadr, an epidemiologist at Columbia University’s Mailman School of Public Health in New York City. “We don’t see it that way because it’s not evenly distributed: There are hot spots. There also are some populations, especially MSM, who have risks of acquiring HIV that are higher than in sub-Saharan Africa. Ask

### Online

sciencemag.org

Slideshow and podcast (<http://scim.ag/hiv2012>).

people on the street, and nine of 10 would say, ‘We took care of HIV, it’s not a problem any more.’ And *that’s* the problem.”

MSM accounted for 61% of the estimated 50,000 new infections in the country in 2009, according to the latest CDC figures. Heterosexuals made up the second-largest risk group, with 27% of new infections, and the remaining 12% were injecting drug users, or IDUs (3% of whom were also MSM). Although blacks make up only 14% of the population, they accounted for 44% of new infections. Rates of infection are six times higher for black males than white males, and black females have a whopping 15 times higher rate of infection than white females. Black MSM between the ages of 13 and 29 were the only group that saw an increase in new infections between 2006 and 2009; the number climbed by 48%. One in five newly infected people were Latino, which is also disproportionately high compared with whites.

CDC divides the United States into four regions—Northeast, South, West, and Midwest—to assess HIV/AIDS. “There are striking geographic differences,” says CDC



**Sitting tall.** With his family’s support, Alexander (right) has overcome his HIV-induced gloom.

PHOTO: MALCOLM LINTON; MAP SOURCE: AIDSvU.ORG



epidemiologist Jonathan Mermin.

The Midwest has the fewest cases. In the West, five small neighboring states that together are home to under 5 million people—Wyoming, North and South Dakota, Idaho, and Montana—each report fewer than 1000 people who have a diagnosed HIV/AIDS infection, but California has 106,000, making it second to only New York (128,000). The South has the heaviest burden, with 43% of the country's HIV-infected people. A recent report about the HIV/AIDS "crisis" in the South by the Duke University Center for Health Policy and Inequalities Research in Durham, North Carolina, analyzed CDC data and found that the region has eight of the 10 U.S. states with the highest rate of new infections and the highest death rates from AIDS. Several cities outside the South have been hit especially hard by HIV, including New York, Los Angeles, San Francisco, Chicago, Philadelphia, and Baltimore, which together in 2007 accounted for 30% of all people living with HIV/AIDS. The virus also readily moves back and forth across the U.S.-Mexico border.

The drivers of spread in the country similarly differ from place to place. "It's not one U.S. epidemic; it's multiple microepidemics," says Kenneth Mayer, medical research director at the Fenway Institute in Boston, which specializes in HIV-prevention studies. Mayer notes that transmission in many white and Latino MSM has links to methamphetamine and cocaine use, but drugs play only a small role in the Southern epidemic in black MSM, who often have their own insular subcultures and sexual networks. Women accounted for nearly 70% of the heterosexual spread, and 60% of those infections in 2009 were in black females, who have distinct sexual networks themselves. Needle-exchange programs have dramatically slowed the spread



**Reaching out.** As men at the Sippi Citi club in Jackson, Mississippi, do a "strolling" line dance, a table in one corner staffed by My Brother's Keeper promotes HIV prevention.

among IDUs in some cities, but bans on the use of federal and state funds for such efforts means that they are scarcely used elsewhere. Commercial sex work does not seem to be a major factor in the country, but recent studies are "sorely lacking," Mayer says. Studies of transgenders are few, too, but those that exist indicate extremely high prevalence.

A plethora of research has focused on analyzing why black MSM and heterosexual women, particularly in the South, have become especially vulnerable to HIV. CDC's Gregorio Millett has closely examined the spread in black MSM, and his findings have challenged many hypotheses. As Millett and co-workers explained in the 15 May 2011 issue of *AIDS*, no studies have shown convincing evidence that black MSM have more partners or more frequently have receptive anal sex without a condom, both known risk factors for HIV infection. Citing data from a survey of nearly 10,000 white and black MSM who agreed to take HIV tests, the researchers concluded that the racial disparity in HIV prevalence had no link to incarceration or circumcision, either.

Several studies have reported that black MSM are more likely to have partners of their own race than are white MSM, and Millett's group concluded that this played a key role in explaining their higher prevalence. The researchers found a link between risk of infection and not knowing a partner's HIV status, and they also discovered that black men who knew that they were infected before the study were less likely to be on anti-

retroviral drugs than white men. This double whammy means that uninfected black MSM are more likely to have sex with a highly infectious man than are their white counterparts. Studies have also shown higher rates of sexually transmitted infections such as syphilis in black MSM, which eases spread.

Epidemiologist Adaora Adimora of the University of North Carolina, Chapel Hill, contends that the high rate of HIV in Southern black women reflects higher rates of concurrent partnerships—relationships that overlap—which is linked to the frequent incarceration of men that splits couples. In the July 2006 issue of *Sexually Transmitted Diseases*, Adimora and colleagues describe several studies that support this thesis, including one they did that surveyed HIV-infected women in North Carolina who had no link to IDUs or MSM. Of these 128 women, 37% had had concurrent partnerships within the past year, 89% said one of their last three partners was having sex with someone else, and 82% said one of these men had been incarcerated. According to the U.S. Bureau of Justice Statistics, one in three black men will be incarcerated during their lives, in contrast to one in 17 white men.

As racially skewed as the epidemic is, important factors in the spread of HIV are not confined to race, cautions Kevin Fenton, who directs CDC's National Center for HIV/AIDS, Viral Hepatitis, STD, and TB Prevention. "When I think of the U.S. epidemic, it's easy to be seduced into the narrative of the epidemic in African Americans," Fenton says. "But the real narrative is poverty, disenfranchisement, and a fragmented health-care system weaving together to create big social challenges."

Fenton points to a CDC study published in the 12 August 2011 issue



**Plan man.** Grant Colfax oversees the Obama White House's HIV/AIDS strategy.

of *MMWR* of nearly 15,000 heterosexual, non-IDU adults in 24 high-poverty urban areas. Study participants were predominantly black (72%), followed by Latino (18%) and white (5%). Nearly 2% turned out to be infected. The highest prevalence was seen in men and women who had lower socioeconomic status—regardless of race. Lack of a high school degree, household income below the poverty level, and unemployment were each independently associated with higher prevalence. “The social drivers are so powerful, and what’s exciting about this is when you think through the social-determinants lens, the solutions become different,” Fenton says. “You can’t just rely on testing, linkage to care, and treating people. It’s necessary but not sufficient. Unpack these social determinants and there are new ways to tackle the epidemic.”

### Rebooting

In response to the National HIV/AIDS Strategy, CDC has begun to reallocate how it supports U.S. HIV/AIDS work. In 2012, CDC shuffled \$40 million of its \$338 million budget to have more of an impact in harder-hit locales, and plans call for similar shifts over the next 4 years. CDC also launched the 12 Cities Project that, by the end of 2012, will have pumped \$30 million of new money into improving the response in urban areas that have 44% of the AIDS cases. There’s a concomitant push to cut funding to behavioral modification programs and ideology-driven work such as abstinence education. Instead, CDC wants more high-impact, cost-effective, evidence-based programs that link people to care, target MSM and drug users, and conduct testing at high-incidence locales.

Wilson of the Black AIDS Institute

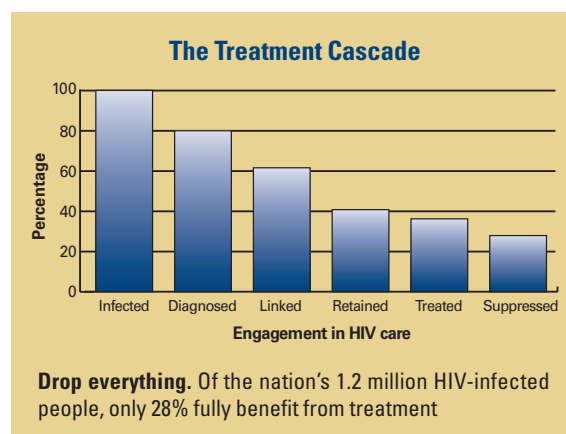
praises the national strategy for spelling out clear, interrelated goals, but he also worries about unintended consequences of the “medicalization” of prevention, as many of the black groups he works with don’t yet have the technical capacity to work with clinics and may lose funding, Wilson says. “With HIV and AIDS, the messenger matters. Having institutions that are from the community and have its trust are critically important,” says Wilson. In May, the Black AIDS Institute’s African American HIV University held a week long teach-in for community-based organizations from around the country to help them adapt to this new world in which treatment as prevention is king.

A key challenge for everyone working in the HIV/AIDS field is to find novel interventions that better address the treatment cascade. More and more clinics have begun working with navigators or mentors to help people overcome issues with housing, food, drug use, incarceration, and transportation. An increasing number of emergency rooms routinely test everyone for HIV. One large-scale clinical trial in Washington, D.C., and the Bronx funded by the U.S. National Institute of Allergy and Infectious Diseases (NIAID) is investigating whether offering financial incentives can help people control their infections. “This is a solvable problem,” says NIAID Director Anthony Fauci (see News Focus). “I mean, c’mon. It’s

a finite problem with a finite solution. So we can do it.”

Fauci, whose lab has made fundamental discoveries about HIV and the immune system, says researchers also have to adjust to this new era that is striving to figure out the best ways to apply existing tools. “The rush that

**Homecare.** San Francisco General found patient Vanessa Romo this housing.



**Cascade brigade.** Nurse Diane Jones’s team at San Francisco General Hospital specializes in retaining patients in care.

you get out of discovery of something that you didn’t know before is a very different feeling than the excitement you get when you see that if you implement proven things that you can actually turn the thing around,” Fauci says. “It isn’t that kind of eureka moment. It’s more of a cause.”

The cause also includes HIV-infected Americans, who from the start of the epidemic have had an astounding influence on both science and society’s response to the disease. Alexander, who is majoring in social work, is part of the new generation of advocates, and he sees himself devoting his career to his version of the cause. “When I first found out I was positive, the social workers were awesome,” he says. “Now there are no text messages, smoke signals, nothing.” If he were a social worker, he’s confident he could use his own experiences to help people through their tough times and to stay on their medication. “I’d like to do outreach to make people not feel bad about being infected,” Alexander says. “That’s where my heart is.”

—JON COHEN





# A Tale of 10 Cities



BIRMINGHAM, ALABAMA

## A Southern HIV/AIDS Program With All the Fixins

FEW PEOPLE WOULD CONFUSE THIS CITY, dubbed the Pittsburgh of the South because of the iron and steel industry that once boomed here, with San Francisco. Yet here in the heart of the Deep South, Michael Saag and his team at the University of Alabama, Birmingham (UAB), now the state's biggest employer, have built a full-service HIV/AIDS center modeled on the widely praised program at San Francisco General Hospital. Not only does UAB's 1917 Clinic, named after its original street address, perform cutting-edge research and pivotal clinical trials, but it has also helped patients overcome the stigma about HIV that is all too prevalent in this part of the country and stay in treatment and on their drugs.

Virologist Robert Schooley, an HIV/AIDS clinical researcher at the University of California, San Diego, says one of the most remarkable aspects of the 1917 Clinic is that it's in his hometown of Birmingham—which is not known for embracing diversity. “Mike has done a great job in putting together

something in a place that had the potential to be incredibly hostile to HIV and anybody with it,” Schooley says.

The 1917 Clinic treats 2000 patients in a multiservice building that features a dentist, social workers, peer mentors, counseling, a pharmacy, and a chaplain. A research team led by Saag, who started the clinic in 1988, has run trials that have helped bring almost every antiretroviral drug to market, tested vaccines, and analyzed critical issues such as stigma and retention in care. “It provides comprehensive, state-of-the-art care in a good environment, and it's one-stop shopping,” says Steven Deeks, a clinician and researcher at San Francisco General Hospital, who recently visited the 1917 Clinic.

In December 1986, Saag spent a day at Deek's hospital to learn from the best. During his visit, he noted how they trained providers all over the city and worked closely with the community. Their clinic, Ward 86 (see p. 175), had an unusually warm, welcoming environment. He asked what they

**Test everyone.** The ER at UAB's hospital checks the HIV status of all adults unless they opt out. Jamey Daniel came in for a toothache.

would do differently if they were starting over, and they said they would create a computer database to track patients, and keep specimens frozen for later study.

The 1917 Clinic now has electronic medical records on 8000 people. As a result of this close monitoring, Saag and his team can easily tap demographic and health information about their entire patient population: nonwhite (55%), white (45%), men who have sex with men (52%), heterosexuals (34%), and injecting drug users (8%). Overall, 71% of the patient population has a fully suppressed viral load, which is similar to San Francisco General's success rate.

UAB's Michael Mugavero has used the database to study retention and linkage to care and assess how the 1917 Clinic and the rest of the country can do better. “We've focused a lot on testing and treatment and forgotten about what's in between,” says Mugavero, a clinical behavioral epidemiologist. A study he co-authored in the 15 January 2009 issue of *Clinical Infectious Diseases* assessed the 60% of patients who missed appointments in the year following their first one—an indicator of health behavior—and found that they subsequently died at twice the rate of patients who kept all appointments. “The fundamental challenge is that at a local, state, and national level we've had inadequate surveillance of individuals after diagnosis, which makes it difficult to determine who is retained in care and then take action,” he says.

Mugavero and other HIV researchers at UAB, which until 2011 included the powerhouse husband-and-wife team of George Shaw and Beatrice Hahn, have made their mark in almost every part of the field from the lab to the clinic to shaping guidelines and policies. Saag has published 240 papers about HIV/AIDS, co-authoring landmark studies about the diversity of viral genotypes in each infected person and the value of measuring viral levels to help manage a person's disease.

Clinicians and staff members at the

1917 Clinic have taken several progressive approaches to addressing the local epidemic. UAB's hospital emergency room runs HIV tests on all patients 19 to 64 years old unless they opt out. "It's an unusual opportunity to counsel, test, and link to care," says ER specialist James Galbraith, who spearheaded the program. A new machine at the hospital, the Abbott ARCHITECT, can detect signs of HIV in people within 8 days of infection, during the acute phase in which people have extremely high viral loads and are more likely to transmit. The nonprofit group AIDS Alabama provides housing for clinic patients, drives them to medical appointments, helps recruit people for AIDS vaccine trials the clinic runs, and conducts media campaigns for testing.

Each week, the clinic holds a discussion group for patients, called Heartsong@1917, and the people who attend tell heartbreaking stories of stigma and discrimination. Lisa J., an African American who served in the Army, says she travels 137 kilometers to come to the clinic because she lives in a small, white town that has enough trouble



Peer mentor Janet Johnson (center) with two HIV-infected peers she helps.

with her race. "I'm from New York City and everything is open," Lisa says. "Come down to the Bible Belt and everything's not like that. I have two children, and I don't want them to be shunned." She says if people in her town knew she was infected, "I'd have to watch how I crossed the street."

Janet Johnson, who sits on the clinic's patient advisory board, says she became infected by injecting drugs, transmitted the virus to her newborn in 1986, and then went clean. She lived in the small town of Arab, 105 kilometers from Birmingham, where "I had to fight for him to go to school and go to the Baptist Church because he might scratch, bite, or poop," she says. Their infections caused such divisions in their church

that they left for a Pentecostal congregation. "My little boy passed away in '99 from AIDS, and he never weighed more than 50 pounds [23 kilograms]," says Johnson, whose husband also died from AIDS. She started using again. By 2002, her CD4 white blood cells, which HIV destroys, had dropped from the normal range of more than 600 per microliter to a life-threatening four.

Johnson started on antiretroviral drugs, entered drug treatment, and found housing with AIDS Alabama. Today, she has an undetectable viral load and a normal CD4 count. She joined a clinical trial at 1917 Clinic, which subsequently began to provide her dental care, and she then joined the staff as a peer mentor who helps others find housing, transportation, and the like. "For us to win the HIV battle, we have to take care of the whole person, not just bits and pieces," Johnson says.

That could be 1917 Clinic's motto.

—JON COHEN

## JACKSON, MISSISSIPPI

# By the People, For the People

AROUND MIDNIGHT ON A RECENT weeknight, a gay club on the west side of town called Sippi Citi suddenly came alive with troupes of dancing men. Some appropriated choreographed routines called J-setting from the majorettes at Jackson State University, while others line-danced in the strolling fashion made popular by the Greek sororities and fraternities at historically black colleges. Adding to the wild incongruity, they shimmied and strutted to a misogynistic hip-hop song about a scheming woman taking advantage of her boyfriend. All in all, it was a perfect place to have outreach workers from My Brother's Keeper stationed in front of a table littered with pamphlets about HIV and other sexually transmitted diseases, advertisements to get tested, and male and female condoms.

My Brother's Keeper is the only community-based organiza-

tion in the state that focuses on those who bear the brunt of the HIV/AIDS epidemic in Mississippi: young black men who have sex with men (MSM). At the end of 2009, 78% of Mississippi's 8142 people living with HIV were black, even though blacks



Community center. My Brother's Keeper taps the bar scene to get out its message.

make up only 37.5% of the population, according to the latest data from the U.S. Centers for Disease Control and Prevention (CDC). A 2008 report from the Mississippi Department of Health found a 48% increase between 2005 and 2007 in HIV in young black men. Mississippi has a higher rate of gonorrhea and chlamydia than any state, and according to a report in the 2 January 2012 issue of *AIDS* co-authored by CDC researchers, it had the country's highest HIV case fatality rate between 2001 and 2007.

Mississippi is one of the poorest states in the nation, and as Human Rights Watch noted in its 2011 report on HIV/AIDS in Mississippi, *Rights at Risk*, half of the residents who know their HIV status do not receive basic health care for their disease. "Save yourself a transatlantic airline fare to a developing country," Craig Thompson, head of the STD/HIV Office for the state's health department, told Human Rights Watch. "Just come to Mississippi, where we have a vast underserved population."

In addition to doing outreach work at clubs like Sippi Citi, My Brother's Keeper offers HIV counseling and testing, trains young men to modify their risky sexual behavior, and partners with CDC and others to do research about the vulnerable young black MSM the



group serves. Founded in 1998 by HIV/AIDS advocate Mark Colomb (who died last year), the group has also tried to combat homophobia in this most conservative city, holding an annual gay pride event—but they do it at a hotel, not in the street. “To be gay here is just not the thing to do,” says June Gipson, who runs My Brother’s Keeper and has a Ph.D. in urban higher education. “We had our biggest Pride last year, and we had 200 people in the room. We hadn’t had but 20 in the past. We probably never will have a parade.”

To better address the health-care needs of African-American MSM, Gipson has teamed up with Leandro Mena, an infectious-disease specialist and researcher at the University of Mississippi Medical Center. Together, they’re creating the state’s first clinic designed for lesbian, gay, bisexual, and transgender people.



**Overtime.** June Gipson (left), shown here outside of a gay club, does prevention education late into the night.

“We want to establish a culturally competent, logistically appropriate place to transfer information,” Mena says. They hope to open the clinic by year’s end. “There’s a significant gay-identified, younger population that has stig-

because of their credibility. “I don’t see any other organization in this state that has a similar potential to establish a relationship with that community,” Mena says. “And that’s because they are part of it.” —JON COHEN

## ATLANTA, GEORGIA

# And the Band Played On, Vol. 2

**AND THE BAND PLAYED ON, THE 1987 EPIC** tome about the early years of the AIDS epidemic, featured Atlanta prominently, largely because what is now called the U.S. Centers for Disease Control and Prevention (CDC) is based here. But author Randy Shilts, who died of AIDS 7 years later, made nary a mention of the city’s epidemic: At that point, the virus had made little headway here. Today, if its large public hospital, Grady Memorial, is any measure, Atlanta has one of the most out-of-control epidemics in the country. “We see a lot of people coming in with three or four T cells and life-threatening opportunistic infections,” says Jeffrey Lennox, chief of infectious diseases at Grady. “We’re seeing a surge in very young men who have sex with men [MSM] who, like most teenagers, don’t take many precautions.”

On a balmy morning in late May, Lennox, who is also on the faculty at Emory University, leads the daily rounds at Grady with eight young doctors rotating through

what’s called the Special Immunology Service. Grady, which receives patients from all over the state, averages about 40 beds a day occupied by AIDS patients. The cases today include horrific opportunistic infections that, since the advent of powerful antiretroviral drugs, are rarely seen in U.S. hospitals nowadays: the skin-blotching Kaposi’s sarcoma, blinding *Mycobacterium avium* complex, seizure-inducing toxoplasmosis, and brain-damaging progressive multifocal leukoencephalopathy. Several patients have dementia and mumble, one is on a respirator, and a few have dangerous forms of tuberculosis that require the doctors to don facemasks. “It’s the ignored epidemic,” Lennox says. “Atlanta is the black San Francisco. It’s a huge mecca for gay black men.”



**Grassroots messaging.** Evolution Project’s Markese Sanders, prevention promoter.

Pregnant HIV-infected women provide another window into the severity of the local epidemic. Ponce de Leon Center, Grady’s sister outpatient HIV/AIDS clinic that treats a stagger-

ing 5000 patients a year, has seen six women in the past 6 months who recently transmitted the virus to their babies—which antiretroviral drugs coupled with C-sections can almost always prevent.

Clinic pediatrician Rana Chakraborty says the root of the problem is that Georgia doesn’t enforce its own laws. He points to a study presented at the American College of Obstetrics and Gynecology meeting in 2010 that surveyed 64 obstetrical hospitals in the state to see whether their HIV-screening policies comported with Georgia law. More than half of the hospitals did not have the proper HIV rapid test needed during labor and delivery, and fewer still had the proper antiretroviral drugs on hand to intervene. “It goes hand in hand with stigma down here,” Chakraborty says, noting that this is the Bible Belt. “It’s just one of those things people don’t want to talk about.”

Similar issues complicate prevention work with MSM. “It’s really difficult to get people involved in prevention,” says Markese Sanders, who recently completed a neuroscience undergraduate degree at Emory and now works at the Evolution Project, a drop-in center for young, black MSM. “You can’t convince them that HIV is a problem and that it’s their community. I had a trans lady get offended when I offered her a test.”

Scant data are available from Grady and Ponce to help Lennox and his colleagues assess whether treatment might be having an effect on prevention, as they’ve just started to build an electronic patient database, Lennox says. “We have this overwhelming

tidal wave of patients hitting us day after day,” he says. “We could have written a ton of papers, but we’re drowning.”

Yet researchers here do often collaborate on national studies that are helping to clarify why so many patients have difficulty fully suppressing HIV. Emory’s Carlos del Rio, who heads clinical research at Ponce, co-authored a widely referenced paper published online 15 March in *Clinical Infectious Diseases* that closely examines the gaps in the continuum of care, or “treatment cascade” (see p. 168). For the difficult populations they treat—including young black MSM, teens who were infected at birth, and many crack cocaine users—del

Rio says they need new models of care, such as clinics that don’t require appointments and that offer food or coffee. He is now helping to run a 10-city study, Project Hope, that asks how best to achieve viral suppression in HIV-infected substance abusers. The study will evaluate the effectiveness of adding a “patient navigator” to the standard care, to help patients deal with clinic visits and the like, and giving financial rewards for treatment compliance. “We need to rethink our approach to the epidemic,” he says.

Lennox says Atlanta clearly has benefited from the introduction in late 1995 of potent combinations of antiretroviral drugs: AIDS deaths peaked at Grady in 1994, dropping

from 990 a year to about 200 now. Still, he’s disappointed that the city hasn’t made more progress. “As frustrating as it was back then to try and help people you couldn’t help, it’s more frustrating now because a significant part of our populations are those who are hardest to engage in treatment,” Lennox says. “If they had been tested earlier when they weren’t sick and there was a network to get them into treatment and give them rides to the clinic and not lose them to follow-up, none of this would be necessary. I would love to close down the AIDS ward at Grady Memorial Hospital. I just don’t see it happening anytime soon.”

—JON COHEN

## SAN FRANCISCO, CALIFORNIA

# A Concerted Effort to Lighten the Load

**MOUPALI DAS AND HER COLLEAGUES AT THE** San Francisco Department of Public Health (DPH) were struck by something missing in a provocative article, “AIDS in America—Forgotten but Not Gone,” that ran in the 18 March 2010 issue of *The New England Journal of Medicine*. A bar graph in the perspective made a stark point: The prevalence of HIV among men who have sex with men (MSM) and other at-risk populations in some U.S. cities on the East Coast approaches that seen in eight sub-Saharan African countries. But if the graph had included San Francisco MSM, as Das and her colleagues later showed in an adaptation of the figure, the bar would have stood taller than the hardest hit country on the graph, South Africa.

San Francisco has a population of 800,000, which is tiny compared with South Africa’s 50 million, but the city has suffered as mightily from HIV as anywhere in the world. As of 2010, 15,861 HIV-infected people lived here, 85% to 90% of whom are male. According to DPH studies, 87% of the males infected with HIV are MSM, and one in four MSM in the city lives with the virus. “This is very different from other epidemics in the United States,” says Das, who directs HIV-prevention research for DPH. So is the response.

The city has made great strides on several fronts over the past few years. After DPH ramped up testing efforts, the percentage of HIV-infected MSM who didn’t know their status dropped from 23 in 2004 to six in 2011. The average CD4 count of 400 at diagnosis is more than twice as high as the rest

of the nation, where many people seek treatment at such late stages that it becomes difficult to save them. DPH works closely with San Francisco General Hospital—Das sees patients there once a week—and, following its lead, issued a policy in 2010 that made San Francisco the first U.S. city to endorse antiretroviral treatment for all HIV-infected people, regardless of their CD4 counts. The hospital’s venerable HIV/AIDS clinic, Ward 86, has pioneered aggressive efforts to link some of the city’s poorest and most troubled people to top-notch care and keep them on the antiretroviral drugs. And in one of its latest innovations, DPH has mapped the amount of virus—the so-called community viral load—in every neighborhood and risk group, which helps guide both treatment and prevention efforts.

California requires labs to report viral load tests of all HIV-infected people, which allowed Das and colleagues—including Grant Colfax, who has since become the Obama Administration’s top domestic HIV/AIDS official (see p. 168)—to analyze com-

munity viral load between 2004 and 2008. In a groundbreaking study published in June 2010 in *PLoS ONE*, they reported a drop in the city’s HIV levels that corresponded with a decrease in the number of new infections. But transgenders, who predominantly live in the neighborhoods known as the Tenderloin and South of Market, had a three times higher viral load than average. “Communi-

ty viral load is one marker that gives a snapshot of the whole continuum” of success and failures, Das says. “We’re doing a little bit better than the rest of the United States in getting people to undetectable HIV levels, but we still have a long way to go.”

## Wards of Ward 86

Some of the challenges facing the campaign are evident in General Hospital’s Ward 86, which takes only patients who have no insurance—and that puts the doctors, nurses, and social workers there on the front line.

First thing on a Friday morning in May, as patients start to fill the waiting room at Ward 86, a team known as PHAST begins to hunt for people who missed their appointments the day before. PHAST stands for Positive Health Access to Services and Treatment, and for the past 10 years, the program has singled out HIV-infected people who have had trou-



**Residency requirement.** Stable housing helped Connie Sprinkle stay on meds.



ble taking care of their disease or who are newly diagnosed. PHAST enrolls people who live in a fog in Fog City, sleeping on the streets, shooting heroin and smoking meth, or wrestling with paranoia and schizophrenia. "People get lost," says Diane Jones (see photo, p. 171), the nurse who runs the program. "Their lives are very chaotic."

After reviewing the previous day's appointment log, Sandra Torres, a social worker, discovers that half of the 20 PHAST patients scheduled for a visit didn't show up. A few rescheduled, and a few others called and said they couldn't make it. "But three are absolutely no-shows," Torres says. "We don't know what's going on."

Torres phones the first no-show, a 49-year-old man who found out he was infected 10 years ago after a PCP overdose hospitalized him. She leaves a message on his voice mail. "He's problematic," she says after hanging up. "He hasn't had labs since October, and his CD4 count was 68 and his viral load was 54,000. He hasn't been here since February. He reports 100% adherence." His blood work suggests anything but.

The second no-show, who like the first is an MSM, has a full voice mailbox. "He's concerning because he likely has anal cancer," Torres says. In September, PHAST's outreach worker went to his house and spoke with him. Torres phones his pharmacy and learns that he hasn't picked up any medication in 3 months. They'll send the outreach worker to his house again.

The third patient is/was an injecting drug user; Torres e-mails him and also leaves a message at his methadone clinic.

Sometimes, the no-shows die, or they move or change clinics without telling anyone. But the PHAST team frequently locates the patients and then connects them to housing, substance treatment, transportation, counseling—or whatever else helps them help themselves. During the past year, 529 people enrolled in PHAST, and 79% of them initially were not receiving antiretroviral drugs. Now, 71% of these patients are taking the drugs. More than a third of the patients "graduated": They kept appointments, refilled medications, and used the emergency room and urgent care appropriately. Another 129 moved on to long-term residential care, switched clinics, or are locked up. Seven died, and 47 did not contact the program for 6 months and fell into



**Takes a village.** San Francisco Department of Public Health's Moupali Das charts community viral load to guide treatment and prevention.

the "lost to follow-up" category.

Diane Havlir of the University of California, San Francisco, who heads the HIV/AIDS program at the hospital and is also a co-chair of the international AIDS conference that will be held next week, notes that when they look at all 2669 patients who received treatment at Ward 86 last year, only 75.4% had undetectable viral loads. "We don't know all the answers," Havlir says. "We have to study what we're doing and better understand the science of delivering care."

Connie Sprinkle, 58, shows the challenges faced by both the PHAST patients and the Ward 86 staff. "Most of my life has just been running and doing what I have to do to survive," says Sprinkle, who is also known as Mama Peaches. Sprinkle told *Science* that molestations by a relative led her to start running away from home at 10 and using heroin at 13. She had her own child at 16 and the next year began dancing in strip clubs. Forgery soon sent her to the penitentiary for a 3-year stint. She was diagnosed with an HIV infection at Ward 86 in 1985, the first year the test became available. It came as little surprise, she says. "I was a

hooker and did IV drugs. I was homeless. I did everything that was wrong."

Sprinkle took AZT when it came to market 2 years later, but the drug made her sick and she stopped after a week. Same thing happened with ddI, the second antiretroviral that came to market. "That made me sicker," she says. "What's the benefit of being sick when you don't feel sick?" By the early '90s, she'd stopped dancing and selling sex and was living in cars and surviving on Social Security income. She rarely visited Ward 86.

Three years ago, suffering from a serious case of *Clostridium difficile*, Sprinkle returned to the ward for help. "My boyfriend of 24 years said he'd had enough of the smell, and he brought me up with my bags and everything," she says. "And he left." Tests showed her CD4 cell count was just 14.

The PHAST team found Sprinkle housing at the city-run Laguna Honda, which has 24-hour care for residents, and she eventually moved to a permanent-care facility, Leland House, supported by the federal Housing Opportunities for Persons with AIDS program. The staff dispenses the antiretroviral drugs and watches her take them each day, which Sprinkle bluntly says she wouldn't do on her own. "There's some ambivalence about the will to live," she says.

Today, Sprinkle's CD4 count is 275 and her viral load is undetectable. So in addition to stabilizing her life and her HIV infection, with PHAST's help, Sprinkle has done her small part to decrease the community viral load—a concept, she says, that had never crossed her mind.

—JON COHEN

## LOS ANGELES, CALIFORNIA

# Life in the Fast Lane: HIV and Meth

STEVEN SHOPTAW RECENTLY HAD A CASE that flapped this unflappable clinical psychologist—and dramatically explains how methamphetamine use on the West Coast has become so intimately linked to HIV in men who have sex with men (MSM).

Shoptaw\* works at the University of California, Los Angeles (UCLA), and runs the Vine Street Clinic, a center for meth research and treatment. He says a longtime patient put an ad on Craigslist that effectively offered men the chance to use him and leave. The rules: No condoms, he was the bottom, and he wore a blindfold. Hyped on crystal meth for 3 days, the HIV-infected Latino

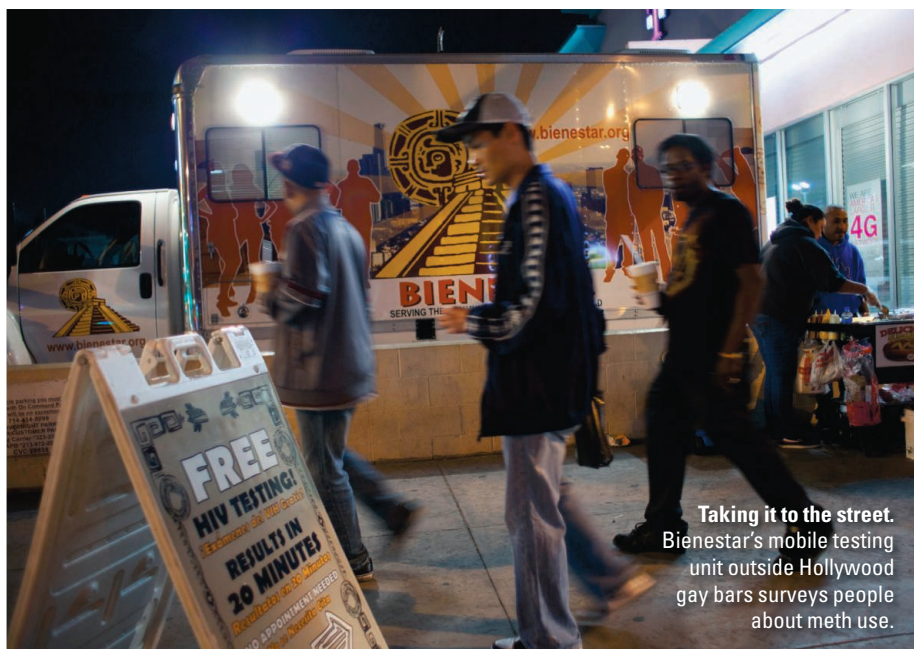
man in his 30s reported that dozens of men came to his hotel room and helped him live out his fantasy. "For many MSM, when they get under the influence of stimulants, particularly meth, it's all accelerator and no brake," says Shoptaw, who has worked closely with his UCLA colleague Cathy Reback, a research sociologist, to document meth's role in the LA epidemic and test interventions. "There's no way they can stop engaging in some extreme form of sexual activity. Meth facilitates extreme sexual behavior that's just not there when men are not high."

Meth, which comes in both a crystalline form ("ice") and a fine powder ("speed"), is

typically smoked or snorted; some users inject it, but there's scant evidence that sharing of syringes occurs and contributes to the spread of HIV. Studies show that meth has gained little popularity in black MSM communities or in MSM who live in the Northeast, Midwest, or South. "It's a real West Coast phenomenon," says Shoptaw, whose clients are evenly split between Latinos and whites. Although the drug is also used by many heterosexuals and leads them to extreme sex, Shoptaw says they have such low levels of HIV in their communities that it hasn't been a factor in transmission. "Even in the presence of a lot of risky behavior, if it's not where the virus is circulating, meth is just a drug problem," he says.

Shoptaw and Reback received widespread attention when they reported in the November 2006 *Journal of Urban Health* about studies in Los Angeles that showed how HIV prevalence in MSM climbed in lockstep with the intensity of meth use. At one extreme, 86% of MSM at a residential treatment facility for drug addiction reported that they were HIV-infected; among recreational users, it was a still-high 23%. Studies have also shown that HIV-infected meth users on antiretroviral drugs (ARVs) have trouble sticking to their treatment regimen. "The simplest explanation is that meth makes you forget to use your ARVs," Shoptaw says.

Shoptaw, Reback, and others have



**Taking it to the street.** Bienestar's mobile testing unit outside Hollywood gay bars surveys people about meth use.

shown that cognitive behavioral therapy—especially if it's "gay-specific"—and a "contingency management" strategy that financially rewards people for staying clean can cut meth use in MSM. Text messaging, which sends notes like "2 much tweak & freak is harsh 2 ur body" at strategic times, can decrease use, too. Several different types of drugs are also being studied, including

some that try to boost the dopamine levels that meth depletes and others that reduce inflammation in the brain caused by the drug. Reback says more men are coming into treatment, but the prevalence of HIV in regular meth users stubbornly remains around 60%. "We haven't put a dent in it."

—JON COHEN

\*Steven Shoptaw is married to the author's cousin.

## SAN DIEGO, CALIFORNIA, AND TIJUANA, MEXICO

# My Virus Is Your Virus

THE TIJUANA RIVER CANAL, A CONCRETE edifice that abuts the Mexican side of the border here, has a sidewalk along its upper ridge that sports a view of what to many locals represents both heaven and hell. Heaven is the opulent Land of Plenty, which stretches as far as the eye can see to the north. Hell is immediately below in the canal's basin—a fetid, garbage-strewn horror that has become home to heroin addicts, many of them deportees from the United States, some infected with HIV.



**Breaching borders.** Steffanie Strathdee (left) and Thomas Patterson track regional spread of HIV.

Men gather in clumps along the sidewalk, putting lighters to spoons that hold the local heroin known as black tar, burning off

the impurities in this version of the opiate. They cook and inject openly, despite the border guards on the San Diego side, who, stationed on a hill in an SUV to deter fence jumpers, watch them through binoculars. Some of the heavily tattooed men have ink on their faces, and several wear syringes balanced behind their ears like pencils. But when they see Susi

Leal, a health promoter who stopped shooting up herself 12 years ago, they smile wide, and there is nothing unsettling about them at all. Leal works with a U.S.-government-funded HIV/AIDS research study in which these men are participating, and it has shown how readily the virus makes a mockery of the border and creates one regional epidemic.

The 8-year-old project, El Cuete—slang for both syringe and being high—is run by a binational team of researchers from the University of California, San Diego (UCSD), located less than 50 km north. "The epidemics of HIV, TB, and syphilis are linked between San Diego and Tijuana," says UCSD epidemiologist Steffanie Strathdee, principal investigator of the project. "You can't just draw the line and say it's their problem, it's not ours."

Strathdee and her husband, UCSD psychologist Thomas Patterson, have published a flood of studies that take a cross-border perspective on HIV, examining the histories and viral status of 3000 injecting drug users (IDUs) in Tijuana, including the canal dwell-





**Painful reality.** Many deported heroin users who live in the Tijuana River Canal consider California home.

ers. A second, overlapping study they run has done similar work with more than 1000 sex workers in Tijuana. And Patterson conducted a third study that has involved 800 men who buy sex in Tijuana, half of whom live in San Diego. A common theme in all of their studies—which they review in a policy forum they co-authored for the June *Annals of Epidemiology*—is that many of these people, by force or free will, go back and forth between Tijuana and southern California, sometimes carrying the virus with them.

Their studies have shown that more than half the male IDUs in Tijuana were deported from the United States. In the canal, several men say they went to America as toddlers and were kicked out in their 20s or 30s after being arrested, most on drug-related charges. “I think more in English than in Spanish,” explains one man, who says he was a San Diego resident for 28 of his 30 years. Another says he was a pastor in Los Angeles for 10 years. Most feel the pull of children and wives back in California; several have multiple deportations on their records. A comparison of male IDUs who had been deported to those who had not found a fourfold higher risk of HIV infection among the deportees, underscoring that mobility and the attendant social upheaval puts people at risk. Patterson says deported women engage in higher risk behavior, too, including sex work. “They get down here in the middle of the night and don’t have any language skills or context to work,” he says.

Strathdee and Patterson have found that

fewer than half of the sex workers and IDUs in Tijuana had been tested for HIV before they joined one of their studies—a huge missed opportunity both to treat and prevent spread (see p. 168). Female IDUs who sold sex and had a sexually transmitted infection such as syphilis have the highest prevalence documented, 12%, which dropped to 10% if they only injected drugs. IDU sex workers said they shot up with clients more than half the time. Patterson’s study of male clients from San Diego and Tijuana found a 5%

## NEW YORK, NEW YORK

# Miracle on 34th Street: Success With Injectors

HIV TYPICALLY SPREADS MORE READILY between people who share needles than in sexual networks, which means a large community of injecting drug users (IDUs) can mark the emergence of an epidemic with great precision. This dense city of about 8 million residents had an estimated 200,000 IDUs in the late 1970s, more than any city in the world. In 1978, Beth Israel Medical Center collected blood samples of users to study liver disease. A retrospective analysis of the samples conducted by Beth Israel’s Don Des Jarlais and colleagues found that 10% were already infected with HIV. By 1981, the prevalence had jumped to 50%, which helped make the Big Apple the center of the country’s AIDS epidemic. “Over half the

prevalence in both groups. Interestingly, in the largest study they did of male IDUs, only 4% of them tested positive for HIV, which is high, but not for IDUs. (They suspect that female IDUs in their study had much higher prevalence primarily because they have higher syphilis rates.)

Although sharing needles is the norm in Tijuana, Daniel Ciccarone, a clinician and researcher at University of California, San Francisco, notes in the May 2009 *International Journal of Drug Policy* that users of black tar heroin—the most popular form of the drug throughout the western United States—have a lower prevalence of HIV than that of those who shoot white or brown versions. He contends that the main factor likely slowing HIV’s spread is that black tar gums up needles and syringes, which frequently have to be cleaned before reuse or thrown out.

Strathdee notes that there were more than 40 million legal crossings from Tijuana to San Diego last year—it is the world’s busiest land border—and she says the two countries have to stop pointing fingers at each other when it comes to HIV/AIDS. She hopes her team’s research will help end the “blame game” and lead both countries to develop a more coordinated approach for treatment and prevention. “We’re absolutely sitting on a time bomb,” Strathdee says. “All of these people are going to fall through the cracks, and it’s going to blow back to both countries. If we don’t do something soon, it’s really going to get out of control.” **—JON COHEN**

injectors were infected before we even knew about AIDS,” says Des Jarlais, as he walks up to the Lower East Side Harm Reduction Center for a visit. New infections occurred in this IDU population at the staggering rate of 13% per year.

Today, studies by Des Jarlais and others have shown that the incidence of HIV in New York City IDUs is 1%. “We’re running out of new infections,” says Des Jarlais, a social psychologist who directs research at Beth Israel’s Baron Edmond de Rothschild Chemical Dependency Institute.

Although the city’s IDU population has dwindled to an estimated 100,000, that doesn’t explain the steep drop in incidence. The main reason is that users stopped shar-

## Pay Now, Benefits May Follow

**BRONX, NEW YORK**—As a celebrated study known in shorthand as HPTN 052 unequivocally proved last year, antiretroviral treatment is prevention: When people reduce the amount of HIV in their bodies, they are less likely to infect others. But for it to work, people, of course, have to learn that they are infected, seek care, and then take their medicine—and there's a steep drop-off between each of these steps, which collectively is called the "treatment cascade" (see p. 168). Now, an innovative and ambitious follow-on trial, dubbed HPTN 065, is taking place both here and in Washington, D.C., to see if it can build on its sister study. "We have to make a dent at every step of the cascade," says Wafaa El-Sadr, the study's principal investigator and an epidemiologist at Columbia University's Mailman School of Public Health.

The HIV Prevention Trials Network (HPTN), sponsored by the U.S. National Institute of Allergy and Infectious Diseases, will spend \$32 million on HPTN 065. The study began in September 2010 and will ultimately involve 10,000 people in the Bronx and D.C., both of which are hard-hit by HIV/AIDS, particularly in African-American and Latino communities. In addition to launching major testing campaigns, the study will assess whether giving cash incentives to people who test positive will encourage them to seek care, thereby reducing their viral loads. Only half of the nearly 40 sites that provide testing and care will offer the incentives, which allows HPTN 065 to determine whether they have an impact. As an added control, the study is also examining data from patients in



**Rewarding experience.** Wafaa El-Sadr (left) and a patient who earned a gift card by suppressing HIV.

Houston, Texas; Chicago, Illinois; Philadelphia, Pennsylvania; and Miami, Florida, which have no similar large-scale campaigns to test and treat. Health departments in each city are collaborating with the study investigators.

The HPTN 065 team recognizes that paying people to take care of their own health might seem absurd, but weight-loss and smoking-cessation programs have successfully used "contingency management" or "conditional cash transfers." El-Sadr adds that the designers of HPTN 065 consulted closely with the community and thought long and hard about how best to do this. "Before we introduced our financial incentive, we had to think so carefully about what can happen that's good and what can undermine what you're trying to do," El-Sadr says. "And we want to use incentives that, if they are effective, will be cost-effective for health systems."

The study offers no financial incentive for testing—as El-Sadr points out, the same negative people might keep coming back just for the cash. Instead, it gives people who find out they are positive a coupon they can redeem for \$125 worth of Visa gift cards if they show up for a clinic visit and complete laboratory tests. Patients who keep their appointments, take their antiretroviral drugs as instructed, and reduce the amount of HIV in their blood to undetectable levels receive gift cards loaded with \$70 up to four times per year. The reward gives new meaning to the credit card company's tag line, "Life Takes Visa."

The researchers plan to complete the trial by February 2014. **—J.C.**

ing needles, Des Jarlais says—thanks in large part to this Harm Reduction Center and many other groups doing similar work. "In the beginning, there was nothing at all

like this," Des Jarlais says about the center, which last year took in 200,000 used syringes and gave out 250,000 clean ones. The 24-person staff also offers HIV testing, help finding housing, and counseling. "This is a full-service organization, and that's the key to its success," Des Jarlais says.

As Des Jarlais and colleagues explain in an article in the January 2011 issue of *Substance Use & Misuse* that looks at HIV in IDUs in New York City over the past 25 years, the logic of providing clean needles to people who shoot up heroin, cocaine, and other illicit drugs did not immediately win over the public or politicians.

"Syringe exchange was considered as early as 1985 but encountered very strong opposition," they note. An article in the same issue recounted that police, conservative politicians, and heroin-weary African-American communities were wary of seeming to condone drug use. Indeed, the U.S. Congress in 1988 outright banned the funding of needle-exchange programs. "With such strong resistance to syringe exchange, punitive drug laws, and the federal ban on syringe exchange funding, it is, in fact, quite remarkable that so much was subsequently accomplished," wrote Dalia Heller and Denise Paone, who worked on the issue at the New York City Department of Health and Mental Hygiene.

Local laws and policies began to change in the early 1990s in response to vocal AIDS activists who illegally distributed clean needles and confronted lawmakers, citing scientific evidence that syringe exchange slowed HIV's spread. As Des Jarlais and colleagues detail, the increase in syringe-exchange programs directly correlates with a precipi-



**Swap, meet.** Don Des Jarlais at Lower East Side Harm Reduction Center, which runs a popular needle exchange and hangout.

CREDITS: MALCOLM LINTON



tous drop in HIV incidence among IDUs. Heller, who is now a visiting scholar at the City University of New York, says there was also a “diffusion of benefit” from the prevention message that came along with syringe-exchange programs. “Syringe exchange was strong at getting the word out, which was almost as important as getting the needles out,” Heller says.

Des Jarlais says syringe exchange did not single-handedly turn around New York’s HIV/AIDS epidemic in IDUs, stressing that the growth of programs that provide opiate addicts with substitution drugs such as methadone and buprenorphine, which are

taken orally, has played a major role. “In the early days of the epidemic, drug-treatment programs didn’t want anything to do with people with HIV,” he says. “People were scared.” Today, Beth Israel runs 18 methadone clinics around the city, the largest such program in the world.

Des Jarlais says to take the next step and eradicate the spread of HIV in IDUs would require more effectively coupling drug substitution, counseling, and antiretroviral treatment with syringe exchange. But he says it offers a huge payoff for a small investment. “If I had limited money, and a lot of places in the world have extremely limited money,

I’d do syringe exchange first,” Des Jarlais says. “It’s the cheapest intervention and can be done with a wide variety of staff. You don’t even need M.D.s.”

To Des Jarlais’s “profound regret,” the lesson of New York City and syringe exchange has fallen on deaf ears in too many locales—including in the U.S. Congress, which lifted the ban on federal funding in 2009 only to reinstate it 2 years later. “I’m extremely frustrated that people are not applying what we know,” he says. “HIV prevention for people who inject drugs can be remarkably effective. It’s about having the political will to apply what we know.”

—JON COHEN



**Time heals.** With help from Josiah Rich (left), Robert Quintana’s health improved when he was locked up.

## PROVIDENCE, RHODE ISLAND

# HIV and the Cell: The Prisoner’s Dilemma

JOSIAH RICH BELIEVES THAT ONE OF THE most important places to stanch the AIDS epidemic is in the nation’s prisons. “If you think that treatment can get us out of this HIV epidemic, which I think it can, these are exactly the people we need to focus on,” says Rich, a clinician and researcher here at Brown University who treats HIV-infected inmates in the cluster of correctional facilities in nearby Cranston.

As Rich notes, the United States incarcerates roughly 10 million prisoners each year—the most in the world—and people behind bars disproportionately come from the highest risk groups for HIV infection:

injecting drug users, heterosexuals who have concurrent relationships, the impoverished, the homeless, and African Americans and Latinos. Some 150,000 HIV-infected people are released from jails and prisons each year. That’s 12.5% of all the infected people in the country.

Over the past 18 years, Rich has conducted pioneering research about HIV/AIDS in prisoners and helped Rhode Island create one of the most progressive and effective programs to help people both behind bars and when they’re on the outside. “Many prisoners are not getting treated, and even ones who are getting treated, we’re not keeping them in treat-

ment when they get out,” Rich says.

People unaware of their HIV status are three times more likely to transmit their infection, and they also, obviously, will not seek treatment for it. Since 2006, the U.S. Centers for Disease Control and Prevention has recommended “opt-out” testing for all prisoners, noting in a “guidance for correctional settings” that less than half of all state prisons that year reported that they offered it. Rhode Island, in contrast, a small state of just over 1 million people, began mandatory testing of all convicted prisoners in 1989 and has an opt-out policy for people in jails who have not yet been sentenced. One-third of all HIV diagnoses in the state during the following decade were made while people were locked up, Rich reported in the October 2002 issue of *AIDS Education and Prevention*.

Although transmission can occur in prison, Rich has helped document that few people become infected behind bars. Much more typical is a patient he saw one morning this spring. Robert Quintana has struggled with heroin addiction since he was a teen and is now doing a 5-year stint for a drug-related burglary. As Rich palpates Quintana’s liver, the 43-year-old patient says there’s no comparison between the medical treatment he’s receiving at this minimum-security facility versus that at the Massachusetts prison he called home between 1991 and 2000. “It’s a really big difference,” says Quintana, who takes antiretroviral drugs for his HIV and a treatment that he hopes will cure his hepatitis C infection. “They actually care over here. There, it was take it or leave it. ‘You don’t take medicine now? Fuggedaboutit.’ Here, I’ve only missed a couple of doses.”

CREDIT: MALCOLM LINTON

For Quintana and HIV-infected prisoners in Rhode Island—and in many other locales—prison becomes a place to improve their health. But that progress typically evaporates soon after release. A study Rich co-authored that examined Texas prisoners between 2004 and 2007 asked whether they filled their

prescriptions for antiretroviral drugs upon release. After 2 months, 70% had not picked up their pills, as Rich and colleagues reported in the 25 February 2009 *Journal of the American Medical Association*.

Rich and his Rhode Island colleagues have shown how to extend the benefits from inside

to outside through Project Bridge, which began at Miriam Hospital in Providence in 1996. The project has a social work team that helps inmates for the first 18 months after release. At the end of that period, 90% of participants were still in care.

—JON COHEN

## BALTIMORE, MARYLAND

# Dancing the Night Away; Keeping HIV at Bay

**TO UNDERSTAND THE SPREAD OF HIV AND** effectively intervene, researchers have long sought out people at risk, from gay men and injecting drug users in some populations to young women and migrant men in others. But there has been a push in the past few years to focus on venues where the uninfected and infected mingle. And in Baltimore, two venues that are receiving increased attention from researchers and public health officials have little in common other than the fact that they both involve dancing: clubs that stage “house/ball” events popular with African-American men who have sex with men (MSM), and bars that feature strippers who cater to all races of heterosexual men. “They are such different populations and the dynamics are so different,” says Susan Sherman, a behavioral scientist at Johns Hopkins Bloomberg School of Public Health (JHSPH) here, who studies exotic dancers. “The link is we try to meet people at places where risk is generated.”

The house/ball community, made famous in the 1990 documentary *Paris Is Burning*, draws hordes of young MSM to jam-packed clubs to watch dancers strut down runways in front of a panel of judges. The dancers often belong to different “houses” and compete in gender-bending competition categories including butch queen and schoolboy. “Go to a gay bar in Baltimore, and there are two black guys,” says Chris Beyrer, an epidemiologist at JHSPH, who recently attended his first ball with a younger researcher now working with the house/ball community. “At the ball, there are hundreds of people dancing.”

The Baltimore City Health Department has a youth outreach coordinator, Keith Holt, who is part of the community and stages an annual ball called Know Your Status. “Some people have made ballroom their life, and there’s a lot of risky behavior,” Holt says. On 13 June, Baltimore Mayor Stephanie Rawling-Blake announced a new HIV/AIDS awareness campaign, Status Update, that fea-

tures posters of people in different category costumes with this ribald pun: “Have Balls. Get Tested.”

No studies have specifically analyzed the HIV/AIDS prevalence in the house/ball community here, but researchers have included the events in venue-based testing in Baltimore, which helped reveal that the city has a severe epidemic in MSM. As JHSPH behavioral scientist Danielle German and colleagues reported in the 1 May 2011 *Journal of Acquired Immune Deficiency Syndromes*, they did surveys and testing in MSM venues as part of the National HIV Behavioral Surveillance, a system organized by the U.S. Centers for Disease Control and Prevention (CDC) to assess prevalence in different high-risk communities. The results of the first survey, which took place in 2004 and 2005, caught the city off guard. “Baltimore has this striking black MSM epidemic that nobody had any idea about,” German says.

A second survey in 2008 tested 448 men, 71% black and 23% white, regardless of whether they had tested positive before. The prevalence was 37.5%, and a startling 78.4% of the men did not know their status. German has done intensive studies to understand why so many of the MSM did not know their status, noting that it is more of a problem here than in other test cities. Jamal Hailey, an African-American MSM who manages HIV-prevention programs at the University of Maryland, Baltimore, and conducted field research for the study, says he thinks the rampant pov-

erty and depression in Baltimore are the main factors. “A lot of people are just trying to make it,” says Hailey, whose own father died from AIDS 13 years ago. “So getting an HIV test isn’t at the top of their to-do lists.”

In the past 2 years, JHSPH’s Sherman has published four papers about the dancers who work at the two dozen strip clubs on East Baltimore Street—an area called “The Block.” One study of 98 strippers, published in the 1 April 2011 issue of *Drug and Alcohol Dependence*, found that although the women don’t see themselves as sex workers, 42% of those surveyed traded sex for money or other valuables, and they were three times more likely to do this if they smoked crack cocaine. Half of the women said they started to smoke crack or shoot heroin after they became



**Site visits.** Baltimore’s HIV prevention efforts target—and stage—competitive dances at gay clubs.

exotic dancers. “These women have limited negotiating power,” says Sherman, stressing that this puts their health at risk. “They come and they go, and there’s no union.”

No researchers have systematically tested the exotic dancers on The Block for HIV, but then there’s little sex-worker research done in the United States. “We don’t really talk about sex workers because we somehow feel it’s not a major driver of HIV spread, but we’re not tracking it,” says Kevin Fenton, director of



CDC's National Center for HIV/AIDS, Viral Hepatitis, STD, and TB Prevention.

Sherman now hopes to conduct both HIV incidence and prevalence studies of women who dance on The Block and elsewhere in the

state—if the clubs and women see that it's in their best interests. "If we could just create some sort of council where different people could talk together—dancers, managers, and owners—then maybe they could make it rou-

tine that condoms are part of sex acts," Sherman says. Their goal is not to "save women from dancing," she says, but to reduce the risks they face from HIV and other diseases when they step down off the stage. **—JON COHEN**

## WASHINGTON, DISTRICT OF COLUMBIA

# HIV/AIDS Response Renovated in Capital

**SEVEN YEARS AGO, A PUBLIC-POLICY** nonprofit called DC Appleseed issued a scathing report about the sorry state of the response to HIV/AIDS in the nation's capital, which it said "lags far behind that of many other cities across the nation." The report called the epidemic in this city of 600,000 people a "public health crisis" and faulted the government for its fragmented leadership, marginal attempts to distribute condoms, weak programs for people with substance-abuse problems, and nonexistent surveillance data. "This challenge is of life-and-death importance," the report concluded. "Simply put, business cannot go on 'as usual.'"

It hasn't. And that's coming from DC Appleseed, a nonpartisan group with outposts around the country that organizes teams of attorneys and other volunteers to analyze local problems and then take action.

Although D.C. remains among the hardest-hit cities in the nation, the nonprofit's most recent report says it "has made steady and significant improvements in its overall response to HIV/AIDS." Condom distribution jumped from 115,000 in 2006 to more than 5 million in 2011. The number of publicly supported HIV tests performed tripled between 2007 and 2011, making the District "a national leader." Surveillance updates have "improved greatly" in both quality and regularity, and all these actions have had results.

According to the 2011 annual report from D.C.'s Department of Health, newly diagnosed infections in general dropped by nearly 24% between 2006 and 2010, and the decrease was 71% in injecting drug users. Other recent improvements include chlamydia and gonorrhea cases leveling off, AIDS deaths decreasing, and people learning of their infections at an earlier stage of the disease when they are easier to treat.

The city also has more HIV/AIDS research projects under way than ever before, including a massive study funded by the U.S. National

Institutes of Health (NIH) called HPTN 065 (see p. 179) that aims to find and treat infected people. "Before 2006, there was virtually no research in the District," says epidemiologist Many Magnus, who works here at George Washington University (GW).

Angela Fulwood Wood, who runs a large clinic that's participating in HPTN 065, the Family and Medical Counseling Service (FMCS), credits the city's progress to the nexus of the health department, academia,



**Patient pursuer.** Robin Thomas of Recapture Blitz tracks down no-shows and returns them to care.

and providers. "We've all grown," Wood says.

Heralded as the changes have been, the city still has a serious HIV/AIDS problem. More than 14,000 HIV-infected people lived in D.C. in 2010, an adult prevalence of 2.7%. African Americans are much more heavily affected, accounting for 91.5% of the female cases and 67.6% of the males. The main modes of transmission are men who have sex with men, or MSM (40.5%), heterosexual contact (28%), and injecting drug users (15.1%).

In the wake of the 2005 DC Appleseed report, D.C.'s Department of Health hired an up-and-coming epidemiologist, Tiffany West, from the U.S. Centers for Disease Control and Prevention (CDC) in Atlanta to right its surveillance ship. GW's Magnus and Alan Greenberg, who previously ran CDC's HIV

epidemiology, soon teamed up with West and her staff. "Public-private partnerships really did help us get a different level of technical support that was required to build this program from scratch," West says. In 2010, NIH also formed the D.C. Partnership for HIV/AIDS Progress, which links its researchers to the Department of Health and also helps fund the city's role in HPTN 065 and other multisite studies.

Wood's team from FMCS works with the health department on several innovative interventions. The group now offers HIV testing at both the Department of Motor Vehicles and the Income Maintenance Administration (welfare) office in the most economically strapped part of the city. Based on Wood's idea, FMCS launched Recapture Blitz to track down patients who disappear. Robin Thomas, an FMCS community health worker, phones missing patients and also drives to their homes to see why they haven't come in for care. "My job is to settle people down," says Thomas, who is HIV-infected herself. "I try to see what's getting in their way and how we can help, whether it's transportation or going to the doctor's appointment with them." A half-dozen clinics now do this in D.C., and in 2010, they found about one-third of the lost patients, half of whom made and kept appointments.

Taking a page from the health department in San Francisco (see p. 175), West and her staff gather data from mandated reporting of lab tests of HIV-infected people to calculate "community viral load," which theoretically should give them a better handle on which neighborhoods are having success or difficulty controlling their infections.

When West took the job here, she dreamed of creating a surveillance program that, like the health departments in San Francisco and New York, was science-driven, understood the community, and could use its findings to inform policies and programs. Recently, she says, people from those cities have knocked on her door. "I never would have thought in a million years that they'd come ask us for technical assistance, but they're doing that right now," she says. "We've literally went from worst to first." **—JON COHEN**

## REVIEW

# Broadly Neutralizing Antibodies Present New Prospects to Counter Highly Antigenically Diverse Viruses

Dennis R. Burton,<sup>1,2\*</sup> Pascal Poignard,<sup>1,4</sup> Robyn L. Stanfield,<sup>3</sup> Ian A. Wilson<sup>3\*</sup>

Certain human pathogens avoid elimination by our immune system by rapidly mutating the surface protein sites targeted by antibody responses, and consequently they tend to be problematic for vaccine development. The behavior described is prominent for a subset of viruses—the highly antigenically diverse viruses—which include HIV, influenza, and hepatitis C viruses. However, these viruses do harbor highly conserved exposed sites, usually associated with function, which can be targeted by broadly neutralizing antibodies. Until recently, not many such antibodies were known, but advances in the field have enabled increasing numbers to be identified. Molecular characterizations of the antibodies and, most importantly, of the sites of vulnerability that they recognize give hope for the discovery of new vaccines and drugs.

Mutation and recombination in genetic material have allowed the evolution of the living world and of our species. But these mechanisms also cause us great problems, notably in the many faces of cancer and from the onslaught of certain highly antigenically diverse pathogens that can change sequence rapidly enough to avoid timely elimination by our immune system. Pathogens that can rapidly change their antigenic profiles include RNA viruses such as HIV, influenza virus, and hepatitis C virus (HCV); bacteria such as *Streptococcus pneumoniae*; and protozoa such as *Plasmodium falciparum*, which causes human malaria, and *Trypanosoma brucei*, which causes sleeping sickness. Preventing infection by these pathogens through design and development of vaccines has proven challenging. Antigenic diversity has also caused notable difficulties in developing certain classes of drugs against these pathogens, in particular those targeting surface-associated glycoproteins. For drugs that are successfully introduced, the ability of many pathogens to rapidly generate variants can lead to drug resistance. Recent breakthroughs in the generation and characterization of broadly neutralizing antibodies against the highly antigenically diverse viruses HIV, influenza virus, and HCV have helped identify potential targets for vaccines and drugs and presented new opportunities to counter these viruses. These types of approaches may also

help in designing strategies to counter other highly antigenically diverse pathogens.

Sequence variability of pathogens is not confined to surface antigens and is not only the result of immune pressure; replication in the host, transmission, and survival of a pathogen may also depend on genetic diversification. It is instructive to consider highly antigenically diverse pathogens in the general context of pathogen variability. A number of pathogens have evolved rapid genetic diversification, including various bacteria and protozoa, but the champions of diversity are viruses. RNA viruses in particular have high mutation rates, largely because of the involvement of virus-encoded error-prone RNA and DNA polymerases in their replication cycle, leading to mutation rates as high as  $1.5 \times 10^{-3}$  mutations per nucleotide per genomic replication (*1*). Certain DNA viruses, especially single-strand DNA viruses, can also have high mutation and substitution rates, sometimes as high or higher than RNA viruses (*1*). For many viruses, sequence variability is crucial to escape host immune cellular and humoral responses, leading to great antigenic diversity in the proteins targeted by the adaptive immune system. However, other variable viruses have evolved modes of replication and transmission that allow them to survive without the need to escape the pressure of their host's adaptive immune responses, for example, by transmitting from one host to the next before an effective immune response is mounted. As a consequence, these viruses do not display a high level of antigenic diversity despite an inherent capacity to do so. Therefore, high sequence diversity per se is not necessarily an obstacle to vaccine development, and effective vaccines have been developed against relatively highly diverse viruses such as measles virus, hepatitis B virus, polio virus, and rabies virus. Conversely, vaccines have been difficult to develop against pathogens with low

diversity, such as herpes simplex virus. However, high antigenic diversity, in which there is a very high level of variability in the viral protein sites principally targeted by the immune system (immunodominant or immunoprominent epitopes), does consistently impair vaccine development. Classical vaccine approaches will tend to afford protection against a very limited fraction of circulating virus populations. Because the most important contributors to protection by the majority of antiviral vaccines are neutralizing antibodies targeting the surface envelope (Env) proteins, the highly dynamic antigenic diversity of these proteins is the major obstacle to the development of practical vaccines for viruses such as HIV, influenza virus, and HCV.

## Disease Impacts

HIV establishes a chronic infection that, over a period of years and if left untreated, leads to AIDS. About 25 million people have died of AIDS, and about 35 million are currently infected (*2*). The epicenter of the plague is sub-Saharan Africa, with an adult infection rate reaching 5%. The high relative cost of treatment has begun to consume a large proportion of development aid to this region with diverse negative consequences. Influenza virus infection produces acute respiratory and systemic symptoms and leads to between one-quarter and one-half million deaths on average per year and societal costs of billions of dollars annually in health care and lost productivity (*3*). At 10- to 50-year intervals, the virus triggers recurring deadly pandemics; the great influenza pandemic of 1918 killed about 50 million people worldwide (*4*), and the other pandemics of the past century in 1957, 1968, and 2009 caused millions of deaths. HCV chronically infects 120 to 170 million people globally (*5*) and is a major cause of chronic liver disease and liver cancer in the developing world. The societal costs of HCV in the United States are expected to approach \$85 billion by 2024 (*6*).

## Antibody Discovery

HIV, influenza, and HCV show great sequence heterogeneity in their Env proteins, which are the essential targets of an effective antibody response. This heterogeneity is seen between different isolates or strains, particularly in their surface-exposed amino acid residues. Nevertheless, at least two regions on these viral Env proteins are expected to be both conserved and accessible, even if only transiently in some instances, to permit virus infection. All enveloped viruses are required to bind to one or more receptors on their target host cell and have a mechanism for entry into that cell. Therefore, the Env proteins contain a receptor binding site(s) and the viral fusion machinery, both of which are likely to be exposed, at least transiently, during cell attachment and viral entry. However, these conserved accessible regions may be relatively small; for example,

<sup>1</sup>Department of Immunology and Microbial Science and International AIDS Vaccine Initiative (IAVI) Neutralizing Antibody Center, The Scripps Research Institute, La Jolla, CA 92037, USA.

<sup>2</sup>Ragon Institute of Massachusetts General Hospital, Massachusetts Institute of Technology, and Harvard University, Cambridge, MA 02129, USA. <sup>3</sup>Department of Molecular Biology, Skaggs Institute for Chemical Biology, and IAVI Neutralizing Antibody Center, The Scripps Research Institute, La Jolla, CA 92037, USA. <sup>4</sup>IAVI, New York, NY 10038, USA.

\*To whom correspondence should be addressed. E-mail: burton@scripps.edu (D.R.B.); wilson@scripps.edu (I.A.W.)



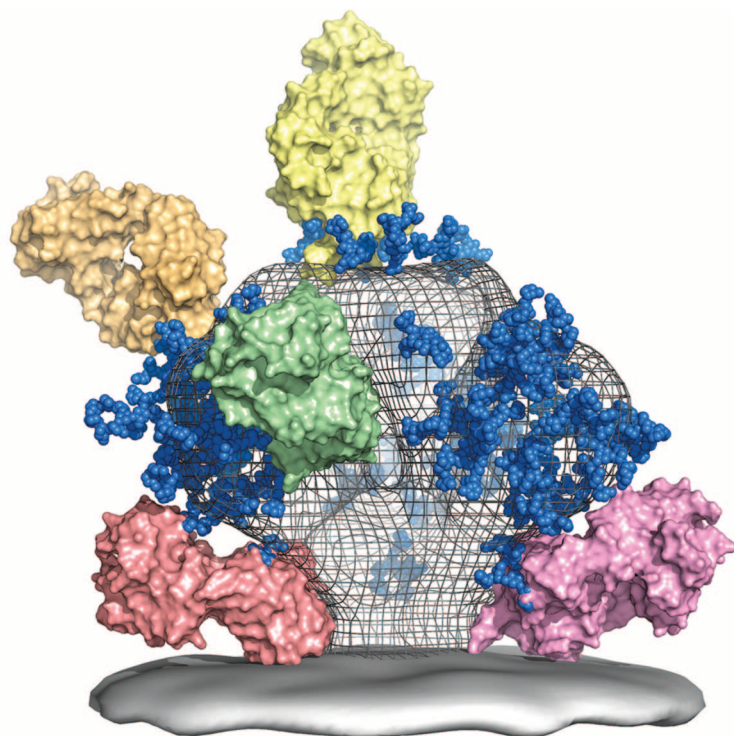


**Fig. 1.** A model of the HIV-1 Env spike with select bnmAbs bound. The spike model is derived from cryoelectron tomography from (73), Electron Microscopy (EM) Data Bank codes EM-5019 and EM-5021. The Fabs are color-coded in the figures to represent different sites of interaction on the Env proteins. The pinkish red Fabs bind to the Env stem that houses the fusion machinery, the green Fabs bind at or around the receptor binding site (CD4 receptor for HIV-1 and sialylated glycans for influenza, as shown in Fig. 2), and the yellow Fabs bind and penetrate the glycan shield for HIV-1. Anti-HIV Fabs shown are PG9 [bright yellow, on top, Protein Data Bank (PDB) code 3u4e] (34), PGT128 (orange-yellow, 3tyg) (33), VRC01 (green, 3ngb) (32), 4E10 (salmon at bottom left, 2fx7) (74), and 2F5 (pink at bottom right, 2f5b) (75). Carbohydrates (Man<sub>5</sub>, blue spheres) were modeled onto an unliganded YU2 gp120 core (3tgq) (76) with GlyProt (77) from glycosciences.de, except for the glycans binding to PGT128 and PG9, which were taken directly from their structures in complex with outer domain (33) and scaffold (34), respectively. The locations of PG9, 4E10, and 2F5 are approximate; however, the VRC01 and PGT128 were docked by superposition of gp120 core and outer domain, respectively, with the unliganded YU2 gp120 model (that is invisible under the EM mesh). Figure was made with Pymol (78).

the hemagglutinin (HA) protein that mediates influenza viral entry is only required to recognize a relatively small glycan moiety, containing a terminal sialic acid, as its receptor on target cells. The small size of the receptor severely limits the conserved footprint that can be specifically recognized by an antibody in order to acquire cross-reactivity against different strains and subtypes. For HIV-1, that footprint is larger because the receptor is a protein, CD4, but CD4 has a molecular width of only a single immunoglobulin (Ig) domain. An antibody antigen-binding fragment (Fab) has twice that width, with two Ig domains. Suggestions that antibody footprint-sized conserved regions may be exposed at the Env surface came originally from observations of serum cross-neutralizing activity against diverse influenza and HIV isolates (7, 8) from individuals infected with the corresponding viruses. Serum cross-neutralizing activity could arise, in principle, from a combination of a large number of antibodies

directed to variable regions. However, the isolation of individual monoclonal antibodies (mAbs) that were able to neutralize in vitro multiple, diverse isolates [broadly neutralizing monoclonal antibodies, bnmAbs (9)] confirmed the presence of conserved antibody footprint-sized accessible regions on Env antigens on the viral surface. BnmAbs to HIV were first isolated from infected individuals in 1992 by electrofusion (10) and by phage display (11) but only shown convincingly to be broadly neutralizing to primary, as distinct from laboratory-adapted, virus isolates in 1994 (12, 13). A mouse bnmAb to influenza virus was isolated and characterized in 1993 (14), and a mouse bnmAb to HCV was first generated in 2001 (15) and shown to be broadly functional in 2005 (16). Until the late 2000s, only a small number of bnmAbs against these viruses had been isolated and characterized, but in the past 3 years an explosion in the rate of generation and characterization of such Abs has occurred. These exciting

breakthroughs have unearthed many novel Abs with unexpected epitopes, as well as novel modes of antibody-antigen recognition, and have suggested a plethora of new vaccine and drug targets.

For many years, only a handful of bnmAbs against HIV, all human, were known (17, 18). Of these Abs, two that were directed to the Env glycoprotein gp120 (b12, 2G12) and two to the transmembrane Env glycoprotein gp41 (2F5, 4E10) were the most notable and were intensely studied. Importantly, these bnmAbs were all shown to protect against free virus challenge in relatively robust macaque models of HIV infection (19–22). Crystal structures of these mAbs in complex with Env antigens were determined, and a variety of novel antibody features were identified in their hypervariable regions (23, 24). These features included long heavy-chain variable complementarity-determining regions 3 (HCDR3s), which had scarcely been reported at that time, antibody domain exchange to recognize a glycan cluster on gp120 (2G12), and very hydrophobic HCDR3s (2F5, 4E10), which appeared to be associated with recognition of epitopes very close to the virus membrane (i.e., membrane proximal external region) for the two anti-gp41 mAbs.

Many immunogens have been designed based, to varying degrees, on molecular understanding of the interaction of these bnmAbs with HIV Env antigens. No immunogen tested to date has “re-elicited” antibodies with broadly neutralizing character. Several explanations have been proposed, including the limitations imposed by the availability of such a small panel of bnmAbs, that make the drawing of general conclusions for immunogen design hazardous. Therefore, considerable effort by a number of laboratories went into the discovery of more bnmAbs. Two factors appear to have been most crucial in the success of that effort: first, the screening of large cohorts of infected donors to identify individuals with broadly neutralizing sera by using reproducible high-throughput neutralization assays (25) and, second, the application of novel single B cell technologies to samples from these donors to facilitate the isolation of bnmAbs from a background of many other non-neutralizing antibodies against Env (anti-Env). The application of direct neutralization screening to a large number of B cells (about 30,000) from a donor with broad and potent serum-neutralizing activity led to the isolation of a pair of bnmAbs to a novel epitope in 2009 (26). The new mAbs were about an order of magnitude more potent in standard neutralization assays than the previously identified bnmAbs while generally maintaining or improving breadth. This development was quickly followed by the sorting of B cells using an engineered gp120 molecule to identify a potent bnmAb directed to the CD4 binding site of gp120 of similarly enhanced potency and even greater breadth (27). The application of direct neutralization screening to further donors with broadly neutralizing sera led to the

identification of yet more bnmAbs that targeted novel mixed glycan/protein epitopes on gp120 with even greater potency (28). Larger panels of highly potent anti-CD4bs bnmAbs have also been isolated by single B cell sorting using Env baits and specially designed polymerase chain reaction (PCR) primers to account for a high degree of antibody mutation (29). Engineering of one such mAb has generated remarkable potency and breadth (30). Deep sequencing of antibody repertoires from donors from whom bnmAbs have been isolated has revealed many additional potent related mAbs (31). BnmAb targets on HIV Env are represented in Fig. 1.

The structures of many of the newer HIV bnmAbs in complex with Env antigens (31–34), together with analysis of the bnmAb sequences, provide opportunities and potential lessons for vaccine and drug discovery. Several new targets are available for immunogen and drug design, and the understanding of existing targets has also been greatly enhanced. For example, recognition of a favored vaccine target, the CD4 binding site, has now been shown to not necessarily require a long HCDR3 but appears to be strongly dependent on certain gene segments of the variable region of immunoglobulin heavy chain ( $V_H$ ) (29, 32). High-affinity glycan recognition on Env can also be achieved by conventional antibodies in the absence of 2G12-like domain exchange (33). Other recurring themes of HIV bnmAbs have been a relatively high degree of somatic hypermutation, a prevalence of insertions and deletions in the antibody variable regions, and an inability of germline versions of the bnmAbs to bind Env (26–29, 35–38). It is still unclear whether a high degree of hypermutation reflects a general property of HIV Abs that has arisen because of the chronic antigen stimulation from natural infection or is a requirement for the evolution of such Abs toward broad cross-reactivity. The affinity threshold required for the Env-germline antibody to trigger a response is also unclear. Nevertheless, a number of immunogens are currently being designed to bind to germline, as well as mature, antibodies to activate naive B cells (37).

Besides informing vaccine design, the discovery of conserved exposed regions, particularly associated with the glycan shield of gp120 (Fig. 1), provides a number of new potential viral entry inhibitor targets.

For influenza virus, the first bnmAb was isolated in 1993 by immunization of a mouse with H2N2 virus (HA subtype 2, neuraminidase sub-

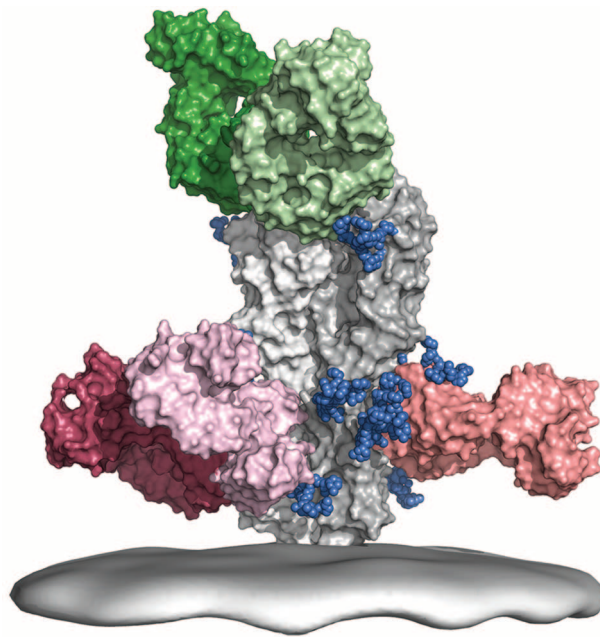


**Fig. 2.** A model of the influenza virus spike with select bnmAbs bound. Anti-influenza virus Fabs are 2D1 (top, light green, 3lzf) (79), CH65 (top, dark green, 3sm5) (48), Fl6 (bottom right, link pink, 3ztj) (44), CR6261 (bottom center, salmon, 3 gbm) (41), and CR8020, (bottom left, red, 3sdy) (43). The HA trimer spike is from the 1918 strain (gray, 3r2x) (56), with Man<sub>9</sub> carbohydrates (blue spheres) modeled on with GlyProt (77) to give approximate dimensions for the attached glycans. EM-5021 membrane density was used to approximate the membrane surface.

type 2) and shown to neutralize group 1 viruses bearing HAs of subtypes 1, 2, 5, 6, and 9 (14). The antibody was proposed to bind to a conserved region in the stem of HA, in contrast to typical strain-specific antibodies that bind to hypervariable regions on the head of HA (Fig. 2). In 2008 and 2009, a number of novel human bnmAbs that cross-neutralized group 1 subtypes were isolated from phage libraries by different laboratories. The antibodies had remarkably similar sequences to one another, close to the corresponding human germline sequence of the  $V_H1-69$  family with relatively few somatic mutations; showed similar patterns of group I subtype neutralization (representing 10 of the 16 known flu subtypes); and were protective in mouse models (39–42). Structural studies showed this group of  $V_H1-69$  bnmAbs recognized a conserved region of the stem of HA by using the heavy chain alone (42, 43) (Fig. 2). More recently, high-throughput screening of immortalized antibody-secreting cells generated a bnmAb that recognizes this conserved region in a different way, using both heavy and light chains, and is able to neutralize both group 1 and group 2 viruses (44). In addition, a different cell-based method has been used to isolate a bnmAb that binds to a second site on the stem of HA, again quite close to the virus membrane; neutralizes group 2 viruses; and protects mice against virus challenge (43) (Fig. 2). Furthermore, bnmAbs have recently been described that target the head re-

gion of HA (39, 45–48) around the receptor binding site. One of these bnmAbs neutralizes selected isolates from both group 1 and 2 viruses (49), but most neutralize only a single subtype. The structure of a mAb that broadly neutralizes viruses from the H1 subtype does so by targeting an epitope that overlaps the HA receptor binding site (48) (Fig. 2).

The holy grail of influenza virus vaccine research is a universal vaccine that protects against all strains and subtypes of the virus, including seasonal and pandemic strains, and thereby renders the annual vaccine redundant. If the vaccine is long-acting as, for example, the yellow fever or smallpox vaccines, it could be given at a relatively young age and protect into old age. There is a great need for such a vaccine because current seasonal influenza vaccines tend to be less effective in elderly individuals as the capacity of the immune system wanes (50). Also, the vaccine needs to be reformulated annually to include the best predictions of which strains will circulate in any given year, and the match is not often optimal. Indeed, the efficacy and effectiveness of current influenza vaccines

may be notably lower than previously thought (50). Furthermore, the vaccine takes some months to develop and manufacture, which can be problematic in the face of a potential pandemic or epidemic. As a new approach to the standard live or inactivated influenza vaccines, the identification of the stem of HA as a vaccine target has already led to design of “headless” HA immunogens, which have thus far produced modest improvements in neutralization breadth (51, 52), and the engineering of scaffolds incorporating crucial structural elements recognized by the stem bnmAbs. A number of different immunization strategies are also being intensively investigated, resulting in some success in improving the breadth of neutralizing anti-influenza virus responses (53, 54). It is also worth noting that the pandemic H1N1 vaccine does induce broadly cross-reactive antibodies to the HA stem region (55). Lastly, as with HIV, the influenza bnmAbs identify promising drug targets, and, indeed, a small protein has been computationally designed to bind to the HA stem region defined by bnmAbs and experimentally shown to neutralize influenza virus by inhibiting critical HA conformational changes required for fusion (56) by a mechanism similar to that used by the stem antibodies. Presumably, a small-molecule drug could also be targeted to this region and used to specifically inhibit influenza virus infection.

For HCV, the first bnmAb was isolated in 2001 (15) and shown to be broadly neutralizing



in 2005 (16). The mouse bnmAb and a human bnmAb identified later (57) define a continuous epitope on the E2 Env glycoprotein of the virus and inhibit interaction of E2 with the receptor CD81. In the past few years, a range of human and murine bnmAbs, mostly directed to discontinuous epitopes on E2, have been identified (58–63), with one report of a bnmAb directed to the E1 glycoprotein (64). Of note, a single bnmAb was shown to provide protection against HCV quasi-species challenge in an animal model (60). Unfortunately, no structure is yet available for E2 or the E1 E2 complex, limiting the value of the bnmAbs for immunogen and drug design. However, the crystal structure of a human bnmAb complexed with a peptide corresponding to a continuous epitope on E2 (57) has recently been determined (65), providing a template for immunogen design.

For the highly antigenically diverse viruses described above, an effective vaccine would seek to induce antibodies that recognize conserved regions and neutralize as broadly as possible. Challenges will always remain because of the diverse sequences and constant antigenic variation in these viruses, which will lead to differences in neutralization sensitivity across the spectrum of circulating isolates and could lower overall efficacy of vaccine-induced antibody responses or, as in the case of dengue virus, enhance disease (66).

Lastly, we have focused here on harnessing the information derived from bnmAbs to help define vaccine and drug targets on highly antigenically diverse viruses. These bnmAbs may also have direct application as prophylactic and/or therapeutic passively administered reagents. For HIV in a prophylactic setting, one might consider systemic passive administration of bnmAbs for high-risk individuals or topical application in a microbicide. In a therapeutic setting, combining passively administered antibody with anti-retroviral drugs could be considered. One advantage of systemic antibody is long half-life, but a serious disadvantage is high cost. This problem could be ameliorated by the expression of bnmAbs from vectors such as adeno-associated viruses (67, 68). For influenza virus, therapy with bnmAbs could be considered, especially given indications that antibody administration relatively late in disease course may be beneficial (69). For HCV, a clear application of bnmAbs is to prevent re-infection of the grafted liver that typically occurs after a liver transplant (70).

## Summary

Highly antigenically diverse pathogens are a major health concern and are particularly difficult to counter through vaccination. The generation of a whole new armamentarium of broadly neutralizing antibodies to several highly antigenically diverse viruses in the past 3 to 4 years has revealed new and unexpected vulnerabilities in these previously impregnable viruses. The stage is now

well and truly set for rational vaccine design based on exploiting these vulnerabilities. Immunogen design based on computational approaches is advancing rapidly (71, 72). Small-animal models expressing human antibody repertoires suitable for immunogen evaluation are being evaluated and developed. Technologies for the detailed evaluation of antibody responses, including deep sequencing and single B cell approaches, will facilitate iterative improvements of immunogens. Immunization strategies based on a better understanding of the antibody requirements for broad neutralization and of the roles of innate immunity and T cell help in eliciting the appropriate antibody responses will also likely be crucial. The challenges are manifest, but the advances made against HIV-1, influenza viruses, and HCV may have ramifications and implications that go well beyond these highly diverse viruses to the many other microbial pathogens that threaten the health and well-being of mankind.

## References and Notes

1. S. Duffy, L. A. Shackleton, E. C. Holmes, *Nat. Rev. Genet.* **9**, 267 (2008).
2. United Nations Program on HIV/AIDS (UNAIDS), "How to get to zero: Faster. Smarter. Better." UNAIDS World Aids Day Report (UNAIDS, Geneva, 2011).
3. D. Graham-Rowe, *Nature* **480**, S2 (2011).
4. C. F. Basler, P. V. Aguilar, *Antiviral Res.* **79**, 166 (2008).
5. C. W. Shepard, L. Finelli, M. J. Alter, *Lancet Infect. Dis.* **5**, 558 (2005).
6. "Combating the silent epidemic of viral hepatitis: Action plan for the prevention, care and treatment of viral hepatitis" (United States Department of Health and Human Services, Washington, DC, 2011); [www.hhs.gov/ash/initiatives/hepatitis/actionplan\\_viralhepatitis2011.pdf](http://www.hhs.gov/ash/initiatives/hepatitis/actionplan_viralhepatitis2011.pdf).
7. P. N. Graves, J. L. Schulman, J. F. Young, P. Palese, *Virology* **126**, 106 (1983).
8. L. K. Vujcic, G. V. Quinlan Jr., *AIDS Res. Hum. Retroviruses* **11**, 783 (1995).
9. D. R. Burton, *Nat. Rev. Immunol.* **2**, 706 (2002).
10. A. Buchacher et al., in *Vaccines '92: Modern Approaches to New Vaccines Including Prevention of AIDS*, F. Brown, R. Chanock, H. S. Ginsberg, R. Lerner, Eds. (Cold Spring Harbor Laboratory Press, Cold Spring Harbor, NY, 1992), pp. 191–194.
11. C. F. Barbas 3rd et al., *Proc. Natl. Acad. Sci. U.S.A.* **89**, 9339 (1992).
12. A. J. Conley et al., *Proc. Natl. Acad. Sci. U.S.A.* **91**, 3348 (1994).
13. D. R. Burton et al., *Science* **266**, 1024 (1994).
14. Y. Okuno, Y. Isegawa, F. Sasao, S. Ueda, *J. Virol.* **67**, 2552 (1993).
15. A. Owsianka, R. F. Clayton, L. D. Loomis-Price, J. A. McKeating, A. H. Patel, *J. Gen. Virol.* **82**, 1877 (2001).
16. A. Owsianka et al., *J. Virol.* **79**, 11095 (2005).
17. D. R. Burton et al., *Nat. Immunol.* **5**, 233 (2004).
18. J. R. Mascola, D. C. Montefiori, *Annu. Rev. Immunol.* **28**, 413 (2010).
19. J. R. Mascola, *Curr. Mol. Med.* **3**, 209 (2003).
20. A. J. Hessel et al., *Nat. Med.* **15**, 951 (2009).
21. A. J. Hessel et al., *PLoS Pathog.* **5**, e1000433 (2009).
22. A. J. Hessel et al., *J. Virol.* **84**, 1302 (2010).
23. D. R. Burton, R. L. Stanfield, I. A. Wilson, *Proc. Natl. Acad. Sci. U.S.A.* **102**, 14943 (2005).
24. D. C. Douek, P. D. Kwong, G. J. Nabel, *Cell* **124**, 677 (2006).
25. L. Stamatos, L. Morris, D. R. Burton, J. R. Mascola, *Nat. Med.* **15**, 866 (2009).
26. L. M. Walker et al., *Science* **326**, 285 (2009); 10.1126/science.1178746.
27. X. Wu et al., *Science* **329**, 856 (2010); 10.1126/science.1187659.
28. L. M. Walker et al., *Nature* **477**, 466 (2011).
29. J. F. Scheid et al., *Science* **333**, 1633 (2011); 10.1126/science.1207227.
30. X. Wu et al., *Science* **333**, 1593 (2011); 10.1126/science.1207532.
31. R. Diskin et al., *Science* **334**, 1289 (2011); 10.1126/science.1213782.
32. T. Zhou et al., *Science* **329**, 811 (2010); 10.1126/science.1192819.
33. R. Pejchal et al., *Science* **334**, 1097 (2011); 10.1126/science.1213256.
34. J. S. McLellan et al., *Nature* **480**, 336 (2011).
35. D. Corti et al., *PLoS ONE* **5**, e8805 (2010).
36. M. Huber et al., *J. Virol.* **84**, 10700 (2010).
37. X. Xiao et al., *Biochem. Biophys. Res. Commun.* **390**, 404 (2009).
38. M. Bonsignori et al., *J. Virol.* **85**, 4998 (2011).
39. A. K. Kashyap et al., *Proc. Natl. Acad. Sci. U.S.A.* **105**, 5986 (2008).
40. M. Throsby et al., *PLoS ONE* **3**, e3942 (2008).
41. D. C. Ekiert et al., *Science* **324**, 246 (2009); 10.1126/science.1171491.
42. J. Sui et al., *Nat. Struct. Mol. Biol.* **16**, 265 (2009).
43. D. C. Ekiert et al., *Science* **333**, 843 (2011); 10.1126/science.1204839.
44. D. Corti et al., *Science* **333**, 850 (2011); 10.1126/science.1205669.
45. N. Ohshima et al., *J. Virol.* **85**, 11048 (2011).
46. J. C. Krause et al., *J. Immunol.* **187**, 3704 (2011).
47. J. C. Krause et al., *J. Virol.* **85**, 10905 (2011).
48. J. R. Whittle et al., *Proc. Natl. Acad. Sci. U.S.A.* **108**, 14216 (2011).
49. R. Yoshida et al., *PLoS Pathog.* **5**, e1000350 (2009).
50. M. T. Osterholm, N. S. Kelley, A. Sommer, E. A. Belongia, *Lancet Infect. Dis.* **12**, 36 (2012).
51. G. Bommakanti et al., *Proc. Natl. Acad. Sci. U.S.A.* **107**, 13701 (2010).
52. J. Steel et al., *mBiol.* **1**, e000018-10 (2010).
53. C. J. Wei et al., *Science* **329**, 1060 (2010); 10.1126/science.1192517.
54. J. Wrammert et al., *J. Exp. Med.* **208**, 181 (2011).
55. G. M. Li et al., *Proc. Natl. Acad. Sci. U.S.A.* **109**, 9047 (2012).
56. S. J. Fleishman et al., *Science* **332**, 816 (2011).
57. T. J. Broering et al., *J. Virol.* **83**, 12473 (2009).
58. D. J. Schofield et al., *Hepatology* **42**, 1055 (2005).
59. D. E. Johansson et al., *Proc. Natl. Acad. Sci. U.S.A.* **104**, 12629 (2007).
60. M. Law et al., *Nat. Med.* **14**, 25 (2008).
61. Z. Y. Keck et al., *J. Virol.* **82**, 6061 (2008).
62. M. C. Sabo et al., *J. Virol.* **85**, 7005 (2011).
63. E. Giang et al., *Proc. Natl. Acad. Sci. U.S.A.* **109**, 6205 (2012).
64. J. C. Meunier et al., *J. Virol.* **82**, 966 (2008).
65. L. Kong et al., *Proc. Natl. Acad. Sci. U.S.A.* **109**, 9499 (2012).
66. S. B. Halstead, *Adv. Virus Res.* **60**, 421 (2003).
67. P. R. Johnson et al., *Nat. Med.* **15**, 901 (2009).
68. A. B. Balazs et al., *Nature* **481**, 81 (2012).
69. W. Gerhard, *Curr. Top. Microbiol. Immunol.* **260**, 171 (2001).
70. R. Eren et al., *J. Virol.* **80**, 2654 (2006).
71. M. L. Azoitei et al., *Science* **334**, 373 (2011).
72. J. S. McLellan et al., *J. Mol. Biol.* **409**, 853 (2011).
73. J. Liu, A. Bartsch, M. J. Borgnia, G. Sapiro, S. Subramaniam, *Nature* **455**, 109 (2008).
74. R. M. Cardoso et al., *J. Mol. Biol.* **365**, 1533 (2007).
75. S. Bryson, J. P. Julien, R. C. Hynes, E. F. Pai, *J. Virol.* **83**, 11862 (2009).
76. Y. D. Kwon et al., *Proc. Natl. Acad. Sci. U.S.A.* **109**, 5663 (2012).
77. A. Bohne-Lang, C. W. von der Lieth, *Nucleic Acids Res.* **33**, W214 (2005).
78. The PyMOL Molecular Graphics System, Version 1.5.0.1. Schrödinger, LLC.
79. R. Xu et al., *Science* **328**, 357 (2010).

**Acknowledgments:** We acknowledge the financial support of the NIH, the IAVI, and the Ragon Institute. We thank C. Corbaci for help in preparation of the manuscript and all of our past and present laboratory members for their many contributions to our research efforts.

10.1126/science.1225416

# Attenuated Vaccines Can Recombine to Form Virulent Field Viruses

Sang-Won Lee,<sup>1</sup> Philip F. Markham,<sup>1</sup> Mauricio J. C. Coppo,<sup>1</sup> Alistair R. Legione,<sup>1</sup> John F. Markham,<sup>3</sup> Amir H. Noormohammadi,<sup>2</sup> Glenn F. Browning,<sup>1</sup> Nino Ficorilli,<sup>1</sup> Carol A. Hartley,<sup>1</sup> Joanne M. Devlin<sup>1\*</sup>

**L**ive attenuated herpesvirus vaccines are widely used in human and veterinary medicine. The risk of vaccines recombining to generate virulent natural recombinants has been raised, but disease outbreaks caused by herpesvirus vaccine recombination have never been reported (1).

The herpesvirus infectious laryngotracheitis virus (ILTV or gallid herpesvirus 1) causes mild to severe respiratory disease in poultry worldwide. Economic losses result from mortality and decreased egg production. Attenuated ILTV vaccines are used widely (2). Concurrent with the introduction of a new vaccine, novel, genotypically distinct viruses (referred as class 8 and 9 viruses) were isolated from geographically distinct Australian regions starting in 2008 (3). These virulent strains have been associated with outbreaks causing mortality rates of up to 17.6% (4). In Australia, three ILTV vaccines are available. The closely related Australian-origin vaccines SA2 and A20 (Pfizer, Australia) are classified genotypically as class 1 viruses on the basis of patterns seen in polymerase chain reaction–restriction fragment length polymorphism (RFLP) analysis (5). The European-origin Serva vaccine strain (Intervet) was first registered in Australia in 2006 and has a class 7 genotype (3). The SA2 and A20 genomes are divergent from the Serva genome, having only 99.2% nucleotide sequence identity with it (6). The contemporaneous introduction of the Serva vaccine and emergence of new

classes of virulent ILTV (classes 8 and 9), together with genetic relatedness of viruses causing recent isolates, led to the hypothesis that the class 8 and 9 viruses may represent subpopulations of viruses within the Serva vaccine or may have arisen after in vivo passages of the Serva vaccine (3).

We performed whole-genome sequencing and comparative sequence analysis of the class 8 and 9 viruses and the three vaccine strains. In genome alignments, much of the class 8 and 9 sequences were almost identical to Serva. Single-nucleotide polymorphisms (SNPs) were clustered in distinct genomic regions unique to each class. The sequence in these regions was identical (class 8) or almost identical (class 9) to the sequences of SA2 and A20 (Fig. 1A). These results are consistent with interspecies recombination between the co-circulating Australian-origin and European-origin vaccines giving rise to virulent class 8 and 9 field strains.

To confirm the likelihood of recombination, we compared the sequences of the class 8 and 9 viruses to those of Serva, SA2, and A20 by using Simplot. Two points of crossover were detected for each virus (Fig. 1, B and C). These corresponded to the recombination regions identified in genome alignments.

To determine whether other class 8 and 9 isolates had the same recombinant genomes as the two fully sequenced isolates, we performed in silico restriction fragment length polymor-

phism (RFLP) analysis with the genomes of the sequenced class 8 and 9 viruses. We also performed specific PCRs to amplify the recombination crossover points of additional class 8 and 9 isolates from different disease outbreaks. The in silico RFLP patterns were consistent with in vitro RFLP analyses of other class 8 and 9 viruses submitted to our diagnostic laboratory. The PCRs revealed that the same recombinant genomes were present in other isolates (figs. S1 and S2).

Lastly, the pathogenicity of class 8 and 9 viruses was studied in specific-pathogen-free chickens. Each recombinant had a distinct in vivo phenotype. After correcting for multiple hypothesis testing, both recombinants had significantly increased virulence or replication compared with their parent strains (fig. S3).

The rapid emergence of two virulent recombinants suggests that recombination between attenuated herpesvirus vaccines and resultant restoration of virulence may be rare but can bring about a fitness advantage, with severe consequences. The findings from this study raise concerns about the use of multiple distinct attenuated herpesvirus vaccines under conditions that favor recombination. These findings have implications for the use of herpesviruses, and possibly other DNA viruses, as attenuated vaccines or vaccine vectors.

## References and Notes

1. E. Thiry *et al.*, *Rev. Med. Virol.* **15**, 89 (2005).
2. T. J. Bagust, R. C. Jones, J. S. Guy, *Rev. Sci. Tech.* **19**, 483 (2000).
3. H. P. Blacker, N. C. Kirkpatrick, A. Rubite, D. O'Rourke, A. H. Noormohammadi, *Aust. Vet. J.* **89**, 89 (2011).
4. J. M. Devlin *et al.*, *Vaccine* **29**, 5699 (2011).
5. N. C. Kirkpatrick, A. Mahmoudian, D. O'Rourke, A. H. Noormohammadi, *Avian Dis.* **50**, 28 (2006).
6. S. W. Lee *et al.*, *Vaccine* **29**, 9583 (2011).

**Acknowledgments:** The Rural Industries Research and Development Corporation, Australia, funded this study. This work is supported by NICTA, which is funded by the Australian government as represented by the Department of Broadband, Communications and the Digital Economy and the Australian Research Council through the ICT Centre of Excellence program. Sequence data for the class 8 and 9 viruses have been deposited in GenBank under accession nos. JN804826 and JN804827, respectively. The three reference sequences are Serva, GenBank accession no. HQ\_630064; SA2, GenBank accession no. JN596962; A20, GenBank accession no. JN596963.

## Supplementary Materials

[www.sciencemag.org/cgi/content/full/337/6091/188/DC1](http://www.sciencemag.org/cgi/content/full/337/6091/188/DC1)

Materials and Methods

Figs. S1 to S3

References (7–12)

28 November 2011; accepted 26 April 2012

10.1126/science.1217134

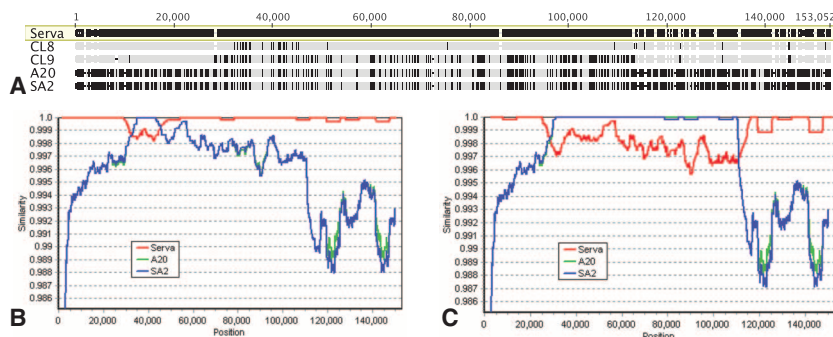


**Fig. 1.** Whole-genome alignments and similarity plots. (A) Alignment of the class 8 (CL8), class 9 (CL9), SA2, and A20 genome sequences with the Serva genome sequence. Vertical black lines indicate single-nucleotide differences from the Serva sequence. Dashes indicate single-base gaps. (B and C) Similarity plots of the sequences of the CL8 (B) and CL9 (C) genomes with those of Serva, A20, and SA2. The results indicate that the class 9 virus was derived from A20 and Serva. One parent of the class 8 virus could not be defined because the recombinant region was identical to both SA2 and A20. All recombinations were significant ( $P < 10^{-3}$ , maximum  $\chi^2$  test).

<sup>1</sup>Asia-Pacific Centre for Animal Health, Faculty of Veterinary Science, The University of Melbourne, Parkville, Victoria 3010, Australia. <sup>2</sup>Asia-Pacific Centre for Animal Health, Faculty of Veterinary Science, The University of Melbourne, Werribee, Victoria 3030, Australia. <sup>3</sup>National ICT Australia (NICTA) Victoria Research Laboratory, Department of Electrical and Electronic Engineering, School of Engineering, The University of Melbourne, Victoria 3010, Australia.

\*To whom correspondence should be addressed. E-mail: devlinj@unimelb.edu.au



# Crystal Structure of the Heterodimeric CLOCK:BMAL1 Transcriptional Activator Complex

Nian Huang,<sup>1\*</sup> Yogarany Chelliah,<sup>2,3\*</sup> Yongli Shan,<sup>2</sup> Clinton A. Taylor,<sup>1,4</sup> Seung-Hee Yoo,<sup>2</sup> Carrie Partch,<sup>1,2,3†</sup> Carla B. Green,<sup>2</sup> Hong Zhang,<sup>1‡</sup> Joseph S. Takahashi<sup>2,3‡</sup>

The circadian clock in mammals is driven by an autoregulatory transcriptional feedback mechanism that takes approximately 24 hours to complete. A key component of this mechanism is a heterodimeric transcriptional activator consisting of two basic helix-loop-helix PER-ARNT-SIM (bHLH-PAS) domain protein subunits, CLOCK and BMAL1. Here, we report the crystal structure of a complex containing the mouse CLOCK:BMAL1 bHLH-PAS domains at 2.3 Å resolution. The structure reveals an unusual asymmetric heterodimer with the three domains in each of the two subunits—bHLH, PAS-A, and PAS-B—tightly intertwined and involved in dimerization interactions, resulting in three distinct protein interfaces. Mutations that perturb the observed heterodimer interfaces affect the stability and activity of the CLOCK:BMAL1 complex as well as the periodicity of the circadian oscillator. The structure of the CLOCK:BMAL1 complex is a starting point for understanding at an atomic level the mechanism driving the mammalian circadian clock.

The basic helix-loop-helix PER-ARNT-SIM (bHLH-PAS) proteins, CLOCK and BMAL1 (ARNTL), are the primary transcriptional activators within the circadian clock mechanism of mammals. Since the molecular identification of the *Clock* gene 15 years ago (1, 2), the transcriptional network that drives circadian oscillations has been systematically identified (3–5). CLOCK and BMAL1 heterodimerize and interact with E-box regulatory elements in the *Period* (*Per1* and *Per2*) and *Cryptochrome* (*Cry1* and *Cry2*) genes to activate their transcription during the daytime (6, 7). Their protein products, PER and CRY, accumulate, dimerize, and translocate into the nucleus at night, where they interact directly with CLOCK:BMAL1 to repress their own transcription (7–10). As the PER:CRY repressor complex is targeted for degradation by specific E3 ubiquitin ligase complexes (11–14), repression is relieved, and CLOCK:BMAL1 then activate a new round of transcription to begin the circadian cycle anew. This cell-autonomous, autoregulatory transcriptional feedback loop takes ~24 hours to complete and forms the core mechanism of the circadian clock in mammals (5).

CLOCK and BMAL1 belong to a family of transcriptional regulators that contain bHLH and PAS domains. In mammals, these bHLH-PAS transcription factors participate in a wide array of functions, including responses to environmental contaminants [Aryl hydrocarbon receptor (AHR)], hypoxia [Hypoxia inducible factor (HIF)], neurogenesis (SIM1), synaptic plasticity (NPAS4), and circadian regulation (CLOCK, NPAS2, and BMAL1) (15), and most of them remain poorly characterized at the structural level. In contrast, the structures of individual PAS domains and their interactions with small-molecule ligands such as heme and flavin cofactors are well understood, especially among microorganisms and plants, in which PAS domains serve important roles in two-component signaling and blue-light detection (16, 17). Although the PAS fold is widely conserved, it has intrinsic flexibility and can adapt to different conformations depending on bound ligands or interacting partners (16). Here, we present the three-dimensional (3D) structure of the bHLH-PAS domains from the mouse CLOCK:BMAL1 heterodimer at 2.3 Å resolution.

**Overall structure of CLOCK:BMAL1.** To obtain stable CLOCK:BMAL1 complexes suitable for crystallographic analysis, we used protein constructs containing the bHLH and the two tandem PAS-A and PAS-B domains (Fig. 1A). N-terminal His-tagged mouse CLOCK (residues 26 to 384) and native mouse BMAL1 (residues 62 to 447) constructs were coexpressed in Sf9 insect cells and copurified (supplementary materials, materials and methods). To confirm that the resulting heterodimeric protein binds DNA, we assayed the affinity of binding to oligonucleotides containing the canonical E-box sequence (CACGTG) from the *mPer1* and *mPer2* promoters and observed dissociation constants ( $K_{ds}$ ) of ~10 nM (Fig. 1B and

fig. S1). Crystals of CLOCK:BMAL1 were obtained that diffracted to 2.3 Å at synchrotron sources. The phases of CLOCK:BMAL1 were determined by means of the single-wavelength anomalous dispersion (SAD) method, using selenomethionine-labeled CLOCK:BMAL1 crystals (fig. S2). Data collection and refinement statistics are shown in table S1.

The 3D structure of CLOCK:BMAL1 reveals a tightly intertwined heterodimer (Fig. 1C, middle) with all three domains—the N-terminal bHLH domain and two tandem PAS domains (PAS-A and PAS-B)—involved in dimerization interactions. Each domain interacts primarily with the corresponding domain of its partner subunit so that CLOCK bHLH interacts with BMAL1 bHLH, and CLOCK PAS-A (or PAS-B) interacts with BMAL1 PAS-A (or PAS-B). Although the primary sequences of these three domains are similar in CLOCK and BMAL1 (figs. S3 and S4), the spatial arrangement of these domains with respect to one another is strikingly different in the two subunits (Fig. 1C). In BMAL1, the second helix of the bHLH domain ( $\alpha_2$ ) is nearly continuous with the N-terminal flanking helix ( $\alpha'$ ) of the PAS-A domain despite insertion of a ~15-residue flexible loop (L1) (Fig. 1C, right). In contrast, in CLOCK there is a ~23 Å displacement between the end of  $\alpha_2$  and the beginning of the PAS-A  $\alpha'$  helix (Fig. 1C, left). As a consequence, the CLOCK PAS-A domain is in direct contact with the  $\alpha_2$  helix of its bHLH domain, whereas there are no direct contacts between the BMAL1 PAS-A and bHLH domains.

The asymmetry of the CLOCK:BMAL1 complex is also reflected in the divergent electrostatic potential distributions on the two subunits. The BMAL1 subunit has an overall positive electrostatic potential with an isoelectric point (pI) of 9.01 (and 8.55 for the PAS-A/B domains). The CLOCK subunit, on the other hand, has an overall negative electrostatic potential, with a pI of 5.86 for the bHLH-PAS domains (and 5.28 for the PAS-A/B domain only). In the 3D CLOCK:BMAL1 complex structure, the exposed CLOCK PAS domain surfaces have a largely negative electrostatic potential, whereas the exposed BMAL1 PAS domains are mostly positively charged or neutral (Fig. 1D). These electrostatic features of the CLOCK:BMAL1 heterodimer produce an interesting dichotomy in the potential interaction interfaces of the complex and are consistent with prior work that suggest that the PER1, PER2, CRY1, and CRY2 proteins differentially interact with CLOCK and BMAL1 (8, 18–20).

**The PAS-A domains.** Although all three domains of the CLOCK and BMAL1 subunits are involved in intermolecular interactions, the heterodimeric interfaces between the individual PAS domains are of particular interest. The CLOCK:BMAL1 heterodimer has long flexible loops interspersed with canonical PAS secondary structure elements in both PAS-A domains. In the BMAL1 PAS-A domain, a total of ~60 residues

<sup>1</sup>Department of Biochemistry, University of Texas Southwestern Medical Center, Dallas, TX 75390, USA. <sup>2</sup>Department of Neuroscience, University of Texas Southwestern Medical Center, Dallas, TX 75390, USA. <sup>3</sup>Howard Hughes Medical Institute, University of Texas Southwestern Medical Center, Dallas, TX 75390, USA. <sup>4</sup>Molecular Biophysics Graduate Program, Division of Basic Science, University of Texas Southwestern Medical Center, Dallas, TX 75390, USA.

\*These authors contributed equally to this work.

†Present address: Chemistry and Biochemistry Department, University of California, Santa Cruz, Santa Cruz, CA 95064, USA.

‡To whom correspondence should be addressed. E-mail: joseph.takahashi@utsouthwestern.edu (J.S.T.); zhang@chop.swmed.edu (H.Z.)

in three loop regions are disordered in the crystal structure, whereas in the CLOCK PAS-A domain, a single loop of ~25 residues is disordered. Despite this high degree of flexibility, the two PAS-A domains adopt a typical PAS fold (Fig. 2A) and are structurally similar to each other, with a root mean square deviation (RMSD) of only 0.62 Å over 79  $C_{\alpha}$  atoms. As seen in typical PAS domains, the core of CLOCK and BMAL1 PAS-A domains contains a five-stranded antiparallel  $\beta$  sheet ( $A\beta$ ,  $B\beta$ ,  $G\beta$ ,  $H\beta$ , and  $I\beta$ ) and several  $\alpha$  helices ( $C\alpha$ ,  $D\alpha$ ,  $E\alpha$ , and  $F\alpha$ ) flanking the concave surface of the sheet. In contrast to the PAS-B domains (Fig. 2A), both PAS-A domains in the two subunits contain an N-terminal flanking helix ( $A'\alpha$ ) external to the canonical PAS-domain fold. The  $A'\alpha$  helices of the CLOCK and BMAL1 PAS-A domains pack in between the  $\beta$ -sheet faces of the two domains to mediate the heterodimeric PAS-A interactions (Fig. 2B). The  $A'\alpha$  helix of CLOCK PAS-A makes extensive contacts with the  $\beta$ -sheet face of BMAL1 PAS-A, whereas the  $A'\alpha$  helix of

BMAL1 interacts with the  $\beta$ -sheet face of CLOCK PAS-A (Fig. 2B). This domain-swapped helical interface is reminiscent of a number of other PAS domain proteins, such as the N-terminal PAS domain of the nitrogen fixation regulatory protein NifL from *Azotobacter vinelandii* (Fig. 2C) (21) and the N-terminal domain of the transcriptional factor TyrR from *Escherichia coli* (22).

The CLOCK:BMAL1 PAS-A dimer interface is largely mediated by conserved hydrophobic interactions. Specifically, Phe<sup>104</sup>, Leu<sup>105</sup>, and Leu<sup>113</sup> on the  $A'\alpha$  helix of CLOCK (corresponding residues on BMAL1 PAS-A are Phe<sup>141</sup>, Leu<sup>142</sup>, and Leu<sup>150</sup>) contact a hydrophobic region on the  $\beta$ -sheet face of BMAL1 PAS-A composed of residues Leu<sup>159</sup> on strand  $A\beta$ , Thr<sup>285</sup> and Tyr<sup>287</sup> on  $H\beta$ , and Val<sup>315</sup> and Ile<sup>317</sup> on strand  $I\beta$  (Fig. 2D). A similar interface can be found between the  $A'\alpha$  helix of BMAL1 and CLOCK PAS-A domain (Fig. 2E). As a result, the two PAS-A domains in CLOCK:BMAL1 form a parallel dimer related by an approximate twofold symmetry, with an ex-

tensive buried surface area (~1950 Å<sup>2</sup>) and topologically complex interface between the two subunits. Many of the residues observed in the CLOCK:BMAL1 PAS-A dimer interface are conserved among bHLH-PAS transcription factors (fig. S4), suggesting that these proteins may share a common PAS-A domain dimerization mode.

**The PAS-B domains.** An ~15-residue linker (L2) connects the PAS-A and PAS-B domains in each of the CLOCK and BMAL1 subunits, although the linker conformation and the relative spatial arrangement of the two PAS domains in the two subunits are different (Fig. 1C). In CLOCK, a large portion of L2 is buried between the interface of CLOCK and BMAL1 and is well ordered (Fig. 1C). In contrast, in BMAL1, L2 between PAS-A and PAS-B is solvent-exposed and very flexible, as indicated by high atomic displacement parameters (B-factors). The PAS-B domains of CLOCK and BMAL1 are related predominantly by a ~26 Å translation and are stacked in a roughly parallel fashion (Fig. 3A)

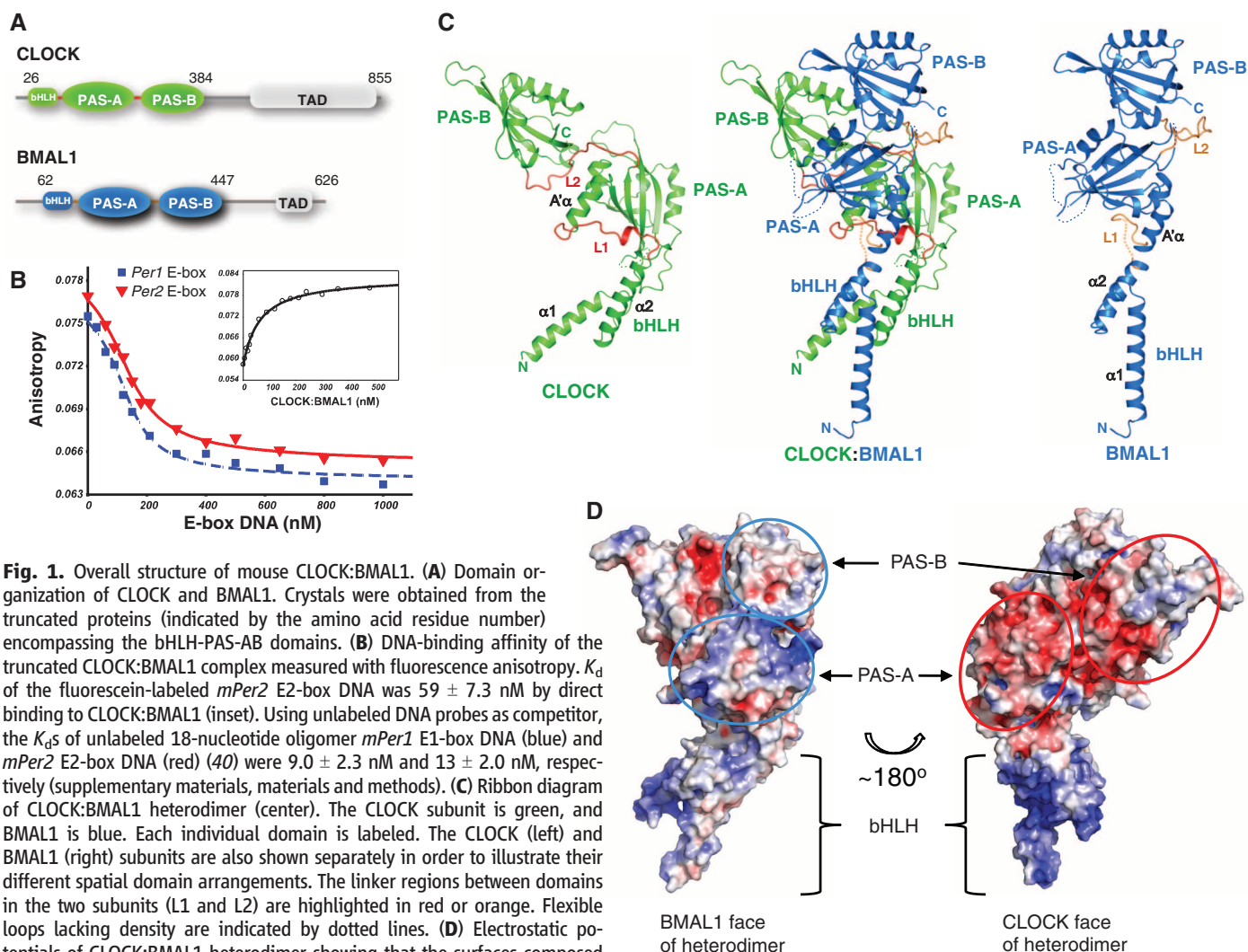


**Fig. 1.** Overall structure of mouse CLOCK:BMAL1. **(A)** Domain organization of CLOCK and BMAL1. Crystals were obtained from the truncated proteins (indicated by the amino acid residue number) encompassing the bHLH-PAS-AB domains. **(B)** DNA-binding affinity of the truncated CLOCK:BMAL1 complex measured with fluorescence anisotropy.  $K_d$  of the fluorescein-labeled *mPer2* E2-box DNA was  $59 \pm 7.3$  nM by direct binding to CLOCK:BMAL1 (inset). Using unlabeled DNA probes as competitor, the  $K_d$ s of unlabeled 18-nucleotide oligomer *mPer1* E1-box DNA (blue) and *mPer2* E2-box DNA (red) (40) were  $9.0 \pm 2.3$  nM and  $13 \pm 2.0$  nM, respectively (supplementary materials, materials and methods). **(C)** Ribbon diagram of CLOCK:BMAL1 heterodimer (center). The CLOCK subunit is green, and BMAL1 is blue. Each individual domain is labeled. The CLOCK (left) and BMAL1 (right) subunits are also shown separately in order to illustrate their different spatial domain arrangements. The linker regions between domains in the two subunits (L1 and L2) are highlighted in red or orange. Flexible loops lacking density are indicated by dotted lines. **(D)** Electrostatic potentials of CLOCK:BMAL1 heterodimer showing that the surfaces composed of CLOCK PAS domains (right, red ovals) have mostly negative potentials, whereas the surfaces of BMAL1 PAS domains (left, blue ovals) are mostly positive or neutral. The colors are ramped from negative potential  $-5 k_B T/q$  (where  $k_B$  is the Boltzmann constant,  $T$  is the temperature, and  $q$  is the magnitude of the charge on an electron) (red) to positive  $5 k_B T/q$  (blue).



different from the antiparallel  $\beta$ -sheet interface seen for the isolated PAS-B domain complex of HIF-2 $\alpha$ :ARNT (Fig. 3B) (23). The  $\beta$  sheet of BMAL1 PAS-B makes contacts with the helical face of CLOCK PAS-B, burying a patch of hydrophobic residues on both subunits. Several surface-exposed hydrophobic residues on both CLOCK and BMAL1 PAS-B become mostly or partially buried upon dimerization, including Tyr<sup>310</sup>, Val<sup>315</sup>, and Leu<sup>318</sup> of CLOCK and Phe<sup>423</sup>, Trp<sup>427</sup>, and Val<sup>435</sup> of BMAL1, resulting in  $\sim 700$  Å<sup>2</sup>

of buried surface area (Fig. 3, C and E). Most prominently within these hydrophobic interactions, BMAL1 Trp<sup>427</sup>, located on the short HI loop (connecting the H $\beta$  and I $\beta$  strands), intrudes into a hydrophobic cleft created between the F $\alpha$  helix and the AB loop of CLOCK PAS-B (Fig. 3, D and F), and partially stacks against the indole ring of CLOCK Trp<sup>284</sup>.

**CLOCK:BMAL1 heterodimer conformation and transactivation function.** To probe the relationship between the observed conformation of

the CLOCK:BMAL1 heterodimer and its function, we generated a series of mutations predicted to perturb the interfaces between each of the three domains (Fig. 4A). For the bHLH domains, the C-terminal halves of the  $\alpha$ 1 helices, together with the  $\alpha$ 2 helices of both CLOCK and BMAL1, participate in the formation of a canonical four-helical bHLH bundle in the heterodimer similar to that observed in USF1 and MYC:MAX (fig. S3A) (24–26). As seen in other bHLH proteins, the core of this four-helical bundle is highly hydrophobic (26, 27), indicating that dimerization of the bHLH domains should help stabilize the CLOCK:BMAL1 complex. The proper conformation of the bHLH domain is also critical for E-box DNA recognition because the DNA-binding  $\alpha$ 1 helices need to be positioned precisely to interact with the major groove sites of the E-box DNA duplex (24, 26, 27). Indeed, when the bHLH hydrophobic core residues Leu<sup>57</sup> and Leu<sup>74</sup> of CLOCK and Leu<sup>95</sup> and Leu<sup>115</sup> of BMAL1 are mutated to glutamate, the transactivation activity of these full-length CLOCK:BMAL1 mutants are eliminated, as demonstrated by measuring E-box-driven luciferase reporter gene activity in human embryonic kidney (HEK) 293T cells with transiently transfected CLOCK and BMAL1 mutant proteins (Fig. 4B).

We examined the dimerization of these mutants in living cells through a bimolecular fluorescence complementation (BiFC) assay, in which the N- and C-terminal fragments of the fluorescent protein Venus (Ven-N and Ven-C) were fused to the C-termini of truncated bHLH-PAS domain constructs of CLOCK and BMAL1, respectively (supplementary materials). Dimerization of CLOCK and BMAL1 brings the two Venus fragments into close proximity to facilitate the formation of an intact fluorescent protein, thus providing a fluorescent readout for protein-protein interactions in living cells (28). The BiFC data showed that mutation at the bHLH hydrophobic core reduced formation of a stable heterodimeric complex (Fig. 4C and fig. S5). Furthermore, three of these bHLH domain mutations—CLOCK L74E (C:L74E), BMAL1 L95E, and L115E (B:L95E and B:L115E)—also destabilized the full-length CLOCK:BMAL1 heterodimer, as shown with co-immunoprecipitation (co-IP) assays (Fig. 4D) (In the mutants, other amino acids were substituted at certain locations; for example, L74E indicates that leucine at position 74 was replaced by glutamic acid. Single-letter abbreviations for the amino acid residues are as follows: A, Ala; C, Cys; D, Asp; E, Glu; F, Phe; G, Gly; H, His; I, Ile; K, Lys; L, Leu; M, Met; N, Asn; P, Pro; Q, Gln; R, Arg; S, Ser; T, Thr; V, Val; W, Trp; and Y, Tyr).

Next, we mutated residues involved in PAS-A and PAS-B domain interfaces in order to test their effects on transactivation activity and CLOCK:BMAL1 heterodimer formation. To examine the PAS-A domain interface, we made the following mutations: L113E (on A' $\alpha$ ) and F122D (on A $\beta$ ) of CLOCK and L150E (on A' $\alpha$ ) and I317D (on I $\beta$ ) of BMAL1. We then performed transactivation,

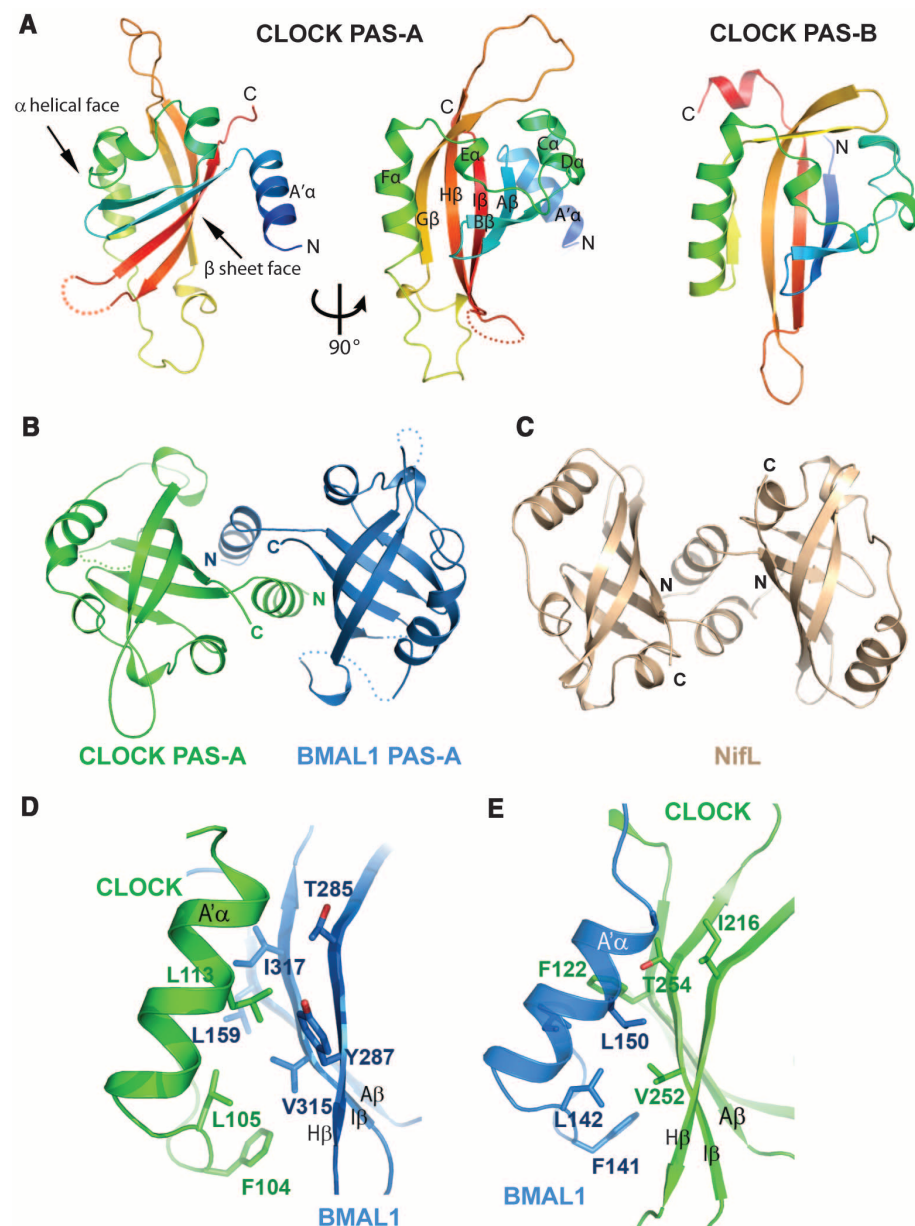


**Fig. 2.** Structure and interaction of the PAS-A domains of CLOCK:BMAL1. (A) Ribbon representations of CLOCK PAS-A domain. Secondary structures are color ramped from blue to red and labeled from the A' $\alpha$  helix located N-terminal to the canonical PAS domain fold, in an alphabetical progression through the whole domain. The CLOCK PAS-B domain is also shown for comparison. (B) Dimerization of the two PAS-A domains in CLOCK:BMAL1, looking down the approximate twofold symmetry axis. (C) Similar domain-swapped structure of the redox-sensing PAS domain of NifL from *A. vinelandii* (PDB 2GJ3). (D) Detailed interface between A' $\alpha$  helix of CLOCK PAS-A (green) and the  $\beta$  sheet face of BMAL1 PAS-A (blue). (E) The corresponding interface between A' $\alpha$  helix of BMAL1 PAS-A and the  $\beta$  sheet face of CLOCK PAS-A.

BiFC, and co-IP assays (Fig. 4). Single mutations of C:L113E, C:F122D, or B:L150E were not sufficient to reduce dimerization or transactivation activity (Fig. 4, B to D). However, BMAL1 mutant I317D had decreased transcriptional activity [~80% of wild type (control)] (Fig. 4B) and decreased affinity for CLOCK, as demonstrated through the BiFC and co-IP experiments (Fig. 4, C and D, and fig. S5). Furthermore, when opposing CLOCK and BMAL1 PAS-A domain interface residues were doubly mutated, as in C:L113E+B:I317D, the association between full-length CLOCK and BMAL1 subunits was not detectable under the assay conditions, and transactivation activity was reduced to ~25% of the control (Fig. 4, B to D).

To examine the unusual interface between the PAS-B domains of the CLOCK:BMAL1 heterodimer, we made the following PAS-B domain mutations: W284A and V315R on the CLOCK helical face and W427A, F423R, and V435R on the  $\beta$ -sheet face of BMAL1. Single mutations in either CLOCK or BMAL1 PAS-B domains had a limited effect on the transactivation activity by the full-length mutant protein (Fig. 4B), although the activities of C:W284A, C:V315R, and B:F423R were reduced by ~20 to 30% compared with the wild-type (WT) protein (Fig. 4B). Additionally, the BiFC signal of mutants C:W284A, C:V315R, and B:V435R decreased dramatically compared with the WT protein (Fig. 4C and fig. S5), indicating that the PAS-B domain interactions of these mutants may be altered. The effect of these single mutations on the interactions of the full-length proteins, as measured with co-IP, was more subtle, with partially weakened interactions for mutants C:W284A and B:W427A (Fig. 4D). The double BMAL1 PAS-B domain mutant B:F423R/V435R and the combined CLOCK:BMAL1 mutant C:W284A+B:W427A showed a decreased interaction in both co-IP and BiFC assays as well as a reduction in transactivation activity (Fig. 4, B to D). These data support the unusual PAS-B domain interface observed in the crystal structure involving the helical face of CLOCK and the  $\beta$ -sheet face of BMAL1 and specifically indicate that contact between CLOCK Trp<sup>284</sup> and BMAL1 Trp<sup>427</sup> is important for PAS-B interaction.

**CLOCK:BMAL1 mutants alter circadian cycling in cells.** To examine the functional consequences of mutations that compromise CLOCK:BMAL1 heterodimer formation and transactivation potential, we assessed circadian rhythms in mouse *Per2<sup>Luc</sup>* fibroblasts overexpressing mutant CLOCK or BMAL1 constructs introduced by lentiviral vectors (supplementary materials, materials and methods, and fig. S6). On the basis of in vivo transgenic experiments, we can infer that CLOCK levels are rate limiting and that overexpression of CLOCK leads to a shortening of circadian period in both constitutively expressed or conditionally expressed transgenic mice (2, 29). In contrast, overexpression of BMAL1 can have no effect or can lengthen circadian period (30), and these effects of BMAL1 overexpression are

consistent with the hypothesis that BMAL1 is normally in excess of CLOCK. Higher overexpression of BMAL1 can lead to period lengthening, possibly by the sequestering of CLOCK via a squelching mechanism (31). Thus, we can assay the function of WT CLOCK and BMAL1 by overexpression in PER2::luciferase-cycling cell assays (32) and, by extension, infer loss-of-function mutations by their inability to mimic WT function or, in contrast, dominant-negative mutations by their disruption of normal rhythms.

Control *Per2<sup>Luc</sup>* fibroblasts overexpressing green fluorescent protein (GFP) had robust luciferase rhythms, with a period of 23.1 hours (fig. S6). Cells overexpressing WT CLOCK or BMAL1 exhibited rhythms with either shorter (~22.0 hours) or longer (24.6 hours) periods,

respectively (fig. S6A). Both the CLOCK mutants tested (C:L57E and C:W284A) failed to mimic WT CLOCK and had period values similar to those of the GFP control cells (~23 hours) and therefore behaved as loss-of-function mutations. The C:L57E mutant abolished transactivation by full-length CLOCK:BMAL1 and reduced dimerization of the truncated heterodimer (Fig. 4, B and C). Although the C:W284A PAS-B mutant had only a 20% reduction in activity in transactivation assays (Fig. 4B), it weakened CLOCK:BMAL1 dimerization significantly (Fig. 4, C and D) and failed to mimic the function of WT CLOCK on circadian periodicity. Overexpression of BMAL1 mutants within the bHLH and PAS-A domains had different effects on the period of circadian rhythms (fig. S6). Overexpression of

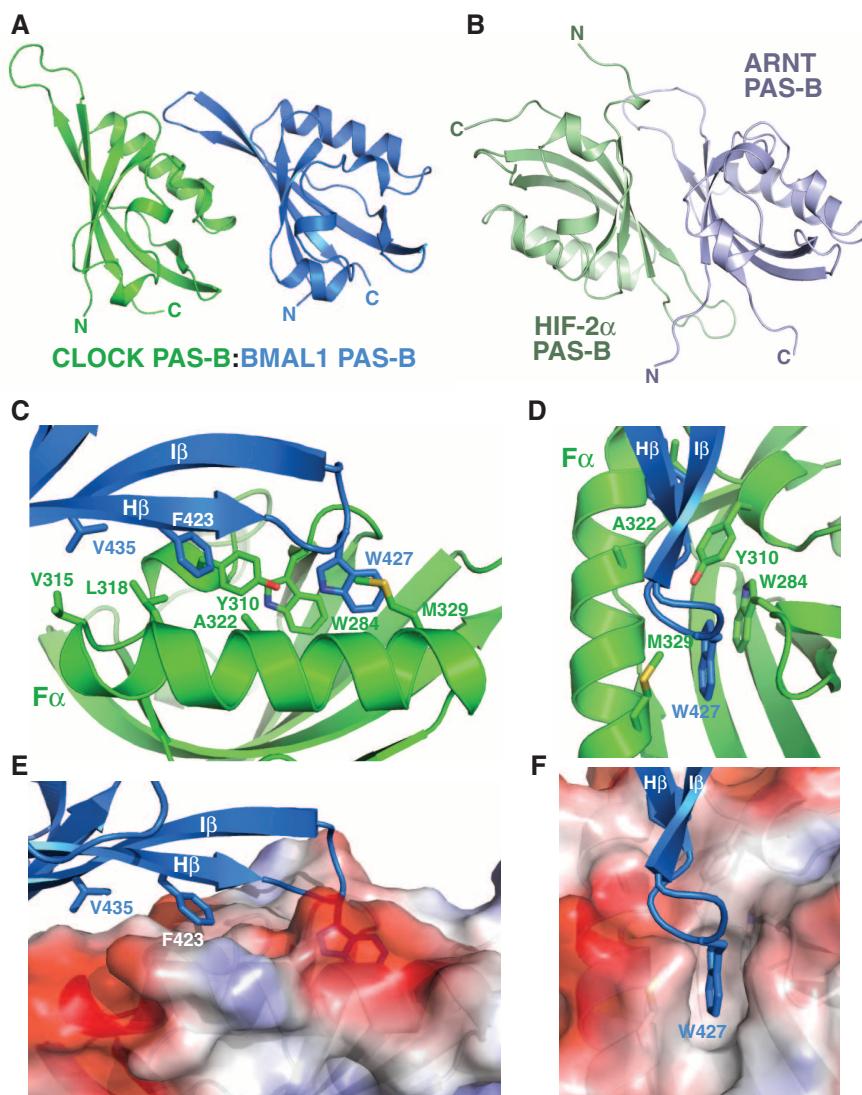


**Fig. 3.** Interface between CLOCK:BMAL1 PAS-B domains. (A) The spatial arrangement of the two PAS-B domains in CLOCK:BMAL1. (B) Antiparallel orientation of  $\beta$  sheet-mediated interaction between isolated HIF-2 $\alpha$ :ARNT PAS-B domains (PDB 3F1P). (C) Detailed interface between CLOCK:BMAL1 PAS-B domains. (D) Front-facing view of CLOCK:BMAL1 PAS-B interface highlighting role of BMAL1 Trp<sup>427</sup> and CLOCK Trp<sup>284</sup> interaction. (E) Side view of PAS-B interface displaying surface electrostatic potential of CLOCK PAS-B. (F) Front-facing view of CLOCK surface electrostatic potential displaying the binding pocket for BMAL1 Trp<sup>427</sup>. The color scheme used is the same as in Fig. 1D.



the bHLH mutant B:L95E led initially to a longer period (25.1 hours) for the first 3 days, followed by disruption of circadian rhythmicity, whereas overexpression of the PAS-A mutant B:I317D led to a shorter period (~23.8 hours) as compared with that of the cells overexpressing WT BMAL1 (24.6 hours) and thus behaved as a partial loss-of-function mutation.

**Discussion.** Here, we present the x-ray structure of the mouse CLOCK:BMAL1 transcriptional activator complex, which is a central regulator in the circadian clock. With the CLOCK:BMAL1 complex structure in hand, it will now be possible to analyze the multiprotein complexes involved in mammalian circadian clock mechanisms at an atomic level. Existing genetic and biochemical data indicate that the negative regulators CRY and PER physically interact with CLOCK:BMAL1 to form the major repressive clock complex containing CLOCK:BMAL1 and PER:CRY (9, 10, 18, 33). Although the structural details of these interactions have not been

elucidated, the binding of CRY and/or PER to CLOCK:BMAL1 could affect DNA binding, modulate transactivation potential, or modify interactions with coactivators and corepressors. Previous work suggests that CRY interacts with the PAS-B domain of CLOCK near its  $\beta$ -sheet face and also with a C-terminal region of BMAL1 (18, 19, 33). Specifically, mutations of residues Gly<sup>332</sup>, His<sup>360</sup>, Gln<sup>361</sup>, Trp<sup>362</sup>, and Glu<sup>367</sup> of the CLOCK PAS-B domain interfere with repression by CRY. In the crystal structure, these residues are located on the HI loop of the solvent-exposed  $\beta$ -sheet face of the CLOCK PAS-B domain, fully accessible for interaction with CRY (Fig. 5). The electrostatic distribution of CLOCK PAS domains is also consistent with the idea that CLOCK is the site for CRY binding because CRY is a highly positively charged protein (pI = 8.24 for CRY1) and would complement the negative surface charge on CLOCK (Fig. 1D). Thus, the unusual spatial arrangement of the PAS-B domains of CLOCK:BMAL1 observed in the crystal struc-

ture is consistent with the earlier biochemical data on the PAS-B domain function. The tandem PAS domains in BMAL1 have a spatial arrangement similar to that observed in the crystal structures of the mouse and *Drosophila* PER tandem PAS domains (fig. S7) (34–37). This suggests that the tandem PAS domains in BMAL1 and PER may have a deeper degree of structural and/or functional conservation than was previously appreciated, which may have implications for how the PAS-A and PAS-B domains of PER2 interact with either CLOCK or BMAL1 (10).

Trp<sup>362</sup> of CLOCK—implicated in an interaction with CRY—corresponds to Trp<sup>427</sup> of BMAL1, which was shown here to interact with CLOCK (Fig. 3, D and F). Moreover, a tryptophan residue at the same position is also conserved in the *Drosophila* and mouse PER proteins (Trp<sup>482</sup> of dPER and Trp<sup>419</sup> of mPER2) and are shown in the crystal structures to be involved in the interaction with a second PER protein to form homodimers (35). These observations highlight a potentially

**Fig. 4.** Functional analysis of CLOCK:BMAL1 mutants.

(A) Locations of domain interface mutants in CLOCK (green) and BMAL1 (blue). (B) *Per2* promoter:Luciferase reporter assays to evaluate the effects of structure-based mutations on transactivation by full-length CLOCK:BMAL1. Data are an average of two independent experiments performed in duplicate. (C) BiFC experiments on the same set of mutants in truncated CLOCK:BMAL1 constructs. The fluorescent intensities of WT and mutant CLOCK:BMAL1 bHLH-PAS-AB constructs (supplementary materials, materials and methods) were quantified by using data from three independent experiments. (D) co-IP experiments assessing the association of CLOCK and BMAL1 in full-length WT and mutant proteins. Anti-FLAG affinity gel was used to precipitate FLAG-tagged CLOCK along with the tightly associated BMAL1, which is HA-tagged. The Western blots using an antibody to HA were then performed to detect the association of WT and mutant CLOCK and BMAL1 constructs. The co-IP data are representative of at least three independent replicates, with the exception of C:W284A, which had stronger co-IP interaction in other experiments, but on average was weaker than WT CLOCK.

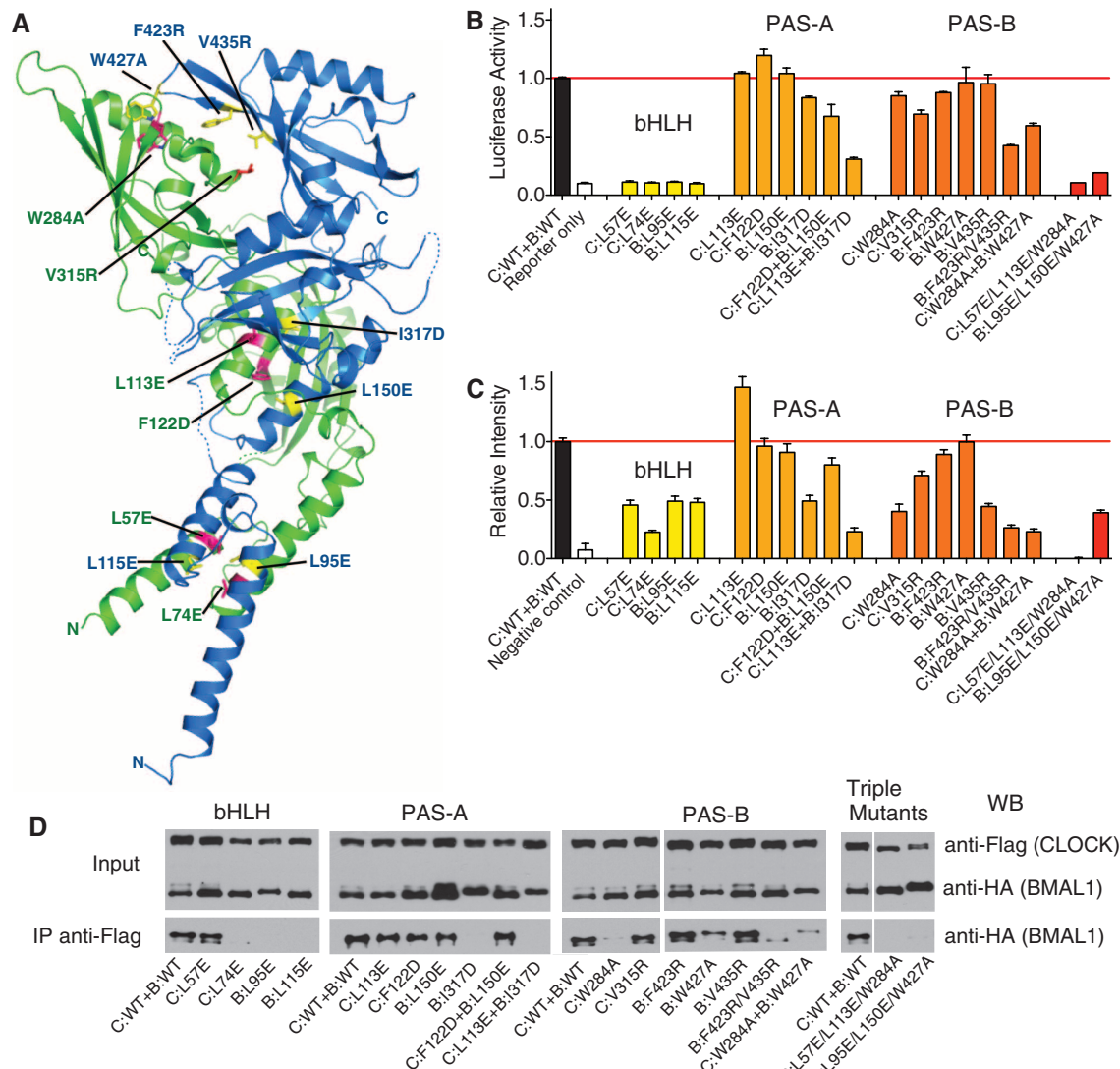
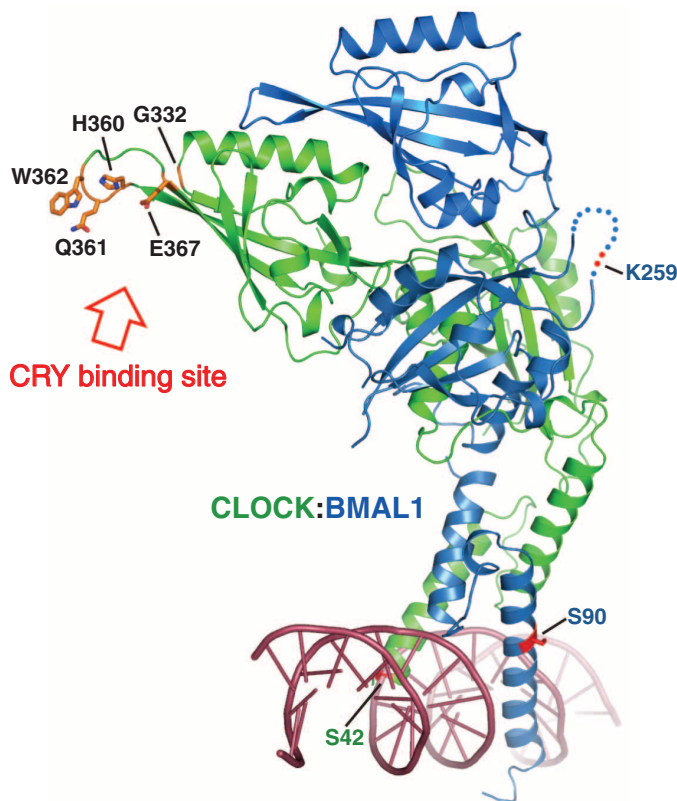


**Fig. 5.** Mutations that reduce repression of CLOCK: BMAL1 transactivation by CRY localize to CLOCK PAS-B HI loop. CRY-derepressing mutations arising from a random mutagenesis screen: G332E, H360Y, E367K (18), or directed mutagenesis study Q361P/W362R (19) are predominantly found on the  $\beta$  sheet face of CLOCK PAS-B domain and are fully solvent-accessible. Residues mutated in these studies are in orange. The locations of the SUMOylation site on BMAL1 PAS-A (K259) (41), the Casein kinase 2 phosphorylation site on BMAL1 (S90) (42), and the phosphorylation site on CLOCK (S42) (43) are also indicated. A double-strand DNA is modeled on the basis of the superposition with USF-DNA complex structure (25).



conserved functional role for the tryptophan residue located at the HI loop of the PAS-B domains of these clock proteins.

The CLOCK:BMAL1 PAS-B domain interface reveals details of a mode of PAS protein-protein interaction involving the  $\alpha$ -helical face of CLOCK PAS-B and the  $\beta$ -sheet face of BMAL1 PAS-B (Fig. 3, C to F, and fig. S8A). The same region (between F $\alpha$  and the AB loop) on the helical face of PER PAS-B is used for intramolecular interactions with a C-terminal  $\alpha$  helix ( $\alpha$ E) containing nuclear exporting signal residues (helix  $\alpha$ E is equivalent to J $\alpha$  in canonical PAS nomenclature) (fig. S8B) (37). Similarly, ARNT has been shown by means of nuclear magnetic resonance studies to use the same helical region for interacting with a family of helical coactivator proteins that are required for transactivation by the heterodimeric HIF:ARNT complex (38, 39). Moreover, the same region of many bacterial and plant PAS proteins binds to small-molecule ligands such as flavin cofactors, flavin adenine dinucleotide, and flavin mononucleotide (fig. S8C) (16). Overall, these data highlight the remarkable structural plasticity and adaptability of PAS domains. Because CLOCK:BMAL1 is a prototypical bHLH-PAS protein family member, the structural features of the CLOCK:BMAL1 complex may be shared by other bHLH-PAS proteins. It will be important in future work to determine the structures of additional heterodimeric bHLH-PAS proteins such as HIF:ARNT and AHR:ARNT and observe the structural basis by which these homologous proteins confer their distinct and pathway-specific functions.

The structure of CLOCK:BMAL1 has revealed the locations of previously identified sites on these proteins that affect their inhibition by CRY. It has also revealed an unexpected similarity in the orientation of the tandem PAS-A and PAS-B domains of BMAL1 to that found in the PERIOD proteins. These observations provide a starting point for the determination of how the CRY and PER proteins interact with and repress CLOCK:BMAL1, which in turn should yield insight into the detailed biochemical mechanism by which this transcriptional feedback loop drives the circadian clock.

#### References and Notes

1. D. P. King *et al.*, *Cell* **89**, 641 (1997).
2. M. P. Antoch *et al.*, *Cell* **89**, 655 (1997).
3. S. M. Reppert, D. R. Weaver, *Nature* **418**, 935 (2002).
4. P. L. Lowrey, J. S. Takahashi, *Annu. Rev. Genomics Hum. Genet.* **5**, 407 (2004).
5. P. L. Lowrey, J. S. Takahashi, *Adv. Genet.* **74**, 175 (2011).
6. N. Gekakis *et al.*, *Science* **280**, 1564 (1998).
7. K. Kume *et al.*, *Cell* **98**, 193 (1999).
8. E. A. Griffin Jr., D. Staknis, C. J. Weitz, *Science* **286**, 768 (1999).
9. C. Lee, J. P. Etchegaray, F. R. Cagampang, A. S. Loudon, S. M. Reppert, *Cell* **107**, 855 (2001).
10. R. Chen *et al.*, *Mol. Cell* **36**, 417 (2009).
11. T. Shirogane, J. Jin, X. L. Ang, J. W. Harper, *J. Biol. Chem.* **280**, 26863 (2005).
12. S. Reischl *et al.*, *J. Biol. Rhythms* **22**, 375 (2007).
13. L. Busino *et al.*, *Science* **316**, 900 (2007).
14. S. M. Siepka *et al.*, *Cell* **129**, 1011 (2007).
15. B. E. McIntosh, J. B. Hogenesch, C. A. Bradfield, *Annu. Rev. Physiol.* **72**, 625 (2010).
16. A. Möglich, R. A. Ayers, K. Moffat, *Structure* **17**, 1282 (2009).
17. J. T. Henry, S. Crosson, *Annu. Rev. Microbiol.* **65**, 261 (2011).
18. T. K. Sato *et al.*, *Nat. Genet.* **38**, 312 (2006).
19. W. N. Zhao *et al.*, *Nat. Cell Biol.* **9**, 268 (2007).
20. R. Ye, C. P. Selby, N. Ozturk, Y. Annayev, A. Sancar, *J. Biol. Chem.* **286**, 25891 (2011).
21. J. Key, M. Hefti, E. B. Purcell, K. Moffat, *Biochemistry* **46**, 3614 (2007).
22. D. Verger, P. D. Carr, T. Kwok, D. L. Ollis, *J. Mol. Biol.* **367**, 102 (2007).
23. T. H. Scheuermann *et al.*, *Proc. Natl. Acad. Sci. U.S.A.* **106**, 450 (2009).
24. A. R. Ferré-D'Amaré, G. C. Prendergast, E. B. Ziff, S. K. Burley, *Nature* **363**, 38 (1993).
25. A. R. Ferré-D'Amaré, P. Pognonec, R. G. Roeder, S. K. Burley, *EMBO J.* **13**, 180 (1994).
26. S. K. Nair, S. K. Burley, *Cell* **112**, 193 (2003).
27. P. C. Ma, M. A. Rould, H. Weintraub, C. O. Pabo, *Cell* **77**, 451 (1994).
28. T. K. Kerppola, *Nat. Rev. Mol. Cell Biol.* **7**, 449 (2006).
29. H. K. Hong *et al.*, *PLoS Genet.* **3**, e33 (2007).
30. E. L. McDearmon *et al.*, *Science* **314**, 1304 (2006).
31. M. Ptashne, *Nature* **335**, 683 (1988).
32. S. H. Yoo *et al.*, *Proc. Natl. Acad. Sci. U.S.A.* **101**, 5339 (2004).
33. Y. B. Kiyohara *et al.*, *Proc. Natl. Acad. Sci. U.S.A.* **103**, 10074 (2006).
34. O. Yildiz *et al.*, *Mol. Cell* **17**, 69 (2005).
35. S. Hennig *et al.*, *PLoS Biol.* **7**, e94 (2009).
36. H. A. King, A. Hoelz, B. R. Crane, M. W. Young, *J. Mol. Biol.* **413**, 561 (2011).
37. N. Kucera *et al.*, *Proc. Natl. Acad. Sci. U.S.A.* **109**, 3311 (2012).
38. C. L. Partch, P. B. Card, C. A. Amezcu, K. H. Gardner, *J. Biol. Chem.* **284**, 15184 (2009).
39. C. L. Partch, K. H. Gardner, *Proc. Natl. Acad. Sci. U.S.A.* **108**, 7739 (2011).
40. S. H. Yoo *et al.*, *Proc. Natl. Acad. Sci. U.S.A.* **102**, 2608 (2005).
41. L. Cardone *et al.*, *Science* **309**, 1390 (2005).
42. T. Tamaru *et al.*, *Nat. Struct. Mol. Biol.* **16**, 446 (2009).
43. H. Yoshitane *et al.*, *Mol. Cell. Biol.* **29**, 3675 (2009).

**Acknowledgments:** This work was supported by the Howard Hughes Medical Institute (J.S.T.), American Heart Association grant 10GRNT4310090 (H.Z.), NIH grant R01 GM090247 (C.B.G.), and R01 GM081875 (K. Gardner). We thank N. Grishin and K. Gardner for helpful discussions; S. Padrick for help with the fluorescence polarization assay; M. Rosen for use of his fluorometer; D. Tomchick and H. Aronovich for technical assistance; and C. Ralston, L. Steinhour, and C. Brautigam for help with data collection. The Berkeley Center for Structural Biology is supported in part by NIH, the National Institute of General Medical Sciences, and the Howard Hughes Medical Institute. The Advanced Light Source is supported by the Director, Office of Science, Office of Basic Energy Sciences, of the U.S. Department of Energy under contract DE-AC02-05CH11231. Results shown in this report are derived from work performed at Argonne National Laboratory, Structural Biology Center at the Advanced Photon Source. Argonne is operated by UChicago Argonne, LLC, for the U.S. Department of Energy, Office of Biological and Environmental Research under contract DE-AC02-06CH11357. J.S.T. is an investigator, Y.C. is a research specialist 3, and C.P. was an associate in the Howard Hughes Medical Institute. J.S.T. is a cofounder of, a Scientific Advisory Board member of, and a paid consultant for ReSet Therapeutics, a biotechnology company aimed at discovering small-molecule therapies that modulate circadian activity for a variety of disease indications. C.B.G. is on the Scientific Advisory Board of, is a paid consultant for, and owns stock in ReSet Therapeutics. Atomic coordinates for the reported crystal structures have been deposited with the Protein Data Bank (PDB) under accession code 4F3L.

#### Supplementary Materials

www.sciencemag.org/cgi/content/full/science.1222804/DC1  
Materials and Methods  
Figs. S1 to S8  
Tables S1 and S2  
References (44–67)  
Movie S1

3 April 2012; accepted 15 May 2012  
Published online 31 May 2012;  
10.1126/science.1222804



# MMS19 Assembles Iron-Sulfur Proteins Required for DNA Metabolism and Genomic Integrity

Oliver Stehling,<sup>1\*</sup> Ajay A. Vashisht,<sup>2\*</sup> Judita Mascarenhas,<sup>1</sup> Zophonias O. Jonsson,<sup>2†</sup> Tanu Sharma,<sup>2</sup> Daili J. A. Netz,<sup>1</sup> Antonio J. Pierik,<sup>1</sup> James A. Wohlschlegel,<sup>2‡</sup> Roland Lill<sup>1‡</sup>

Instability of the nuclear genome is a hallmark of cancer and aging. MMS19 protein has been linked to maintenance of genomic integrity, but the molecular basis of this connection is unknown. Here, we identify MMS19 as a member of the cytosolic iron-sulfur protein assembly (CIA) machinery. MMS19 functions as part of the CIA targeting complex that specifically interacts with and facilitates iron-sulfur cluster insertion into apoproteins involved in methionine biosynthesis, DNA replication, DNA repair, and telomere maintenance. MMS19 thus serves as an adapter between early-acting CIA components and a subset of cellular iron-sulfur proteins. The function of MMS19 in the maturation of crucial components of DNA metabolism may explain the sensitivity of MMS19 mutants to DNA damage and the presence of extended telomeres.

Maintaining genomic stability is a key cellular function, and its impairment has been implicated in a variety of diseases, including cancer (1–3). The process has been connected to mitochondrial function and to the biogenesis of iron-sulfur (Fe-S) proteins, and it may be relevant for the neurodegenerative disorder Friedreich's ataxia (4–6). The observation that multiple DNA replication and repair enzymes require Fe-S clusters for function has suggested a link between genomic stability and Fe-S protein biogenesis (7–12); however, in vivo evidence is lacking and the molecular basis of these connections is unclear.

The synthesis of Fe-S clusters and their assembly into proteins as inorganic cofactors cannot occur without a dedicated and conserved biosynthetic pathway (13, 14). Mitochondrial Fe-S proteins are matured by the iron-sulfur cluster (ISC) assembly machinery. Extramitochondrial Fe-S protein biogenesis depends on both the ISC and CIA (cytosolic iron-sulfur protein assembly) machineries. Cytosolic Fe-S clusters are first assembled on the CIA scaffold complex CFD1-NBP35 (15–18) and are then transferred to apoproteins with the help of Cia1 [human CIAO1 (19)] and Nar1 [human IOP1 (20, 21)].

Mutants in eukaryotic MMS19 (also known as MET18 in yeast) show a variety of phenotypes, including defects in methionine synthesis, sensitivity to genotoxic stress [e.g., by methyl methanesulfonate (MMS)], and the presence of

extended telomeres (22–25). A molecular function explaining these diverse cellular roles is unknown. Previous proteomic studies identified an interaction between yeast Mms19 and (putative) CIA components potentially linking

MMS19 to Fe-S protein biogenesis (26, 27). Here, we show that MMS19 is a component of the “CIA machinery” that transfers Fe-S clusters to various DNA metabolism-associated Fe-S proteins. These findings explain the previously described MMS19 mutant phenotypes.

## Yeast Mms19 is a late-acting CIA component.

The interaction of yeast Mms19 (gene *YIL128w*) with two late-acting members of the CIA machinery, Cia1 and Cia2 [gene *YHR122w* (19, 26–28)], was validated by coimmunoprecipitation (29) (fig. S1A). The potential role of Mms19 in cellular Fe-S protein biogenesis was examined by depleting the protein in a *GAL* promoter-regulatable MMS19 yeast strain and measuring <sup>55</sup>Fe incorporation into known Fe-S target proteins (Leu1, Rli1, and Ntg2) by immunoprecipitation and scintillation counting (30). Mms19 depletion resulted in decreased <sup>55</sup>Fe-S cluster binding to these proteins (Fig. 1A). The decrease in <sup>55</sup>Fe binding by Leu1 correlated with loss of its enzymatic activity, whereas the activity of the non-Fe-S protein alcohol dehydrogenase was unchanged (Fig. 1B). These results were similar to those for depletion of the CIA proteins Nbp35

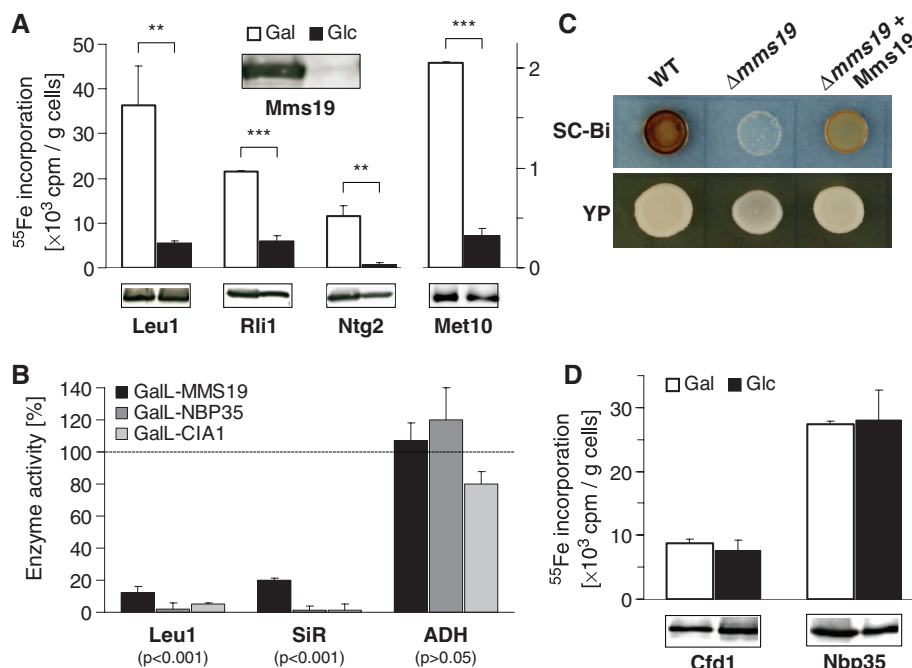


**Fig. 1.** Yeast Mms19 is a CIA component acting late in cytosolic Fe-S protein maturation. (A) <sup>55</sup>Fe incorporation into cytosolic Fe-S proteins. Gal-GFP-MMS19 yeast cells producing Rli1-HA, Ntg2-HA, or Met10-HA were grown in minimal medium (SC) containing galactose (Gal) or glucose (Glc). After radiolabeling with <sup>55</sup>Fe, cell extracts were analyzed for the indicated Fe-S proteins by immunoblotting, and associated <sup>55</sup>Fe was quantified by immunoprecipitation and scintillation counting. (B) Enzyme activities of the cytosolic Fe-S proteins isopropylmalate isomerase (Leu1) and sulfite reductase (SiR), and of alcohol dehydrogenase (ADH), were measured in extracts of indicated cells grown for 36 hours in glucose-containing SC and plotted relative to wild-type cell activities. (C) SiR activity was measured in wild-type (WT) and  $\Delta$ mms19 cells without and with a Mms19-encoding plasmid on SC (SC-Bi) or YP glucose plates containing bismuth ammonium citrate and sodium sulfite. Sulfide produced by SiR after growth for 3 days yields Bi<sub>2</sub>S<sub>3</sub> (brown precipitate). (D) Mms19 acts late in biogenesis. <sup>55</sup>Fe incorporation into the indicated CIA proteins was measured as in (A) for Gal-GFP-MMS19 cells with plasmids encoding Cfd1-TAP and Nbp35-TAP. Values are means  $\pm$  SD. \*\**P* < 0.01, \*\*\**P* < 0.001.

<sup>1</sup>Institut für Zytobiologie und Zytopathologie, Philipps-Universität Marburg, Robert-Koch-Str. 6, 35033 Marburg, Germany, and Max-Planck-Institut für terrestrische Mikrobiologie, Karl-von-Frisch-Str. 10, 35043 Marburg, Germany. <sup>2</sup>Department of Biological Chemistry, David Geffen School of Medicine, University of California, Los Angeles, CA 90095, USA.

\*These authors contributed equally to this work.

†Present address: Institute of Biology, University of Iceland, Sturlugata 7, 101 Reykjavík, Iceland.

‡To whom correspondence should be addressed. E-mail: jwohl@mednet.ucla.edu (J.A.W.); lill@staff.uni-marburg.de (R.L.)

and Cia1 (19). The defect in Leu1 activity did not result from impaired methionine biosynthesis in *mms19* mutants, because other methionine synthesis mutants showed normal Leu1 activity (fig. S2A). Mms19 was also required for  $^{55}\text{Fe}$ -S cluster assembly and for the sulfite reductase activity of the Met5-Met10 complex, which supplies sulfur for methionine biosynthesis in a CIA-dependent manner (Fig. 1, A to C, and fig. S2B). Together, these findings explain the methionine auxotrophy of *mms19* mutants and identify Mms19 as a CIA component. As previously found for CIA defects, both mitochondrial Fe-S protein maturation (fig. S3, A and B) and cellular iron metabolism (fig. S3C) were unaffected by Mms19 deficiency. To clarify when Mms19 acted in the CIA pathway (13), we investigated its requirement for Fe-S cluster assembly on the early-acting CIA proteins Cfd1 and Nbp35. Mms19 depletion had no detrimental effect on the  $^{55}\text{Fe}$ -S maturation of these factors (Fig. 1D), which suggests that Mms19 functions late in cytosolic Fe-S protein assembly as a partner of Cia1 and Cia2.

**Yeast Mms19 assembles and interacts with Fe-S proteins involved in DNA metabolism.** To explain the sensitivity of *mms19* mutants to DNA-damaging agents (22), we analyzed the requirement of yeast Mms19 for the maturation of several Fe-S cluster-containing DNA repair enzymes.  $^{55}\text{Fe}$  radiolabeling showed that the Rad3 DNA helicase bound a Fe-S cluster in vivo (Fig. 2A) (7) and that its maturation was dependent on Mms19 and the ISC CIA machinery. Similar findings were made for the human Rad3 ortholog XPD (xeroderma pigmentosum protein D) when expressed in yeast (Fig. 2B). Mutations in Fe-S cluster-coordinating residues of XPD or the disease-relevant residue Arg<sup>112</sup> destroyed Fe-S cluster binding (fig. S4A). Mms19 specifically coimmunoprecipitated with Rad3, Met10 (Fig. 2, C and D), and several other Fe-S proteins, including the DNA helicase/nuclease Dna2 (Fig. 2D and fig. S4B), Rli1, and the DNA glycosylase Ntg2 (fig. S1B).

**Human MMS19 matures only a subset of Fe-S proteins.** Mammalian MMS19 has been identified as part of a protein complex including XPD and two putative CIA components, CIAO1 and FAM96B (homolog of yeast Cia2). It has been functionally implicated in DNA repair, chromosome segregation, and transcription (24, 31, 32), yet no connection to Fe-S protein assembly has been proposed. To examine whether human MMS19 plays an evolutionarily conserved role in Fe-S protein biogenesis, we depleted MMS19 by RNA interference (RNAi) in HeLa cells, using three different small interfering RNA (siRNA) oligos either alone or as a pool (33). Efficient MMS19 silencing was achieved by three consecutive siRNA transfections performed at 3-day intervals (fig. S5, A and B). We first tested the possible role of MMS19 in the maturation of two well-studied Fe-S proteins, cytosolic aconitase IRP1 (iron regulatory protein 1) and GPAT [glutamine phosphoribosylpyrophosphate amidotransferase

(16)]. For IRP1, the enzyme activity, protein level, and binding capacity to iron-responsive RNA elements (IREs) were unchanged upon MMS19 depletion (Fig. 3A and fig. S6, A to C). Similarly, no effects on GPAT protein levels were observed (Fig. 3A and fig. S7). Because Fe-S cluster binding is essential for GPAT stability, GPAT abundance is a reliable measure of its maturation (16).

These negative results prompted us to hypothesize that MMS19 plays a specialized role in Fe-S cluster maturation of a subset of target proteins. We therefore developed two additional assays for cytosolic Fe-S protein biogenesis. First, we examined the enzymatic activity of the Fe-S protein dihydropyrimidine dehydrogenase [DPYD (34)] by following the conversion of [4- $^{14}\text{C}$ ]thymine into [4- $^{14}\text{C}$ ]dihydrothymine by thin-layer chromatography and autoradiography (Fig. 3B and fig. S8, A to C). In contrast to IRP1 and GPAT, DPYD activity was severely impaired upon MMS19 depletion. This decrease was also observed upon depletion of the ISC proteins

Nfs1 and frataxin and the CIA component Nbp35, consistent with this effect being a Fe-S cluster assembly defect. Although DPYD protein levels were also depleted (Fig. 3C and fig. S8, D and E), the respective decreases were less pronounced relative to enzyme activities. The lower DPYD levels were likely indirect effects of apoprotein degradation. Next, we measured the amounts of the POLD1 subunit of DNA polymerase  $\delta$ , the homolog of yeast Fe-S protein Pol3 (10). Because impaired Fe-S protein assembly frequently results in apoprotein degradation (Fig. 3C) (16), Fe-S protein levels can be used to estimate their biogenesis. POLD1 levels were strongly decreased in MMS19-depleted cells (Fig. 3D and fig. S9). Similar effects were observed during RNAi-mediated depletion of Nfs1, frataxin, and Nbp35. Because CIA depletion should not affect mitochondrial Fe-S proteins (fig. S3) (16, 21), we measured the levels and activities of mitochondrial aconitase (mtAco) and succinate dehydrogenase (SDH). They remained unchanged upon

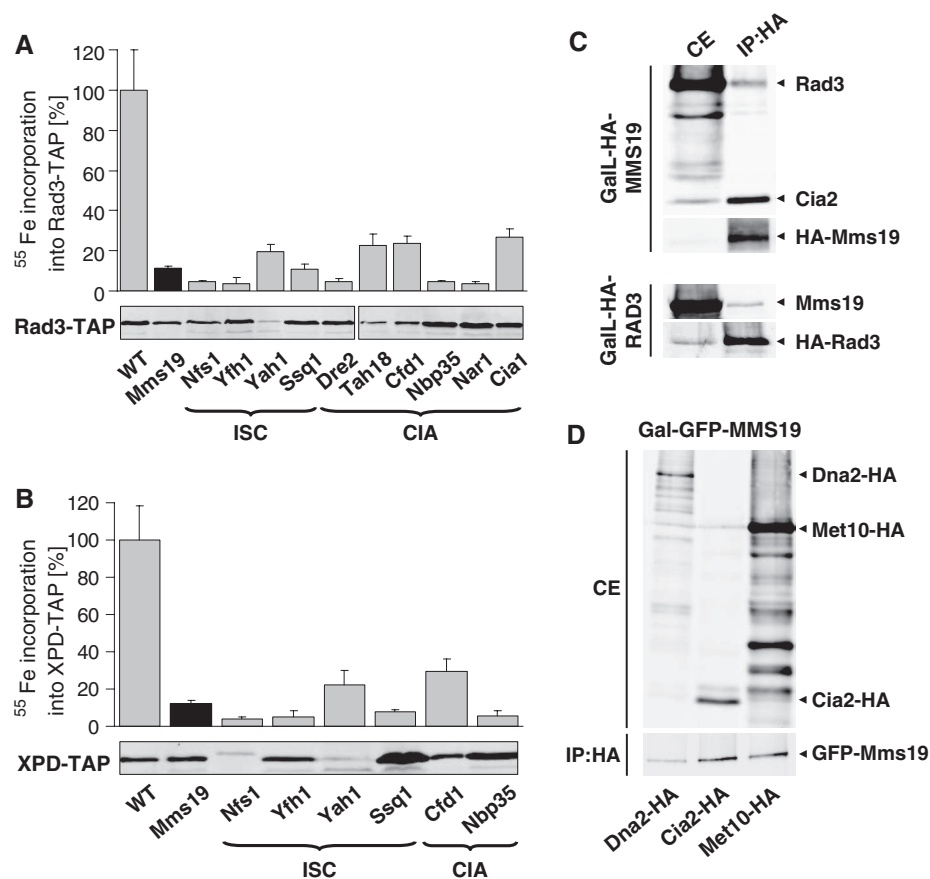


**Fig. 2. Yeast Mms19 interacts with and assembles Fe-S clusters into DNA helicases.** (A and B)  $^{55}\text{Fe}$  incorporation into plasmid-encoded Rad3-TAP (A) and human XPD-TAP (B) was measured in yeast strains deficient in the indicated ISC and CIA proteins. The TAP-tagged proteins were visualized by immunostaining. Values are means  $\pm$  SD. For all depletions,  $P < 0.001$ . (C) MMS19 binds to Rad3 and Cia2. Extracts from overnight cultures of GalL-HA-MMS19 (top) and GalL-HA-RAD3 cells (bottom) grown in SC galactose medium were used for immunoprecipitation with anti-HA beads. Cell extracts (CE) and immunoprecipitates (IP:HA) were immunostained for the indicated proteins. (D) Interaction of Mms19 with target Fe-S proteins. Extracts of Gal-GFP-MMS19 cells producing C-terminally HA-tagged Dna2, Cia2, or Met10 were used for immunoprecipitation with anti-HA beads. Bound proteins were analyzed by immunostaining (anti-HA, top; anti-GFP, bottom).



MMS19 depletion (fig. S10). Collectively, these results suggest that MMS19 is required for Fe-S cluster assembly of DPYD and POLD1 and may act as a specialized CIA factor with specificity for a subset of cytosolic-nuclear Fe-S proteins.

**Human MMS19 is part of the CIA targeting complex.** To define those Fe-S proteins that require MMS19 function, we used a proteomic approach to identify MMS19 interaction partners. MMS19-associated protein complexes were affinity-purified from a human embryonic kidney (HEK) 293 cell line stably expressing hemagglutinin- and FLAG-tagged MMS19 (HA-FLAG-MMS19) and were then analyzed using multidimensional protein identification technology [MudPIT (35)]. We identified a wide range of putative MMS19-interacting proteins including known and putative Fe-S proteins and the characterized and putative CIA components CIAO1, IOP1, and FAM96B (table S4). For some of these proteins, the MMS19 interaction was confirmed by coimmunoprecipitation of HA-

FLAG-MMS19 from stable HEK293 cells followed by immunoblotting with specific antibodies. Endogenous CIAO1, FAM96B, IOP1, FANCI, XPD, RTEL1, and POLD1 copurified only in extracts containing HA-FLAG-MMS19 (Fig. 3E). The interaction between XPD and MMS19 was confirmed for endogenous levels (fig. S11). These data validate the proteomic data and show that MMS19 associates with both CIA factors and Fe-S target proteins, including many involved in DNA metabolism.

The strong interactions of MMS19, CIAO1, and FAM96B, as assessed by normalized spectral abundance factors (table S4) and coimmunoprecipitation studies (Fig. 3E), indicate that these three proteins likely form a complex that we term the CIA targeting complex. The results for human MMS19 agree with our yeast data and suggest that this complex acts late in Fe-S protein biogenesis to facilitate Fe-S cluster transfer from the CIA scaffold complex Cfd1-Nbp35 to Fe-S target proteins.

**Fe-S protein assembly defects augment sensitivity of cells to DNA damage.** The association of MMS19 with multiple DNA replication and repair proteins led us to examine whether the integrity of Fe-S protein biogenesis might be a general requirement for efficient cellular DNA damage repair. We first tested this idea in yeast and assessed whether depleting ISC or CIA components elicited effects on the DNA damage response pathway. Rad53 phosphorylation was observed in strains defective in Fe-S protein assembly after exposure to low levels of MMS (36). These MMS levels were not sufficient to trigger Rad53 phosphorylation in wild-type yeast, which suggests that the former strains accumulated higher levels of DNA damage (Fig. 4A). We then analyzed the effects of Fe-S protein deficiencies on the expression of *RNR3* and *HUG1*, two genes transcriptionally induced in response to DNA damage (37). Reporter plasmids in which the *RNR3* and *HUG1* promoters controlled luciferase expression were introduced into different regulatable

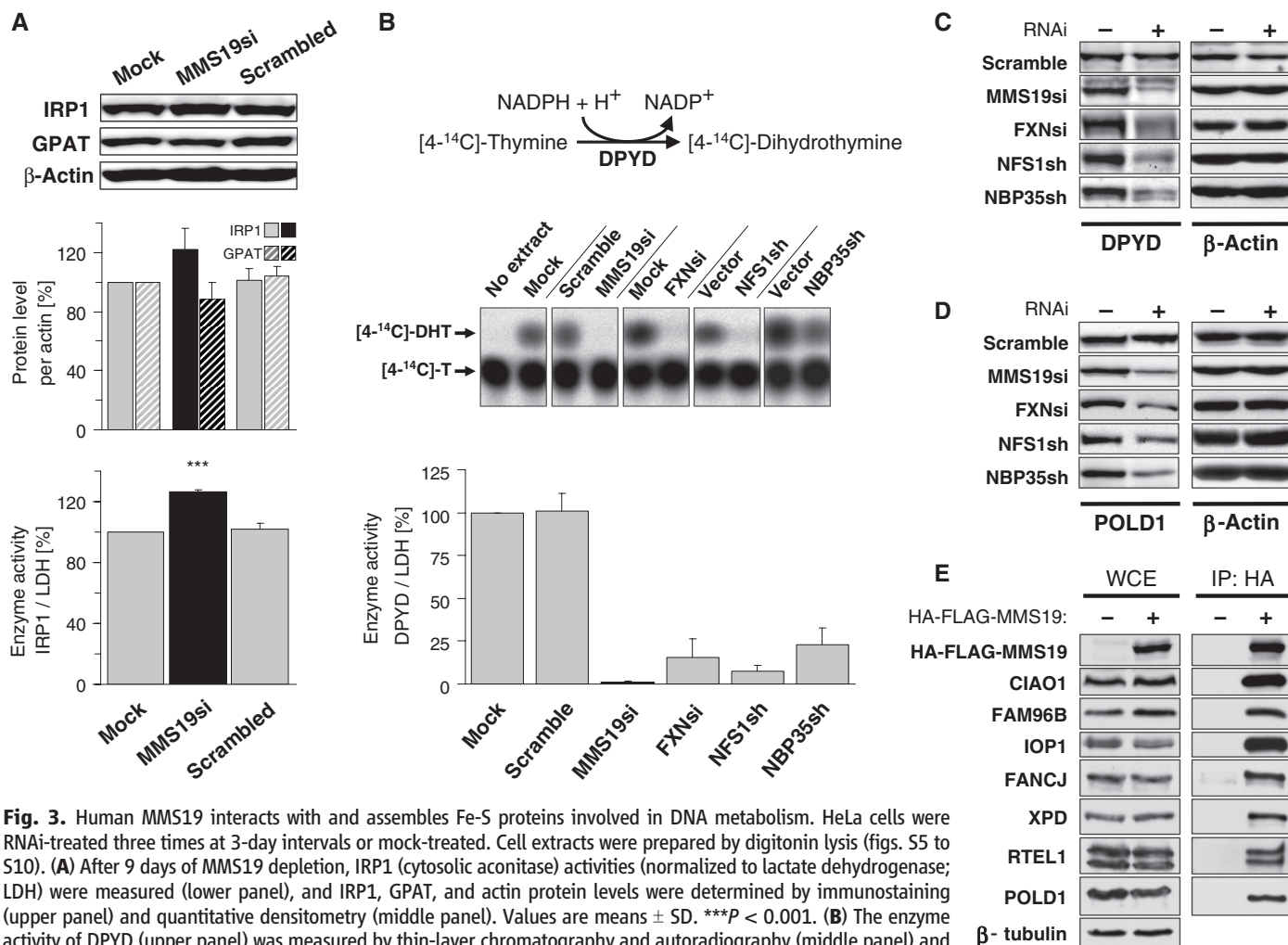


**Fig. 3.** Human MMS19 interacts with and assembles Fe-S proteins involved in DNA metabolism. HeLa cells were RNAi-treated three times at 3-day intervals or mock-treated. Cell extracts were prepared by digitonin lysis (figs. S5 to S10). **(A)** After 9 days of MMS19 depletion, IRP1 (cytosolic aconitase) activities (normalized to lactate dehydrogenase; LDH) were measured (lower panel), and IRP1, GPAT, and actin protein levels were determined by immunostaining (upper panel) and quantitative densitometry (middle panel). Values are means  $\pm$  SD. \*\*\* $P$  < 0.001. **(B)** The enzyme activity of DPYD (upper panel) was measured by thin-layer chromatography and autoradiography (middle panel) and quantitated by phosphorimaging (lower panel). As controls, HeLa cells were RNAi-depleted for frataxin (FXN), NFS1, and NBP35. Values are means  $\pm$  SD. For all depletions,  $P$  < 0.001. **(C and D)** Levels of DPYD (C) and POLD1 (D) protein were measured by immunostaining in cell extracts depleted for the indicated proteins. **(E)** Interaction of human MMS19 with Fe-S proteins and CIA components. Flp-In-TREx-293 cells lacking or stably expressing inducible 3xHA-3xFLAG-MMS19 were induced with doxycycline (500 ng/ml) overnight. Whole-cell extracts (WCE) were subjected to anti-HA immunoprecipitation (IP:HA) followed by immunostaining for the indicated proteins.

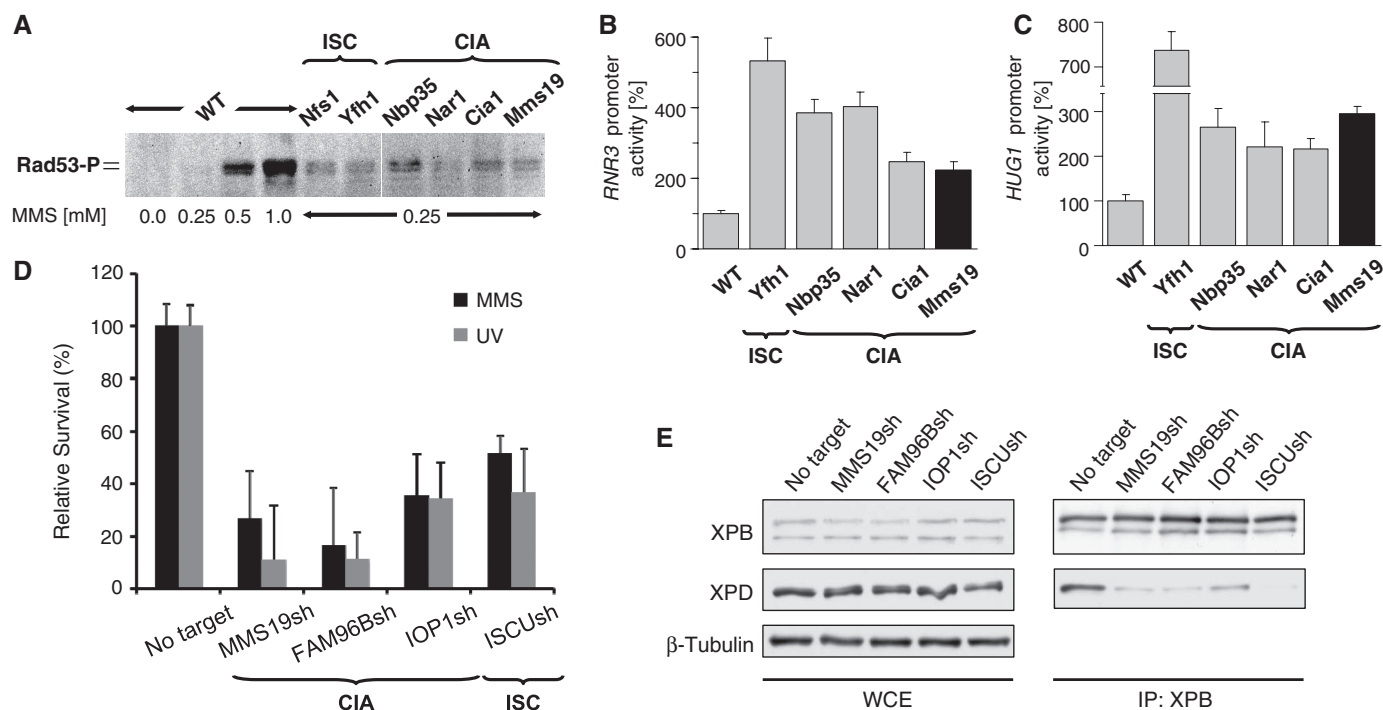


**Fig. 4.** Defects in Fe-S protein assembly show increased DNA damage sensitivity. **(A)** Activation of Mec1-dependent DNA damage pathway in yeast. Wild-type yeast (WT) and strains deficient in the indicated proteins were treated with the indicated concentrations of MMS. Extracts were immunostained for phospho-Rad53 (Rad53-P). **(B and C)** Induction of DNA damage-inducible *RNR3* or *HUG1*. Yeast strains depleted for the indicated proteins were transformed with plasmids encoding *RNR3* or *HUG1* promoter-regulated luciferase and were exposed to 0.25 mM MMS. Values are means  $\pm$  SD. For all depletions,  $P < 0.01$ . **(D)** Depletion of the indicated proteins by shRNAs in

HEK293 cells results in increased sensitivity to UV- and MMS-induced DNA damage. Stable knockdown cell lines were treated with UV (20 J/m<sup>2</sup>) or 20  $\mu$ M MMS. Cell viability relative to the corresponding untreated cell line (No target) was measured using the MTS cell proliferation assay (Promega) 7 days after treatment. Values are means  $\pm$  SEM ( $n = 3$ ); for all depletions,  $P < 0.05$ . **(E)** Fe-S protein biogenesis is required for incorporation of XPD into TFIIH. HEK293 cell extracts (WCE) from (D) were used for immunoprecipitation with XBP antibodies (IP:XBP) followed by immunoblotting for the indicated proteins.

ISC and CIA strains. A factor of 2 to 6 increase in luciferase activity was detected in ISC- and CIA-depleted strains relative to wild-type cells (Fig. 4, B and C). These results indicate that inactivation of Mms19 or other Fe-S protein assembly components leads to up-regulation of the DNA damage response. We finally tested whether the requirement of intact Fe-S protein assembly for DNA damage repair was conserved in humans. HEK293 cell lines expressing short hairpin RNA (shRNA) constructs for silencing MMS19, FAM96B, the CIA protein IOP1, or the mitochondrial scaffold protein ISCU were generated (fig. S12). Depletion of ISC or CIA factors severely diminished the survival of HEK293 cells after ultraviolet (UV) irradiation or MMS treatment (Fig. 4D). Together, these data suggest that the previously observed DNA repair and metabolism defects of MMS19-defective cells may be the consequence of impaired Fe-S protein biogenesis and may not be related to a dedicated function of MMS19 in DNA maintenance (24, 25).

The increased DNA damage sensitivity in cells with impaired Fe-S protein biogenesis may include the loss of nucleotide excision repair because maturation of XPD is defective. The requirement of the Fe-S cluster of XPD for its DNA helicase activity in vitro (7) led us to investigate whether inactive apo-XPD is integrated into the

transcription factor complex TFIIH in ISC- or CIA-depleted cells. XPD could be detected in TFIIH immunoprecipitated with endogenous XBP from control cells but not from cells depleted of MMS19, FAM96B, IOP1, or ISCU; these findings suggest that the inability to assemble Fe-S clusters on XPD prevented its incorporation into the TFIIH complex (Fig. 4E). The inability of cells impaired in Fe-S protein biogenesis to form functional TFIIH complexes may provide, at least in part, the mechanistic basis for the increased sensitivity of MMS19 mutants to UV- and MMS-induced DNA damage. Other Fe-S cluster-containing substrates of the CIA targeting complex, such as DNA2, FANCI, and RTEL1, play key roles in maintaining genome stability and the response to other types of DNA damage [i.e., DNA double-strand breaks and DNA interstrand cross-links (3)]. Hence, impairment of Fe-S protein biogenesis (e.g., by mutations in ISC and CIA proteins) may lead to the simultaneous inactivation of multiple DNA repair pathways and thereby promote genomic instability.

Our study clarifies the functional role of MMS19 in DNA maintenance and provides insights into the mechanism of cytosolic Fe-S protein biogenesis (11, 13). MMS19 exerts its function as part of a CIA targeting complex involved in the maturation of a subset of Fe-S proteins, in-

cluding those with functions in DNA replication, DNA repair, and telomere stability (fig. S13). By undergoing direct interaction with target Fe-S proteins, MMS19 (and its putative functional partners CIAO1 and FAM96B) may serve an adapter function between Fe-S cluster synthesis and insertion into apoproteins. This conserved function of MMS19 can explain possibly all of the previously described phenotypes associated with MMS19 defects. Mitochondria perform an essential role in cellular Fe-S protein biogenesis and, as shown here, in nuclear DNA metabolism. These functions, and not adenosine triphosphate production, may explain the maintenance of these endosymbiotic organelles even in anaerobic eukaryotes (38). Moreover, the crucial role of mitochondria in DNA metabolism and genome maintenance may be relevant to neurodegenerative phenotypes associated with mitochondrial diseases, including Friedreich's ataxia.

#### References and Notes

1. M. A. McMurray, D. E. Gottschling, *Curr. Opin. Microbiol.* **7**, 673 (2004).
2. J. H. Hoeijmakers, *N. Engl. J. Med.* **361**, 1475 (2009).
3. A. Ciccia, S. J. Elledge, *Mol. Cell* **40**, 179 (2010).
4. J. R. Veatch, M. A. McMurray, Z. W. Nelson, D. E. Gottschling, *Cell* **137**, 1247 (2009).
5. G. Karthikeyan, L. K. Lewis, M. A. Resnick, *Hum. Mol. Genet.* **11**, 1351 (2002).



6. R. Thierbach *et al.*, *Biochem. J.* **432**, 165 (2010).
7. J. Rudolf, V. Makrantonis, W. J. Ingledew, M. J. Stark, M. F. White, *Mol. Cell* **23**, 801 (2006).
8. S. Klinge, J. Hirst, J. D. Maman, T. Krude, L. Pellegrini, *Nat. Struct. Mol. Biol.* **14**, 875 (2007).
9. J. T. Yeeles, R. Cammack, M. S. Dillingham, *J. Biol. Chem.* **284**, 7746 (2009).
10. D. J. Netz *et al.*, *Nat. Chem. Biol.* **8**, 125 (2012).
11. A. Sheftel, O. Stehling, R. Lill, *Trends Endocrinol. Metab.* **21**, 302 (2010).
12. M. F. White, M. S. Dillingham, *Curr. Opin. Struct. Biol.* **22**, 94 (2012).
13. R. Lill, *Nature* **460**, 831 (2009).
14. H. Ye, T. A. Rouault, *Biochemistry* **49**, 4945 (2010).
15. A. Roy, N. Solodovnikova, T. Nicholson, W. Antholine, W. E. Walden, *EMBO J.* **22**, 4826 (2003).
16. O. Stehling *et al.*, *Mol. Cell. Biol.* **28**, 5517 (2008).
17. U. Mühlenhoff *et al.*, *Cell Metab.* **12**, 373 (2010).
18. D. J. Netz *et al.*, *Nat. Chem. Biol.* **6**, 758 (2010).
19. J. Balk, D. J. Aguilar Netz, K. Tepper, A. J. Pierik, R. Lill, *Mol. Cell. Biol.* **25**, 10833 (2005).
20. J. Balk, A. J. Pierik, D. J. Netz, U. Mühlenhoff, R. Lill, *EMBO J.* **23**, 2105 (2004).
21. D. Song, F. S. Lee, *J. Biol. Chem.* **283**, 9231 (2008).
22. L. Prakash, S. Prakash, *MGG* **176**, 351 (1979).
23. S. H. Askree *et al.*, *Proc. Natl. Acad. Sci. U.S.A.* **101**, 8658 (2004).
24. S. Ito *et al.*, *Mol. Cell* **39**, 632 (2010).
25. H. Kou, Y. Zhou, R. M. Gorospe, Z. Wang, *Proc. Natl. Acad. Sci. U.S.A.* **105**, 15714 (2008).
26. A. C. Gavin *et al.*, *Nature* **440**, 631 (2006).
27. S. Ben-Aroya *et al.*, *Mol. Cell* **30**, 248 (2008).
28. E. Weerapana *et al.*, *Nature* **468**, 790 (2010).
29. See supplementary materials on Science Online.
30. A. J. Pierik, D. J. A. Netz, R. Lill, *Nat. Protoc.* **4**, 753 (2009).
31. F. Li, R. Martienssen, W. Z. Cande, *Nature* **475**, 244 (2011).
32. T. Seroz *et al.*, *Nucleic Acids Res.* **28**, 4506 (2000).
33. O. Stehling *et al.*, *Methods Mol. Biol.* **372**, 325 (2007).
34. K. D. Schnackerz, D. Dobritzsch, Y. Lindqvist, P. F. Cook, *Biochim. Biophys. Acta* **1701**, 61 (2004).
35. A. A. Vashisht *et al.*, *Science* **326**, 718 (2009).
36. A. Pelliccioli *et al.*, *EMBO J.* **18**, 6561 (1999).
37. M. G. Benton, N. R. Glasser, S. P. Palecek, *Mutat. Res.* **633**, 21 (2007).
38. A. V. Goldberg *et al.*, *Nature* **452**, 624 (2008).

**Acknowledgments:** We thank D. R. Dean and D. E. Gottschling for fruitful discussions, and C. Doré, S. A. Freibert, M. Funke, G. Köpf, B. Niggemeyer, R. Rösser, M. Stümpfig, and H. Webert for experimental help. Supported by Deutsche Forschungsgemeinschaft grants (SFB 593), Gottfried-Wilhelm Leibniz program and GRK 1216, von Behring-Röntgen Stiftung, Max-Planck Gesellschaft, Feldberg Foundation, Fonds der chemischen Industrie (all to R.L.), Rhön Klinikum AG (A.J.P. and R.L.), NIH grant GM089778 (J.A.W.), the University of California Cancer Research Coordinating Committee (J.A.W.), and the Jonsson Cancer Center at UCLA (J.A.W.).

#### Supplementary Materials

www.sciencemag.org/cgi/content/full/science.1219723/DC1  
Materials and Methods  
Figs. S1 to S13  
Tables S1 to S4  
References (39–64)

27 January 2012; accepted 14 May 2012  
Published online 7 June 2012;  
10.1126/science.1219723

# An Overlapping Protein-Coding Region in Influenza A Virus Segment 3 Modulates the Host Response

B. W. Jagger,<sup>1,2</sup> H. M. Wise,<sup>1\*</sup> J. C. Kash,<sup>2</sup> K.-A. Walters,<sup>3</sup> N. M. Wills,<sup>4</sup> Y.-L. Xiao,<sup>2</sup> R. L. Dunfee,<sup>2</sup> L. M. Schwartzman,<sup>2</sup> A. Ozinsky,<sup>3</sup> G. L. Bell,<sup>1†</sup> R. M. Dalton,<sup>1‡</sup> A. Lo,<sup>1</sup> S. Efstathiou,<sup>1</sup> J. F. Atkins,<sup>4,5</sup> A. E. Firth,<sup>1§</sup> J. K. Taubenberger,<sup>2§</sup> P. Digard<sup>1\*§</sup>

Influenza A virus (IAV) infection leads to variable and imperfectly understood pathogenicity. We report that segment 3 of the virus contains a second open reading frame (“X-ORF”), accessed via ribosomal frameshifting. The frameshift product, termed PA-X, comprises the endonuclease domain of the viral PA protein with a C-terminal domain encoded by the X-ORF and functions to repress cellular gene expression. PA-X also modulates IAV virulence in a mouse infection model, acting to decrease pathogenicity. Loss of PA-X expression leads to changes in the kinetics of the global host response, which notably includes increases in inflammatory, apoptotic, and T lymphocyte–signaling pathways. Thus, we have identified a previously unknown IAV protein that modulates the host response to infection, a finding with important implications for understanding IAV pathogenesis.

**I**nfluenza A virus (IAV) is a single-stranded, segmented, negative-sense RNA virus of the Orthomyxoviridae family (1). Its ecology is complex, encompassing diverse host species,

such as both wild and domesticated birds and several mammalian species, including humans, dogs, horses, and pigs. IAV virulence varies widely, depending on virus and host and ranging from completely asymptomatic to nearly 100% lethal. IAV pandemics over the past 100 years have shown case fatality rates varying from ~2% (1918 H1N1) to around 0.05% (2009 H1N1). Although some aspects of this variability can be explained, IAV pathogenesis remains imperfectly understood and difficult to predict (2).

IAV genome segment 3 produces a single, unspliced mRNA that encodes a subunit of the viral RNA-dependent RNA polymerase complex (PA). PA provides an RNA-endonuclease activity—contained in an N-terminal domain—that cleaves capped RNA fragments from cellular pre-mRNAs to provide primers for viral transcription (3–5). Ectopic expression of PA from plasmid has been shown to inhibit the accumulation of other coexpressed proteins, a phenomenon proposed to result from proteo-

lytic activity, either nonspecific (6) or possibly resulting from degradation of RNA polymerase II (7, 8). A genome-wide survey of IAV synonymous codon usage aimed at identifying RNA packaging signals discovered a highly conserved internal region in segment 3 that did not correlate with any known or predicted RNA structural or functional motifs (9, 10). Here, we present evidence that the reduced synonymous variation in this region reflects a hitherto unrecognized overlapping open reading frame (termed here “X-ORF”) that is accessed by ribosomal frameshifting to produce a distinct PA-related polypeptide with a role in host-cell shutoff, modulation of host gene expression, and, consequently, limitation of viral pathogenesis.

To further investigate the unexplained region of conservation in IAV segment 3, we measured synonymous site conservation in an alignment of >1000 representative segment 3 sequences. The observed number of synonymous substitutions in a nine-codon sliding window was compared with the number expected under a null model of neutral evolution at synonymous sites (11). This analysis confirmed the presence of the 5′- and 3′-terminal conserved regions involved in genome packaging (10), as well as an additional region of prominent synonymous site conservation between PA codons 190 and 253 (Fig. 1A). Furthermore, there was a notable absence of stop codons in the +1, but not the +2, reading frame within this region (Fig. 1B), suggestive of an overlapping ORF (X). As noted previously (10), there are no conserved AUG codons that could initiate independent translation of this ORF, nor could we identify any conserved splice donor-acceptor combinations that might allow access to it. However, a highly conserved UCC UUU CGU C motif was identified near the 5′ end of the X-ORF (table S1), despite the fact that both Ser (UCC) and Arg (CGU), in principle, could each be encoded by any of five other codons.

We hypothesized that +1 ribosomal frameshifting on this motif could lead to expression of

<sup>1</sup>Division of Virology, Department of Pathology, University of Cambridge, Cambridge CB2 1QP, UK. <sup>2</sup>Viral Pathogenesis and Evolution Section, Laboratory of Infectious Diseases, National Institute of Allergy and Infectious Diseases, National Institutes of Health, Bethesda, MD 20892, USA. <sup>3</sup>Institute for Systems Biology, Seattle, WA 98109, USA. <sup>4</sup>Department of Human Genetics, University of Utah, Salt Lake City, UT 84112, USA. <sup>5</sup>BioSciences Institute, University College Cork, Cork, Ireland.

\*Present address: The Roslin Institute, University of Edinburgh, Easter Bush, Midlothian EH25 9RG, Scotland, UK.

†Present address: Cambridge Institute for Medical Research, Wellcome Trust–Medical Research Council Building, Addenbrooke’s Hospital, Hills Road, Cambridge CB2 0XY, UK.

‡Present address: Department of Molecular and Cellular Biology, Centro Nacional de Biotecnología, Consejo Superior de Investigaciones Científicas (Spanish National Research Council, CSIC), Cantoblanco, 28049 Madrid, Spain.

§To whom correspondence should be sent. E-mail: aef24@cam.ac.uk (A.E.F.); taubenbergerj@niaid.nih.gov (J.K.T.); paul.digard@roslin.ed.ac.uk (P.D.).

X as a fusion with the N-terminal domain of PA ( $PA_N$ ). Frameshifting in the +1 direction can be stimulated by a slow-to-decode codon in the ribosomal A-site, which results in a pause in decoding that may allow a proportion of ribosomes to shift reading frame (12). Frameshifting efficiency depends on the relative speed with which the 0 frame and +1 frame A-site codons can be decoded, the potential for P-site codon:anticodon re-pairing in the +1 reading frame, and the relative stability of the P-site codon:anticodon duplex in the two alternative reading frames, as well as other poorly defined factors that may involve the E-site codon. Thus, +1 slippage might occur when UUU is positioned in the ribosomal P-site with the rare codon CGU in the A-site. CGU is one of the most seldom used codons in both mammalian and avian genomes. Both UUU and UUC are translated by a single transfer RNA  $tRNA^{Phe}$  isoacceptor whose anticodon, GAA, has a higher affinity for UUC than for UUU, which favors P-site re-pairing to UUC in the +1 frame (13). Such a frameshift (FS) event would produce a 29-kD fusion protein, termed PA-X, comprising the

N-terminal endonuclease domain of PA (4, 5) and, in most isolates, a novel 61-amino acid C terminus from the X-ORF (Fig. 1C). In a minority of isolates, largely of the 2009 pandemic H1N1 lineage, a shorter 41-amino acid X domain is predicted.

The frameshifting hypothesis was tested by cloning the putative FS site and flanking sequences from influenza A/Puerto Rico/8/1934 (H1N1) (PR8) segment 3 between *Renilla* and firefly luciferase ORFs such that a +1 FS event would give rise to a fusion product of the two reporter polypeptides (14). These constructs were in vitro translated in rabbit reticulocyte lysates, which demonstrated frameshifting at an efficiency of ~1.3% in a wild-type (WT) construct, whereas mutation of the FS motif from UUU CGU to UUC AGA reduced frameshifting to ~0.2% (Fig. 1D). Further mutagenesis of the region supported the proposed mechanism of frameshifting stimulated by a combination of the rare (A-site) codon CGU, the (E-site) codon UCC, and possibly more distal elements in the 5' flanking sequence (fig. S1).

To test if frameshifting occurred in the context of full-length IAV segment 3, we in vitro trans-

lated plasmids containing WT and mutant A/Brevig Mission/1/1918 (1918) segment 3. The WT segment produced full-length PA and several smaller polypeptide species, including a ~29-kD product (Fig. 1E, lane 2). The last-named species co-migrated with the polypeptide produced from a plasmid in which cytosine 598 (the base predicted to be “skipped” during the FS event; see Fig. 1C and fig. S2 for details on the 1918 mutations used) had been deleted to put the X-ORF in frame with the  $PA_N$  coding region (delC) (Fig. 1E, lane 4). This band was much reduced when the FS site was mutated (lane 3), whereas a faster-migrating species was seen when a premature termination codon (PTC) was introduced into the X-ORF (Fig. 1E, lane 5). Next, we raised an antiserum against an X-derived peptide and subjected selected in vitro translation products to immunoprecipitation. Both the delC product and the corresponding species from WT 1918 translation reactions were precipitated by the antiserum against X (anti-X), but not preimmune antisera (Fig. 1E and fig. S3, A to C). However, no anti-X-specific product was precipitated from

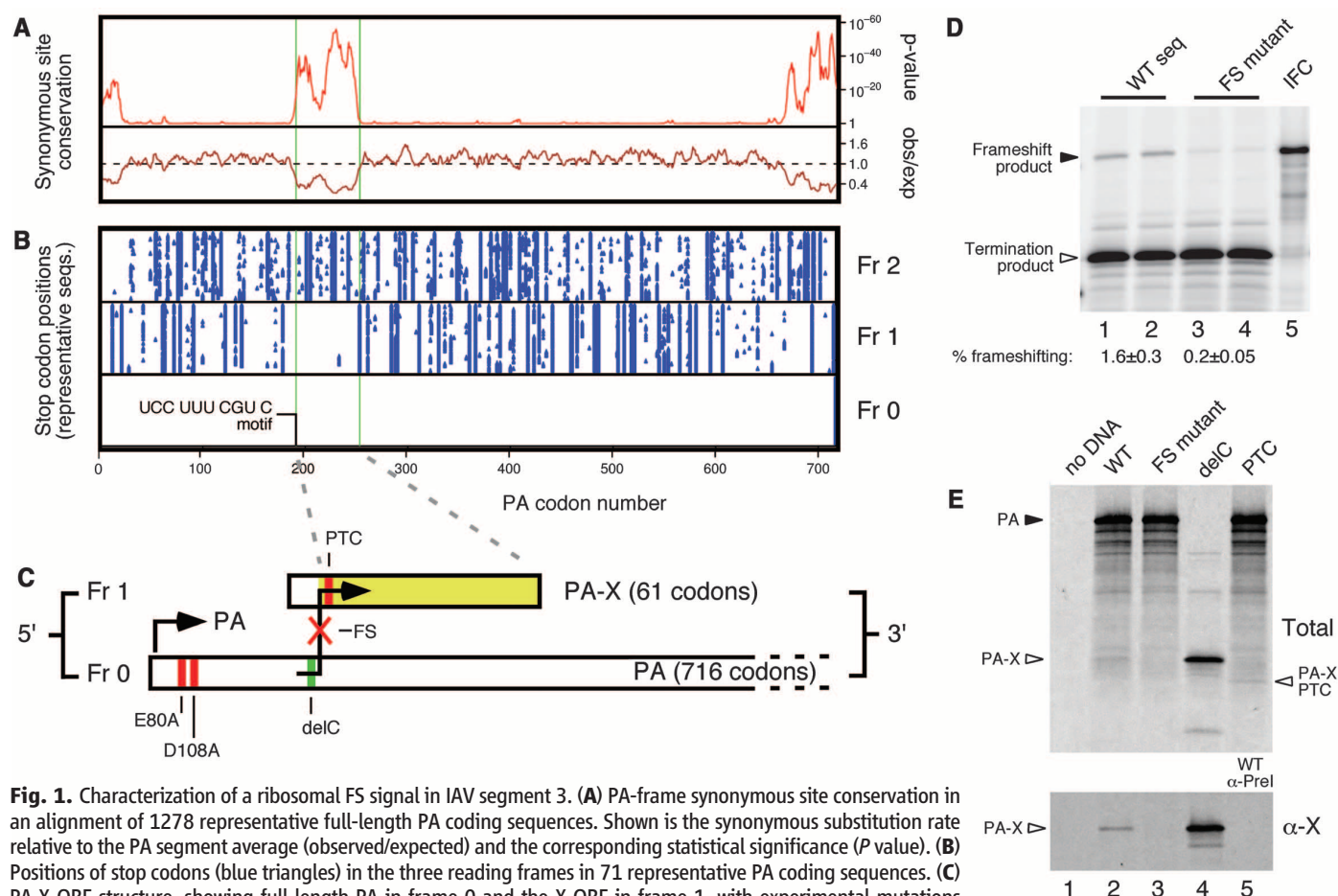


**Fig. 1.** Characterization of a ribosomal FS signal in IAV segment 3. **(A)** PA-frame synonymous site conservation in an alignment of 1278 representative full-length PA coding sequences. Shown is the synonymous substitution rate relative to the PA segment average (observed/expected) and the corresponding statistical significance ( $P$  value). **(B)** Positions of stop codons (blue triangles) in the three reading frames in 71 representative PA coding sequences. **(C)** PA-X ORF structure, showing full-length PA in frame 0 and the X-ORF in frame 1, with experimental mutations indicated. **(D)** and **(E)** Detection of frameshifting in rabbit reticulocyte lysate by SDS–polyacrylamide gel electrophoresis (SDS–PAGE) and autoradiography of in vitro translated (IVT) reactions. **(D)** Dual reporter constructs separated by the putative ribosomal frameshifting signal from PR8 segment 3 along with 100-nucleotide 5′- and 3′-flanking sequences. WT, wild-type sequence; FS mutant, shift site UUU CGU mutated to UUC AGA; IFC, in-frame control. The calculated frameshifting efficiencies (means  $\pm$  SEM,  $n = 4$ ) are shown. **(E)** IVT reactions were programmed with full-length segment 3 constructs from the 1918 virus and analyzed before (total) or after ( $\alpha$ -X) immunoprecipitation with rabbit 1918 X antiserum. Lane 5 of the bottom panel shows a WT IVT immunoprecipitated with a preimmune bleed. Polypeptides of interest are indicated.



the FS mutant samples. We also detected X-ORF expression in plasmid transfected cells that again was dependent on an intact FS site and was sensitive to the introduction of a premature X-ORF stop codon (fig. S3, D and E). Thus, the X-ORF is accessed by ribosomal frameshifting.

Next, we considered the potential function of the PA-X polypeptide. Because it incorporates the PA endonuclease domain, but not the PA C-terminal domain that interacts with the PB1 subunit of the viral polymerase, we hypothesized that it might act independently of the polymerase as an mRNA endonuclease. By analogy to the herpes simplex virus vhs protein (15), PA-X might therefore have a role in host-cell shutoff, a phenomenon seen in many virus infections in which cellular gene expression is inhibited to hinder the induction of an antiviral response, as well as to divert ribosomes toward translation of viral mRNAs (16). To test this, we used plasmids encoding  $\beta$ -galactosidase ( $\beta$ -gal) or the PR8 nucleoprotein (NP) as reporters in cotransfection assays with WT or mutant forms of 1918 segment 3. The WT 1918 segment 3 potently repressed

$\beta$ -gal expression (Fig. 2A), consistent with previous observations (6). However, this activity was abolished by the FS mutation and weakened by the insertion of a PTC in X; both of these alterations are silent in the PA gene (fig. S2). Furthermore, the delC construct, which expresses PA-X but not PA, exhibited strong repressive activity (Fig. 2A). The same pattern of repression by the delC construct or WT segment 3 was seen when NP was used as the reporter, and again, the activity was abolished by the FS mutation (Fig. 2, B and C). The inhibitory activity of segment 3 was originally proposed to result from protease activity (6), whereas our hypothesis predicted an effect on RNA, mediated by the endonuclease activity. To test this, we introduced mutations known to abolish PA endonuclease activity in which alanine replaces aspartic acid at position 108 and glutamic acid at position 80 (D108A and E80A, respectively) (4). These mutations eliminated the repressive activity on protein expression, whether in the background of otherwise WT segment 3 or in the delC construct (Fig. 2, A to C). Furthermore, as predicted by the messenger RNA

endonuclease (mRNase) hypothesis, examination of NP reporter gene mRNA levels showed that WT segment 3 and the delC construct reduced mRNA accumulation severalfold compared with FS-mutant, endonuclease-mutant, and control cotransfections, in a manner that correlated with reporter protein abundance (Fig. 2, C and D). Overall, these data indicate that the ability of segment 3 to inhibit plasmid-mediated gene expression is a property mediated by PA-X, not PA, and support the hypothesis that repression results from an mRNA endonuclease activity.

We next sought to determine whether PA-X is expressed during viral infection and what consequence this has for virus replication. Accordingly, we generated sets of viruses based around the 1918 segment 3, with or without mutations affecting PA-X expression: either the fully reconstructed 1918 virus, or reassortants between PR8 and 1918, where either all 1918 ribonucleoprotein genes (segments 1 to 3 and 5; 1918 RNP) or only 1918 segment 3 (1918 PA) were introduced. To test if PA-X could be detected during infection, radiolabeled cell lysates were prepared from cells infected with parental or FS mutant viruses containing the 1918 segment 3 and immunoprecipitated with anti-X or preimmune sera. A polypeptide of the expected molecular weight (migrating above a prominent M1/NS1 background band) was precipitated by anti-X but not by the preimmune bleed from cells infected with parental but not FS mutant viruses (Fig. 3A), which confirmed expression of PA-X during virus infection. Western blot analysis showed that the synonymous FS site mutation did not affect PA accumulation in infected cells (Fig. 3B).

To test the effect of the loss of PA-X expression on virus growth, end-point titers of low-multiplicity infections of Madin-Darby canine kidney (MDCK) cells or embryonated chicken eggs were determined. FS mutant viruses propagated efficiently in either system, and although the 1918 RNP-FS virus grew in MDCKs to titers  $\sim 1/10$ th of those seen in WT virus and somewhat lower titers in eggs (Fig. 3C), the differences were not statistically significant. In addition, no differences were seen when single- or multicycle growth kinetics of the 1918 viruses was tested in MDCK cells (fig. S4, A and B). Next, we tested whether altering PA-X expression had an effect on host-cell shutoff. Cells were infected with WT, FS, or PTC 1918 RNP viruses, and protein synthesis was monitored across a time course of infection by metabolic labeling. All infections produced abundant quantities of virus polypeptides from 4 hours after infection, with the expected pattern of delayed late gene M1 and hemagglutinin (HA) expression (Fig. 3D). In the case of the WT virus, this was accompanied by reduced background cellular protein synthesis from 4 to 6 hours onward. Host-cell shutoff, however, was highly attenuated in cells infected with the FS mutant virus and delayed in cells infected with the PTC virus. Densitometric quantification of actin synthesis (the most prominent cellular polypeptide in these experiments)

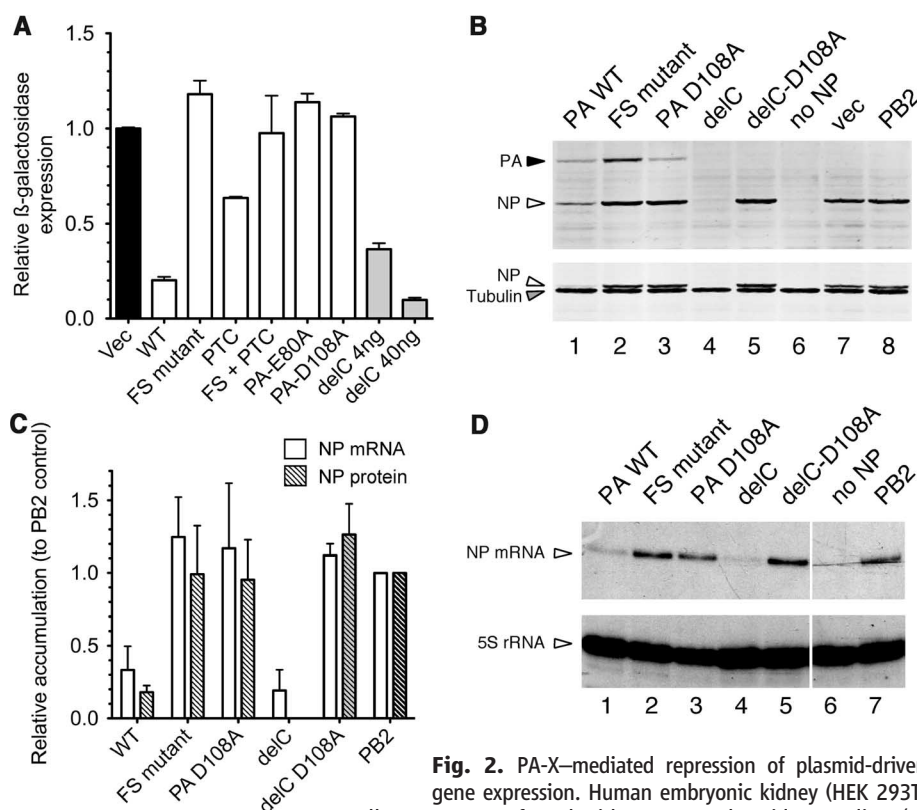


**Fig. 2.** PA-X-mediated repression of plasmid-driven gene expression. Human embryonic kidney (HEK 293T) cells were cotransfected with reporter plasmids encoding (A)  $\beta$ -galactosidase or (B to D) IAV NP, as well as the indicated "effector" plasmids (400 ng unless indicated otherwise). (A)  $\beta$ -Galactosidase accumulation was measured by enzymatic assay. Values plotted are the means  $\pm$  SEM of three experiments normalized to the level seen with an empty plasmid vector as effector. (B) NP, PA, and tubulin (as a loading control) accumulation was measured by Western blot and (C) quantified from replicate experiments using LiCor Odyssey software. Note in (B) that the same membrane was reprobbed for tubulin; residual NP staining is apparent as a doublet running just above tubulin. (D) NP mRNA and 5S rRNA (as a loading control) were measured by urea-PAGE and autoradiography of radioactive primer extension assays. (C) NP mRNA accumulation from (D) was quantified by densitometry. Values plotted in (C) are the means  $\pm$  range of two independent experiments, normalized to the control where the PB2 subunit of the viral polymerase was cotransfected in place of PA.

factor" plasmids (400 ng unless indicated otherwise). (A)  $\beta$ -Galactosidase accumulation was measured by enzymatic assay. Values plotted are the means  $\pm$  SEM of three experiments normalized to the level seen with an empty plasmid vector as effector. (B) NP, PA, and tubulin (as a loading control) accumulation was measured by Western blot and (C) quantified from replicate experiments using LiCor Odyssey software. Note in (B) that the same membrane was reprobbed for tubulin; residual NP staining is apparent as a doublet running just above tubulin. (D) NP mRNA and 5S rRNA (as a loading control) were measured by urea-PAGE and autoradiography of radioactive primer extension assays. (C) NP mRNA accumulation from (D) was quantified by densitometry. Values plotted in (C) are the means  $\pm$  range of two independent experiments, normalized to the control where the PB2 subunit of the viral polymerase was cotransfected in place of PA.

at 8 hours confirmed the significantly reduced ability of the PA-X mutant viruses to inhibit cellular gene expression (Fig. 3E and fig. S4C). These data supported the hypothesis that PA-X has a function in host-cell shutoff.

We next investigated the impact of mutating PA-X expression on pathogenesis in an experimental mouse model of influenza infection, using the fully reconstructed 1918 pandemic virus. The 1918 virus background was chosen to evaluate changes in pathogenicity because it induces clinical symptoms in mice without prior adaptation. Additionally, recent data suggest that the current human population may be protected from the 1918 H1N1 virus because of prior infection by, or immunization against, the 2009 H1N1 pandemic virus (17, 18). Because PA-X is a conserved feature of IAV and because PA-X-deficient viruses exhibited decreased host-cell shutoff capacity *in vitro*, it was expected that such viruses would be attenuated *in vivo*. To follow the clinical course of infection, 100 plaque-forming units (PFU) of 1918-WT, -FS, or -PTC viruses were inoculated intranasally into BALB/c mice, and daily weights were taken in an Animal Biosafety Level 3+ select agent-approved laboratory (in accordance with the select agent guidelines of the National Institutes of Health and Centers for Disease Control and Prevention and under the supervision of the NIH Select Agent Program and the NIH Department of Health and Safety). The 1918-FS-infected mice displayed more weight loss than the 1918-WT-infected mice at a dose of 100 PFU [ $P < 0.0001$  8 days post infection (DPI)], whereas 1918-PTC-infected mice displayed an intermediate disease severity phenotype ( $P = 0.008$  versus WT,  $P = 0.007$  versus FS, at 8 DPI) (Fig. 4A). Although no survival differences were observed between 1918-WT and 1918-FS at doses of 10 PFU and 1000 PFU, survival of the 1918-FS-infected mice at a dose of 100 PFU was significantly decreased compared with WT ( $P < 0.0001$ ) (Fig. 4B). This difference corresponded with a  $<1$  log decrease in the calculated 50% mouse lethal dose ( $MLD_{50}$ ), from  $10^{2.4}$  PFU for the 1918-WT virus to  $10^{1.6}$  PFU for the 1918-FS virus. Virus-infected mice were humanely killed on 3, 5, and 8 days post inoculation, and lungs were harvested for virus titration and histopathologic examination. Viral replication in lungs was similar among 1918-WT-, 1918-FS-, and 1918-PTC-infected mice at these three time points (Fig. 4C). Similarly, there was no apparent difference in the histopathologic changes, nature of the inflammatory infiltrate, or viral antigen distribution among the viruses (fig. S5).

Global transcriptional profiling was also performed on 3, 5, and 8 DPI to determine whether changes in PA-X expression affected the character of the host response compared with a nonlethal dose of the WT 1918 influenza virus infection. Gene expression analysis was performed on RNA isolated from the lungs of individual infected mice (four per group) and compared with

a pool of RNA isolated from control animals by oligonucleotide microarray. “Heat map” profiles of sequences showing a twofold or higher change in expression relative to mock controls of the individual animals showed that at each time point, at a dose of 100 PFU, 1918-FS and -PTC viruses induced a host transcriptional response different from that of the 1918-WT virus, particularly at earlier time points (Fig. 4D). However, comparison of the host response to 1918-FS and 1918-PTC viral infection showed a high degree of similarity to responses of mice infected with a five times as high, lethal dose of the 1918-WT virus (fig. S6). Thus, mutation of PA-X in the 1918-FS and 1918-PTC viruses changed the kinetics and magnitude of the host response in infected mice.

Although a subset of cellular genes were expressed in greater amounts in animals infected with the mutant viruses (especially at earlier time points), in general, there was a significant reduction of cellular gene expression in the lungs of mice infected with PA-X-deficient 1918 viruses, similar to that previously reported for lethal infections with the 1918-WT virus (19). Further analysis of sequences showing differential expression between 1918-WT and 1918-FS or -PTC viruses was therefore done to identify potential

cellular pathways associated with the moderately increased pathogenicity of the mutant viruses. Standard *t* tests identified ~5000 genes that showed significantly different expression levels (at least twofold difference in median expression level,  $P < 0.01$ ) between 1918-WT and either 1918-FS or -PTC viruses at each time point (fig. S7). Although genetically distinct strategies were used to compromise PA-X expression in the 1918-FS and -PTC mutant viruses, the host response to these two viruses was similar. Many genes identified as differentially regulated in 1918-FS as compared with 1918-WT were also differentially regulated in 1918-PTC (fig. S7). Fewer differences in gene expression were observed between 1918-FS- and 1918-PTC-infected animals, which further emphasized the similarity in the response of host gene expression to these viruses. Moreover, in concordance with global expression data (fig. S6), the host response at 8 DPI of 1918-FS- and 1918-PTC-infected animals was more similar to that of animals given a lethal 500 PFU dose of 1918-WT than to the comparable 100 PFU 1918-WT-infected animals (fig. S7).

Gene ontology analysis indicated that sequences showing differential expression between 1918-WT and 1918-FS infection were associated

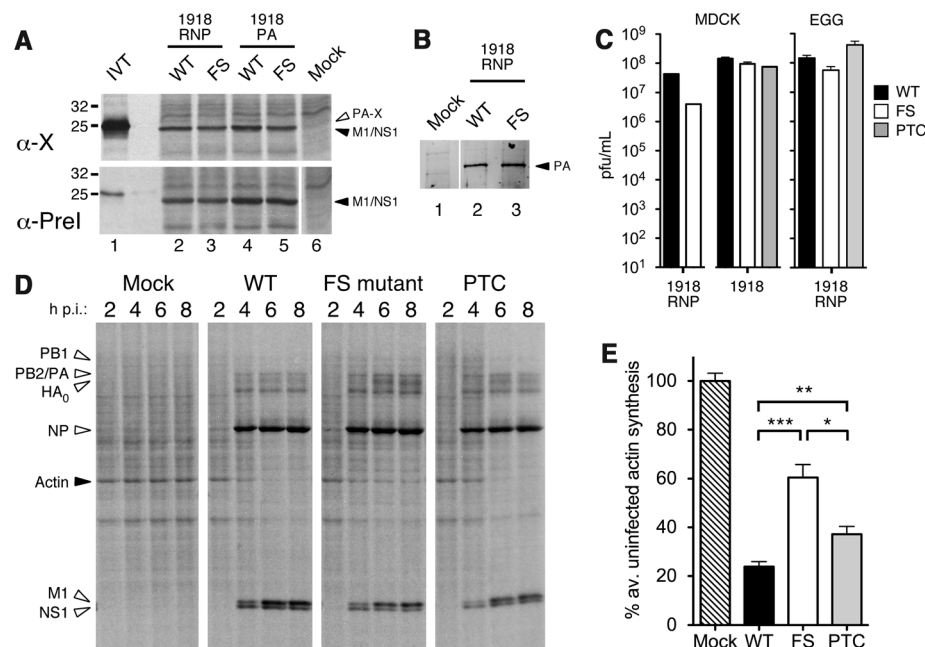


**Fig. 3.** Characterization of PA-X mutant viruses. (A) MDCK cells infected with the indicated viruses were metabolically labeled with [ $^{35}$ S]methionine from 3 to 8 hours post infection. Cell lysates were immunoprecipitated with anti-X or the corresponding preimmune (Prel) serum, and bound fractions were analyzed by SDS-PAGE and autoradiography. Aliquots of IVT PA-X were run in parallel as markers. The migration of molecular mass standards is also indicated. (B) Lysates from cells infected with the indicated viruses were analyzed by Western blotting for PA. (C) Virus titers from MDCK cells (infected at a multiplicity of infection of ~0.001) or embryonated eggs (inoculated with 1000 PFU) were determined by plaque assay. Data are the means  $\pm$  SEM of two to six separate inoculations, except for 1918-PTC, which was grown once. (D and E) Lysates from MDCK cells infected with the indicated 1918 RNP viruses and metabolically labeled for 45-min periods ending at the times shown were (D) analyzed by SDS-PAGE and autoradiography. (E) Actin synthesis at 8 hours post infection was quantified by densitometry. Data plotted are means  $\pm$  SEM of three independent experiments. Two-tailed *P* values are indicated: \*\*\* $P < 0.0001$ ; \*\* $P = 0.003$ ; \* $P = 0.01$ .



predominantly with inflammation or immune response, apoptosis, cell differentiation, and tissue remodeling (Fig. 4E). Interestingly, the majority of differentially regulated immune response and/or inflammation sequences were related to lymphocyte activation and/or proliferation or other aspects of cell-mediated immunity, including interferon- $\gamma$  (IFN- $\gamma$ ), the chemokine receptor CCR5, CD28, and interleukin-7 (IL-7) and (IL-15) signaling (Fig. 4F). Many of these genes were more highly induced in the 1918-FS- and 1918-PTC-infected animals relative to 1918-WT-infected animals. Many of the differentially regulated apoptosis-related genes are also functionally related to lymphocytes, including Fas pathway signaling and lymphotoxins, similar to genes examined in previous high-dose 1918 studies (19). In addition, several major histocompatibility complex (MHC) class I-associated genes showed up-regulation earlier in 1918-FS (by 3 DPI) compared with 1918-WT (8 DPI) (fig. S8). By contrast, sequences involved in cell adhesion, including many integrins and extracellular matrix components, showed decreased expression during infection with 1918-FS and -PTC viruses. Collectively, these data support

the hypothesis that PA-X plays a role in modulating host gene expression during infection with the 1918 pandemic virus.

The data presented here—derived from genomic, biochemical, functional, and in vivo studies—demonstrate the existence of a 13th protein, termed PA-X, in the IAV proteome. PA-X is a fusion protein incorporating the N-terminal endonuclease domain of the PA protein with a short C-terminal domain, encoded by an overlapping ORF (“X”) in segment 3 that is accessed by +1 ribosomal frameshifting. Ribosomal frameshifting has not been previously reported in IAV. The proteins PB1-N40 (20) and PB1-F2 (21) are also recent discoveries in the IAV proteome, and it is interesting that the X-ORF exhibits greater codon-level conservation than does PB1-F2, which is also expressed from an overlapping ORF (10, 22, 23). We show functional data primarily for the 1918 pandemic virus, but on the basis of the conserved nature of the FS sequence (98%; table S1) and the prevalence of the downstream X-ORF (>99.5% of IAV genomes contain either 61- or 41-codon X-ORFs), as well as its codon-level conservation (Fig. 1A),

we predict that expression of PA-X is a nearly universal feature of IAV. Note that there are lineage-specific differences in the distribution of X-ORF lengths. The ~75% of sequenced isolates that have a 61-codon X-ORF represent virtually all host species and HA/NA subtypes, whereas the ~25% of isolates with a 41-codon X-ORF are overwhelmingly from the 2009 H1N1 swine-origin pandemic virus plus, a minority subset of swine H3N2 and swine H1N2 viruses, the parental source of the 2009 pandemic segment 3 (24). Functional analyses of the differences in these PA-X variants will require additional experimentation. Although the biochemical properties of PA-X [including the function(s) of the X-domain] await a full characterization, cotransfection reporter assays suggest that PA-X can act as an mRNAse by virtue of the PA<sub>N</sub> endonuclease domain, in a manner evocative of the herpes simplex virus vhs protein (15). Thus, the substrate range and specificity of PA-X will be particularly interesting areas for further research.

PA-X expression was not required for viral replication, and indeed, by virtue of its expression mechanism, only low levels of the protein

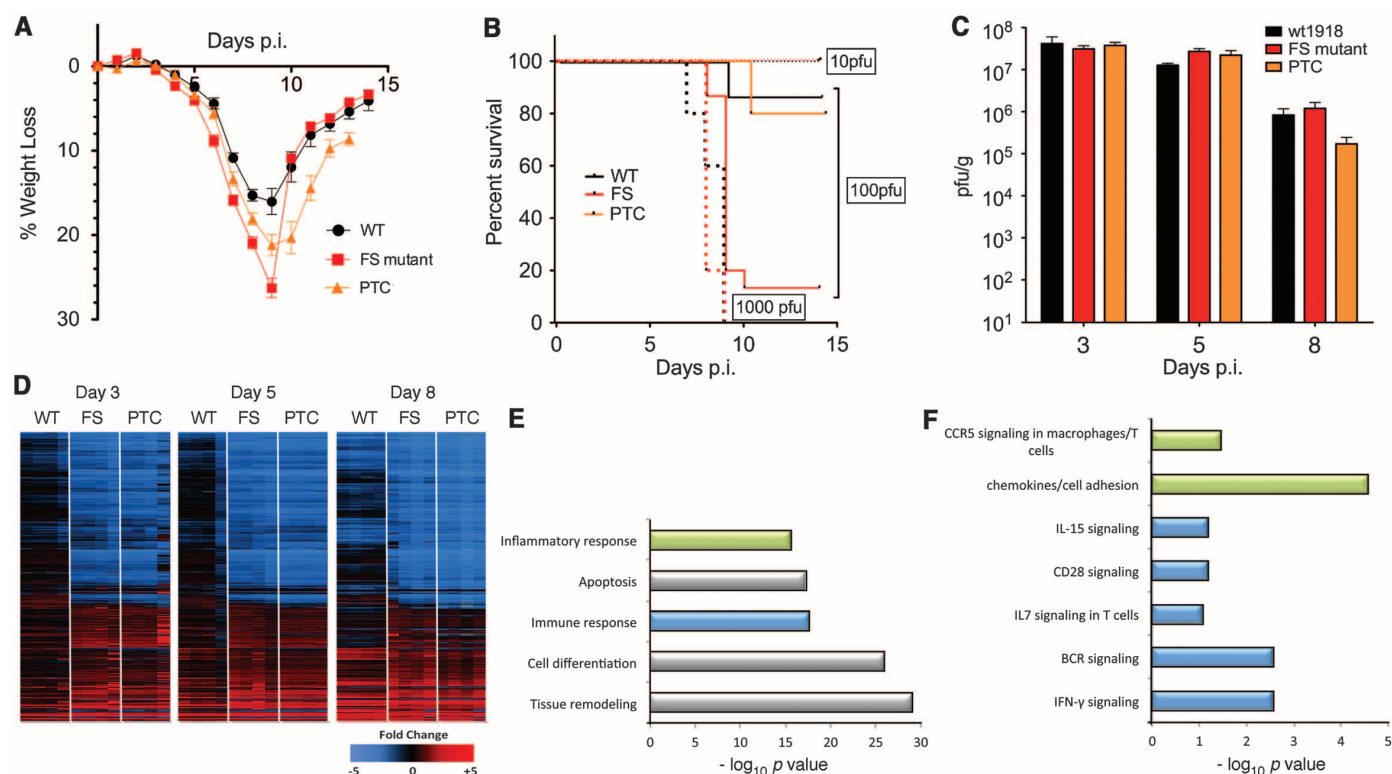


**Fig. 4.** Mutation of PA-X affects IAV pathogenicity in a murine model. **(A)** Mean weight loss of mice infected with 100 PFU of 1918-WT, -FS, and -PTC viruses ( $n = 15$ , 15, and 10, respectively). Mice were humanely killed when they lost  $\geq 25\%$  of their initial body weight; no mice were found dead. Error bars represent  $\pm$ SEM. **(B)** Survival proportions of mice infected with 10 (dotted line), 100 (solid line), or 1000 (squares in line) PFU of 1918-WT, -FS, and -PTC viruses. Data for WT and FS in (A) and (B) are pooled results obtained with two independently rescued sets of viruses, one set of which was subjected to high-throughput, full-genome sequencing to confirm that the only changes between WT and FS were those deliberately introduced in PA. **(C)** Mean infectious titers of 1918 viruses in homogenized mouse lungs. Error bars represent the SEM. **(D)** Expression profile heat maps generated

from whole-lung RNA isolated from mice killed at 3, 5, and 8 DPI ( $n = 4$  per virus, per time point), displaying sequences that showed a  $\geq 2$ -fold difference from mock-infected mouse lungs in at least one experimental group. Each column represents data from an individual experiment; rows represent unique sequences; and row-gene identities are preserved across time points. Genes in red are up-regulated, those in blue are down-regulated, and those in black do not differ compared with a pool of RNA isolated from six mock-infected control mice. **(E)** and **(F)** Gene ontology analysis of sequences whose expression levels differed significantly ( $P < 0.01$ ,  $\geq 2$ -fold expression level difference) between 1918-WT- and -FS-infected lung tissue at 3 DPI with 100 PFU. **(E)** Top-scoring functional categories. **(F)** Top pathways within color-coded functional categories.

were expressed during WT viral infection. However, PA-X-deficient viruses differed from the WT counterpart in their ability to cause host-cell shutoff and, moreover, caused greater clinical disease in a mouse model of IAV infection, an outcome related to an accelerated host response as assessed by microarray. PA-X is thus an accessory IAV protein that plays a consequential role at the virus-host interface. We hypothesize that defective control of host gene expression by the mutant viruses in the minority of infected lung cells provokes an altered cascade of host responses from the majority of uninfected cells. The nature of these host gene expression changes—including marked early overexpression of MHC class I genes in 1918-FS or -PTC infections, compared with 1918-WT infections—suggests that these perturbations in host response pathways affect lymphocyte activation and immune cell function that lead to an immunopathogenic inflammatory response (19). This may explain the lack of significant differences in weight loss in mice infected with 1918-WT versus 1918-FS and -PTC viruses until 5 to 8 DPI, which coincides with the appearance of influenza-specific cytotoxic T lymphocytes (25).

Taken together, these data contribute substantially to our understanding of IAV replication and pathogenesis and further suggest promising lines of inquiry into the anti-IAV immune response, as well as the factors driving IAV evolution. It is noteworthy that the outcome of infection with PA-X-null viruses was altered in the absence of differences in viral replication, as this suggests

that host immunopathology is of central importance in determining the character of disease and could therefore be a fruitful target for new therapeutics aimed at ameliorating severe IAV illness (19, 26).

#### References and Notes

1. P. Palese, M. L. Shaw, in *Fields Virology*, D. M. Knipe, Howley, P.M., Ed. (Lippincott Williams & Wilkins, Philadelphia, 2007), vol. 2, pp. 1647–1690.
2. J. K. Taubenberger, J. C. Kash, *Cell Host Microbe* **7**, 440 (2010).
3. K. Hara, F. I. Schmidt, M. Crow, G. G. Brownlee, *J. Virol.* **80**, 7789 (2006).
4. P. Yuan *et al.*, *Nature* **458**, 909 (2009).
5. A. Dias *et al.*, *Nature* **458**, 914 (2009).
6. J. J. Sanz-Ezquerro, S. de la Luna, J. Ortín, A. Nieto, *J. Virol.* **69**, 2420 (1995).
7. A. Rodriguez, A. Pérez-González, A. Nieto, *J. Virol.* **81**, 5315 (2007).
8. F. T. Vreede, A. Y. Chan, J. Sharps, E. Fodor, *Virology* **396**, 125 (2010).
9. E. C. Hutchinson, J. C. von Kirchbach, J. R. Gog, P. Digard, *J. Gen. Virol.* **91**, 313 (2010).
10. J. R. Gog *et al.*, *Nucleic Acids Res.* **35**, 1897 (2007).
11. A. E. Firth, N. M. Wills, R. F. Gesteland, J. F. Atkins, *Nucleic Acids Res.* **39**, 6679 (2011).
12. J. F. Atkins, R. F. Gesteland, *Recoding: Expansion of Decoding Rules Enriches Gene Expression* (Springer, Heidelberg, Germany, ed. 1, 2010).
13. J. Eisinger, B. Feuer, T. Yamane, *Nat. New Biol.* **231**, 126 (1971).
14. G. Grentzmann, J. A. Ingram, P. J. Kelly, R. F. Gesteland, J. F. Atkins, *RNA* **4**, 479 (1998).
15. J. R. Smiley, *J. Virol.* **78**, 1063 (2004).
16. F. Weber, O. Haller, *Biochimie* **89**, 836 (2007).
17. J. D. Easterbrook *et al.*, *Influenza Other Respi. Viruses* **5**, 198 (2011).
18. B. Manicassamy *et al.*, *PLoS Pathog.* **6**, e1000745 (2010).
19. J. C. Kash *et al.*, *Nature* **443**, 578 (2006).
20. H. M. Wise *et al.*, *J. Virol.* **83**, 8021 (2009).

21. W. Chen *et al.*, *Nat. Med.* **7**, 1306 (2001).
22. E. C. Holmes, D. J. Lipman, D. Zamarin, J. W. Yewdell, *Science* **313**, 1573 (2006).
23. R. Zell *et al.*, *J. Gen. Virol.* **88**, 536 (2007).
24. R. J. Garten *et al.*, *Science* **325**, 197 (2009).
25. S. A. Valkenburg *et al.*, *Microbes Infect.* **13**, 489 (2011).
26. K. B. Walsh *et al.*, *Proc. Natl. Acad. Sci. U.S.A.* **108**, 12018 (2011).

**Acknowledgments:** A.E.F. is supported by the Wellcome Trust (088789). P.D. was supported by the U.K. Medical Research Council (G0700815) and Wellcome Trust (073126). This work was supported in part by the intramural funds of the NIH and the National Institute of Allergy and Infectious Diseases (NIAID), NIH. J.F.A. is supported by Science Foundation Ireland (08/IN.1/B1889). K.-A.W. and A.O. were funded by Defense Threat Reduction Agency contract HDTRA-1-08-C-0023, the Luxembourg Centre for Systems Biomedicine, and the University of Luxembourg. G.L.B. and A.L. were supported by studentships from the U.K. Biotechnology and Biological Sciences Research Council and the Cambridge Infectious Disease Consortium, respectively. We thank the Comparative Medicine Branch (NIAID, NIH) for assistance with animal studies and M. Howard (Utah) for the pDluc variant of the dual luciferase vector. We also thank a number of colleagues for helpful discussion, including J. Gog and L. Tiley (University of Cambridge), W. Barclay (Imperial College London), Y. J. Tao (Rice University), J. I. Cohen, K. Subbarao, K. C. Zoon, D. C. Wilson, M. M. Gottesman, R. Wyatt, and H. Metzger (NIH). B.W.J., P.D., and J.K.T. are also thankful for the support of the NIH-Oxford-Cambridge Research Scholars program. The Gene Expression Omnibus accession no. for microarray data is GSE38112.

#### Supplementary Materials

www.sciencemag.org/cgi/content/full/science.1222213/DC1  
Materials and Methods

Supplementary Text

Figs. S1 to S8

Table S1

References (27–33)

20 March 2012; accepted 31 May 2012

Published online 28 June 2012;

10.1126/science.1222213

## REPORTS

# Spin-Polarized Light-Emitting Diode Based on an Organic Bipolar Spin Valve

Tho D. Nguyen,<sup>1</sup> Eitan Ehrenfreund,<sup>1,2</sup> Z. Vally Vardeny<sup>1,\*</sup>

The spin-polarized organic light-emitting diode (spin-OLED) has been a long-sought device within the field of organic spintronics. We designed, fabricated, and studied a spin-OLED with ferromagnetic electrodes that acts as a bipolar organic spin valve (OSV), based on a deuterated derivative of poly(phenylene-vinylene) with small hyperfine interaction. In the double-injection limit, the device shows ~1% spin valve magneto-electroluminescence (MEL) response, which follows the ferromagnetic electrode coercive fields and originates from the bipolar spin-polarized space charge-limited current. In stark contrast to the response properties of homopolar OSV devices, the MEL response in the double-injection device is practically independent of bias voltage, and its temperature dependence follows that of the ferromagnetic electrode magnetization. Our findings provide a pathway for organic displays controlled by external magnetic fields.

The quest for a spin-polarized organic light-emitting diode (spin-OLED) (1–3), in which the electroluminescence (EL) intensity is

sensitive to the spin polarization of the injected carriers, has been a goal in the field of organic spintronics since the successful implementation of

an organic spin valve (OSV) based on the small molecule aluminum tris(8-hydroxyquinoline) (Alq<sub>3</sub>) (4). Despite several attempts at spin-OLEDs (1, 5) in which Alq<sub>3</sub> was used as the organic interlayer between two ferromagnetic (FM) electrodes in a vertical configuration, this goal has not been achieved as yet. The main obstacle in realizing such a device has been the relatively high bias voltage  $V_b$  needed for reaching substantive EL efficiency in the device at low temperatures. For example,  $V_b > 10$  V is needed for EL of Alq<sub>3</sub> with FM electrodes at temperature  $T = 10$  K, but the OSV performance sharply deteriorates with  $V_b$  and is limited to <1 V for practical operation (4, 6, 7).

We report the realization of a spin-OLED based on a bipolar OSV device that exhibits magneto-electroluminescence (MEL) on the order of ~1% at  $V_b \approx 3.5$  V, with emission intensity modulation that follows the coercive fields

<sup>1</sup>Department of Physics and Astronomy, University of Utah, Salt Lake City, UT 84112, USA. <sup>2</sup>Physics Department and Solid State Institute, Technion-Israel Institute of Technology, Haifa 32000, Israel.

\*To whom correspondence should be addressed. E-mail: val@physics.utah.edu



of the FM electrodes. Two important technical advances enabled this achievement. First, our devices are based on a deuterated organic polymer interlayer with superior spin transport properties that has a smaller hyperfine interaction than polymers based on hydrogen side groups (7). Second, we deposited a thin LiF buffer layer in front of the FM cathode to improve the electron injection efficiency (8). The bipolar OSV response has substantially different voltage, temperature, and thickness dependencies relative to the response in homopolar OSV based on the same organic interlayer. These differences are caused in part by the spin-aligned space charge-limited current (SCLC) operation upon reaching double-injection conditions during bipolar operation.

The device operation scheme (Fig. 1A) shows the injected electrons and holes initially forming polaron pairs (PPs) at the appropriate  $V_b$  needed for bipolar injection. These species are precursor excitations to singlet excitons (SEs) that may recombine radiatively and emit EL. With non-FM electrodes (Fig. 1A, panel 1), the net electron-hole bimolecular rate coefficient  $b$  for forming PPs did not depend on the magnetic field. Under the assumption of SCLC operation, the fraction of current from electron-hole recombination was inversely proportional to the rate  $b$  (9). When the OLED device was driven with FM electrodes that inject spin-aligned carriers, the rate  $b$  became field-dependent (Fig. 1A, panels 2 and 3) because the external magnetic field changed the mutual magnetization directions of the spin-injecting FM electrodes. Thus, the PP formation rate, EL intensity (MEL), and current density (magnetoconductivity, MC) all become field-dependent. This operation scenario of spin-OLED is more realistic than the simple model described in (2, 6) because the intermediate step of PP formation, as well as the spin mixing among its spin singlet ( $PP_s$ ) and spin triplet ( $PP_t$ ) configurations, is explicitly considered (10, 11). In fact, the spin-mixing channel is responsible for a variety of effects in OLED devices with non-FM electrodes (such as monotonic MC and MEL responses) that we term “intrinsic” MC and MEL responses (7, 11, 12), as well as EL quantum efficiency that is not limited to 25% (13).

The spin-OSV device was designed to achieve efficient EL emission at relatively low  $V_b$  (Fig. 1C), with sizable spin injection capability from the FM electrodes and with large spin diffusion length in the organic interlayer. We show the spin-OLED device structure in Fig. 1B. For the anode, we used the half-metal FM  $\text{La}_{0.7}\text{Sr}_{0.3}\text{MnO}_3$  (LSMO), which has a coercive field  $B_c \approx 5$  mT at cryogenic temperatures (Fig. 2D); the cathode was a FM Co thin film ( $B_c \approx 35$  mT at cryogenic temperatures; Fig. 2D) capped with an Al layer for corrosion protection. The organic interlayer film, with thickness  $d$  ranging from 18 to 50 nm, was based on deuterated poly(dioctyloxy)phenyl vinylene (D-DOO-PPV), a  $\pi$ -conjugated polymer in which all the hydrogen atoms closest to the backbone chain were replaced by deuterium

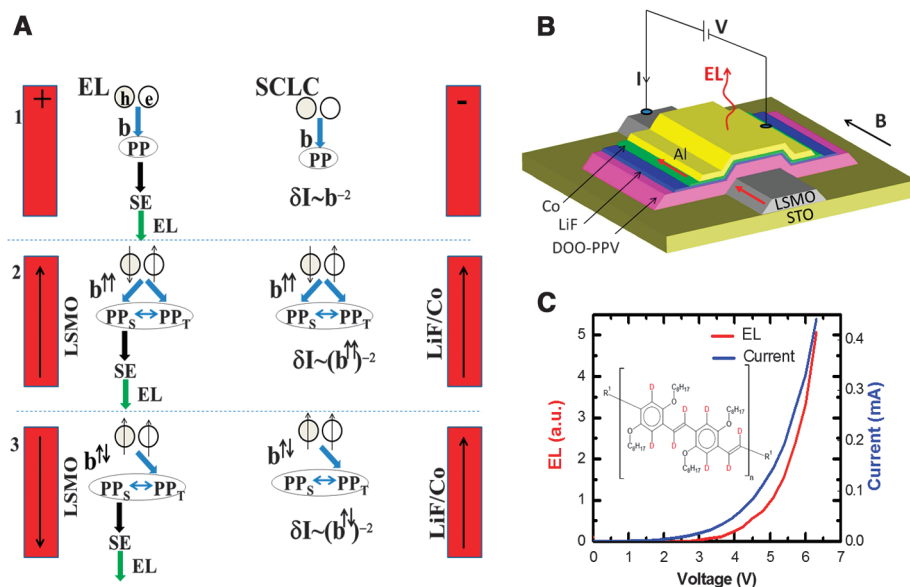


**Fig. 1.** (A) Spin-OLED device operation under the condition of unbalanced electron-hole space charge limited current (SCLC): (1) OLED with non-FM electrodes; the “recombination” current  $\delta I$  is inversely related to the efficiency of PP formation via the bimolecular recombination coefficient  $b$ ; also,  $EL \propto \delta I$ . (2 and 3) OLED with FM electrodes:  $b$  becomes magnetic field-dependent via the spin injection of the FM electrodes, giving rise to spin-dependent current and EL. (B) The spin-OLED device structure, where the D-DOO-PPV organic layer thickness is  $\sim 25$  nm and LiF buffer layer thickness is  $\sim 1.5$  nm. Here the in-plane magnetic field (black arrow) causes the FM magnetizations (red arrows) to align parallel to each other. The EL emission (wavy red line) is collected through the Co/Al thin electrode. (C) The device  $I$ - $V$  and  $EL$ - $V$  characteristics; the EL onset is at  $V_0 \approx 3.5$  V. Inset: D-DOO-PPV polymer chemical structure.

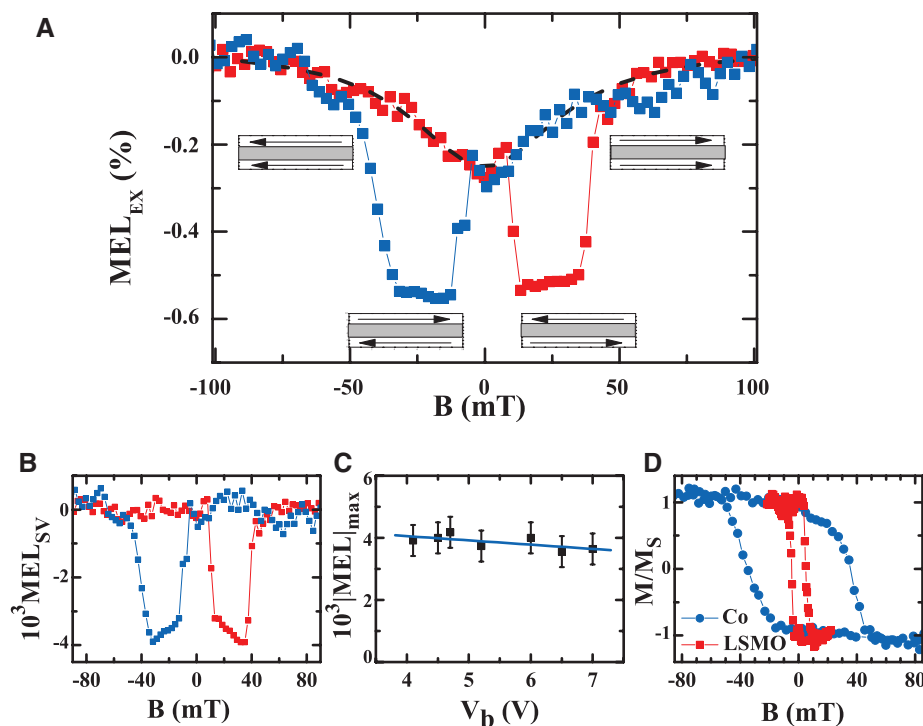


**Fig. 2.** Magneto-electroluminescence (MEL) response of a spin-OLED device. (A) Obtained  $MEL_{EX}(B)$  response for up (red) and down (blue)  $B$ -sweeps, measured at  $V_b = 4.5$  V and  $T = 10$  K, for device A ( $d = 25$  nm,  $d' = 1.5$  nm). The black dashed line describes the nonhysteretic, intrinsic MEL background response for an up-sweep. The horizontal arrows mark the relative electrode magnetization directions. (B) The net  $MEL_{SV}(B)$  response after subtraction of the background MEL from the measured MEL response shown in (A). (C) The bias voltage dependence of the maximum  $MEL_{SV}$  value. (D) Magneto-optic Kerr effect (MOKE) measurements of the LSMO and Co/LiF electrodes at 10 K that show coercive fields  $B_c(\text{FM1}) \approx 5$  mT and  $B_c(\text{FM2}) \approx 35$  mT, respectively.

(Fig. 1C, inset). It was previously shown (7) that the hyperfine interaction in D-DOO-PPV is considerably reduced, thus increasing the spin diffusion length  $\lambda_S$  to  $\sim 45$  nm; this is about 3 times the value of  $\lambda_S$  in H-DOO-PPV polymer. In addition, a thin LiF layer (thickness  $d'$  ranging from 0.8 to 1.5 nm) was deposited as a buffer layer between the organic layer and Co electrode to improve electron injection (14) and to block the formation of Co inclusions (4, 15).

The turn-on voltage  $V_0$  for sizable EL emission at the double-injection condition was reached at  $V_0 \approx 3.5$  V (Fig. 1C); this value was  $V_0 \approx 10$  V without the LiF layer (8). Because  $V_0$  is still relatively high in the spin-OLED device, we conjecture that hole injection is more efficient than electron injection. This difference led to unbalanced charge injection; most of the current density was carried by the holes, whereas the EL intensity was limited by the minority electron injection from the Co/LiF cathode. Under these conditions, the “intrinsic” MEL and MC responses (7), those unrelated to the spin valve, were small (figs. S1 to S3), and this allowed us to readily study the spin valve-related MEL response.

At cryogenic temperatures, the FM LSMO (FM1) and Co (FM2) electrodes in the spin-OLED had nominal spin injection degrees of polarization of  $P_1 \approx 95\%$  and  $P_2 \approx 30\%$  [which may depend on the environment; see (16)]. However,  $P_2$  substantially dropped because of the LiF buffer layer (8, 17). Because  $B_c(\text{FM1}) \neq B_c(\text{FM2})$ , we could switch their relative magnetization directions between parallel ( $\uparrow\uparrow$ ) and antiparallel ( $\uparrow\downarrow$ ) relative

alignments by sweeping the external magnetic field  $B$  (horizontal arrows in Fig. 2A), whereby the device resistance, conductance, and EL intensity depended on the relative magnetization orientations of the FM electrodes. We thus measured  $\text{MEL}(B)$  and  $\text{MC}(B)$  at various bias voltages, temperatures, and device thicknesses.

A typical EL( $B$ ) response of a D-DOO-PPV spin-OLED measured at 10 K is plotted as  $\text{MEL}_{\text{EX}}(B) \equiv [\text{EL}(B) - \text{EL}(\uparrow\uparrow)]/\text{EL}(\uparrow\uparrow)$  in Fig. 2A for a device with  $d = 25$  nm and LiF  $d' = 1.5$  nm. The EL( $B$ ) response had two components: (i) a hysteretic negative  $\text{MEL}_{\text{SV}}$  component and (ii) a nonhysteretic positive  $\text{MEL}_{\text{LSMO}}$  component (black dashed line in Fig. 2A). The  $\text{MEL}_{\text{SV}}$  response component consisted of a downward sharp jump of  $\sim 0.4\%$  in the antiparallel magnetization configuration between 4 and 30 mT that followed the electrodes' coercive fields (Fig. 2D). The  $\text{MEL}_{\text{LSMO}}$  response was caused by the magnetic properties of the LSMO electrode (4) combined with the “intrinsic” MEL response (7); it was a monotonic function of  $|B|$  and symmetric with respect to  $B = 0$  (fig. S2). A similar MEL component was measured before in FM-OLED devices based on  $\text{Alq}_3$  at room temperature (1) and was ascribed to the non-spin valve MEL response of the organic interlayer. In that case, the sudden change in the EL( $B$ ) response at the electrodes' respective  $B_c$  values was positive with increasing  $B$ , and was thus interpreted as having been caused by the stray field  $B_S$  that arises from the proximity of the FM electrodes to the organic interlayer. We measured  $B_S$  of the LSMO and

Co/LiF electrodes in our device (figs. S2 and S3). For devices with one FM electrode, we found  $B_S(\text{LSMO}) \approx 0.7$  mT (fig. S2) and  $B_S(\text{Co}) \approx 3.5$  mT (fig. S3) at cryogenic temperatures. However, the average  $B_S$  increased when two FM electrodes were deposited; in this case, we measured  $B_S \approx 4$  mT (fig. S4), which is somewhat greater than in devices with one FM electrode but is too small for explaining the  $\text{MEL}_{\text{SV}}$  sharp response in our devices, given that the intrinsic MEL response is weak (fig. S1). In addition, the  $\text{MEL}_{\text{SV}}$  response was negative, in contrast to the positive MEL jump related to the stray field ( $I$ ) (fig. S4).

Moreover, the MEL was isotope-dependent. We measured the MEL response in devices with different DOO-PPV isotopes (7). The spin diffusion length was isotope-dependent, and the spin valve-related MEL response indeed depended on the polymer isotope (fig. S5). Thus, the MEL response cannot be interpreted as arising from the stray fields that influence the intrinsic MEL response, as in ( $I$ ). We thus conjecture that the obtained  $\text{MEL}_{\text{SV}}$  response in the bipolar OSV is a genuine spin valve effect.

To facilitate data analysis, we subtracted the nonhysteretic  $\text{MEL}_{\text{LSMO}}$  response [component (ii)] from the  $\text{MEL}_{\text{EX}}(B)$  response (Fig. 2A) to obtain the “net” spin valve-related response [component (i)],  $\text{MEL}_{\text{SV}}(B) \equiv \text{MEL}_{\text{EX}} - \text{MEL}_{\text{LSMO}}$  (Fig. 2B).  $\text{MEL}_{\text{SV}}(B)$  displayed the typical hysteretic spin valve characteristic response with sharp jumps at the LSMO and Co coercive fields. Moreover, one of the most prominent features

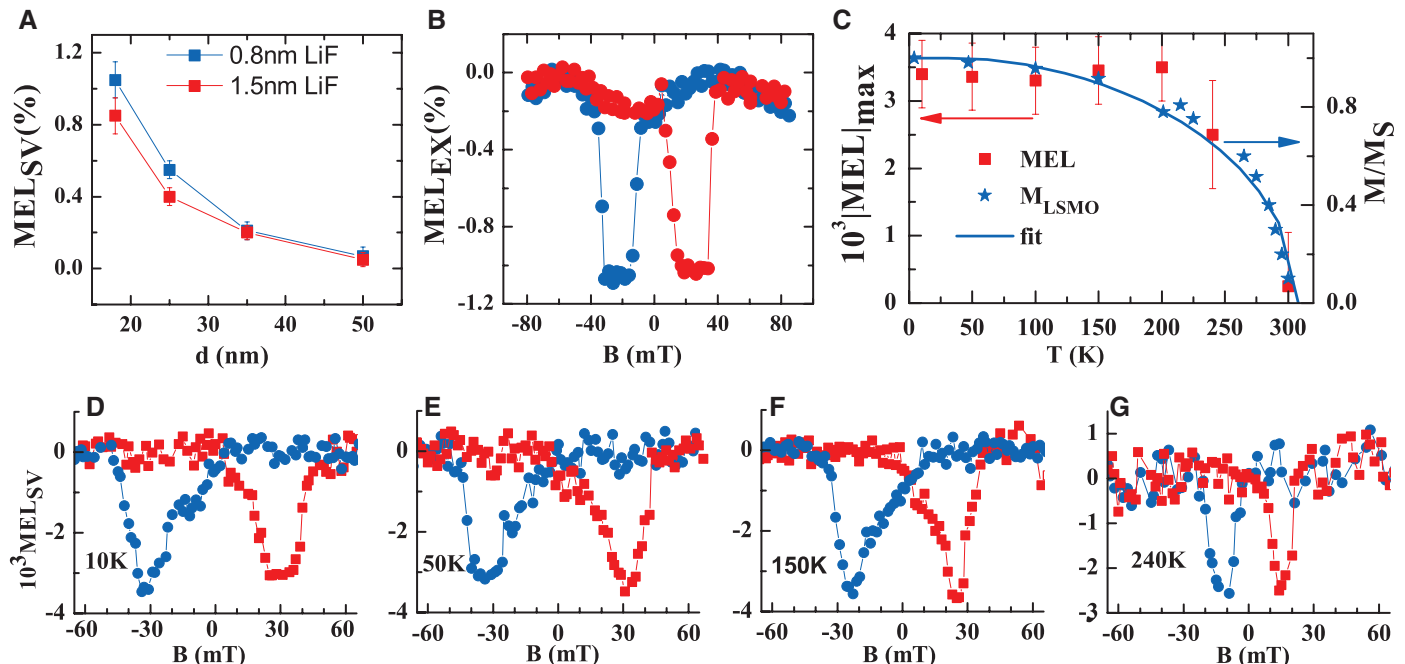


**Fig. 3.** (A) The maximum  $\text{MEL}_{\text{SV}}$  response of spin-OLED devices at various polymer thicknesses  $d$  and LiF buffer layer thicknesses  $d'$  of 0.8 nm (red squares) and 1.5 nm (blue squares), measured at  $T = 10$  K and  $V_0 = 4.5$  V. (B) The optimum  $\text{MEL}_{\text{SV}}(B)$  response of  $\sim 1.1\%$  measured for a device with  $d = 18$  nm and  $d' = 0.8$  nm. (C) The maximum  $\text{MEL}_{\text{SV}}(T)$  response at  $V_0 = 5$  V

(red squares) for a spin-OLED device with  $d = 25$  nm and  $d' = 1.5$  nm; the LSMO bulk magnetization versus  $T$  measured by superconducting quantum interference device (SQUID) (blue stars); and its fit using the Brillouin function  $B_J(T/T_c)$  with  $J = 5/2$  and  $T_c = 307$  K (blue line). (D to G)  $\text{MEL}(B)$  response at selected temperatures.



of the  $MEL_{SV}(B)$  response is the very weak dependence of its maximum value,  $MEL_{max} \equiv \max(|MEL_{SV}(B)|)$ , on  $V_b$  (Fig. 2C). This response substantially differs from the strong decrease of the magnetoresistance  $MR_{max}$  with  $V_b$  in homopolar OSV devices (4, 18, 19). It is thus clear that the performance of the bipolar OSV device degrades less with  $V_b$  relative to a homopolar OSV based on the same organic layer (see below).

We measured the OSV “figure of merit”  $MEL_{max}$  at 10 K and  $V = 4.5$  V for various device thicknesses  $d$  and LiF buffer layer thicknesses  $d'$  (Fig. 3A). We found that  $MEL_{max}$  decreases as  $d$  and  $d'$  increase. The decreased performance with increasing LiF  $d'$  may be readily explained as arising from the decrease of the cathode spin polarization  $P_2$  with the LiF buffer layer thickness (8). The decreased performance with increasing organic layer  $d$  may be caused by a finite “effective” spin diffusion length  $\lambda_S$  at the bipolar injection condition reached here. From the device thickness dependence shown in Fig. 3A we estimate  $\lambda_S \approx 25$  nm, which is different from  $\lambda_S = 45$  nm obtained at small bias voltage (7). The best device performance, a  $MEL_{max}$  value of 1.1% (Fig. 3B), was obtained for a bipolar OSV device having  $d = 18$  nm and  $d' = 0.8$  nm (Fig. 3A). Further decreases of  $d$  and  $d'$  caused the OLED devices to become unstable.

In Fig. 3, D to G, we show  $MEL_{SV}(B)$  response at various temperatures, and summarize  $MEL_{max}$  versus temperature relative to the measured LSMO bulk magnetization,  $M(T)$  in Fig. 3C. The  $MEL_{max}(T)$  values almost perfectly follow the

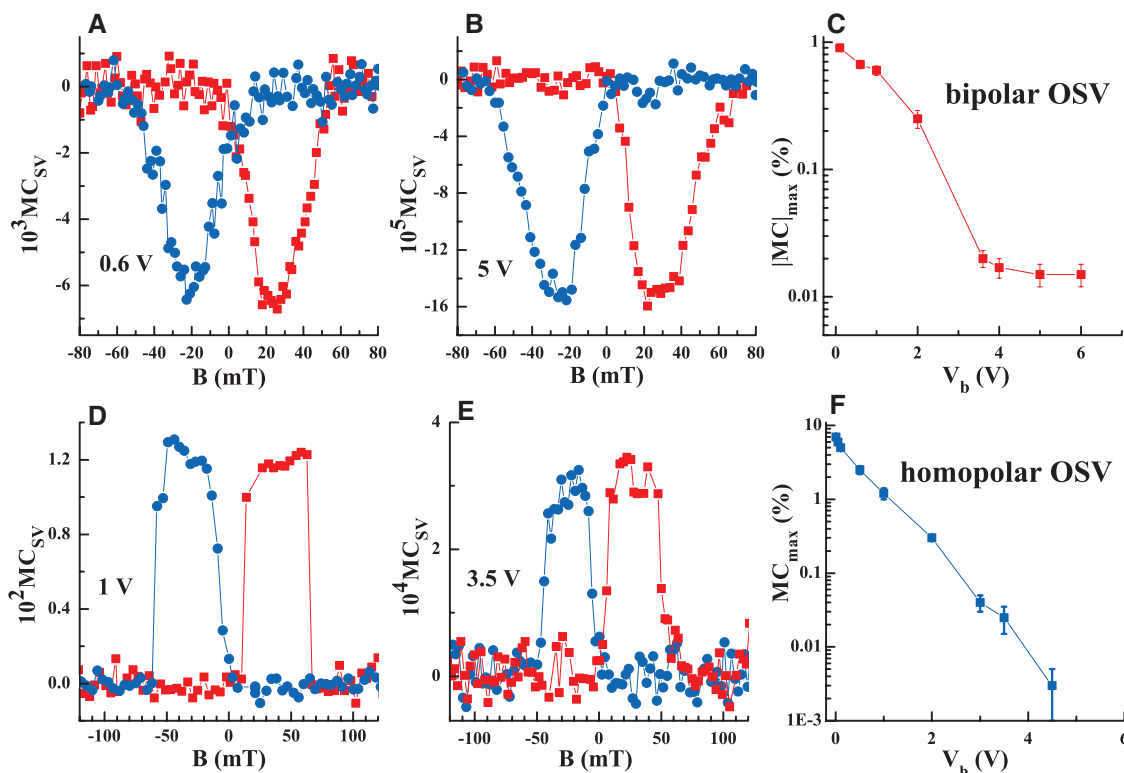
$M(T)$  response. This behavior is in stark contrast to  $MR_{max}(T)$  in homopolar OSV devices, where a much steeper temperature dependence was observed (20–23) and was explained (21, 22) as having been caused by the LSMO surface magnetization decreasing with  $T$  (23).

To better compare the homopolar and bipolar OSV devices, we show in Fig. 4 the effect of the LiF buffer layer on the device magnetoconductance  $MC(B)$  response. The measured response,  $MC_{EX}(B) \equiv [I(B) - I(\uparrow\uparrow)]/I(\uparrow\uparrow)$ , shows a nonhysteretic background that is similar to that observed in the  $MEL_{EX}(B)$  response in Fig. 2A. We again subtracted this background MC response to obtain the net response  $MC_{SV}(B)$ , which is shown in Fig. 4, A and B, for the bipolar (LiF/Co cathode) OSV device and in Fig. 4, D and E, for the homopolar (Co cathode) OSV device. The opposite sign of the two MC response sets demonstrates that the LiF layer reverses the cathode spin polarization in agreement with (8). In Fig. 4, C and F, we show  $MC_{max} \equiv \max(|MC_{SV}(B)|)$  as a function of  $V_b$  for the homopolar and bipolar OSV devices. Surprisingly, we see that although the  $MC_{max}(V_b)$  dependence of the bipolar OSV device sharply decreased for  $V_b < 3.5$  V, it abruptly leveled off at  $V_0$  and became practically independent of bias voltage. This outstanding property of the bipolar OSV device facilitates the realization of spin-OLED at  $V_b > V_0$ .

In the following, we analyze the spin-OLED device response under conditions of unbalanced bipolar current density  $J$  where the electron current density  $J_e$  is injection-limited and  $J_e \ll J$ . Under these conditions, most of the device cur-

rent density is carried by the hole current  $J_h$  along with an additional small “recombination current”  $J_R$  caused by the electron-hole “recombination” that leads to PP formation (Fig. 1A).  $J_h$ , which is the sole current through the device for  $V_b < V_0$ , gives rise to the bias voltage-dependent  $MC_{SV}$  that is usually observed in homopolar OSV devices (7). The homopolar  $MC_{SV}$  appears to follow a Jullière-type behavior (4, 17):  $MC_{SV}(V_b < V_0) \propto 2P_1P_2/(1 + P_1P_2)$ , where  $P_1$  and  $P_2$  are the cathode and anode spin polarizations, respectively.  $J_R$ , however, turns on at  $V_b \geq V_0$  and is responsible for the voltage-independent  $MEL_{SV}$  and  $MC_{SV}$  responses. These latter responses appear to follow a novel “recombination-modified” Jullière-type behavior: Both  $MC_{SV}(V_b > V_0)$  and  $MEL_{SV}$  are proportional to  $P_1P_2\Delta b$ , where  $\Delta b = b^{uu} - b^{ud}$ , and  $b^{uu}$  and  $b^{ud}$  are the spin-dependent bimolecular recombination rate constants for up-up and up-down electron-hole relative spin directions, respectively. Note that although both  $MC_{SV}(V_b < V_0)$  and  $MC_{SV}(V_b > V_0)$  are proportional to  $P_1P_2$ , only  $MC_{SV}(V_b < V_0)$  is voltage-dependent. We thus conclude that the homopolar  $MC_{SV}$  voltage dependence cannot be caused by the FM electrode polarization as originally postulated (4), but rather originates within the device volume by a mechanism that does not affect the recombination current  $J_R$ . The electron-hole recombination products that are the singlet ( $PP_S$ ) and triplet ( $PP_T$ ) polaron pairs intermix through an intersystem crossing enabled via a variety of spin mixing interactions, such as the hyperfine, exchange, and spin-orbit interactions. Both same-spin polarized and opposite-spin polarized electron-hole

**Fig. 4.** Magnetoconductance (MC) response of bipolar and homopolar OSV devices based on D-DOO-PPV and measured at 10 K ( $d = 25$  nm,  $d' = 1.5$  nm). (A and B)  $MC(B)$  response of bipolar OSV device measured at  $V_b = 0.6$  V and 5 V, respectively, at positive (red) and negative (blue)  $B$ -sweeps. (C) Maximum  $MC_{SV}$  value versus  $V_b$  for the bipolar device. (D and E)  $MC(B)$  response of homopolar OSV device measured at  $V_b = 1$  V and 3.5 V, respectively, at positive (red) and negative (blue)  $B$ -sweeps. (F) Maximum  $MC_{SV}$  value versus  $V_b$  for the homopolar device.



“recombination” contribute, albeit not equally, to the steady-state  $PP_S$  density and eventually to EL (7).

To understand the obtained bipolar OSV properties, we extend the classical bipolar SCLC Parmenter-Ruppel (PR) model (9) to include FM electrodes under the condition of unbalanced current density without the effect of traps (24). In this case the  $J$ - $V$  relation is given by

$$J = \frac{9\epsilon\epsilon_0\mu_h V^2}{8d^3} + \frac{3\mu_e\mu_h J_e}{2\mu_R^2} = J_h + J_R \quad (1)$$

where  $\epsilon$  is the dielectric constant;  $\mu_h$ ,  $\mu_e$ , and  $\mu_R = \epsilon\epsilon_0 b/2e$  are the hole, electron, and recombination mobilities, respectively;  $b$  is the bimolecular recombination coefficient in the reaction rate  $R_{pp} = bnp$  in which electrons of density  $n$  and holes of density  $p$  generate weakly coupled PP species (see supplementary text);  $J_h$  ( $\gg J_e$ ) is the hole majority SCLC density; and  $J_R$  is the recombination current density. Although  $J_R$  was originally ignored by PR because  $J_R \ll J_h$ , here we keep this term because it is the only term that leads to EL emission.

For FM electrodes, the fraction of spin-polarized electrons injected by the cathode FM1 and collected by FM2 is  $(1 \pm P_1 P_2)/2$  for  $\uparrow\uparrow$  and  $\uparrow\downarrow$  electrode magnetization directions, respectively, and the same is true for the fraction of spin-polarized holes that is injected by the anode FM2 and collected by FM1; here we assumed for simplicity that the spin diffusion length  $\lambda_s \gg d$ . In this case the spin-sensitive bimolecular recombination coefficients  $b^{uu}$  and  $b^{ud}$  cause  $J_R$  to depend on the mutual magnetization directions of the FM electrodes. The electrode magnetization-dependent SCLC can then be written as

$$J^{\uparrow\uparrow(\uparrow\downarrow)} = \frac{1}{2}(1 \pm P_1 P_2)J_h + \frac{3\mu_e\mu_h J_e}{2(\mu_R^{\uparrow\uparrow(\uparrow\downarrow)})^2} \quad (2)$$

where  $\mu_R^{\uparrow\uparrow(\uparrow\downarrow)} = (\epsilon\epsilon_0 b/2e)[1 \pm P_1 P_2 \Delta b/2b]$  are the recombination mobilities for parallel and antiparallel electrode magnetizations, respectively (see supplementary text). Thus, the magnetoconductance, defined as  $MC = (J^{\uparrow\uparrow} - J^{\uparrow\downarrow})/J^{\uparrow\uparrow}$  is composed of two components,  $MC_h$ , from the majority hole current, and  $MC_R$  from the recombination current. When  $J_R \ll J \approx J_h$ , these two components are

$$MC_h = \frac{2P_1 P_2}{1 + P_1 P_2}$$

$$MC_R = \frac{J_R}{J_h} \frac{2P_1 P_2}{[1 - (P_1 P_2 \Delta b/2b)]^2} \frac{\Delta b}{b} \quad (3)$$

where  $J_h$  and  $J_R$  are given in Eq. 1 with  $\mu_R = (\mu_R^{\uparrow\uparrow} + \mu_R^{\uparrow\downarrow})/2$  and  $b = (b^{uu} + b^{ud})/2$ . Note that  $MC_h$  has the form of the Jullière formula (17) for a homopolar OSV, which is derived here for

the case of SCLC, whereas the new term  $MC_R$  is related to both electrode polarizations as well as the difference,  $\Delta b$ . For LSMO ( $P_1 \approx 1$ ) and Co/LiF [ $P_2 \approx 0.04$  at small  $V_b$  (Fig. 4F)],  $(P_1 P_2)^2 \approx 10^{-3} \ll 1$  and thus  $MC_h \approx 2P_1 P_2$ , whereas  $MC_R \approx 2P_1 P_2 (J_R/J_h)(\Delta b/b)$ . We conclude that both  $MC_h$  and  $MC_R$  are proportional to  $P_1 P_2$  and thus disappear in an OLED with non-FM electrodes.

The EL emission results from the radiative recombination of singlet excitons that emerge from their  $PP_S$  precursor. Thus, the EL intensity is directly proportional to the steady-state  $PP_S$  density  $N_{PPS}$ . The intermixing of  $PP_S \leftrightarrow PP_T$  means that  $N_{PPS}$  is determined by both singlet and triplet channels,

$$N_{PPS}^{\uparrow\uparrow(\uparrow\downarrow)} = \frac{R_S^{\uparrow\uparrow(\uparrow\downarrow)}}{\kappa_S} + \frac{R_T^{\uparrow\uparrow(\uparrow\downarrow)}}{\kappa_T} \quad (4)$$

where

$$R_{S(T)}^{\uparrow\uparrow(\uparrow\downarrow)} \propto \frac{b^{ud(uu)} J_e}{\mu_R^{\uparrow\uparrow(\uparrow\downarrow)}} \quad (5)$$

is the singlet (triplet) channel “recombination” (or PP formation) rate, and  $\kappa_{S(T)}$  designates the effective singlet (triplet) channel reaction rate, which is spin- and magnetization-independent. Using a rate equation approach to calculate  $N_{PPS}$ , we find

$$MEL = \frac{EL^{\uparrow\uparrow} - EL^{\uparrow\downarrow}}{EL^{\uparrow\uparrow}} = \frac{(\mu_R^{\uparrow\uparrow})^{-1} - (\mu_R^{\uparrow\downarrow})^{-1}}{(\mu_R^{\uparrow\uparrow})^{-1}}$$

$$= \frac{2P_1 P_2 \Delta b/2b}{1 + P_1 P_2 \Delta b/2b} \quad (6)$$

(see supplementary text). All spin-independent rates cancel out from the MEL expression. When comparing Eqs. 3 and 6, for bipolar OSV, MC and MEL have the same sign, and MEL is greater than MC by the factor  $J_h/J_R$  ( $\gg 1$ ).

Figure 4C shows two regimes in the  $MC_{SV}(V_b)$  response for the bipolar OSV. For  $V_b < V_0$  (i.e., the hole-only injection regime),  $MC_{SV}$  decreases by a factor of  $\sim 50$  between  $V_b \approx 0$  and  $V_b = 3.5$  V, similar to the homopolar OSV based on D-DOO-PPV (Fig. 4F). However, for  $V_b > V_0$  (i.e., the bipolar injection regime),  $MC_{SV}(V_b)$  is practically voltage-independent, unlike  $MC_{SV}(V_b)$  of the homopolar device (Fig. 4F). Note that  $EL_{SV}$  is also voltage-independent (Fig. 2C). We thus conclude that homopolar OSV devices become less efficient at large  $V_b$ , but less so for bipolar operation. Our SCLC model separates  $MC_{SV}$  into two different components: namely, the “homopolar MC” component ( $MC_h$  in Eq. 3) and the “recombination MC” component ( $MC_R$  in Eq. 3). We conjecture that the homopolar MC component decreases with  $V_b$ , whereas the recombination MC component does not depend on  $V_b$ . For  $V_b < V_0$ , the bipolar  $MC(V_b)$  response is dominated by the hole-only OSV that monotonically decreases with  $V_b$ . However, as bipolar injection sets in at  $V_0$ , the

voltage-independent  $MC_R$  takes over and the  $MC(V_b)$  response becomes  $V_b$ -independent. Simultaneously, MEL is given by Eq. 6 and thus is also independent of bias voltage. MC and MEL also have the same sign for  $V_b > V_0$ , as predicted by Eqs. 3 and 6. In addition, the obtained ratio  $MEL_{SV}/MC_{SV} \approx 25$  measured at  $V_b > 4$  V (Figs. 2C and 4C) is in agreement with the larger MEL predicted by our model, where  $MEL/MC \approx J_h/J_R \gg 1$ .

The performance of homopolar OSV devices severely degrades with  $V_b$  (7, 16, 19). Two possible mechanisms might explain this behavior: (i) a decrease of the spin injection efficiency of the electrodes with increasing  $V_b$  via the term  $P_1 P_2$ , and (ii) voltage-dependent processes that occur in the organic layer. Because both  $MC_h$  and  $MC_R$  are proportional to  $P_1 P_2$  (Eq. 3), but only  $MC_h$  degrades with  $V_b$ , we conjecture that the observed  $MC_{SV}(V_b)$  decrease cannot originate from a decrease of  $P_1 P_2$  dependence on  $V_b$ . By adding the screened Frenkel effect to the homopolar SCLC operation, the  $MC_{SV}(V_b)$  decrease was recently explained as arising from the magnetic field-dependent “screening length”  $\lambda_{sc}$  (25). Such a mechanism would not affect the “recombination current” in a bipolar OSV for electron-hole distances  $r < \lambda_{sc}$ , and this may explain the voltage-independent response of the spin-OLED.

Our results provide a pathway toward organic displays controlled by external magnetic fields, but such applications would require a larger MEL and room-temperature operation. These requirements might be achieved by choosing different FM electrodes and/or organic interlayers. Finally, we note the possibility of manipulating the EL emission colors in spin-OLEDs by an external magnetic field, unlike inorganic spin-LEDs.

## References and Notes

- G. Salis, S. F. Alvarado, M. Tschudy, T. Bruntschwiler, R. Allenspach, *Phys. Rev. B* **70**, 085203 (2004).
- V. A. Dediu, L. E. Hueso, I. Bergenti, C. Taliani, *Nat. Mater.* **8**, 707 (2009).
- V. Dediu, M. Murgia, F. C. Matocotta, C. Taliani, S. Barbanera, *Solid State Commun.* **122**, 181 (2002).
- Z. H. Xiong, D. Wu, Z. V. Vardeny, J. Shi, *Nature* **427**, 821 (2004).
- A. H. Davis, K. Bussmann, *J. Appl. Phys.* **93**, 7358 (2003).
- I. Bergenti *et al.*, *Org. Electron.* **5**, 309 (2004).
- T. D. Nguyen *et al.*, *Nat. Mater.* **9**, 345 (2010).
- L. Schulz *et al.*, *Nat. Mater.* **10**, 39 (2011).
- R. H. Parmenter, W. Ruppel, *J. Appl. Phys.* **30**, 1548 (1959).
- M. Yunus, P. P. Ruden, D. L. Smith, *Appl. Phys. Lett.* **93**, 123312 (2008).
- J. Kalinowski, M. Cocchi, D. Virgili, P. Di Marco, V. Fattori, *Chem. Phys. Lett.* **380**, 710 (2003).
- O. Mermer *et al.*, *Phys. Rev. B* **72**, 205202 (2005).
- M. Wohlgenannt, K. Tandon, S. Mazumdar, S. Ramasesha, Z. V. Vardeny, *Nature* **409**, 494 (2001).
- H. Ishii, K. Seki, *IEEE Trans. Electron. Dev.* **44**, 1295 (1997).
- Y. Q. Zhan *et al.*, *Appl. Phys. Lett.* **94**, 053301 (2009).
- C. Barraud *et al.*, *Nat. Phys.* **6**, 615 (2010).
- M. Jullière, *Phys. Lett. A* **54**, 225 (1975).
- H. Vinzelberg *et al.*, *J. Appl. Phys.* **103**, 093720 (2008).
- J.-W. Yoo *et al.*, *Phys. Rev. B* **80**, 205207 (2009).
- S. Majumdar, H. S. Majumdar, R. Laiho, R. Osterbacka, *J. Alloy. Comp.* **423**, 169 (2006).
- F. J. Wang, C. G. Yang, Z. V. Vardeny, X. G. Li, *Phys. Rev. B* **75**, 245324 (2007).
- V. Dediu *et al.*, *Phys. Rev. B* **78**, 115203 (2008).
- J. H. Park *et al.*, *Phys. Rev. Lett.* **81**, 1953 (1998).



24. P. N. Murgatroyd, *J. Phys. D* **3**, 151 (1970).  
 25. D. Sun *et al.*, *Phys. Rev. Lett.* **104**, 236602 (2010).

**Acknowledgments:** Supported by NSF grant DMR-1104495 and MRSEC, DMR-1121252 program at the UoU (T.D.N. and Z.V.V.), Israel Science Foundation grant ISF 472/11 (E.E.), and Israel-USA BSF grant 2010135 (Z.V.V. and E.E.). The D-DOO-PPV

polymer synthesis was supported by U.S. Department of Energy grant DE-FG02-04ER46109. We thank X.-G. Li (USTC) for providing the LSMO substrates. The authors declare no conflict of interest associated with this work. A patent disclosure related to the spin-OLED invention was recently filed with the University of Utah, disclosure no. 5249, which has been filed as a provisional patent application.

## Supplementary Materials

www.sciencemag.org/cgi/content/full/337/6091/204/DC1  
 Supplementary Text  
 Figs. S1 to S5

17 April 2012; accepted 31 May 2012  
 10.1126/science.1223444

# Dislocation-Driven Deformations in Graphene

Jamie H. Warner,<sup>1\*</sup> Elena Roxana Margine,<sup>1</sup> Masaki Mukai,<sup>2</sup> Alexander W. Robertson,<sup>1</sup> Feliciano Giustino,<sup>1</sup> Angus I. Kirkland<sup>1</sup>

The movement of dislocations in a crystal is the key mechanism for plastic deformation in all materials. Studies of dislocations have focused on three-dimensional materials, and there is little experimental evidence regarding the dynamics of dislocations and their impact at the atomic level on the lattice structure of graphene. We studied the dynamics of dislocation pairs in graphene, recorded with single-atom sensitivity. We examined stepwise dislocation movement along the zig-zag lattice direction mediated either by a single bond rotation or through the loss of two carbon atoms. The strain fields were determined, showing how dislocations deform graphene by elongation and compression of C-C bonds, shear, and lattice rotations.

The two-dimensional (2D) structure of graphene provides unusual mechanical (1) and electronic properties (2), which can be influenced by defects and dislocations (3, 4). Defects and strain can lead to spin and magnetism in graphene that may be important for extending graphene's electronic applications to spin-based technology (5, 6). Understanding how dislocations deform graphene helps build an accurate description of both elasticity and plasticity in graphene (7–9). Studying dislocation movement (creep and climb), the interaction between dislocation pairs, and how the strain fields respond is key for developing complete structural models of graphene. So far, deep insights into dislocations in graphene have been primarily from a theoretical perspective (10–12).

Experimental investigation of dislocations in graphene at the atomic level needs high-resolution imaging, with spatial resolution sufficient to unambiguously resolve individual carbon atoms. Low-voltage transmission electron microscopy (TEM) can resolve the lattice structure of carbon-based materials such as graphitic nanomaterials and graphene (13–19) with high contrast and minimal damage. Improvement in the information limit in high-resolution TEM (HRTEM) requires the reduction of both spherical and chromatic aberration, with the latter having a notable effect at low voltages. Spherical aberration correction in HRTEM, combined with low accelerating voltage operation to reduce knock-on damage [at less than 90 kV (20)], enables

imaging of light-element atoms (including C, B, and N) in nanomaterials and molecules (14).

To image single-carbon atom dynamics in graphene using HRTEM, sufficient information transfer to unambiguously resolve the atomic positions is necessary. At low accelerating voltage, this cannot be achieved by spherical aberration correction alone and requires reducing chromatic aberration. Electron optical correction of chromatic aberration has been successfully reported (21, 22). Alternatively, the use of a monochromator to reduce the energy spread in the incident electron beam provides a way of limiting chromatic effects (23). There have been several reports of HRTEM imaging of graphene both with (24) and without (25, 26) monochromation at an accelerating voltage of 80 kV, but only relatively small differences in the resolution of images have been demonstrated. Indirect exit-wave reconstruction has also been used to characterize a fully resolved atomic structure for a monolayer/bilayer interface (27). However, this technique requires numerous images to generate the complex exit wave and is thus not suitable for the investigation of real-time single-atom dynamics, which are essential for monitoring structural transformations.

In this paper, we present low-voltage HRTEM imaging of dislocation dynamics in graphene, using both spherical aberration correction and monochromation of the electron beam using a double Wien filter (figs. S1 to S4). Graphene samples were prepared using chemical vapor deposition (CVD) on copper foils (28) and were transferred onto silicon nitride TEM grids with 2- $\mu$ m holes (see the supplementary materials for details) (29).

Figure 1A shows a single HRTEM image of monolayer graphene containing a pair of edge

dislocations aligned in opposite directions with (1,0) form, consisting of a pentagon-heptagon pair (10). Previous work has suggested the presence of a single dislocation in graphene (19) and a pair of dislocations in reduced graphene oxide (30), but the image resolution in those studies was not sufficient to resolve the individual atomic positions required to determine the exact structure. Figure 1B shows an atomic model, and Fig. 1C shows the multislice HRTEM image simulation for the dislocation pair observed in Fig. 1A.

There are five possible mechanisms that describe how these dislocation pairs could have formed: during the CVD growth, electron beam sputtering of carbon dimers along a zig-zag lattice direction, from surface adatom incorporation, from a mono vacancy, or from a Stone-Wales defect (figs. S5 to S7). Initial observation of the area of the sample in Fig. 1 showed that it was free from dislocations and monovacancies (fig. S8), which indicates that the dislocations were

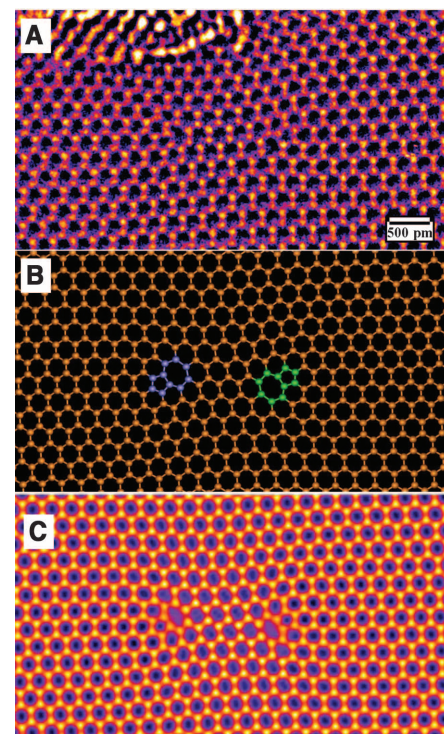


**Fig. 1.** Imaging edge dislocations. (A) HRTEM image showing two opposing (1,0) edge glide dislocations in graphene. (B) Structural model representing the dislocation pair (blue and green) in (A). (C) HRTEM image simulations using the atomic model in (B) as a supercell. False color is used for the images to aid visual inspection.

<sup>1</sup>Department of Materials, University of Oxford, Parks Road, Oxford OX1 3PH, UK. <sup>2</sup>JEOL, 3-1-2 Musashino, Akishima, Tokyo 196-8558, Japan.

\*To whom correspondence should be addressed. E-mail: jamie.warner@materials.ox.ac.uk



formed after synthesis, probably through energy supplied by electron beam irradiation. The dislocation pairs we observed did not share a common glide plane, indicating that one dislocation had moved along the armchair direction at some stage. This process is known to stabilize dislocation dipoles and prevent their rapid annihilation (7).

Having two dislocations in graphene leads to strain fields that depend on their separation. We mapped the strain fields using the geometric phase analysis (GPA) method (31). Figure 2A shows a HRTEM image of a pair of dislocations in graphene, and Fig. 2B shows the corresponding GPA phase map obtained from Bragg spot *b* (fig. S9i). The phase map has two discontinuities of  $2\pi$ , which is typical of dislocations (31). The strain tensor was made symmetric, leading to strain fields  $\epsilon_{xx}$ ,  $\epsilon_{xy}$ , and  $\epsilon_{yy}$ , and a rotation  $\omega$  (in radians), shown in Fig. 2, C to F, respectively. The color scale mapping (Fig. 2C) has range  $-1$  (black) to  $+1$  (white). The strain  $\epsilon_{xy}$  (Fig. 2D) corresponds to shear with values ranging from  $\sim 8$  to  $77\%$  at distances of  $0.1$  to  $0.02$  nm from the dislocation core. The lattice rotation (Fig. 2F) has values ranging from  $\sim 15^\circ$  to  $\sim 63^\circ$  at distances of  $0.1$  to  $0.02$  nm from the dislocation core. The strain maps in Fig. 2 show that the strain fields from each dislocation core extend far enough to intersect. A similar analysis of regions of graphene containing closed loops of heptagons and pentagons did not produce such extended strain, and examination of pairs of dislocations with different separation lengths revealed the extent of the intersection (figs. S9 to S11). We compared the 2D profile of the strain fields to those predicted by the isotropic elastic, Peierls-Nabarro (PN), and Foreman (FM) dislocation theory models (fig. S12). The dislocations in graphene can be described by a PN model, but improvement is seen with the FM model, with fitting parameter of  $a = 1.5$  (figs. S13 and S14).

During imaging, once the dislocation pair appeared (Fig. 3, A to D), it remained stable for 129 s under electron beam irradiation before a rapid transformation within 1 to 2 s to a new stable configuration (Fig. 3, B and E). This transformation corresponds to the minimum step single bond rotation along the zig-zag lattice direction, similar to dislocation creep. The dislocations remained stable in this configuration for a further 180 s and then rapidly transformed by the loss of two carbon atoms to move horizontally along the zig-zag lattice direction (Fig. 3, C and F), similar to dislocation climb. Tracking of the strain fields with dislocation movement showed that they remained focused around the dislocation cores and the central region between them (fig. S15).

We used density functional theory (DFT) in order to gain insights into the formation energy and bond lengths of the observed dislocation pair. The experimental studies have shown that a stable dislocation pair requires a mixture of glide (Stone-Wales bond rotation) and climb (removal

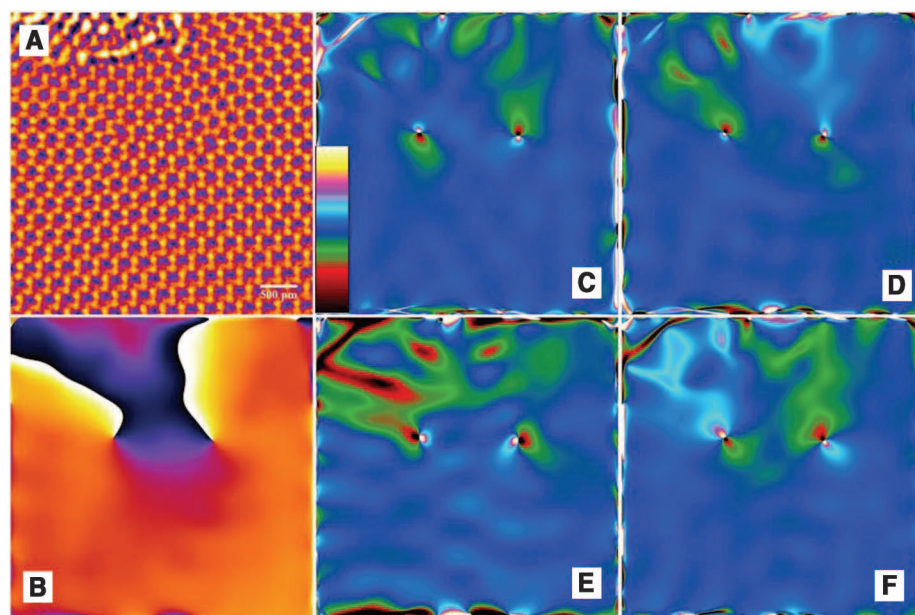


**Fig. 2.** Strain field mapping. (A) HRTEM image of a dislocation pair in graphene. GPA was applied to the HRTEM image in (A) to determine (B) the phase map, (C)  $\epsilon_{xx}$ , (D)  $\epsilon_{xy}$ , (E)  $\epsilon_{yy}$ , and (F) rotation (in radians). The color scale for (C) to (F) is shown in (C), with a range of  $-0.5$  (black) to  $+0.5$  (white). For the phase map in (B), the color map is black ( $0$ ) to white ( $2\pi$ ).

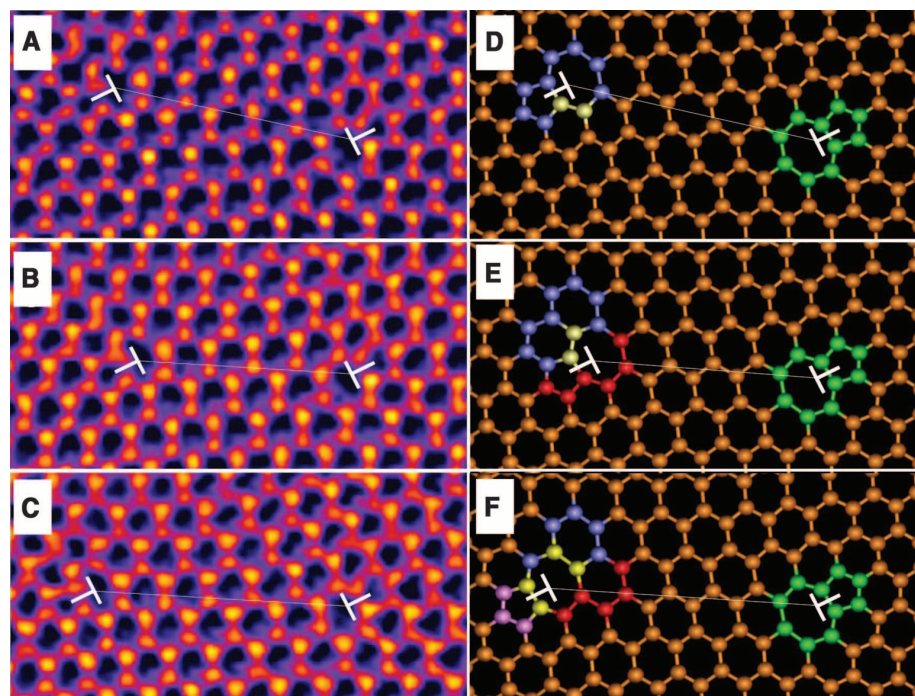


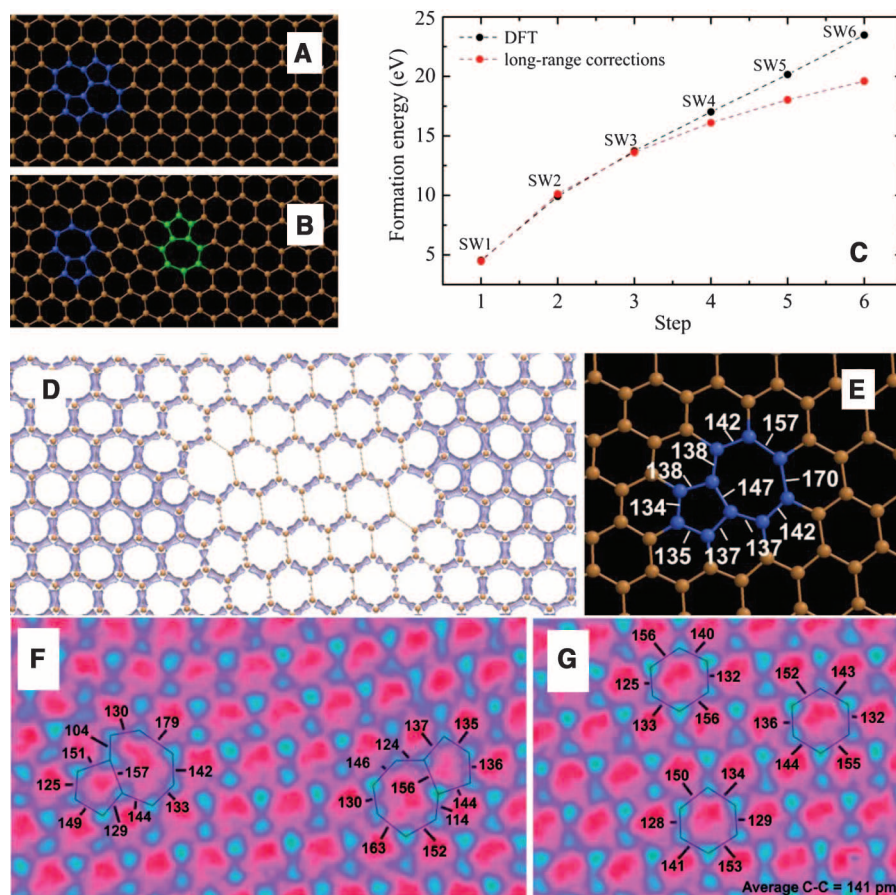
**Fig. 3.** Real-time dislocation dynamics. HRTEM images showing changes in the position of an edge glide dislocation with time under continuous electron beam irradiation. (A) Time =  $0$  s. (B) Time =  $141$  s. (C) Time =  $321$  s. (D to F) Atomic models illustrating the structures inferred from (A) to (C), respectively. The white T indicates the position of dislocation.

of two atoms) processes. These two mechanisms enable a pentagon-heptagon pair to migrate through a 2D lattice as a composite object. Our calculations of various stages of separated dislocation pairs in pristine graphene mediated by Stone-Wales bond rotations (Fig. 4, A to C) revealed

that for each subsequent step, the formation energy increase is at most  $5.4$  eV. The DFT formation energies of these structures for up to six bond rotations are shown in Fig. 4C as black dots. The formation energies incorporating corrections for long-range strain field interactions



**Fig. 4.** (A and B) Atomistic models obtained within DFT for one and four Stone-Wales bond rotations (steps 1 and 4). (C) Formation energy at each step (one dislocation is stationary and the other one is moving along the glide direction). The black dots represent the DFT data. The red dots represent the DFT data corrected for long-range strain-field interactions. (D) Total charge density of the structure shown in Fig. 3B. (E) C-C bond lengths in picometers for the structure in Fig. 4D extracted from the DFT calculations. (F) HRTEM image [Ice color look-up table (LUT)] of a dislocation pair with measurements of bond lengths in picometers. (G) HRTEM image (ice color LUT) of pristine graphene with measurement of bond lengths in picometers. The average C-C bond length was determined as  $141 \pm 10$  pm.



between periodic replicas of the dislocation pairs are shown by red dots in the same figure (fig. S16). The calculation details are provided in the supplementary materials. Another way of splitting two pentagon-heptagon dipoles in graphene consists of removing one carbon dimer at a time along the zig-zag direction. The formation energies involved in these processes are similar to those calculated here [see Jeong *et al.* (12)]. At each transition step (bond rotation or dimer removal), an energy activation barrier must be overcome. For a bond rotation (glide step), the energy barrier lies in the range of 5 to 10 eV, depending on the local atomic configuration of the  $sp^2$ -bonded carbon structure (20, 32). For each climb step, the energy barrier to remove a carbon dimer from the side of a pentagon is in the range of 9 to 12 eV (33). Overall, these energy barriers are comparable with the energy that is transferred by 80-keV electrons to carbon atoms, and therefore the processes described here are viable.

We calculated the formation energy of the dislocation pair in Fig. 1A to be 30.6 eV. Long-range strain-field corrections (Fig. 4C) reduce this to 26.7 to 28.5 eV. Our DFT formation energy is comparable with those reported for a dislocation obtained by removing a zig-zag carbon chain and for a haeckelite structure, when the number of missing carbon atoms is the same (12). The presence of the structural defects causes

elongation of the C-C bonds of the hexagons between the two dislocation dipoles (average bond length, 147 pm) and a substantial depletion of charge in this region (Fig. 4D). Overall, the bond length values vary from 134 to 170 pm for the pentagon-heptagon pair and from 136 pm to 141 pm in the graphene region with the lowest strain. The longest bond of the heptagon rings of 170 pm is similar to the 168 pm value reported in (12) for the dislocation structure with 10 vacancy units. All the bond lengths in our pentagon-heptagon dipole are shown in Fig. 4E.

Figure 4F shows an experimental HRTEM image with direct measurements of the bond lengths for a dislocation pair. The left dislocation has bond lengths from 104 to 179 pm, and the right from 114 to 163 pm. Bond lengths measured in regions of graphene where the elastic strain was minimal (Fig. 4G) were between 125 and 156 pm (hexagon 1), 132 and 155 pm (hexagon 2), and 128 and 153 pm (hexagon 3), yielding an average of  $141 \pm 10$  pm, which agrees well with expected values. This corresponds to a maximum of 26% compression and 27% elongation of certain individual C-C bonds. The bonds with contraction or elongation are at the same position in each dislocation. The position of elongation matches that predicted by DFT, with some discrepancies likely to arise from possible warping and rippling of the graphene. Bond elongation cannot mistakenly arise because of a 2D projec-

tion of an out-of-plane distortion, such as rippling, and therefore is real.

We have shown that edge dislocations result in substantial deformation of the atomic structure of graphene, with bond compression or elongation of  $\pm 27\%$ , plus shear strain and lattice rotations. If dislocation pairs are separated by less than 1.5 nm, the individual strain fields associated with each dislocation core intersect, and the presence of one dislocation affects the other. Energy from electron beam irradiation induced variation in the distance between the two dislocations in the pair, and tracking of the strain field showed that it remained localized around the core. Monochromatization of the electron beam for HRTEM using a double Wien filter led to substantially improved image resolution that enabled the position of single carbon atoms to be accurately mapped.

#### References and Notes

1. C. Lee, X. Wei, J. W. Kysar, J. Hone, *Science* **321**, 385 (2008).
2. K. S. Novoselov *et al.*, *Science* **306**, 666 (2004).
3. A. Mesaros, D. Sadri, J. Zaanen, *Phys. Rev. B* **79**, 155111 (2009).
4. J.-H. Chen, L. Li, W. G. Cullen, E. D. Williams, M. S. Fuhrer, *Nat. Phys.* **7**, 535 (2011).
5. R. R. Nair *et al.*, *Nat. Phys.* **8**, 199 (2012).
6. N. Levy *et al.*, *Science* **329**, 544 (2010).
7. A. Carpio, L. L. Bonilla, *Phys. Rev. B* **78**, 085406 (2008).
8. S. Chen, D. C. Chrzan, *Phys. Rev. B* **84**, 214103 (2011).

9. R. Grantab, V. B. Shenoy, R. S. Ruoff, *Science* **330**, 946 (2010).
10. O. V. Yazyev, S. G. Louie, *Phys. Rev. B* **81**, 195420 (2010).
11. E. Cockayne *et al.*, *Phys. Rev. B* **83**, 195425 (2011).
12. B. W. Jeong, J. Ihm, G.-D. Lee, *Phys. Rev. B* **78**, 165403 (2008).
13. J. H. Warner, N. P. Young, A. I. Kirkland, G. A. D. Briggs, *Nat. Mater.* **10**, 958 (2011).
14. O. L. Krivanek *et al.*, *Nature* **464**, 571 (2010).
15. K. Suenaga, M. Koshino, *Nature* **468**, 1088 (2010).
16. J. Kotakoski, A. V. Krashenninnikov, U. Kaiser, J. C. Meyer, *Phys. Rev. Lett.* **106**, 105505 (2011).
17. J. C. Meyer *et al.*, *Nat. Mater.* **10**, 209 (2011).
18. P. Y. Huang *et al.*, *Nature* **469**, 389 (2011).
19. A. Hashimoto, K. Suenaga, A. Gloter, K. Urita, S. Iijima, *Nature* **430**, 870 (2004).
20. F. Banhart, J. Kotakoski, A. V. Krashenninnikov, *ACS Nano* **5**, 26 (2011).
21. B. Kabius *et al.*, *J. Electron Microsc. (Tokyo)* **58**, 147 (2009).
22. M. Haider, P. Hartel, H. Müller, S. Uhlemann, J. Zach, *Microsc. Microanal.* **16**, 393 (2010).
23. M. Mukai *et al.*, *Microsc. Microanal.* **11**, 2134 (2005).
24. J. C. Meyer *et al.*, *Nano Lett.* **8**, 3582 (2008).
25. J. H. Warner *et al.*, *Nat. Nanotechnol.* **4**, 500 (2009).
26. Z. Liu, K. Suenaga, P. J. F. Harris, S. Iijima, *Phys. Rev. Lett.* **102**, 015501 (2009).
27. J. R. Jinschek, E. Yucelen, H. A. Calderon, B. Freitag, *Carbon* **49**, 556 (2011).
28. X. Li *et al.*, *Science* **324**, 1312 (2009).
29. A. W. Robertson *et al.*, *ACS Nano* **5**, 6610 (2011).
30. C. Gómez-Navarro *et al.*, *Nano Lett.* **10**, 1144 (2010).
31. M. J. Hÿtch, E. Snoeck, R. Kilaas, *Ultramicroscopy* **74**, 131 (1998).
32. Y. Kim, J. Ihm, E. Yoon, G.-D. Lee, *Phys. Rev. B* **84**, 075445 (2011).
33. F. Ding, K. Jiao, Y. Lin, B. I. Yakobson, *Nano Lett.* **7**, 681 (2007).

**Acknowledgments:** J.H.W. thanks the Royal Society and Balliol College for support. Financial support from the Engineering and Physical Sciences Research Council (grant EP/F028784/1) is gratefully acknowledged. E.R.M. was funded by Marie Curie Intra-Euronpean Fellowships project

FP7-PEOPLE-2009-IEF-252586. F.G. acknowledges support from the European Research Council under EU FP7/ERC grant no. 239578. J.H.W. produced the samples; performed the HRTEM, GPA analysis, image simulations, and dislocation theory; analyzed the results; and wrote the paper. M.M. developed and installed the monochromator. A.I.K. developed the HRTEM methods and assisted with the analysis and writing the paper. A.W.R. assisted with the GPA analysis and HREM image simulations. E.R.M. and F.G. designed and analyzed the calculation and assisted with writing the paper. E.R.M. performed the calculations.

#### Supplementary Materials

www.sciencemag.org/cgi/content/full/337/6091/209/DC1  
Materials and Methods  
Supplementary Text  
Figs. S1 to S16  
References (34–47)

6 December 2011; accepted 10 May 2012  
10.1126/science.1217529

# A Reduced Organic Carbon Component in Martian Basalts

A. Steele,<sup>1\*</sup> F. M. McCubbin,<sup>1,2</sup> M. Fries,<sup>3</sup> L. Kater,<sup>4</sup> N. Z. Boctor,<sup>1</sup> M. L. Fogel,<sup>1</sup> P. G. Conrad,<sup>5</sup> M. Glamoclija,<sup>1</sup> M. Spencer,<sup>6</sup> A. L. Morrow,<sup>6</sup> M. R. Hammond,<sup>6</sup> R. N. Zare,<sup>6</sup> E. P. Vicenzi,<sup>7</sup> S. Siljeström,<sup>8,9</sup> R. Bowden,<sup>1</sup> C. D. K. Herd,<sup>10</sup> B. O. Mysen,<sup>1</sup> S. B. Shirey,<sup>11</sup> H. E. F. Amundsen,<sup>12</sup> A. H. Treiman,<sup>13</sup> E. S. Bullock,<sup>14</sup> A. J. T. Jull<sup>15</sup>

The source and nature of carbon on Mars have been a subject of intense speculation. We report the results of confocal Raman imaging spectroscopy on 11 martian meteorites, spanning about 4.2 billion years of martian history. Ten of the meteorites contain abiotic macromolecular carbon (MMC) phases detected in association with small oxide grains included within high-temperature minerals. Polycyclic aromatic hydrocarbons were detected along with MMC phases in Dar al Gani 476. The association of organic carbon within magmatic minerals indicates that martian magmas favored precipitation of reduced carbon species during crystallization. The ubiquitous distribution of abiotic organic carbon in martian igneous rocks is important for understanding the martian carbon cycle and has implications for future missions to detect possible past martian life.

Organic carbon in macromolecular reduced form has been detected in several martian meteorites, but there is little agreement on its provenance on Mars. Hypotheses for its origin include terrestrial contamination (1, 2), chondritic meteoritic input (3), thermal decomposition of carbonate minerals (4–6), direct precipitation from aqueous fluids (4), and the remains of ancient biota (7). Confirming the presence and understanding the source and formation of this reduced carbon has implications for the carbon budget of Mars, its putative carbon cycle, carbon availability for biotic chemistry, life detection, and how to detect organic compounds on future Mars missions.

Eleven martian meteorites, including samples of the recent Tissint meteorite fall, were studied with confocal Raman imaging spectroscopy (CRIS). Macromolecular carbon (MMC) was identified in 10 of these meteorites associated with small (2 to 20  $\mu\text{m}$ ) metal oxide grains (hereafter referred to as spinel or oxide) that are

ubiquitous as inclusions within olivine and/or pyroxene grains (Fig. 1 and fig. S1) (8). All of the MMC that we report here was located at least several microns below the top surface of the thin sections we analyzed (Fig. 1). The association of MMC with spinel is observed in recent falls (Tissint and Zagami), as well as older finds (DaG 476 and SAU 019) (table S1), making it unlikely to be terrestrial contamination (9).

MMC is characterized by the diagnostic disordered “D” Raman peak at  $\sim 1350$  and the graphitic ordered peak at  $\sim 1590\text{ cm}^{-1}$  (Fig. 2, A and B) (10, 11). MMC was initially detected within olivine-hosted melt inclusions in DaG 476 in association with oxide and pyroxene (table S1). DaG 476 is an olivine-phyric shergottite with olivine comprising 15 to 17% of the mode (fig. S1, A to E) (12). The oxides are fine-grained spinel-group minerals that appear to be magnetite or chromite based on the Raman peak positions. They are distributed throughout the olivine with enough grains below the surface to allow study

of associated MMC that is completely encased within a silicate host (Fig. 1, A to F). With a combination of transmitted and reflected light, we determined the distance from the oxides to the surface and confirmed their isolation from any visible cracks (Fig. 1G). Figure 1G shows a three-dimensional (3D) CRIS depth profile of MMC occurring with spinel at a distance of 5 to 10  $\mu\text{m}$  into the surface of DaG 476. Scanning electron microscopic (SEM) investigations of DaG 476 and SAU 130 showed oxides containing a carbon film that is texturally and chemically consistent with the MMC observed by CRIS (fig. S3) and is neither carbonate nor terrestrial microbial contamination (12–14).

Transmitted-light microscopy images and CRIS peak maps of a number of oxide grains hosted by pyroxenes in ALH 84001 and olivines from northwest Africa (NWA) 1110 demonstrate the co-occurrence of MMC phases with oxides in other meteorites analyzed (Fig. 1, H and I). In the

<sup>1</sup>Geophysical Laboratory, Carnegie Institution of Washington, 5251 Broad Branch Road, NW, Washington, DC 20015, USA.

<sup>2</sup>Institute of Meteoritics, Department of Earth and Planetary Sciences, University of New Mexico, Albuquerque, NM 87131, USA. <sup>3</sup>Planetary Science Institute, 1700 East Fort Lowell, Suite 106, Tucson, AZ 85719, USA. <sup>4</sup>Witec GmbH, Lise-Meitner-Strasse 6, D-89081, Ulm, Germany. <sup>5</sup>NASA Goddard Space Flight Centre, 8800 Greenbelt Road, Greenbelt, MD 20771, USA. <sup>6</sup>Department of Chemistry, Stanford University, Stanford, CA 94305, USA. <sup>7</sup>Museum Conservation Institute, Smithsonian Institution, 4210 Silver Hill Road, Suitland, MD 20746, USA. <sup>8</sup>Department of Geological Sciences, Stockholm University, 10691 Stockholm, Sweden. <sup>9</sup>Department of Chemistry and Materials, SP Technical Research Institute of Sweden, 501 15 Borås, Sweden. <sup>10</sup>Department of Earth and Atmospheric Sciences, University of Alberta, Edmonton, AB T6G 2E3, Canada. <sup>11</sup>Department of Terrestrial Magnetism, Carnegie Institution of Washington, 5241 Broad Branch Road, NW, Washington, DC 20015, USA. <sup>12</sup>Earth and Planetary Exploration Services, Jacob Aals Gate 44b, 0364 Oslo, Norway. <sup>13</sup>Lunar and Planetary Institute, 3600 Bay Area Boulevard, Houston, TX 77058, USA. <sup>14</sup>Department of Mineral Sciences, Smithsonian Institution, Washington, DC 20013–7012, USA. <sup>15</sup>University of Arizona, 1118 East Fourth Street, Tucson, AZ 85721, USA.

\*To whom correspondence should be addressed. E-mail: astelee@ciw.edu



case of NWA 1110 (Fig. 1), the oxides are zoned with chromite cores and iron-rich (magnetite) rims, with MMC predominantly associated with the chromite phase. In general, two types of associations were observed: (i) pyroxene + oxide + MMC hosted in olivine and (ii) oxide + MMC hosted in pyroxene. Minor phases such as pyrrhotite and apatite are sometimes observed.

We have used the G-band peak center and full width at half maximum (FWHM) to indicate the maturity level and crystallinity of MMC (15, 16). The MMC data (Fig. 2B) show a large range of G-band peak shapes and on the whole are indicative of amorphous to poorly ordered graphitic carbon in the range recorded for carbonaceous chondrites and interplanetary dust particles (IDPs) (16). The MMC in Tissint and Zagami appears to have a higher degree of graphitic order than that seen in the other martian meteorites except NWA 1110. Within individual meteorites (i.e., ALH 84001 and DaG 476), there is substantial variation in the G-band parameters (Fig. 2B). This variation may indicate different formation conditions or mild heating after MMC formation.

To further elucidate the chemical composition of the amorphous to poorly ordered graphitic carbon measured by CRIS, we conducted laser desorption laser ionization mass spectrometry ( $L^2MS$ ) analysis (17) on exposed olivine phenocrysts from a crushed sample of DaG 476 to identify any possible polycyclic aromatic hy-

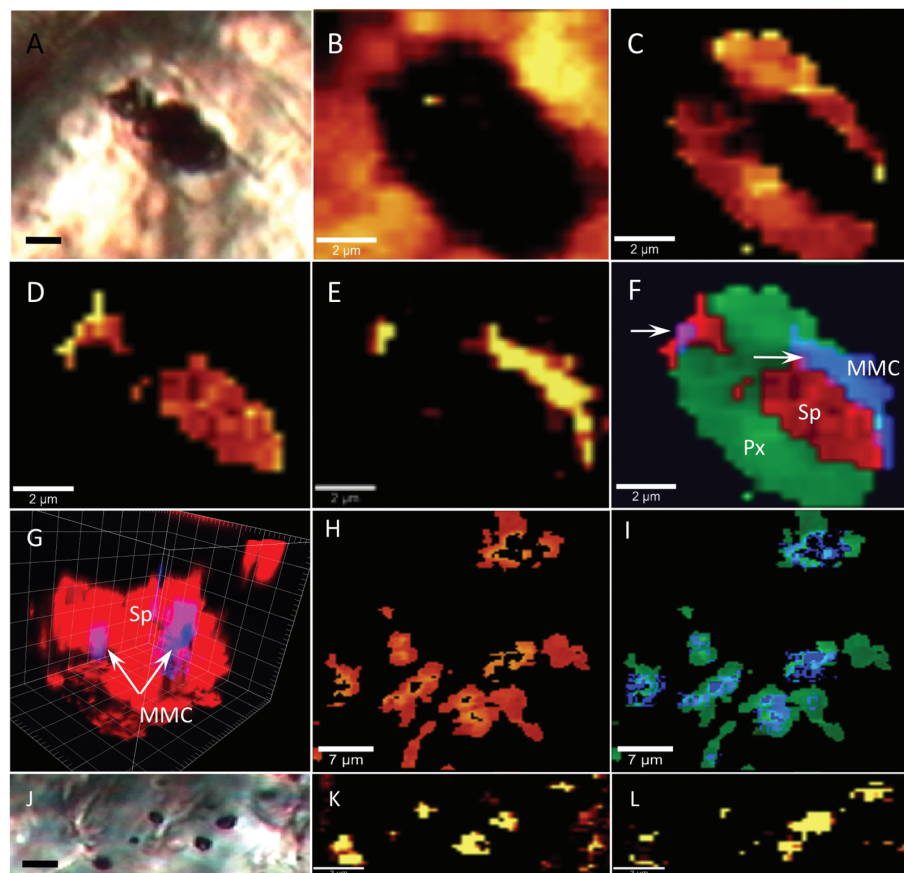
drocarbons (PAHs) associated with the MMC (9). Compared with MMC extracted from a Murchison reference standard and several controls, DaG 476 contains a range of PAHs, including phenanthrene (and alkylated derivatives), pyrene, perylene, and anthracene similar to that seen in the Murchison meteorite (fig. S4). Apart from chrysene, the major PAH molecules observed are similar to those seen previously in ALH 84001 (7), although the degree of alkylation of phenanthrene is more pronounced in DaG 476. The degree of alkylation of phenanthrene has been used as an indicator of parent-body processing in carbonaceous chondrites and does not necessarily represent an indicator of biogenicity or contamination (7, 18). Substantial PAHs were not present on the surface of the samples or controls and were only detected when the inclusions were revealed after etching of the silicate minerals. Furthermore, the controls show that no PAHs were added to the samples during analysis (9). The lack of dibenzothiophene (184 atomic mass units), a ubiquitous contaminant associated with PAHs from terrestrial sources, also indicates that the PAHs measured were not terrestrial (7). Previous studies of the MMC of carbonaceous chondrites by  $L^2MS$  and CRIS show similar PAH distributions and Raman G-band parameters to those observed in the present study (18, 19). Thus, the PAHs found in DaG 476 must be indigenous to this meteorite and a component of

the MMC detected by Raman spectroscopy. We expect that PAHs are a probable constituent of the MMC found in the other martian meteorites analyzed.

The presence of PAHs in the martian meteorites we studied is in accord with current models and observations documenting MMC and PAH synthesis over a diverse range of pressure and temperature conditions, including temperatures  $>3000$  K in the solar nebula and 1400 K in industrial blast furnaces (20). The distribution of PAHs and MMC alone cannot distinguish whether the carbon was produced biologically or abiotically (21); thus, textural relationships between MMC and any coexisting mineral phases become paramount to determining the possible mechanism of formation and incorporation in crystallizing silicates. Because MMC was always associated with igneous phases, we conclude that it crystallized from the host magma. This textural relationship negates any biological origin of the MMC and PAHs.

We analyzed bulk samples of DaG 476, SAU 130, and Dhofar 019 for  $^{14}C$  (table S1) (9) to determine the presence of a young (terrestrial) C component. The  $^{14}C$  measurements suggest that although modern terrestrial carbon was present in all the meteorites, there was also a portion of organic carbon that is probably indigenous to Mars (9), which is consistent with previous results from Nakhla and ALH 84001 (1, 22, 23).

**Fig. 1.** (A) Transmitted-light image of a single inclusion 4  $\mu m$  below the surface of DaG 476 (scale bar, 3  $\mu m$ ). (B to F) Raman maps of the same inclusion as (A) (the lighter the color, the more intense the mapped peak). (B) Olivine ( $\sim 820$   $cm^{-1}$ ), (C) pyroxene ( $\sim 1005$   $cm^{-1}$ ), (D) spinel-group oxide ( $\sim 670$   $cm^{-1}$ ), (E) MMC (carbon G-band  $1580$   $cm^{-1}$ ), (F) red-green-blue color image. Green, Px, pyroxene; red, Sp, spinel-group oxide; blue, MMC. White arrows show the joint occurrence of oxides and MMC. (G) A CRIS 3D depth profile through a melt inclusion 5 to 20  $\mu m$  into the sample surface within DaG 476. Red, Sp, spinel-group oxide; blue, MMC (grid is in 2- $\mu m$  increments). MMC is visualized as blue when in isolation and as purple when with oxides. (H) Raman peak images of peak center shift map of oxide from 660 to 720  $cm^{-1}$  (lighter orange, higher wave number, more chromite rich; darker orange, lower wave number, magnetite rich) in inclusions in NWA1110 (scale bar 7  $\mu m$ ). (I) Blue-green image of peak center shift map showing the occurrence of MMC with higher-wave number chromite-rich phase. Blue, MMC; green, spinel-group oxide. (J) Transmitted-light image of inclusions within pyroxenes in ALH 84001. Scale bar, 3  $\mu m$ . (K and L) Raman peak maps of (K) spinel-group oxide and (L) MMC. Scale bars, 3  $\mu m$ .



The stable carbon isotope compositions ( $\delta^{13}\text{C}$ ) for Zagami, NWA 998, SaU 130, and DaG 476 are consistent with previous results of MMC in martian meteorites (24); however, our results averaged  $\sim 16$  parts per million (ppm) C for the shergottites, about four times as much as previous results (24) (table S1). This difference is consistent for both falls and finds and may be due to differences in analytical techniques, interference from low levels of terrestrial contamination, or sample heterogeneity.

The Tissint meteorite, which fell in July 2011 in the Moroccan desert, represented a unique opportunity to study a minimally contaminated

martian sample. It has 14 ppm of reduced C with a  $\delta^{13}\text{C}$  of  $-17.8 \pm 1.9$  per mil (‰), similar to the other martian meteorites. The similarity of the C content and  $\delta^{13}\text{C}$  of Tissint with the other martian meteorites and the presence of C without substantial  $^{14}\text{C}$  supports the finding that much of its carbon is of martian origin. Combining ours and other studies, igneous martian rocks could contain an average of  $\sim 20 \pm 6$  ppm of reduced carbon with a  $\delta^{13}\text{C}$  of  $\sim -19.8 \pm 4.3\%$ . Grady *et al.*, (24) speculated that the carbon they detected was along grain boundaries and within silicate inclusions. Our in situ and bulk investigations corroborate their findings and suggest that some of the carbon

occurs as a PAH-containing MMC phase within mineral-hosted crystalline melt inclusions.

The MMC-bearing oxides are fully encapsulated in igneous crystals of olivine and/or pyroxene, suggesting that such oxides are also igneous in origin. Inclusions consisting primarily of oxide (+MMC) are likely microphenocrysts encapsulated by the growing silicate crystals, whereas multiphase inclusions represent melt inclusions with oxide microphenocrysts (Fig. 3). The disordered nature of the MMC and the presence of PAHs in the MMC-containing assemblages indicate that the MMC precipitated in contact with the oxides as an insoluble organic

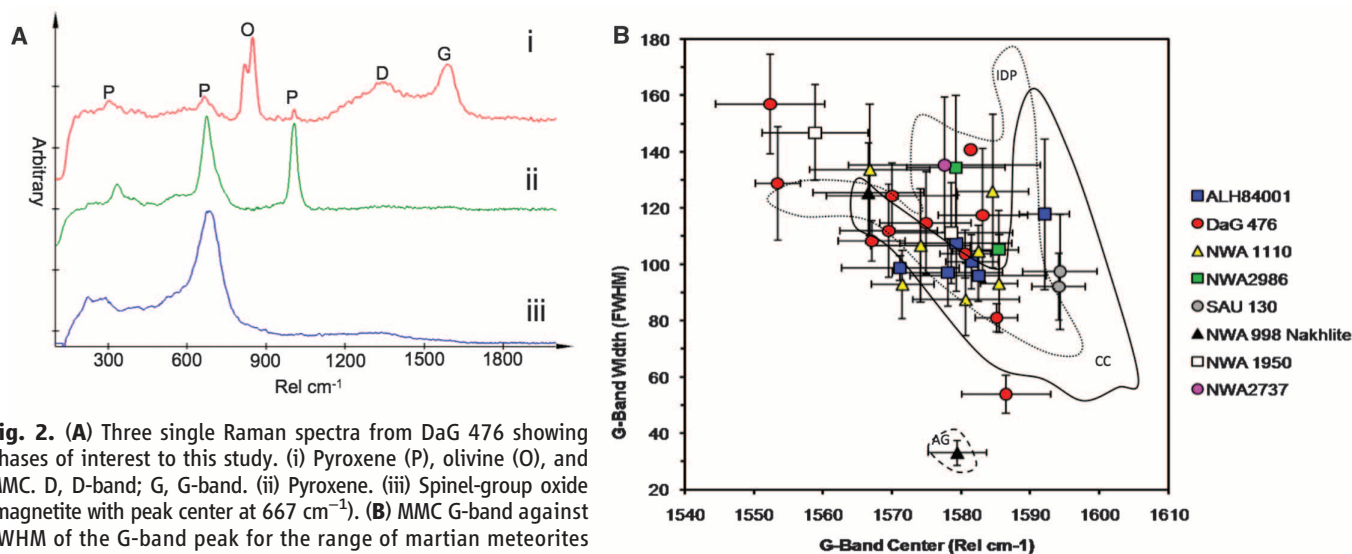
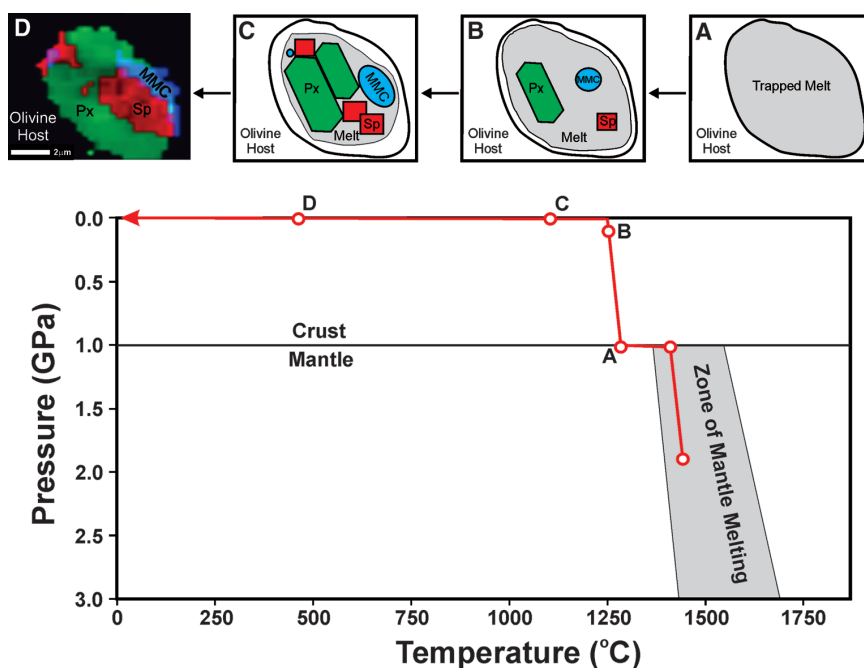


**Fig. 2.** (A) Three single Raman spectra from DaG 476 showing phases of interest to this study. (i) Pyroxene (P), olivine (O), and MMC. D, D-band; G, G-band. (ii) Pyroxene. (iii) Spinel-group oxide (magnetite with peak center at  $667\text{ cm}^{-1}$ ). (B) MMC G-band against FWHM of the G-band peak for the range of martian meteorites in which MMC has been detected. The area bordered by a black line is the variation in these parameters observed in carbonaceous chondrites (CC); the area bordered by a dotted black line shows the parameters exhibited by interplanetary dust particles (IDP). AG is a standard

spectrum of graphite and represents ordered crystalline carbon; disorder in the MMC increases with decreasing G-band center and increasing FWHM (19).

**Fig. 3.** Proposed crystallization sequence for the MMC-bearing melt inclusions along with a pressure-temperature schematic illustrating the process that correlates to each of the crystallization sequence panes [(A) to (D)]. (A) Trapping of liquid in olivine. (B) Ascent and cooling allow inclusion to begin to crystallize. (C) Continued crystallization of melt inclusion during cooling. (D) CRIS image of a trapped inclusion in olivine from DaG 476. Black arrows indicate the direction of the crystallization sequence. The depth of melting (1 to 3 GPa or 75 to 225 km depth) is within the pressure range of experimentally determined multiple saturation points for shergottites shown to be representative of liquid compositions [i.e., (26, 40)]. Phenocryst growth at higher pressure may take place at the base of the martian crust as it acts as a natural density barrier for melts to pond and begins to crystallize [as proposed by (41)].





carbon phase that was sensitive to the redox state of the magma. It has been hypothesized that the martian mantle is saturated with respect to graphite and that the oxygen fugacities ( $f_{O_2}$ ) of the mantle sources for the martian meteorites are buffered by fluids in the C-O-H system (25, 26), consistent with  $f_{O_2}$  recorded by many of the martian meteorites (table S1) (9, 27–29). Substantial amounts of hydrogen occur in martian magmatic source regions (30, 31), indicating that if the martian mantle is graphite saturated, partial melts of the mantle would have contained substantial C-O-H components. Trapping of a C-O-H-bearing melt in the mineral host would have led to the early saturation in a graphite + C-O-H fluid-phase in the melt inclusion that would have increased in volume as the rock cooled and crystallized (Fig. 3). Importantly, C-O-H fluid + graphite is the structural equivalent of MMC, if the C-O-H fluid and graphite were to form a single phase. The formation of a single MMC phase is further supported by the lack of void space within the inclusions coupled with the absence of any gaseous species identified by CRIS (i.e.,  $H_2O$ ,  $CO_2$ , or  $CH_4$ ) in the many hundreds of inclusions analyzed. This observation indicates that MMC formation was probably not by catalysis of volatiles with the oxide phases, unless this catalysis occurred while the volatile components were dissolved in the silicate melt. The formation mechanism that we propose for MMC production is supported by experimental data on the C-O-H system in which low  $f_{O_2}$  and high  $f_{H_2}$  conditions produced MMC and PAHs at 1000 K (32). In that study, formation of  $CH_4$  and crystalline graphite were inhibited, allowing for the formation of MMC, including PAHs. The C:H ratio of the fluid changes the size and distribution of polycyclic aromatic species, and MMC may shift toward graphitic at low  $f_{H_2}$  and to very amorphous at higher  $f_{H_2}$ , explaining the MMC G-band parameter heterogeneity seen in our study (32) (Fig. 2B).

From the crystallization ages of these martian meteorites (table S1), it appears that some portion of the martian carbon budget has existed as MMC from at least 4.2 billion years ago to 190 million years ago (33, 34). Hirschmann and Withers (25) postulated on the formation of a martian atmosphere from a reduced mantle and concluded that  $CO_2$  degassing to the martian surface may have been severely limited. Our results confirm the presence of reduced MMC species in reduced (less than quartz-fayalite-magnetite) igneous rocks, and therefore support the central tenet of the Hirschmann and Withers (25) study. However, the lack of MMC in inclusions in the most oxidized sample (Nakhl) illustrates the possible effects of the redox state of the martian magmas on the preservation of these carbon species during crystallization. This, in turn, has an effect on their distribution at the surface and within the crust (35, 36).

Our analyses did not detect  $CH_4$  or  $CO_2$  within any igneous inclusions. Methane detected in

the atmosphere of Mars has been explained by both abiotic and biotic processes (37, 38), although there is some doubt to its presence at all (39). Our data cannot prove a link between igneous processes and the presence of putative methane; however, the reduced conditions implied by the presence of MMC could affect carbon in the atmosphere on Mars tentatively supporting abiotic production of  $CH_4$  (37, 38). The youngest MMC-bearing meteorite (~190 million years old), demonstrates that reduced carbon phases have been generated recently in Mars' history and, therefore, that the martian reduced carbon budget was in flux during the late Amazonian, hinting that a true martian carbon cycle may still be active.

Our results imply that primary organic carbon is nearly ubiquitous in martian basaltic rocks. It formed through igneous, not biological, processes and was delivered over most of martian geologic history to the surface as recently as the late Amazonian. Therefore, a positive detection of organics (especially PAHs) on Mars by Mars Science Laboratory, even if coupled with isotopically "light"  $\delta^{13}C$  values, may be detecting this abiotic reservoir. Furthermore, the origin of the carbon in mantle rocks is strong evidence that this carbon was indigenous to the martian interior because the absence of extensive plate tectonics would have prevented exchange between surface and near-surface carbon reservoirs (9). Consequently, the storage of carbon within Mars occurred very early in its history, at the time of planet-wide differentiation (9), which has also been suggested for hydrogen storage on Mars (31). This process is likely not unique to Mars and could have been widely responsible for the production and delivery of abiotic organic carbon to the surfaces of the other terrestrial planets, including early Earth.

#### References and Notes

- A. J. T. Jull, C. Courtney, D. A. Jeffrey, J. W. Beck, *Science* **279**, 366 (1998).
- T. Stephan, E. K. Jessberger, C. H. Heiss, D. Rost, *Meteorit. Planet. Sci.* **38**, 109 (2003).
- L. Becker, B. Popp, T. Rust, J. L. Bada, *Earth Planet. Sci. Lett.* **167**, 71 (1999).
- A. Steele *et al.*, *Meteorit. Planet. Sci.* **42**, 1549 (2007).
- A. H. Treiman, *Astrobiology* **3**, 369 (2003).
- M. Y. Zolotov, E. L. Shock, *Meteorit. Planet. Sci.* **35**, 629 (2000).
- D. S. McKay *et al.*, *Science* **273**, 924 (1996).
- Any MMC found to be incompletely enclosed within its silicate host (i.e., in cracks, grain boundaries, at the surface of the sample, or associated with weathering or contaminating phases) was treated as contamination and discounted from this study.
- Materials, methods, and supporting text are available as supplementary materials on Science Online.
- M. Fries, A. Steele, *Science* **320**, 91 (2008).
- A. Steele *et al.*, *Science* **329**, 51 (2010).
- J. Zipfel, P. Scherer, B. Spettel, G. Dreibus, L. Schultz, *Meteorit. Planet. Sci.* **35**, 95 (2000).
- A. Steele *et al.*, *Meteorit. Planet. Sci.* **35**, 237 (2000).
- J. Toporski, A. Steele, *Astrobiology* **7**, 389 (2007).
- O. Beyssac, B. Goffe, C. Chopin, J. N. Rouzaud, *J. Metamorph. Geol.* **20**, 859 (2002).
- G. D. Cody *et al.*, *Earth Planet. Sci. Lett.* **272**, 446 (2008).
- The detection sensitivity of the  $L^2MS$  technique is in the femtomolar range for PAHs.
- S. Messenger *et al.*, *Astrophys. J.* **502**, 284 (1998).
- S. A. Sandford *et al.*, *Science* **314**, 1720 (2006).
- M. Y. Zolotov, E. L. Shock, *J. Geophys. Res. Solid Earth* **105**, 539 (2000).
- J. D. Pasteris, B. Wopenka, *Astrobiology* **3**, 727 (2003).
- A. J. T. Jull, J. W. Beck, G. S. Burr, *Geochim. Cosmochim. Acta* **64**, 3763 (2000).
- A. J. T. Jull, in *Meteorites and the Early Solar System II*, D. S. Lauretta, H. Y. McSween Jr., Eds. (Univ. of Arizona Press, Tucson, AZ, 2006), pp. 889–905.
- M. M. Grady, A. B. Verchovsky, I. P. Wright, *Int. J. Astrobiol.* **3**, 117 (2004).
- M. M. Hirschmann, A. C. Withers, *Earth Planet. Sci. Lett.* **270**, 147 (2008).
- K. Righter, H. Yang, G. Costin, R. T. Downs, *Meteorit. Planet. Sci.* **43**, 1709 (2008).
- C. D. K. Herd, *Meteorit. Planet. Sci.* **38**, 1793 (2003).
- M. Wadhwa, *Rev. Mineral. Geochem.* **68**, 493 (2008).
- M. Wadhwa, *Science* **291**, 1527 (2001).
- F. M. McCubbin *et al.*, *Earth Planet. Sci. Lett.* **292**, 132 (2010).
- F. M. McCubbin *et al.*, *Proc. 43rd Lunar Planet. Sci. Conf.* **43**, 1121 (2012).
- R. V. Eck, E. R. Lippincott, M. O. Dayhoff, Y. T. Pratt, *Science* **153**, 628 (1966).
- L. E. Borg, D. S. Draper, *Meteorit. Planet. Sci.* **38**, 1713 (2003).
- T. J. Lapen *et al.*, *Science* **328**, 347 (2010).
- R. V. Morris *et al.*, *Science* **329**, 421 (2010).
- J. R. Michalski, P. B. Niles, *Nat. Geosci.* **3**, 751 (2010).
- S. K. Atreya, P. R. Mahaffy, A. S. Wong, *Planet. Space Sci.* **55**, 358 (2007).
- M. J. Mumma *et al.*, *Science* **323**, 1041 (2009).
- K. Zahnle, R. S. Freedman, D. C. Catling, *Icarus* **212**, 493 (2011).
- D. S. Musselwhite, H. A. Dalton, W. S. Kiefer, A. H. Treiman, *Meteorit. Planet. Sci.* **41**, 1271 (2006).
- F. M. McCubbin, H. Nekvasil, D. H. Harrington, S. M. Elardo, D. H. Lindsley, *J. Geophys. Res. Planets* **113**, (E11), E11013 (2008).

**Acknowledgments:** This work was funded by NASA Astrobiology Science and Technology for Exploring Planets (NNX09AB74G to A.S., P.G.C., A.H.T., and M.L.F.), NASA Mars Fundamental Research Program (NNX08AN61G to A.S.), the W. M. Keck Foundation (2007–6–29 to M.L.F. and A.S.), NASA Astrobiology Institute (NNA09DA81A to A.S., S.B.S., N.Z.B., B.O.M., and M.L.F.), and the Carnegie Institution of Washington. F.M.M. acknowledges financial support from NASA Cosmochemistry (NNX11AG76G to F.M.M.). A.S. thanks J. Strope for identification of suitable meteorite samples, C. Agee (University of New Mexico) for the Tissint sample, and L. Welzenbach, T. Gooding, and T. Rose for their assistance in thin-sectioning the meteorites and the use of the Scanning Electron Microscope in the Department of Mineral Sciences, National Museum of Natural History, Smithsonian Institution, Washington, DC. C.D.K.H. thanks D. Hnatyshin for assistance with oxygen fugacity calculations. This work was supported by Natural Science and Engineering Research Council of Canada grant 261740 "The Geology of Mars from Studies of Martian Meteorites" to C.D.K.H.  $L^2MS$ ,  $^{14}C$ , and additional Raman data have been included in the supplementary materials.

#### Supplementary Materials

www.sciencemag.org/cgi/content/full/science.1220715/DC1  
Materials and Methods  
Supplementary Text  
Figs. S1 to S4  
Table S1  
References (42–72)

17 February 2012; accepted 3 May 2012  
Published online 24 May 2012;  
10.1126/science.1220715

# Ice Volume and Sea Level During the Last Interglacial

A. Dutton<sup>1,2\*</sup> and K. Lambeck<sup>1,3</sup>

During the last interglacial period, ~125,000 years ago, sea level was at least several meters higher than at present, with substantial variability observed for peak sea level at geographically diverse sites. Speculation that the West Antarctic ice sheet collapsed during the last interglacial period has drawn particular interest to understanding climate and ice-sheet dynamics during this time interval. We provide an internally consistent database of coral U-Th ages to assess last interglacial sea-level observations in the context of isostatic modeling and stratigraphic evidence. These data indicate that global (eustatic) sea level peaked 5.5 to 9 meters above present sea level, requiring smaller ice sheets in both Greenland and Antarctica relative to today and indicating strong sea-level sensitivity to small changes in radiative forcing.

**F**orecasting the nature of future sea-level rise requires an understanding of potential ice-sheet instability under sustained global warming conditions. One approach to elucidate ice-sheet behavior during warm climate periods is to investigate geologic records during periods when the size and configuration of the cryosphere was largely analogous to that of today (*1*).

The last interglacial period (LIG)—also known as marine isotope stage (MIS) 5e, MIS 5.5, or the Eemian stage in Western Europe (*2*)—is a clear choice for such a study because there are more empirical data than for any prior interglacial period. The LIG is usually described as having a eustatic sea level (ESL) some +4 to 6 m higher than today (*3, 4*) and with a global mean temperature that was similar or perhaps slightly warmer than the preindustrial state (*5–7*). In contrast, a recent study suggested that ESL was in fact significantly higher, peaking between +6.6 and 9.4 m (*8*). The difference between ESL at +4 and ESL at +9 m higher than present is important: The former can be largely accounted for through thermal expansion of seawater, loss of mountain glaciers, and partial loss of the Greenland ice sheet, but higher levels require a contribution from Antarctica (*9, 10*).

The focus of this Report is twofold: one, to present a new global database of U-Th ages and elevations of fossil LIG corals and, two, by correcting this record for contributions from the glacio-hydro-isostatic process during glacial cycles, to establish an independent estimate of ice volumes during the LIG compared with the present. We have compiled and normalized age-elevation data of LIG fossil corals into a database containing 711 U-Th measurements from 16 sites around the globe, six of which

are considered tectonically stable (Fig. 1) (database S1) (*11*). To interpret these data, we provide insight into how deformations of Earth's solid surface and gravity field in glacial-interglacial cycles influence the position of the LIG shorelines that are observed today. This analysis highlights the difference in observed sea level at field sites around the globe versus the eustatic sea-level signal that primarily reflects changes in the volume of land-based ice. We argue that glacial isostatic adjustment is a critical element in assessing field observations of LIG sea level and cannot be ignored when discussing the observed differences reported between sites.

Resolving the magnitude and timing of maximum sea level during the LIG requires well-dated sea-level markers and an appreciation of the processes that produce changes in sea level relative to land. One common approach is to use elevations of LIG corals that grow near the sea surface, which can potentially be extremely accurately and precisely dated by using U-series geochronometry (*12, 13*).

The primary strength of coral-based sea-level reconstructions is their potential to deliver an extremely well-resolved record with respect to both time and elevation, whereas the principal weakness lies in paleodepth uncertainties of the corals

and in the geochemical alteration of skeletal aragonite. Thus, coral age-elevation data provide a minimum estimate of sea-level position, with some uncertainty in absolute age that is related to ambiguous effects of diagenesis or variability in seawater uranium isotope composition ( $\delta^{234}\text{U}$ ) through time (*13*).

Coral U-Th data from uplifting sites are valuable because multiple oscillations in sea-level rise are expressed geomorphically as different terraces, whereas in tectonically stable areas overprinting and reworking during prolonged sea-level highstands will often mask oscillations. However, it is not possible to reconstruct the precise absolute elevation of LIG sea level by using coral U-Th data from uplifting sites, because assumptions about the magnitude and constancy of uplift rates become a substantial source of uncertainty when extrapolating back in time. An additional confounding factor is that tectonically active sites have uplift or subsidence rates that are calculated on the basis of assumptions about LIG sea-level timing and position—hence, the argument can become circular. However, rapid oscillations in ESL can be inferred from geographically widespread observations including uplifted sites, and in fact global prevalence of sea-level oscillations is a prerequisite before “real” ESL or ice-volume oscillations are invoked.

The best ESL indicators are from tectonically stable localities that are geographically distant, or far field, from former ice-sheet margins (*14*). Although it has been common practice to equate sea-level observations from far-field sites to glacio-eustatic changes in sea level, even far-field sites are sensitive to glacio-isostatic processes that cause local, or relative sea level (RSL), observations to depart significantly from the ESL curve during both the Holocene (*14, 15*) and the LIG (*16*). In the following discussion, we first examine how RSL differs from ESL because of the glacio-hydro-isostatic process and then combine this knowledge with the observational record to interpret maximum ESL during the LIG (*11*).

LIG and earlier interglacial shorelines above or below present sea level have been attributed to differences in polar ice volumes compared with

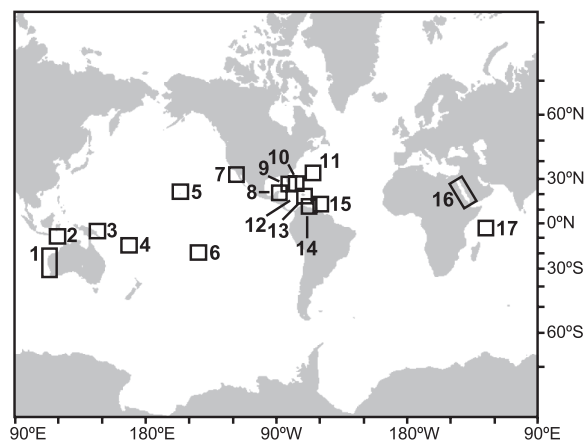


**Fig. 1.** Geographic distribution of LIG reefs in our coral U-Th database. Localities are as follows: 1, Western Australia; 2, Sumba Island, Indonesia; 3, Huon Peninsula, Papua New Guinea; 4, Vanuatu; 5, Oahu; 6, Mururoa Atoll, French Polynesia; 7, California/Mexico coast and islands; 8, Xcaret, Yucatan; 9, Florida Keys; 10, Bahamas; 11, Bermuda; 12, Jamaica; 13, Haiti; 14, Curaçao; 15, Barbados; 16, Red Sea coast; 17, Seychelles (granitic islands). Coral U-Th data sources are listed in database S1.

<sup>1</sup>Research School of Earth Sciences, The Australian National University, 1 Mills Road, Canberra, ACT 0200, Australia. <sup>2</sup>Department of Geological Sciences, University of Florida, Post Office Box 112120, Gainesville, FL 32611, USA. <sup>3</sup>Département des Géosciences, Ecole Normale Supérieure, Paris, France.

\*To whom correspondence should be addressed. E-mail: adutton@ufl.edu



today, vertical tectonic movement, residual isostatic response to previous and subsequent ice loads, or a combination of these processes depending on the locality. The +4- to 6-m benchmark for LIG sea level has been widely held as a de facto ESL and used as an indicator for establishing tectonic stability at sites around the globe (e.g., 3, 17, 18). This approach is not valid because LIG sea-level position and timing, like their Holocene counterparts, can be expected to vary between locations depending on the position relative to former and subsequent ice sheets and the response to isostatic adjustments to ice and water loading and gravitational effects (16, 19). In other words, the elevation of peak LIG sea level seen today is not expected to be the same across Earth's surface, nor will the timing of peak sea level be synchronous.

Glacio-hydro-isostatic effects include the deformation and gravitational and rotational responses of the solid earth and ocean surfaces to changes in ice and water loads. In regions proximal to large ice sheets (near- to intermediate-field sites), changes in ice loading dominate the isostatic signal. For example, along much of the United States Atlantic coast and across the Caribbean, the unloading of the North American ice sheet results in a slowly rising sea level, superimposed on the eustatic change, throughout the interglacial until the onset of the next phase of glaciation, mainly because of subsidence of a broad peripheral bulge in Earth's surface that developed around the ice sheet during the preceding glacial period (Fig. 2B).

At far-field sites, the change in water load dominates the shorter wavelengths of the spa-

tial pattern of sea-level change because, in a first approximation, the ocean floor loading during the deglaciation phase depresses the sea floor relative to the continent. Therefore, in the absence of any changes in ice volume during an interglacial period, far-field, continental coastal sea levels will fall. In this instance, a small-amplitude highstand develops at the time melting ceased and decays by a few meters during the interglacial period (Fig. 2A).

Sea-level observations from geologic archives measure past positions of sea level relative to present sea level. However, the elevations of paleoshorelines—including those of the LIG—will continue to evolve because the relaxation of the mantle to the last glacial cycle is not yet complete (19). At sites near field to the last glacial maximum ice sheets, for example, sea levels will continue to rise into the future, so that at some later time the LIG shorelines seen today will be seen at a lower elevation. At far-field sites, present sea level will continue to fall (in the absence of other processes), and presently raised LIG reefs will appear at higher elevations even though no additional water has been removed from the oceans. Thus at neither near- nor far-field sites is there a simple relation between observed sea levels and ice volumes during interglacials: The actual relation requires knowledge of the ice sheets before, during, and after the interglacial; of Earth's rheological response to the ice-water loads; and of the evolution of the ocean basin shape during the glacial cycles (19–21).

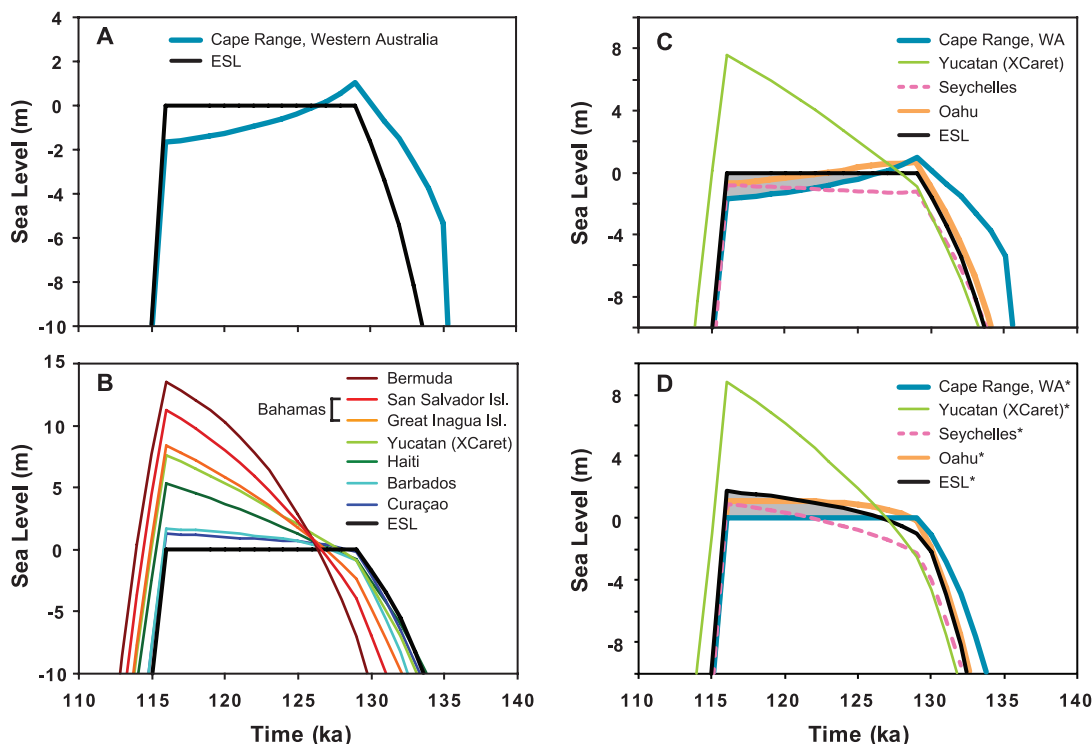
To approximate the magnitude of the isostatic and gravitational effects, we used a reference ice model in which grounded ice volumes during

the LIG are set constant and equal to present ice volume for the duration of the period (11, 22). The predicted LIG RSL curves have several notable characteristics (Fig. 2). The first relates to the different character of sea-level response at different sites. In particular, for the reference ice model (see ESL curve in Fig. 2, A to C) a highstand is predicted to occur early in the interglacial at far-field localities, whereas in the near field it occurs at the end of the interglacial. Thus, if observational data from the Yucatan and Western Australia (WA) were plotted on the same diagram without correcting for the differences in isostatic response, the resulting curve would show two peaks (Fig. 2C). Therefore, if RSL data from multiple sites have not been corrected for isostatic contributions, their superposition can result in synthetic sea-level oscillations that misrepresent the ESL history.

The second notable feature relates to the timing when sea levels first reach present-day sea level. At the far-field sites, this occurs earlier, by 3 to 4 thousand years, than at sites in the near field, and considerable variation can also occur between far-field sites depending on their positions relative to the principal ice sources and on the coastline geometry.

A third characteristic illustrated by the forward model is the gradient of the LIG highstand across the Caribbean (Fig. 2B), which is similar in behavior to the observationally better-constrained Holocene sea-level rise along the United States Atlantic coast (23). The amplitude and gradient of this sea-level pattern are critically dependent on the adopted North American ice sheet for the two glacial cycles, with the average

**Fig. 2.** RSL predictions during the LIG for (A) Cape Range, Western Australia, (B) several sites across the Caribbean-Atlantic region, and (C and D) several disparate sites display the differences in timing and magnitude of RSL (colored lines) compared with ESL (heavy black line). ESL is set equal to zero (present sea level) for the duration of the LIG in this forward model in all cases except (D), where the ESL function is defined to have a gradual increase during the LIG (denoted by asterisks), similar to the pattern seen in the Holocene. Gray shaded areas in (C) and (D) are the magnitude of the sum of the isostatic and gravitational effects at Cape Range that cause RSL to depart from the ESL curve. ka, thousand years ago.



elevation of LIG sea level at any site providing primarily a constraint on the last glacial maximum ice volume and the rate of RSL change providing a constraint on the MIS 6 ice sheet. The latter remains poorly understood; hence, data from this area do little to constrain LIG ESL unless the knowledge of the ice-sheet history can first be improved. The present disparity between the maximum predicted RSL in our forward model and maximum LIG observations in this region indicates that modification of the MIS 2 and/or MIS 6 ice sheet will be required to bring the model in line with the observations. Fortunately, the far-field sites are not sensitive to the distribution of ice volume between the various ice sheets, allowing us to place reasonable constraints on maximum LIG ESL by using the existing ice model.

The nature of these predicted RSL patterns provides the necessary context to evaluate the geochronological data. Synthesis of U-Th data for fossil corals is complicated by a number of factors, including (i) the use of different screening criteria to accept or reject data, (ii) different decay constants used to calculate ages, (iii) inconsistent application of open-system models, (iv) uncertainty in the past uranium-isotope composition of seawater, (v) lack of stratigraphic information paired with geochronological data to interpret sea-level position, and (vi) the use of different sea-level benchmarks for elevation measurements. We have normalized our database for all these factors with the exception of (iv) and (v), the first of which remains ambiguous and the second we consider where enough information is provided.

Coral age-elevation data confirm the isostatic modeling predictions in that different sites display a variety of behaviors during the LIG sea-level highstand, including both stable and rising sea-level patterns (24) (Fig. 3). A pattern of rising RSL is expected in the Bahamas and the Yucatan even for the nominal scenario where ESL remains constant throughout the LIG (Fig. 2B). In fact, a progression toward younger ages with increasing elevation is observed in reef growth at both of these sites (25, 26).

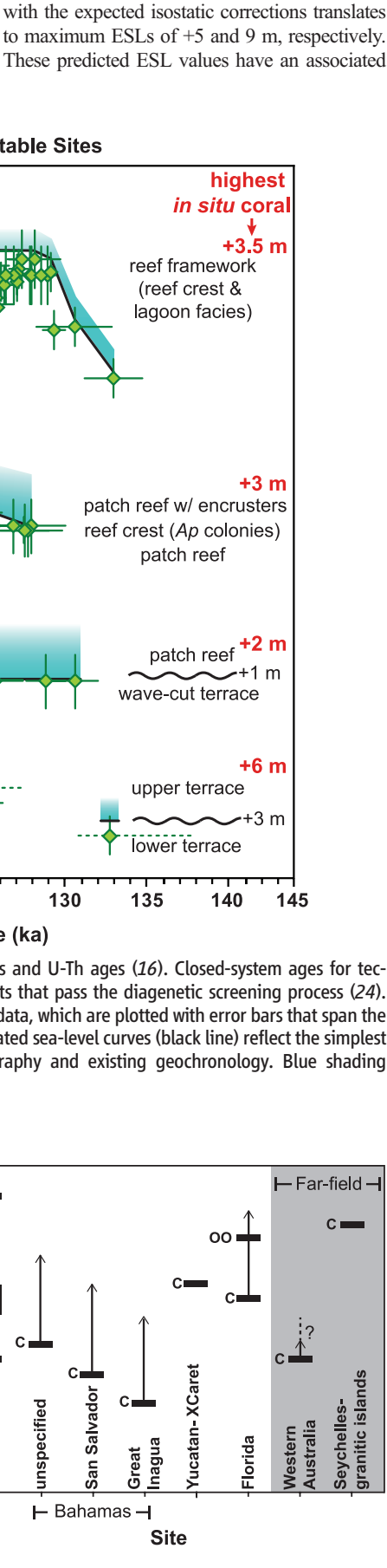
Evidence for rapid sea-level rise occurring late in the LIG rests largely on high notches observed in the Bahamas and Bermuda (27) and the presence of a second, higher LIG terrace that defines a back-stepping reef architecture in the Yucatan (26). The model results show that, even with no change in LIG ESL, a late peak is expected at these localities and that there is no need to invoke a rapid change in ESL or ice volume to explain these field observations (Fig. 2).

To determine the magnitude of peak LIG ESL, we combined model-derived corrections for the noneustatic component with observational data from tectonically stable, far-field localities where RSL is dominantly a function of ESL (11). Maximum elevations of in situ LIG corals at (assumed) tectonically stable sites indicate local sea-level positions ranging from +2 to 8 m above present

(28) (Fig. 4). Consideration of elevation data from the only two sites in our database that are both far field and stable (WA and the Seychelles) along with the expected isostatic corrections translates to maximum ESLs of +5 and 9 m, respectively. These predicted ESL values have an associated

**Fig. 3.** RSL reconstruction based on coral elevations and U-Th ages (16). Closed-system ages for tectonically stable localities with five or more data points that pass the diagenetic screening process (24). Data are shown with 2σ errors except for the Yucatan data, which are plotted with error bars that span the range of ages on replicates from the same coral. Indicated sea-level curves (black line) reflect the simplest interpretations that are consistent with reef stratigraphy and existing geochronology. Blue shading indicates likely paleodepth of corals.

**Fig. 4.** Elevation of the highest in situ corals at all of the tectonically stable sites in our database along with associated sedimentary sea-level markers at these sites, where C indicates in situ coral; OO, oolite shoal; SB, subtidal facies; and SW, storm wash deposits. Arrows indicate paleodepth of corals as estimated in the original data sources; in Western Australia, we estimate a minimum paleodepth of 1 m because the modern reef crest remains unexposed at low tide. Gray shading highlights the only two sites far field from former Northern Hemisphere ice-sheet margins. Data sources are listed in database S1.





error of  $\pm 1.5$  m that includes uncertainties associated with the ice and earth model parameters. The +5-m estimate from WA has its basis in LIG fossil reefs that outcrop discontinuously along some 1300 km of coastline at the same elevation, whereas it has not been independently established that the few closely spaced localities in the granitic Seychelles are indeed tectonically stable (11). We attribute part of the discrepancy in our maximum-elevation estimates from WA and the Seychelles to an underestimation in WA. The highest corals we surveyed there (+3.5 m) are planed off, implying that sea level may have easily reached +4.0 m (RSL), which translates to a +5.5 m ESL. In contrast, the highest in situ coral that we surveyed in the Seychelles was capped by an intertidal facies, suggesting that the coral grew right up to the sea surface and represents a maximum estimate of sea-level position. This result is remarkably similar to the +6.6- to 9.4-m range determined from a separate compilation of LIG sea-level markers by using a statistical analysis method to account for the role of isostatic effects (8) yet still leaves a considerable 3- to 4-m uncertainty on the elevation of peak sea level, highlighting the need for additional observations from far-field, tectonically stable sites.

The absolute timing of peak sea level during the LIG period remains uncertain because of the temporal resolution of the data as well as uncertainty in  $\delta^{234}\text{U}$  of LIG seawater, which affects the interpretation of the U-Th ages regardless of whether closed-system ages or modeled open-system ages are used to define the chronology. Because the overall pattern in elevation for the closed-system U-Th data in Fig. 3 (i.e., relatively stable in WA and slightly increasing in the Bahamas and the Yucatan) will hold even if an open-system interpretation is invoked, we can infer that maximum sea level was more likely achieved during the latter portion of the sea-level highstand. This effect is apparent in Fig. 2D, where the isostatic effect is greater in WA at the end of the highstand, implying that a rising ESL is required to maintain or raise RSL at this site in the latter portion of the highstand.

Despite differences in the timing and elevation of LIG sea level at globally distributed fossil reefs, we have demonstrated that many of the different patterns observed in coral age-elevation data can provide a consistent interpretation of LIG sea level when the glacio-hydro-isostatic processes are quantitatively modeled. These latter processes are well understood and quantifiable for more recent times, but their magnitudes and rates are less certain for the LIG—particularly for the near-field sites under the influence of the North American ice sheet—because of the limited knowledge of the ice sheets during the preceding glacial maximum. Hence, to construct an ESL curve for the LIG, we suggest a strategy that uses the evidence from the far-field sites to estimate the ESL during the LIG and then uses the

near-field sites as indicators of the MIS 6 ice-sheet parameters.

The two far-field locations for which accurately dated LIG information is available, WA and the Seychelles, indicate a discrepancy of up to 3 to 4 m in peak LIG ESL, similar to the range estimated independently (8). This large uncertainty in the current best estimate of the peak LIG ESL highlights the need for additional, stratigraphically controlled, data from additional far-field localities that are stable at a level better than 0.01 mm/year. Can either location be considered stable at this level? The other requirement is improvements in the isostatic modeling, particularly in the ice models for the penultimate glaciation, but also in some of the model assumptions made: For example, are the effective rheological parameters that describe the earth's deformation on time scales of  $10^4$  years also valid on the longer time scale? Lastly, we need to address outstanding issues surrounding the interpretation of absolute ages from coral U-Th data and in relating absolute chronologies of sea-level change to paleoclimate records from ice and deep-sea cores to better understand the temporal interplay between climate, ice sheets, and sea-level change.

The need to improve upon the uncertainty in the LIG ESL estimates is best seen in terms of its consequences on melting from both Greenland and Antarctica during the LIG. Current modeling and data-based estimates converge on a 2- to 4-m contribution to ESL from Greenland (9, 10, 29–31) and on a maximum contribution of +3.3 m from West Antarctica (32). Thus, the lower limit estimate of the peak LIG ESL (+5.5 m) is consistent with such contributions from both Greenland and West Antarctica, but the upper limit (+9 m) implies additional melt-water contribution from adjacent sectors in East Antarctica.

## References and Notes

- M. Siddall *et al.*, *J. Quat. Sci.* **25**, 19 (2009).
- The timing and duration of the LIG are generally defined on the basis of the presence of climatically warm indicators in the geologic record. Here, we are interested in the timing of the last interglacial sea-level highstand, defined as the period of time when ESL exceeded that of the present.
- H. H. Veeh, *J. Geophys. Res.* **71**, 3379 (1966).
- C. H. Stirling, T. M. Esat, K. Lambeck, M. T. McCulloch, *Earth Planet. Sci. Lett.* **160**, 745 (1998).
- P. U. Clark, P. Huybers, *Nature* **462**, 856 (2009).
- N. P. McKay, J. T. Overpeck, B. L. Otto-Bliesner, *Geophys. Res. Lett.* **38**, L14605 (2011).
- Proxy data compiled by (5, 6) indicate that the last interglacial was warmer by 1.5° to 2°C or 0.7°C, respectively, relative to the pre-anthropogenic global average.
- R. E. Kopp, F. J. Simons, J. X. Mitrovica, A. C. Maloof, M. Oppenheimer, *Nature* **462**, 863 (2009).
- K. M. Cuffey, S. J. Marshall, *Nature* **404**, 591 (2000).
- B. L. Otto-Bliesner, S. J. Marshall, J. T. Overpeck, G. H. Miller, A. Hu, *Science* **311**, 1751 (2006).
- Materials and methods are available as supplementary materials on Science Online.
- R. L. Edwards, C. D. Gallup, H. Cheng, in *Uranium-Series Geochemistry*, B. Bourdon, G. M. Henderson, C. C. Lundström, S. P. Turner, Eds. (Mineralogical Society of America, Washington, DC, 2003), vol. 52, pp. 363–406.
- C. H. Stirling, M. B. Andersen, *Earth Planet. Sci. Lett.* **284**, 269 (2009).
- W. E. Farrell, J. A. Clark, *Geophys. J. R. Astron. Soc.* **46**, 647 (1976).
- G. A. Milne, J. X. Mitrovica, *Quat. Sci. Rev.* **27**, 2292 (2008).
- K. Lambeck, M. Nakada, *Nature* **357**, 125 (1992).
- L. Ferranti *et al.*, *Quat. Int.* **145–146**, 30 (2006).
- J.-C. Plazait, J.-L. Reyss, A. Choukri, C. Cazala, *Carnets Géol. CG2008*, 1 (2008).
- E.-K. Potter, K. Lambeck, *Earth Planet. Sci. Lett.* **217**, 171 (2003).
- M. E. Raymo, J. X. Mitrovica, *Nature* **483**, 453 (2012).
- K. Lambeck, A. Purcell, A. Dutton, *Earth Planet. Sci. Lett.* **315**, 4 (2012).
- The magnitude of the isostatic effect for different ice models defining ESL will only vary by ~10% of the amount that ESL changes, which is well within the uncertainty of elevation measurements of LIG deposits; therefore, we can use the forward model to effectively estimate the magnitude of the isostatic correction in far-field localities.
- S. E. Engelhart, B. P. Horton, B. C. Douglas, W. R. Peltier, T. E. Tornqvist, *Geology* **37**, 1115 (2009).
- Fig. 3 includes all sites with at least five data points meeting the following diagenetic criteria: (i)  $\delta^{234}\text{U}$  within 5 per mil (‰) of modern seawater (147‰), (ii) <2% calcite (if mineralogy was reported), and (iii)  $^{232}\text{Th}$  < 2 parts per billion.
- J. H. Chen, H. A. Curran, B. White, G. J. Wasserburg, *Geol. Soc. Am. Bull.* **103**, 82 (1991).
- P. Blanchon, A. Eisenhauer, J. Fietzke, V. Liebetrau, *Nature* **458**, 881 (2009).
- P. J. Hearty, J. T. Hollin, A. C. Neumann, M. J. O'Leary, M. T. McCulloch, *Quat. Sci. Rev.* **26**, 2090 (2007).
- The upper end of this range is defined by LIG fossil reefs in the granitic Seychelles that we have recently resurveyed and rise to elevations of +8 m.
- N. Lhomme, G. K. C. Clarke, S. J. Marshall, *Quat. Sci. Rev.* **24**, 173 (2005).
- E. J. Colville *et al.*, *Science* **333**, 620 (2011).
- L. Tarasov, W. R. Peltier, *J. Geophys. Res.* **108**, 2143 (2003).
- J. L. Bamber, R. E. M. Riva, B. L. A. Vermeersen, A. M. LeBrocq, *Science* **324**, 901 (2009).

**Acknowledgments:** We acknowledge useful discussions with many of our colleagues, including T. Esat, E.-K. Potter, and members of the PALSEA (Paleo-Constraints on Sea Level Rise) working group funded by Past Global Changes/IMAGES (International Marine Past Global Change Study). We also extend our gratitude to many authors who provided additional information or data to supplement their U-Th measurements that appear in database S1. This project has been partially funded by the Australian Research Council and the Australian National University. K.L. was partly funded by the Chaire Internationale de Recherche Blaise Pascal financée par l'Etat et la Région Ile-de-France. Data compiled for this review are available in the supplementary materials and are archived online at the World Data Center for Paleoclimatology.

## Supplementary Materials

www.sciencemag.org/cgi/content/full/337/6091/216/DC1  
Materials and Methods

Fig. S1

References (33–71)

Database S1

17 March 2011; accepted 30 May 2012  
10.1126/science.1205749

# Rapid Progression of Ocean Acidification in the California Current System

Nicolas Gruber,<sup>1\*</sup> Claudine Hauri,<sup>1</sup> Zouhair Lachkar,<sup>1</sup> Damian Loher,<sup>1</sup> Thomas L. Frölicher,<sup>2</sup> Gian-Kasper Plattner<sup>3</sup>

Nearshore waters of the California Current System (California CS) already have a low carbonate saturation state, making them particularly susceptible to ocean acidification. We used eddy-resolving model simulations to study the potential development of ocean acidification in this system up to the year 2050 under the Special Report on Emissions Scenarios A2 and B1 scenarios. In both scenarios, the saturation state of aragonite  $\Omega_{\text{arag}}$  is projected to drop rapidly, with much of the nearshore region developing summer-long undersaturation in the top 60 meters within the next 30 years. By 2050, waters with  $\Omega_{\text{arag}}$  above 1.5 will have largely disappeared, and more than half of the waters will be undersaturated year-round. Habitats along the sea floor will become exposed to year-round undersaturation within the next 20 to 30 years. These projected events have potentially major implications for the rich and diverse ecosystem that characterizes the California CS.

Though it has been known for decades that the oceanic uptake of anthropogenic  $\text{CO}_2$  will lead to a reduction in the pH of seawater (1, 2), the amplitude of these changes was thought to be too small to harm marine organisms or lead to appreciable changes in the biogeochemical cycling of elements in the ocean. Only when the first experimental results revealed that certain marine organisms respond sensitively to this  $\text{CO}_2$ -induced reduction in pH or to the associated changes in marine carbonate chemistry (ocean acidification) did the scientific community begin to realize that this is a potentially serious issue (3–6). The carbonate saturation state,  $\Omega$ , is of particular relevance, especially for organisms that build part of their structures out of mineral forms of  $\text{CaCO}_3$ . This saturation state describes whether seawater is super- or undersaturated with regard to mineral forms of  $\text{CaCO}_3$ , such as calcite or the less stable forms aragonite and high magnesium carbonate (7). When  $\Omega > 1$ , seawater is supersaturated, whereas  $\Omega < 1$  characterizes seawater that is undersaturated. Currently, almost all of the surface ocean waters are substantially supersaturated with regard to aragonite (global mean saturation state of aragonite,  $\Omega_{\text{arag}}$ , of  $\sim 3.0$ ) (8). However, upwelling regions such as the Southern Ocean (9, 10) and the Eastern Boundary Upwelling Systems (11) have a naturally lower pH and a substantially lower saturation state, because the upwelled waters are enriched in  $\text{CO}_2$  from the remineralization of organic matter in the ocean interior and, thus, have low pH and  $\Omega$ .

Recent observations in the California Current System (California CS), one of the four major Eastern Boundary Upwelling Systems, revealed that waters with  $\Omega_{\text{arag}} < 1$  are being transported onto the continental shelf during strong upwelling events and are even reaching the surface ocean in a few nearshore locations (11). Though the upwelling of waters with low pH and  $\Omega_{\text{arag}}$  is a naturally occurring event along the West Coast of the United States (12, 13), model- and

data-based estimates suggest that the increase in atmospheric  $\text{CO}_2$  since preindustrial times has contributed to the severity of the event by lowering the pH by  $\sim 0.1$  and  $\Omega_{\text{arag}}$  by  $\sim 0.4$  (11, 12). With atmospheric  $\text{CO}_2$  likely to increase further, it is important to assess how the California CS will evolve in the future and what levels of ocean acidification it might experience in the coming decades. This is especially relevant because the California CS constitutes one of the most productive ecosystems in the world with a high biodiversity (14, 15) and important commercial fisheries (16), yet the California CS may be especially prone to reaching widespread undersaturation soon due to its low initial pH and  $\Omega_{\text{arag}}$ . Thus far, global ocean models have failed to recognize ocean acidification in Eastern Boundary Upwelling Systems (17), because their coarse resolution is insufficient to resolve the local dynamics responsible for bringing the waters with low pH and  $\Omega_{\text{arag}}$  to the surface (9, 18, 19). We have overcome this limitation by using a regional model at eddy-resolving resolution and investigate the progression of ocean acidification in the California CS from 1995 until 2050 under two future  $\text{CO}_2$  scenarios: the high-emissions scenario A2 and the low-emissions scenario B1, both from the Special Report on Emissions Scenarios (SRES) (20). We contrast these projections into the future with results from a simulation of the preindustrial state (i.e., from 1750). We put particular emphasis on the changes in the saturation state  $\Omega_{\text{arag}}$  in the nearshore 10-km region of the

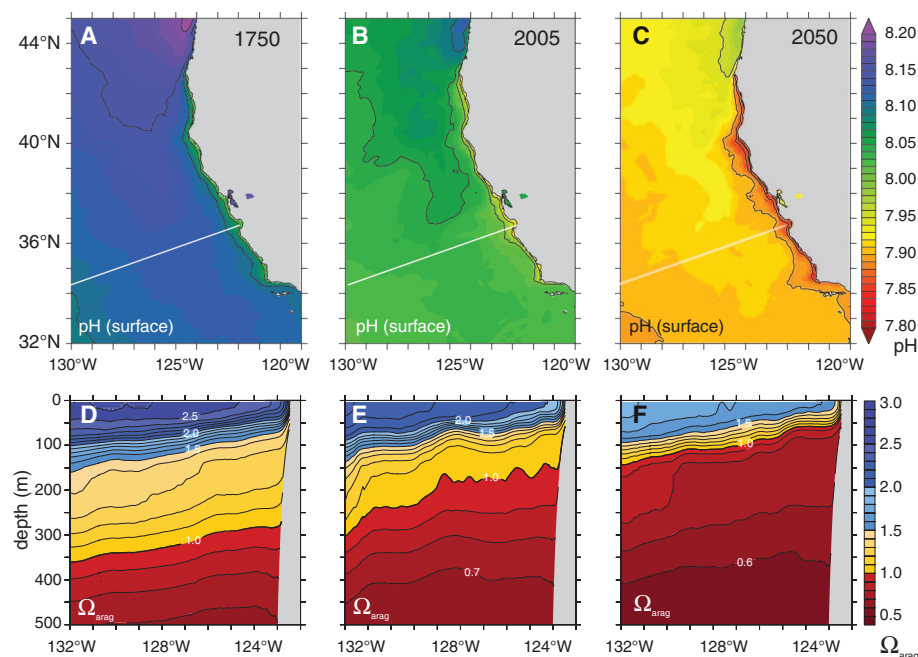


**Fig. 1.** Temporal evolution of ocean acidification in the California CS from 1750 until 2050 for the A2 scenario. (A to C) Maps illustrating the evolution of annual mean surface pH, showing the decrease in pH for 1750, 2005, and 2050. (D to F) Offshore depth sections depicting the general decrease of the annual mean saturation state of seawater with regard to aragonite ( $\Omega_{\text{arag}}$ ) and the shoaling of the saturation depth (i.e.,  $\Omega_{\text{arag}} = 1$ ) for the same three years. The white lines in (A) to (C) indicate the position of the offshore section.

<sup>1</sup>Environmental Physics, Institute of Biogeochemistry and Pollutant Dynamics, ETH Zürich, Zürich, Switzerland. <sup>2</sup>Atmospheric and Oceanic Sciences Program, Princeton University, Princeton, NJ, USA. <sup>3</sup>Climate and Environmental Physics, University of Bern, Bern, Switzerland.

\*To whom correspondence should be addressed. E-mail: nicolas.gruber@env.ethz.ch



central California CS [Point Conception (34°35'N) to the California/Oregon border (42°0'N)], where upwelling is strongest.

The model we employ is a California CS setup of the Regional Oceanic Modeling System (ROMS) (21), to which we have coupled a simple nitrogen-based ecosystem model and a full description of the marine inorganic carbon system (see supplementary materials for details and model evaluation) (22, 23). For all simulations, the model is forced with present-day climatological boundary conditions based on observations, except for atmospheric CO<sub>2</sub> and for the lateral boundary conditions of dissolved inorganic carbon.

For the preindustrial time-slice simulation, the atmospheric partial pressure of CO<sub>2</sub> ( $P_{\text{CO}_2}$ ) was prescribed at 280 parts per million (ppm), whereas for the transient simulations, atmospheric  $P_{\text{CO}_2}$  increased from 364 ppm in 1995 to 492 ppm (B1 scenario) and 541 ppm (A2 scenario), respectively, in 2050. The preindustrial case and the A2 scenario were run with our standard configuration at 5-km horizontal resolution, whereas we employed a coarser-resolution configuration of 15 km to explore the sensitivity of our results to the scenarios.

For the time period between 1750 and 2005, the model simulations suggest that surface-ocean

pH decreased from an annual mean of  $8.12 \pm 0.03$  to  $8.04 \pm 0.03$  (1 SD of the spatial mean) for the whole California CS (Fig. 1). Over the same time period, the annual mean surface ocean  $\Omega_{\text{arag}}$  decreased from  $2.58 \pm 0.19$  to  $2.27 \pm 0.20$ , reflecting the reduction of the carbonate ion concentration from the titration of the CO<sub>2</sub> that the ocean has taken up from the atmosphere. In the nearshore 10 km of the central California coast, annual mean surface pH and  $\Omega_{\text{arag}}$  in 1750 were already as low as  $8.03 \pm 0.03$ , and  $1.94 \pm 0.14$ , respectively, reflecting the upwelling of waters with naturally low pH and  $\Omega_{\text{arag}}$  due to the substantial addition of respired CO<sub>2</sub> to these waters. The uptake of anthropogenic CO<sub>2</sub> from the atmosphere until 2005 decreased the surface pH and  $\Omega_{\text{arag}}$  in this region by about the same amount as for the whole domain, yielding annual mean values of  $7.95 \pm 0.04$  and  $1.67 \pm 0.16$ , respectively.

For atmospheric  $P_{\text{CO}_2}$  following the SRES A2 scenario, our model simulation predicts an even sharper decrease until 2050 to an annual mean surface pH and  $\Omega_{\text{arag}}$  for the whole domain of  $7.92 \pm 0.03$  and  $1.77 \pm 0.16$ , respectively, and for the nearshore 10-km environment of the central California CS to  $7.82 \pm 0.04$  and  $1.26 \pm 0.12$ , respectively. pH and  $\Omega_{\text{arag}}$  reach even lower values in summer, when upwelling is at its maximum (13). In the summer of 2050, for example, our model projects that large stretches of the nearshore 10 km of the central California CS will be undersaturated (see supplementary materials), although the mean  $\Omega_{\text{arag}}$  remains slightly supersaturated ( $1.05 \pm 0.13$ ).

These changes are not confined to the surface ocean, as anthropogenic CO<sub>2</sub> is transported from the surface to depth, causing changes in the carbonate chemistry there as well (Fig. 1, D to F). As a result, the aragonite saturation horizon, which was located at ~350 m in the offshore region and at ~300 m in the nearshore, shoaled generally by ~150 m from 1750 until 2005 and is projected to shoal by another 100 to 150 m between 2005 and 2050. In 2050, the annual mean aragonite saturation horizon is as shallow as 100 m in the offshore region, but shoals to less than 50 m in the nearshore regions in the annual mean. In the summer, the aragonite saturation horizon breaks to the surface in many parts of the central California CS (fig. S4). Thus, ocean acidification will severely reduce the habitat for organisms that are sensitive to the saturation state, particularly for those who cannot tolerate undersaturated conditions for an extended period of time.

The reduction of habitats of organisms sensitive to ocean acidification becomes even more evident when considering the volume of water with a particular range of saturation states within the nearshore 10 km of the central California CS (Fig. 2). In 1750, our model simulates that ~16% of the waters in the euphotic zone (0 to 60 m) in that region had an  $\Omega_{\text{arag}}$  value above 2, with the majority (60%) having an  $\Omega_{\text{arag}}$

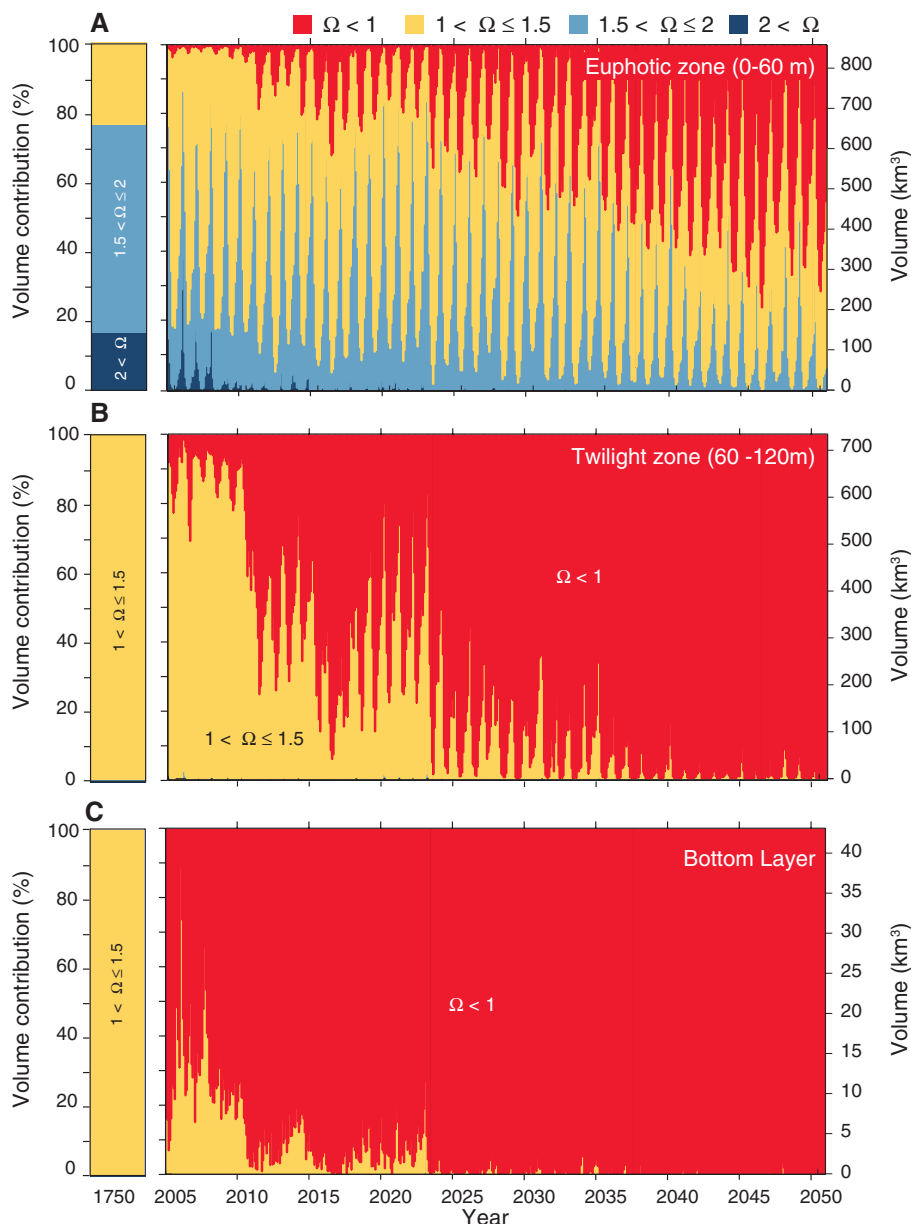


**Fig. 2.** Temporal evolution of the volume of seawater with a particular  $\Omega_{\text{arag}}$  in the nearshore 10 km of the central California CS for the A2 scenario. The panels depict the evolution (A) in the upper 60 m, (B) in between 60 and 120 m, and (C) in the bottom layer of the model above the shelf sediments (maximum depth: 120 m). Volumes were computed by summing over all regions from Point Conception (34°35'N) to the California/Oregon border (42°0'N).

between 1.5 and 2.0 (Fig. 2A). Only 24% of the waters had an  $\Omega_{\text{arag}}$  between 1.5 and 1.0, and no waters were undersaturated. By 2005, the volume of waters with an  $\Omega_{\text{arag}}$  value greater than 1.5 had dropped to ~20% in the yearly average, with waters with an  $\Omega_{\text{arag}}$  between 1.0 and 1.5 dominating and undersaturated waters appearing seasonally. In the coming decades, waters with  $\Omega_{\text{arag}} < 1$  are projected to expand substantially in the euphotic zone of the central California CS, occupying more than half of the waters in 2050 in the annual mean. In the summer season, this ratio increases to about 70%, with long stretches of the central coast projected to be undersaturated throughout the euphotic zone (fig. S4). By that time, waters with  $\Omega_{\text{arag}} > 1.5$  will have largely vanished.

The progression toward widespread and persistent undersaturation in the nearshore 10 km is even more dramatic in the upper twilight zone; that is, in the depth range between 60 and 120 m (Fig. 2B). Though nearly all waters in this depth range were supersaturated with respect to aragonite in preindustrial times, a small but persistent volume of undersaturated waters appears by 2005. Within the next 20 to 30 years, the volume of undersaturated waters quickly expands, and by ~2035 in the SRES A2 scenario, nearly the entire twilight zone of the central California coast will be undersaturated year-round.

Undersaturated conditions became common by 2005 in the bottom layer of the model above the shelf sediments of the central California CS (with water depths ranging between 50 and

120 m) (Fig. 2C). This is a substantial change since preindustrial times, for which the model simulated no undersaturated conditions in this layer. Still, ~30% of this layer remains supersaturated in 2005. Our simulations for the waters above the shelf sediments are consistent with data-based reconstructions for the central Oregon coast (13), which also suggest widespread undersaturated conditions for the present but extended periods of supersaturation with regard to aragonite. Such supersaturated conditions are projected to disappear within the next 10 years, so that by the mid-2020s essentially all waters above the shelf sediments will be undersaturated.

Most of these early developments occur regardless of whether atmospheric  $\text{CO}_2$  follows the high (A2) or low (B1)  $\text{CO}_2$  scenario (see supplementary materials). This lack of sensitivity is due to two factors. First, the two scenarios do not differ substantially in their atmospheric  $\text{CO}_2$  levels for the next 20 years; only around 2035 do they begin to deviate more strongly from each other (fig. S5). Second, because surface waters are following the increase in atmospheric  $\text{CO}_2$  relatively closely, the primary determinant for the degree of ocean acidification in the upper ocean is the atmospheric  $\text{CO}_2$  concentration, not its rate of change. This is well illustrated when the saturation state is plotted as a function of atmospheric  $p\text{CO}_2$  rather than time (Fig. 3), resulting in nearly identical outcomes for the two scenarios (fig. S7). This means that the timing of when particular chemical thresholds are reached in the upper ocean depends only

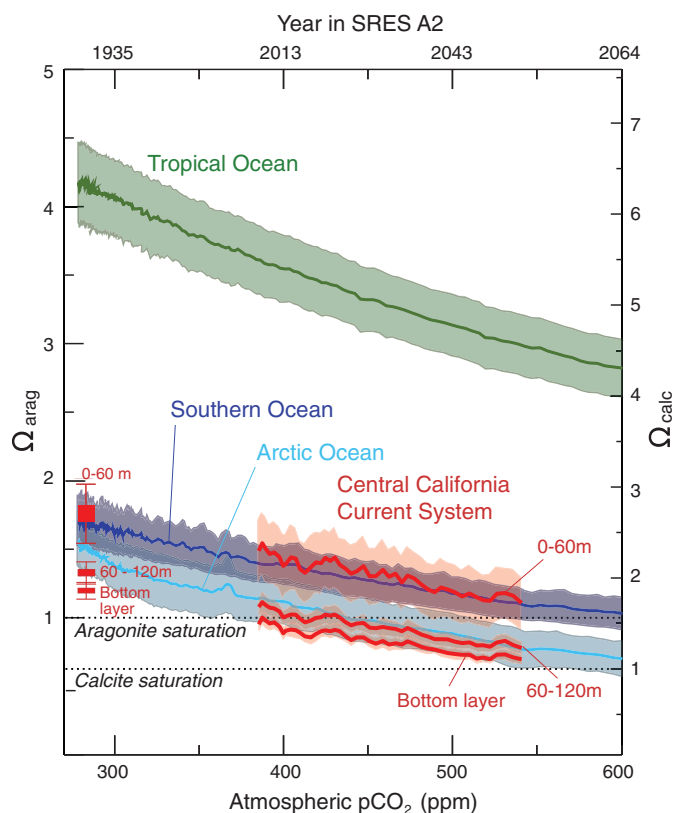
on when the corresponding atmospheric  $\text{CO}_2$  concentration is attained. Our simulation results show that at ~400 ppm, substantial parts of the twilight zone (60 to 120 m) and the habitats along the sea floor on the shelf become undersaturated. Given the present-day atmospheric  $\text{CO}_2$  concentration of 390 ppm and the recent rates of increase in atmospheric  $\text{CO}_2$  of 1.5 ppm/year or more (24), we are virtually certain that a level of 400 ppm will be reached within this decade. When atmospheric  $\text{CO}_2$  reaches ~500 ppm, a level that is crossed by ~2040 in the A2 scenario and a little after 2050 in the B1 scenario, the top 60 m in our model begin to experience extended undersaturated conditions. Thus, unless atmospheric  $\text{CO}_2$  follows a scenario that is much lower than the low-emission B1 pathway, most of the simulated transitions are bound to happen.

The projected evolution of the upper ocean in the nearshore 10 km of the central California CS toward low  $\Omega_{\text{arag}}$  conditions is similar to that projected for the Southern Ocean and the Arctic Ocean (Fig. 3), which have previously been proposed as the first oceanic regions to become undersaturated (9, 18). The upper twilight zone and the bottom layer of the central California CS become undersaturated even faster than the surface Arctic Ocean, highlighting the imminent nature of reaching this threshold.

The progression of ocean acidification may occur even faster or at lower atmospheric  $\text{CO}_2$  concentrations than projected by our model simulations. First, our model tends to overpredict  $\Omega_{\text{arag}}$  in the nearshore regions (see supplementary materials), so that the appearance of certain  $\Omega_{\text{arag}}$  thresholds is probably delayed in the model. A sensitivity test, in which we applied a uniform correction of -0.1 units to  $\Omega_{\text{arag}}$ , revealed that the shifts in the distribution of volumina with a particular saturation state may occur ~10 years earlier than in our standard case (fig. S3). Second, our model is forced with the present-day climatological boundary conditions for all years up to 2050, whereas theoretical considerations (25), model simulations (26), and historical trends (27) suggest that the upwelling favorable winds may increase in the coming decades in response to global warming. This could enhance the upwelling of corrosive water and accelerate the progression toward low  $\Omega_{\text{arag}}$  conditions even further.

Although we are able to project with some confidence the chemical changes associated with the future evolution of ocean acidification in the California CS, the impacts of these chemical changes on organisms, ecosystems, and biogeochemistry remain highly uncertain (6, 28, 29). The limited evidence available suggests that most aragonite-secreting organisms, such as pteropods or oysters, respond negatively to lowered  $\Omega_{\text{arag}}$  (30), with the early-life stages appearing to be particularly sensitive (31). We emphasize here the progression toward undersaturated conditions, as this represents a well-established chemical threshold, but

**Fig. 3.** Temporal evolution of the mean saturation states with regard to aragonite (left y axis) and calcite (right y axis) in the nearshore 10 km of the central California CS as a function of the atmospheric  $p\text{CO}_2$  (lower x axis) and time (upper x axis). The evolutions of three depth layers (0 to 60 m, 60 to 120 m, and the bottom layer of the model above the shelf sediments) are shown. Also shown are the mean evolutions of  $\Omega_{\text{arag}}$  for the tropical ocean, the Southern Ocean, and the Arctic Ocean, as simulated by a global coarse resolution model (18). Shaded curves depict the modeled trajectories including  $\pm 1$  SD of the seasonal variations. All simulations were performed for the A2 scenario.





we must note that none of the organisms studied so far has a simple dose-response curve with a threshold at  $\Omega_{\text{arag}} = 1$  (28). Rather, some organisms or life stages respond negatively at higher  $\Omega_{\text{arag}}$ , whereas others can tolerate undersaturated conditions for some time. In addition, organisms living in the California CS may have had the chance to adapt to the naturally low and variable pH and  $\Omega_{\text{arag}}$  conditions that prevailed before the onset of the industrial revolution, making them potentially less vulnerable to the effects of ocean acidification (32). Regardless of these uncertainties associated with the biological response to ocean acidification, our simulation results indicate that the California CS is moving rapidly toward conditions that are well outside the natural range, with frequent or even persistent undersaturation conditions (Fig. 3). Such conditions probably will be challenging to calcifying and other organisms, as well as the fisheries that depend on them (33).

Although we focused our study on the changes in  $\Omega_{\text{arag}}$ , ocean acidification alters all aspects of the carbonate chemistry in the ocean, including pH and the concentrations of dissolved  $\text{CO}_2$ , bicarbonate, and carbonate (34), each of which can impact physiological processes and, hence, affect marine organisms and ecosystems (35). Yet, the changes in these properties are highly correlated (fig. S7) because they are mechanistically linked through the driver of ocean acidification (i.e., the oceanic uptake of  $\text{CO}_2$  from the atmosphere), which increases dissolved  $\text{CO}_2$  and bicarbonate but decreases pH,  $\Omega_{\text{arag}}$ , and carbonate with predictable ratios (34). Therefore, regardless of whether the parameter affecting a biological process is  $\Omega_{\text{arag}}$  or the dissolved  $\text{CO}_2$  concentration, the changes are unprecedented.

In addition, ocean acidification will not be operating in isolation, but its impact could be potentially worsened with synergistic effects of ocean warming and deoxygenation (35, 36), both of which have been noted to occur in the California CS (37, 38) and probably get more severe with time (39). Thus, specific attention should be given to the development of ocean acidification in this very rich and productive ecosystem, as well as to some of the other Eastern Boundary Current Systems where similar conditions prevail.

#### References and Notes

- W. Stumm, J. J. Morgan, *Aquatic Chemistry: An Introduction Emphasizing Chemical Equilibria in Natural Waters* (Wiley Interscience, New York, ed. 1, 1970).
- W. S. Broecker, Y.-H. Li, T.-H. Peng, in *Impingement of Man on the Oceans*, D. W. Hood, Ed. (Wiley, New York, 1971), pp. 287–324.
- J.-P. Gattuso, M. Frankignoulle, I. Bourge, S. Romaine, R. W. Buddemeier, *Global Planet. Change* **18**, 37 (1998).
- J. A. Kleypas et al., *Science* **284**, 118 (1999).
- U. Riebesell et al., *Nature* **407**, 364 (2000).
- S. C. Doney, V. J. Fabry, R. A. Feely, J. A. Kleypas, *Annu. Rev. Mar. Sci.* **1**, 169 (2009).
- A. Mucci, *Am. J. Sci.* **283**, 780 (1983).
- R. A. Feely, S. C. Doney, S. C. Cooley, *Oceanography* **22**, 36 (2009).
- J. C. Orr et al., *Nature* **437**, 681 (2005).
- B. I. McNeil, R. J. Matear, *Proc. Natl. Acad. Sci. U.S.A.* **105**, 18860 (2008).
- R. A. Feely, C. L. Sabine, J. M. Hernandez-Ayon, D. Ianson, B. Hales, *Science* **320**, 1490 (2008).
- C. Hauri et al., *Oceanography* **22**, 60 (2009).
- L. W. Juranek et al., *Geophys. Res. Lett.* **36**, L24601 (2009).
- M.-E. Carr, *Deep Sea Res. Part II* **49**, 59 (2002).
- B. A. Block et al., *Nature* **475**, 86 (2011).
- R. Costanza et al., *Nature* **387**, 253 (1997).
- C. Turley et al., *Mar. Pollut. Bull.* **60**, 787 (2010).
- M. Steinacher, F. Joos, T. L. Frölicher, G.-K. Plattner, S. C. Doney, *Biogeosciences* **6**, 515 (2009).
- F. Joos, T. L. Frölicher, M. Steinacher, G.-K. Plattner, in *Ocean Acidification*, J.-P. Gattuso, L. Hansson, Eds. (Oxford Univ. Press, Oxford, 2011), chap. 14, pp. 272–290.
- N. Nakicenovic et al., *Special Report on Emissions Scenarios: A Special Report of Working Group III of the Intergovernmental Panel on Climate Change* (Cambridge Univ. Press, New York, 2000).
- A. F. Shchepetkin, J. C. McWilliams, *Ocean Model.* **9**, 347 (2005).
- N. Gruber et al., *Nat. Geosci.* **4**, 787 (2011).
- Z. Lachkar, N. Gruber, *Biogeosciences* **8**, 2961 (2011).
- P. Tans, R. F. Keeling, Recent Mauna Loa Data, Electronic Data (National Oceanic and Atmospheric Administration Earth System Research Laboratory, Scripps Institution of Oceanography, Boulder, CO, 2012); [www.esrl.noaa.gov/gmd/ccgg/trends/](http://www.esrl.noaa.gov/gmd/ccgg/trends/).
- A. Bakun, *Science* **247**, 198 (1990).
- N. S. Diffenbaugh, M. A. Snyder, L. C. Sloan, *Proc. Natl. Acad. Sci. U.S.A.* **101**, 27 (2004).
- D. Gutiérrez et al., *Geophys. Res. Lett.* **38**, L07603 (2011).
- K. J. Kroeker, R. L. Kordas, R. N. Crim, G. G. Singh, *Ecol. Lett.* **13**, 1419 (2010).
- J. P. Barry, S. Widdicombe, J. M. Hall-Spencer, in *Ocean Acidification*, J.-P. Gattuso, L. Hansson, Eds. (Oxford Univ. Press, Oxford, 2011), chap. 10, pp. 192–209.
- V. J. Fabry, B. A. Seibel, R. A. Feely, J. C. Orr, *ICES J. Mar. Sci.* **65**, 414 (2008).
- A. Barton, B. Hales, G. G. Waldbusser, C. Langdon, R. Feely, *Limnol. Oceanogr.* **57**, 698 (2012).
- M. D. Ohman, B. E. Lavanios, A. W. Townsend, *Geophys. Res. Lett.* **36**, L18608 (2009).
- S. R. Cooley, S. C. Doney, *Environ. Res. Lett.* **4**, 024007 (2009).
- J. C. Orr, in *Ocean Acidification*, J. P. Gattuso, L. Hansson, Eds. (Oxford Univ. Press, Oxford, 2011), chap. 3, pp. 41–66.
- H. O. Pörtner, *Mar. Ecol. Prog. Ser.* **373**, 203 (2008).
- N. Gruber, *Philos. Trans. R. Soc. London Ser. A* **369**, 1980 (2011).
- S. J. Bograd et al., *Geophys. Res. Lett.* **35**, L12607 (2008).
- F. Chan et al., *Science* **319**, 920 (2008).
- R. F. Keeling, A. Kortzinger, N. Gruber, *Annu. Rev. Mar. Sci.* **2**, 199 (2010).

**Acknowledgments:** This work was supported by ETH Zürich and the European Project on Ocean Acidification, which received funding from the European Community's Seventh Framework Programme (FP7/2007-2013) under grant agreement no. 211384. T.L.F. was supported by the Carbon Mitigation Initiative project at Princeton Univ., sponsored by BP and Ford Motor Company. We thank J. C. McWilliams and his group at the Univ. of California Los Angeles for the long-term collaboration on the development of ROMS.

#### Supplementary Materials

[www.sciencemag.org/cgi/content/full/science.1216773/DC1](http://www.sciencemag.org/cgi/content/full/science.1216773/DC1)  
Supplementary Text  
Figs. S1 to S8  
References

17 November 2011; accepted 30 May 2012  
Published online 14 June 2012;  
10.1126/science.1216773

## Clovis Age Western Stemmed Projectile Points and Human Coprolites at the Paisley Caves

Dennis L. Jenkins,<sup>1\*†</sup> Loren G. Davis,<sup>2\*</sup> Thomas W. Stafford Jr.,<sup>3,4\*</sup> Paula F. Campos,<sup>3,5\*</sup> Bryan Hockett,<sup>6</sup> George T. Jones,<sup>7</sup> Linda Scott Cummings,<sup>8</sup> Chad Yost,<sup>8</sup> Thomas J. Connolly,<sup>1</sup> Robert M. Yohe II,<sup>9</sup> Summer C. Gibbons,<sup>9</sup> Maanasa Raghavan,<sup>3</sup> Morten Rasmussen,<sup>3</sup> Johanna L. A. Paijmans,<sup>10</sup> Michael Hofreiter,<sup>10</sup> Brian M. Kemp,<sup>11</sup> Jodi Lynn Barta,<sup>11,12</sup> Cara Monroe,<sup>11,13</sup> M. Thomas P. Gilbert,<sup>3\*</sup> Eske Willerslev<sup>3\*†</sup>

The Paisley Caves in Oregon record the oldest directly dated human remains (DNA) in the Western Hemisphere. More than 100 high-precision radiocarbon dates show that deposits containing artifacts and coprolites ranging in age from 12,450 to 2295  $^{14}\text{C}$  years ago are well stratified. Western Stemmed projectile points were recovered in deposits dated to 11,070 to 11,340  $^{14}\text{C}$  years ago, a time contemporaneous with or preceding the Clovis technology. There is no evidence of diagnostic Clovis technology at the site. These two distinct technologies were parallel developments, not the product of a unilinear technological evolution. "Blind testing" analysis of coprolites by an independent laboratory confirms the presence of human DNA in specimens of pre-Clovis age. The colonization of the Americas involved multiple technologically divergent, and possibly genetically divergent, founding groups.

**D**espite increasing evidence for pre-Clovis sites in North and South America (1–6), debate continues as to whether the technological tradition that led to Clovis was the first to arrive in the Americas. Was Clovis the first in a long, unilinear technological evolu-

tion spreading throughout the Americas? Or were other Pleistocene technological complexes involved (6–10)? In the American Far West, the Western Stemmed Tradition (WST) is recognized as the oldest nonfluted lithic technology. Stemmed points were present earlier in East

Asia and Siberia, and the basic form could have arrived in the Americas before Clovis developed (11–15). Like Clovis, the WST is a New World development sharing basic morphological and technological characteristics with Old World forms.

Western Stemmed (WS) projectile points are generally narrow bifaces with sloping shoulders, and many have relatively thick contracting bases (Fig. 1, A to C). They were commonly made on flakes by broad collateral, midline, percussion flaking and finished by pressure flaking. In this, they are morphologically and technologically distinct from the generally broader, concave-based, fluted Clovis points made on large bifacial preforms often thinned by overshot flake technology (16–19) (Fig. 1D). Prismatic blades—long, narrow flakes with triangular cross sections driven from specially prepared cores—are common to Clovis sites outside of western North America (16, 17) and are less common to WST assemblages. Most dated WS projectile points are younger than Clovis, and it has been proposed that they evolved from a single tradition. The possible exceptions are WS projectile points found in strata dated to the Clovis era at the Smith Creek Cave, Cooper's Ferry, and Bonneville Estates Rockshelter sites. The association of the dates with the points at these sites has not been confirmed and is not widely accepted (fig. S1) (13, 20–24). Here, we describe WST assemblages—including human coprolites—at the Paisley Caves and show that these date to between 11,070 and 11,340 radiocarbon years before the present ( $^{14}\text{C}$  yr B.P.), confirming that they overlap or precede Clovis (20).

We continued to excavate the Paisley Caves from 2009 through 2011. To resolve the question of stratigraphic integrity, we acquired 121 new AMS (accelerator mass spectrometry) radiocarbon dates on samples of terrestrial plants (e.g., *Artemisia* sp., *Atriplex* sp.), macrofossils from coprolites, bone collagen, and water-soluble extracts recovered from each of these categories. To date, a total of 190 radiocarbon dates have been produced from the Paisley Caves (tables S1 to S9). These are distributed throughout four

of the caves, although the primary set of high-precision dates represents six dating columns in Caves 2 and 5. DNA analysis has been completed on 65 coprolites from the site. To investigate whether non-endogenous human DNA may have leached into samples, we also tested Camelidae, Felidae, and Caprinae coprolites for the presence of ancient human DNA (25).

Middens of wood rat (*Neotoma* sp.) are common in the Paisley Caves, particularly in the North Block of Cave 5 (fig. S2). To investigate whether excavations by rodents disturbed the stratigraphic integrity of the deposits, we dated two profiles there (Fig. 2A and tables S2 and S3) (25). The dates in each are stratigraphically and chronologically well ordered. Beginning just below a layer of Mount Mazama O tephra—dated to  $6790 \pm 15$   $^{14}\text{C}$  yr B.P. in Cave 2 and  $\sim 6850$  years regionally (26)—the ages in profiles I and II range from  $6980 \pm 15$  to  $12,450 \pm 30$   $^{14}\text{C}$  yr B.P. WS projectile point 1294-PC-5/6D-47-1 (Fig. 1B), a biface, a polished probable food-processing stone (fig. S3), and eight pieces of lithic debitage were recovered from lithostratigraphic units LU1 and LU2 in the North Block,

which are of late Pleistocene–early Holocene age. Projectile point 1294-PC-5/6D-47-1 was recovered from sifted LU2 [LU1a in (4)] sediments in excavation unit 5/6D (fig. S2) and may date from 11,135 to 11,600  $^{14}\text{C}$  yr B.P. (Table 1) (25).

A trench connecting the North and South Blocks provided continuous stratigraphic exposure across the mouth of Cave 5 (fig. S2). Profiles III and IV, at the intersection of this trench with the South Block, reveal well-stratified, highly indurated sandy sediments (LU2 and LU3) underlain by gravelly LU1 deposits. Ages here range from  $7700 \pm 20$  to  $12,410 \pm 25$   $^{14}\text{C}$  yr B.P. (Fig. 2, B and C, and tables S4 and S5). Organic materials in basal LU1 sediments of profile III date to  $12,410$   $^{14}\text{C}$  yr B.P. The lower portion of overlying LU2 is dated between  $11,070 \pm 25$  and  $12,405 \pm 25$   $^{14}\text{C}$  yr B.P. and is composed of more organic, loamy, and gravelly sand, varying portions of which are highly indurated. The upper portion is dated between  $10,855 \pm 30$   $^{14}\text{C}$  yr B.P. and  $\sim 9500$   $^{14}\text{C}$  yr B.P.

Rodent disturbances were traceable as oval voids filled with loose organic sediments intruded into less organic, compact to cemented LU2 sandy-

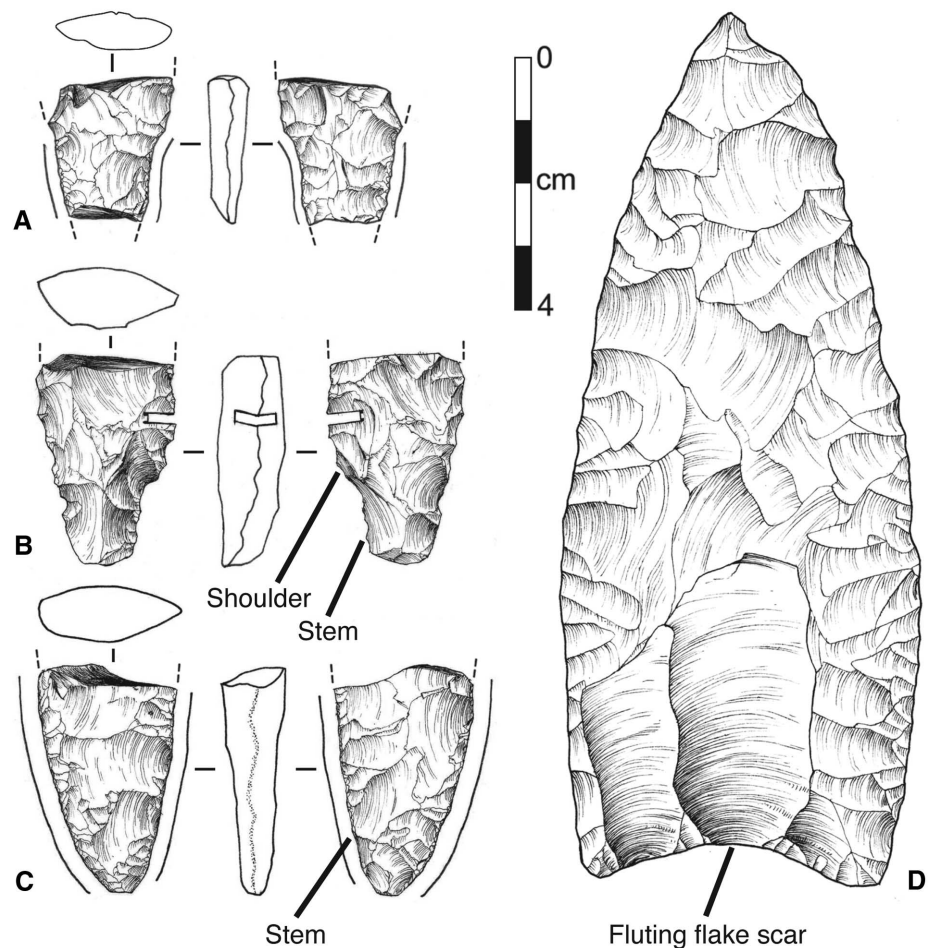


**Fig. 1.** Western Stemmed projectile point fragments. (A) 1961-PC-5/18a-10-1. (B) 1294-PC-5/6D-47-1. (C) 1895-PC-5/16A-24. (D) Clovis point from Dent site, Colorado. Edges of (A) and (C) are intensely ground, as indicated by lines paralleling edges and stippling in edge-on view. The notch in (B) is an obsidian hydration cut. [Illustrations by Eric Carlson and George T. Jones]

<sup>1</sup>Museum of Natural and Cultural History, University of Oregon, Eugene, OR 97403, USA. <sup>2</sup>Department of Anthropology, Oregon State University, Corvallis, OR 97331, USA. <sup>3</sup>Centre for GeoGenetics, University of Copenhagen, DK 1350 Copenhagen, Denmark. <sup>4</sup>Stafford Research Laboratories Inc., 200 Acadia Avenue, Lafayette, CO 80026, USA. <sup>5</sup>Museu da Ciência, Universidade de Coimbra, Largo Marquês de Pombal, 3000-272 Coimbra, Portugal. <sup>6</sup>Bureau of Land Management, Nevada State Office, 1340 Financial Boulevard, Reno, NV 89502, USA. <sup>7</sup>Department of Anthropology, Hamilton College, Clinton, NY 13323, USA. <sup>8</sup>PaleoResearch Institute, 2675 Youngfield Street, Golden, CO 80401, USA. <sup>9</sup>Anthropology Program, California State University, Bakersfield, CA 93311, USA. <sup>10</sup>Department of Biology, University of York, York YO10 5DD, UK. <sup>11</sup>Department of Anthropology and School of Biological Sciences, Washington State University, Pullman, WA 99164, USA. <sup>12</sup>Department of Biological and Health Sciences, Madonna University, Livonia, MI 48150, USA. <sup>13</sup>Department of Anthropology, University of California, Santa Barbara, CA 93106, USA.

\*These authors contributed equally to this work.

†To whom correspondence should be addressed. E-mail: djenkins@uoregon.edu (D.L.); ewillerslev@snm.ku.dk (E.W.)





A Camelidae coprolite was recovered in situ below the silt lens at 1365.85 m (table S11). It produced a macrofossil age of  $12,125 \pm 30$   $^{14}\text{C}$  yr B.P.; however, the age of its water-soluble extract was  $11,315 \pm 25$   $^{14}\text{C}$  yr B.P. This is the only instance of fractions differing by hundreds of years between macrofossils and their extracted solutes in 12 such tests (25). Three coprolites containing ancient human DNA (aDNA)—results from two of which were replicated by laboratories in Copenhagen and York in blind testing and found to relate to mitochondrial DNA founding haplogroup A (25)—were recovered in close horizontal proximity. Dates on the macroflora and solute fractions, respectively, from these three coprolites were  $12,265 \pm 25$  and  $12,260 \pm 30$   $^{14}\text{C}$  yr B.P.;  $12,165 \pm 25$  and  $12,050 \pm 25$   $^{14}\text{C}$  yr B.P., and  $11,205 \pm 25$  and  $11,250 \pm 25$   $^{14}\text{C}$  yr B.P. (tables S1 and S12). The two oldest of these were recovered lower in the deposits of adjacent excavation unit 5/11B (fig. S2). Presumably, they would have been contaminated in the manner of the Camelidae coprolite had water reached them. Their concordant ages indicate that the effects of water were limited spatially, stratigraphically, and in volume. The new human aDNA

**Table 1.** Western Stemmed projectile point proveniences and their bracketing radiocarbon dates. Two independent laboratories provided the dual dates for specimen 1294-PC-5/6D-47-1.

Specimen no.	Unit	Elevation (m)	Upper bracketing age and elevation (m)	Lower bracketing age and elevation (m)
1294-PC-5/6D-47-1	5/6D	1366.06 to 1366.01	10,050 ± 50 (1366.40 to 1366.35) 10,965 ± 50	12,140 ± 70 (1365.91 to 1365.86) 12,260 ± 60
1895-PC-5/16A-24	5/16A	1365.93	11,070 ± 25 (1365.97)	11,340 ± 50 (1365.88)
1895-PC-5/16A-23-6A	5/16A	1366.01 to 1365.96	10,855 ± 30 (1366.05 to 1366.00)	11,070 ± 25 (1365.97)
1961-PC-5/18a-10-1	5/18a	1366.10 to 1366.05	10,200 ± 35 (1366.09)	10,855 ± 30 (1366.05 to 1366.00)

results (table S12) confirm our previous findings that humans with DNA founding haplogroup A had occupied the site in pre-Clovis times (3).

In Cave 2, dates for profiles V and VI, beginning at the base of the Mount Mazama tephra, range between  $6790 \pm 15$  and  $12,320 \pm 35$   $^{14}\text{C}$  yr B.P. (Fig. 4 and fig. S5). All Cave 2 dates between  $10,980 \pm 20$  and  $12,425 \pm 30$   $^{14}\text{C}$  yr B.P. come from LU1 and LU2, both of which are easily distinguished from LU3 by their low organic, sand, and gravel content. LU1 contains water-rounded boulders and sandy gravels. It is covered by up to 30 cm of brown gravelly sand (LU2). The LU2 sands are partially capped by a thin alluvial silt lens with a mean age of  $11,035$   $^{14}\text{C}$  yr B.P. *Artemisia* charcoal from the surface of hearth 2/6-4 at elevation 1365.48 m was dated to  $10,020 \pm 30$   $^{14}\text{C}$  yr B.P., whereas *Artemisia* charcoal recovered at lower elevations—1365.40 m and 1365.35 to 1365.30 m from within the hearth depression—was dated to  $11,005 \pm 30$  and  $11,055 \pm 35$   $^{14}\text{C}$  yr B.P. (Fig. 4B and table S1). Because the younger sample was taken from the LU2-LU3 stratigraphic boundary where charcoal is common, and LU2—into which the hearth was excavated—is an incombustible, low-organic matrix, the  $10,020 \pm 30$   $^{14}\text{C}$  yr B.P. sample is interpreted as younger charcoal associated with LU3. We accept the age of  $11,005$   $^{14}\text{C}$  yr for this hearth. The hearth was surrounded by obsidian debitage and burned bone. Stone artifacts in undisturbed LU2 deposits at and below the hearth include 228 pieces of lithic debitage, a biface, a polished and chipped probable food-processing stone (fig. S6), and a flake tool. The pre-Clovis context of the probable food-processing stone at elevation 1365.28 m (not associated with the hearth) is established by dates on an *Artiodactyla* rib ( $11,930 \pm 25$   $^{14}\text{C}$  yr B.P.) and an *Equus* sp. maxilla ( $11,740 \pm 25$   $^{14}\text{C}$  yr B.P.) found below and above it at elevations of 1365.25 and 1365.31 m, respectively. LU2 transitions abruptly upward into more organic LU3 sediments that are rich in bat guano and are dated between  $6790 \pm 15$  and  $10,585 \pm 30$   $^{14}\text{C}$  yr B.P. (table S1).

DNA can be carried through sedimentary deposits by water (rain, sheet wash, capillary fringe solutions) and urine (3, 27). We initially (3, 28–30) addressed the question of DNA leaching by testing sediment around the coprolites, as well as *Neotoma* fecal pellets, for human aDNA; however, no human aDNA was detected. *Neotoma* sp. (wood rat) aDNA was extracted from *Neotoma* fecal pellets, and *Callospermophilus lateralis*

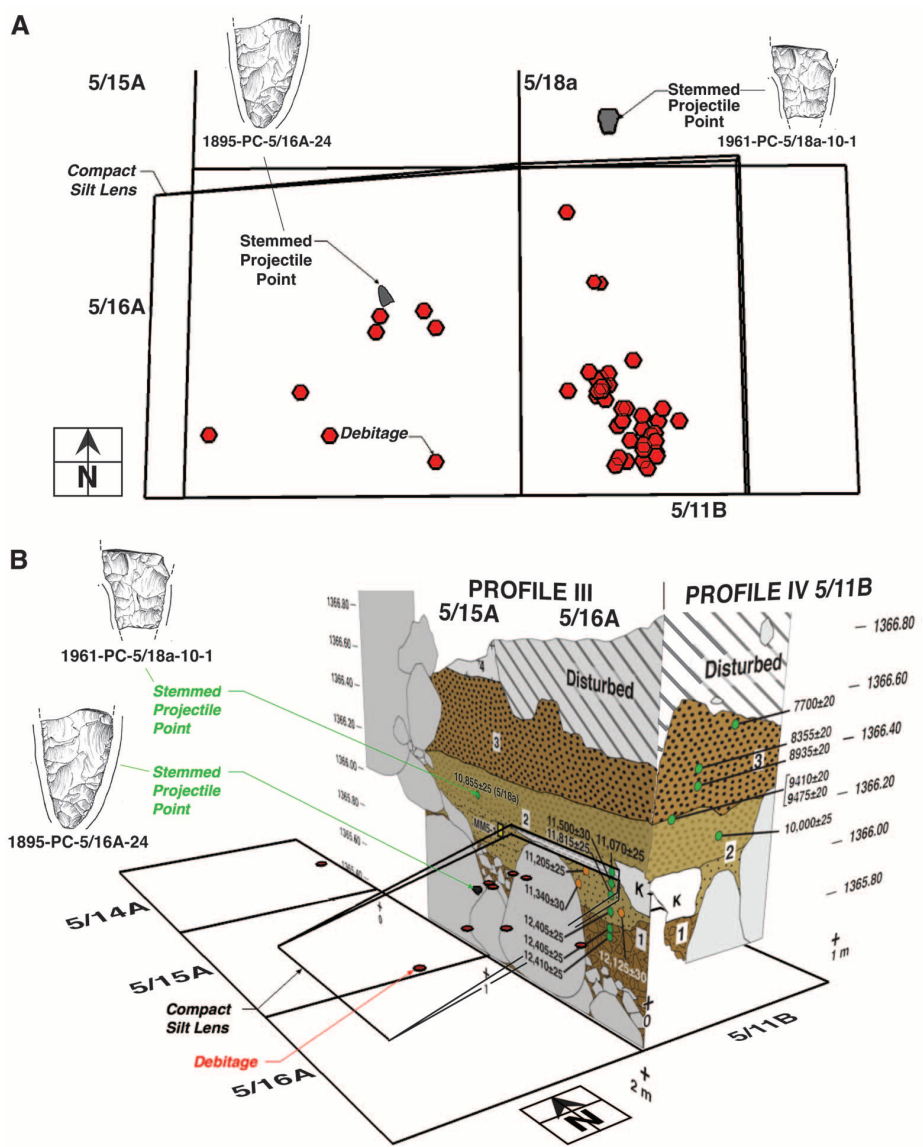


**Fig. 3.** (A) Horizontal distribution of Western Stemmed projectile points and in situ lithic debitage in excavation units 5/16A and 5/18A. (B) Vertical distribution of artifacts relative to acceptably dated coprolites and dating column samples.

(golden-mantled ground squirrel) aDNA was obtained from rodent bones near the coprolites, demonstrating that endogenous DNA survives in the material and the aDNA extraction techniques were producing reliable results (3, 28). Further tests were undertaken to investigate for potential leaching of modern DNA or aDNA

by attempting to extract human aDNA from dry *Neotoma* urine and from *Neotoma*, pronghorn, and mountain sheep fecal pellets. Again, no human aDNA was detected.

DNA moving in rainwaters or urine could contaminate underlying coprolites with younger DNA. To detect DNA translocation, we made



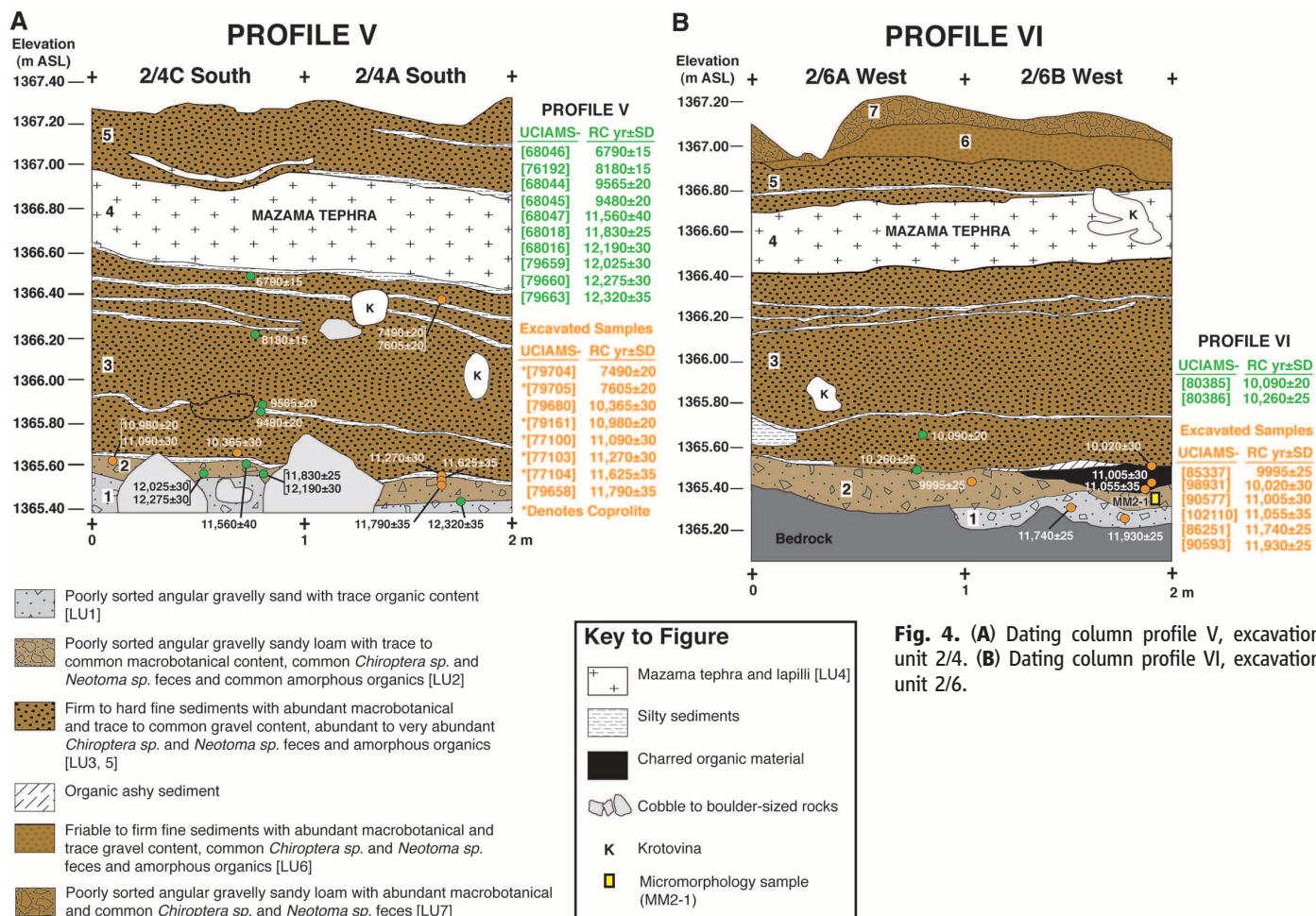


**Fig. 4. (A)** Dating column profile V, excavation unit 2/4. **(B)** Dating column profile VI, excavation unit 2/6.

26  $^{14}\text{C}$  measurements on paired macrofossils and water-soluble fractions on nine coprolites and three 1-cm-thick sediment samples. Younger solutes would indicate potential DNA contamination from younger overlying strata (table S9).

In seven coprolites, paired fractions had statistically similar ages. Another coprolite's solutes were 165  $^{14}\text{C}$  yr older than macrofossils, and a camelid coprolite's solutes were 810  $^{14}\text{C}$  yr younger than macrofossils. Sediment solutes and macrofossils exhibit differential dating of 85 to 180  $^{14}\text{C}$  yr. Urine-cemented sands accumulating at ~1 cm per 50 to 80 years have time-averaging problems, whereas instantaneous deposits such as coprolites enable accurate solute-macrofossil interpretations.

Radiocarbon data, mummified macrofossils, and struvite accumulations are evidence that the Paisley Caves rarely experienced wetting events that could transport aDNA into older strata. Radiocarbon measurements detect nanograms of carbon contamination, but a few hundred exogenous DNA base pairs—femtogram and smaller amounts—could be present and not detectable by  $^{14}\text{C}$  dating. Younger DNA contamination is not indicated but could exist.

Deposition in the caves is generally rapid, normally burying human-size (diameter 2 to >3 cm)

coprolites below the penetration depth of surface water or urine within 225 radiocarbon years. If human DNA were introduced into nonhuman coprolites, it was most likely within a few hundred years of deposition, not thousands of years. Previous DNA findings of mitochondrial founding haplogroup A were confirmed by obtaining matching sequences from coprolites in blind test experiments at two independent laboratories, of which one (1830-PC-5/11B-33-101) is dated to a pre-Clovis age ( $12,165 \pm 25$   $^{14}\text{C}$  yr B.P.), one to about Clovis times ( $11,205 \pm 25$   $^{14}\text{C}$  yr B.P.), and one to the mid-Holocene ( $5750 \pm 15$   $^{14}\text{C}$  yr B.P.). The Paisley Caves' archaeology, geoarchaeology, and DNA analyses all indicate initial human occupation of the northern Great Basin by at least 12,300  $^{14}\text{C}$  yr B.P. (3, 28).

The only chronologically diagnostic late Pleistocene technology at the Paisley Caves is related to the WST. We have firmly dated two WS projectile points to Clovis (10,800 to 11,050  $^{14}\text{C}$  yr B.P.) (31) and earlier times (Table 1) and stratigraphically dated a third to about the same or even earlier times. There is no evidence of diagnostic Clovis technology in the site assemblage (25).

Although stemmed points and seaworthy watercraft were present in late Pleistocene Asia

thousands of years before the Paisley Caves were occupied, there is no direct correlate for WST technology in Asia. The Paisley Caves evidence suggests that the WST and Clovis complexes were contemporaneous and parallel—not unilinear—North American technological developments (18, 19). The Paisley Caves evidence supports the hypothesis that the WST was an indigenous development in the far western United States, whereas Clovis may have developed independently in the Plains and Southeast (11, 19).

#### References and Notes

1. T. D. Dillehay et al., *Science* **320**, 784 (2008).
2. J. M. Adovasio, D. R. Pedler, in *Entering America: Northeast Asia and Beringia Before the Last Glacial Maximum*, D. B. Madsen, Ed. (Univ. of Utah Press, Salt Lake City, 2004), chap. 5.
3. M. T. P. Gilbert et al., *Science* **320**, 786 (2008).
4. D. L. Jenkins, in *Paleoindian or Paleoarchaic: Great Basin Human Ecology at the Pleistocene-Holocene Transition*, K. Graf, D. Schmidt, Eds. (Univ. of Utah Press, Salt Lake City, 2007), chap. 4.
5. M. R. Waters et al., *Science* **334**, 351 (2011).
6. B. T. Lepper, R. Bonnicksen, *New Perspectives on the First Americans* (Center for the Study of the First Americans, Texas A&M Univ. Press, College Station, TX, 2004).
7. D. J. Meltzer, *First Peoples in a New World: Colonizing Ice Age America* (Univ. of California Press, Berkeley, 2009).

8. R. Bonnicksen, K. L. Turnmire, Eds., *Ice Age Peoples of North America: Environments, Origins, and Adaptations of the First Americans* (Center for the Study of the First Americans, Texas A&M Univ. Press, College Station, TX, 2005).
9. G. Haynes, *The Early Settlement of North America: The Clovis Era* (Cambridge Univ. Press, Cambridge, 2002).
10. G. Haynes, *Paleoanthropology* **2009**, 271 (2009).
11. C. Beck, G. T. Jones, *Am. Antiq.* **75**, 81 (2010).
12. J. M. Erlandson et al., *Science* **331**, 1181 (2011).
13. A. Bryan, in *The Archaeology of Smith Creek Canyon, Eastern Nevada*, D. R. Tuohy, D. L. Rendall, Eds. (Anthropological Papers No. 17, Nevada State Museum, Carson City, NV, 1979), pp. 162–253.
14. A. Bryan, D. R. Tuohy, in *Ice Age Peoples of North America: Environments, Origins, and Adaptations of the First Americans*, R. Bonnicksen, K. L. Turnmire, Eds. (Center for the Study of the First Americans, Texas A&M Univ. Press, College Station, TX, 2005), pp. 249–263.
15. F. Ikawa-Smith, in *Entering America: Northeast Asia and Beringia Before the Last Glacial Maximum*, D. B. Madsen, Ed. (Univ. of Utah Press, Salt Lake City, 2004), chap. 10.
16. B. A. Bradley, M. B. Collins, C. A. Hemmings, *Clovis Technology* (International Monographs in Prehistory no. 17, Ann Arbor, MI, 2010).
17. M. R. Waters, C. D. Pevney, D. L. Carlson, *Clovis Lithic Technology: Investigation of a Stratified Workshop at the Gault Site, Texas* (Center for the Study of the First Americans, Texas A&M Univ. Press, College Station, TX, 2011).
18. C. Beck, G. T. Jones, in *Meetings at the Margins: Prehistoric Cultural Interactions in the Intermountain* West, D. Rhode, Ed. (Univ. of Utah Press, Salt Lake City, 2012), chap. 2.
19. L. G. Davis, S. C. Willis, S. J. Macfarlan, in *Meetings at the Margins: Prehistoric Cultural Interactions in the Intermountain West*, D. Rhode, Ed. (Univ. of Utah Press, Salt Lake City, 2012), chap. 3.
20. L. G. Davis, C. E. Schweger, *Geochronology* **19**, 685 (2004).
21. J. A. Willig, C. M. Aikens, in *Early Human Occupation in Far Western North America: The Clovis-Archaic Interface*, J. A. Willig, C. M. Aikens, J. L. Fagan, Eds. (Anthropological Papers No. 21, Nevada State Museum, Carson City, NV, 1988), pp. 1–40.
22. T. Goebel, K. Graf, B. Hockett, D. Rhode, in *On Shelter's Ledge: Histories, Theories and Methods of Rockshelter Research*, M. Kornfeld, S. Vasil'ev, L. Miotti, Eds. (British Archaeological Reports, Oxford, 2007), pp. 147–161.
23. K. Graf, in *Paleoindian or Paleoarchaic: Great Basin Human Ecology at the Pleistocene-Holocene Transition*, K. Graf, D. Schmidt, Eds. (Univ. of Utah Press, Salt Lake City, 2007), chap. 5.
24. R. L. Kelly, *Quat. Int.* **109–110**, 133 (2003).
25. See supplementary materials on Science Online.
26. C. R. Bacon, *J. Volcanol. Geotherm. Res.* **18**, 57 (1983).
27. J. Haile et al., *Mol. Biol. Evol.* **24**, 982 (2007).
28. See supplementary materials in (3).
29. H. Poinar et al., *Science* **325**, 148a (2009).
30. M. T. P. Gilbert et al., *Science* **325**, 148b (2009).
31. M. R. Waters, T. W. Stafford Jr., *Science* **315**, 1122 (2007).

**Acknowledgments:** Support for the Paisley Caves Project was provided by NSF grant 0924606; the Danish National Research Foundation; the U.S. Bureau of Land Management; the

archaeological field school and the Museum of Natural and Cultural History, University of Oregon; the Keystone Archaeological Research Fund, Oregon State University; the Bernice Peltier Huber Charitable Trust; the Great Basin Paleoindian Research Unit of the University of Nevada, Reno; Playa Fellowship Residency grants; and D. Dana, A. Hurley, S. Kohntopp, R. Engle, Origer Associates Inc., and other private contributors. P. Bauman and Enertek Solutions provided high-tech lighting in the caves in 2011. D. Kennett and B. J. Culleton contributed ultrafiltration and XAD AMS radiocarbon dating of three paleontological and two cordage samples. M. Rondeau analyzed all of the lithic debitage and tools from reliable contexts at the site, verifying Jones' analysis. E. Carlson illustrated the projectile points. T. Goebel, D. Grayson, D. Madsen, and an anonymous individual reviewed drafts of the manuscript. G. McDonald, E. Scott, and E. Davis identified paleontological specimens and consulted us about taxonomy. Paisley Caves archaeological materials are stored at the University of Oregon under accession nos. 1294, 1374, 1704, 1829, 1830, 1895, 1896, and 1961. The 16S rRNA sequences have been deposited in GenBank under accession nos. JQ734469 to JQ734473.

# Supplementary Materials

www.sciencemag.org/cgi/content/full/337/6091/223/DC1  
Materials and Methods  
Figs. S1 to S12  
Tables S1 to S19  
References (32–47)

27 December 2011; accepted 31 May 2012  
10.1126/science.1218443

# Extinction Debt and Windows of Conservation Opportunity in the Brazilian Amazon

Oliver R. Wearn,<sup>1,2</sup> Daniel C. Reuman,<sup>1,3</sup> Robert M. Ewers<sup>1\*</sup>

Predicting when future species extinctions will occur is necessary for directing conservation investments but has proved difficult. We developed a new method for predicting extinctions over time, accounting for the timing and magnitude of habitat loss. We applied this to the Brazilian Amazon, predicting that local extinctions of forest-dependent vertebrate species have thus far been minimal (1% of species by 2008), with more than 80% of extinctions expected to be incurred from historical habitat loss still to come. Realistic deforestation scenarios suggest that local regions will lose an average of nine vertebrate species and have a further 16 committed to extinction by 2050. There is a window of opportunity to dilute the legacy of historical deforestation by concentrating conservation efforts in areas with greatest debt.

In recent decades, there have been unprecedented rates of habitat loss, fragmentation, and degradation, especially in the species-rich tropics (1), leading to estimates of resulting species extinctions that are rarely less than catastrophic (2). Extinction does not, however, immediately follow changes in habitat extent or quality. Instead, a process of time-delayed community “relaxation” usually occurs (3, 4), where species progressively disappear over time. The term “extinction debt” (5) refers to any future biodiversity losses that current or past habitat

destruction will incur but which have yet to be realized because of time delays in extinction. This time delay offers a window of conservation opportunity, during which it is possible to restore habitat or implement alternative measures to safeguard the persistence of species that are otherwise committed to extinction.

The Brazilian Amazon harbors some 40% of the world's tropical forest (6) and a substantial proportion of global biodiversity (7) but has also been host to the majority of tropical deforestation that has occurred in recent decades (1). There has been much debate over the future of the Brazilian Amazon and especially the prospects for biodiversity in the region (6, 8, 9). Quantitative estimates of resulting species loss have rarely been made (10), although we know that the number of threatened bird species in the Amazon is likely

to triple over the coming decades because of the continued process of deforestation (11).

To address this problem, we built a modeling framework that expands on the species-area relationship (SAR) (12, 13). SARs provide a powerful way of estimating the final, equilibrium level of extinction caused by habitat losses (14, 15) but provide no information on the timing of extinctions or on the extinction debt remaining at a given time. Our improved framework gives estimates of extinctions and debt remaining at all times during and after a sequence of habitat destruction events.

Assume that at time  $t = 0$  we have a patch of uniform habitat of area  $A(0)$  and initial equilibrium species richness  $S(0) = S_{eq}(0) = cA(0)^z$ . Here,  $z$  is the exponent of the SAR and  $c$  is a constant (12). The patch is subjected to a subsequent pattern of habitat destruction, so that the remaining area  $A(t)$  at time  $t$  is less than  $A(0)$ . If  $S_{eq}(t) = cA(t)^z$  is the equilibrium number of species that would eventually remain if habitat destruction ceased at time  $t$ , then we assume, following empirical (16) and theoretical (3, 17) expectations, that the rate of community relaxation to this equilibrium is proportional to the difference between current richness,  $S(t)$ , and equilibrium richness:

$$\frac{dS}{dt} = -k(S - S_{eq}) = -k(S - cA^z) \quad (1)$$

Here,  $k$  is a relaxation rate constant (10). The solution to this is

$$S(t) = S(0)e^{-kt} + e^{-kt} \int_0^t kcA(\tau)^z e^{k\tau} d\tau \quad (2)$$

which can easily be computed numerically for any temporal pattern of habitat destruction  $A(t)$ .

<sup>1</sup>Imperial College London, Silwood Park, Ascot SL5 7PY, UK.  
<sup>2</sup>Zoological Society of London, Institute of Zoology, London NW1 4RY, UK. <sup>3</sup>Rockefeller University, New York, NY 10065, USA.  
\*To whom correspondence should be addressed. E-mail: r.ewers@imperial.ac.uk



Extinction that has occurred at time  $t$  is  $E(t) = S(0) - S(t)$ , and extinction debt is  $D(t) = S(t) - S_{eq}(t)$ . Model predictions for simple and complex patterns of habitat destruction through time are compared in Fig. 1.

We used the temporal trajectory of forest cover for the entire Brazilian Amazon to estimate current and future levels of extinction and extinction debt in communities of forest-dependent mammals, birds, and amphibians and quantified the uncertainty in our estimates by using Monte Carlo randomizations based on a quantitative review of the primary literature (10, 13) (fig. S1). Deforestation trajectories were determined from previously published deforestation maps for 1978, 1988, 1992, and 1998 and then annually for the period 2000 to 2008 (10). We assumed that deforestation began in 1970 and used three alternative interpolation strategies to backcast annual changes in forest cover between 1970 and 2000 (10). Predictions of future forest cover (2009 to 2050) were made according to four development scenarios. The first two, business as usual (BAU) and governance (GOV), are spatially explicit deforestation simulations that differ in their assumptions about compliance with environmental law, protected area network expansion, and overall trends in deforestation rates over the

coming decades resulting from the expansion of agriculture and rural development (8, 10). Given rapid declines in deforestation rates for the Brazilian Amazon from 2005 to 2010 (9), we consider the most likely future to more closely approximate the GOV than the BAU scenario. We also explored the outcomes of two scenarios of strongly targeted deforestation reduction. The strong reduction (SR) scenario leads to an 80% reduction (per 50 km by 50 km grid cell) in absolute deforestation rate by 2020, whereas the end of deforestation (EOD) scenario eliminates deforestation by 2020 (9). These targeted programs have their bases in recent pledges by the Brazilian government and potential reductions in deforestation proposed in 2009, respectively, that may have been achievable with greatly expanded investment in forest conservation in the region (9).

Extinctions and the extinction debt of forest-dependent vertebrates in the Brazilian Amazon arising from deforestation over the past four decades are predicted to be minimal but are likely to rapidly accumulate over the coming four decades, making the biodiversity changes observed over the past four decades pale by comparison (Fig. 2). However, applying the SAR to predict extinctions at this spatial scale is problematic because of spatial heterogeneity in species richness and habitat loss. Species richness is highest in the western Amazon (figs. S6 to S8), whereas deforestation has been concentrated in the relatively species-poor southeast

Amazon, meaning that a SAR-based approach will likely overestimate extinction rates when applied at such large spatial scales. Although our predictions of present-day extinction debt closely matched the number of threatened species on the Red List (18) (Fig. 2A), the model predicted that between 4 and 10 forest-dependent species should have been driven extinct from the Brazilian Amazon (10), yet no extinctions have been observed. We therefore focused our analyses at a much finer spatial resolution, dividing the Brazilian Amazon into a grid with 50-km spacing (10) and placing our emphasis on predicting local extinctions.

For each grid cell, we used cell-specific trajectories of past and future forest loss to estimate current and future levels of local extinction and extinction debt (10). We attempted to validate model predictions at this scale against lists of forest-dependent bird species from four intensively sampled regions within the Brazilian Amazon, finding a positive, but nonsignificant, correlation between observed and predicted species loss (10). Most of the species we modeled are widely distributed, suggesting that global extinctions will be lower than predicted local extinctions. Nonetheless, focusing on local extinctions is particularly important given their immediate consequences for ecosystem function and service provision at local scales (19).

Despite the loss of more than 81 million ha of forest over recent decades in the Brazilian

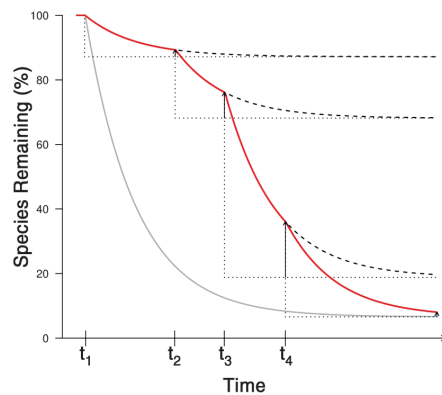


**Fig. 1.** Trajectories of community relaxation under single- and multiple-episode habitat loss. The gray line illustrates the species relaxation trajectory modeled with a single episode of habitat loss at  $t_1$ . The red line illustrates a more complex pattern of habitat destruction, with habitat lost in four discrete episodes ( $t_1$ ,  $t_2$ ,  $t_3$ , and  $t_4$ ) giving rise to a composite relaxation curve as modeled under Eq. 2. Dashed black lines show the unrealized tail end of each relaxation curve; gray dotted lines highlight the shifting equilibrium number of species; the arrow lengths indicate the size of the extinction debt that remains to be paid before each new episode of habitat loss occurs. Over long enough time frames, both patterns of habitat destruction result in the same equilibrium number of species, but modeling deforestation as a single-episode event (gray line) greatly overestimates the severity of extinction at finite times relative to the loss that occurs in the multiple-episodes case (red line).

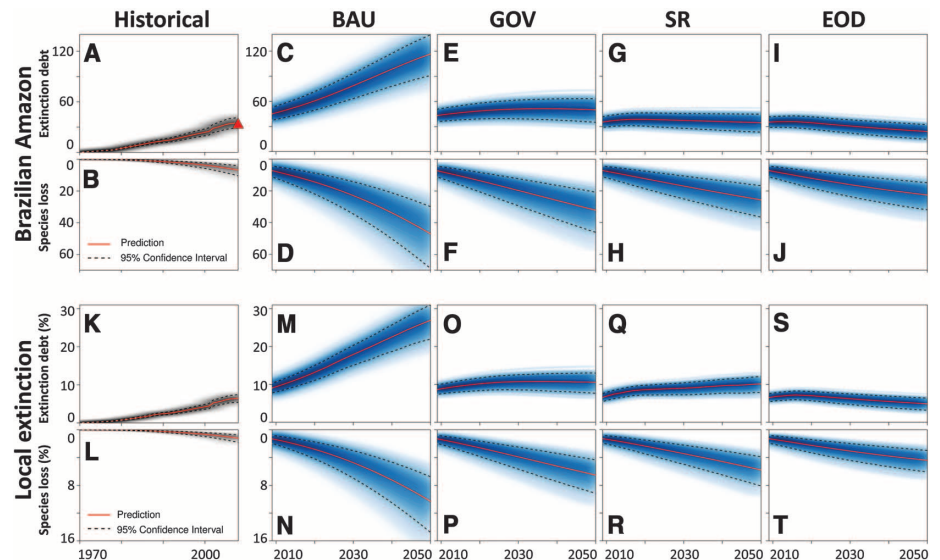


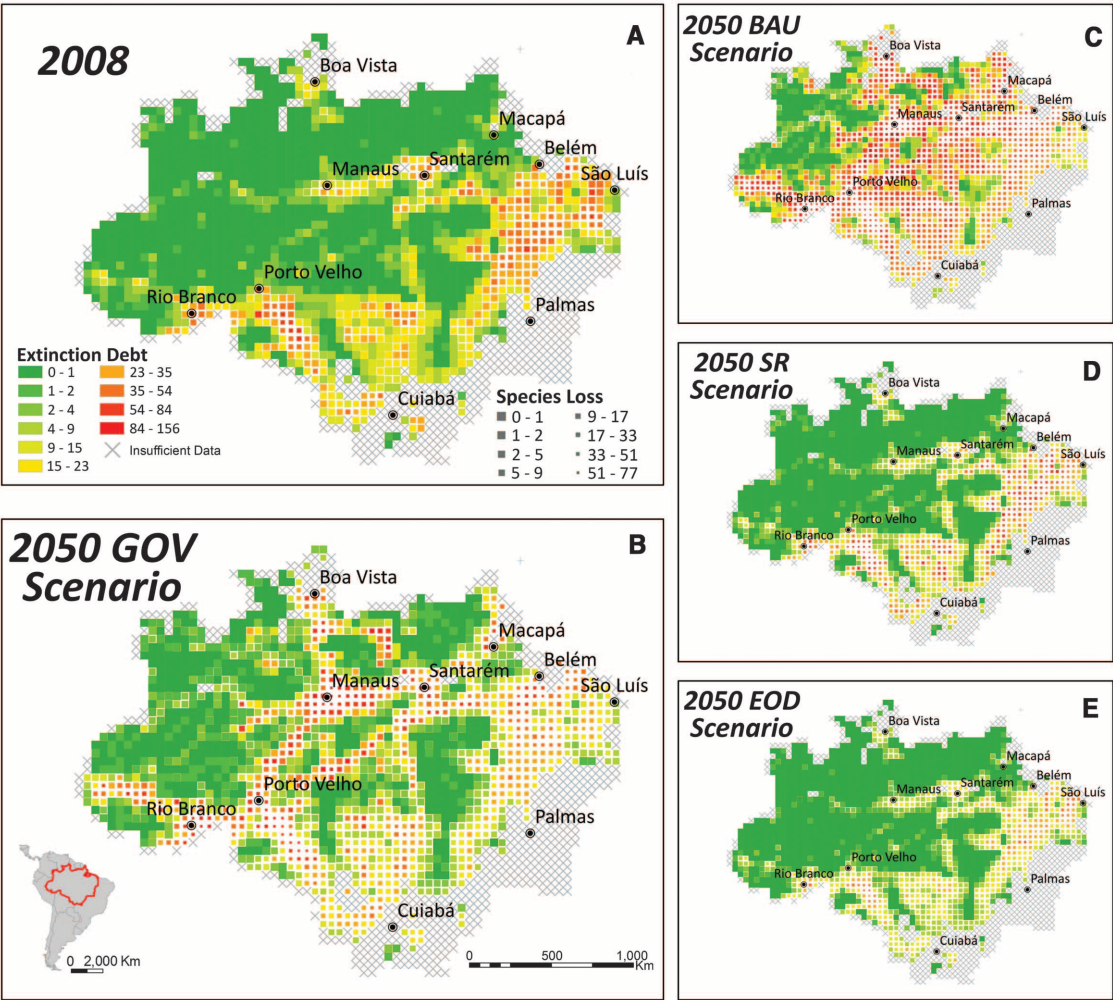
**Fig. 2.** Historical trends of absolute and relative species loss and extinction debt between 1970 and 2008 (using the “interpolated clearance” scheme of Table 1) and predicted future trends through 2050 under four scenarios: BAU, GOV, SR, and EOD. (A to J) Species loss and extinction debt were estimated at the scale of the Brazilian Amazon and represent the cumulative numbers of forest-dependent mammals, birds, and amphibians. The red triangle in (A) shows the number of species classified as threatened on the Red List (Critical, Endangered, or Vulnerable categories). (K to T) Relative species loss and extinction debt were estimated in grid cells (50 km by 50 km), and values were calculated as a percentage of initial species richness and averaged across grid cells. In all panels, uncertainties arising from model parameterization were incorporated by using Monte Carlo simulations (10), with background color saturation corresponding to the density of simulation runs. Dotted lines give 95% confidence bands. Exact values of species loss and extinction debt estimates are in Table 1 and tables S1 and S2.

Amazon, estimated species losses from bird, mammal and amphibian communities to 2008 were modest in both relative (Fig. 2 and Table 1) and absolute (0.16 to 0.93 species per cell across scenarios of forest loss and across taxa; table S1) terms. Relative losses are slightly higher for mammals and birds than for amphibians (for mammals, 0.8 to 1.1%; birds, 0.8 to 1.0%; and

**Table 1.** Estimates of relative (%) species loss and extinction debt in the Brazilian Amazon (mean values per 2500 km<sup>2</sup> grid cell) for the present (2008) and future (2050) under various scenarios of forest loss. Means, confidence intervals (CIs), and ranges were calculated across Monte Carlo simulations of the extinction debt model with values of *z* and *k* distributed according to the uncertainty in our estimates of these quantities. Estimates for 2008 have their basis in incomplete knowledge of annual forest cover trajectories between 1970 and 2000 and so were generated by using three different methods of interpolating the temporal trajectory of forest cover. Ranges given are across grid cells. Absolute values are given separately for birds, mammals, and amphibians in tables S1 and S2.

Scenario	Species loss (%)		Extinction debt (%)	
	Mean (95% CI)	Range	Mean (95% CI)	Range
2008				
Immediate clearance	1.36 (0.85–2.03)	0–33.35	6.33 (5.23–7.31)	0–68.92
Interpolated clearance	1.20 (0.74–1.81)	0–28.25	6.49 (5.43–7.45)	0–72.47
Delayed clearance	1.07 (0.65–1.62)	0–26.31	6.62 (5.58–7.60)	0–74.17
2050				
Business-as-usual	10.30 (6.76–14.79)	0–56.82	26.94 (21.97–30.99)	0–91.23
Governance	6.52 (4.33–9.15)	0–56.82	10.56 (7.67–13.02)	0–74.35
Strong reduction	5.79 (3.89–8.09)	0–56.87	10.12 (7.85–12.05)	0–80.62
End of deforestation	4.40 (2.97–6.08)	0–56.87	4.88 (3.19–6.39)	0–60.19

**Fig. 3.** Spatial patterns of absolute species loss (represented by the sizes of squares) and extinction debt (represented by colors) in the Brazilian Amazon to 2008 (A) and for 2050 under four scenarios: GOV (B), BAU (C), SR (D), and EOD (E). Smaller squares have suffered greatest extinction, whereas redder squares have the largest extinction debts and are expected to experience the greatest future losses of species without conservation attention. Large and red squares are intact but imperiled and are where the greatest gains could be expected from conservation actions. Values are cellwise means across Monte Carlo simulations and were summed across birds, mammals, and amphibians.



amphibians, 0.6 to 0.7%). In contrast to the modest species losses, a considerable extinction debt has accumulated (Fig. 2 and Table 1). We estimate that the Brazilian Amazon holds an average extinction debt of 2.22 to 2.32 mammal species, 4.51 to 4.71 birds, and 1.00 to 1.05 amphibians per cell (table S2). Thus, between 80 and 90% of all local extinctions expected to be incurred from historical habitat loss have yet to be realized (tables S1 and S2).

Estimates of average species loss and extinction debt conceal substantial and systematic spatial variation across the Brazilian Amazon (Fig. 3, fig. S3, and movies S1 to S4). As a result, the prognosis for an average grid cell belies important regional differences in species loss and extinction debt. The state of Maranhão, followed by Tocantins, Pará, and Rondônia, were the first to experience widespread settlement (see fig. S2 for the locations of all place names), and their early accumulation of extinction debt and species losses reflects this (fig. S3). Central Rondônia is a key region of species loss, especially because species richness is higher here than in the eastern Amazon. By the late 1980s and early 1990s, Roraima and Acre had also begun to collect extinction debt (fig. S3). Meanwhile, Amapá and



Amazonas show only negligible quantities of either species loss or debt to the current day, reflecting their de facto conservation granted by virtue of their inaccessibility (fig. S3).

Heterogeneity in species richness patterns also affects the absolute estimates of species loss and extinction debt. With much of the species diversity concentrated in the northern and western portions of the Amazon but the forest loss concentrated on the “arc of deforestation” in the east and south, extinctions to the present day have been less severe than they might have been: just 0.37 to 0.47 mammals, 0.73 to 0.93 birds, and 0.16 to 0.20 amphibians per cell. There is a relative absence of extinction debt hot spots in southern Amazonia (Fig. 3) considering that this region suffered the highest annual rates of deforestation over the last decade (20). This is due partly to the lower spatial aggregation, in general, of deforestation patterns and also the lower species richness of forest-dependent vertebrates (figs. S6 to S8).

Under the GOV scenario, debt continues to accumulate over the next 15 years, after which the debt begins to decline again (Fig. 2 and movie S2). By contrast, the accumulation of debt under the BAU scenario continues until near exhaustion of each cell’s forest estate (outside of protected areas) (Fig. 2 and movie S1). By 2050, average species losses per cell under the GOV scenario are expected to lie in the range from two to three (5.5%) mammals, three to seven (5.3%) birds, and one to two (4.5%) amphibians (Table 1 and table S1). In addition, cells will have accrued an additional three to five (9.6%) mammals, 7 to 11 (9.5%) birds, and two to three (8.5%) amphibians as outstanding debt (Table 1 and table S2), leaving between 60 and 70% of expected extinctions still to be realized. Compared with the BAU scenario, the other three scenarios would likely reduce species losses up to 2050 by one- to two-thirds (GOV, 38 to 42%; SR, 50 to 56%; EOD, 62 to 68%; movies S1 to S4). The extinction debt burden is also greatly reduced, by 62 to 64%, 69 to 75%, and 85 to 88%, for the GOV, SR, and EOD scenarios, respectively.

The systematic spatial variation in patterns of extinction debt continues under the modeled scenarios of forest loss to 2050. Under the BAU scenario, the main corridors of extinction debt result from federally sponsored highway-paving programs (10), compounded by population growth and influx at the margins of major urban centers (especially Manaus) as well as by emerging deforestation foci at the intersections of newly paved highways (figs. S2 and S6). As a result, all states except Maranhão and Tocantins still accumulate debt in 2050 and show increasing rates of species loss (fig. S4). In Maranhão and Tocantins, most of the forest outside protected areas will be lost by mid-century, causing extinction debt to peak around 2025 and decline thereafter with continued species losses (fig. S4). Under the increased frontier governance of the GOV scenario, most states show declining extinc-

tion debts, and rates of species loss, by 2030. The notable exception to this is Amazonas, which is still accumulating debt in 2050 (fig. S4).

Although the overall spatial patterns of species loss and extinction debt are determined by patterns of habitat loss, there are important differences in the patterns between the three vertebrate groups that arise from nuances in the spatial distribution of species richness between the three groups (figs. S6 to S8). This means that, in the present day, areas with the highest extinction debt are not entirely consistent across taxa (fig. S5). Moreover, these areas are not conserved across time for the three groups (fig. S6). Under the GOV scenario, peak debt for all groups converges onto central Amazonia (figs. S6 to S8). Under the BAU scenario, however, deforestation reaches the regions of highest species richness for each group, and peak areas of debt begin to echo peak regions of species richness for the different taxa: Mammalian extinction debt is comparatively high in the northern Brazilian Amazon (fig. S6), bird extinction debt is comparatively high in the central Amazon (fig. S7), whereas amphibian extinction debt is comparatively high in the western Brazilian Amazon (fig. S8).

Across all scenarios, incorporating time delays in extinction led to lower estimates of current extinction and extinction to 2050 than have previously been reported (21–23). On the basis of our empirically derived estimate of  $k$ , the relative relaxation rate, it will take on the order of centuries for communities to fully equilibrate, whereas we have estimated extinctions only up to 2050. Limiting the time frame reduces our extinction estimates below the expected species losses at equilibrium. The 2050 time frame is, however, one that we believe is sufficiently immediate to be relevant to present-day conservation decision-making.

Comparing the four scenarios allows us to assess the impact of “lost” conservation opportunities. The EOD scenario appeared feasible when first published in 2009 (9) but appears much less so now in the face of recently voted changes to the Brazilian Forest Code that may weaken controls on deforestation rates (24). Similarly, the Brazilian government targets that form the basis of the SR scenario now also seem unlikely to be achieved. Comparing the predicted outcome of the EOD and SR scenarios with the outcome of the more likely GOV and BAU scenarios shows the impact of present-day decision-making on future biodiversity, with failure to reach these ambitious targets reflected in increased extinction and larger accumulations of extinction debt for decades to come.

Even under the worst-case scenario that we modeled, the window of conservation opportunity extends beyond 2050 for most species, although opportunity does diminish progressively through time. The future of biodiversity in the Brazilian Amazon currently stands at a critical juncture. Under BAU, the Amazon will continue

to collect extinction debt for decades to come. On the other hand, with an ambitious program of basinwide conservation investment (9), the Brazilian Amazon could enter 2050 with minimal (less than 5%) species loss and extinction debt. In all scenarios and without forest regeneration in key areas, species will still be going extinct more than three decades after deforestation has halted.

Across two decades of monitoring, the years 2009 and 2010 were the lowest deforestation figures yet recorded (20), providing support for the notion that Brazil has at least departed from the BAU trajectory (9). This progress, although promising, is potentially threatened by recently voted changes to the Brazilian Forest Code (24), which have already been linked to a spike in deforestation rates in 2011 (25) and which may drive the deforestation trajectory back toward the BAU scenario. It is therefore premature to assert that a new development paradigm for the Brazilian Amazon has permanently emerged, but even so the declines in deforestation rates over the period 2005 to 2010 have helped widen the window of conservation opportunity for the highly biodiverse Brazilian Amazon. Continuing legislative and other land development and conservation choices made in the coming months and years will accordingly widen or narrow this window.

#### References and Notes

1. F. Achard *et al.*, *Science* **297**, 999 (2002).
2. S. L. Pimm, G. J. Russell, J. L. Gittleman, T. M. Brooks, *Science* **269**, 347 (1995).
3. J. M. Diamond, *Proc. Natl. Acad. Sci. U.S.A.* **69**, 3199 (1972).
4. T. M. Brooks, S. L. Pimm, J. O. Oyugi, *Conserv. Biol.* **13**, 1140 (1999).
5. D. Tilman, R. M. May, C. L. Lehman, M. A. Nowak, *Nature* **371**, 65 (1994).
6. W. F. Laurance *et al.*, *Science* **291**, 438 (2001).
7. R. A. Mittermeier *et al.*, *Proc. Natl. Acad. Sci. U.S.A.* **100**, 10309 (2003).
8. B. S. Soares-Filho *et al.*, *Nature* **440**, 520 (2006).
9. D. Nepstad *et al.*, *Science* **326**, 1350 (2009).
10. Materials and methods are available as supplementary materials on Science Online.
11. J. P. Bird *et al.*, *Divers. Distrib.* **18**, 273 (2011).
12. M. L. Rosenzweig, *Species Diversity in Space and Time* (Cambridge Univ. Press, Cambridge, 1995).
13. S. Drakare, J. J. Lennon, H. Hillebrand, *Ecol. Lett.* **9**, 215 (2006).
14. S. L. Pimm, R. A. Askins, *Proc. Natl. Acad. Sci. U.S.A.* **92**, 9343 (1995).
15. T. Brooks, A. Balmford, *Nature* **380**, 115 (1996).
16. G. Ferraz *et al.*, *Science* **315**, 238 (2007).
17. R. H. MacArthur, E. O. Wilson, *The Theory of Island Biogeography* (Princeton Univ. Press, Princeton, NJ, 1967).
18. World Conservation Union, 2008 IUCN Red List of Threatened Species (IUCN, 2008); [www.iucnredlist.org](http://www.iucnredlist.org).
19. G. Ceballos, P. R. Ehrlich, *Science* **296**, 904 (2002).
20. Instituto Nacional de Pesquisas Espaciais (INPE), Projeto PRODES: Monitoramento da Floresta Amazônica Brasileira por Satélite (2009); [www.obt.inpe.br/prodes/](http://www.obt.inpe.br/prodes/).
21. C. E. V. Grelle, *Oryx* **39**, 347 (2005).
22. S. P. Hubbell *et al.*, *Proc. Natl. Acad. Sci. U.S.A.* **105** (suppl. 1), 11498 (2008).
23. K. J. Feeley, M. R. Silman, *Proc. Natl. Acad. Sci. U.S.A.* **106**, 12382 (2009).
24. J. P. Metzger *et al.*, *Science* **329**, 276 (2010).
25. S. N. Hayashi, C. M. Souza Jr., A. Verissimo, “Mato Grosso SAD alerta” (Belém, Brasil, 2011); [www.imazon.org.br/publicacoes/transparencia-florestal/sad-alerta/sad-alerta-mato-grosso-abril-2011](http://www.imazon.org.br/publicacoes/transparencia-florestal/sad-alerta/sad-alerta-mato-grosso-abril-2011).

26. R. S. Ridgely et al., *Digital Distribution Maps of the Birds of the Western Hemisphere, version 3.0* (NatureServe, Arlington, VA, 2007).

**Acknowledgments:** R. Bernard provided GIS assistance, and T. Gardner, J. Barlow, and A. Lees commented on the manuscript and provided data. The UK Natural Environment Research Council supported O.R.W. and

D.C.R. and the European Research Council supported R.M.E. during this work. Data were obtained from online sources (10, 18, 26).

#### Supplementary Materials

www.sciencemag.org/cgi/content/full/337/6091/228/DC1  
Materials and Methods

Figs. S1 to S8  
Tables S1 and S2  
References (27–118)  
Movies S1 to S4

11 January 2012; accepted 18 May 2012  
10.1126/science.1219013

# Structural Basis for Allosteric Regulation of GPCRs by Sodium Ions

Wei Liu,<sup>1\*</sup> Eugene Chun,<sup>1\*</sup> Aaron A. Thompson,<sup>1\*</sup> Pavel Chubukov,<sup>1</sup> Fei Xu,<sup>1</sup> Vsevolod Katritch,<sup>1</sup> Gye Won Han,<sup>1</sup> Christopher B. Roth,<sup>2</sup> Laura H. Heitman,<sup>3</sup> Adriaan P. IJzerman,<sup>3</sup> Vadim Cherezov,<sup>1†</sup> Raymond C. Stevens<sup>1†</sup>

Pharmacological responses of G protein–coupled receptors (GPCRs) can be fine-tuned by allosteric modulators. Structural studies of such effects have been limited due to the medium resolution of GPCR structures. We reengineered the human A<sub>2A</sub> adenosine receptor by replacing its third intracellular loop with apocytochrome b<sub>562</sub>RIL and solved the structure at 1.8 angstrom resolution. The high-resolution structure allowed us to identify 57 ordered water molecules inside the receptor comprising three major clusters. The central cluster harbors a putative sodium ion bound to the highly conserved aspartate residue Asp<sup>2.50</sup>. Additionally, two cholesterol molecules stabilize the conformation of helix VI, and one of 23 ordered lipids intercalates inside the ligand-binding pocket. These high-resolution details shed light on the potential role of structured water molecules, sodium ions, and lipids/cholesterol in GPCR stabilization and function.

G protein–coupled receptors (GPCRs) encompass the largest and most diverse family of membrane proteins in eukaryotes, sharing a common architecture of seven-transmembrane (7-TM)  $\alpha$  helices. GPCRs transduce a variety of signals across the cell membrane that regulate diverse biological and (patho)physiological processes and, hence, are favored drug targets. Ligand-dependent GPCR activation triggers dramatic conformational changes in the 7-TM helical bundle that are coupled to activation of G proteins and other downstream effectors. Over the past 4 years, breakthroughs in protein engineering and crystallography have yielded structures of 14 different GPCRs responding to diffusible ligands in different functional states (1–9), providing the basic structural framework for understanding ligand binding and activation mechanisms. However, despite the progress in GPCR stabilization for crystallographic studies, the resolution of GPCR structures has remained in the range of 2.2 to 3.5 Å (1). The function of GPCRs relies on a specific lipid environment and often strongly depends on the presence of cholesterol and ions (10–12). Our understanding of the structural mechanism of such effects has been limited due to the absence of higher-resolution GPCR structures.

We replaced the third intracellular loop (ICL3) of the human A<sub>2A</sub> adenosine receptor (A<sub>2A</sub>AR) with a thermostabilized apocytochrome b<sub>562</sub>RIL (BRIL) (13, 14) and determined the crystal structure of this chimeric protein [referred to as A<sub>2A</sub>AR-BRIL- $\Delta$ C (15)] in complex with a high-affinity, subtype-selective antagonist, ZM241385, at 1.8 Å resolution (table S1). The high resolution enabled us to identify a comprehensive network of 57 internal water molecules, a highly conserved binding site for a sodium ion, three cholesterol molecules, and 23 lipid acyl chains bound to the receptor.

The ligand binding and functional characteristics of the A<sub>2A</sub>AR-BRIL- $\Delta$ C fusion protein were extensively characterized and compared with the A<sub>2A</sub>AR-WT (wild-type) and A<sub>2A</sub>AR- $\Delta$ C (C-terminal truncation) constructs. Antagonist [<sup>3</sup>H]ZM241385 radioligand-binding and agonist-displacement assays confirmed that the ligand recognition site of the A<sub>2A</sub>AR-BRIL- $\Delta$ C fusion protein is very similar to that of both the A<sub>2A</sub>AR-WT and A<sub>2A</sub>AR- $\Delta$ C constructs (fig. S1). The BRIL insertion did not have an impact on receptor expression and trafficking to the cell plasma membrane (fig. S2), but, as expected, the insertion prevented the receptor construct from activating available G<sub>s</sub> proteins (fig. S3).

The high-resolution receptor structure is nearly identical to the original 2.6 Å resolution crystal structure of A<sub>2A</sub>AR-T4L- $\Delta$ C/ZM241385 [Protein Data Bank identification number (PDB ID) 3EMJ] (16), with an all-atom root mean square deviation of 0.45 Å over 81% of A<sub>2A</sub>AR (excluding terminal residues 1 to 9, 305 to 307, the

distal part of ECL2 147 to 162, and residues 199 to 232 flanking ICL3). The conformations of the cytoplasmic ends of helices V and VI near the BRIL junction sites closely resemble the conformations in the A<sub>2A</sub>AR structure with unmodified ICL3 (13, 17), in contrast to a distorted conformation caused by the T4L fusion in A<sub>2A</sub>AR-T4L- $\Delta$ C/ZM241385 (16). A distal part of the extracellular loop 2 (ECL2), which was missing in all inactive-state structures of A<sub>2A</sub>AR, is fully resolved (fig. S4). Most importantly, the higher resolution revealed atomic details for the structurally conserved regions, including intricate networks of water molecules, sodium ion, lipids, and cholesterol.

The 1.8 Å-resolution structure of A<sub>2A</sub>AR-BRIL- $\Delta$ C/ZM241385 contains 177 structured waters, 57 of which occupy the interior of the 7-TM bundle. The interior waters form an almost-continuous channel extending from the ligand-binding site to the site of G protein interaction (Fig. 1A), which is composed of three bulky water-molecule clusters as well as several scattered waters. The channel has two narrow “bottlenecks” restricted by Trp246<sup>6.48</sup> and Tyr288<sup>7.53</sup> (18) to slightly less than the diameter of one water molecule (2.4 and 2.0 Å, respectively). Rearrangements of the receptor backbone and side chains upon activation disrupt the channel continuity in these sites (Fig. 1B), substantially reducing its volume.

The first of the three water clusters, the extracellular (EC) cluster, located inside the orthosteric ligand-binding pocket, plays a role in ligand binding and selectivity (Fig. 1C and fig. S5) (19). One of the waters in this cluster stabilizes the conformation of a nonproline kink in helix III by forming hydrogen bonds with both the main-chain carboxyl of Ile80<sup>3.28</sup> and the main-chain nitrogen of Val84<sup>3.32</sup>. In the active-like state of agonist-bound A<sub>2A</sub>AR structures (20, 21), the kink in helix III straightens, thereby precluding water binding, which points to a role of water rearrangement at this location in A<sub>2A</sub>AR activation. This ligand-induced and water-mediated conformational change is accompanied by an overall activation-related shift of helix III (20).

The second, central water cluster includes a sodium ion and 10 water molecules that completely fill a cavity in the middle of the 7-TM bundle (Fig. 1D). The central cluster spans a distance of more than 13 Å between two functionally important and conserved residues, Trp246<sup>6.48</sup> and Tyr288<sup>7.53</sup>. Three water molecules from this cluster were previously observed in the A<sub>2A</sub>AR-T4L- $\Delta$ C/ZM241385 complex (fig. S6A) (16),

<sup>1</sup>Department of Molecular Biology, The Scripps Research Institute, 10550 North Torrey Pines Road, La Jolla, CA 92037, USA. <sup>2</sup>Receptos, San Diego, CA 92121, USA. <sup>3</sup>Division of Medicinal Chemistry, Leiden/Amsterdam Center for Drug Research, Post Office Box 9502, 2300RA Leiden, Netherlands.

\*These authors contributed equally to this work.

†To whom correspondence should be addressed. E-mail: vcherezov@scripps.edu (V.C.); stevens@scripps.edu (R.C.S.)



and positions of 4 of the 10 waters are similar to those found in bovine rhodopsin (PDB ID 1U19) (fig. S6B) (22), suggesting that such an internal network is common in class A GPCRs and could be important for their function (23, 24). Finally, the intracellular (IC) cluster containing ~20 water molecules is found near the conserved D[E]RY motif (D, Asp; E, Glu; R, Arg; Y, Tyr) (Fig. 1E), which is inferred in the sta-

bilization of different functional receptor states and in interactions with G proteins and other effectors.

Evidence for the presence of a sodium ion in the central water cluster came from a strong spherical electron density with a distorted octahedral coordination and short distances to coordinating atoms in its neighborhood. Such geometry was poorly compatible with the presence of a

water molecule. However,  $\text{Na}^+$  modeled in this density is coordinated by five oxygen atoms, including OD1 of Asp52<sup>2.50</sup> (2.45 Å), OG of Ser91<sup>3.39</sup> (2.54 Å), and three waters (2.20, 2.45, and 2.59 Å) (Fig. 2A and fig. S7), which is in excellent agreement with coordination and distances for  $\text{Na}^+$  in protein structures (25). Moreover, the presence of  $\text{Na}^+$  in the structure is consistent with conditions employed during purification (0.8 M  $\text{Na}^+$ ) and crystallization (~0.15 M  $\text{Na}^+$ ). Allosteric effects of  $\text{Na}^+$  on ligand binding, stability, and crystallization of A<sub>2A</sub>AR have been documented in previous studies (11, 16, 26). We confirmed the allosteric effects of physiological concentrations of  $\text{Na}^+$  on agonist and antagonist binding and thermal stability of A<sub>2A</sub>AR (Fig. 3 and table S2).

During the past 40 years, allosteric modulation by  $\text{Na}^+$  has been observed for many GPCRs and was linked to motifs in helix II, including the highly conserved Asp<sup>2.50</sup> (27). Mutation of this residue has been the subject of many studies on a multitude of receptors; in the GPCRDB database (28), Asp<sup>2.50</sup> is mentioned more than 100 times for dozens of receptors of human origin and from other species. Asp<sup>2.50</sup> has not been mutated in the A<sub>2A</sub>AR, but in the closely homologous A<sub>1</sub> and A<sub>3</sub> adenosine receptors, the  $\text{Na}^+$  effect was largely abrogated when the residue was mutated to alanine or asparagine, respectively (29, 30). Despite this indirect evidence, the nature of  $\text{Na}^+$  interactions with GPCRs remained hypothetical (31, 32), and the sodium ion remained undetected in crystal structures of GPCRs solved at medium resolution.

In this high-resolution A<sub>2A</sub>AR structure, we were able to determine the precise location of  $\text{Na}^+$ , as well as to resolve the complete network of water molecules around the sodium ion and conformations of all residues involved in direct or water-mediated coordination. The central water cluster harboring  $\text{Na}^+$  is surrounded by and engaged in hydrogen bonding with several highly conserved residues, including Asn24<sup>1.50</sup>, Asp52<sup>2.50</sup>, Ser91<sup>3.39</sup>, Trp246<sup>6.48</sup>, Asn280<sup>7.45</sup>, Asn284<sup>7.49</sup>, and Tyr288<sup>7.53</sup> (Fig. 2A). Structural alignment of these residues from known GPCR structures reveals a well-preserved site capable of binding  $\text{Na}^+$  along with several water molecules (Fig. 2, C and D). Small deviations were observed in bovine rhodopsin, in which Asn<sup>7.45</sup> is substituted with a serine residue and Asn<sup>7.49</sup> adopts a different rotamer, and in CXCR4 where Asn<sup>7.45</sup> is replaced with a histidine. Interestingly, in many olfactory receptors, Ser<sup>3.39</sup> is substituted with a glutamate, resulting in two acidic side chains pointing inside the central water cluster, which may favor binding of a divalent cation in this site.

The central water cluster with  $\text{Na}^+$  likely plays an important role in receptor activation. Comparison between the inactive and active-like states of A<sub>2A</sub>AR (PDB ID 3QAK) suggests that, upon activation, the inward movement of helix VII in this region collapses the pocket from 200

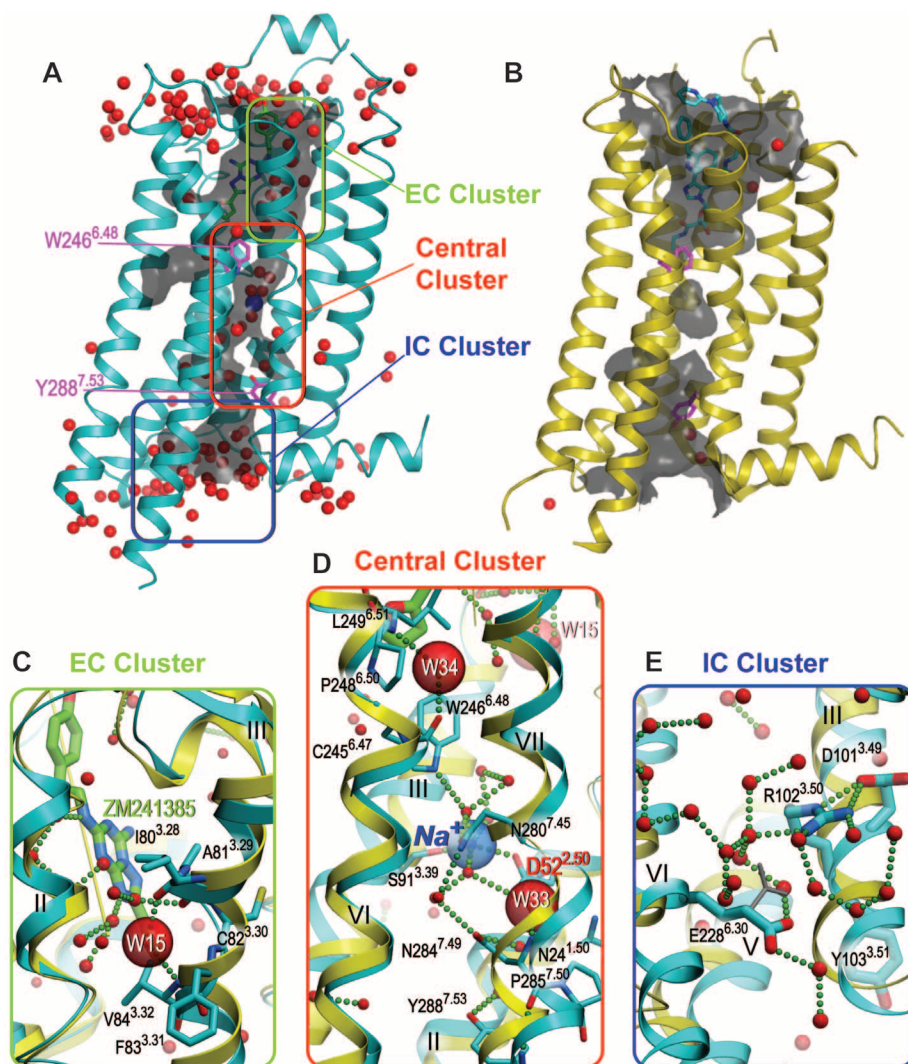


**Fig. 1.** Distribution of ordered waters in A<sub>2A</sub>AR. In all panels, the antagonist-bound, high-resolution structure is shown in light blue, the agonist-bound structure in the active-like state (PDB ID 3QAK) is shown in yellow, waters are represented as red spheres, and salt bridges and hydrogen bonds are depicted as small green spheres. (A) Interior water molecules in the A<sub>2A</sub>AR-BRIL-ΔC/ZM241385 structure form an almost-continuous water channel [gray; calculated using the program HOLLOW (38)] containing three major water clusters. (B) The channel is disrupted in the structure in the active-like state (PDB ID 3QAK). (C) Close-up view of the EC water cluster deep in the ligand-binding pocket. The water molecule W15 (shown as a large red semitransparent sphere) stabilizes the kink in helix III. I, Ile; A, Ala; C, Cys; V, Val; F, Phe. (D) Close-up view of the central cluster, which includes waters and a sodium ion (blue transparent sphere). Water molecules W34 and W33 stabilizing the proline-induced kinks in helices VI and VII are shown as large red semitransparent spheres. L, Leu; P, Pro; N, Asn; S, Ser. (E) Close-up view of the IC cluster around the D[E]RY motif in helix III. Despite their close proximity, Arg102<sup>3.50</sup> and Glu228<sup>6.30</sup> do not form an ionic interaction; instead both amino acids form hydrogen bonds with neighboring waters. An alternative rotamer of Glu228<sup>6.30</sup>, which potentially makes a 3.0 Å contact with Arg102<sup>3.50</sup> side chain, is shown in a gray stick representation. W246 is Trp246, but W15, W33, and W34 are waters 15, 33, and 34.

to 70 Å<sup>3</sup> and shifts it toward helix VI (Fig. 2B). The resulting pocket in the active-like state can accommodate a maximum of three water molecules and does not provide sufficient coordination for Na<sup>+</sup>. This comparison suggests that high-affinity agonist binding and the presence of Na<sup>+</sup> in this site are mutually exclusive, which is consistent with the observed negative allosteric effects of Na<sup>+</sup> on binding of agonists (Fig. 3 and table S2) (16, 20).

The high-resolution structure also allows us to investigate off-target interactions of the diuretic and sodium-channel blocker amiloride with GPCRs that were first documented by Howard *et al.* (33) and Nunnari *et al.* (34); they demonstrated that amiloride and derivatives non-competitively displaced a radiolabeled antago-

nist from the α<sub>2</sub>-adrenergic receptor by enhancing the radioligand's dissociation rate. Moreover, Howard *et al.* (33) provided evidence that NaCl competed with amiloride, suggesting that Na<sup>+</sup> and amiloride share an allosteric binding site. We docked amiloride into the central cluster cavity (fig. S8), with only minor changes in the conformations of the surrounding side chains; i.e., Trp246<sup>6.48</sup>. Multiple docking runs consistently led to an amiloride orientation in which its charged guanidinium group interacts with Asp52<sup>2.50</sup>, whereas other polar groups form a network of hydrogen bonds with residues in the pocket, mimicking polar interactions in the Na<sup>+</sup>/water cluster. Successful docking of bulkier amiloride derivatives, such as 5-(*N,N*-hexamethylene)amiloride, required more substantial rearrangements of sev-

eral side chains and possibly the main chain, which would potentially perturb the conformation of the deepest part of the orthosteric ligand-binding pocket. This result is consistent with the higher potencies of such derivatives in accelerating orthosteric antagonists' off rates (11). This docking study also corroborates the results of our experiments (Fig. 3), in which amiloride reduced [<sup>3</sup>H]ZM241385 binding (probably due to the conformational changes in Trp246<sup>6.48</sup>), inhibited binding of the agonist [<sup>3</sup>H]NECA, and competed with Na<sup>+</sup> ions for the same binding site.

The 1.8 Å structure includes 23 ordered lipid chains and three cholesterol molecules per receptor. Together, they form an almost-complete lipid bilayer around each protein molecule, mediating crystal contacts (Fig. 4, A and B, and fig. S9). Lipids

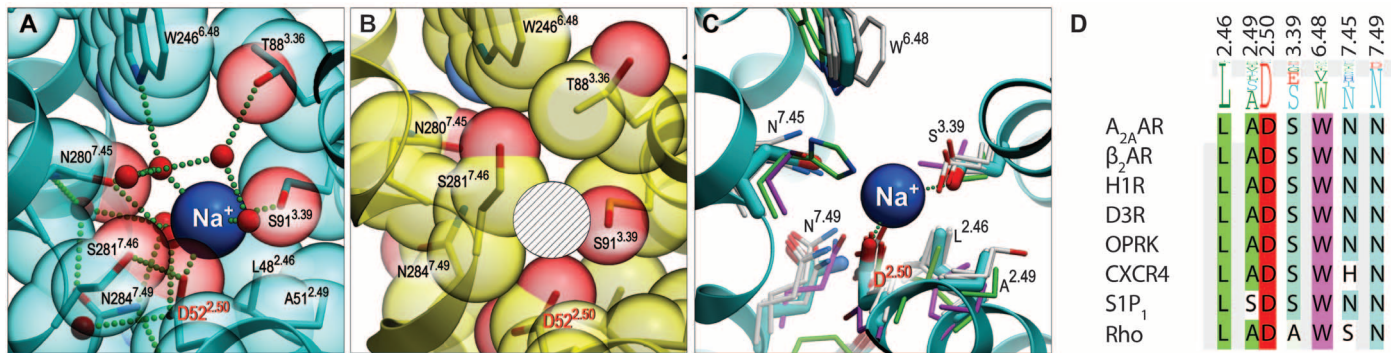


**Fig. 2.** Structural details of the Na<sup>+</sup> allosteric site in the inactive and active-like state A<sub>2A</sub>AR. (A) Sodium ion (blue sphere) in the middle of the 7-TM bundle coordinated by highly conserved Asp52<sup>2.50</sup>, Ser91<sup>3.39</sup>, and three water molecules. The receptor is shown as a ribbon, and residues lining the Na<sup>+</sup> cavity are shown as sticks. Transparent spheres with carbon atoms are colored light blue; oxygen atoms are transparent and red. Water molecules in the cluster are shown as small red spheres, whereas the salt bridge between Na<sup>+</sup> and Asp52<sup>2.50</sup> and hydrogen bonds are shown as green

dotted lines. T, Thr. (B) The pocket collapses in the active-like state A<sub>2A</sub>AR-T4L-ΔC/UK432,097 structure, precluding Na<sup>+</sup> binding at this site (the hatched sphere designates the position of Na<sup>+</sup> in the inactive structure). (C) Structural conservation of the allosteric pocket among solved GPCR structures. (A<sub>2A</sub>AR, light blue; CXCR4, green; rhodopsin, purple; all other, gray). (D) Sequence conservation of the pocket residues among all class A GPCRs (shown as a residue profile in the top row) and among the solved GPCR structures. H, His.

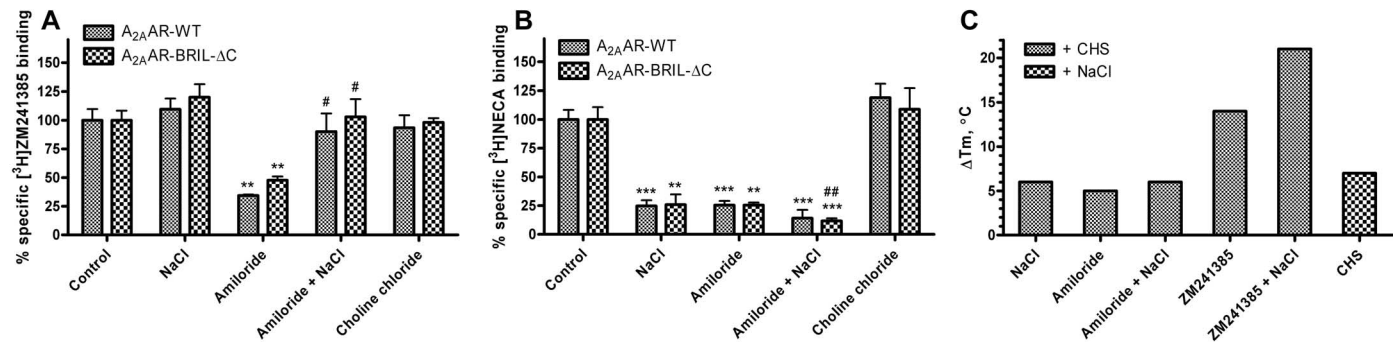


**Fig. 3.** Modulation of A<sub>2A</sub>AR by sodium ions, amiloride, and cholesterol. (A) [<sup>3</sup>H]ZM241385 or (B) [<sup>3</sup>H]NECA equilibrium binding to A<sub>2A</sub>AR-WT and A<sub>2A</sub>AR-BRIL-ΔC constructs transiently expressed on human embryonic kidney 293 cell membranes in the presence of buffer (control) or buffer supplemented with 150 mM NaCl, 100 μM amiloride, combinations of 100 μM amiloride and 150 mM NaCl, and 150 mM choline chloride. The figures represent data combined from three separate experiments performed in duplicate. Differences in specific binding were analyzed by a Student's *t* test. Significant differences were observed for the effect of modulators on control binding (\*\**P* < 0.01, \*\*\**P* < 0.001), as well as for the effect of NaCl on amiloride modulation (#*P* < 0.05, ##*P* < 0.01). There was no significant effect of choline chloride on [<sup>3</sup>H]ZM241385

or [<sup>3</sup>H]NECA binding, which is further proof that Na<sup>+</sup> rather than Cl<sup>−</sup> ions caused the effect of NaCl. Error bars indicate SEM of three separate experiments. (C) Shifts in thermostability of A<sub>2A</sub>AR-BRIL-ΔC construct purified in detergent micelles upon addition of 150 mM NaCl, 100 μM amiloride, combinations of 100 μM amiloride and 150 mM NaCl, 1 μM ZM241385 and 150 mM NaCl, and 0.01% CHS. Experiments with ZM241385 were repeated six times, with a SD of less than 1°C. The composition of the control buffer was 25 mM Hepes pH 7.5, 0.05% *n*-dodecyl β-D-maltoside (DDM), and 0.01% CHS for all samples except for the study of the effect of CHS, in which the control buffer was 25 mM Hepes pH 7.5, 0.05% DDM, and 800 mM NaCl. ΔT<sub>m</sub>, shift in the melting temperature.



on the EC side have stronger electron densities and appear to be more ordered. All three cholesterol molecules in this structure are bound to the EC half of the receptor and have low average B-factors (25 to 27 Å<sup>2</sup>) in comparison to other lipids (41 to 61 Å<sup>2</sup>). Two of these cholesterol molecules (CLR1 and CLR3) are bound to symmetry-related receptors and mediate crystal-lattice packing by forming face-to-face interactions. The third cholesterol molecule (CLR2) does not participate in crystal contacts. Interestingly, CLR2 and CLR3 occupy hydrophobic grooves along helix VI and form extensive contacts with the aromatic ring of Phe255<sup>6,57</sup>, which is sandwiched between these cholesterol molecules (Fig. 4C and fig. S10). In the adenosine family of receptors, position 6.57 is conserved as Ile, Val, or Phe: hydrophobic residues that all could support the type of stacking interaction observed in this structure. In addition, CLR2 forms a hydrogen bond (2.7 Å) with the main-chain carboxyl of Ser263, and the hydroxyl of CLR3 has a polar interaction with sulfur of Cys259 (3.8 Å) in

ECL3, the loop that is stabilized by the Cys259-Cys262 disulfide bond. Specific binding and conformational stabilization of this region of helix VI by cholesterol molecules may play a functional role in A<sub>2A</sub>AR by fixing the position of Asn253<sup>6,55</sup> in the ligand-binding pocket of the receptor (Fig. 4C). This key residue exists in all adenosine receptors and anchors the exocyclic amine of the ligand's central core in both agonist and antagonist complexes (20). Such direct cholesterol binding to A<sub>2A</sub>AR is also consistent with observations that addition of cholesterol hemisuccinate (CHS) increases the thermostability of the receptor purified in detergent micelles (Fig. 3).

Although most lipid chains form nonspecific hydrophobic contacts filling grooves on the protein surface, several interactions of lipids with A<sub>2A</sub>AR may be specific: for example, interactions between the lipids' polar groups and the main-chain and side-chain polar groups of ECL1 and ECL3. In addition, one lipid (OLA) intercalates inside the TM bundle between helices I and VII, thereby protruding into the ligand-

binding pocket (Fig. 4D). This lipid molecule apparently stabilizes the conformation of the first eight N-terminal residues of helix I, which do not make any direct contacts with the rest of the helical bundle.

It is intriguing to speculate that GPCRs are allosteric machines (35–37), controlled in part by ions like sodium, membrane components such as lipids and cholesterol, and also water molecules. Although this concept of allostery exceeds its common definition, with increased-resolution eukaryotic membrane protein structures and complementary biophysical studies, it seems likely that we will start to observe the control of membrane proteins, not only by pharmacological ligands, but also by endogenous small molecules at specific binding sites. The small molecules mentioned here can dramatically affect a protein's stability and function, which can have a pronounced effect on the physiological signaling of GPCRs in very important ways.

#### References and Notes

1. V. Katritch, V. Cherezov, R. C. Stevens, *Trends Pharmacol. Sci.* **33**, 17 (2012).
2. S. G. Rasmussen *et al.*, *Nature* **477**, 549 (2011).
3. M. A. Hanson *et al.*, *Science* **335**, 851 (2012).
4. K. Haga *et al.*, *Nature* **482**, 547 (2012).
5. A. C. Kruse *et al.*, *Nature* **482**, 552 (2012).
6. H. Wu *et al.*, *Nature* **485**, 327 (2012).
7. A. Manglik *et al.*, *Nature* **485**, 321 (2012).
8. A. A. Thompson *et al.*, *Nature* **485**, 395 (2012).
9. S. Granier *et al.*, *Nature* **485**, 400 (2012).
10. K. Burger, G. Gimpl, F. Fahrenholz, *Cell. Mol. Life Sci.* **57**, 1577 (2000).
11. Z. G. Gao, A. P. Ijzerman, *Biochem. Pharmacol.* **60**, 669 (2000).
12. A. Göblyös, A. P. Ijzerman, *Biochim. Biophys. Acta* **1808**, 1309 (2011).
13. E. Chun *et al.*, *Structure* **20**, 967 (2012).
14. Materials and methods are available as supplementary materials on Science Online.
15. The construct is based on the sequences of the wild-type human A<sub>2A</sub>AR and the thermostabilized apocytochrome b562 from *E. coli* (M7W, H102I, K106L), referred to as BRIL, including the following features: (i) Residues Ala1 to Leu106 of BRIL were inserted between Lys209 and Gly218 within the A<sub>2A</sub>AR ICL3 region. (ii) C-terminal residues 317 to 412 of A<sub>2A</sub>AR were truncated.
16. V.-P. Jaakola *et al.*, *Science* **322**, 1211 (2008).
17. A. S. Doré *et al.*, *Structure* **19**, 1283 (2011).
18. Superscripts refer to the Ballesteros-Weinstein numbering in which a single most conserved residue among the class A GPCRs is designated x.50, where x is the transmembrane helix number. All other residues on that helix are numbered relative to this conserved position.
19. V. Katritch, I. Kufareva, R. Abagyan, *Neuropharmacology* **60**, 108 (2011).
20. F. Xu *et al.*, *Science* **332**, 322 (2011).
21. G. Lebon *et al.*, *Nature* **474**, 521 (2011).
22. T. Okada *et al.*, *J. Mol. Biol.* **342**, 571 (2004).
23. R. Nygaard, T. M. Frimurer, B. Holst, M. M. Rosenkilde, T. W. Schwartz, *Trends Pharmacol. Sci.* **30**, 249 (2009).
24. T. E. Angel, M. R. Chance, K. Palczewski, *Proc. Natl. Acad. Sci. U.S.A.* **106**, 8555 (2009).
25. M. M. Harding, *Acta Crystallogr. D Biol. Crystallogr.* **58**, 872 (2002).
26. F. Magnani, Y. Shibata, M. J. Serrano-Vega, C. G. Tate, *Proc. Natl. Acad. Sci. U.S.A.* **105**, 10744 (2008).
27. M. S. Parker, Y. Y. Wong, S. L. Parker, *Amino Acids* **35**, 1 (2008).
28. B. Volring *et al.*, *Nucleic Acids Res.* **39**, D309 (2011).
29. H. Barbhaiya, R. McClain, A. Ijzerman, S. A. Rivkees, *Mol. Pharmacol.* **50**, 1635 (1996).

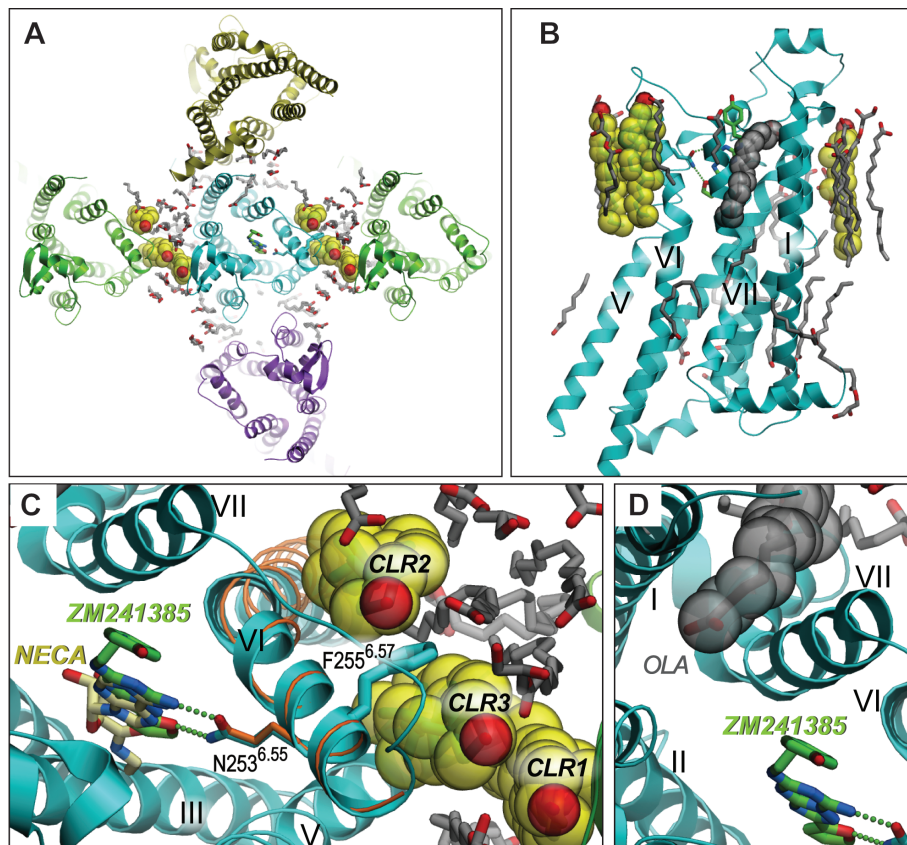


**Fig. 4.** Lipid-receptor interactions. (A) Top view of A<sub>2A</sub>AR (light blue ribbon) including crystallographic neighbors (green, translational symmetry; purple, rotational; yellow, antiparallel arrangement). Cholesterol molecules are shown as balls with yellow carbons; lipid molecules are shown as sticks with gray carbons. (B) Side view of A<sub>2A</sub>AR. (C) Potential stabilizing effect of two cholesterol molecules, CLR2 and CLR3, on the conformation of helix VI. Side chains Phe255<sup>6,57</sup> and Asn253<sup>6,55</sup> of the A<sub>2A</sub>AR-BRIL-ΔC/ZM241385 complex are shown as sticks with light blue carbons. The superimposed active-like state A<sub>2A</sub>AR-T4L-ΔC/UK432,097 is shown as an orange ribbon (helix VI only) and sticks (Asn253<sup>6,55</sup> side chain and NECA scaffold of the UK432,097 agonist only). (D) A lipid molecule (OLA, gray balls) is inserted in between helices I and VII inside the ligand-binding pocket.

30. Z. G. Gao *et al.*, *Mol. Pharmacol.* **63**, 1021 (2003).
31. B. S. Zhovrov, V. S. Ananthanarayanan, *J. Biomol. Struct. Dyn.* **15**, 631 (1998).
32. J. Selent *et al.*, *PLoS Comput. Biol.* **6**, e1000884 (2010).
33. M. J. Howard *et al.*, *Mol. Pharmacol.* **32**, 53 (1987).
34. J. M. Nunnari *et al.*, *J. Biol. Chem.* **262**, 12387 (1987).
35. M. Canals *et al.*, *Trends Biochem. Sci.* **36**, 663 (2011).
36. J. P. Changeux, *Annu. Rev. Biophys.* **41**, 103 (2012).
37. T. P. Kenakin, *Br. J. Pharmacol.* **165**, 1659 (2012).
38. B. K. Ho, F. Gruswitz, *BMC Struct. Biol.* **8**, 49 (2008).

**Acknowledgments:** This work was supported by NIH Common Fund in Structural Biology grant P50 GM073197 for technology development, NIH/National Institute of General Medical Sciences (NIGMS) PSI:Biological grant U54 GM094618 for biological studies and structure production, NIGMS grant

R01 GM089857 to V.C., a Dutch Research Council Nederlandse Organisatie voor Wetenschappelijk Onderzoek (NWO) TOP grant (714.011.001: "The crystal structure of the adenosine A<sub>2A</sub> receptor: The follow-up") to A.P.I., and an NWO Veni grant (11188) to L.H.H. We thank J. Velasquez for help on molecular biology; T. Trinh, K. Allin, and M. Chu for help on baculovirus expression; T. Mulder-Krieger and H. de Vries for their technical expertise in the biochemical characterization, G. van Westen for his educated comments on the crystal structure; M. Mileni for reviewing the final structure; J. P. Changeux for discussions on GPCR allostery and the potential for allosteric stabilizers; K. Kadyshchinskaya for assistance with figure preparation; A. Walker for assistance with manuscript preparation; J. Smith, R. Fischetti, and N. Sanishvili for assistance in development and use of the minibeam and beamtime at GM/CA-CAT beamline 23-ID at the Advanced Photon Source, which is supported by National Cancer Institute

grant Y1-CO-1020 and NIGMS grant Y1-GM-1104. Coordinates and the structure factors have been deposited in the Protein Data Bank under the accession code (4E1Y). R.C.S. is a founder and on the Board of Directors of Receptos, a GPCR structure-based drug discovery company. R.C.S., C.B.R., A.A.T., W.L., F.X., E.C., and V.K. are inventors on a patent applied for jointly by The Scripps Research Institute and Receptos on the use of fusion proteins to crystallize GPCRs.

# Supplementary Materials

www.sciencemag.org/cgi/content/full/337/6091/232/DC1

Materials and Methods

Figs. S1 to S10

Tables S1 and S2

References (39–57)

17 January 2012; accepted 18 May 2012

10.1126/science.1219218

# Molecular Architecture and Assembly Principles of *Vibrio cholerae* Biofilms

Veysel Berk,<sup>1,2\*</sup> Jiunn C. N. Fong,<sup>3</sup> Graham T. Dempsey,<sup>4</sup> Omer N. Develioglu,<sup>6</sup> Xiaowei Zhuang,<sup>4,5</sup> Jan Liphardt,<sup>1,2,7</sup> Fitnat H. Yildiz,<sup>3\*</sup> Steven Chu<sup>8\*†</sup>

In their natural environment, microbes organize into communities held together by an extracellular matrix composed of polysaccharides and proteins. We developed an in vivo labeling strategy to allow the extracellular matrix of developing biofilms to be visualized with conventional and superresolution light microscopy. *Vibrio cholerae* biofilms displayed three distinct levels of spatial organization: cells, clusters of cells, and collections of clusters. Multiresolution imaging of living *V. cholerae* biofilms revealed the complementary architectural roles of the four essential matrix constituents: RbmA provided cell-cell adhesion; Bap1 allowed the developing biofilm to adhere to surfaces; and heterogeneous mixtures of *Vibrio* polysaccharide, RbmC, and Bap1 formed dynamic, flexible, and ordered envelopes that encased the cell clusters.

Microbes within biofilms are more resistant to antibiotics; immune clearance; and osmotic, acid, and oxidative stresses as compared with planktonic cells (1–7). Despite advances in identifying the polysaccharide and proteinaceous constituents of the biofilm extracellular matrix, the mechanisms by which these factors yield a mechanically defined and spatially organized biofilm are largely unknown (8–10). *Vibrio cholerae* biofilm formation involves the production of *Vibrio* polysaccharide (VPS) and three matrix proteins (RbmA, RbmC, and Bap1) predicted to contain carbohydrate-binding domains (fig. S1A) (11–13). To investigate the molecular mechanisms of biofilm development, we

used a *V. cholerae* rugose variant with increased capacity to form biofilms (11). We inserted Myc, FLAG, and human influenza hemagglutinin epitopes into its genome at the 3' ends of the *rbmA*, *rbmC*, and *bap1* genes, respectively (fig. S1B), allowing us to label these matrix proteins in vivo by supplementing the growth medium with corresponding cyanine dye-labeled primary antibodies (Fig. 1).

We used four-color confocal imaging to validate this labeling strategy and obtain a diffraction-limited overview of biofilm architecture (Fig. 1, A to C, and movie S1). Cells were mainly organized into elongated clusters whose boundaries were defined by three-dimensional (3D) envelopes of the RbmC (red) and Bap1 (green) proteins (Fig. 1C, red arrow). Within the envelope that encases the cell clusters, the relative Bap1 signal was highest in those areas with the least RbmC (Fig. 1A and figs. S5 and S6). Deletion of either RbmC or Bap1 did not impair cluster formation or the resultant architecture of the envelope (Fig. 1D and fig. S7) (11, 14). The cell clusters had a regular width of  $2.2 \pm 0.3 \mu\text{m}$  ( $n = 42$  clusters), whereas their length varied from 2 to 8  $\mu\text{m}$  (fig. S8). Each cell within a cluster contacted the cluster boundary and, thus, the interstitial space between clusters, perhaps facilitating nutrient delivery and waste disposal.

However, although Bap1 and RbmC share 47% peptide sequence similarity (11), their spa-

tial distributions differed notably at the interface between the coverslip and the cell clusters (fig. S9). Bap1 was concentrated at the biofilm-surface interface (14), whereas RbmC was absent from the interface (Fig. 1, B and C, and fig. S9). Moreover, a *bap1* deletion strain had a more severely altered biofilm phenotype than a *rbmC* deletion strain (11, 14), all pointing to Bap1 having two separable functions—namely, encasing cell clusters and attaching cells to the surface.

In contrast to RbmC and Bap1, we detected RbmA throughout the biofilm (Fig. 1, A to C) (14). Strains lacking RbmA have reduced colony corrugation and are less resistant to detergent treatment (12) but can still adhere to surfaces. Surprisingly, deletion of *rbmA* caused loss of cell ordering into clusters and associated RbmC-Bap1 envelopes, although both of these proteins were clearly present within the biofilm (Fig. 1D and fig. S7). Thus, Bap1 appears to help the biofilm to adhere to surfaces, RbmC and Bap1 appear to encapsulate cell clusters, and RbmA appears to participate in cell-cell adhesion (movies S2 to S6) (11, 12, 14).

To further test these hypotheses and learn how biofilms assemble, we imaged living biofilms as they developed from a single founder cell into mature biofilms (Fig. 2A and fig. S10). We followed matrix protein secretion and organization with a continuous in situ immunostaining approach (15) in which labeled primary antibodies were added to the growth medium (Fig. 2A). At the time of initial attachment, individual founder cells did not have detectable RbmA, RbmC, and Bap1 on their surface. The first matrix protein to appear postattachment was RbmA, which accumulated at discrete sites on the cell surface. After the first cell division, the newly formed daughter cell remained attached to the founder cell, unlike in planktonic cells, where the two cells quickly separate (Fig. 2A).

Bap1 then appeared at the junction between the two cells and also on the substrate near the cells (Fig. 2A). Bap1 gradually accumulated radially over distances of tens of micrometers from its initial location on or near the founder cell (Fig. 2, A and B). The founder cell and its immediate environment had notably more Bap1 than the rest of the biofilm for the entire 6.5-hour

<sup>1</sup>Department of Physics, University of California, Berkeley, CA 94720, USA. <sup>2</sup>Molecular and Cellular Biology, University of California, Berkeley, CA 94720, USA. <sup>3</sup>Department of Microbiology and Environmental Toxicology, University of California, Santa Cruz, CA 95064, USA. <sup>4</sup>Biophysics Program, Harvard University, Cambridge, MA 02138, USA. <sup>5</sup>Department of Chemistry and Chemical Biology, Department of Physics, and Howard Hughes Medical Institute (HHMI), Harvard University, Cambridge, MA 02138, USA. <sup>6</sup>Department of Otorhinolaryngology, Taksim Training and Research Hospital, Istanbul, Turkey. <sup>7</sup>Physical Biosciences Division, Lawrence Berkeley National Laboratory, Berkeley, CA 94720, USA. <sup>8</sup>U.S. Department of Energy, 1000 Independence Avenue, SW, Washington, DC 20585, USA.

\*To whom correspondence should be addressed. E-mail: vberk@berkeley.edu (V.B.); fyildiz@ucsc.edu (F.H.Y.); correspondence to S.C. should be addressed to vberk@berkeley.edu. †Formerly of the Departments of Physics and Molecular and Cellular Biology, University of California, Berkeley, CA 94720, USA.



**Fig. 1.** *V. cholerae* biofilm structure. (A) Optical section of biofilm 4  $\mu\text{m}$  above the coverslip. Images are pseudocolored in blue (cells), gray (RbmA), red (RbmC), and green (Bap1). RbmA localizes around and within cell clusters; RbmC and Bap1 encase cell clusters. Cells were counterstained with 4',6-diamidino-2-phenylindole (DAPI). Scale bars, 3  $\mu\text{m}$ . (B) Three-dimensional biofilm architecture. Colors are as in (A). (C) Enlargement of the boxed region in (B). The red arrow indicates one cell cluster. The red signal is now rendered partially transparent to allow visualization of cells within an RbmC-containing cluster. (D) Comparison of biofilm architecture formed by rugose (Rg) and  $\Delta\text{rbmA}$  (A-) strains. RbmA is required for cell cluster formation. Scale bars, 2  $\mu\text{m}$ .

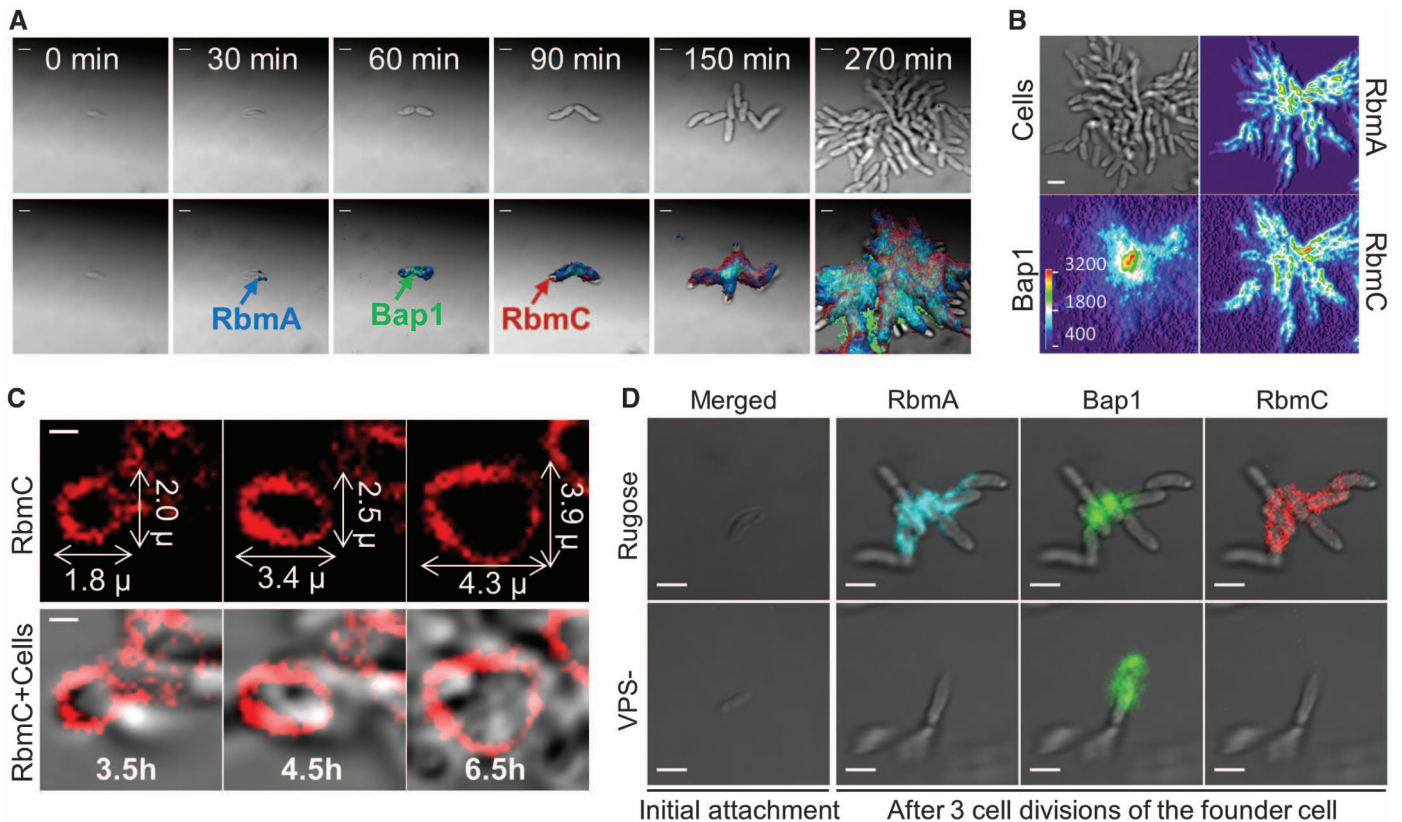
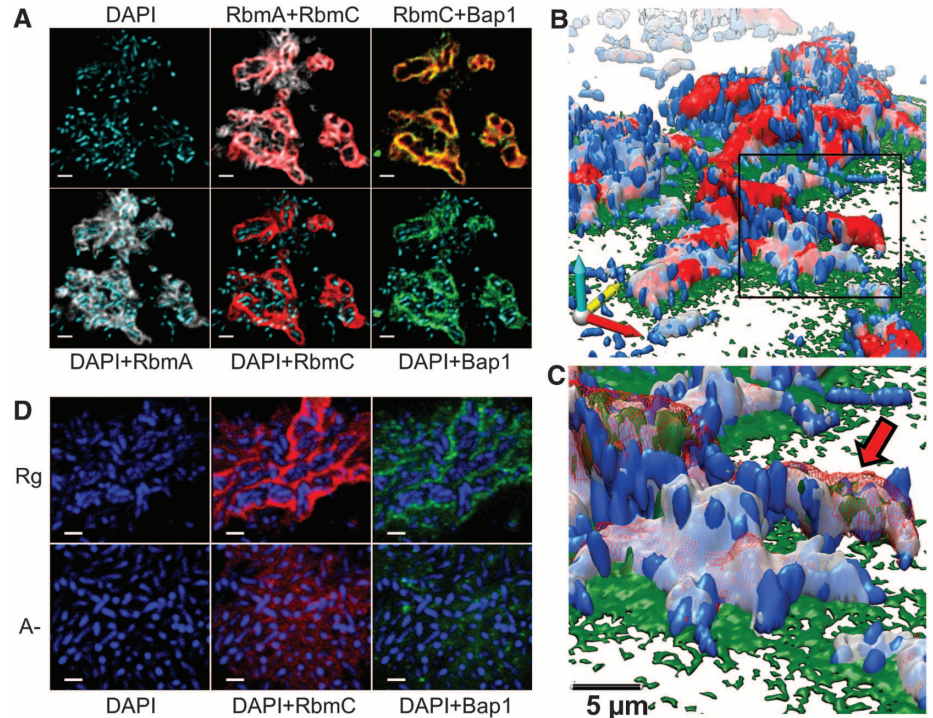


**Fig. 2.** Time-lapse CLSM imaging of *V. cholerae* biofilm development and cluster formation. (A) Expression and subsequent distribution of matrix proteins followed by time-lapse CLSM using continuous direct immunostaining. Cell outlines (bright field) are gray; RbmA, Bap1, and RbmC are shown in blue, green, and red, respectively. Scale bars, 2  $\mu\text{m}$ . (B) Bright-field biofilm image and corresponding fluorescent channel surface plots of Bap1, RbmA, and RbmC obtained 4.5 hours postinoculation. Fluorescence intensity is color-coded

according to the color scale bar. Bap1 spread from a central point corresponding to the founder cell position, whereas RbmA and RbmC were more homogeneously distributed through the biofilm cells. Scale bar, 3  $\mu\text{m}$ . (C) Gradual expansion of the RbmC-containing cluster tracked by time-lapse CLSM. Scale bars, 1  $\mu\text{m}$ . (D) Inability to produce VPS (VPS-) prevents retention of daughter cells, as well as accumulation of RbmA and RbmC and also blocks biofilm formation. Scale bars, 3  $\mu\text{m}$ .

duration of the experiment. The radially symmetrical distribution of Bap1 relative to the founder cell suggests that Bap1 is continuously secreted into solution by the founder cell and other early members of the young biofilm, after which it accumulates on nearby surfaces (Fig. 2B and fig. S11).

The third matrix protein, RbmC, first appeared after 90 min at discrete sites on the cell surface. Later in biofilm development, the RbmC-Bap1 envelopes formed and then grew by expansion in all directions, with the size of the RbmC-Bap1 envelope doubling within three cell divisions to accommodate the new cell mass (Fig. 2C). Biofilm formation thus involves the temporally sequenced and spatially heterogeneous secretion of matrix proteins, which may have complementary architectural functions—namely, retention of daughter cells after division by RbmA, surface functionalization by Bap1, and encapsulation of the cell clusters by RbmC/Bap1.

Next, we investigated how the RbmC and Bap1 matrix proteins interact with VPS during biofilm formation. VPS is a polysaccharide thought to form a polymeric network that gives mechanical continuity to the biofilm (8, 16–19). *V. cholerae* cells lacking either VPS (VPS<sup>−</sup>) or all three matrix proteins (ABC<sup>−</sup>) were unable to form 3D biofilms (fig. S12). The parent strain biofilm phenotype could be recovered by coculturing VPS<sup>−</sup> and ABC<sup>−</sup> strains, showing that heterologous provision of these four materials is sufficient to restore normal biofilm formation (figs. S1A and S12). VPS<sup>−</sup> cells could stick to surfaces, but subsequently produced daughter cells did not accumulate and were instead lost in the growth medium (Fig. 2D and movie S5) (20). Although RbmA, RbmC, and Bap1 proteins were synthesized (figs. S13 and S14), they did not accumulate on the surface of VPS<sup>−</sup> cells (Fig. 2D). Bap1 was detected on the substrate near the founder cell (Fig. 2D), as expected if Bap1's main function is

to adhere to diverse substrates and tether the biofilm (14). Thus, VPS is required for accumulation of the RbmA, RbmC, and Bap1 on the cell surface, which, in turn, is needed for formation of mature biofilms (13, 14).

Because VPS was required for accumulation of matrix proteins on the cell surface, we wondered whether the opposite was also true. We directly stained the VPS with a Cy3-labeled wheat germ agglutinin (WGA), which recognizes *N*-acetylglucosamine sugars in the VPS (21). RbmC was essential for sustained incorporation of VPS throughout *V. cholerae* biofilms (fig. S15A). Without RbmC, there were occasional bright dots of VPS within the colony but at a much lower density than in the parent strain biofilm (fig. S15A). Thus, sustained retention of VPS is co-dependent with retention of RbmC (Fig. 2D and fig. S15). The VPS staining also confirmed that the RbmC/Bap1 envelopes contained VPS, as expected (Fig. 1A and fig. S15B).

Three-dimensional biofilm development requires a specific, mutually interdependent series of protein/VPS synthesis, secretion, capture, and cross-linking steps. However, the ~200-nm spatial resolution of confocal laser scanning microscopy (CLSM) (22, 23) was insufficient to directly visualize these developmental intermediates. We thus constructed a multicolor 3D superresolution imaging apparatus using stochastic optical reconstruction microscopy (23–28) with a localization precision of 19, 21, and 42 nm in *x*, *y*, and *z* (full width at half maximum) (fig. S16). As before, we added labels to the growth medium and imaged living biofilms. With the use of a Cy3-WGA reagent, VPS was first detected at several discrete sites on the cell surface at time *t* = 15 min postattachment (Fig. 3A, white arrows). Over the next 2 hours, the number of VPS spots, as well as their intensity, increased slowly. At *t* = 60 min postattachment, 3D superresolution images of VPS organization showed that the polymer was primarily organized into 50- to 200-nm diameter spheroids protruding away from the cell surface (Fig. 3B, white arrow). It appears that VPS is progressively extruded from the cell as a flexible polymer that, like all relaxed flexible polymers, adopts an isotropic, spherical configuration.

*Pseudomonas aeruginosa* biofilms have been reported to self-heal within minutes after mechanical disruption beyond their yield point, implying that relatively transient interactions are responsible for maintaining the *P. aeruginosa* matrix (29). How could such recovery be possible if the VPS (or Psl in *P. aeruginosa*) were irreversibly cross-linked by matrix proteins such as RbmC? We used two-color 3D superresolution imaging to visualize the organization of VPS and RbmC within a biofilm (15). The superresolution microscope has wide dynamic range and can detect single VPS and RbmC molecules. VPS and RbmC were not homogeneously distributed within the mature biofilm, but both matrix components were confined to the envelopes encasing

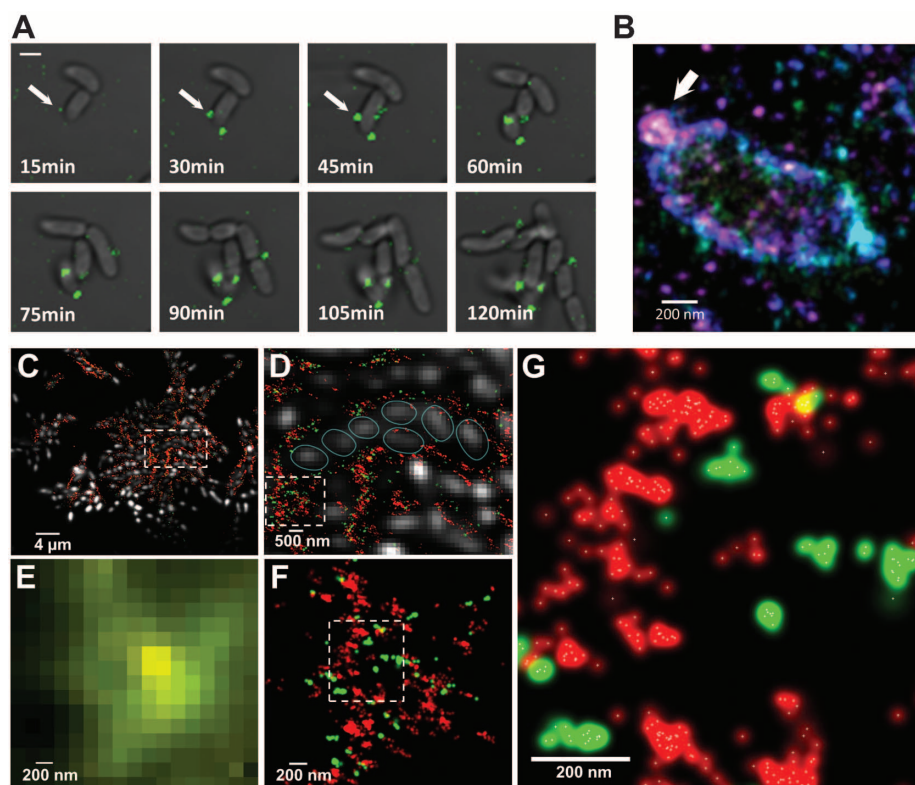


**Fig. 3.** Exopolysaccharide secretion, initial organization, and molecular architecture of *V. cholerae* biofilms. (A) Time-lapse CLSM images of VPS (green) production and secretion in *V. cholerae* cells during biofilm formation. Fluorescent images of VPS are merged with bright-field images of cells. White arrows indicate VPS. Scale bar, 2  $\mu$ m. (B) Three-dimensional superresolution image of a single *V. cholerae* cell. The white arrow indicates a ball-like structure of VPS on the surface of the *V. cholerae* cell early in biofilm formation. Color corresponds to height: -300 nm (violet) to +300 nm (red). (C) Three-dimensional two-color superresolution image (200-nm *z*-section) of a rugose variant biofilm showing molecular organization of VPS (red) and RbmC (green) around cell clusters. Cells were counterstained with DAPI (white). (D) Enlarged boxed region in (C) showing organization of cells within the VPS/RbmC-enclosed cluster. Individual cells were outlined (light blue) for clarity. (E) Enlarged boxed region in (D) as it appears in conventional, diffraction-limited microscopy, showing unresolved VPS and RbmC signals. (F) Superresolution image of the same region in (E), showing distribution of RbmC and the VPS polymers in a biofilm matrix. (G) Enlarged boxed region in (F). White symbols indicate the center of a Gaussian fit to each localization events.



the cell clusters and to the interstitial space between clusters (Fig. 3, C and D). The mechanism(s) by which bacteria achieve such spatial segregation of materials within the biofilm and, thus, generate a matrix architecture with submicrometer features are unknown. Moreover, most RbmC signal was not uniformly distributed within the VPS matrix (Fig. 3, E to G). Hence, RbmC and VPS may have homophilic (RbmC-RbmC or VPS-VPS) and heterophilic (RbmC-VPS) interactions, where RbmC may act as a reversible cross-linker of VPS. VPS organization must also be dynamic; otherwise, the cells could not sharply repartition RbmC and VPS into the envelopes and interstitial spaces (Fig. 3D).

We used a matrix-labeling strategy to observe in real time as *V. cholerae* biofilms develop with single-protein and single-polymer precision, revealing assembly principles and intermediates. Cells organize into clusters within the biofilm, and the mature biofilm is a composite of these clusters. An envelope composed of VPS, Bap1, and RbmC encloses these clusters, and RbmA is required for their formation. The VPS/Bap1/RbmC envelope is structured on the molecular level by an unknown mechanism(s) and is capable of reforming, stretching, and expanding to accommodate cell growth.

## References and Notes

1. J. W. Costerton, P. S. Stewart, E. P. Greenberg, *Science* **284**, 1318 (1999).
2. L. Hall-Stoodley, P. Stoodley, *Trends Microbiol.* **13**, 7 (2005).
3. M. R. Parsek, P. K. Singh, *Annu. Rev. Microbiol.* **57**, 677 (2003).
4. P. S. Stewart, J. W. Costerton, *Lancet* **358**, 135 (2001).
5. T.-F. Mah et al., *Nature* **426**, 306 (2003).
6. G. G. Anderson, G. A. O'Toole, *Curr. Top. Microbiol. Immunol.* **322**, 85 (2008).
7. A. Reisner, N. Høiby, T. Tolker-Nielsen, S. Molin, *Contrib. Microbiol.* **12**, 114 (2005).
8. H.-C. Flemming, J. Wingender, *Nat. Rev. Microbiol.* **8**, 623 (2010).
9. D. López, H. Vlamakis, R. Kolter, *Cold Spring Harbor Perspect. Biol.* **2**, a000398 (2010).
10. M. Harmsen, L. Yang, S. J. Pamp, T. Tolker-Nielsen, *FEMS Immunol. Med. Microbiol.* **59**, 253 (2010).
11. J. C. N. Fong, F. H. Yildiz, *J. Bacteriol.* **189**, 2319 (2007).
12. J. C. N. Fong, K. Karplus, G. K. Schoolnik, F. H. Yildiz, *J. Bacteriol.* **188**, 1049 (2006).
13. J. C. N. Fong, K. A. Syed, K. E. Klose, F. H. Yildiz, *Microbiology* **156**, 2757 (2010).
14. C. Absalon, K. Van Dellen, P. I. Watnick, *PLoS Pathog.* **7**, e1002210 (2011).
15. Materials and methods are available as supplementary materials on Science Online.
16. I. W. Sutherland, *Microbiology* **147**, 3 (2001).
17. E. Karatan, P. Watnick, *Microbiol. Mol. Biol. Rev.* **73**, 310 (2009).
18. F. H. Yildiz, X. S. Liu, A. Heydorn, G. K. Schoolnik, *Mol. Microbiol.* **53**, 497 (2004).
19. S. S. Branda, S. Vik, L. Friedman, R. Kolter, *Trends Microbiol.* **13**, 20 (2005).
20. S. Moorthy, P. I. Watnick, *Mol. Microbiol.* **52**, 573 (2004).
21. I. J. Goldstein, C. E. Hayes, *Adv. Carbohydr. Chem. Biochem.* **35**, 127 (1978).
22. J. B. Pawley, B. R. Masters, *J. Biomed. Opt.* **13**, 029902 (2008).
23. S. W. Hell, *Science* **316**, 1153 (2007).
24. M. J. Rust, M. Bates, X. Zhuang, *Nat. Methods* **3**, 793 (2006).
25. E. Betzig et al., *Science* **313**, 1642 (2006).
26. M. Bates, B. Huang, G. T. Dempsey, X. Zhuang, *Science* **317**, 1749 (2007).
27. B. Huang, W. Wang, M. Bates, X. Zhuang, *Science* **319**, 810 (2008).
28. S. T. Hess, T. P. K. Girirajan, M. D. Mason, *Biophys. J.* **91**, 4258 (2006).
29. O. Lieleg, M. Caldara, R. Baumgärtel, K. Ribbeck, *Soft Matter* **7**, 3307 (2011).

**Acknowledgments:** We thank B. Huang for providing image processing software and D. J. Wozniak, J. H. D. Cate, X. Nan, A. Arkin, and A. Yildiz for critical evaluation of the manuscript. This work is supported by the NSF [grant PHY-0647161 (J.L.)] and the NIH [grants AI055987 (F.H.Y.) and GM096450 and GM068518 (X.Z.)]. X.Z. is a HHMI Investigator. J.L. acknowledges support from the U.S. Department of Energy Office of Basic Energy Sciences (FWP SISGRKN) and Lawrence Berkeley National Laboratory.

## Supplementary Materials

www.sciencemag.org/cgi/content/full/337/6091/236/DC1  
Materials and Methods  
Figs. S1 to S17  
Tables S1 and S2  
References (30–40)  
Movies S1 to S6

5 April 2012; accepted 22 May 2012  
10.1126/science.1222981

# Oscillatory Dynamics of Cdc42 GTPase in the Control of Polarized Growth

Maitreyi Das,<sup>1\*</sup> Tyler Drake,<sup>2\*</sup> David J. Wiley,<sup>1</sup> Peter Buchwald,<sup>1</sup> Dimitrios Vavylonis,<sup>2</sup> Fulvia Verde<sup>1,3,†</sup>

Cells promote polarized growth by activation of Rho-family protein Cdc42 at the cell membrane. We combined experiments and modeling to study bipolar growth initiation in fission yeast. Concentrations of a fluorescent marker for active Cdc42, Cdc42 protein, Cdc42-activator Scd1, and scaffold protein Scd2 exhibited anticorrelated fluctuations and oscillations with a 5-minute average period at polarized cell tips. These dynamics indicate competition for active Cdc42 or its regulators and the presence of positive and delayed negative feedbacks. Cdc42 oscillations and spatial distribution were sensitive to the amounts of Cdc42-activator Gef1 and to the activity of Cdc42-dependent kinase Pak1, a negative regulator. Feedbacks regulating Cdc42 oscillations and spatial self-organization appear to provide a flexible mechanism for fission yeast cells to explore polarization states and to control their morphology.

The conserved guanosine triphosphatase (GTPase) Cdc42 establishes cell polarity by regulating the cytoskeletal asymmetry required for normal cell function, differentiation, and motility (1, 2). In budding yeast, Cdc42 breaks the symmetry of spherical cells by clustering in one area of the membrane, the site of bud growth, through a “winner-take-all” positive-feedback mechanism (3–6). However, such a

mechanism cannot explain how multiple growing zones form simultaneously in other cells. Fission yeast cells initially grow in a monopolar fashion, from the tip that existed before division (the old end), and activate bipolar growth that includes the new end as well, once a minimal cell length has been achieved [“new end take off” (NETO)] (7). Fission yeast is thus an ideal system to study how Cdc42 is distributed at multiple sites.

To characterize Cdc42 during the transition to bipolar growth, we used a fluorescent fusion protein [Cdc42/Rac interactive binding peptide–green fluorescent protein (GFP), CRIB-GFP] that binds specifically to activated, guanosine triphosphate (GTP)–bound Cdc42 (8). In larger bipolar cells, CRIB-GFP intensities at cell ends showed out-of-phase oscillations with an average period of

5 min (Fig. 1, A and B; movies S1 and S2, and tables S2 and S3). Oscillations were detectable in more than 50% of cells (table S2), when imaging every 15 s instead of 1 min (Fig. 1C), and in three dimensions (Fig. 1D). The rest of the cells displayed anticorrelated fluctuations without obvious periodicity. For shorter cells, nongrowing ends still had detectable CRIB-GFP fluorescence, albeit at lower intensities than the older, growing ends (fig. S1). The tip intensities still underwent anticorrelated oscillations and fluctuations, but around asymmetric averages, unlike longer cells (table S2).

We visualized fluorescently labeled scaffold protein Scd2, which is proposed to mediate Cdc42 activation by binding to the Cdc42 GEF (guanine nucleotide exchange factor) Scd1 and to Cdc42 (9, 10). Scd2-GFP intensity at the cell tips oscillated and fluctuated much like CRIB-GFP intensity (fig. S2 and table S2), as did Scd1-3xGFP and Cdc42-GFP (fig. S3). Thus, CRIB-GFP oscillations and fluctuations appear to reflect the activated Cdc42 protein complex.

To understand how GTP-Cdc42 levels might influence the NETO transition, we measured instantaneous cell growth rates along with CRIB-GFP intensity in cells undergoing NETO, which occurs in cells longer than 9  $\mu\text{m}$  (7). Intensities at both new and old ends fluctuated strongly over time (Fig. 1E). The instantaneous growth rate was correlated with abundance of CRIB-GFP at both old and new ends; cell tips with a CRIB-GFP tip fraction below 0.2 grew slower than tips with the fraction above 0.2 (Fig. 1F). Varied degrees of asymmetry were also observed at intermediate lengths in a population of asynchronous

<sup>1</sup>Department of Molecular and Cellular Pharmacology (R-189), University of Miami Miller School of Medicine, Post Office Box 016189, Miami, FL 33101, USA. <sup>2</sup>Department of Physics, Lehigh University, 16 Memorial Drive East, Bethlehem, PA, 18015, USA. <sup>3</sup>Marine Biological Laboratory, 7 MBL Street, Woods Hole, MA 02543, USA.

\*These authors contributed equally to this work.

†To whom correspondence should be addressed. E-mail: fverde@med.miami.edu

cells (Fig. 1G, region II). These findings indicate that NETO is a noisy transition driven by GTP-Cdc42 redistribution.

To determine the essential requirements for the transition from oscillating monopolar (asymmetric) to oscillating bipolar (symmetric) states during cell elongation, we developed a coarse-grained mathematical model (Fig. 2A) (11–14). Instead of describing specific molecular interac-

tions, we took into consideration several experimental observations to predict system behavior. We assumed that tips compete for Cdc42 or its effectors and regulators, on the basis of observed GTP-Cdc42 anticorrelations. We also assumed that positive and delayed negative feedbacks combine to generate oscillations, as they do in the bacterial Min system (15). We added noise to represent random concentration fluctuations and

to capture the observed variability (fig. S4A). The model reproduced the observed time courses: dominant-tip oscillations in short cells (with anti-correlated lagging tip) and out-of-phase oscillations at both tips in long cells (Fig. 2B). Allowing different rate constants at the two tips caused them to oscillate around slightly different averages, as observed in many cells (fig. S4B). The model also predicted varied Cdc42 asymmetry in

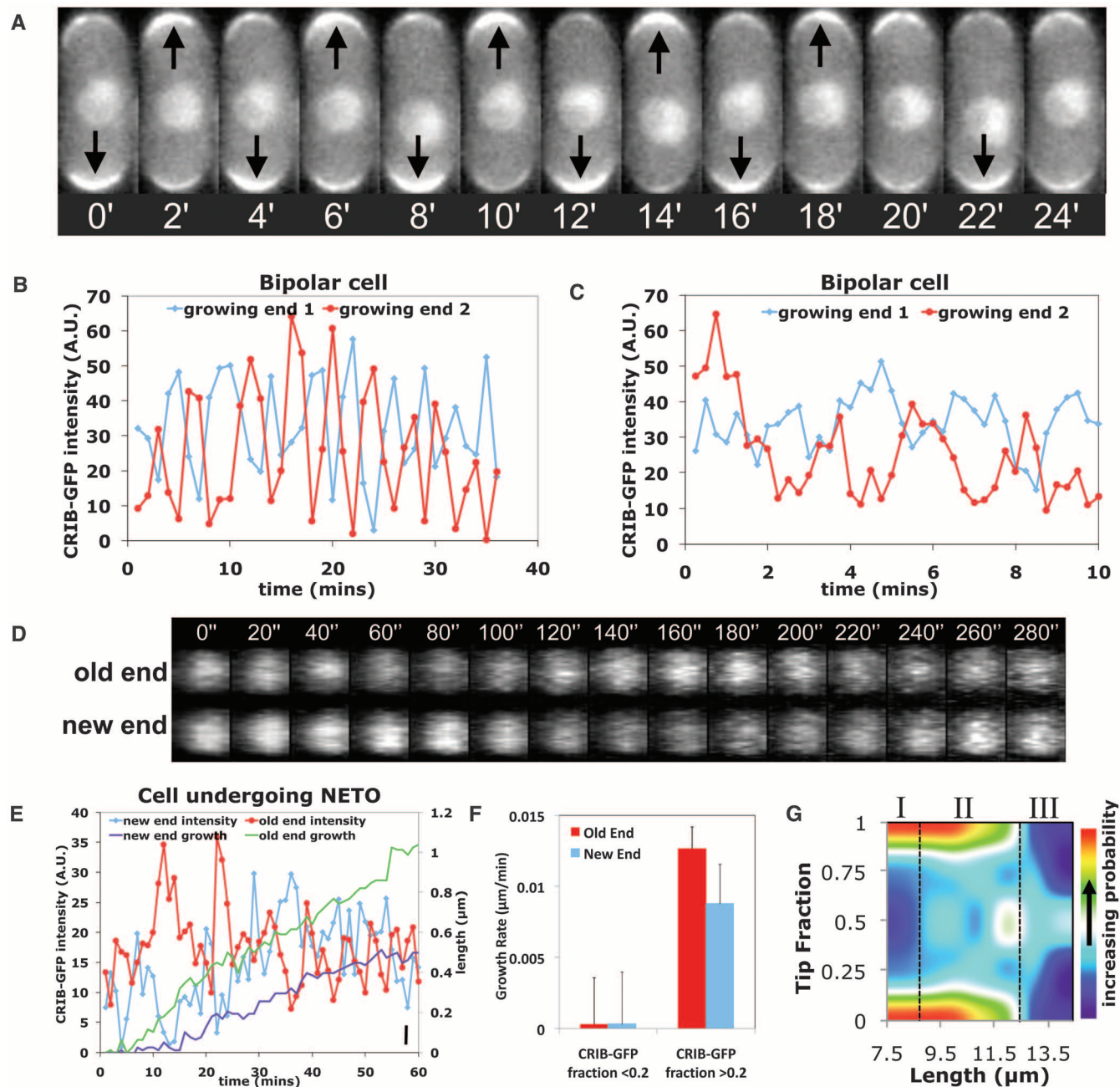


**Fig. 1.** Oscillations and fluctuations of CRIB-GFP fluorescence at fission yeast cell tips. (A) CRIB-GFP fluorescence at cell tips in a bipolar cell (2-min intervals). (B) Old (red) and new end (blue) CRIB-GFP intensity in a bipolar cell (1-min intervals). A.U., arbitrary units. (C) As in (B), for 15-s intervals. (D) Three-dimensional reconstruction of confocal Z-stack images of a bipolar cell showing CRIB-GFP at the old and new end (20-s intervals). (E) Old (red) and new end (blue) CRIB-GFP intensity and cell growth at the old (green) and new

(purple) ends in a cell undergoing NETO. The cell was 8.3  $\mu\text{m}$  long at time 0. Bar, bottom right: 1 pixel = 0.1  $\mu\text{m}$ . (F) Instantaneous growth rate, binned by CRIB-GFP tip fraction (ratio of intensity at one tip over sum of tip intensities) and tip type (old or new). Error bars indicate SEM. (G) Heat-map of CRIB-GFP tip fraction versus cell length in wild-type cells (smoothed data,  $n = 653$ ). Note three regions: asymmetric, short cells (I); intermediate-length region with large intensity variations (II); symmetric, longer cells (III).



cells with similar length (Fig. 2C, “coexistence region”; and fig. S5), as in Fig. 1G.

According to the mathematical model, changes in abundance or activity of Cdc42, or of its regulators, can shift the system to more asymmetric or symmetric states. It indicated that cells with a lower rate of Cdc42 activation (or decreased total amounts of GTP-Cdc42 or Cdc42 GEFs), favor asymmetric states, because the lagging tip is influenced more severely by the accumulation of GTP-Cdc42 at the dominant tip and by the resulting depletion of the cytoplasmic pool (figs. S5A and S6A). To test this, we analyzed CRIB-GFP in *gef1Δ* cells, which lack one of the two Cdc42

GEFs and thus exhibit decreased amounts of global active GTP-Cdc42 (16) but otherwise grow at a normal rate (table S5). Most (75%;  $n = 12$ ) *gef1Δ* cells had lower amounts of CRIB-GFP at the new tips in time-lapse recordings (Fig. 2, D and E; and movie S3). CRIB-GFP tip fractions in *gef1Δ* cells ( $n = 381$ ) were asymmetric (Fig. 2F), consistent with the model.

In our model, increasing cell size increases the total amount of active Cdc42 or of Cdc42 GEFs. In the presence of noise, this is predicted to decouple oscillations, because one tip can no longer deplete the pool available to the other. Thus, we studied *cdc25-22* cells that delay entry

into mitosis, owing to a mutation in a cell-cycle control gene, and become longer than wild-type cells at permissive temperatures (17). Consistent with this prediction, we found less anticorrelation between CRIB-GFP tip signals in longer *cdc25-22* cells (Fig. 2, D, G, and H; and table S3).

To test if Cdc42 GEF availability influences the anticorrelation of Cdc42 oscillations, we overexpressed Gef1. This eliminated the anticorrelation of CRIB-GFP signal at the cell tips (Fig. 2, I and J; and movie S4). Increased amounts of Gef1 also led to increased symmetry of CRIB-GFP and Cdc42-target formin For3 (18) (Fig. 2, D and I; and fig. S6, B, C, and D). This agrees

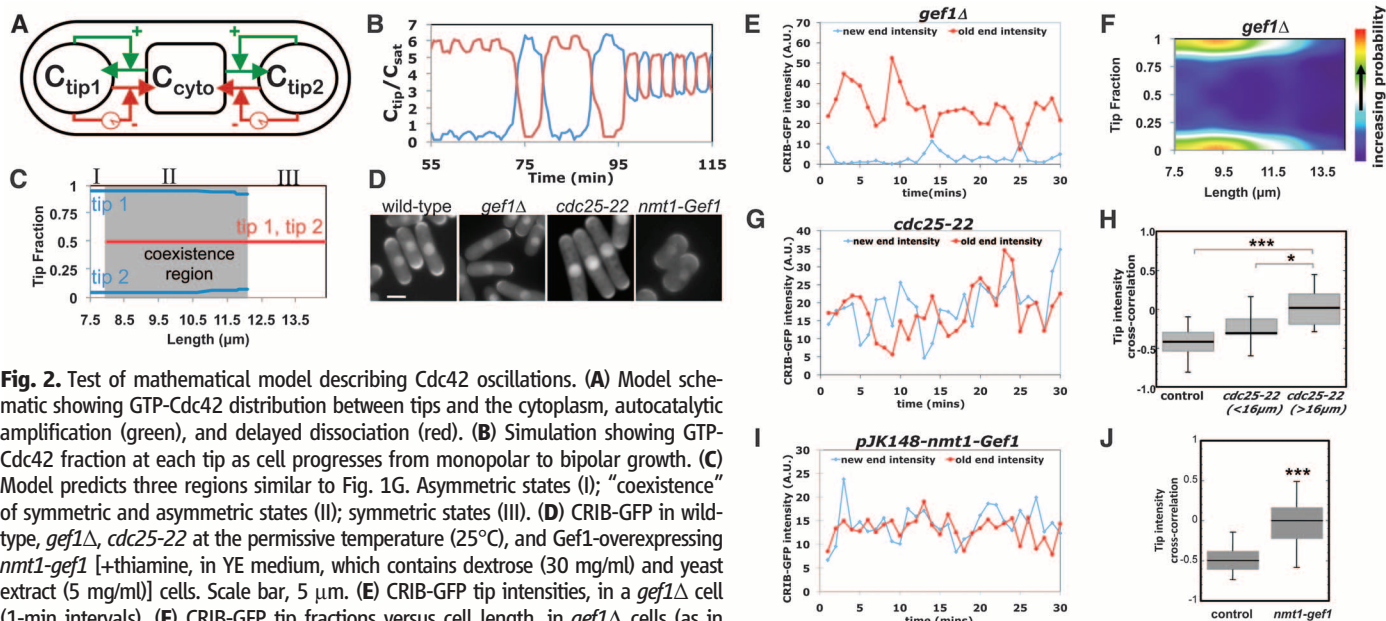


**Fig. 2.** Test of mathematical model describing Cdc42 oscillations. (A) Model schematic showing GTP-Cdc42 distribution between tips and the cytoplasm, autocatalytic amplification (green), and delayed dissociation (red). (B) Simulation showing GTP-Cdc42 fraction at each tip as cell progresses from monopolar to bipolar growth. (C) Model predicts three regions similar to Fig. 1G. Asymmetric states (I); “coexistence” of symmetric and asymmetric states (II); symmetric states (III). (D) CRIB-GFP in wild-type, *gef1Δ*, *cdc25-22* at the permissive temperature (25°C), and Gef1-overexpressing *nmt1-gef1* [+thiamine, in YE medium, which contains dextrose (30 mg/ml) and yeast extract (5 mg/ml)] cells. Scale bar, 5 μm. (E) CRIB-GFP tip intensities, in a *gef1Δ* cell (1-min intervals). (F) CRIB-GFP tip fractions versus cell length, in *gef1Δ* cells (as in Fig. 1G,  $n = 381$ ). (G) CRIB-GFP tip intensities, in a *cdc25-22* cell at 25°C. (H) Anticorrelation of CRIB-GFP tip intensities decreases with respect to wild-type cells and with increasing cell length in *cdc25-22* mutants ( $*P = 0.03$ ,  $***P = 0.00039$ , Student’s  $t$  test). (I) CRIB-GFP tip intensities of cell moderately overexpressing Gef1 (+thiamine, in YE medium). (J) CRIB-GFP tip anticorrelation decreases in cells moderately overexpressing Gef1 ( $***P = 5.7 \times 10^{-6}$ , Student’s  $t$  test). Whiskers in (H) and (J) indicate the full range of data.

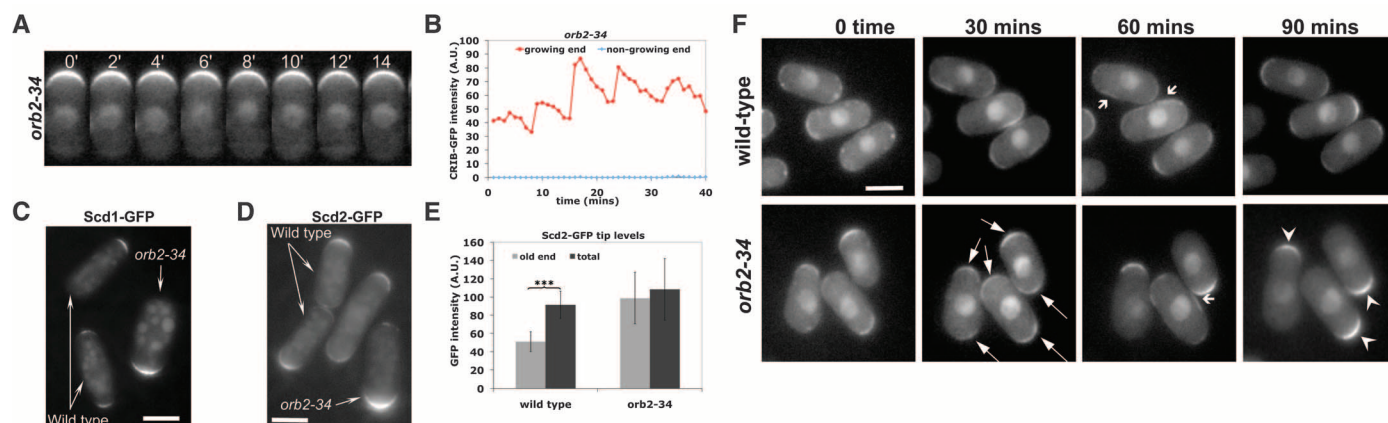


**Fig. 3.** Negative regulation of Cdc42 by the kinase Pak1. (A) Fluorescence of CRIB-GFP in *orb2-34* (*pak1/shk1* mutant allele) cells (25°C) at growing cell tip (2-min intervals). (B) CRIB-GFP fluorescence at growing (red) and nongrowing (blue) tips in an *orb2-34* cell (1-min intervals). (C) Scd1-GFP, in wild-type and *orb2-34* cells visualized in the same field. (D) Scd2-GFP, in wild-type and *orb2-34* cells visualized in the same field. (E) Scd2-GFP tip intensity in wild-type (old end, total) and *orb2-34* mutant cells (growing end, total) visualized in the same field ( $***P < 0.0001$ , Student’s  $t$  test). Error bars indicate SD. (F) Recovery following mild LatA treatment (10 μM, 10 min) in wild-type and *orb2-34* cells. Both show symmetric (thin arrows) and transiently ectopic (wide arrows) CRIB-GFP after treatment. *orb2-34* mutants progressively revert to monopolar distribution (arrow heads). Scale bar, 5 μm.

type (old end, total) and *orb2-34* mutant cells (growing end, total) visualized in the same field ( $***P < 0.0001$ , Student’s  $t$  test). Error bars indicate SD. (F) Recovery following mild LatA treatment (10 μM, 10 min) in wild-type and *orb2-34* cells. Both show symmetric (thin arrows) and transiently ectopic (wide arrows) CRIB-GFP after treatment. *orb2-34* mutants progressively revert to monopolar distribution (arrow heads). Scale bar, 5 μm.

with the model, which predicts that increasing Cdc42 activation rate (or total amounts of active Cdc42 or Cdc42 GEFs) (fig. S6A) leads to more symmetrical GTP-Cdc42 distribution.

Autocatalytic activation within the Cdc42 complex (9, 10, 19, 20) and actin-mediated transport (21) are likely contributors to positive feedback, as in budding yeast (3–6). Much less is known about negative feedback (22), a required mechanism for oscillations. To identify possible mechanisms, we analyzed CRIB-GFP in morphological mutants (fig. S7, A and B), including *orb2-34* and *tea1Δ*, which are monopolar (23, 24); *rdi1Δ* (encoding the Rho guanine nucleotide dissociation inhibitor); and *rga4Δ* (encoding the only known Cdc42 GTPase-activating protein) (8, 25). *orb2-34* mutants oscillated asymmetrically, but with a longer period and a decreased amplitude of CRIB-GFP oscillations (table S2 and Fig. 3, A and B). Conversely, *rdi1Δ* and *rga4Δ* mutants displayed normal, mostly symmetrical oscillations; *tea1Δ* mutants fluctuated asymmetrically (fig. S7C).

Amounts of CRIB-GFP, Cdc42 GEF Scd1-GFP, and scaffold Scd2-GFP at the one growing tip of *orb2-34* cells were increased compared with the same complexes in control cells (Fig. 3, C, D, and E; and fig. S8, A and B). No localization change was seen for Gef1-3xYFP (yellow fluorescent protein) or Rga4-GFP (fig. S8C) (8). The intensity of Scd2-GFP signal (Fig. 3E) or Scd1-GFP at the growing tip in *orb2-34* cells roughly equaled the total fluorescence at both tips (new end plus old end) in control cells (Fig. 3E). Amounts of total protein were not changed (fig. S7D). Thus, *orb2* regulates intracellular distribution of Scd1 and Scd2. In the model, this behavior is expected when the maximal active Cdc42 allowable at each tip increases (fig. S8E). In mutant cells unable to suppress maximal tip accumulation, the growing tip could function as a “sink,” entrapping Scd1 and Scd2.

To confirm that *orb2-34* mutants remain monopolar because of their inability to redis-

tribute Scd1, Scd2, or other regulators, we destabilized the actin-dependent (21) localization of Scd1 by exposing cells for 10 min to latrunculin A (LatA). In *orb2-34* and wild-type cells, CRIB-GFP, Scd1-GFP, and Scd2-GFP became symmetric in the first hour after LatA removal (Fig. 3F and fig. S9), consistent with reports of brief actin depolymerization promoting bipolar growth in monopolar cells *cdc10<sup>ts</sup>* and *ssp1Δ* (13, 26). However, 90 min after LatA removal, *orb2-34* cells reaccumulated these markers at one tip, which could be different than the tip originally growing, whereas wild-type cells remained largely symmetric (Fig. 3F and fig. S9). This agrees with the model's prediction of lack of a symmetric attractor for cells with reduced negative feedback and convergence to a symmetric attractor for wild-type cells after a perturbation (fig. S4A).

*orb2-34*, a mutant allele of *pak1* (also known as *shk1*) (23) contains a point mutation [Glu replaces Gly<sup>517</sup> (G517E); see (12)] in the Pak1 kinase domain that decreases its activity (fig. S7, E and F). Pak1, a Cdc42-dependent kinase (27, 28), localizes to tips in an Scd1 and Scd2-dependent manner (21). Negative regulation of Cdc42 could thus be linked to its own activation, as expected from a negative-feedback loop. It might occur through Scd2, a substrate of Pak1 (20), consistent with findings in *Saccharomyces cerevisiae*, where the Pak1 homolog Cla4 negatively regulates the interaction of the scaffold protein Bem1, an Scd2 homolog with Cdc42 GEF Cdc24 (29).

Increased accumulation of Cdc42 GEFs at the membrane, by Gef1 overexpression or loss of negative inhibition (*orb2-34* mutants), dampens Cdc42 fluctuations (fig. S10A). These mutants are wider, possibly because increasing tip-bound Cdc42 results in growth over a wider area (16) (fig. S10, B and C). We suggest that wild-type cells regulate diameter by maintaining Cdc42 activity at the tips within a normal range and activate bipolar growth by Cdc42 redistribution (Fig. 4A). Oscillations and fluctuations may regulate cell morphology and help the switch to

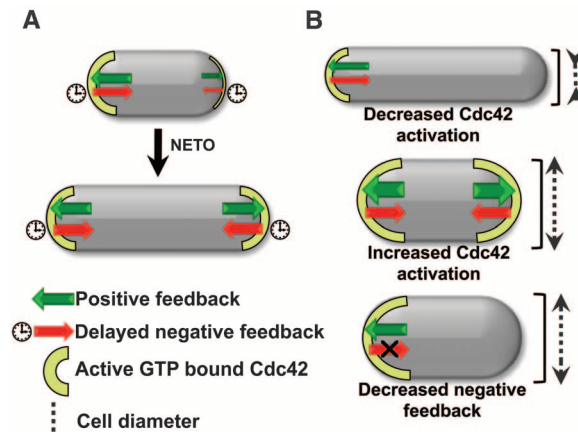
bipolar growth. Before NETO, accumulation of Cdc42 at the old end provides a kinetic barrier to bipolar symmetry by depleting the resources available to the new end. Oscillations and fluctuations may relieve this depletion, giving the new end a chance to take off by allowing the system to reach an otherwise inaccessible state of bipolarity (figs. S11 and S12). Mutations affecting Cdc42 regulation may alter the system's dynamics, by promoting a different pattern of Cdc42 distribution and changing cell diameter and symmetry (Fig. 4B).

Fission yeast Cdc42 oscillations and fluctuations might represent exploratory behavior, a general strategy among self-organizing biological systems (30). Despite the associated energy cost, biological systems may benefit because they acquire the ability to quickly reach states that would otherwise be difficult to access. Fluctuations of Cdc42 activity allows fission yeast to rapidly respond to changing intracellular conditions, such as cell volume and length. In an environment with changing external cues, such as nutrient or pheromone gradients, Rho GTPase fluctuations may allow eukaryotic cells to adapt and redirect the direction of growth.

## References and Notes

1. S. J. Heasman, A. J. Ridley, *Nat. Rev. Mol. Cell Biol.* **9**, 690 (2008).
2. P. Perez, S. A. Rincón, *Biochem. J.* **426**, 243 (2010).
3. J. E. Irazoqui, A. S. Gladfelter, D. J. Lew, *Nat. Cell Biol.* **5**, 1062 (2003).
4. R. Wedlich-Soldner, S. C. Wai, T. Schmidt, R. Li, *J. Cell Biol.* **166**, 889 (2004).
5. L. Kozubowski et al., *Curr. Biol.* **18**, 1719 (2008).
6. B. D. Slaughter, A. Das, J. W. Schwartz, B. Rubinstein, R. Li, *Dev. Cell* **17**, 823 (2009).
7. J. M. Mitchison, P. Nurse, *J. Cell Sci.* **75**, 357 (1985).
8. H. Tabebe, K. Nakano, R. Maximo, K. Shiozaki, *Curr. Biol.* **18**, 322 (2008).
9. M. Endo, M. Shirouzu, S. Yokoyama, *J. Biol. Chem.* **278**, 843 (2003).
10. E. Wheatley, K. Rittinger, *Biochem. J.* **388**, 177 (2005).
11. The model [see (12)] has two populations of Cdc42 associated with each tip,  $C_{tip1}$  and  $C_{tip2}$ , and one in the cytoplasm,  $C_{cyto}$ . We assumed competition for Cdc42 but similar results are obtained for Cdc42 GEFs or GTP-Cdc42. The total amount,  $C_{tot} \equiv C_{tip1} + C_{tip2} + C_{cyto}$ , increases in proportion to cell volume  $V$ . Association to the tips obeys  $dC_{tipj}/dt = \lambda^+ C_{cyto}/V - k^- C_{tipj}$ ,  $j = 1, 2$ . Here,  $\lambda^+$  and  $k^-$  represent rate constants;  $V$  is the cell volume. Autocatalytic activation,  $\lambda^+(C_{tip}) = (\lambda_0^+ + \lambda_n^+ C_{tip}^n) \exp(-C_{tip}/C_{sat})$ , with  $n \geq 2$ , generates asymmetry by allowing one tip to deplete the cytoplasmic pool and preventing the other tip from gathering Cdc42. Saturation at level  $C_{sat}$  recovers bipolarity for long cells. Oscillations result by assuming Cdc42 triggers its own removal (delayed negative feedback):  $k^-(C_{tip}) = k_0^- \{ (1 - \epsilon/2) + \epsilon C_{tip}(t - \tau)^h / [C_{tip}(t)^h + C_{tip}(t - \tau)^h] \}$ . Here,  $\epsilon$  determines the delayed dissociation strength,  $\tau$  is delay time, and  $h$  gives the nonlinearity of the effect.
12. Materials and methods are available as supplementary materials on Science Online.
13. A. Csikász-Nagy, B. Györfy, W. Alt, J. J. Tyson, B. Novák, *Yeast* **25**, 59 (2008).
14. A. S. Howell et al., *Cell* **139**, 731 (2009).
15. H. Meinhardt, P. A. de Boer, *Proc. Natl. Acad. Sci. U.S.A.* **98**, 14202 (2001).
16. P. M. Coll, Y. Trillo, A. Ametazurra, P. Perez, *Mol. Biol. Cell* **14**, 313 (2003).
17. P. Fantes, *Nature* **279**, 428 (1979).
18. S. G. Martin, S. A. Rincón, R. Basu, P. Pérez, F. Chang, *Mol. Biol. Cell* **18**, 4155 (2007).
19. E. C. Chang et al., *Cell* **79**, 131 (1994).
20. E. Chang et al., *Mol. Cell Biol.* **19**, 8066 (1999).

**Fig. 4. Model of self-organization of Cdc42 at the cell tips and control of cell morphogenesis. (A)** In wild-type cells, Cdc42 recruitment or activation balances Cdc42 removal or deactivation, limiting GTP-Cdc42 tip level and thus setting cell diameter at a normal range. Increased GEF availability promotes bipolar Cdc42 activation at the new cell tip as cell size increases. **(B)** Changes in the system's dynamics alter Cdc42 distribution. Decreased Cdc42 activation (*gef1Δ* mutants) increases Cdc42 asymmetry and decreased cell diameter. GEF overexpression increases Cdc42 activation at both tips, which leads to increased diameter. Decreased negative feedback (*orb2-34* mutants) leads to the accumulation of most Cdc42 activity at one single tip and results in monopolar growth. Increased active Cdc42 levels at the growing end results in increased cell diameter.





21. F. D. Kelly, P. Nurse, *Mol. Biol. Cell* **22**, 3801 (2011).
22. E. M. Ozbudak, A. Becskei, A. van Oudenaarden, *Dev. Cell* **9**, 565 (2005).
23. F. Verde, D. J. Wiley, P. Nurse, *Proc. Natl. Acad. Sci. U.S.A.* **95**, 7526 (1998).
24. J. Mata, P. Nurse, *Cell* **89**, 939 (1997).
25. M. Das *et al.*, *Mol. Biol. Cell* **18**, 2090 (2007).
26. I. Rupes, Z. Jia, P. G. Young, *Mol. Biol. Cell* **10**, 1495 (1999).
27. S. Marcus *et al.*, *Proc. Natl. Acad. Sci. U.S.A.* **92**, 6180 (1995).
28. S. Ohtlie *et al.*, *EMBO J.* **14**, 5908 (1995).
29. M. P. Gulli *et al.*, *Mol. Cell* **6**, 1155 (2000).
30. E. Karsenti, *Nat. Rev. Mol. Cell Biol.* **9**, 255 (2008).

**Acknowledgments:** We thank E. Karsenti, C. Luetje, S. Lemmon, G. D'Urso, and T. K. Harris for critically reading the manuscript; M. Ioannidou and K. Zhang for help with data analysis; B. Skibbens and Yi Hu for facilitating experiments; and K. Shiozaki, P. Perez, and S. Martin for various strains. This work was supported by NSF grant 0745129, NIH grant 1R01GM095867, and a University of Miami NSF ADVANCE award 0820128 to F.V., and by NIH grant R21GM083928 and a Lehigh University Class of 68 Faculty Fellowship to D.V. T.D. was supported by a Sigma Xi grant-in-aid and as a Graduate Assistance in Areas of National Need Fellow through the U.S. Department of Education.

## Supplementary Materials

www.sciencemag.org/cgi/content/full/science.1218377/DC1  
Materials and Methods  
Supplementary Text  
Figs. S1 to S12  
Tables S1 to S4  
References (31–51)  
Movies S1 to S4

23 December 2011; accepted 4 May 2012  
Published online 17 May 2012;  
10.1126/science.1218377

# MMS19 Links Cytoplasmic Iron-Sulfur Cluster Assembly to DNA Metabolism

Kerstin Gari,<sup>1</sup> Ana María León Ortiz,<sup>1</sup> Valérie Borel,<sup>1</sup> Helen Flynn,<sup>2</sup> J. Mark Skehel,<sup>2</sup> Simon J. Boulton<sup>1\*</sup>

The function of many DNA metabolism proteins depends on their ability to coordinate an iron-sulfur (Fe-S) cluster. Biogenesis of Fe-S proteins is a multistep process that takes place in mitochondria and the cytoplasm, but how it is linked to nuclear Fe-S proteins is not known. Here, we demonstrate that MMS19 forms a complex with the cytoplasmic Fe-S assembly (CIA) proteins CIAO1, IOP1, and MIP18. Cytoplasmic MMS19 also binds to multiple nuclear Fe-S proteins involved in DNA metabolism. In the absence of MMS19, a failure to transfer Fe-S clusters to target proteins is associated with Fe-S protein instability and preimplantation death of mice in which *Mms19* has been knocked out. We propose that MMS19 functions as a platform to facilitate Fe-S cluster transfer to proteins critical for DNA replication and repair.

MMS19 is a highly conserved HEAT repeat protein that was first identified in *Saccharomyces cerevisiae* as being required for the removal of ultraviolet radiation (UV)-induced pyrimidine dimers (1). *mms19Δ* cells are impaired for both nucleotide excision repair (NER) and RNA polymerase II transcription, which is complemented in vitro by addition of the NER/transcription complex TFIIH but not by purified Mms19 (2). Consistently, *mms19Δ* cells display reduced protein levels of the TFIIH component Rad3, and overexpression of Rad3 can restore NER proficiency, suggesting a function for Mms19 in stabilizing Rad3 rather than a direct role in DNA metabolism (3). Human MMS19 also interacts with two components of TFIIH: XPB and the Rad3 homolog XPD (4). Moreover, MMS19 and XPD interact independently of TFIIH and were proposed to play a role in mitotic spindle formation and chromosome segregation (5). *Schizosaccharomyces pombe* Mms19 is part of a different complex composed of Rik1, Dos1, and the catalytic subunit of DNA polymerase  $\epsilon$ , which links DNA replication to heterochromatin silencing (6). A molecular explanation of how MMS19 affects so many different processes has remained elusive.

We found MMS19 as an interaction partner of the Regulator of Telomere Length protein RTEL1. RTEL1 is a helicase implicated in telomere-length regulation and the maintenance of genomic stability (7, 8); it acts as an anti-recombinase to counteract toxic recombination and limit crossing over during meiosis (7, 9). RTEL1 belongs to the same family of Rad3-like SF2 helicases as XPD, the Fanconi Anemia protein J (FANCF), and the Warsaw Breakage Syndrome protein ChlR1, which all bind an iron-sulfur (Fe-S) cluster (10).

Mass spectrometry (MS) analysis identified MMS19 as the most abundant interaction partner of RTEL1 (fig. S1A). This interaction was confirmed by means of reciprocal co-immunoprecipitation experiments (Fig. 1A) and was confined to the cytoplasm, principally because the vast majority of MMS19 is cytoplasmic (Fig. 1B and fig. S1B).

To gain insight into the function of MMS19, we purified cytoplasmic MMS19-containing complexes and identified additional interaction partners by using MS and co-immunoprecipitation (Fig. 1, C and D). The cytoplasmic MMS19 complex contained many other nuclear genome stability factors, including XPD, FANCF, DNA polymerase  $\delta$ , DNA primase (Pri2), and DNA2, all of which are known to coordinate an Fe-S cluster (10–13). In total, we identified 12 known Fe-S proteins in the cytoplasmic MMS19 complex (fig. S1C). This complex also contained CIAO1, IOP1 (also known as NARFL), and MIP18 (also known as FAM96B) (Fig. 1D and fig. S1C), three members of the cytoplasmic Fe-S assembly (CIA) machinery (14, 15). Co-immunoprecipitation and

gel filtration studies confirmed that MMS19 forms a stable complex with MIP18, CIAO1, and IOP1 (Fig. 2, A and B, and fig. S2, A and B). Furthermore, small interfering RNA (siRNA)-mediated depletion of MMS19 resulted in a dramatic down-regulation of the CIA component MIP18, suggesting that MIP18 is unstable in the absence of MMS19 (Fig. 2C). Taken together, these data raised the possibility that MMS19 may physically link the CIA machinery to target Fe-S cluster proteins.

To address whether MMS19 could play a direct role in Fe-S cluster biogenesis, we used a well-established assay to study Fe-S metabolism in *Saccharomyces cerevisiae*, which can be grown in Fe-free conditions and subsequently pulse-labeled with radioactive <sup>55</sup>Fe (16). Known Fe-S proteins were immunoprecipitated in the presence or absence of Mms19, and <sup>55</sup>Fe incorporation was measured by means of liquid scintillation counting. In the absence of Mms19, incorporation of <sup>55</sup>Fe into target proteins was reduced between three- and 10-fold (Fig. 2D and fig. S2C), which was comparable with loss of Cia1, the yeast homolog of CIAO1 [Fig. 2D; compare left with right and (17)]. These data indicate that Mms19 is indeed required for Fe-S cluster biogenesis.

We next tested whether human XPD could incorporate <sup>55</sup>Fe when overexpressed in yeast. This was indeed the case, and <sup>55</sup>Fe incorporation was reduced when Mms19 was depleted (Fig. 3A). However, the interpretation of this result was complicated by the fact that considerably less GFP-XPD was immunoprecipitated in the absence of Mms19, possibly because Fe-S cluster transfer by Mms19 is required for protein folding and stability of XPD. This instability is reminiscent of the reduced levels of Rad3 observed in *mms19Δ* yeast cells (3). We then addressed whether the absence of MMS19 had a similar impact on XPD stability in human cells. In an inducible XPD overexpression system, siRNA-mediated depletion of MMS19 led to a decrease in the levels of XPD, corresponding to a reduction to 10% relative to control siRNA (Fig. 3B). The protein level of the point mutant C190S XPD, which is mutated in one of the four cysteines that coordinate the Fe-S cluster and is therefore predicted to display diminished Fe-S cluster incorporation, was also reduced when compared with wild-type XPD, and it was further decreased upon depletion of MMS19 (Fig. 3B).

<sup>1</sup>DNA Damage Response Laboratory, London Research Institute, Cancer Research UK, Clare Hall, South Mimms EN6 3LD, UK. <sup>2</sup>Protein Analysis and Proteomics Laboratory, London Research Institute, Cancer Research UK, Clare Hall, South Mimms EN6 3LD, UK.

\*To whom correspondence should be addressed. E-mail: simon.boulton@cancer.org.uk

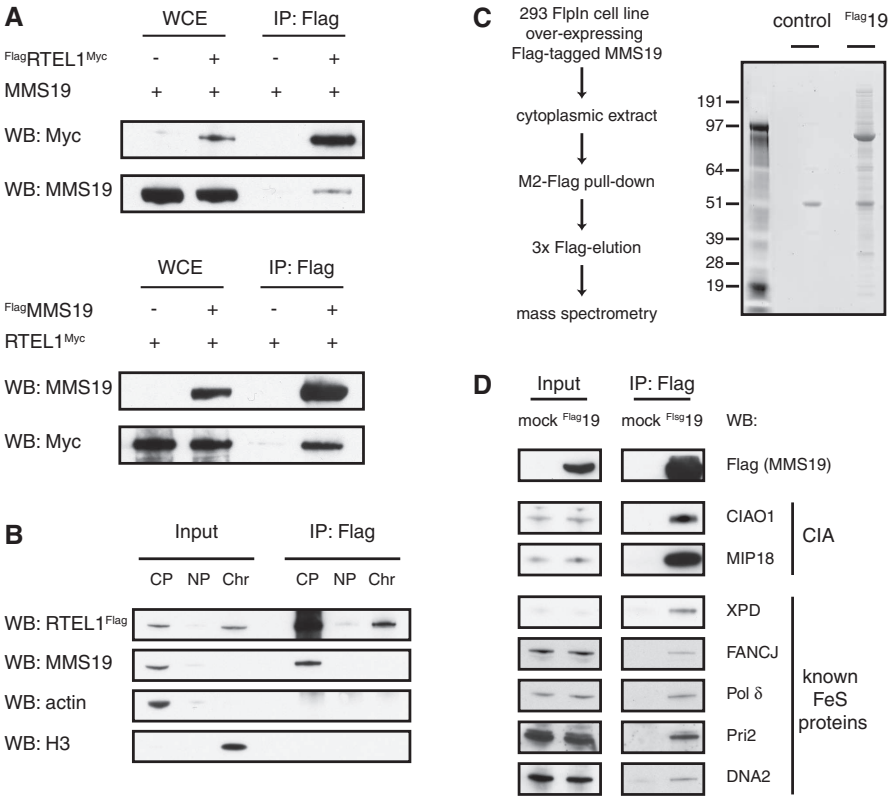


**Fig. 1.** Interaction network of MMS19. **(A)** Reciprocal co-immunoprecipitations of RTEL1 and MMS19 overexpressed in HEK 293T cells. **(B)** Fractionation of HeLa cells stably overexpressing RTEL1<sup>Flag</sup> into cytoplasm (CP), nucleoplasm (NP), and chromatin (Chr) and immunoprecipitation with M2-Flag beads. **(C)** Schematic of experiment. SYPRO ruby (Molecular Probes, Eugene, OR)—stained gel showing <sup>Flag</sup>MMS19-containing (<sup>Flag</sup>19) and control (mock) complexes. Asterisk indicates <sup>Flag</sup>MMS19. **(D)** Immunoprecipitation of <sup>Flag</sup>MMS19 (<sup>Flag</sup>19) stably overexpressed in HEK 293 cells and verification of endogenous interaction partners by means of Western blot.

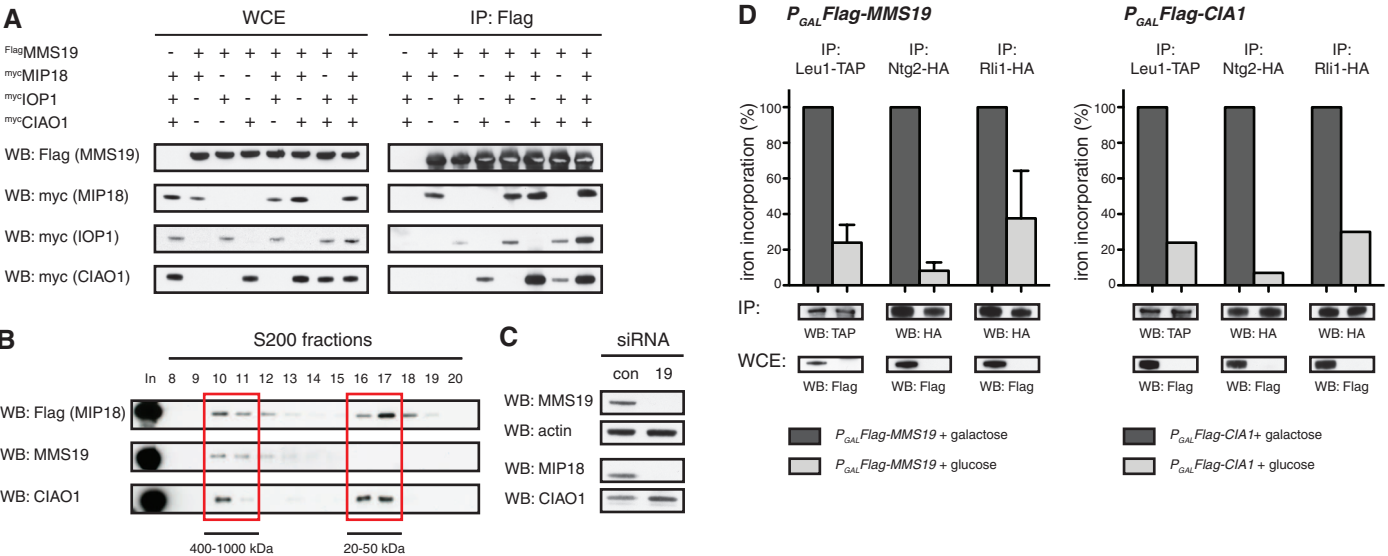


**Fig. 2.** MMS19 is part of the CIA machinery. **(A)** Co-immunoprecipitations of <sup>Flag</sup>MMS19 and members of the CIA machinery overexpressed in HEK 293T cells. **(B)** Superdex 200 10/300 GL (GE Healthcare, Uppsala, Sweden) gel filtration analysis of complexes containing <sup>Flag</sup>MIP18, MMS19, and CIAO1 overexpressed in Sf9 insect cells. In [Superdex 200 input], eluate of Flag-immunoprecipitation. **(C)** Effect of MMS19 depletion on MIP18 and CIAO1. 19, siRNA MMS19; con, siRNA control. **(D)** Incorporation of <sup>55</sup>Fe into target

proteins measured by means of liquid scintillation counting. Galactose-driven promoters replace the endogenous promoters of *Mms19* (left) and *Cia1* (right); expression was switched on (+ galactose) or switched off (+ glucose) for 40 hours. Western blots show immunoprecipitated Fe-S proteins and depletion efficiency of Mms19 and Cia1 in WCEs. Counts were normalized to levels of immunoprecipitated proteins. Error bars indicate SDs from three independent experiments.



*mms19* $\Delta$  yeast cells were sensitive to hydroxyurea (HU), which inhibits ribonucleotide reductase and reduces nucleotide pools (fig. S4B). Cell-cycle analysis further showed that wild-type yeast accumulate in *S* phase after HU treatment, whereas *mms19* $\Delta$  yeast are impaired for *S* phase entry (fig. S4C). Under conditions of HU treatment,

Rad53 phosphorylation was induced in wild-type strains but was largely impaired in the absence of Mms19 (Fig. 4B). By extension, whereas HeLa cells treated with control siRNA induced phosphorylation of Chk1<sup>S345</sup> and RPA in response to HU treatment, MMS19-depleted cells failed to do so (Fig. 4C). These data suggest that MMS19

deficiency in yeast or human cells confers an inability to efficiently enter *S* phase under limiting nucleotide pools. This may be due to the reduced levels of DNA polymerase  $\delta$  (Fig. 4A) and potentially additional Fe-S proteins, such as Pri2, DNA2, and DNA polymerase  $\epsilon$ . In agreement with an essential role in DNA metabolism, *Mms19* $\beta$ -*GEO* gene trap mice are embryonically dead before the implantation stage (fig. S5), and attempts to isolate *Mms19*-deficient embryos or cells were unsuccessful, suggesting that Mms19 is essential for cell viability in mice.

Collectively, these data identify MMS19 as a key factor involved in Fe-S cluster assembly, which affects the stability of multiple Fe-S proteins. We propose that MMS19 functions as part of the CIA machinery to facilitate Fe-S cluster transfer to target Fe-S proteins [as depicted in our model (fig. S6)]. The fact that MMS19 affects multiple proteins required for genome stability provides a plausible explanation for DNA replication problems and the early embryonic death of mice in which *Mms19* has been knocked out. This study also provides molecular insight to explain the previously reported phenotypes associated with MMS19 deficiency (5, 6) and why defects in mitochondrial Fe-S cluster biogenesis confer genome instability (19).

#### References and Notes

1. L. Prakash, S. Prakash, *Mol. Gen. Genet.* **176**, 351 (1979).
2. S. Lauder et al., *Mol. Cell. Biol.* **16**, 6783 (1996).
3. H. Kou, Y. Zhou, R. M. C. Gorospe, Z. Wang, *Proc. Natl. Acad. Sci. U.S.A.* **105**, 15714 (2008).
4. T. Seroz et al., *Nucleic Acids Res.* **28**, 4506 (2000).
5. S. Ito et al., *Mol. Cell* **39**, 632 (2010).
6. F. Li, R. Martienssen, W. Z. Cande, *Nature* **475**, 244 (2011).
7. L. J. Barber et al., *Cell* **135**, 261 (2008).
8. H. Ding et al., *Cell* **117**, 873 (2004).
9. J. L. Youds et al., *Science* **327**, 1254 (2010).
10. J. Rudolf, V. Makrantonis, W. J. Ingledew, M. J. R. Stark, M. F. White, *Mol. Cell* **23**, 801 (2006).
11. D. J. A. Netz et al., *Nat. Chem. Biol.* **8**, 125 (2012).
12. S. Klinge, J. Hirst, J. D. Maman, T. Krude, L. Pellegrini, *Nat. Struct. Mol. Biol.* **14**, 875 (2007).
13. J. T. P. Yeates, R. Cammack, M. S. Dillingham, *J. Biol. Chem.* **284**, 7746 (2009).
14. R. Lill, *Nature* **460**, 831 (2009).
15. E. Weerapana et al., *Nature* **468**, 790 (2010).
16. A. J. Pierik, D. J. A. Netz, R. Lill, *Nat. Protoc.* **4**, 753 (2009).
17. J. Balk, D. J. Aguilar Netz, K. Tepper, A. J. Pierik, R. Lill, *Mol. Cell. Biol.* **25**, 10833 (2005).
18. R. Chanet, M. Heude, *Curr. Genet.* **43**, 337 (2003).
19. J. R. Veatch, M. A. McMurray, Z. W. Nelson, D. E. Gottschling, *Cell* **137**, 1247 (2009).

**Acknowledgments:** Research in the laboratories of S.J.B. and M.J.S. is supported by Cancer Research UK. The laboratory of S.J.B. is also funded by a European Research Council Advanced Investigator Grant (RecMitMei). S.J.B. is a recipient of a Royal Society Wolfson Research Merit Award. K.G. is funded by long-term fellowships from the Federation of European Biochemical Societies and the Human Frontier Science Program. The authors declare no conflict of interest.

#### Supplementary Materials

www.sciencemag.org/cgi/content/full/science.1219664/DC1  
Materials and Methods  
Figs. S1 to S6  
Table S1

25 January 2012; accepted 14 May 2012  
Published online 7 June 2012;  
10.1126/science.1219664

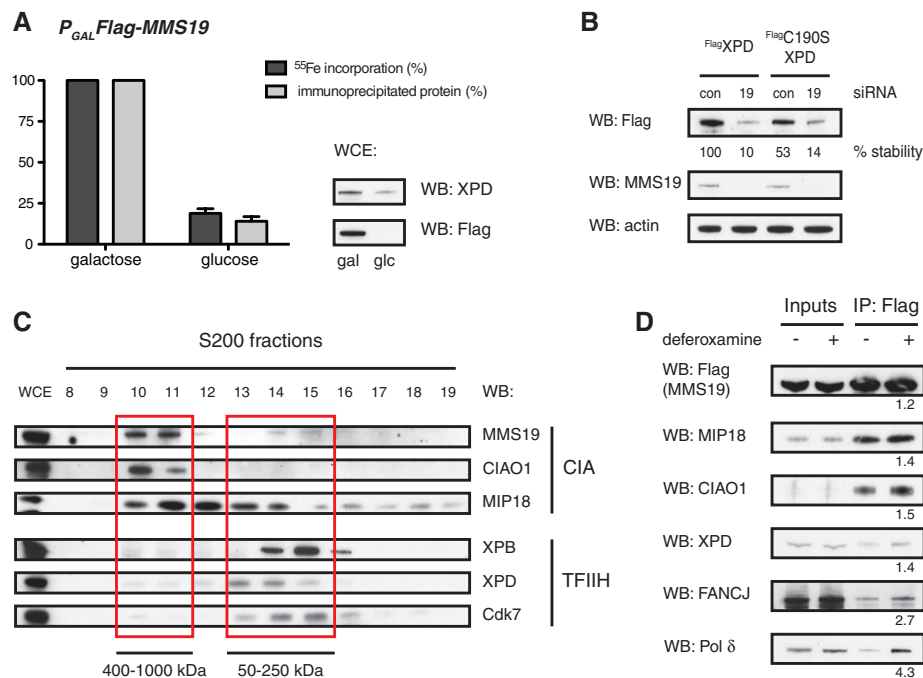


**Fig. 3.** XPD requires MMS19 function for Fe-S cluster incorporation and protein stability. **(A)** Incorporation of <sup>55</sup>Fe into ectopically expressed human GFP-XPD in yeast. A galactose-driven promoter replaces the endogenous promoter of *Mms19*; expression was switched on (+ galactose) or switched off (+ glucose) for 40 hours. Western blots show depletion efficiency of Mms19 and the levels of XPD in WCEs. Graph depicts <sup>55</sup>Fe incorporation and amount of immunoprecipitated protein. Error bars indicate SDs from three independent experiments. **(B)** Tetracycline-induced expression of stably integrated Flag-XPD or FlagC190S XPD after treatment of HeLa cells for 7 days with MMS19 (19) or control (con) siRNAs. **(C)** Fractionation of HeLa WCEs by means of Superdex 200 gel filtration and Western blot analysis of CIA proteins and TFIIF components. **(D)** Flag-MMS19 complexes were pulled down from WCEs of HEK 293 cells treated with or without 125  $\mu$ M deferoxamine for 18 hours and analyzed by means of Western blot. Numbers below blots indicate fold increase in deferoxamine-treated samples as compared with control samples (from three independent experiments).

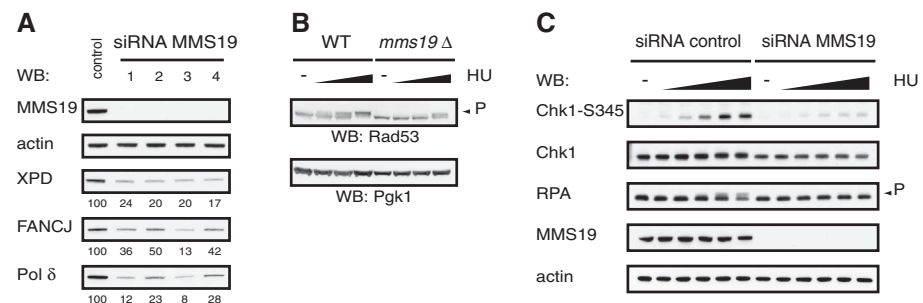


**Fig. 4.** MMS19 impacts on DNA metabolism. **(A)** Levels of Fe-S proteins in WCEs of HeLa cells treated with four different siRNAs against MMS19. Western blots show a representative experiment, and numbers below blots indicate protein stability in percent relative to control siRNA. **(B)** Rad53 phosphorylation in response to increasing doses of HU. Wild-type and *mms19* $\Delta$  yeast cells were treated for 3 hours with 0, 2, 20, and 200 mM HU, TCA-precipitated, and analyzed by means of Western blot. Arrowhead indicates Rad53 phosphorylation. **(C)** Chk1 and RPA phosphorylation in HeLa cells treated with control and MMS19 siRNA in response to increasing doses of HU (0, 0.05, 0.1, 0.25, 0.5, and 1 mM HU for 20 hours). Arrowhead indicates RPA phosphorylation.

## New Products



### DUCTLESS CHEMICAL FUME HOODS

Aura ductless fume hoods provide state-of-the-art construction and safety features. Each Aura ductless fume hood has advanced safety monitoring and controls. EverSafe II microprocessor safety controller monitors and adjusts fume hood face velocity to the user preset value. EverSafe II, not guesswork, keeps the Aura face velocity ideal for containment of potentially toxic gases and vapors. Aura has been ASHRAE 110 tested and provides unsurpassed containment from toxic fumes and vapors. Breathe easier knowing EverSafe II is working for your safety. Filtrak positive filter sealing system is installed in each Aura ductless hood. This cam-driven filter sealing system has a built-in filter position indicator and alerts the end user if the filtration bed is not properly sealed. Filtrak provides safe and easy filter maintenance and replacement. Aura ductless fume hoods are available in 30, 42, and 54 inch widths. ESD models are available for applications involving volatile chemicals.

**Mystaire**

For info: 877-328-3912 | [www.mystaire.com](http://www.mystaire.com)

### WIDEPORE UHPLC COLUMNS

The new SecurityGuard ULTRA system protects widepore ( $\geq 200$  Å) UHPLC columns typically used in the analysis of biomolecules. The SecurityGuard ULTRA system dramatically extends the lifetime of columns packed with sub-2 micron fully porous or core-shell particles by protecting against the damaging effects of chemical contaminants and microparticulates introduced by the sample, mobile phase, or system. These contaminants can also affect method sensitivity, quantitation, and peak identification. The new SecurityGuard ULTRA product is ideal for virtually any manufacturer's UHPLC, sub-2 micron, or core-shell widepore columns including the Phenomenex Aeris widepore XB-C18, XB-C8, and C4 products. By reducing the frequency of column replacements, as well as the need for troubleshooting and system down time, SecurityGuard ULTRA saves chromatographers time and money. Pressure-rated up to 20,000 psi (1,378 bar), these widepore guard cartridges have no significant impact on chromatography, backpressure, or dead volume.

**Phenomenex**

For info: 310-212-0555 | [www.phenomenex.com](http://www.phenomenex.com)

### FISH PROBES

Agilent SureFISH probes are the next generation of tools for fluorescent in situ hybridization (FISH) assays, delivering a comprehensive menu of the industry's highest resolution probes for a wide range of molecular analysis applications. Agilent SureFISH probes deliver dramatically better performance compared to existing FISH products. SureFISH probes enable users to specifically detect aberrations in regions of the genome as small as 50 kb as well as aberrations near highly repetitive regions. They provide higher resolution and faster hybridization times than competing technologies and are designed to enable users to meet American College of Medical Genetics guidelines for clinical cytogenetics. Agilent offers an extensive menu of FISH probes for constitutional and cancer applications. The initial menu includes hundreds of SureFISH probes for the most common regions, to accommodate a wide range of cytogenetic research needs.

**Agilent Technologies**

For info: 800-227-9770 | [www.agilent.com/genomics/SureFISH](http://www.agilent.com/genomics/SureFISH)

### MAGNETIC STIRRER

The Tornado Plus System is the ideal synthesis solution for stirring both viscous samples and for the dispersion of delicate solids in solution where conventional magnetic stirring is not suitable. Tornado Plus allows scientists to use a single overhead stirrer to simultaneously deliver high-torque mechanical stirring to six round-bottom flasks from 50 to 250 mL. Tornado also provides controlled heating and cooling from  $-65^{\circ}\text{C}$  to  $+180^{\circ}\text{C}$ , making it ideal for applications such as crystallization studies, process optimization, polymer research, or the synthesis of building blocks. Tornado features a unique PEEK 'pinch-grip' stirrer guide mechanism which allows rapid, tool-free exchange of stirrer shafts and operation under an inert atmosphere. Choose from centrifugal, anchor, or propeller style PTFE stirrers, which are matched to each flask size. Tornado accepts a range of round bottom flasks from 50 to 250 mL, including flasks with one or two sidearms, internal baffles, and special azeotropic flask options.

**Radleys**

For info: +44-(0)-1799-513320 | [www.radleys.com](http://www.radleys.com)

### MINI STIRRER

The new SM5 Mini Stirrer packs the power to stir volumes up to 1 L and even offers a choice of three stylish fascia designs. This versatile and economical magnetic stirrer is very simple to operate, providing stirring speeds of 350 to 2,000 rpm. The SM5 is lightweight yet strong, constructed from polypropylene with a chemically resistant polycarbonate top. The SM5 is the smallest in the company's comprehensive range of magnetic stirrers. A robust casing incorporates silver-based BioCote antimicrobial protection for enhanced safety. The power to mix an impressive 1 L at adjustable speeds makes the SM5 an attractive option for any lab. The new Mini Stirrer has fun twist with a choice of three different fascia designs: blue with the Stuart logo, a Bibby Scientific image, or an abstract blue swirl.

**Bibby Scientific**

For info: +44-(0)-1785-812121 | [www.bibby-scientific.com](http://www.bibby-scientific.com)

Electronically submit your new product description or product literature information! Go to [www.sciencemag.org/products/newproducts.dtl](http://www.sciencemag.org/products/newproducts.dtl) for more information.

Newly offered instrumentation, apparatus, and laboratory materials of interest to researchers in all disciplines in academic, industrial, and governmental organizations are featured in this space. Emphasis is given to purpose, chief characteristics, and availability of products and materials. Endorsement by *Science* or AAAS of any products or materials mentioned is not implied. Additional information may be obtained from the manufacturer or supplier.



# Introducing the BD FACSJazz™

Perfectly tuned cell sorting from BD Biosciences.



## Breathtaking solo performance.

The BD FACSJazz™ system begins a new era in cell sorting with stellar performance, benchtop fit, and an affordable price.

The BD FACSJazz can be configured with up to 3 lasers and 8 parameters to support your application needs—offloading sorting demand at core labs or meeting the needs of individuals.

Requiring less than 2 x 2 ft (50 x 50 cm) of bench space, the BD FACSJazz also addresses biosafety concerns with an optional custom



Helping all people  
live healthy lives

designed biosafety cabinet that meets Class II Type A2 NSF 49 and EU 12469 standards.

In addition to factory-optimized settings, the BD FACSJazz comes standard with BD FACSTM Software sorter software to simplify use. This innovative software is specifically designed for cell sorting and features comprehensive control for acquisition, sorting, and analysis.

For legendary results, just add your creativity. Learn how at [bdbiosciences.com/go/jazz](http://bdbiosciences.com/go/jazz)

Class 1 Laser Product.  
For Research Use Only. Not for use in diagnostic or therapeutic procedures.  
BD, BD Logo and all other trademarks are property of Becton, Dickinson and Company. © 2012 BD  
23-14201-00

**BD Biosciences**  
2350 Qume Drive  
San Jose, CA 95131  
[bdbiosciences.com](http://bdbiosciences.com)



# cell sciences®

## cytokine center

Browse our web site of recombinant proteins, including cytokines, growth factors, chemokines and neurotrophins. Daily shipping and competitive pricing are offered. Bulk quantities of many proteins available. Cell Sciences also carries corresponding antibodies and ELISA kits.



### LIST OF PROTEINS

4-1BBL	Caspase-3	sFlt-1 (D3)	IL-2	MEC	sRANK
4-1BB Receptor	Caspase-6	sFlt-1 (D4)	IL-3	Mek-1	sRANKL
6 Ckine	CD4	sFlt-1 (D5)	IL-4	MIA	RANTES
ACAD8	CD14	sFlt-1 (D7)	sIL-4 Receptor	Midkine	RELM- $\alpha$
ACAT2	CD22	Flt3-Ligand	IL-5	MIG / CXCL9	RELM- $\beta$
gAcrp30/Adipolean	CD40 Ligand / TRAP	sFlt-4	IL-6	MIP-1 $\alpha$ / CCL3	Resistin
Activin A	CD95 / sFas Ligand	sFlt-4/ Fc Chimera	sIL-6 Receptor	MIP-1 $\beta$ / CCL4	RPTP $\beta$
ACY1	CD105 / Endoglin	Follistatin	IL-7	MIP-3 / CCL23	RPTP $\gamma$
ADAT1	CHIPS	FSH	IL-8 (72 a.a.)	MIP-3 $\alpha$ / CCL20	RPTP $\mu$
Adiponectin	CNTF	Fractalkine/ CX3C	IL-8 (77 a.a.)	MIP-3 $\beta$ / CCL19	SCF
ADRP	Collagen	G-CSF	IL-9	MIP-4 (PARC) / CCL18	SCGF- $\alpha$
AITRL	CREB	$\alpha$ -Galactosidase A	IL-10	MIP-5 / CCL15	SCGF- $\beta$
Akt1	CTACK/CCL27	Galectin-1	IL-11	MMP-3	SDF-1 $\alpha$
Alpha-Feto Protein (AFP)	CTGF	Galectin-3	IL-12	MMP-7	SDF-1 $\beta$
Alpha-Galactosidase A	CTGFL/WISP-2	Gastrointestinal CA	IL-13	MMP-13	Secretin
Angiopoietin-1 (Ang-1)	CTLA-4/Fc	GCP-2	IL-13 analog	Myostatin	SF20
Angiopoietin-2 (Ang-2)	CXCL16	GDF-3	IL-15	Nanog	SHP-2
Angiostatin K1-3	Cytokeratin 8	GDF-9	IL-16 (121 a.a.)	NAP-2	STAT1
Annexin-V	DEP-1	GDF-11	IL-16 (130 a.a.)	Neurturin	c-Src
apo-SAA	Desmopressin	GDNF	IL-17	NFAT-1	TACI
Apolipoprotein A-1	Disulfide Oxidoreductase	GLP-1	IL-17B	beta-NGF	TARC
Apolipoprotein E2	E-selectin	Glucagon	IL-17D	NOGGIN	TC-PTP
Apolipoprotein E3	ECGF	Goserelin	IL-17E	NOV	TECK
Apolipoprotein E4	EGF	GM-CSF	IL-17F	NP-1	TFF2
APRIL	Elafin/SKALP	GPBB	IL-19	NT-1/BCSF-3	TGF- $\alpha$
Artemin	EMAP-II	GRO $\alpha$	IL-20	NT-3	TGF- $\beta$ 1
ATF2	ENA-78	GRO $\beta$	IL-22	NT-4	TGF- $\beta$ 2
Aurora A	Endostatin	GRO $\gamma$	IL-31	Ocreotide	TGF- $\beta$ 3
Aurora B	Enteropeptidase	GRO/MGSA	Insulin	Oncostatin M	Thymosin $\alpha$ 1
BAFF	Eotaxin	Growth Hormone	IP-10	Osteoprotegerin (OPG)	sTIE-1/Fc Chimera
BAFF Receptor	Eotaxin-2	Growth Hormone BP	JE	OTOR	sTIE-2/Fc Chimera
BCA-1 / BLC / CXCL13	Eotaxin-3 (TSC)	GST-p21/WAF-1	JNK2a1	Oxytocin	TL-1A
BCMA	EPHB2	HB-EGF	JNK2a2	p38- $\alpha$	TNF- $\alpha$
BD-1	EPHB4	HCC-1	KC / CXCL1	Parathyroid Hormone	TNF- $\beta$
BD-2	Eptifibatide	HGF	KGF	PDGF-AA	sTNFR1
BD-3	Erk-2	Histidyl-tRNA synthetase	L-asparaginase	PDGF-AB	sTNFR2
BDNF	Erythropoietin (EPO)	Histrelin	LAG-1	PDGF-BB	TPO
Bivalirudin	Exodus-2	HRG1- $\beta$ 1	LALF Peptide	Persephin	TRAIL/Apo2L
BMP-2	Fas Ligand	I-309	LAR-PTP	PF-4	sTRAIL R-1 (DR4)
BMP-4	Fas Receptor	I-TAC	LC-1	PIGF-1	sTRAIL R-2 (DR5)
BMP-7	FGF-1 (acidic)	IFN- $\alpha$	LBP	PIGF-2	TSH
BMP-13	FGF-2 (basic)	IFN- $\alpha$ A	LD-78 $\beta$	PKA $\alpha$ -subunit	TSLP
sBMPR-1A	FGF-4	IFN- $\alpha$ 2a	LDH	PKC- $\alpha$	TWEAK
Brain Natriuretic Protein	FGF-5	IFN- $\alpha$ 2b	LEC/NCC-4	PKC- $\gamma$	TWEAK Receptor
BRAK	FGF-6	IFN- $\beta$	Leptin	Pleiotrophin	Urokinase
Breast Tumor Antigen	FGF-7/ KGF	IFN- $\gamma$	LIGHT	PLGF-1	VEGF121
C5a	FGF-8	IFN-Omega	LIX	Polymyxin B (PMB)	VEGF145
C5L2 Peptide	FGF-9	IGF-I	LKM	PRAS40	VEGF165
C-10	FGF-10	IGF-II	LL-37	PRL-1	VEGF-C
C-Reactive Protein	FGF-16	proIGF-II	Lymphotactin	PRL-2	VEGF-C I525
C-Src	FGF-17	IGFBP-1	sLYVE-1	PRL-3	EG-VEGF
Calbindin D-9K	FGF-18	IGFBP-2	M-CSF	Prokineticin-2	VEGF-E
Calbindin D-28K	FGF-19	IGFBP-3	MCP-1 (MCAF)	Prolactin	HB-VEGF-E
Calbindin D-29K	FGF-20	IGFBP-4	MCP-2	Protirelin	sVEGFR-1
Calmodulin	sFGFR-1 (IIIc) / Fc Chimera	IGFBP-4	MCP-3	PTHrP	sVEGFR-2
Calcitonin Acetate	sFGFR-2 (IIIc) / Fc Chimera	IGFBP-5	MCP-4	PTP1B	sVEGFR-3
Carbonic Anhydrase III	sFGFR-3 / Fc Chimera	IGFBP-6	MCP-5	PTP-IA2	WISP-1
Carcino-embryonic Antigen	sFGFR-4 / Fc Chimera	IGFBP-7	MDC (67 a.a.)	PTP-MEG2	WISP-2
Cardiotrophin-1	sFlt-1 (native)	IL-1 $\alpha$	MDC (69 a.a.)	PTP-PEST	WISP-3
		IL-1 $\beta$	MDH		WNT-1



# Personal Flow Cytometry from BD Biosciences

BD Pharmingen™ reagents and BD Accuri™ C6



Best-in-class meets  
best time to buy.



**10% OFF**



**40% OFF**

Now you can speed discovery with the power of multiparameter cell analysis using the best-in-class BD Accuri™ C6 personal flow cytometer. Never before have the power and insight of personal flow cytometry been more within reach. Today, you can take advantage of an unprecedented value package including 10% savings on the BD Accuri C6 and 40% savings on the high quality BD reagents you'll use with it for a full two years.

With this package, you get 4-color cell analysis in an affordable, transportable, and easy-to-use

format that serves both novice and experienced researchers well, right from the benchtop.

The software's intuitive interface guides you through workflows, making it easy to begin collecting and analyzing data—even if you have little flow cytometry know-how. Setup and maintenance are also simplified to increase availability and up-time.

Take advantage of this value package today at [bdbiosciences.com/go/accuri](http://bdbiosciences.com/go/accuri).

***Flow cytometry within reach.™***



Helping all people  
live healthy lives

Some limitations apply. Visit [bdbiosciences.com/go/accuri](http://bdbiosciences.com/go/accuri) for more information.  
BD flow cytometers are Class 1 Laser Products. For Research Use Only. Not for use in diagnostic or therapeutic procedures.  
BD, BD Logo and all other trademarks are property of Becton, Dickinson and Company. © 2012 BD  
23-14402-00

**BD Biosciences**  
2350 Qume Drive  
San Jose, CA 95131  
[bdbiosciences.com](http://bdbiosciences.com)

LOCATION: Jackson Park Health Club  
ARTICLE: *An Electronic Second Skin*  
DATE: Sep 21, 7:43am

LOCATION: University Faculty Lounge  
ARTICLE: *The Visual Impact of Gossip*  
DATE: Sep 21, 4:22pm

LOCATION: Gyro King  
ARTICLE: *Cavemen Craved Carbs, Too*  
DATE: Sep 21, 1:13pm

LOCATION: Hemlock Bar  
ARTICLE: *Quantum Simulation of Frustrated Classical Magnetism in Triangular Optical Lattices*  
DATE: Sep 21, 9:21pm

LOCATION: Bed  
ARTICLE: *Consciousness: What, How and Why*  
DATE: Sep 21, 10:56pm



## A new way to look at science

The new *Science* Reader app for iPad® from AAAS puts *Science* in your hands, wherever you go. Read abstracts, career advice, and highlights from our newest journals, *Science Signaling* and *Science Translational Medicine*. Plus, AAAS members can access full text articles from *Science*. Visit [iTunes App Store<sup>SM</sup>](#) or [content.aaas.org/ipad](http://content.aaas.org/ipad) for details.





## New Products



### DUCTLESS CHEMICAL FUME HOODS

Aura ductless fume hoods provide state-of-the-art construction and safety features. Each Aura ductless fume hood has advanced safety monitoring and controls. EverSafe II microprocessor safety controller monitors and adjusts fume hood face velocity to the user preset value. EverSafe II, not guesswork, keeps the Aura face velocity ideal for containment of potentially toxic gases and vapors. Aura has been ASHRAE 110 tested and provides unsurpassed containment from toxic fumes and vapors. Breathe easier knowing EverSafe II is working for your safety. Filtrak positive filter sealing system is installed in each Aura ductless hood. This cam-driven filter sealing system has a built-in filter position indicator and alerts the end user if the filtration bed is not properly sealed. Filtrak provides safe and easy filter maintenance and replacement. Aura ductless fume hoods are available in 30, 42, and 54 inch widths. ESD models are available for applications involving volatile chemicals.

**Mystaire**

For info: 877-328-3912 | [www.mystaire.com](http://www.mystaire.com)

### WIDEPORE UHPLC COLUMNS

The new SecurityGuard ULTRA system protects widepore ( $\geq 200$  Å) UHPLC columns typically used in the analysis of biomolecules. The SecurityGuard ULTRA system dramatically extends the lifetime of columns packed with sub-2 micron fully porous or core-shell particles by protecting against the damaging effects of chemical contaminants and microparticulates introduced by the sample, mobile phase, or system. These contaminants can also affect method sensitivity, quantitation, and peak identification. The new SecurityGuard ULTRA product is ideal for virtually any manufacturer's UHPLC, sub-2 micron, or core-shell widepore columns including the Phenomenex Aeris widepore XB-C18, XB-C8, and C4 products. By reducing the frequency of column replacements, as well as the need for troubleshooting and system down time, SecurityGuard ULTRA saves chromatographers time and money. Pressure-rated up to 20,000 psi (1,378 bar), these widepore guard cartridges have no significant impact on chromatography, backpressure, or dead volume.

**Phenomenex**

For info: 310-212-0555 | [www.phenomenex.com](http://www.phenomenex.com)

### FISH PROBES

Agilent SureFISH probes are the next generation of tools for fluorescent in situ hybridization (FISH) assays, delivering a comprehensive menu of the industry's highest resolution probes for a wide range of molecular analysis applications. Agilent SureFISH probes deliver dramatically better performance compared to existing FISH products. SureFISH probes enable users to specifically detect aberrations in regions of the genome as small as 50 kb as well as aberrations near highly repetitive regions. They provide higher resolution and faster hybridization times than competing technologies and are designed to enable users to meet American College of Medical Genetics guidelines for clinical cytogenetics. Agilent offers an extensive menu of FISH probes for constitutional and cancer applications. The initial menu includes hundreds of SureFISH probes for the most common regions, to accommodate a wide range of cytogenetic research needs.

**Agilent Technologies**

For info: 800-227-9770 | [www.agilent.com/genomics/SureFISH](http://www.agilent.com/genomics/SureFISH)

### MAGNETIC STIRRER

The Tornado Plus System is the ideal synthesis solution for stirring both viscous samples and for the dispersion of delicate solids in solution where conventional magnetic stirring is not suitable. Tornado Plus allows scientists to use a single overhead stirrer to simultaneously deliver high-torque mechanical stirring to six round-bottom flasks from 50 to 250 mL. Tornado also provides controlled heating and cooling from  $-65^{\circ}\text{C}$  to  $+180^{\circ}\text{C}$ , making it ideal for applications such as crystallization studies, process optimization, polymer research, or the synthesis of building blocks. Tornado features a unique PEEK 'pinch-grip' stirrer guide mechanism which allows rapid, tool-free exchange of stirrer shafts and operation under an inert atmosphere. Choose from centrifugal, anchor, or propeller style PTFE stirrers, which are matched to each flask size. Tornado accepts a range of round bottom flasks from 50 to 250 mL, including flasks with one or two sidearms, internal baffles, and special azeotropic flask options.

**Radleys**

For info: +44-(0)-1799-513320 | [www.radleys.com](http://www.radleys.com)

### MINI STIRRER

The new SM5 Mini Stirrer packs the power to stir volumes up to 1 L and even offers a choice of three stylish fascia designs. This versatile and economical magnetic stirrer is very simple to operate, providing stirring speeds of 350 to 2,000 rpm. The SM5 is lightweight yet strong, constructed from polypropylene with a chemically resistant polycarbonate top. The SM5 is the smallest in the company's comprehensive range of magnetic stirrers. A robust casing incorporates silver-based BioCote antimicrobial protection for enhanced safety. The power to mix an impressive 1 L at adjustable speeds makes the SM5 an attractive option for any lab. The new Mini Stirrer has fun twist with a choice of three different fascia designs: blue with the Stuart logo, a Bibby Scientific image, or an abstract blue swirl.

**Bibby Scientific**

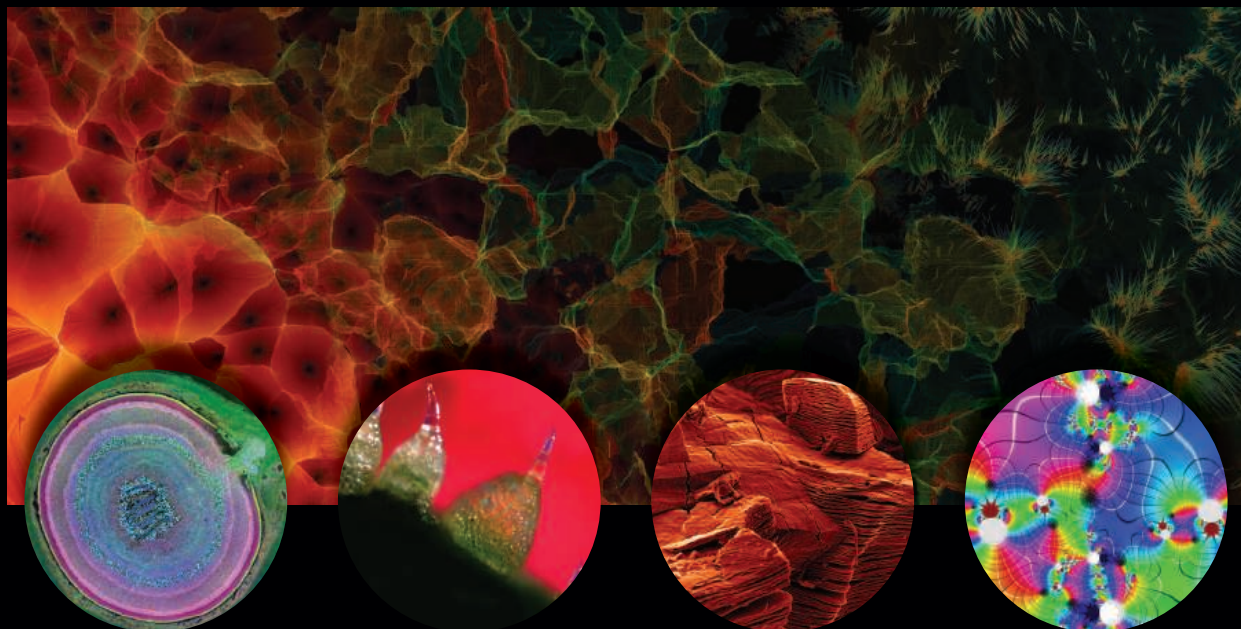
For info: +44-(0)-1785-812121 | [www.bibby-scientific.com](http://www.bibby-scientific.com)

Electronically submit your new product description or product literature information! Go to [www.sciencemag.org/products/newproducts.dtl](http://www.sciencemag.org/products/newproducts.dtl) for more information.

Newly offered instrumentation, apparatus, and laboratory materials of interest to researchers in all disciplines in academic, industrial, and governmental organizations are featured in this space. Emphasis is given to purpose, chief characteristics, and availability of products and materials. Endorsement by *Science* or AAAS of any products or materials mentioned is not implied. Additional information may be obtained from the manufacturer or supplier.

INTERNATIONAL SCIENCE & ENGINEERING  
VISUALIZATION CHALLENGE

# CALL FOR ENTRIES



ENTRY DEADLINE: SEPTEMBER 28, 2012

SCIENCE AND ENGINEERING'S MOST POWERFUL STATEMENTS  
ARE NOT MADE FROM WORDS ALONE

Visualization in all its forms has the power to illuminate and educate. It explains and makes clear all aspects of the world around us. It feeds insight and provokes curiosity.

The National Science Foundation (NSF) and the journal *Science*, published by the American Association for the Advancement of Science, invite you to participate in this year's Challenge. The competition recognizes scientists, engineers, visualization specialists, and artists who produce innovative work in visual communication.

Winning entries will be published in *Science* and *Science Online*, and will be displayed on the NSF web site.

## Award Categories

- Photography
- Illustrations
- Informational Posters and Graphics
- Videos
- Interactive Video Games

COMPLETE ENTRY INFORMATION:  
[WWW.NSF.GOV/NEWS/SCIVIS](http://WWW.NSF.GOV/NEWS/SCIVIS)





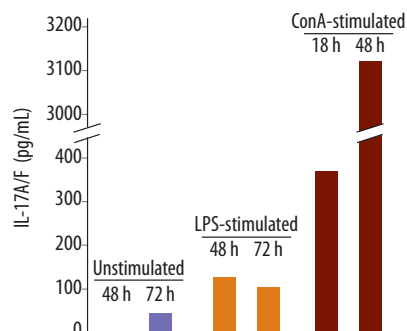
# Quantikine® ELISA Kits

## Setting the Standard for the Life Science Industry

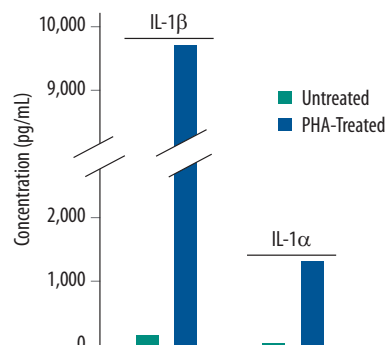
R&D Systems has over 25 years of experience developing and manufacturing products for cytokine research and today we offer **the most referenced selection of ELISA kits in the industry**. Our Quantikine ELISA Kits are designed to provide the highest levels of specificity, accuracy, and sensitivity in analyte quantification. For each kit we develop, we take every step possible to ensure that it will provide customers with reliable, consistent results without the need for further assay optimization. These standards have made Quantikine Kits the top choice of life science researchers.

- More than 300 complete, ready-to-run Quantikine ELISA Kits are currently available
- Each Quantikine ELISA measures a specific protein in a designated set of complex sample types utilizing two highly specific antibodies
- During development, each kit undergoes rigorous testing to ensure optimal assay performance

Measurement of IL-17A/F in Mouse Spleen Cell Culture Supernates using the Mouse IL-17A/F Heterodimer Quantikine ELISA Kit



Measurement of IL-1 $\beta$  and IL-1 $\alpha$  in Supernates from Human PBMCs using the Human IL-1 $\alpha$  Quantikine or the IL-1 $\beta$  QuantiGlo ELISA Kit



For more information, please visit our website at  
[www.RnDSystems.com/ELISAQuality](http://www.RnDSystems.com/ELISAQuality)

For research use only. Not for use in diagnostic procedures.

R&D Systems, Inc. [www.RnDSystems.com](http://www.RnDSystems.com)

R&D Systems Europe, Ltd. [www.RnDSystems.com](http://www.RnDSystems.com)

R&D Systems China Co., Ltd. [www.RnDSystemsChina.com.cn](http://www.RnDSystemsChina.com.cn)

**R&D**  
SYSTEMS®

There's only one

**Science**



## Science Careers Advertising

For full advertising details, go to [ScienceCareers.org](http://ScienceCareers.org) and click For Employers, or call one of our representatives.

### Tracy Holmes

Worldwide Associate Director  
Science Careers  
Phone: +44 (0) 1223 326525

### UNITED STATES & CANADA

E-mail: [advertise@sciencecareers.org](mailto:advertise@sciencecareers.org)  
Fax: 202-289-6742

### Tina Burks

United States/Canada/  
South America  
Phone: 202-326-6577

### Marci Gallun

Sales Administrator  
Phone: 202-326-6582

### Online Job Posting Questions

Phone: 202-312-6375

### EUROPE & REST OF WORLD

E-mail: [ads@science-int.co.uk](mailto:ads@science-int.co.uk)  
Fax: +44 (0) 1223 326532

### Simone Jux

Phone: +44 (0)1223 326529

### Lucy Nelson

Phone: +44 (0)1223 326527

### Kelly Grace

Phone: +44 (0) 1223 326528

### JAPAN

#### Yuri Kobayashi

Phone: +81-50-3696-5100  
E-mail: [ykobayas@aaas.org](mailto:ykobayas@aaas.org)

### CHINA & TAIWAN

#### Ruolei Wu

Phone: +86-1367-1015-294  
E-mail: [rwu@aaas.org](mailto:rwu@aaas.org)

All ads submitted for publication must comply with applicable U.S. and non-U.S. laws. *Science* reserves the right to refuse any advertisement at its sole discretion for any reason, including without limitation for offensive language or inappropriate content, and all advertising is subject to publisher approval. *Science* encourages our readers to alert us to any ads that they feel may be discriminatory or offensive.

**Science Careers**

From the journal *Science*



## Professor and Director

### Tata – Cornell Agriculture and Nutrition Institute (TACO-AN)

*Cornell is a community of scholars, known for intellectual rigor and engaged in deep and broad research, teaching tomorrow's thought leaders to think otherwise, care for others, and create and disseminate knowledge with a public purpose.*

Cornell University invites applications for a tenure-able Full Professor with responsibility for establishing a long-term research and education institute supported by an endowment designed to help reduce poverty and malnutrition in rural India. The founding director will conduct research and lead a multidisciplinary research and training program focused on the design and evaluation of innovative interventions that link agriculture, food systems and human nutrition, including the impacts of nutrition and agriculture policies on poverty and nutritional status. The goal of the institute is to enhance individual and institutional capacity in the areas of agriculture, nutrition and rural development. The institute will support multidisciplinary action research and educational programs conducted by collaborative teams from Indian universities, government and non-governmental organizations, and Cornell.

**Duties and Responsibilities:** The TACO-AN Director will be an internationally recognized expert who will lead and direct this India-based research and education program. The director will develop a comprehensive framework and strategic plan, establish program priorities and directions, and be responsible for program implementation. The director is expected to provide engagement opportunities for Cornell faculty and Indian colleagues from several disciplines through the administration and selection of projects for funding. S/he is expected to seek synergistic linkages with proposed or on-going projects of other organizations that are consistent with the TACO-AN program objectives, and to engage broadly with the Cornell University community. The director of this university-wide institute will report to the Dean of the College of Agriculture and Life Sciences who represents the Provost and other college deans. An established international advisory board will advise the director regarding program development. The donor and the President of Cornell University provide ultimate programmatic and financial oversight for the endowment. In academic matters related to his/her position as a tenured faculty member, the professor will report to his/her department chair.

The TACO-AN Director will be a faculty member based in Ithaca, NY at Cornell University appointed in either the College of Agriculture and Life Sciences or the College of Human Ecology. The appointment will be in an appropriate academic department depending on the interests and expertise of the successful applicant. The director is expected to work closely with an India-based associate director to identify appropriate research problems in India, develop collaborative partnerships and funding opportunities, support Cornell research activities, network with Indian educational and development partners, and facilitate communications with program collaborators and beneficiaries in India.

The successful candidate will devote half of his/her time to research and 50% effort to TACO-AN administration, which includes mentoring, teaching and advising students involved in the program, as well as program leadership. In addition to responsibility for financial and programmatic management, the director will be expected to leverage the endowment's funds by obtaining external research and training funding. Program management responsibilities will include: 1) managing the TACO-AN competitive grants program designed to bring new faculty and students into the program, and 2) monitoring and evaluation of TACO-AN program components. Because TACO-AN offers the opportunity to do long term longitudinal research, the director is expected to anticipate and plan new activities and programmatic themes as appropriate. The director will be expected to promote the TACO-AN program within and through Cornell. In addition, it is expected that the appointee will devote half of his/her time to research on agriculture, food and nutrition using a systems approach.

**Qualifications:** Candidates for the Director are expected to have a strong background and expertise in agriculture and food systems, population health, and nutrition in resource limited settings and a PhD, MD, DVM or equivalent degree. International experience is required and experience in India is desirable.

**Application procedure:** Submit electronically a letter of application, curriculum vitae, selected reprints, statement of research goals and plans, and names and addresses of three references to Renee Hoffman at [rmh6@cornell.edu](mailto:rmh6@cornell.edu).

Review of applications will begin September 1, 2012 and will continue until the position is filled.

Find us online at <http://hr.cornell.edu/jobs> or [Facebook.com/CornellCareers](https://www.facebook.com/CornellCareers)



*Diversity and inclusion have been and continue to be a part of our heritage.  
Cornell University is a recognized EEO/AA employer and educator.*



## Tenure Track Assistant Professor Department of Earth and Atmospheric Sciences

College of Agriculture & Life Sciences (CALS) – Cornell University – Ithaca, NY

*Cornell is a community of scholars, known for intellectual rigor and engaged in deep and broad research, teaching tomorrow's thought leaders to think otherwise, care for others, and create and disseminate knowledge with a public purpose.*

The Department of Earth and Atmospheric Sciences (EAS) at Cornell University invites applications for an Assistant Professor in the subject area of extreme weather during climate change. The successful candidate will develop a high quality research program investigating the multi-scale processes linking climate to extreme weather phenomena, such as thunderstorms, tornadoes, tropical and extra-tropical cyclones, flooding, and droughts, and their impacts. The incumbent could take an Earth system approach to the subject, emphasizing the interactions of atmospheric, oceanic and land-surface processes in the climate system, including future climate change scenarios. The incumbent will also be a committed educator, enthusiastically teaching undergraduate and graduate courses, advising undergraduate and graduate students, and supervising students at all levels in research. The ideal candidate will be able to interact in teaching and research with colleagues having similar interests at Cornell University, particularly in the Colleges of Engineering and of Agriculture and Life Sciences, in which the Department of EAS is jointly located. The responsibilities of the position will be split between research (50%) and teaching (50%).

**Qualifications Required:** A Ph.D. in atmospheric science, Earth system science, or a related science or engineering discipline.

**Salary/Benefits:** Salary is commensurate with qualifications and experience. Cornell University provides an attractive fringe benefits package.

Please submit applications to: [extreme-weather-search@cornell.edu](mailto:extreme-weather-search@cornell.edu) as a single PDF (15 mb maximum) that includes (1) a cover letter addressed to the Search Committee Chair, Professor Stephen Colucci, and providing the names and contact information for three individuals who are willing to write letters of recommendation; (2) a curriculum vitae; (3) a research plan; and (4) a statement of teaching interests.

Applications will be reviewed beginning September 4, 2012. The position will remain open until filled, with an anticipated start in Fall 2013.

*College of Agriculture and Life Sciences  
Developing Leaders. Improving Lives. Shaping the Future.*

Find us online at <http://hr.cornell.edu/jobs> or  
[Facebook.com/CornellCareers](https://www.facebook.com/CornellCareers)



*Diversity and inclusion have been and continue to be a part of our heritage.  
Cornell University is a recognized EEO/AA employer and educator.*

## THE UNIVERSITY OF KANSAS

### ASSISTANT PROFESSOR OF PHARMACOLOGY/TOXICOLOGY

Applications are invited for a tenure track position at the level of Assistant Professor in Pharmacology and Toxicology at the University of Kansas, School of Pharmacy. The Pharmacy School at the University of Kansas has a strong history of competitive research and ranks second nationally in total NIH funding. Candidates must hold a Ph.D., M.D., or equivalent degree and have at least three years of postdoctoral research experience. Candidates should demonstrate a strong potential to develop/maintain an externally funded research program in pharmacology or toxicology. Individuals with research expertise in drug metabolism and disposition, or translational aspects of neurodegeneration and regeneration related to Alzheimer's disease, diabetes, or traumatic brain injury are especially sought. Prospective faculty are also expected to actively participate in teaching in the graduate and professional pharmacy programs of the department. To aid faculty research, core facilities exist for proteomics, DNA microarray analyses, molecular modeling, high-throughput screening, peptide synthesis, quantitative bio-behavioral assessments and confocal/electron microscopy. The University of Kansas is especially interested in hiring faculty members who can contribute to four key campus-wide strategic initiatives: (1) Sustaining the Planet, Powering the World; (2) Promoting Well-Being, Finding Cures; (3) Building Communities, Expanding Opportunities; and (4) Harnessing Information, Multiplying Knowledge. See <http://www.provost.ku.edu/planning/themes/> for more information. To apply go to <http://www.ku.edu/employment/> under faculty searches and look for position #00209874. Additionally, three letters of recommendation should be emailed to Dr. Rick Dobrowsky at [dobrowsky@ku.edu](mailto:dobrowsky@ku.edu). Review of applications begins August 1, 2012. Position will remain opened until filled.

*Under-represented minorities and women are encouraged to apply. University of Kansas prohibits discrimination on the basis of race, color, ethnicity, religion, sex, national origin, age, ancestry, disability, status as a veteran, sexual orientation, marital status, parental status, gender identity, gender expression and genetic information in the University's programs and activities. The following person has been designated to handle inquiries regarding the non-discrimination policies: Director of the Office of Institutional Opportunity and Access, IOA@ku.edu, 1246 W. Campus Road, Room 153A, Lawrence, KS, 66045, (785)864-6414, 711 TTY.*



JOHNS HOPKINS  
MEDICINE

### Urology Director of Research The Brady Urological Institute

We seek an individual with a strong background in urologic research and a track record of collaborative interactions, successful funding, program development and a desire to mentor residents, fellows, medical students, and graduate students. Candidates must also have demonstrated focus on translational research in urology.

Please forward letters of application, with curriculum vitae to:  
Search Committee

Attention: Beverly Comegys ([bcomegys@jhmi.edu](mailto:bcomegys@jhmi.edu))  
James Buchanan Brady Urological Institute  
The Johns Hopkins Hospital  
600 North Wolfe Street  
Marburg 105  
Baltimore, MD 21287

*The Johns Hopkins University is an Equal Opportunity Employer and does not discriminate based on race, color, gender, religion, age, sexual orientation, national or ethnic origin, disability, marital status, veteran status, or any other occupationally irrelevant criteria. The University promotes affirmative action for minorities, women, disabled persons, and veterans. The Johns Hopkins University is a smoke-free environment and as such, prohibits smoking in all facilities. The Johns Hopkins University is a drug-free workplace.*

# What type of mark will you make?



## Janssen Research & Development

The Biotechnology Center of Excellence (CoE) within Janssen Research & Development, LLC, discovers and develops some of the most innovative technology platforms and biologic medicines today. We are a world leader in monoclonal antibody technology and have a strong pipeline of novel antibodies in development.

Promising areas of focus for the Janssen R&D Biotechnology CoE include antibody engineering/analysis, alternative scaffolds, and therapeutic peptides.

We are looking for scientists from around the globe with a driven, passionate, and pioneering spirit to join our team in Spring House, PA, and La Jolla, CA.

This is an outstanding opportunity to make a difference in the lives of people living with chronic diseases through cutting-edge research and development.

We are recruiting scientific leaders with BS, MS, and/or PhD degrees and expertise in the following specialties:

- Molecular Biology
- Protein Biochemistry
- Antibody Engineering
- Cell Biology
- Phage Display
- MS Analysis of Proteins
- Assay Biology
- Biologics Toxicology
- Biologics Clinical Pharmacology
- Pharmacokinetics/ Pharmacodynamics
- Cell Therapy



**BE VITAL**  
[careers.jnj.com](http://careers.jnj.com)

For more information about these positions, please send your CV and/or cover letter inquiry by e-mail to [aarmstr1@its.jnj.com](mailto:aarmstr1@its.jnj.com).





## VICTORIA UNIVERSITY OF WELLINGTON

Victoria University delivers internationally-acclaimed results in teaching and research, as well as programmes of national significance and international quality.

As one of Wellington's largest and most established employers, we're committed to providing our staff with opportunities for rewards, recognition and development, all within a dynamic and inclusive culture where innovation and diversity are highly valued.

### ASSOCIATE PROFESSOR/PROFESSOR IN FISHERIES SCIENCE

#### School of Biological Sciences

We seek a Senior Fisheries Biologist, with a strong track record in internationally recognised research, with significant experience in both securing and leading externally-funded research programs together with experience in teaching and supervision of students.

The successful candidate will be expected to promote Victoria University of Wellington as a leading provider of fisheries research, by advancing national and international research networks and leading School activities in outreach programmes in fisheries biology. The successful applicant will be expected to work with government research agencies, and New Zealand or international fishing industry research organisations.

We are seeking a Fisheries Biologist and would welcome applications from specialists in a wide range of fields, including stock assessment, population modelling, or resource sustainability. Experience of academic leadership is expected for all professorial candidates.

For further information contact Associate Professor Phil Lester, phil.lester@vuw.ac.nz

**Applications close 6th August 2012**

Victoria University of Wellington is an EEO employer and actively seeks to meet its obligations under the Treaty of Waitangi.

For more information and to apply online visit <http://vacancies.vuw.ac.nz>

**Reference A177-12Q**



Maine Medical Center Research Institute (MMCRI) is a leading NIH-funded biomedical research institute and division of Maine Medical Center, a major academic affiliate of Tufts University School of Medicine.

## FACULTY POSITIONS AT MMCRI MAINE MEDICAL CENTER RESEARCH INSTITUTE Portland, Maine

Applications are invited for faculty positions at all levels (Assistant, Associate and Full Professor equivalent) in the Center for Molecular Medicine.

Candidates should complement existing strengths in the areas of stem cell biology, vascular and cardiovascular biology, metabolism, bone biology, cancer, and basic and translational studies of human disease. Applicants must have an MD and/or PhD degree or equivalent. Physician-scientists are encouraged to apply. Candidates for senior-level positions should have an independently funded research program. Applications are strongly encouraged from those seeking a highly supportive, collegial and collaborative environment.

Positions include competitive start-up/transition packages, and opportunities for faculty appointments at Tufts University School of Medicine and the University of Maine. MMCRI maintains core facilities in flow cytometry/FACS, mouse transgenic technologies, proteomics, bioinformatics support, confocal microscopy, metabolic phenotyping, small animal in vivo imaging including microCT and MRI, and translational and clinical research. Salary, benefits, and resources are nationally competitive.

MMCRI is an expanding biomedical research institute on the scenic southern coast of Maine. The greater Portland area features a high quality of life with outstanding recreational and cultural opportunities.

Candidates should provide a CV, brief statement of research interests, and contact information for three professional references to Tom Gridley PhD, Chair, Faculty Recruiting Committee ([gridlt@mmc.org](mailto:gridlt@mmc.org)). Learn more about us at [www.mmc.org](http://www.mmc.org).

We are an Equal Opportunity Employer.



**Science Careers**

*There's only one  
GALILEO GALILEI*

For your career in science,  
there's only one



**Science**

**ScienceCareers.org**

Career advice | Job postings | Job Alerts | Career Forum  
Crafting resumes/CVs | Preparing for interviews



Science For A Better Life

HealthCare

[www.myBayerjob.com](http://www.myBayerjob.com)

**Lucia Rosano** wants to make the world a better place - for everyone. As a bioscientist at Bayer, Lucia knows she is doing just that. Searching for solutions and never giving up. That is the passion that unites all of us at Bayer. We call it the Bayer Spirit. If you feel it, too, then it is high time we had a chance to talk about a career at Bayer.

## Postdoc within the IMI EU consortium PREDECT

Bayer Pharma AG, Berlin, Germany

PREDECT is a unique European IMI-funded partnership between academic and industrial partners, aiming to develop novel, advanced, complex in vitro and in vivo models for breast, prostate and lung cancers that represent, with better fidelity, the complexity of a human tumor in situ and should lead to greater predictivity of clinical efficacy.

**Job description** Bayer Pharma AG participates in PREDECT with a focus on the development and evaluation of improved in vivo and in vitro / ex vivo models for breast cancer research. Within this project there is a unique opportunity for a postdoctoral fellow to work at a cutting-edge public private interphase. Based on existing xenograft and syngeneic tumor models tissue slice culture technology and complex spheroid co-culture systems using tumor and stromal cells will be established and applied to novel GEMMs in close collaboration with other consortium members. The aim of the project is an in depth characterization of the above mentioned models and evaluation of their predictivity including the analysis of cellular and molecular responses to genetic perturbations or to targeted therapeutics. As postdoctoral fellow, you will be responsible for project planning, design and set-up of experiments, analysis and reporting and actively participating in PREDECT meetings in close collaboration with the principal investigator and consortium collaborators.

**Your qualifications** You hold a PhD in the field of molecular biology, cell biology, cancer biology, or biochemistry and have a demonstrated track record of innovative scientific publications. You have already gained expertise in in vitro and in vivo cancer models as well as a sound knowledge of cellular signaling pathways. You show ambition, commitment and effective communication skills and act as a teamplayer. To excel in an international environment, a very good command of spoken and written English is essential.

**Your application** We offer a postdoc position initially for two years with the possibility of an extension for a 3rd year. Initial training will be provided at the University of Helsinki and other PREDECT consortium members as appropriate. Applications for this position should be made online (Reference Code 0000038022) at [www.myBayerjob.de](http://www.myBayerjob.de), submitting a letter of motivation, CV and contact information of 2-3 references. Please contact Dr. Sylvia Gruenewald for further information (email: [sylvia.gruenewald@bayer.com](mailto:sylvia.gruenewald@bayer.com)).

[www.myBayerjob.de](http://www.myBayerjob.de)

Fon +49 214 30 9 97 79



## UT SOUTHWESTERN MEDICAL CENTER



### Faculty Opening for Division Chief July, 2012

The Department of Radiation Oncology at UT Southwestern Medical Center seeks an exceptional senior scientist to head the department's division of Molecular Radiation Biology. Applicants must have a Ph.D. or M.D./Ph.D. and a vigorous and ambitious independent research program in an area of cancer biology that is related to radiation oncology, as well as grant funding and a significant record of peer-reviewed publication. The program should complement and expand existing research strengths within the division, which includes molecular oncology, cell signaling, hypoxia and the DNA damage response. Candidates should have a successful record as the manager of a productive research team and an enthusiasm for promoting collaboration within a multidisciplinary environment.

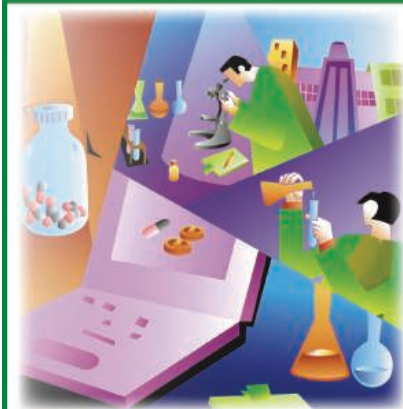
The Division of Molecular Radiation Biology currently has 60 employees, including seven senior Ph.D. investigators and three M.D./Ph.D. translational researchers as well as other junior research faculty, postdoc and graduate student trainees, and lab technicians. There is also significant dedicated administrative support staff. The division has approximately 10,000 square feet of contiguous lab space, including 6 large labs and core space for tissue culture, microscopy, and other shared resources.

The appointment will be at the level of Professor, with tenure (contingent upon approval by the institutional promotion and tenure committee). A generous start up package will include substantial lab space and funding for equipment or faculty/staff/trainees. Of particular note, the Cancer Prevention and Research Institute of Texas (CPRIT) has awarded over \$106 million in grants to investigators at UT Southwestern, including funding opportunities for recruitment of pre-eminent cancer investigators.

Applicants should email their curriculum vitae, the names of three references, and a brief description of their research goals to the attention of **Dr. Hak Choy** at [Hak.Choi@utsouthwestern.edu](mailto:Hak.Choi@utsouthwestern.edu).

*UT Southwestern is an Equal Opportunity Employer.*

## CAREER TRENDS Running Your Lab



Download your free copy today at  
[ScienceCareers.org/booklets](http://ScienceCareers.org/booklets)

**Science Careers**

From the journal *Science* AAAS

Brought to you by the  
AAAS/Science Business Office

## UCRIVERSIDE UNIVERSITY OF CALIFORNIA

### COOPERATIVE EXTENSION WEED SCIENCE SPECIALIST

The Department of Botany and Plant Sciences invites applications for an Assistant Cooperative Extension Weed Specialist (11-month tenure-track, 90% CE, 10% OR). The Weed Specialist will work with Farm Advisors, other Extension Specialists, faculty, land managers and the industry to conduct research on biology of weedy and invasive plants and their interactions with managed ecosystems, focusing on urban systems. Research could address potential invasiveness of ornamental or biofuel crops; environmental issues associated with herbicide use and other weed control practices; development of integrated weed management practices in nurseries, floriculture, and landscapes; and impacts of weeds and weed management in the urban-agriculture and urban-wildland interfaces. Outreach will center on UC Farm Advisors and clientele who focus on managed ecosystems including urban systems and landscapes, horticulture and floriculture.

The successful applicant is expected to develop a nationally competitive research program and obtain extramural grant funds. Preference will be given to candidates conducting research at the forefront of their field and having a strong working knowledge of weed ecology and control and a desire and ability to work with diverse clientele.

The position will be available October 1, 2012. Applicants must hold a Ph.D. in Plant Science, Ecology, Range Science, Horticulture, Plant Physiology or related fields. Evaluation of applications will begin **August 15, 2012** and continue until the position is filled. Interested individuals should submit (1) a curriculum vitae, (2) a statement of research and extension interests, and 3) have three letters of recommendation sent to: **Chair, Cooperative Extension Specialist Search Committee, c/o Department of Botany and Plant Sciences, 2118 Batchelor Hall, University of California, Riverside, CA 92521-0124; E-mail: [bpscercruit@ucr.edu](mailto:bpscercruit@ucr.edu); FAX: (951) 827-4437.** For additional information on the Department and the campus visit <http://cnas.ucr.edu/> and <http://www.plantbiology.ucr.edu/>.

*UCR has an active career partner program, and is an Affirmative Action Equal Opportunity Employer committed to excellence through diversity.*



**Texas Children's  
Cancer Center**

**BCM**  
Baylor College of Medicine

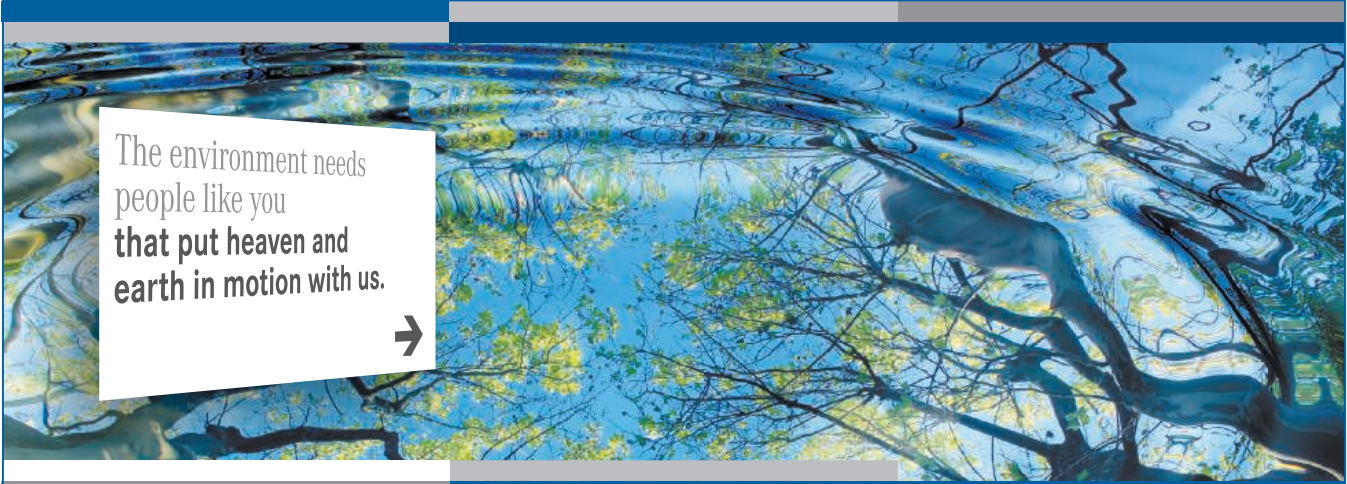
### Center for Personal Cancer Genomics and Therapeutics Faculty Search

We are seeking full time research faculty at all academic levels for the newly formed **Center for Personal Cancer Genomics and Therapeutics** designed to exploit the latest in genome-scale technology to better understand childhood cancer and identify novel targets to improve therapy and outcomes. The Texas Children's Cancer Center is the largest children's cancer center in the US, with over \$21 million annually in federal funding. Candidates with research programs that foster development of new bioinformatics tools, innovative mouse models of cancer or use of model organisms and tissue culture models to carry out functional analyses of large-scale datasets, are encouraged to apply. Previous research experience, including a relevant publication record and history of successful peer-reviewed grant funding, are important. Salary and start-up package will be commensurate with qualifications and prior experience.

Interested candidates should submit curriculum vitae, a summary of past work, a brief research plan, and the names of at least three references. Applications will be accepted until the positions are filled and should be submitted to **Sharon Plon, MD, PhD** by e-mail at [splon@bcm.edu](mailto:splon@bcm.edu).

*Baylor College of Medicine is an Equal Opportunity/Affirmative Action/Equal Access Employer.*

[www.txch.org](http://www.txch.org)



The environment needs  
people like you  
that put heaven and  
earth in motion with us.



## We are recruiting **50 doctoral and post-doctoral candidates** to create new knowledge with us.

You want to investigate major challenges of our society? This requires the best career environment right from the beginning: outstanding education, inspiring science locations and exceptional equipment and infrastructure. The **Helmholtz Centre for Environmental Research – UFZ** offers exciting research topics, excellent supervision, solid structures, interdisciplinary team work and tailored qualification at the UFZ Graduate School HIGRADE – the best conditions to start a successful career.

Join us in addressing the most pressing societal and scientific challenges across ten large integrated projects (IP) in research areas like land use, biological diversity, water, soil, chemicals, health and energy. Find solutions to better understand and manage complex environmental systems together with more than 1,000 competent colleagues at the UFZ. Seek with us after a balance between social development and long-term protection of our livelihoods. Do research for the environment!

### The ten Integrated Projects (IP) are:

- IP 1 Mitigating of land use conflicts
- IP 2 Emerging ecosystems: functional dynamics under global change
- IP 3 Land use aspects of transforming the energy system
- IP 4 Urban transformations
- IP 5 Healthy aquatic ecosystems
- IP 6 Water and solute fluxes in catchments
- IP 7 Water scarcity – Water management in semi-arid regions
- IP 8 Exposome – Environmental pollution and its impacts on human health
- IP 9 Controlling chemicals' fate
- IP10 From local observations to regional predictions

### Interested?

You are an excellent graduate in natural, social or economic sciences? You are, e.g., biologist, hydrologist, engineer or economist with outstanding skills, knowledge and ideas? We invite you to submit an application to the Helmholtz Centre for Environmental Research – UFZ, the international centre of competence for environmental sciences and member of the largest scientific organisation in Germany, the Helmholtz Association. Come to Leipzig, Halle or Magdeburg, three modern and unique science locations with an appealing culture and flair. **Deadline: 10 August 2012**

Have a look at [www.ufz.de/docs](http://www.ufz.de/docs) to see the job offers and at [www.join.ufz.de](http://www.join.ufz.de) to get an impression of the research and life environment at the UFZ locations.

Certainly one of our offers will attract your attention!



## POSITIONS OPEN

### TENURE-TRACK POSITION in Anatomy, Physiology, and Genetics (APG) F. Edward Hebert School of Medicine Uniformed Services University of the Health Sciences

The Department of Anatomy, Physiology, and Genetics, Uniformed Services University School of Health Sciences (USUHS), Bethesda, Maryland, chaired by **Harvey B. Pollard, M.D., Ph.D.**, invites applications for a tenure-track, hard-money position at the **ASSISTANT PROFESSOR** level. The department has strong commitments to medical education and biomedical research and is located in an interactive scientific environment adjacent to the National Institutes of Health and National Library of Medicine. Outstanding core facilities are available to support medical education and biomedical research in cell biology, genomics, and proteomics. The successful applicant will have a Ph.D. and/or M.D. degree and will be expected to contribute to the Department's interdisciplinary Anatomy and Physiology curriculum for first-year medical students, and to establish an independent and extramurally funded research program. Research interest in systems biology and cell signaling is an asset. Candidates should submit curriculum vitae, an outline of their proposed research program, and have three letters of reference sent to: **Gregory P. Mueller, Ph.D., Search Committee Chair, Department APG, USUHS, 4301 Jones Bridge Road, Bethesda, M.D. 20814-4799 (e-mail: [gregory.mueller@usuhs.edu](mailto:gregory.mueller@usuhs.edu))**. Position open until filled. *USUHS is an Equal Opportunity Employer with a strong commitment to racial, cultural, and ethnic diversity.*

### FACULTY POSITIONS-MEDICAL SCHOOL

The Saint James School of Medicine, an international medical school ([website: http://www.sjsm.org](http://www.sjsm.org)), invites applications from candidates with teaching and/or research experience in any of the basic medical sciences for its Caribbean campuses.

Faculty positions are currently available in Anatomy and Pathology. Applicants must be a M.D., D.O., and/or Ph.D.

Teaching experience in the U.S. system is desirable but not required. Retired persons are encouraged to apply. Attractive salary and benefits. Submit curriculum vitae electronically to e-mail: [mjansen@mail.sjsm.org](mailto:mjansen@mail.sjsm.org) or mail to: **HRDS Inc., 1480 Renaissance Drive, Suite 300, Park Ridge, IL 60068.**

### POSTDOCTORAL POSITION/RESEARCH ASSISTANT PROFESSOR Hollings Cancer Center

The Medical University of South Carolina

An outstanding Postdoctoral/Research Assistant Professor (rank dependent upon experience) position is available with the Director of the Hollings Cancer Center (HCC), a National Cancer Institute designated Cancer Center, in Charleston, South Carolina. Working in the laboratory of **Dr. Andrew S. Kraft**, the research will focus on investigating the ability of protein kinases to control the growth and metastasis of prostate cancer using knock-out and knock-in mice, cell culture, and a novel subrenal tissue recombination assay (*Can. Res.* 72:294, 2012; *PNAS* 108:528, 2011). Experience in constructing and studying transgenic knock-in mice is essential and investigators should have a strong background in molecular and cellular biology. Senior investigators will have the opportunity to submit grant applications where appropriate.

Applicants should submit cover letter, curriculum vitae, and the names of three references via the following website: <https://www.jobs.musc.edu>; requisition number 048450.

*The Medical University of South Carolina is an Equal Opportunity Employer, promoting workplace diversity.*



## Nontraditional Careers: Opportunities Away From the Bench Webinar

Want to learn more about exciting and rewarding careers outside of academic/industrial research? View a roundtable discussion that looks at the various career options open to scientists and strategies you can use to pursue a nonresearch career.

**Now Available On Demand**  
[www.sciencecareers.org/webinar](http://www.sciencecareers.org/webinar)

Produced by the  
Science/AAAS Business Office.



# Your career is our cause.

Get help from the experts.

[www.sciencecareers.org](http://www.sciencecareers.org)

- Job Postings
- Job Alerts
- Resume/CV Database
- Career Advice
- Career Forum

**Science Careers**

From the journal *Science* AAAS

# Find your future here.



**Science Careers**

From the journal *Science* AAAS

[www.ScienceCareers.org](http://www.ScienceCareers.org)

## MARKET PLACE

Widely  
Recognized  
Original &  
Guaranteed

# KlenTaq1

8¢/u  
Truncated  
Taq DNA  
Polymerase  
Withstand 99°C

US Pat #5,436,149  
Call: **Ab Peptides**  
Fax: 314•968•8988

e-mail: [abpeps@msn.com](mailto:abpeps@msn.com)  
1•800•383•3362  
[www.abpeps.com](http://www.abpeps.com)